# FUNCTIONAL AND SMART BIOMATERIALS: DEVELOPMENT AND APPLICATION IN REGENERATIVE MEDICINE

EDITED BY: Guicai Li, Hongbo Zhang and Jingan Li

PUBLISHED IN: Frontiers in Bioengineering and Biotechnology

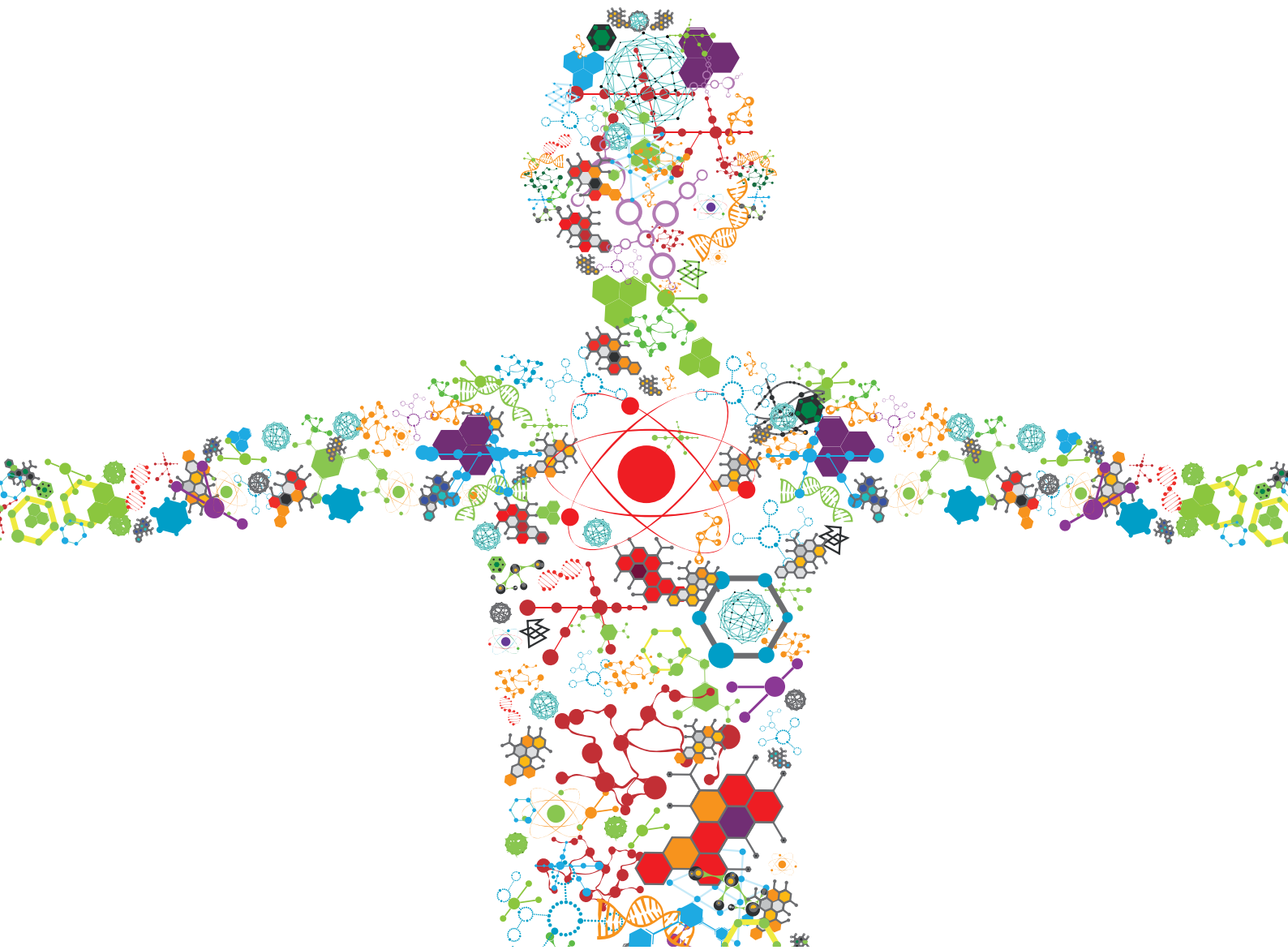

frontiers Research Topics

ISSN 1664-8714
ISBN 978-2-88976-313-9
DOI 10.3389/978-2-88976-313-9

## About Frontiers

Frontiers is more than just an open-access publisher of scholarly articles: it is a pioneering approach to the world of academia, radically improving the way scholarly research is managed. The grand vision of Frontiers is a world where all people have an equal opportunity to seek, share and generate knowledge. Frontiers provides immediate and permanent online open access to all its publications, but this alone is not enough to realize our grand goals.

## Frontiers Journal Series

The Frontiers Journal Series is a multi-tier and interdisciplinary set of open-access, online journals, promising a paradigm shift from the current review, selection and dissemination processes in academic publishing. All Frontiers journals are driven by researchers for researchers; therefore, they constitute a service to the scholarly community. At the same time, the Frontiers Journal Series operates on a revolutionary invention, the tiered publishing system, initially addressing specific communities of scholars, and gradually climbing up to broader public understanding, thus serving the interests of the lay society, too.

## Dedication to Quality

Each Frontiers article is a landmark of the highest quality, thanks to genuinely collaborative interactions between authors and review editors, who include some of the world's best academicians. Research must be certified by peers before entering a stream of knowledge that may eventually reach the public - and shape society; therefore, Frontiers only applies the most rigorous and unbiased reviews.
Frontiers revolutionizes research publishing by freely delivering the most outstanding research, evaluated with no bias from both the academic and social point of view. By applying the most advanced information technologies, Frontiers is catapulting scholarly publishing into a new generation.

## What are Frontiers Research Topics?

Frontiers Research Topics are very popular trademarks of the Frontiers Journals Series: they are collections of at least ten articles, all centered on a particular subject. With their unique mix of varied contributions from Original Research to Review Articles, Frontiers Research Topics unify the most influential researchers, the latest key findings and historical advances in a hot research area! Find out more on how to host your own Frontiers Research Topic or contribute to one as an author by contacting the Frontiers Editorial Office: frontiersin.org/about/contact

# FUNCTIONAL AND SMART BIOMATERIALS: DEVELOPMENT AND APPLICATION IN REGENERATIVE MEDICINE

Topic Editors:
**Guicai Li,** Nantong University, China
**Hongbo Zhang,** Åbo Akademi University, Finland
**Jingan Li,** Zhengzhou University, China

**Citation:** Li, G., Zhang, H., Li, J., eds. (2022). Functional and Smart Biomaterials: Development and Application in Regenerative Medicine. Lausanne: Frontiers Media SA. doi: 10.3389/978-2-88976-313-9

# Table of Contents

frontiers | Frontiers in Bioengineering and Biotechnology

EDITORIAL
published: 17 May 2022
doi: 10.3389/fbioe.2022.920730

# Editorial: Functional and Smart Biomaterials: Development and Application in Regenerative Medicine

*Guicai Li*[1]* *and Hongbo Zhang*[2,3]*

[1]Key Laboratory of Neuroregeneration of Jiangsu and Ministry of Education, Co-innovation Center of Neuroregeneration, NMPA Key Lab for Research and Evaluation of Tissue Engineering Technology Products, Nantong University, Nantong, China, [2]Pharmaceutical Sciences Laboratory, Åbo Akademi University, Turku, Finland, [3]Turku Bioscience Center, University of Turku and Åbo Akademi University, Turku, Finland

**Keywords: functional biomaterials, smart biomaterials, development, application, regenerative medicine**

## Editorial on the Research Topic

## Functional and Smart Biomaterials: Development and Application in Regenerative Medicine

The development of functional and smart biomaterials has emerged the multidisciplinary subjects including medicine, biology, physics, chemistry and materials science, etc., and is playing important role in clinical applications, e.g., facilitating wound healing and restoring other types of biological function (Freudenberg et al., 2016; Shodeinde et al., 2020; Najjari et al., 2022). However, the performance of these biomaterials still need to be further enhanced due to the complicated interactions with components of living systems and the unpredictable responses of body to biomaterials (Kowalski et al., 2018). Thus, a good design and development of functional and smart biomaterials will be a guarantee for their future clinical applications for improving patients' health and life. Today, with the flourishing of biomaterials and regenerative medicine, more and more researcher are joining this field to study the functional and smart biomaterials for various regenerative medicine applications. To highlight the current progress, this Research Topic aims to bring together the latest exciting achievements referring to the development and application of functional and smart biomaterials on regenerative medicine.

Here, we collected a total of 16 papers, which present a broad range of the functional and smart biomaterials design, preparation, evaluation and application for various biological systems; and summarize the current progress of functional and smart biomaterials in regenerative medicine. The papers published in the present topic are briefly introduced below.

Dong et al. highlighted and summarized the various applied polymers in osteonecrosis therapy, then discussed the development of biofunctionalized composite polymers based on the polymers combined with different bioactive substances. Finally, the application of polymers in the treatment of osteonecrosis and future outlook are summarized. This review provided a comprehensive knowledge relevant to the application of polymers in the treatment of osteonecrosis and a meaningful theoretical basis further to advance the treatment of osteonecrosis with biomedical polymer materials.

The ideal orthopedic implant should possess both osteogenic and antibacterial properties and do proper assistance to *in situ* inflammatory cells for anti-microbe and tissue repair. However, aseptic loosening and peri-implant infection remain problems that may lead to implant removal eventually. Titanium and its alloys are dominant material for orthopedic/dental implants due to their stable chemical properties and good biocompatibility. In the review by Lu et al., an overview of the latest strategies to endow titanium implants with bio-function and anti-infection properties were overviewed. The methods for preparing efficient surfaces were stated and the insights into the

OPEN ACCESS

***Edited and reviewed by:***
*Hasan Uludag,*
*University of Alberta, Canada*

***Correspondence:**
*Guicai Li*
*gcli1981@ntu.edu.cn*
*Hongbo Zhang*
*hongbo.zhang@abo.fi*

***Specialty section:***
*This article was submitted to Biomaterials, a section of the journal Frontiers in Bioengineering and Biotechnology*

***Received:*** *15 April 2022*
***Accepted:*** *28 April 2022*
***Published:*** *17 May 2022*

***Citation:***
*Li G and Zhang H (2022) Editorial: Functional and Smart Biomaterials: Development and Application in Regenerative Medicine. Front. Bioeng. Biotechnol. 10:920730. doi: 10.3389/fbioe.2022.920730*

interaction between the devices and the local biological environment were offered. In the end, the challenges in terms of stability and long-term performance were put forward, new substances or surface modification methods with antibacterial and bone-promoting properties need to be explored in the development of ideal materials for bone implantation.

Shu et al. introduced the advantages of hydrogel dressings and the treatment strategies for burns, ranging from external to clinical. They then discussed the development of new hydrogel dressings for wound healing along with skin regeneration, and the functional classifications of hydrogel dressings along with their clinical value for burns. To construct different functional hydrogel dressings according to the different stages of wound healing and ensure that the appropriate therapy is administered when appropriate in the treatment of burn wounds.

Xu et al. analyzed and summarized the construction methods, with or without cells, and repair effects of single layer scaffold and multi-layer scaffold for the treatment of esophageal cancer. The multilayer complex structure of the esophagus should be considered in the repair of the full-thickness or circumferential defect of the esophagus. Besides, the source of an ingenious design and maintenance of the bionic structure and bionic function are the research direction.

Wu et al. explored a novel method for constructing porous collagen membranes via the combined application of bioskiving and sonication. Tuning the power intensity was shown to modulate fibril orientation, and the porous membrane without denatured collagen could be obtained by a 20-min sonication treatment at 90 W. The prepared collagen membrane could also be further mineralized to enhance osteogenesis. Overall, this study offered a rapid and convenient approach for fabricating porous collagen membranes.

In another study, Wu et al. developed a sensitive, specific, and biocompatible integrin αvβ3-targeted superparamagnetic $Fe_3O_4$ nanoparticles (NPs) for the noninvasive magnetic resonance imaging (MRI) of integrin αvβ3. The results established the possibility of $Fe_3O_4$-RGD serving as a feasible MRI agent for the noninvasive diagnosis of IgA nephropathy.

Li et al. investigated the osteogenic differentiation of inducedpluripotent-stem-cell-derived mesenchymal stem cells (iPSC-MSCs) and bone regeneration capacities using N-acetyl cysteine (NAC)-loaded biomimetic nanofibers of hydroxyapatite/silk fibroin (HAp/SF), which demonstrated the promising potential for the use of NAC/HAp/SF for bone tissue engineering.

Zhao et al. synthesized a bioclickable mussel-derived peptide Azide-3,4-dihydroxy-Lphenylalanine ($DOPA_4$) as a polyether ether ketone (PEEK) surface coating modifier and further combined bone morphogenetic protein two functional peptides (BMP2p) with a dibenzylcyclooctyne (DBCO) motif through bio-orthogonal reactions to obtain $DOPA_4$@BMP2p-PEEK, which displayed excellent biocompatibility and osteogenic functions, thus offering insights to engineering surfaces of orthopedic implants.

Liu et al. reported a dual-response nano-carrier of glutathione and acid to achieve the rapid release of encapsulated drug and increase the effective drug concentration in the tumor. In this way, the nanocarrier degraded quickly, realizing the purpose of rapid drug release and efficient antitumor effects, thus showing better clinical application prospects.

Electrospinning is still the convenient and efficient method for constructing tissue engineered implants. Wang et al. prepared nanofibrous membranes with different gelatin/polycaprolactone mass ratios via electrospinning for preventing postoperative cardiac adhesion, also providing potential application for wound dressing and bone regeneration. Kong et al. developed a porous nerve decellularized matrix-chitosan (NDM-CS) scaffold with high antimicrobial activity and high biocompatibility using a one-step electrospinning method for neural tissue engineering.

Hong et al. synthesized the copolymer of 6-arm polyethylene glycol and heparin (PEG-Hep) and then immobilized it on the surface of chitosan (Chi)-modified magnesium alloy surface through electrostatic interaction, which was shown to improve the corrosion resistance and biocompatibility.

Luo et al. covalently immobilized multifunctional baicalin (BCL) onto the surface of the contact lens, thus improving the anti-inflammatory, anti-oxidative stress, and antibacterial capabilities, and displaying great application potential in the surface engineering of ophthalmic medical materials.

Chen et al. proposed a simple UV-photofunctionalization strategy to improve the hemocompatibility of Ag nanoparticles, which provided a new solution idea to improve the hemocompatibility of metal nanoparticles.

Zhang et al. constructed Ag-incorporated polydopamine/tannic acid coating on titanium substrate with improved hydrophilicity, good cytocompatibility, and antibacterial effectiveness, indicating the potential for surface modification of titanium implants.

In summary, the articles collected in this Research Topic demonstrate the development and application of functional and smart biomaterials in regenerative medicine. In prospectively, the functional and smart biomaterials will continue to expand their application and significance in the field of regenerative medicine and tissue engineering.

## AUTHOR CONTRIBUTIONS

All authors listed have made a substantial, direct and intellectual contribution to the work and approved it for publication.

## ACKNOWLEDGMENTS

The authors gratefully acknowledge the financial support of the National Natural Science Foundation of China (32171352), Natural Key Science Research Program of Jiangsu Education Department (19KJA320006), Open Project of Guangxi Key Laboratory of Regenerative Medicine (Guizaizhongkai 202101) and Opening Project of National Engineering Laboratory for Modern Silk, Soochow University (SDGC2147).

## REFERENCES

Freudenberg, U., Liang, Y., Kiick, K. L., and Werner, C. (2016). Glycosaminoglycan-Based Biohybrid Hydrogels: A Sweet and Smart Choice for Multifunctional Biomaterials. *Adv. Mater* 28, 8861–8891. doi:10.1002/adma.201601908

Kowalski, P. S., Bhattacharya, C., Afewerki, S., and Langer, R. (2018). Smart Biomaterials: Recent Advances and Future Directions. *Acs Biomaterials Sci. Eng.* 4, 3809–3817. doi:10.1021/acsbiomaterials.8b00889

Najjari, A., Mehdinavaz Aghdam, R., Ebrahimi, S. A. S., Suresh, K. S., Krishnan, S., Shanthi, C., et al. (2022). Smart Piezoelectric Biomaterials for Tissue Engineering and Regenerative Medicine: a Review. *Biomed. Tech. Berl.* 67 (2), 71–88. doi:10.1515/bmt-2021-0265

Shodeinde, A. B., Murphy, A. C., Oldenkamp, H. F., Potdar, A. S., Ludolph, C. M., and Peppas, N. A. (2020). Recent Advances in Smart Biomaterials for the Detection and Treatment of Autoimmune Diseases. *Adv. Funct. Mater* 30, 1909556. doi:10.1002/adfm.201909556

**Conflict of Interest:** The authors declare that the research was conducted in the absence of any commercial or financial relationships that could be construed as a potential conflict of interest.

frontiers in Bioengineering and Biotechnology

REVIEW
published: 24 September 2021
doi: 10.3389/fbioe.2021.761302

# Polymer Scaffolds-Enhanced Bone Regeneration in Osteonecrosis Therapy

*Hengliang Dong[1†], Tongtong Zhu[1†], Mingran Zhang[1], Dapeng Wang[2], Xukai Wang[1], Guanning Huang[1], Shuaishuai Wang[1] and Minglei Zhang[1]**

[1]Department of Orthopedics, China-Japan Union Hospital of Jilin University, Changchun, China, [2]Department of Orthopedics, Siping Central Hospital, Siping, China

Osteonecrosis without effective early treatment eventually leads to the collapse of the articular surface and causes arthritis. For the early stages of osteonecrosis, core decompression combined with bone grafting, is a procedure worthy of attention and clinical trial. And the study of bone graft substitutes has become a hot topic in the area of osteonecrosis research. In recent years, polymers have received more attention than other materials due to their excellent performance. However, because of the harsh microenvironment in osteonecrosis, pure polymers may not meet the stringent requirements of osteonecrosis research. The combined application of polymers and various other substances makes up for the shortcomings of polymers, and to meet a broad range of requirements for application in osteonecrosis therapy. This review focuses on various applying polymers in osteonecrosis therapy, then discusses the development of biofunctionalized composite polymers based on the polymers combined with different bioactive substances. At the end, we discuss their prospects for translation to clinical practice.

**Keywords: polymer scaffold, bone tissue engineering, osteonecrosis treatment, bone regeneration, functionalization**

OPEN ACCESS

***Edited by:***
*Hongbo Zhang,*
*Åbo Akademi University, Finland*

***Reviewed by:***
*Lesan Yan,*
*Wuhan University of Technology, China*
*Saeid Kargozar,*
*Mashhad University of Medical Sciences, Iran*

****Correspondence:***
*Minglei Zhang*
*zml669@jlu.edu.cn*

*†These authors have contributed equally to this work*

***Specialty section:***
*This article was submitted to Biomaterials, a section of the journal Frontiers in Bioengineering and Biotechnology*

***Received:*** *19 August 2021*
***Accepted:*** *09 September 2021*
***Published:*** *24 September 2021*

***Citation:***
*Dong H, Zhu T, Zhang M, Wang D, Wang X, Huang G, Wang S and Zhang M (2021) Polymer Scaffolds-Enhanced Bone Regeneration in Osteonecrosis Therapy. Front. Bioeng. Biotechnol. 9:761302. doi: 10.3389/fbioe.2021.761302*

## INTRODUCTION

Osteonecrosis is a disease caused by a temporary or permanent loss of blood supply to the bone. The causes of osteonecrosis are extensive, and the pathogenesis is still unclear (Guo et al., 2014; Cui et al., 2021; Hines et al., 2021). The potential pathogenic factors that have been explored include trauma (Pascarella et al., 2019), long-term history of heavy drinking (Chen et al., 2017), hyperlipidemia (Mogensen et al., 2017), history of hormone medication (Li et al., 2018b), decompression sickness (Jones et al., 1993), and blood system diseases such as Gaucher disease (Reed et al., 2018) and sickle cell anemia (Severyns and Gayet, 2021) among others. The loss of blood supply to bone tissue leads to a decrease in the activity of bone cells, which leads to bone destruction (Zhou et al., 2019).

The destruction of bone activates the self-repair response of bone tissue (Shrivats et al., 2014) [including vascular regeneration, new bone formation, and sequestered bone resorption (Mont et al., 1998)]. However, the self-repair response of bone tissue is hindered by the harsh microenvironment of the osteonecrosis site (Zheng et al., 2015). Ineffective repairs such as fibrous tissue repair cannot replace the original bone tissue in terms of structure and support performance. Therefore, osteonecrosis involving joints often leads to the gradual collapse of the articular surface, which in turn causes arthritis (Calder et al., 2001; Hernigou et al., 2020; Cui et al., 2021).

At present, in both basic research on and clinical application of osteonecrosis treatments, there are a large number of studies that report various constructive methods. Systemic management may be unsuitable for osteonecrosis because the unavoidable problems of systemic treatment include insufficient local osteonecrosis concentration and systemic side effects. Recently, researchers to treat osteonecrosis locally through injection of stem cells (Piuzzi et al., 2017), growth factors (Rackwitz et al., 2012; Peng and Wang, 2017), cytokines (Rackwitz et al., 2012; Peng and Wang, 2017; Yang et al., 2018), various drugs (Feng et al., 2017; Guo et al., 2017; Huang et al., 2018), and hormones (Bakhshi et al., 2012; Zhou et al., 2017) at the site of osteonecrosis to achieve local treatment of osteonecrosis. These basic researchs have had varying outcomes. However, such local injection therapies face problems such as leakage, burst release, and loss of biological activity (Li et al., 2009; Tai et al., 2013; Phipps et al., 2016).

In clinical application, surgical treatment is the most important means. Surgical therapies, including core decompression, osteotomy, arthroplasty, and so forth, have been developed in clinical practice, but they are also subject to limitations, such as the narrow scope of application and repeated revision operations (Cao et al., 2016). At present, for the early stage of osteonecrosis, core decompression combined with bone grafting is widely practiced (Andronic et al., 2021). Both autologous bone grafting and allogeneic bone grafting meet the surgical needs. However, autologous bone grafting is limited by insufficient donor supply and secondary damage to and complications at the donor site, and allogeneic bone grafting faces issues such as immune rejection. These problems limit the clinical application of bone grafting (Lord et al., 1988; Stevenson et al., 1996).

Thanks to the development of biotechnology and materials science, many biomaterials are available to make bone substitute materials to cope with the problems in bone grafting. Among them, polymers are widely used in the study of osteonecrosis because of their excellent biocompatibility and biodegradability. This article focuses on applying various polymers in osteonecrosis and elaborates and summarizes the current research. Then, the different functions of various polymers combined with different substances are discussed. Finally, the application of polymers in the treatment of osteonecrosis and future outlook are summarized. We aim to provide a comprehensive review of the application of polymers in the treatment of osteonecrosis and a meaningful theoretical basis further to advance the treatment of osteonecrosis with biomedical polymer materials.

## POLYMERS USED IN OSTEONECROSIS THERAPY

Biocompatibility, biodegradability, and certain mechanical properties are required for biomaterials used in osteonecrosis research (Zhu et al., 2020). Biocompatibility is the primary criterion for tissue engineering materials. It allows cell adhesion, migration, and proliferation without triggering an immune response and severe inflammation (Williams, 2008). Appropriate biodegradability and certain mechanical properties are also characteristics that osteonecrosis repair biomaterials need to have. Biomaterials with appropriate biodegradability and mechanical properties provide sufficient support before new bone is formed in the osteonecrosis area to avoid articular surface collapse and pathologic fracture. Biomaterials are degraded to a certain extent over time, providing enough space to form new bone tissue (Zhang et al., 2019a; Zhu et al., 2020). In addition, this feature also allows biomaterials to be used as carriers of small molecules (Phipps et al., 2016; Zhang et al., 2019a; Zhu et al., 2020). When biomaterials are degraded, the contained substances are released into the environment. The degradation of biomaterials and the absence of any toxic byproducts also avoid the body's immune response to foreign substances and subsequent inflammation (Zhang et al., 2019a; Zhu et al., 2020).

Polymers are mainly divided into two types, natural and synthetic (Zhang et al., 2019a; Zhang et al., 2019b). At present, natural polymers such as alginate, chitosan, and peptide chain hydrogels have been used in various forms for research on osteonecrosis. Because of their inherent extracellular matrix structure, these natural polymers exhibit better biological properties than synthetic polymers in terms of cell proliferation and differentiation and hydrophobicity (Chen et al., 2011). However, synthetic polymers also have some advantages, including better mechanical strength, higher processing capability, and a more controllable degradation rate than natural polymers.

Polymers that are often used in the treatment of osteonecrosis are poly (lactide-co-glycolide) (PLGA), poly (ε-caprolactone) (PCL), polylactide (PLA), poly (propylene fumarate) (PPF) (Chen et al., 2011; Zhu et al., 2020). Various materials have different advantages and disadvantages. Furthermore, it is difficult for a single polymer to meet the requirements of suitable biocompatibility, biodegradability, porosity, and certain mechanical support properties at the same time. In order to overcome these limitations, natural polymers, synthetic polymers, cells, small molecule drugs, and other substances are combined (**Table 1**). These hybrid biomaterials combine the advantages of various materials to meet more requirements, such as better biological activity, more robust mechanical properties, more controllable degradation, and more convenient manufacturing capability (Lee et al., 2014b; Feng et al., 2019).

## Natural Polymers in Osteonecrosis Therapy

Because natural polymers have the characteristics of biocompatibility and biodegradability—and the biological functional molecules on the surface of natural polymers are conducive to cell adhesion, aggregation, proliferation, and differentiation—natural polymers are widely used in tissue engineering. Various natural polymers such as chitosan, alginate, and peptide chain hydrogel have been made into bone substitute materials for osteonecrosis therapy (Zhang et al., 2019a).

### Chitosan and Its Derivatives

Chitosan is a linear polycationic polysaccharide polymer derivative of chitin. A large number of research reports show that chitosan has good biocompatibility, high biodegradability, low allergenicity, antibacterial properties, and wound healing activity. Chitosan can be easily extracted from shellfish and other seafood waste. However, the poor solubility of chitosan in neutral and alkaline media limits the direct application of chitosan in medicine and

**TABLE 1 |** Combined application of polymers.

| Polymer | Additional material combined with polymers | Biologically active factor | Properties | References |
|---|---|---|---|---|
| Chitosan | Alginate | BMMSC and EPCs | Biocompatibility, porosity, low cytotoxicity and excellent cell adhesion, enhanced bone production and angiogenesis, reduced fat production | Xu et al. (2021) |
| Alginate (ALG) | — | SMSCs | Biocompatibility, biodegradability, osteogenesis, injectability, elasticity | Chen et al. (2014) |
| Cervi cornus colla (CCC) | Deproteinized bone | — | Biocompatibility, diameter 15 mm, thickness 3.5 mm, cylindrical shape, pore structure, porosity (72.86 ± 5.45%), compressive strength 4.45 ± 1.02 MPa, degradation rate after 6 weeks is 35.81%, osteogenesis | Wang et al. (2019b) |
| HA | CAP | — | Biocompatibility, biodegradability, osteoconductivity, bone conductivity, promotes osteogenic differentiation and bone regeneration | Wang et al. (2018) |
| Peptide-based hydrogel | — | BMP-2 | Biocompatibility, biodegradability, glue is also liquid in different environments, osteogenesis | Phipps et al. (2016) |
| DBM | — | BFGF, BMP-2 | Biocompatibility, enhanced osteogenesis and angiogenesis, cell adhesion | Peng and Wang, (2017) |
| PLGA | β-TCP | 5% Mg<br>10% Mg<br>15% Mg | Biocompatibility, biodegradability, pore size PT 423.1 ± 77.0, PT 5 M 418.7 ± 33.4, PT, 10M 392.5 ± 30.2, PT 15M 411.5 ± 26.9, porosity PT 59.1 ± 9.7, PT 5M 59.4 ± 3.1, PT 10M 62.4 ± 5.3, PT 15M 65.8 ± 8.0, the connectivity is 100%, compressive strength, PT 1.5 ± 0.1 MPa, PT 5M 2.9 ± 0.2 MPa, PT 10M 3.1 ± 0.2 MPa, PT 15M 3.7 ± 0.2 MPa, osteogenesis | Lai et al. (2019) |
| PLGA | TCP | Icaritin | Biocompatibility, biodegradability, pore structure, compressive strength 47.03 ± 33.58 N, enhanced bone formation | Qin et al. (2015) |
| PLGA | CPC | BMP, VEGF | Biocompatibility, biodegradability, porosity 62.13 ± 4.28%, compressive strength of 6.60 ± 1.02 MPa, osteogenic, angiogenic | Zhang et al. (2016) |
| PCL | TCP | BMMCs | Biocompatibility, pore structure, porosity near section is 15%, the middle section is 40%, the far section is 16%, the 8-weeks degradation rate of the proximal segment 42.5 ± 14.0%, 5.3 ± 1.9% at the middle segment, 5.5 ± 3.2% at the distal segment, osteogenic, vascular | Maruyama et al. (2018) |
| PLA | Nano-hydroxyapatite, collagen | BMMSC | Biocompatibility, biodegradability, pore size of 300 ± 250 μm, porosity of 70–90%, vascularity, osteogenesis | Wang et al. (2019a) |
| PPF | CPC | Ginsenoside Rg1 | Biocompatibility, biodegradability, pore structure, the compressive strength in C/P = 0, C/P = 1 and C/P = 2 groups are 13.66 3.00 MPa, 15.68 3.52 MPa and 21.37 1.06 MPa, respectively, osteogenic, angiogenic | Chang et al. (2010) |

*BMMSC, Bone marrow mesenchymal stem cells; EPCs, endothelial progenitor cells; SMSCs, synovial fluid mesenchymal stem cells; HA, hyaluronic acid; CAP, calcium phosphate; BMP-2, bone morphogenetic protein-2; DBM, demineralized bone matrix; BFGF-2, basic fibroblast growth factor-2; β-TCP, β-tricalcium phosphate; Mg, magnesium; CPC, calcium phosphate; VEGF, vascular endothelial growth factor.*

biomedicine (Prabaharan and Mano, 2005; Bhattarai et al., 2010; Fonseca-Santos and Chorilli, 2017). Chitosan is easily carboxy-methylated to produce carboxymethyl chitosan (CMC). The solubility of CMC in aqueous media is greatly enhanced, while biodegradability and biocompatibility are maintained. Moreover, CMC is easy to modify chemically and has a high affinity for macromolecules in the body. CMC is widely used in biomedicine and various tissue engineering fields (Fonseca-Santos and Chorilli, 2017). Xu et al. (2021) manufactured a carboxymethyl chitosan/alginate scaffold (CMC/ALG) by a lyophilization approach and loaded BMMSC and EPCs on the scaffold. Their research confirmed that the scaffold has good biocompatibility (**Figure 1A**) (porosity, low cytotoxicity, and excellent cell adhesion). The researchers established a rabbit model of steroid-induced osteonecrosis of the femoral head (ONFH) (**Figure 1B**). After CD was performed on the necrotic femoral head, a CMC/ALG/BMMSC/EPC scaffold was implanted into the rabbit femoral head. Two weeks later, the results of radiological evaluation and histological analysis showed that the CMC/ALG/BMMSC/EPC group achieved the best curative effect in the repair of osteonecrosis in each group (**Figure 1C**). They observed that the CMC/ALG/BMMSC/EPC group had significant bone formation and angiogenesis and decreased fat production, which promoted the repair of ONFH.

## Alginate

Alginate is a frequently used biomedical material, often for drug delivery, cell embedding, tissue embedding, and cartilage tissue regeneration (Chen et al., 2014). Alginate has good water solubility and good biocompatibility and can be made into a gel (Majima et al., 2005). Alginate is often made into an injectable gel for surgery (Goodship and Birch, 2005), and many researchers use it for research on osteonecrosis repair.

Chen et al. (2014) embedded synovial fluid mesenchymal stem cells (SMSCs) in alginate beads and observed the biological activity and osteogenic differentiation of synovial mesenchymal stem cells in the internal environment of

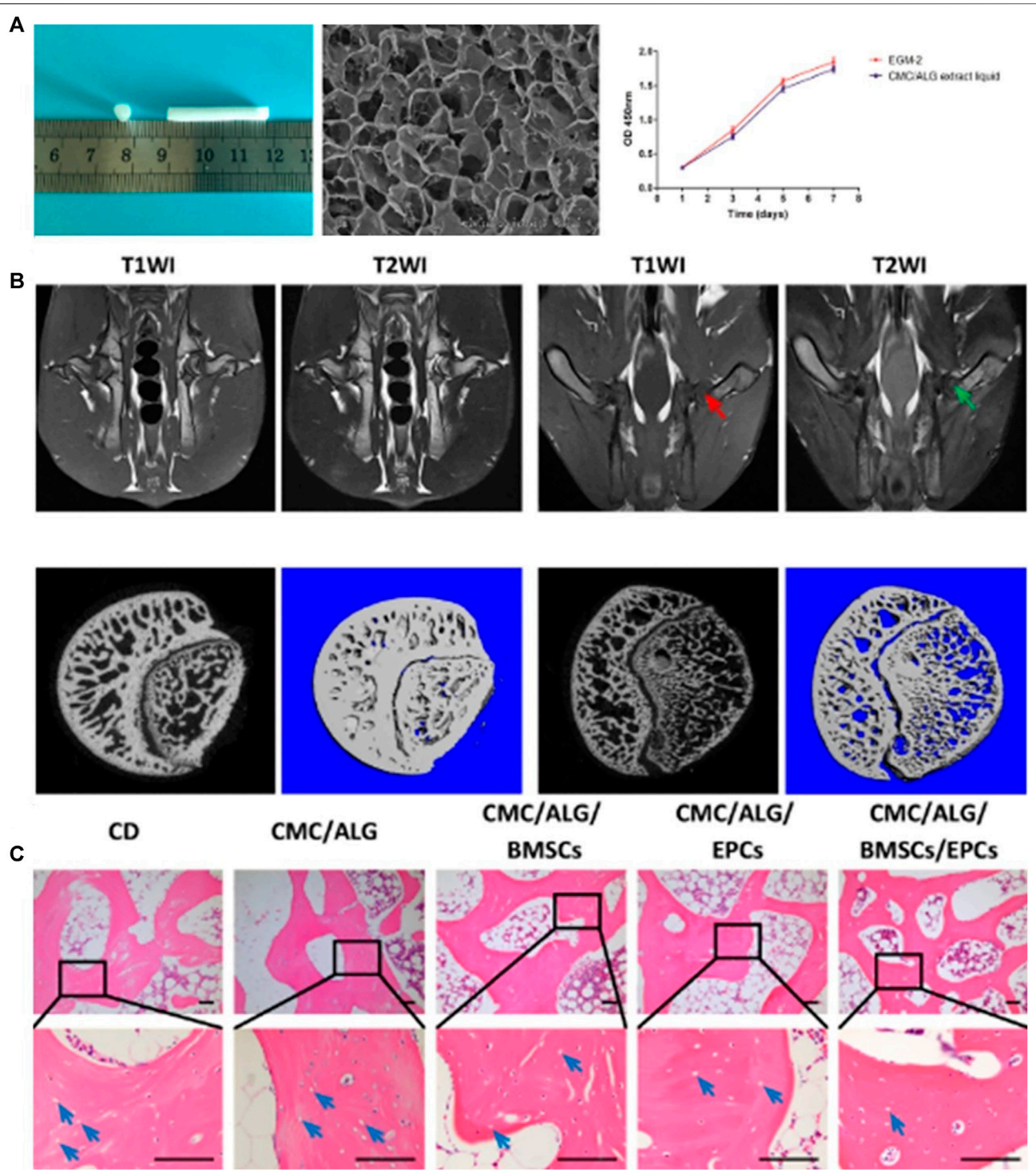


**FIGURE 1 |** BMMSC and EPCs dual-loaded CMC/ALG scaffolds for enhanced bone regeneration in ONFH (Xu et al., 2021). **(A)** Morphology of the scaffold for *in vivo* transplantation. The SEM micrograph showed the porous structure of the scaffold. And CCK-8 assay results confirmed that CMC/ALG scaffolds generated no cytotoxicity effects on BMSC/EPC viability. **(B)** Representative MRI photograph of the normal rabbit and the rabbit model. 2D and 3D micro-CT images of the femoral head in normal group and model group. **(C)** H&E staining of the empty lacuna in the necrotic region of the femoral head for each group. Reproduced with permission (Xu et al., 2021). Copyright 2021, Wiley Periodicals LLC.

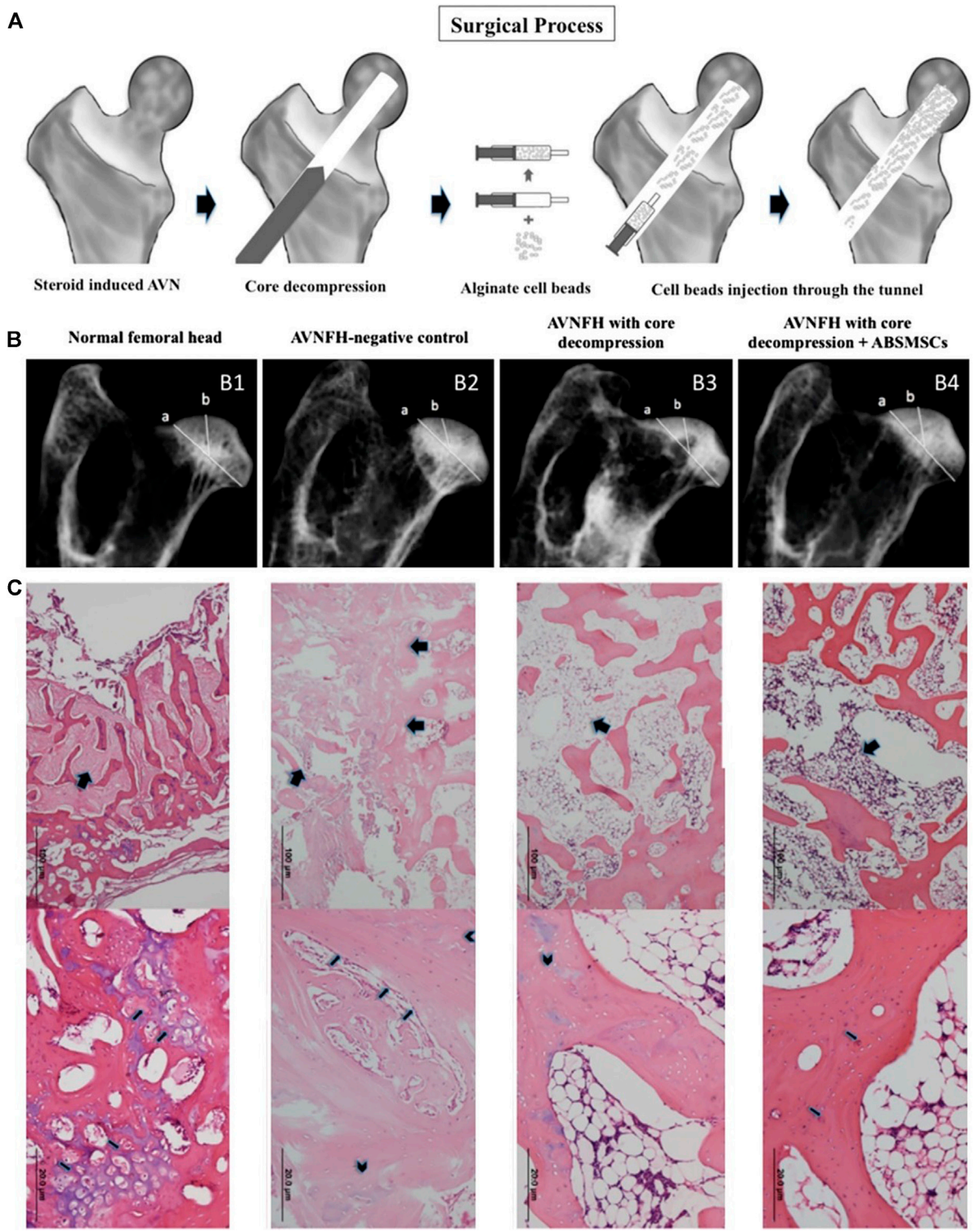


**FIGURE 2 |** The alginate beads loaded with SMSCs promote bone formation and angiogenesis in animal models of femoral head necrosis (Chen et al., 2014). **(A)** Procedures for treating femoral head necrosis in the animal model. Radiographs of harvested femoral heads **(B)** and histological observations **(C)** of different groups. Reproduced with permission (Chen et al., 2014). Copyright 2014, ELSEVIER.

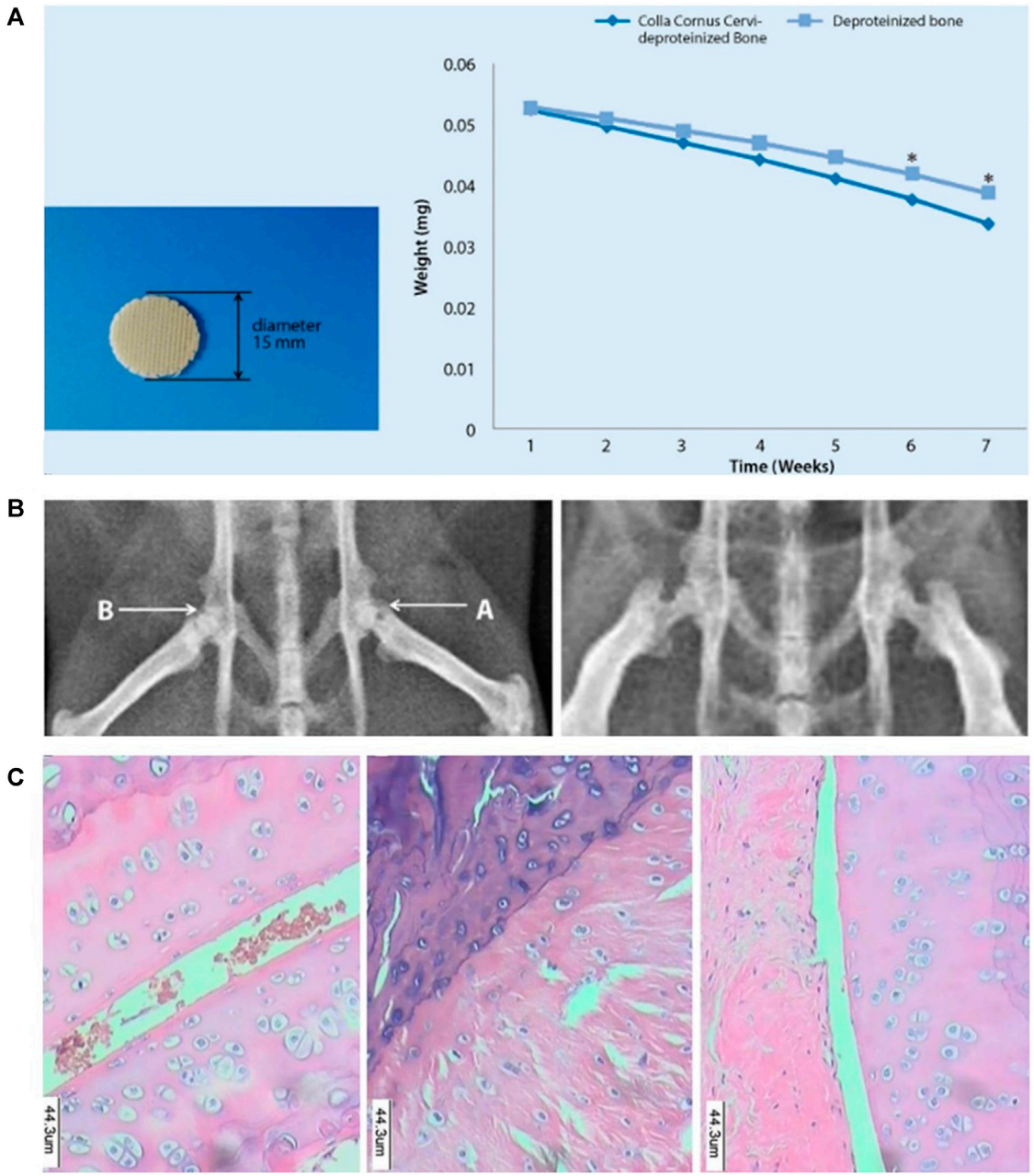


**FIGURE 3 |** CCC deproteinized bone scaffold reduced femoral head necrosis in rats. **(A)** Exterior view of a 3D printed CCC-deproteinized bone scaffold, and scaffold degradation curves. The degradation levels of the CCC-deproteinized bone scaffolds and deproteinizedbone scaffolds after 6 weeks immersion in PBS reached 35.81 and 26.61%, respectively (*$p < 0.05$). **(B)** The femoral head implanted with a CCC-deproteinized bone scaffold and the non-implanted femoral head exhibited different outcome. **(C)** Pathological observation of the femoral head of rat in different groups. Significant alleviation of femoral head necrosis was observed in the rats implanted with CCC-deproteinized bone scaffolds. Reproduced with permission (Wang et al., 2019b). Copyright 2019, SPRINGER.

alginate beads in *in vitro* experiments. The alginate beads embedded with synovial fluid MSCs (ABSMSCs) were implanted into the femoral head of the rabbit model of hormone-induced femoral head necrosis after core decompression surgery (**Figure 2A**).

The results of *in vitro* experiments show that the SMSC in the internal environment of alginate beads have the potential to differentiate into bone. *In vivo*, the hormone-induced femoral head necrosis rabbit model can be treated by core decompression and alginate beads carrying ABSMSCs implantation. This method maintains the density and spherical shape of the femoral head and promotes bone regeneration within the necrotic femoral head (**Figure 2B**). Histological analysis results also showed that compared with other groups, the ABSMSCs

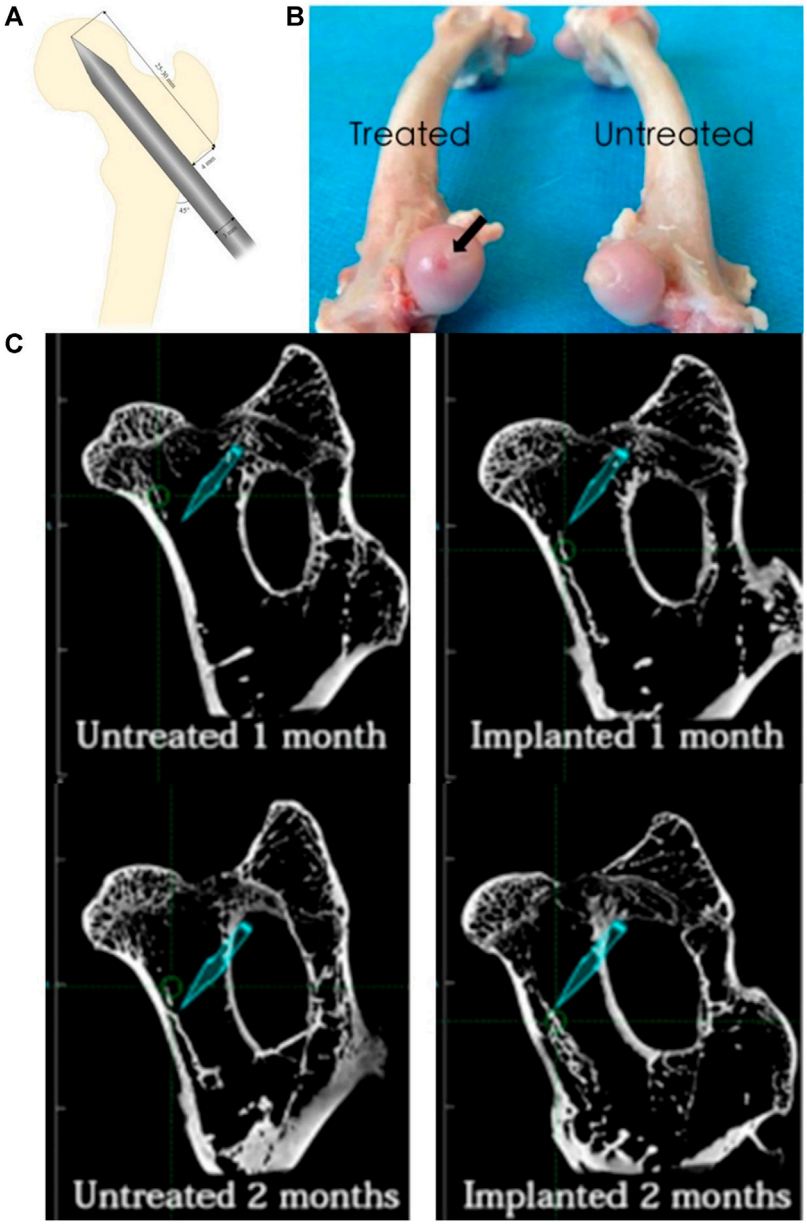


**FIGURE 4 |** HA-BP/CAP composite hydrogel can promote bone regeneration at the site of osteonecrosis (Wang et al., 2018). **(A)** The details regarding the standard animal model of ONFH. **(B)** The subchondral bone of the femoral head in the experimental group presented the establishment of the ONFH animal model because of the dark red area on the surface of the femoral head, while the untreated group appeared normal. **(C)** shows that the amount of bone regeneration at 1 and 2 months after injection of HA-BP/CAP composite hydrogel in the experimental group was significantly greater than that in the control group. Reproduced with permission (Wang et al., 2018). Copyright 2018, 2018 Elsevier Inc.

group had more new bone tissue and new blood vessels in the area of osteonecrosis (**Figure 2C**). Therefore, alginate is also an polymer suitable for osteonecrosis research.

## Cervi Cornus Colla

Cervi Cornus colla (CCC) is a Chinese medicine extracted from deer antlers, and it is a protein-polysaccharide complex. CCC contains 16 amino acids, including glycine, proline, glutamic acid, and so forth. (Choi et al., 2013). CCC has long been used in animal model tests and clinical human experiments. CCC has been used to prevent and treat acute and chronic arthritis, osteoporosis, fractures, hypercholesterolemia, and other diseases (Kim et al., 2013; Li et al., 2014). Wang et al. (2019b) processed the proximal pig femur to obtain a deproteinized bone meal. After mixing the deproteinized bone meal with CCC and synthetic organic materials, CCC-deproteinized bone scaffolds were made by 3D printing technology. The 3D printed CCC-deproteinized bone scaffold had a porous structure, degradability,

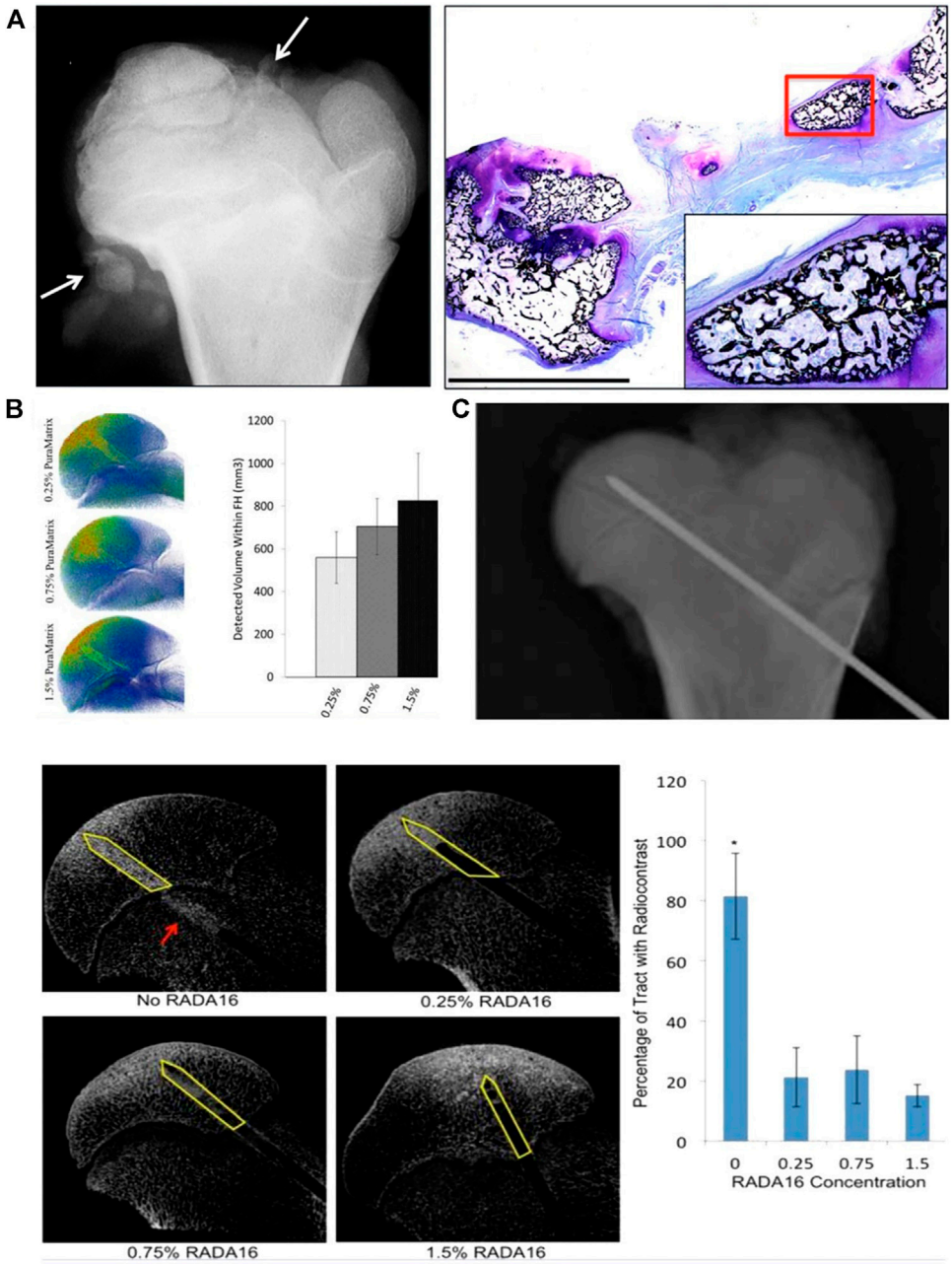


**FIGURE 5 |** A peptide-based hydrogel named RADA16 provides a feasible method for the leakage problem encountered by local injection of BMP-2 in the treatment of femoral head necrosis (Vandermeer et al., 2011; Phipps et al., 2016). **(A)** Radiograph and histological analysis showed heterotopic ossification after local intraosseous administration of ibandronate and BMP-2 (Vandermeer et al., 2011). **(B)** Distribution of different concentrations of RADA16/radiocontrast mixture in the femoral head (Phipps et al., 2016). **(C)** Intraosseous needle introduced in the central region of the femoral head by transphyseal approach for RADA16/radiocontrast infusion (Phipps et al., 2016). **(D)** Micro-CT images showing different amount of backflow of radiocontrast solution down the needle track. Bar graph showing percentage of needle track with radiocontrast backflow after the removal of the needle (Phipps et al., 2016). Reproduced with permission (Vandermeer et al., 2011). Copyright 2011, LIPPINCOTT WILLIAMS & WILKINS. Reproduced with permission (Phipps et al., 2016). Copyright 2016, American Chemical Society.

and excellent mechanical properties (**Figure 3A**). They implanted the scaffold into the femoral head of the mouse model with osteonecrosis of the femoral head (ONFH) to repair osteonecrosis (**Figure 3B**) and found that the CCC deproteinized bone scaffold significantly reduced femoral head necrosis in rats (**Figure 3C**). *In vitro* experiments also showed that osteoblasts aggregated and adhered in the pore structure of the CCC deproteinized bone scaffold, and the CCC-deproteinized bone scaffold enhances the proliferation of osteoblasts (Wang et al., 2019b).

### Hyaluronic Acid

Hyaluronic acid (HA), a natural polysaccharide composed of D-glucuronic acid and D-N-acetyl glucosamine repeating units (Kutlusoy et al., 2017; Rezaeeyazdi et al., 2018), is the main component of the extracellular matrix and an essential structural element in various tissues. HA plays an essential role in angiogenesis and wound healing (Wu et al., 2017; Rezaeeyazdi et al., 2018), and researchers are currently using HA to study osteonecrosis. Wang et al. (2018) combined bisphosphonate (BP)-modified HA (HA-BP) and CAP to create an HA-BP/CAP composite hydrogel. Their *in vitro* experiments confirmed that the composite hydrogel has good biocompatibility. The composite hydrogel material was also injected into the femoral skull tunnel of the ONFH rabbit model as the experimental group. The control group was injected with saline (**Figures 4A,B**). At 1 month and 2 months, the repair of femoral head necrosis of the two rabbit models was compared. As expected, in the radiological evaluation and histological analysis, the experimental group produced more new bone mineral tissue than the control group (**Figure 4C**), demonstrating that this HA-BP/CAP composite hydrogel can promote bone regeneration at the site of osteonecrosis.

### Peptide-Based Hydrogels

Some peptide and protein nanofiber structures have also been extensively studied as biomaterials. As early as 2011, Vandermeer et al. (2011) injected ibandronate combined with BMP-2 into an animal model of ischemic femoral head necrosis. Experiments confirmed that ibandronate combined with BMP-2 could reduce femoral head deformities and at the same time stimulate bone formation. However, they also found that infusion of BMP-2 solution can cause the unnecessary spread of BMP-2 outside the femoral head and produce heterotopic ossification in the hip joint capsule (**Figure 5A**).

Five years later, Phipps et al. (2016), in the same laboratory as Vandermeer *et al.*, used a peptide-based hydrogel called RADA16 to provide a solution to the BMP-2 leakage problem previously encountered by. They believe that this novel method may provide benefits for osteonecrosis therapy.

RADA16 is a peptide-based hydrogel composed of 16 amino acids (Yokoi et al., 2005) and has a β-sheet structure in a saline environment (Zhang et al., 1993). Previous studies have shown that this peptide-based hydrogel is biocompatible, biodegradable, and can support new bone formation (Misawa et al., 2006; Nakahara et al., 2010; Kohgo et al., 2011). In their *in vivo* and *in vitro* experiments, Phipps et al. (2016) used RADA16 as a carrier to deliver BMP-2, retaining the biological activity of BMP-2 and effectively controlling the diffusion of BMP-2 (**Figures 5B,C**). After a mixed injection of RADA16 and a radiographic agent, the backflow of the contrast agent in the porcine femoral head channel was significantly reduced (**Figure 5D**).

The above findings support peptide-based hydrogel as an intraosseous carrier and provide a new solution to the leakage problem in osteonecrosis therapy. They also guide the next steps in studying peptide chain hydrogel in osteonecrosis model experiments.

### Demineralized Bone Matrix

The bone tissue removes the mineralized components and retains the organic matrix and growth factors to obtain demineralized DBM. DBM has strong osteogenic properties because it contains many organic components and growth factors and is often used in bone repair research (Lee et al., 2014a). BFGF can affect gene expression and angiogenesis. Therefore, it is considered to be a critical factor in the process of bone repair (Hu et al., 2015). Peng and Wang (2017) transfected adenovirus-mediated bone morphogenetic protein 2 (Ad-BMP-2) and bFGF into BMMSC. The modified bone marrow mesenchymal stem cells combined with DBM (Ad-BMP2-bFGF-GFP group) were then implanted into an ONFH canine model. This experiment shows that the BMMSC modified by Ad-BMP-2/bFGF combined with DBM can repair the osteonecrosis of the femoral head in the ONFH canine model by promoting bone formation and angiogenesis, and DBM itself has osteoinduction and osteoconduction capabilities. Both radiological evaluation and histological analysis show that the Ad-BMP2-bFGF-GFP group had a larger area of new bone and a higher density of new blood vessels than the other groups.

## Synthetic Polymers in Osteonecrosis Therapy

In recent years, synthetic polymers have received more attention than natural polymers because of their desirable properties in bone engineering, such as porosity, degradation time, and mechanical properties. They have strong shaping abilities and can be made into various shapes according to need (Oh, 2003; Sheikh et al., 2016).

### Poly (Lactide-Co-Glycolide)

Poly (lactide-*co*-glycolide) (PLGA) is currently one of the most successfully developed synthetic biodegradable polymers. Because of its excellent biocompatibility and biodegradability, it has been widely used in research on various human delivery systems (Danhier et al., 2012). PLGA is approved by the U.S. Food and Drug Administration (FDA) and the European Medicines Agency for use in various human drug delivery systems (Kempen et al., 2008). PLGA has extremely low toxicity in the human body because the hydrolyzed metabolites of PLGA are monomeric lactic acid and monomeric glycolic acid, as shown in **Figure 6A**. As endogenous substances in humans, these two monomers are easily metabolized through the human body's Krebs cycle (Kumari et al., 2010).

Lai et al. (2018) established a poly (lactide-coglycolide) (PLGA), β-TCP composite scaffold using low-temperature rapid prototyping (LT-RP) technology. The PLGA/TCP (PT) scaffold has a trabecular pore structure with good biocompatibility, bone conductivity, and biodegradability *in vivo* and *in vitro*. Lai et al. (2019) also added magnesium (Mg) to the PT scaffold to make a PTM scaffold in a follow-up study. The research results show that the PTM scaffold has a good bionic structure and suitable mechanical properties. The PTM scaffold has the dual capabilities of osteogenesis and angiogenesis

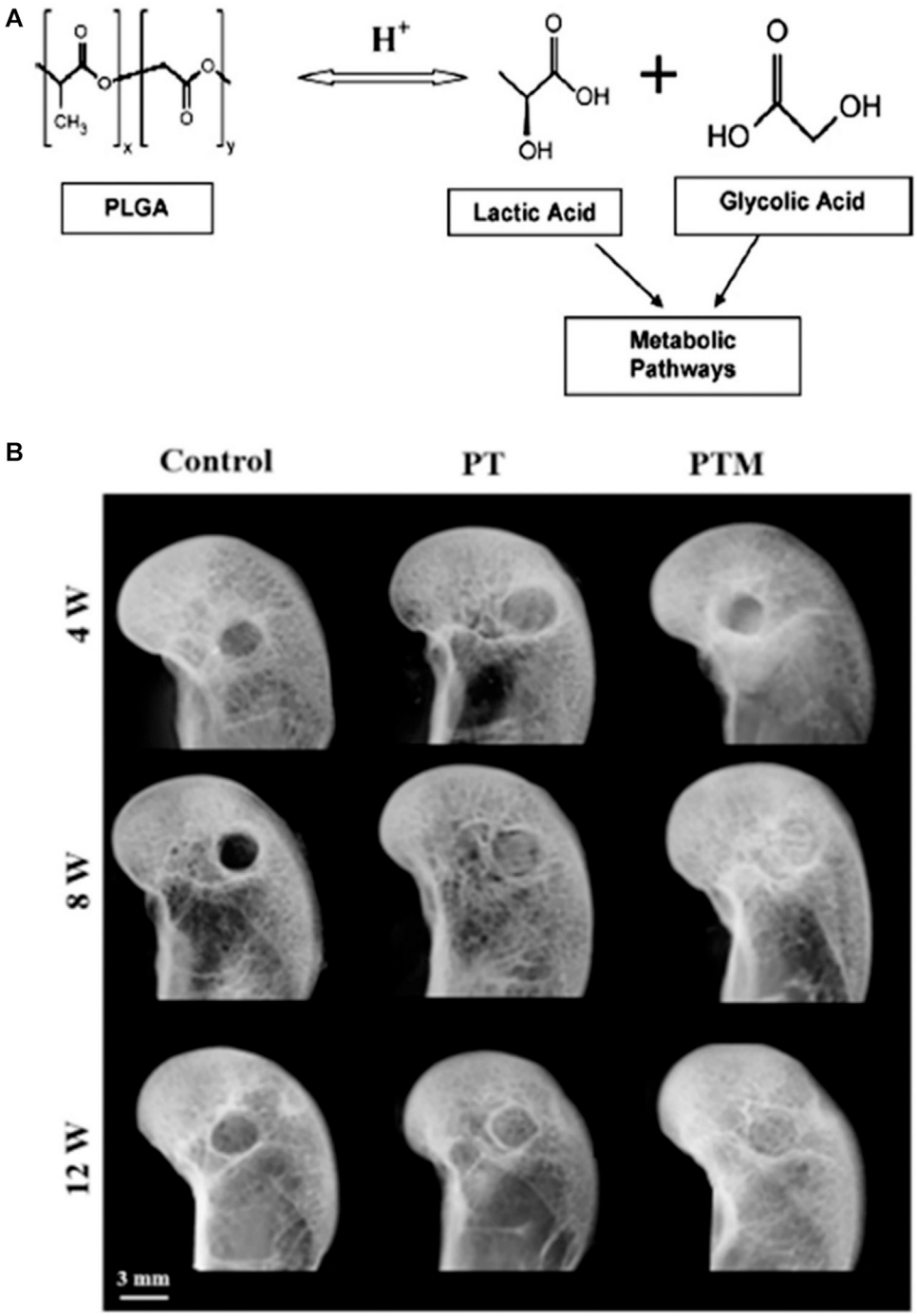


**FIGURE 6 |** PLGA for osteonecrosis therapy. **(A)** Hydrolysis of PLGA (Danhier et al., 2012). **(B)** Representative radiographs showed that new bone formation within bone tunnel at 4, 8, and 12 weeks after surgery (Lai et al., 2019). Reproduced with permission (Danhier et al., 2012). Copyright 2012, Elsevier Ltd. Reproduced with permission (Lai et al., 2019). Copyright 2019, Elsevier Ltd.

(**Figure 6B**). The PTM scaffold is synergistic in enhancing the formation and quality of new bone in the rabbit model of steroid-associated osteonecrosis (SAON), and it has a stronger ability to promote bone formation than the PT scaffold.

Qin et al. (2015) added icaritin to the PLGA/TCP scaffolds to produce PLGA/TCP/icaritin (PTI) scaffolds. A steroid-associated osteonecrosis (SAON) animal model was established, and the PTI and PT scaffolds were implanted in the animal model. A non-implanted scaffold group was the control group. The effects of the

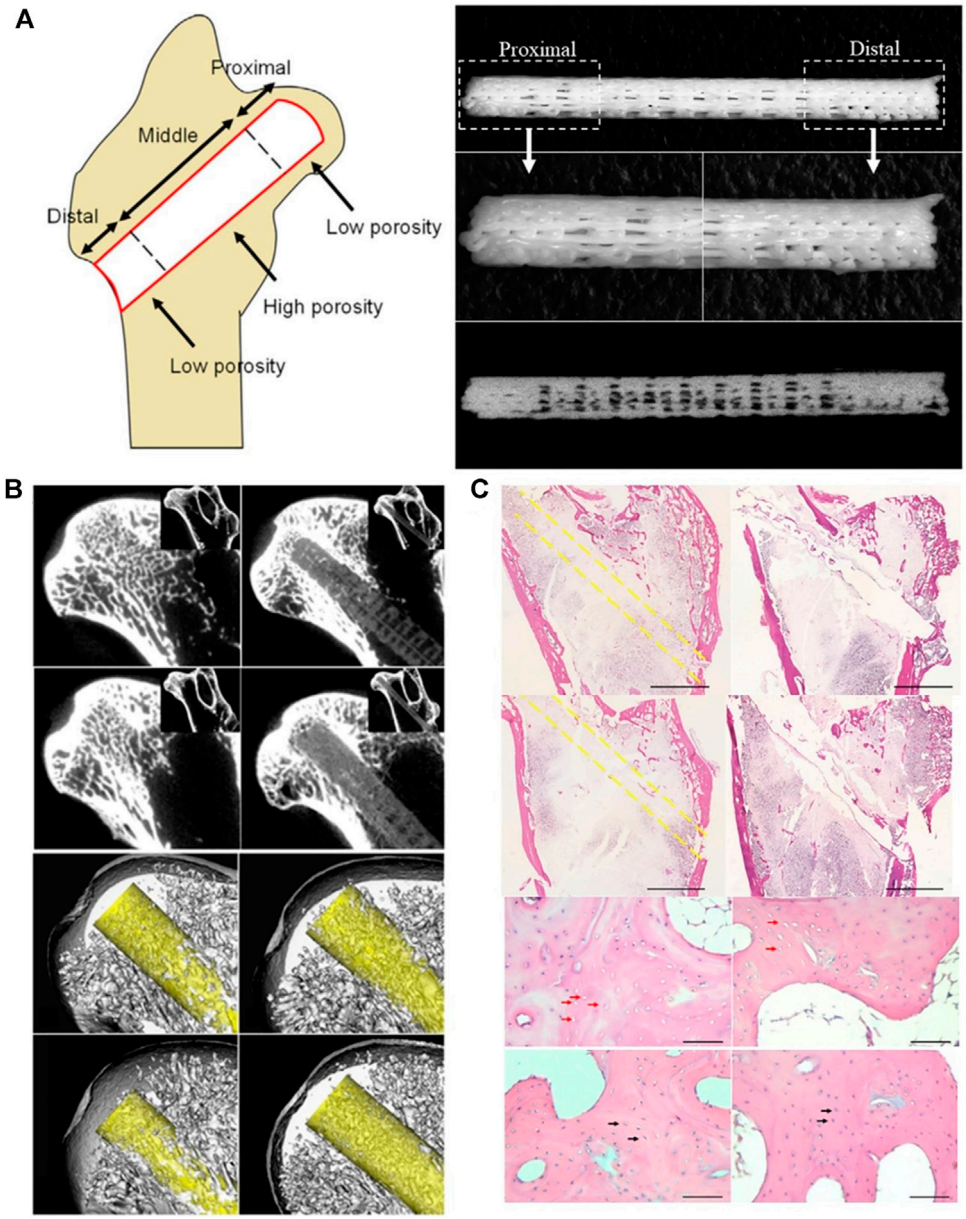


**FIGURE 7 |** FGS and FGS/BMMC could promote bone regeneration in the area of osteonecrosis. **(A)** A schematic image shows how the three segments of FGS with different porosities are distributed in the femoral head. The FGS consisting of three segments of spatially graded porosity, including 4 mm length proximal segment of 15% porosity, 17 mm length middle segment of 40% porosity, and 6 mm distal segment of 15% porosity. **(B)** FGS is degraded at the proximal end, and there is mineralized tissue around it. **(C)** Histological analysis confirmed that there was more new bone formation around FGS than other groups. Reproduced with permission (Maruyama et al., 2018). Copyright 2018, Elsevier Ltd.

PTI scaffold on the recruitment, bone formation, and anti-adipogenesis of bone marrow mesenchymal stem cells (BMMSC) were observed. The results of the study showed that the incidence of femoral head collapse in the PTI stent group was the lowest. Compared with the control group and the PT group, the femoral head cartilage was better preserved in the PTI scaffold group, and more new bone was formed in the bone tunnel.

Zhang et al. (2016) produced a composite PLGA microsphere. This calcium phosphate (CPC) scaffold contained BMP-vascular endothelial growth factor (VEGF)-loaded PLGA microspheres (BMP-VEGF-PLGA-CPC) and exhibited compressive strength equivalent to that of cancellous bone. The composite microspheres showed good biocompatibility and promoted bone formation and angiogenesis in animal experiments. Compared with other scaffold groups, more new mineralized tissue can be observed around the scaffold, and more new blood vessels appear in the newly mineralized tissue in the BMP-VEGF-PLGA-CPC group. Zhang et al. (2016) proposed that the

BMP-VEGF-PLGA-CPC scaffold has a potentially useful application in the treatment of osteonecrosis.

In summary, PLGA is currently one of the most widely used synthetic polymer materials in the field of osteonecrosis research. We believe that PLGA will continue to receive more attention in this field in the future.

### Poly (ε-Caprolactone)

Poly (ε-caprolactone) (PCL) is another polymer material that is widely used in bioengineering. The biocompatibility of PCL is excellent, and the surface chemistry of PCL is suitable for cell attachment, proliferation, and differentiation. Moreover, the degradation byproducts of PCL are non-toxic and can usually be metabolized and eliminated through the body's natural metabolic pathways (Gao et al., 2017). A previous study (Sung et al., 2004) compared the pH level of the environment around the implant after PCL and PLGA scaffolds were implanted under the skin of the mouse back. The study concluded that PCL is less likely to acidify the environment than PLGA and less likely to cause inflammation in the body. Thermoplastic polymers such as PCL can be easily produced by 3D printing technology into controllable, various-shaped, porous scaffolds for various scientific research (Lam et al., 2009; Wang et al., 2019c). However, the degradation rate of PCL in the abdomen of rats is low, and the low degradation rate causes PCL to hinder the production of new cell tissue in the implantation area and may even trigger the body's immune rejection reaction (Qazi et al., 2014; Kargozar et al., 2018; Zhu et al., 2020).

Maruyama et al. (2018) produced PCL/TCP functionally graded scaffold (FGS), which was divided into three porosity-spatially-graded sections. The porosity of the proximal section was 15% to produce a length of 4 mm, the porosity of the middle section was 40% to produce a length of 17 mm, and the porosity of the distal section was 16% to produce a length of 6 mm. The porosity of each segment was similar to that of the human femur (**Figure 7A**). The study also added bone marrow-derived mononuclear cells (BMMCs) to FGS and implanted FGS + BMMCs and FGS into the femoral head of a rabbit steroid-induced osteonecrosis model after CD surgery. The results showed that the degradation rate of the proximal segment of FGS was higher than that of the middle and distal segments. The degradation rate of the proximal part of FGS in the FGS/BMMCs group was higher than that in the FGS group. The addition of TCP increased the degradation rate of PCL to a suitable range. The experimental results also showed that more new bone was formed in the bone tunnel in the FGS group than in the CD group, and the FGS/BMMCS group had the newest bone of each group. The results indicated that both FGS and FGS/BMMCS could promote bone regeneration in the area of osteonecrosis (**Figures 7B,C**).

### Poly(Lactic Acid)

Lactic acid, the precursor of poly (lactic acid) (PLA), is non-toxic to humans. PLA is also one of the most widely used synthetic polymers approved by the FDA for biomedical purposes (Abdalhay et al., 2013; Zhao et al., 2019b; Zhao et al., 2021). Wang et al. (2019a) combined PLA, nano-hydroxyapatite, and collagen PLA to establish a nano-hydroxyapatite/collagen I/poly-L-lactic acid composite scaffold (nHAC/PLA). The BMMSC were cultured on the composite scaffold and implanted into the necrotic femoral head after CD in the ANFH rabbit model (**Figure 8A**). The researchers observed the adhesion of BMMCs to the nHAC/PLA scaffold through an electron microscope, which proved the good biocompatibility of the composite scaffold (**Figure 8B**). The experimental results showed that the nHAC/PLA/BMMSC group had the best therapeutic effect in the treatment of osteonecrosis. Micro-CT and histological analysis showed that the nHAC/PLA/BMMSC group produced more new bone tissue than the CD and nHAC/PLA groups, and the degradation rate of the composite scaffold was also the highest in these groups (**Figures 8C,D**).

### Poly(Propylene Fumarate)

In recent years, polypropylene fumarate (PPF) has attracted widespread attention as a promising biodegradable, injectable, and non-toxic bone cement material (Lee et al., 2006). Chang et al. (2010) study combined polypropylene fumarate (PPF) and CPC. They also studied the effects of different CPC/PPF ratios on their mechanical properties and cytotoxicity (**Figure 9A**). The results show that as the C/P ratio increases (C/P = 0, C/P = 1 and, C/P = 2), the cytotoxicity of the composite bone cement decreases, and the increase in the CPC ratio also enhances the mechanical strength of the composite bone cement. The bone cement composite material added with ginsenoside Rg1 also has an angiogenic effect (**Figure 9B**). They believe that this newly developed angiogenic bone cement composite material has significant development potential in treating femoral head necrosis.

## FUNCTIONALIZED POLYMER MATERIALS IN OSTEONECROSIS THERAPY

Osteonecrosis is a disease caused by the destruction of blood supply and decreased skeletal cell activity (Guo et al., 2014; Cui et al., 2021; Hines et al., 2021). The reconstruction of bone and blood supply in the necrotic area is the top priority in treating osteonecrosis (Zhu et al., 2020). Previously, researchers injected stem cells (Piuzzi et al., 2017), growth factors (Rackwitz et al., 2012; Peng and Wang, 2017), cytokines (Rackwitz et al., 2012; Peng and Wang, 2017; Yang et al., 2018), various drugs (Feng et al., 2017; Guo et al., 2017; Huang et al., 2018), and hormones (Bakhshi et al., 2012; Zhou et al., 2017) directly into the area of osteonecrosis to explore the role of these biological substances that have osteogenic and vascular functions in promoting the repair of osteonecrosis (Maruyama et al., 2018; Zhang et al., 2019a; Zhu et al., 2020). The researchers have achieved practical results.

However, problems related to biologically active substances such as loss of biological activity, short half-life *in vivo*, heterotopic ossification, and lack of effective support remain to be resolved (Phipps et al., 2016; Shi et al., 2017; Zhang et al., 2018a).

Various polymer scaffolds, gels, and microspheres with biocompatibility, biodegradability, porous structure, and

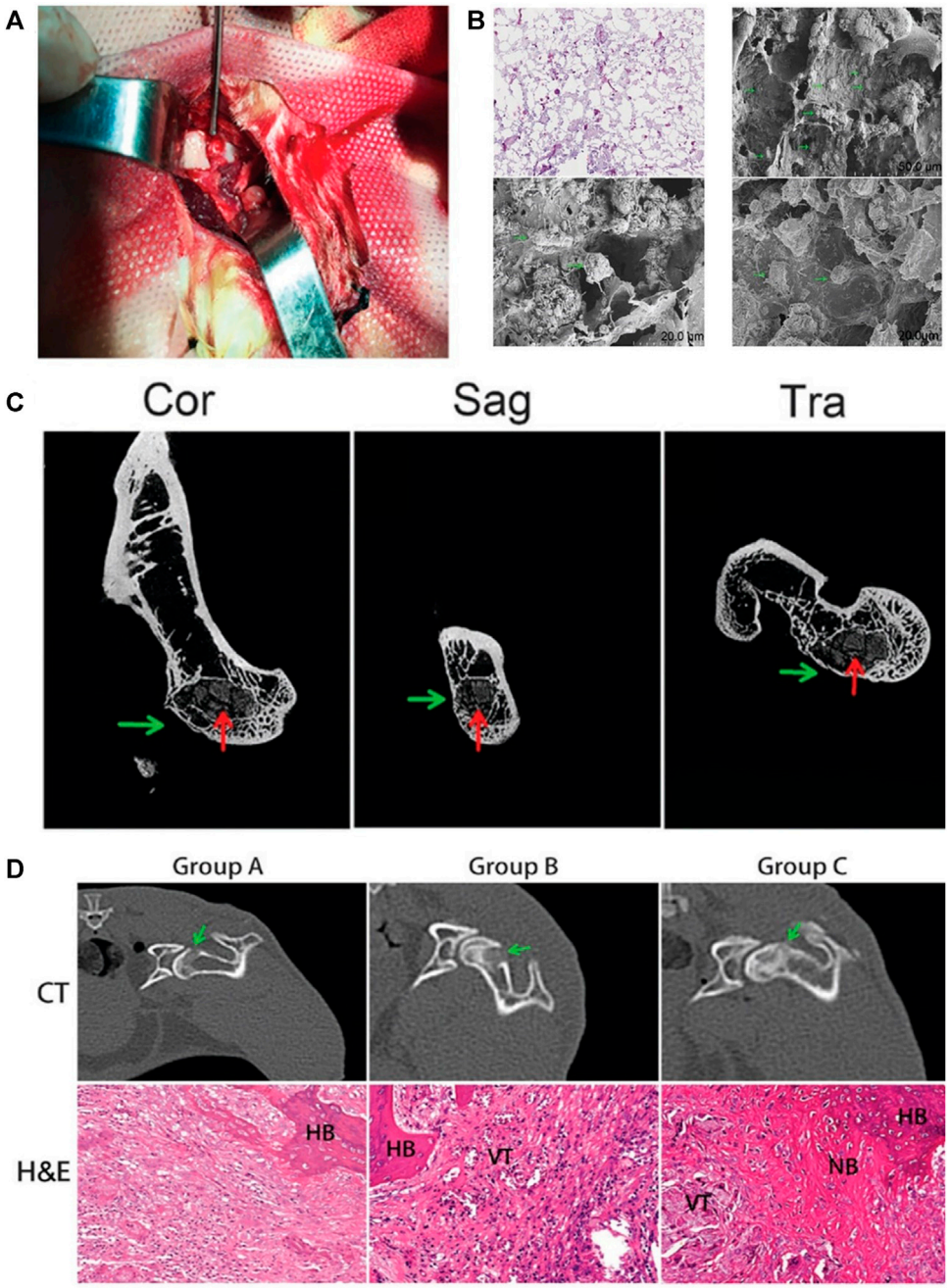


**FIGURE 8 |** PLA-based composite scaffolds may improve the curative effect of CD and provide a strategy for treating ANFH. **(A)** composite scaffolds were implanted into the decompression tunnel. **(B)** A total of 24 h after seeding, hematoxylin and eosin staining and scanning electron microscopy micrographs revealed that BMMSC attach to scaffolds. **(C)** The micro-CT results further showed more bone trabeculae around the decompression tunnel in group C. **(D)** CT images and HE micrographs at 4 weeks post-operation. The CT images suggested that the osteogenesis in the decompression tunnel of group C was significantly higher than that in the other two groups. Histology micrographs of H&E staining of bone tunnels (x200) of the three groups. CT, computerized tomographic scanning; NB, new bone; HB, host bone; VT, vascular tissue; H&E, hematoxylin and eosin. Group A, pure CD; group B, CD + nHAC/PLA; and group C, CD + nHAC/PLA/BMMSC. Reproduced with permission (Wang et al., 2019a). Copyright 2019, Spandidos Publ Ltd.

excellent mechanical support have helped solve the above problems (Zhang et al., 2019a; Zhu et al., 2020). Adding biologically active substances such as stem cells and growth factors to pure polymers to enhance the osteogenesis and angiogenesis function of polymers is considered to be an effective strategy (Zhu et al., 2020). Polymer scaffolds can provide attachment points for biologically active substances, effective support, and slow-release capability, and these

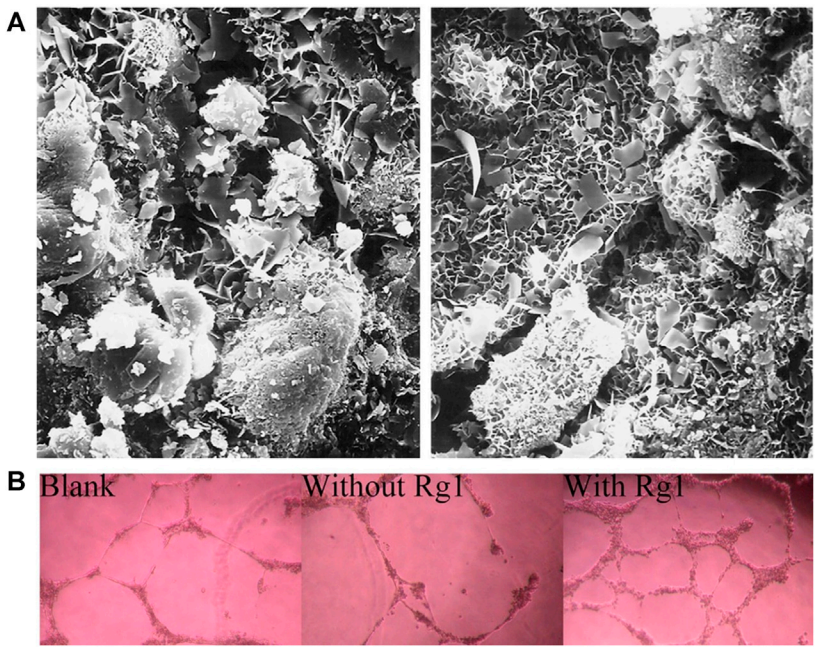


**FIGURE 9 |** The bone cement composite material added with ginsenoside Rg1 to treat osteonecrosis. **(A)** Section morphology observation of the cement in different C/P ratio by scanning electron microscopy. **(B)** Tube formation in different extract-contained media from cements. Reproduced with permission (Chang et al., 2010). Copyright 2010, Elsevier Ltd.

biologically active substances improve the biological activity and mechanical properties of pure polymers. The combination of different biologically active substances [such as stem cells (Fan et al., 2015; Ismail et al., 2017; Peng and Wang, 2017; Maruyama et al., 2018), growth factors (Wang et al., 2009; Garcia et al., 2012; Bai et al., 2014; Phipps et al., 2016; Zhang et al., 2016; Zhu et al., 2017; Chen et al., 2018), small molecule drugs (Tai et al., 2013; Qin et al., 2015; Salarian et al., 2017), metal ions (Salarian et al., 2017; Li et al., 2018a; Lai et al., 2019)] and polymers provides polymers with different functionalities. This strategy has also become a popular area in the research and treatment of osteonecrosis.

## Combination of Polymers and Bioactive Factors With Osteogenesis Function

The addition of bioactive factors with osteogenic function to polymers can enhance the osteogenic properties of polymers, which is conducive to the formation of new bone in the osteonecrosis area and prevents joint collapse and arthritis. Mesenchymal stem cells can differentiate into a variety of cell lines (such as bone cells, osteoblasts, and endothelial cells) (Fan et al., 2015; Hernigou et al., 2015; Sui et al., 2019). Bone marrow mesenchymal stem cells are accessible to culture and expand *in vitro* and accelerate bone regeneration by differentiating into osteoblasts (Le et al., 2020; Song et al., 2020; Zhu et al., 2020; El-Jawhari et al., 2021). Previous studies have shown that bone marrow mesenchymal stem cells secrete a variety of growth factors, cytokines, and other biologically active molecules to regulate the damage and repair process of ischemic tissue after transplantation (Herrmann et al., 2011).

In the study of PCL/TCP FGS (**Figure 7A**) constructed by Maruyama et al. (2018), the FGS/BMMSc group had more new bone formation than the other groups. The FGS/BMMSc group also had a higher FGS degradation rate than the FGS group. It is believed that (Maruyama et al., 2018) this result proves that BMMSc promotes osteogenesis and that proper pretreatment improves the therapeutic effect of bone marrow mesenchymal stem cells. Hypoxic preconditioning induces a compensatory response in bone marrow mesenchymal stem cells by activating endogenous mechanisms, increasing vitality, and reducing cell apoptosis during implantation (Tsai et al., 2012; Fan et al., 2015). Fan et al. (2015) implanted bone marrow mesenchymal stem cells on an absorbable collagen sponge under hypoxic conditions of 2 and 20% oxygen concentration to construct a hypoxic pretreatment functionalized absorbable sponge. They found that, compared with normoxic conditions, hypoxic pretreatment could more effectively overcome the obstacles of cell death *in vitro* and promote the survival and proliferation of bone marrow mesenchymal stem cells *in vitro*.

Some investigators studied SMSC. These cells show the ability to differentiate into bone, cartilage, and fat and can be easily obtained from the joint fluid (Morito et al., 2008). Chen et al. (2014) embedded synovial fluid mesenchymal stem cells (SMSCs) into alginate beads and implanted them into the femoral head of a rabbit model of femoral head necrosis induced by hormones (**Figure 4A**). Through core decompression and ABSMSCs implantation, the density and spherical shape of the femoral head of the rabbit model was maintained, and the bone regeneration within the necrotic femoral head was promoted (**Figures 4B,C**).

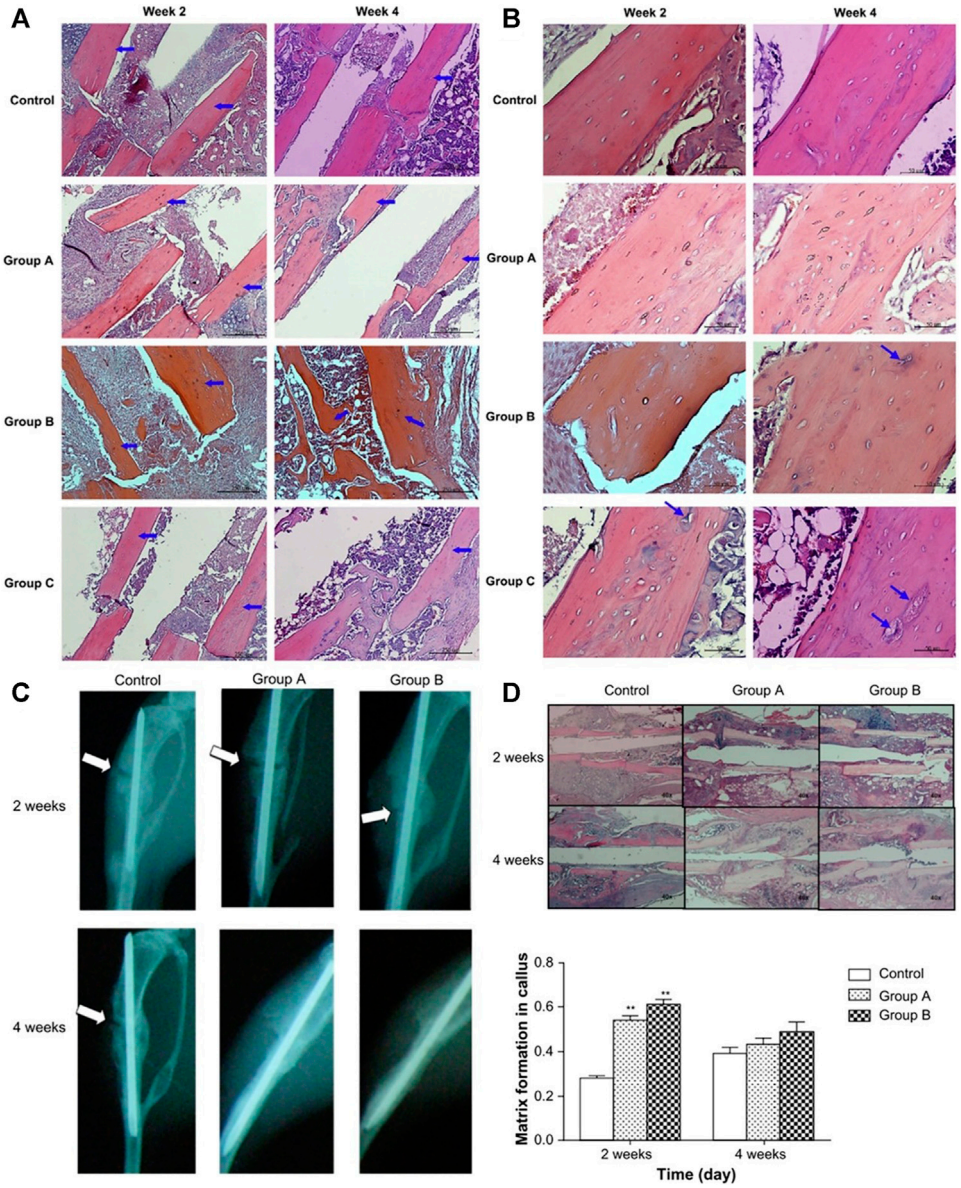


**FIGURE 10 |** Combination of polymers and bioactive factors. Histological specimens from mice tibias were made after 2 and 4 weeks of implantation of different rhBMP-2 carriers (Group A, Group B, Group C) along with control. Original magnification is 400x for **(A)**. Original magnification is 100x for **(B)**. (Group A: 8 mg HAP and 2,500 ng rhBMP-2 within PLGA microspheres, Group B: 1,000 ng rhBMP-2 coating on PLGA microspheres, Group C: 2 mg HAP and 2000 ng rhBMP-2 coating on PLGA microspheres) Blue arrows identify lacunae. (Wang et al., 2009). **(C)** Radiography of mice tibias 2 and 4 weeks after implantation of SIM/PLGA/HAP. No implantation was implanted in the bone fracture of the control group. The meaning of the white arrow has been clarified. (group A, 3 mg SIM/PLGA/HAP; group B, 5 mg SIM/PLGA/HAP) (Tai et al., 2013). **(D)** Hematoxylin-eosin staining and quantification of matrix formation in the callus by Image-Pro Plus. $p < 0.01$ compared with control (Tai et al., 2013). Reproduced with permission (Wang et al., 2009). Copyright 2009, Elsevier Ltd. Reproduced with permission (Tai et al., 2013). Copyright 2013, Dove Medical Press Ltd.

Growth factors can accelerate the differentiation of stem cells into osteoblasts and have been widely used in the study of osteonecrosis (Zuo and Gong, 2012; Zhao et al., 2018b). Among them, the most well-known include bone morphogenetic protein (BMP), vascular endothelial growth factor (VEGF), and BFGF. These factors are often used to transform biological materials. BMP promotes the differentiation of mesenchymal stem cells into osteoblasts in the human body, and is also the main factor in inducing bone and cartilage formation in the body (Ngo et al., 2006; Zhao et al., 2019a). These growth factors are mostly protein structures. In the harsh microenvironment of osteonecrosis, they are susceptible to losing their activity. As a carrier, the polymer scaffold effectively preserves the biological activity of the growth factor, stabilizes the growth factor in the target area, and ensures its release is sustainable (Zhang et al., 2019a; Cui et al., 2020). In addition,

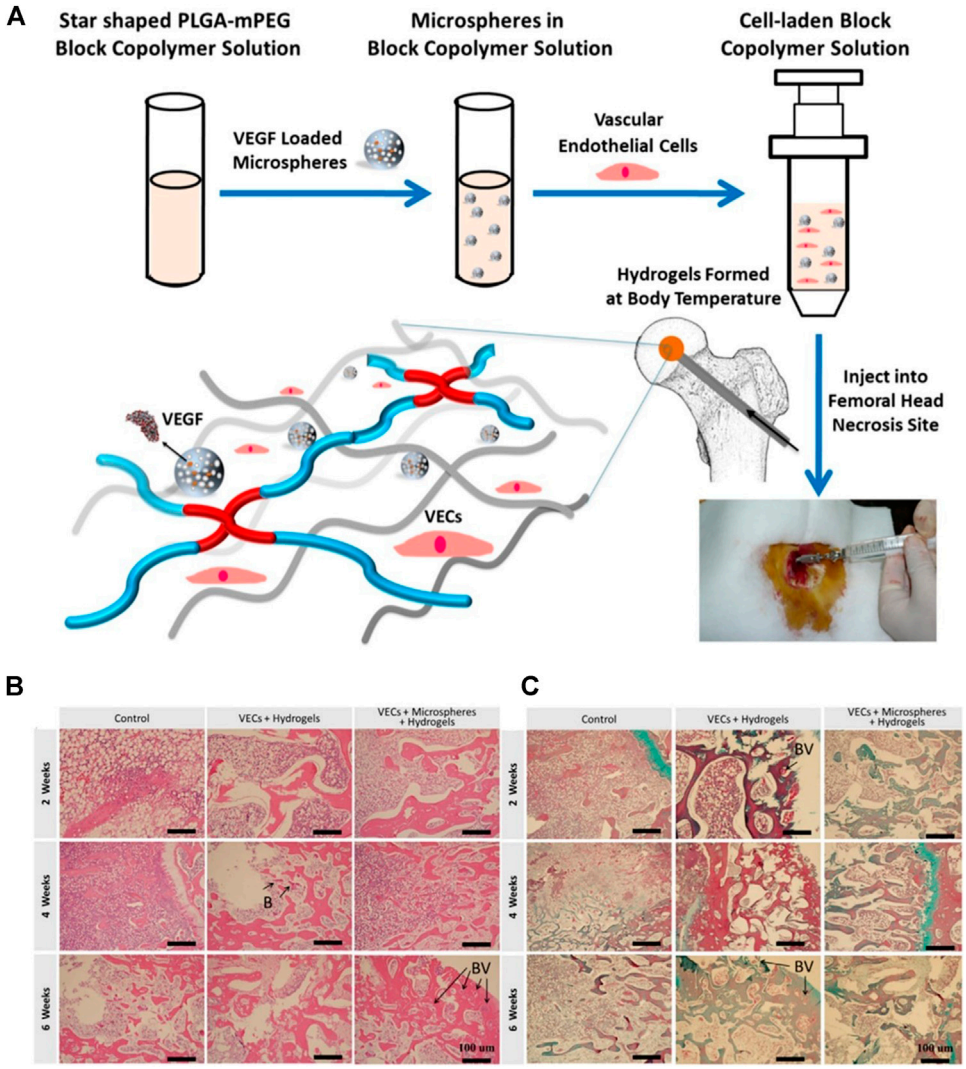


**FIGURE 11 |** Polymer scaffold carrying VEGF is beneficial to vascular regeneration during osteonecrosis. **(A)** Schematic illustration for preparation of injectable hydrogel composite with VEGF loaded microspheres and vascular endothelial cells. Representative histological evaluation of cross sections retrieved at week 2, 4 and 6 after implantation of hydrogels composited with VEGF loaded microspheres. VEGF refers to vascular endothelial growth factor, VECs refers to vascular endothelial cells, **(B)** refers to blood cells, BV refers to blood vessels. The black arrow refers to the position of **(B)** or BV in the figures. Reproduced with permission (Chen et al., 2018). Copyright 2018, Elsevier Ltd.

BMP can stimulate the formation of new blood vessels (van der Bent et al., 2002). Wang et al. (2009) encapsulated BMP-2 in PLGA/hydroxyapatite (HAP) microspheres and found that the microspheres could release a sufficient therapeutic concentration of BMP-2, and the biological activity of BMP-2 was well maintained. The results showed that new bone tissue appeared in the area of osteonecrosis (**Figure 10A**). The addition of BMP therefore improves the osteogenesis of polymers.

Previous studies have shown that oral simvastatin (SIM) has the function of promoting new bone formation in the damaged bone tissue of the human body, but statins are easily degraded during the first liver metabolism (Mundy et al., 1999; Maeda et al., 2001; Song et al., 2003; Baek et al., 2005; Solomon et al., 2005). Tai et al. (2013) took advantage of the biodegradability of PLGA and encapsulated simvastatin in PLGA/HAP composite microspheres to obtain SIM/PLGA/HAP composite microspheres. The SIM/PLGA/HAP composite microspheres have a slow-release function, which effectively avoids rapid loss of simvastatin biological activity in the body. The SIM/PLGA/HAP microspheres were implanted into the osteonecrosis area in a mouse osteonecrosis model, and it was found that the SIM/PLGA/HAP microspheres promoted bone healing in mice and promoted the formation of new bone in the osteonecrosis area (**Figure 10C**). The investigators believed that the SIM/PLGA/HAP system will have a promising future in the treatment of osteonecrosis. Their study also confirmed that statins could promote the repair of osteonecrosis, because the

combination of statins and polymers endows the polymers with osteogenic properties.

## Combination of Polymer and Bioactive Substance With Angiogenesis Function

Sufficient angiogenesis is necessary for the long-term survival of osteoblasts in the necrotic area (Koike et al., 2004; Zhang et al., 2018b). VEGF is considered to be a key regulator of angiogenesis in the process of bone repair (Ferrara et al., 2003). VEGF stimulates the reconstitution of blood supply at the site of necrosis, can induce the adhesion and proliferation of osteoblasts, and also promote the formation of new bone (Bai et al., 2014; Zhang et al., 2016). Chen et al. (2018) loaded VEGF into PLGA copolymer microspheres. VEGF-loaded PLGA copolymer microspheres and vascular endothelial cells (VECs) were composited into to form hydrogels (**Figure 11A**). Then they implanted the hydrogels into the rabbit model of femoral head necrosis. The results showed that the continuous release of VEGF caused a constant increase in new blood vessels, indicating that the polymer carrying VEGF is beneficial to vascular regeneration during osteonecrosis (**Figures 1C**, **11B**).

BFGF, because of its effect on gene expression and angiogenesis, is considered to be a critical factor in the process of bone repair (Hu et al., 2015). used BFGF as a cytokine to transfect BMMSC, co-cultured it with XACB to construct functionalized XACB, and transplanted it into a rabbit model to repair osteonecrosis. The results showed that this method could effectively promote angiogenesis in the avascular necrosis area and significantly improve repair in osteonecrosis.

Some small molecule drugs also promote angiogenesis. The active ingredient of ginseng, ginsenoside Rg1, regulates angiogenesis and stimulates blood vessel formation by up-regulating the expression of nitric oxide and VEGF (Yue et al., 2007). Chang et al. (2010) added Rg1 to a CPC/PPF composite bone cement material, and the results showed that more new blood vessels were formed in the osteonecrotic area when Rg1 bone cement was added (**Figure 9B**). The addition of these bioactive factors with angiogenic activity promotes the angiogenic properties of polymers in osteonecrosis treatment.

## Combination of Polymer and Bioactive Substance With Dual Functions of Osteogenesis and Angiogenesis

Osteogenesis and angiogenesis are the most critical functions of functionalized polymers, and most functionalized polymer bone substitutes are constructed with this goal. The combination of osteogenesis and angiogenesis is more advantageous in osteonecrosis therapy than either process alone. Osteogenesis and angiogenesis are complementary: the new blood vessels provide oxygen and nutrients for the new bone tissue and remove the metabolic waste from the new bone tissue. The pore structure of new bone tissue provides space and mechanical support for new blood vessels.

Many small molecule drugs also promote bone formation and angiogenesis and are cheaper and more stable in the human body than stem cells and growth factors (Lo et al., 2012; Laurencin et al., 2014). Icariin is the active extract of epimedium, which can promote the activity and mineralization of osteoblasts and the formation of capillaries (Yue et al., 2007; Yao et al., 2012; Song et al., 2013; Tang et al., 2015b; Qin et al., 2015). Qin et al. (2015) added icaritin to a PTI composite scaffold. Compared with the simple PLGA/TCP (PT) group, *in vivo* experiments confirmed that the PTI scaffold group had the lowest incidence of femoral head collapse, better cartilage preservation, and more new bone formation in the bone tunnel. Deferoxamine is an iron chelator that stimulates the expression of angiogenic genes and promotes osteogenic differentiation of osteoblasts (Yan et al., 2019). Li et al. (2015) loaded deferoxamine on a gelatin sponge to enhance bone regeneration in patients with osteonecrosis. However, the results showed that the mechanical properties of the composite gel sponge and the sustained release of drugs were insufficient in the repair of osteonecrosis.

Some metal ions (such as strontium (Sr), Mg, and Li) also have dual functions of osteogenesis and angiogenesis, and they are often used in osteonecrosis research. Strontium has a chemical structure similar to calcium and stimulates bone formation, inhibits osteoclast differentiation, and promotes angiogenesis (Bonnelye et al., 2008; Zhao et al., 2018a). Kang et al. (2015) found that a strontium-doped calcium polyphosphate scaffold promotes angiogenesis and osteogenesis in osteonecrosis treatment. As an implantable metal material, Mg has good mechanical properties and biodegradability and can promote bone growth and microvascular expansion. Lai et al. (2019) added Mg to the PT scaffold to make the PTM scaffold, which promoted both osteogenesis and angiogenesis and had the synergistic effect of enhancing the formation of new bone and enhancing the quality of new bone in the rabbit model of osteonecrosis. The PTM scaffold had stronger osteogenic and angiogenic properties than the PT scaffold. Because Li enhances bone formation, promotes vascularization, and inhibits fat production, it has potential value in repairing osteonecrosis (Tang et al., 2015a; Li et al., 2017). As mentioned above, Li et al. (2018a) added Li to the composite scaffold and determined that the composite scaffold has the ability to promote bone formation and vascularization.

Many studies have found that the osteogenesis and angiogenesis functions of various growth factors have a synergistic effect, and their combined application can achieve a better osteonecrosis repair effect than a single growth factor (Garcia et al., 2012; Rackwitz et al., 2012; Bai et al., 2014; Zhang et al., 2016; Peng and Wang, 2017; Zhu et al., 2020). Peng and Wang (2017) transfected BMP-2 and BFGF into BMMSC and then loaded the modified bone marrow mesenchymal stem cells onto DBM. Implanting it into the canine model of ONFH promoted the bone repair effect in the area of osteonecrosis. Zhang et al. (2016) co-loaded BMP and VEGF into PLGA/CPC microspheres. The composite microspheres showed good biocompatibility and promoted bone formation and angiogenesis in animal experiments. Compared with other treatments, more bone and angiogenesis can be seen around the composite microspheres loaded with BMP and VEGF.

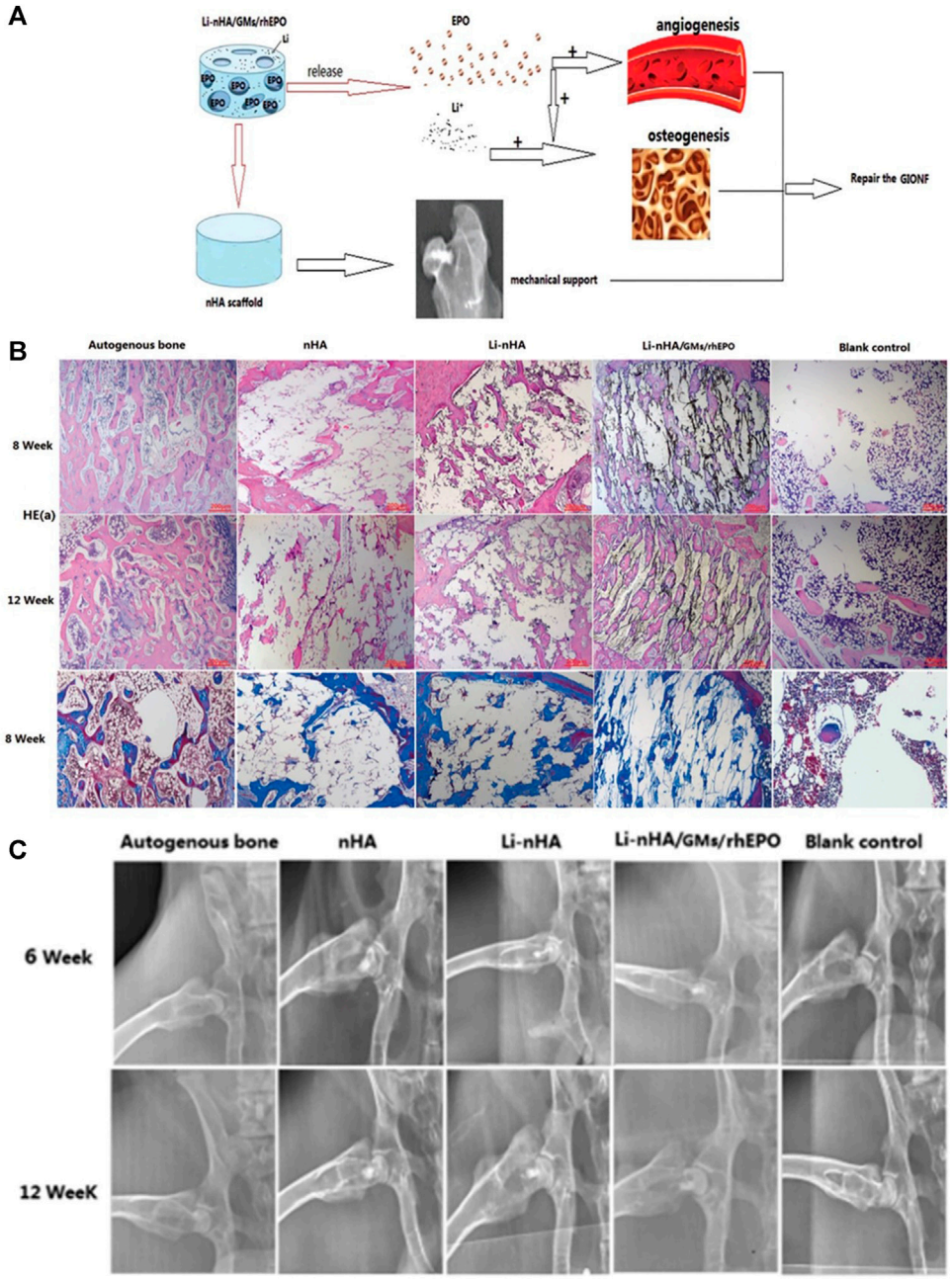


**FIGURE 12 |** Combination of EPO, Li and polymers to treat osteonecrosis. **(A)** Schematic of the composite scaffold design. **(B)** HE staining and Masson staining showing the bone defect repair in the drilling channels. **(C)** X-radiographic examination showing the implants in the femoral head and the morphology of the femoral head. Reproduced with permission (Li et al., 2018a). Copyright 2018, The Royal Society of Chemistry 2018.

EPO is a pleiotropic cytokine that can enhance the function of VEGF and accelerate the differentiation of bone marrow mesenchymal stem cells into osteoblasts. Li et al. (2018a) combined EPO, gelatin, Li, and hydroxyapatite to make a composite scaffold (**Figure 12A**) and evaluated its mechanical properties, release properties, and *in vitro* biological activity. They implanted the scaffold into the femoral head of ONFH rabbits to evaluate the bone formation and angiogenesis ability of the stent *in vivo* and the effect in repairing bone defects. The results showed that the composite scaffold had good mechanical compressive strength. It could continuously release Li and EPO, enhance the formation of new bone and new blood vessel in ONFH rabbits, and had some effect in repairing femoral head necrosis (**Figures 2C**, **12B**).

Many pathological changes occur during the development of osteonecrosis. It is challenging to achieve sufficient therapeutic effects with pure polymer materials. Therefore, functional

polymer materials are being developed. The combination of polymers and biologically active substances achieves targeted therapy and maximizes the effectiveness of each, which is of great significance for the treatment of osteonecrosis.

## CONCLUSION AND FUTURE PERSPECTIVES

Osteonecrosis often affects the articular surface and is especially common in the femoral head. Osteonecrosis that has not been effectively treated will eventually cause the articular surface to collapse, leading to arthritis. The treatment of osteonecrosis has always attracted the attention of the medical community, and various methods have been explored to relieve and treat it. Treatment is mainly divided into two categories, surgical and nonsurgical treatments. At present, the primary clinical treatment is surgery. In the surgical treatment of osteonecrosis, joint replacement surgery is generally considered as a final intervention. Because the life of the artificial joint is limited, it may require multiple revision operations, which undoubtedly increase the pain and economic burden for the patient (Cao et al., 2016). Therefore, investigators continue to explore effective managements for osteonecrosis therapies. One therapy is core decompression combined with bone grafting, which can reduce intramedullary pressure in the necrotic area and trigger revascularization, bone formation, and remodeling by inducing local bone damage. Research on bone graft substitutes has become a significant field of study in osteonecrosis research. With the development of biotechnology and materials science, more potential biomaterials can be used to research osteonecrosis treatment.

A variety of organic and inorganic materials have been studied to treat osteonecrosis (Zhang et al., 2019a; Zhu et al., 2020). Because polymers have advantages over inorganic materials concerning biocompatibility, biodegradability, and mechanical properties, polymers have received more attention than inorganic materials. However, because of the harsh microenvironment of the area of osteonecrosis, pure polymers are not suitable for treating osteonecrosis. The combined application of polymers and various other substances harnesses the advantages of various substances with the strengths of polymers to meet a broader range of requirements in osteonecrosis research. The addition of various substances improves the biological activity and mechanical support performance of pure polymers. Various biologically active substances are added to polymers to produce functionalized polymers. Adding stem cells, growth factors, small molecule drugs, and metal ions to the polymer bone substitute materials endow the polymer with osteogenic and vascular properties that are beneficial in repairing osteonecrosis. Research on functionalized polymer bone substitute materials has become a developing trend.

The relevant experiments mentioned in this review were all carried out in animal models. Animal models of osteonecrosis cannot fully simulate the process of human osteonecrosis. The vast majority of research is limited to animal experiments, and research results cannot soon be translated into clinical practice. Therefore, the development of more ideal animal models for osteonecrosis research is necessary for the future.

The current composites cannot achieve the optimal coordination of various properties, such as the mutual influence between porosity, degradability, and mechanical properties (Zhu et al., 2020). The combined ratio of various materials also affects the properties of composite materials. Future research should mainly focus on improving existing materials and the development of new materials to enhance the properties of various materials.

The reconstruction of human bone tissue is a complex process that involves the synergy of many tissues, cells, and biological factors. We believe that the next step of functionalizing polymer materials should be to add more cells, growth factors, drugs, and other biologically active materials rather than just a few biologically active materials. The interaction between various biologically active factors related to osteonecrosis should also be studied more.

In summary, the creation of various functionalized polymer biomaterials may improve the treatment of osteonecrosis. We believe that future scientific and technological innovations and research can eventually result in significantly better treatment of osteonecrosis.

## AUTHOR CONTRIBUTIONS

HD and TZ contributed equally to this work. HD: Conceptualization, Investigation, Writing—Original Draft, Writing—Review and Editing. TZ: Conceptualization, Investigation, Writing—Review and Editing. Mlz: Conceptualization, Writing—Review and Editing, Supervision, Project administration, Funding acquisition. MrZ: Writing - Review and Editing. DW: Writing—Review and Editing. XW: Writing—Review and Editing. GH: Resources. SW: Writing—Review and Editing.

## FUNDING

This study was financially supported by, the Provincial Health Specific Project of Jilin Province (Grant Nos. 2018SCZ018 and SCZSY201710), the Specific Project for Health Research Talents of Jilin Province (Grant No. 2019SCZ025).

## REFERENCES

Abdal-hay, A., Sheikh, F. A., and Lim, J. K. (2013). Air Jet Spinning of Hydroxyapatite/poly(lactic Acid) Hybrid Nanocomposite Membrane Mats for Bone Tissue Engineering. *Colloids Surf. B: Biointerfaces* 102, 635–643. doi:10.1016/j.colsurfb.2012.09.017

Andronic, O., Weiss, O., Shoman, H., Kriechling, P., and Khanduja, V. (2021). What Are the Outcomes of Core Decompression without Augmentation in Patients with Nontraumatic Osteonecrosis of the Femoral Head? *Int. Orthopaedics (Sicot)* 45 (3), 605–613. doi:10.1007/s00264-020-04790-9

Baek, K. H., Lee, W. Y., Oh, K. W., Tae, H. J., Lee, J. M., Lee, E. J., et al. (2005). The Effect of Simvastatin on the Proliferation and Differentiation of Human Bone Marrow Stromal Cells. *J. Korean Med. Sci.* 20 (3), 438–444. doi:10.3346/jkms.2005.20.3.438

Bai, Y., Leng, Y., Yin, G., Pu, X., Huang, Z., Liao, X., et al. (2014). Effects of Combinations of BMP-2 with FGF-2 And/or VEGF on HUVECs Angiogenesis *In Vitro* and CAM Angiogenesis *In Vivo*. *Cell Tissue Res* 356 (1), 109–121. doi:10.1007/s00441-013-1781-9

Bakhshi, H., Rasouli, M. R., and Parvizi, J. (2012). Can Local Erythropoietin Administration Enhance Bone Regeneration in Osteonecrosis of Femoral Head? *Med. Hypotheses* 79 (2), 154–156. doi:10.1016/j.mehy.2012.04.021

Bhattarai, N., Gunn, J., and Zhang, M. (2010). Chitosan-based Hydrogels for Controlled, Localized Drug Delivery. *Adv. Drug Deliv. Rev.* 62 (1), 83–99. doi:10.1016/j.addr.2009.07.019

Bonnelye, E., Chabadel, A., Saltel, F., and Jurdic, P. (2008). Dual Effect of Strontium Ranelate: Stimulation of Osteoblast Differentiation and Inhibition of Osteoclast Formation and Resorption *In Vitro*. *Bone* 42 (1), 129–138. doi:10.1016/j.bone.2007.08.043

Calder, J. D., Pearse, M. F., and Revell, P. A. (2001). The Extent of Osteocyte Death in the Proximal Femur of Patients with Osteonecrosis of the Femoral Head. *J. Bone Jt. Surg Br.* 83 (3), 419–422. doi:10.1302/0301-620x.83b3.0830419

Cao, H., Guan, H., Lai, Y., Qin, L., and Wang, X. (2016). Review of Various Treatment Options and Potential Therapies for Osteonecrosis of the Femoral Head. *J. Orthopaedic Translation* 4, 57–70. doi:10.1016/j.jot.2015.09.005

Chang, C.-H., Liao, T.-C., Hsu, Y.-M., Fang, H.-W., Chen, C.-C., and Lin, F.-H. (2010). A Poly(propylene Fumarate) - Calcium Phosphate Based Angiogenic Injectable Bone Cement for Femoral Head Osteonecrosis. *Biomaterials* 31 (14), 4048–4055. doi:10.1016/j.biomaterials.2010.01.124

Chen, D., Zhang, C., Huo, H., Ji, C., Sun, M., and Nie, L. (2018). Injectable Temperature-Sensitive Hydrogel with VEGF Loaded Microspheres for Vascularization and Bone Regeneration of Femoral Head Necrosis. *Mater. Lett.* 229, 138–141. doi:10.1016/j.matlet.2018.06.123

Chen, J., Liu, W., Cao, Y., Zhang, X., Guo, Y., Zhu, Y., et al. (2017). MMP-3 and MMP-8 Single-Nucleotide Polymorphisms Are Related to Alcohol-Induced Osteonecrosis of the Femoral Head in Chinese Males. *Oncotarget* 8 (15), 25177–25188. doi:10.18632/oncotarget.15587

Chen, M., Le, D. Q. S., Baatrup, A., Nygaard, J. V., Hein, S., Bjerre, L., et al. (2011). Self-assembled Composite Matrix in a Hierarchical 3-D Scaffold for Bone Tissue Engineering. *Acta Biomater.* 7 (5), 2244–2255. doi:10.1016/j.actbio.2010.12.031

Chen, Y.-P., Chen, W.-C., Wang, K.-C., and Chen, C.-H. (2014). Effectiveness of Synovial Fluid Mesenchymal Stem Cells Embedded in Alginate Beads for Treatment of Steroid-Induced Avascular Necrosis of the Femoral Head. *J. Orthopaedic Sci.* 19 (4), 657–666. doi:10.1007/s00776-014-0568-5

Choi, H.-R., Nam, K.-M., Kim, D.-S., Huh, C.-H., Na, J.-I., and Park, K.-C. (2013). Cervi Cornus Colla (Deer Antler Glue) Induce Epidermal Differentiation in the Reconstruction of Skin Equivalents. *Int. J. Cosmet. Sci.* 35 (3), 281–285. doi:10.1111/ics.12045

Cui, L., Zhang, J., Zou, J., Yang, X., Guo, H., Tian, H., et al. (2020). Electroactive Composite Scaffold with Locally Expressed Osteoinductive Factor for Synergistic Bone Repair upon Electrical Stimulation. *Biomaterials* 230, 119617. doi:10.1016/j.biomaterials.2019.119617

Cui, Q., Jo, W.-L., Koo, K.-H., Cheng, E. Y., Drescher, W., Goodman, S. B., et al. (2021). ARCO Consensus on the Pathogenesis of Non-traumatic Osteonecrosis of the Femoral Head. *J. Korean Med. Sci.* 36 (10), e65. doi:10.3346/jkms.2021.36.e65

Danhier, F., Ansorena, E., Silva, J. M., Coco, R., Le Breton, A., and Préat, V. (2012). PLGA-based Nanoparticles: An Overview of Biomedical Applications. *J. Controlled Release* 161 (2), 505–522. doi:10.1016/j.jconrel.2012.01.043

Deckers, M. M. L., van Bezooijen, R. L., van der Horst, G., Hoogendam, J., van der Bent, C., Papapoulos, S. E., et al. (2002). Bone Morphogenetic Proteins Stimulate Angiogenesis through Osteoblast-Derived Vascular Endothelial Growth Factor A. *Endocrinology* 143 (4), 1545–1553. doi:10.1210/endo.143.4.8719

El-Jawhari, J. J., Ganguly, P., Jones, E., and Giannoudis, P. V. (2021). Bone Marrow Multipotent Mesenchymal Stromal Cells as Autologous Therapy for Osteonecrosis: Effects of Age and Underlying Causes. *Bioengineering* 8 (5), 69. doi:10.3390/bioengineering8050069

Fan, L., Zhang, C., Yu, Z., Shi, Z., Dang, X., and Wang, K. (2015). Transplantation of Hypoxia Preconditioned Bone Marrow Mesenchymal Stem Cells Enhances Angiogenesis and Osteogenesis in Rabbit Femoral Head Osteonecrosis. *Bone* 81, 544–553. doi:10.1016/j.bone.2015.09.005

Feng, X., Li, J., Zhang, X., Liu, T., Ding, J., and Chen, X. (2019). Electrospun Polymer Micro/nanofibers as Pharmaceutical Repositories for Healthcare. *J. Controlled Release* 302, 19–41. doi:10.1016/j.jconrel.2019.03.020

Feng, Z., Zheng, W., Tang, Q., Cheng, L., Li, H., Ni, W., et al. (2017). Fludarabine Inhibits STAT1-Mediated Up-Regulation of Caspase-3 Expression in Dexamethasone-Induced Osteoblasts Apoptosis and Slows the Progression of Steroid-Induced Avascular Necrosis of the Femoral Head in Rats. *Apoptosis* 22 (8), 1001–1012. doi:10.1007/s10495-017-1383-1

Ferrara, N., Gerber, H.-P., and LeCouter, J. (2003). The Biology of VEGF and its Receptors. *Nat. Med.* 9, 669–676. doi:10.1038/nm0603-669

Fonseca-Santos, B., and Chorilli, M. (2017). An Overview of Carboxymethyl Derivatives of Chitosan: Their Use as Biomaterials and Drug Delivery Systems. *Mater. Sci. Eng. C* 77, 1349–1362. doi:10.1016/j.msec.2017.03.198

Gao, M., Zhang, H., Dong, W., Bai, J., Gao, B., Xia, D., et al. (2017). Tissue-engineered Trachea from a 3D-Printed Scaffold Enhances Whole-Segment Tracheal Repair. *Sci. Rep.* 7 (1), 5246. doi:10.1038/s41598-017-05518-3

Garcia, P., Pieruschka, A., Klein, M., Tami, A., Histing, T., Holstein, J. H., et al. (2012). Temporal and Spatial Vascularization Patterns of Unions and Nonunions: Role of Vascular Endothelial Growth Factor and Bone Morphogenetic Proteins. *J. Bone Jt. Surgery-American* 94 (1), 49–58. doi:10.2106/jbjs.J.00795

Goodship, A. E., and Birch, H. L. (2005). Cross Sectional Area Measurement of Tendon and Ligament *In Vitro*: a Simple, Rapid, Non-destructive Technique. *J. Biomech.* 38 (3), 605–608. doi:10.1016/j.jbiomech.2004.05.003

Guo, K. J., Zhao, F. C., Guo, Y., Li, F. L., Zhu, L., and Zheng, W. (2014). The Influence of Age, Gender and Treatment with Steroids on the Incidence of Osteonecrosis of the Femoral Head during the Management of Severe Acute Respiratory Syndrome. *Bone Jt. J.* 96-B (2), 259–262. doi:10.1302/0301-620x.96b2.31935

Guo, P., Gao, F., Wang, Y., Zhang, Z., Sun, W., Jiang, B., et al. (2017). The Use of Anticoagulants for Prevention and Treatment of Osteonecrosis of the Femoral Head. *Medicine* 96 (16), e6646. doi:10.1097/md.0000000000006646

Hernigou, P., Flouzat-Lachaniette, C.-H., Delambre, J., Poignard, A., Allain, J., Chevallier, N., et al. (2015). Osteonecrosis Repair with Bone Marrow Cell Therapies: State of the Clinical Art. *Bone* 70, 102–109. doi:10.1016/j.bone.2014.04.034

Hernigou, P., Hernigou, J., and Scarlat, M. (2020). Shoulder Osteonecrosis: Pathogenesis, Causes, Clinical Evaluation, Imaging, and Classification. *Orthop. Surg.* 12 (5), 1340–1349. doi:10.1111/os.12788

Herrmann, J. L., Abarbanell, A. M., Weil, B. R., Manukyan, M. C., Poynter, J. A., Brewster, B. J., et al. (2011). Optimizing Stem Cell Function for the Treatment of Ischemic Heart Disease. *J. Surg. Res.* 166 (1), 138–145. doi:10.1016/j.jss.2010.05.057

Hines, J. T., Jo, W.-L., Cui, Q., Mont, M. A., Koo, K.-H., Cheng, E. Y., et al. (2021). Osteonecrosis of the Femoral Head: an Updated Review of ARCO on Pathogenesis, Staging and Treatment. *J. Korean Med. Sci.* 36 (24), e177. doi:10.3346/jkms.2021.36.e177

Ho, M.-L., Tai, Y. C., Fu, C. K., Wang, J. K., and Chang, M. L. (2013). Local Delivery of Controlled-Release simvastatin/PLGA/HAp Microspheres Enhances Bone Repair. *Ijn* 8, 3895–3904. doi:10.2147/ijn.S48694

Hu, Y., Zhang, Q., Zhang, L., Tang, X.-X., and He, H.-Y. (2015). Basic Fibroblast Growth Factor Lentiviral Vector-Transfected Sheep Bone Marrow Mesenchymal Stem Cells and Non-specific Osteogenic Gene Expression. *Mol. Med. Rep.* 12 (1), 267–272. doi:10.3892/mmr.2015.3399

Huang, Z., Cheng, C., Cao, B., Wang, J., Wei, H., Liu, X., et al. (2018). Icariin Protects against Glucocorticoid-Induced Osteonecrosis of the Femoral Head in Rats. *Cell Physiol Biochem* 47 (2), 694–706. doi:10.1159/000490023

Ismail, T., Osinga, R., Todorov, A., Haumer, A., Tchang, L. A., Epple, C., et al. (2017). Engineered, Axially-Vascularized Osteogenic Grafts from Human Adipose-Derived Cells to Treat Avascular Necrosis of Bone in a Rat Model. *Acta Biomater.* 63, 236–245. doi:10.1016/j.actbio.2017.09.003

Jones, J. P., Ramirez, S., and Doty, S. B. (1993). The Pathophysiologic Role of Fat in Dysbaric Osteonecrosis. *Clin. Orthopaedics Relat. Res.* 8, 256–264. doi:10.1097/00003086-199311000-00042

Kang, P., Xie, X., Tan, Z., Yang, J., Shen, B., Zhou, Z., et al. (2015). Repairing Defect and Preventing Collapse of Femoral Head in a Steroid-Induced Osteonecrotic of Femoral Head Animal Model Using Strontium-Doped Calcium Polyphosphate Combined BM-MNCs. *J. Mater. Sci. Mater. Med.* 26 (2), 9. doi:10.1007/s10856-015-5402-x

Kargozar, S., Baino, F., Hamzehlou, S., Hill, R. G., and Mozafari, M. (2018). Bioactive Glasses: Sprouting Angiogenesis in Tissue Engineering. *Trends Biotechnol.* 36 (4), 430–444. doi:10.1016/j.tibtech.2017.12.003

Kempen, D. H. R., Lu, L., Hefferan, T. E., Creemers, L. B., Maran, A., Classic, K. L., et al. (2008). Retention of *In Vitro* and *In Vivo* BMP-2 Bioactivities in Sustained Delivery Vehicles for Bone Tissue Engineering. *Biomaterials* 29 (22), 3245–3252. doi:10.1016/j.biomaterials.2008.04.031

Kim, J., Jeong, H.-S., Li, H., Baek, K. J., Kwon, N. S., Yun, H.-Y., et al. (2013). Effects of Cervi Cornus Colla (Deer Antler Glue) in the Reconstruction of a Skin Equivalent Model. *Arch. Dermatol. Res.* 305 (1), 85–89. doi:10.1007/s00403-012-1283-8

Kohgo, T., Yamada, Y., Ito, K., Yajima, A., Yoshimi, R., Okabe, K., et al. (2011). Bone Regeneration with Self-Assembling Peptide Nanofiber Scaffolds in Tissue Engineering for Osseointegration of Dental Implants. *Int. J. Periodontics Restorative Dent* 31 (4), e9–16. doi:10.4012/dmj.2011-028

Koike, N., Fukumura, D., Gralla, O., Au, P., Schechner, J. S., and Jain, R. K. (2004). Creation of Long-Lasting Blood Vessels. *Nature* 428 (6979), 138–139. doi:10.1038/428138a

Kumari, A., Yadav, S. K., and Yadav, S. C. (2010). Biodegradable Polymeric Nanoparticles Based Drug Delivery Systems. *Colloids Surf. B: Biointerfaces* 75 (1), 1–18. doi:10.1016/j.colsurfb.2009.09.001

Kutlusoy, T., Oktay, B., Apohan, N. K., Süleymanoğlu, M., and Kuruca, S. E. (2017). Chitosan-co-Hyaluronic Acid Porous Cryogels and Their Application in Tissue Engineering. *Int. J. Biol. Macromolecules* 103, 366–378. doi:10.1016/j.ijbiomac.2017.05.067

Lai, Y., Cao, H., Wang, X., Chen, S., Zhang, M., Wang, N., et al. (2018). Porous Composite Scaffold Incorporating Osteogenic Phytomolecule Icariin for Promoting Skeletal Regeneration in Challenging Osteonecrotic Bone in Rabbits. *Biomaterials* 153, 1–13. doi:10.1016/j.biomaterials.2017.10.025

Lai, Y., Li, Y., Cao, H., Long, J., Wang, X., Li, L., et al. (2019). Osteogenic Magnesium Incorporated into PLGA/TCP Porous Scaffold by 3D Printing for Repairing Challenging Bone Defect. *Biomaterials* 197, 207–219. doi:10.1016/j.biomaterials.2019.01.013

Lam, C. X. F., Hutmacher, D. W., Schantz, J.-T., Woodruff, M. A., and Teoh, S. H. (2009). Evaluation of Polycaprolactone Scaffold Degradation for 6 Monthsin Vitroandin Vivo. *J. Biomed. Mater. Res.* 90A (3), 906–919. doi:10.1002/jbm.a.32052

Laurencin, C. T., Ashe, K. M., Henry, N., Kan, H. M., and Lo, K. W.-H. (2014). Delivery of Small Molecules for Bone Regenerative Engineering: Preclinical Studies and Potential Clinical Applications. *Drug Discov. Today* 19 (6), 794–800. doi:10.1016/j.drudis.2014.01.012

Le, H., Xu, W., Zhuang, X., Chang, F., Wang, Y., and Ding, J. (2020). Mesenchymal Stem Cells for Cartilage Regeneration. *J. Tissue Eng.* 11, 204173142094383. doi:10.1177/2041731420943839

Lee, J.-S., Hong, J. M., Jung, J. W., Shim, J.-H., Oh, J.-H., and Cho, D.-W. (2014b). 3D Printing of Composite Tissue with Complex Shape Applied to Ear Regeneration. *Biofabrication* 6 (2), 024103. doi:10.1088/1758-5082/6/2/024103

Lee, J. H., Baek, H.-R., Lee, K. M., Lee, H.-K., Im, S. B., Kim, Y. S., et al. (2014a). The Effect of Poloxamer 407-based Hydrogel on the Osteoinductivity of Demineralized Bone Matrix. *Clin. Orthop. Surg.* 6 (4), 455–461. doi:10.4055/cios.2014.6.4.455

Lee, K.-W., Wang, S., Lu, L., Jabbari, E., Currier, B. L., and Yaszemski, M. J. (2006). Fabrication and Characterization of Poly(propylene Fumarate) Scaffolds with Controlled Pore Structures Using 3-dimensional Printing and Injection Molding. *Tissue Eng.* 12 (10), 2801–2811. doi:10.1089/ten.2006.12.2801

Li, C., Zhao, H., Liu, Z., and McMahon, C. (2014). Deer Antler - A Novel Model for Studying Organ Regeneration in Mammals. *Int. J. Biochem. Cel Biol.* 56, 111–122. doi:10.1016/j.biocel.2014.07.007

Li, D., Xie, X., Yang, Z., Wang, C., Wei, Z., and Kang, P. (2018a). Enhanced Bone Defect Repairing Effects in Glucocorticoid-Induced Osteonecrosis of the Femoral Head Using a Porous Nano-Lithium-Hydroxyapatite/gelatin Microsphere/erythropoietin Composite Scaffold. *Biomater. Sci.* 6 (3), 519–537. doi:10.1039/c7bm00975e

Li, J., Fan, L., Yu, Z., Dang, X., and Wang, K. (2015). The Effect of Deferoxamine on Angiogenesis and Bone Repair in Steroid-Induced Osteonecrosis of Rabbit Femoral Heads. *Exp. Biol. Med. (Maywood)* 240 (2), 273–280. doi:10.1177/1535370214553906

Li, L., Peng, X., Qin, Y., Wang, R., Tang, J., Cui, X., et al. (2017). Acceleration of Bone Regeneration by Activating Wnt/β-Catenin Signalling Pathway via Lithium Released from Lithium Chloride/calcium Phosphate Cement in Osteoporosis. *Sci. Rep.* 7, 45204. doi:10.1038/srep45204

Li, Y., Duan, J., Guo, T., Xie, W., Yan, S., Li, B., et al. (2009). *In Vivo* pharmacokinetics Comparisons of Icariin, Emodin and Psoralen from Gan-kang Granules and Extracts of Herba Epimedii, Nepal Dock Root, Ficus Hirta Yahl. *J. Ethnopharmacology* 124 (3), 522–529. doi:10.1016/j.jep.2009.05.008

Li, Z., Yang, B., Weng, X., Tse, G., Chan, M. T. V., and Wu, W. K. K. (2018b). Emerging Roles of MicroRNAs in Osteonecrosis of the Femoral Head. *Cell Prolif* 51 (1), 6. doi:10.1111/cpr.12405

Lo, K. W.-H., Ashe, K. M., Kan, H. M., and Laurencin, C. T. (2012). The Role of Small Molecules in Musculoskeletal Regeneration. *Regenerative Med.* 7 (4), 535–549. doi:10.2217/rme.12.33

Lord, C. F., Gebhardt, M. C., Tomford, W. W., and Mankin, H. J. (1988). Infection in Bone Allografts. Incidence, Nature, and Treatment. *J. Bone Jt. Surg.* 70 (3), 369–376. doi:10.2106/00004623-198870030-00008

Maeda, T., Matsunuma, A., Kawane, T., and Horiuchi, N. (2001). Simvastatin Promotes Osteoblast Differentiation and Mineralization in MC3T3-E1 Cells. *Biochem. Biophysical Res. Commun.* 280 (3), 874–877. doi:10.1006/bbrc.2000.4232

Majima, T., Funakosi, T., Iwasaki, N., Yamane, S.-T., Harada, K., Nonaka, S., et al. (2005). Alginate and Chitosan Polyion Complex Hybrid Fibers for Scaffolds in Ligament and Tendon Tissue Engineering. *J. Orthopaedic Sci.* 10 (3), 302–307. doi:10.1007/s00776-005-0891-y

Maruyama, M., Nabeshima, A., Pan, C.-C., Behn, A. W., Thio, T., Lin, T., et al. (2018). The Effects of a Functionally-Graded Scaffold and Bone Marrow-Derived Mononuclear Cells on Steroid-Induced Femoral Head Osteonecrosis. *Biomaterials* 187, 39–46. doi:10.1016/j.biomaterials.2018.09.030

Misawa, H., Kobayashi, N., Soto-Gutierrez, A., Chen, Y., Yoshida, A., Rivas-Carrillo, J. D., et al. (2006). PuraMatrix Facilitates Bone Regeneration in Bone Defects of Calvaria in Mice. *Cel Transpl.* 15 (10), 903–910. doi:10.3727/000000006783981369

Mogensen, S. S., Schmiegelow, K., Grell, K., Albertsen, B. K., Wehner, P. S., Kampmann, P., et al. (2017). Hyperlipidemia Is a Risk Factor for Osteonecrosis in Children and Young Adults with Acute Lymphoblastic Leukemia. *Haematologica* 102 (5), e175–e178. doi:10.3324/haematol.2016.160507

Mont, M. A., Jones, L. C., Einhorn, T. A., Hungerford, D. S., and Hari Reddi, A. (1998). Osteonecrosis of the Femoral Head. *Clin. Orthopaedics Relat. Res.* 355 (Suppl. l), S314–S335. doi:10.1097/00003086-199810001-00032

Morito, T., Muneta, T., Hara, K., Ju, Y.-J., Mochizuki, T., Makino, H., et al. (2008). Synovial Fluid-Derived Mesenchymal Stem Cells Increase after Intra-articular Ligament Injury in Humans. *Rheumatology* 47 (8), 1137–1143. doi:10.1093/rheumatology/ken114

Mundy, G., Garrett, R., Harris, S., Chan, J., Chen, D., Rossini, G., et al. (1999). Stimulation of Bone Formation *In Vitro* and in Rodents by Statins. *Science* 286 (5446), 1946–1949. doi:10.1126/science.286.5446.1946

Nakahara, H., Misawa, H., Yoshida, A., Hayashi, T., Tanaka, M., Furumatsu, T., et al. (2010). Bone Repair Using a Hybrid Scaffold of Self-Assembling Peptide PuraMatrix and Polyetheretherketone Cage in Rats. *Cel Transpl.* 19 (6), 791–797. doi:10.3727/096368910X508906

Ngo, T. Q., Scherer, M. A., Zhou, F. H., Foster, B. K., and Xian, C. J. (2006). Expression of Bone Morphogenic Proteins and Receptors at the Injured Growth Plate Cartilage in Young Rats. *J. Histochem. Cytochem.* 54 (8), 945–954. doi:10.1369/jhc.6A6939.2006

Oh, S. (2003). Fabrication and Characterization of Hydrophilic Poly(lactic-Co-Glycolic Acid)/poly(vinyl Alcohol) Blend Cell Scaffolds by Melt-Molding Particulate-Leaching Method. *Biomaterials* 24 (22), 4011–4021. doi:10.1016/s0142-9612(03)00284-9

Pascarella, R., Fantasia, R., Sangiovanni, P., Maresca, A., Massetti, D., Politano, R., et al. (2019). Traumatic Hip Fracture-Dislocation: A Middle-Term Follow up Study and a Proposal of New Classification System of Hip Joint Associated Injury. *Injury* 50, S11–S20. doi:10.1016/j.injury.2019.01.011

Peng, W.-X., and Wang, L. (2017). Adenovirus-Mediated Expression of BMP-2 and BFGF in Bone Marrow Mesenchymal Stem Cells Combined with Demineralized Bone Matrix for Repair of Femoral Head Osteonecrosis in Beagle Dogs. *Cel Physiol Biochem* 43 (4), 1648–1662. doi:10.1159/000484026

Phipps, M. C., Monte, F., Mehta, M., and Kim, H. K. W. (2016). Intraosseous Delivery of Bone Morphogenic Protein-2 Using a Self-Assembling Peptide Hydrogel. *Biomacromolecules* 17 (7), 2329–2336. doi:10.1021/acs.biomac.6b00101

Piuzzi, N. S., Chahla, J., Schrock, J. B., LaPrade, R. F., Pascual-Garrido, C., Mont, M. A., et al. (2017). Evidence for the Use of Cell-Based Therapy for the Treatment of Osteonecrosis of the Femoral Head: A Systematic Review of the Literature. *The J. Arthroplasty* 32 (5), 1698–1708. doi:10.1016/j.arth.2016.12.049

Prabaharan, M., and Mano, J. F. (2004). Chitosan-based Particles as Controlled Drug Delivery Systems. *Drug Deliv.* 12 (1), 41–57. doi:10.1080/10717540590889781

Qazi, T. H., Rai, R., and Boccaccini, A. R. (2014). Tissue Engineering of Electrically Responsive Tissues Using Polyaniline Based Polymers: A Review. *Biomaterials* 35 (33), 9068–9086. doi:10.1016/j.biomaterials.2014.07.020

Qin, L., Yao, D., Zheng, L., Liu, W.-C., Liu, Z., Lei, M., et al. (2015). Phytomolecule Icaritin Incorporated PLGA/TCP Scaffold for Steroid-Associated Osteonecrosis: Proof-Of-Concept for Prevention of Hip Joint Collapse in Bipedal Emus and Mechanistic Study in Quadrupedal Rabbits. *Biomaterials* 59, 125–143. doi:10.1016/j.biomaterials.2015.04.038

Rackwitz, L., Eden, L., Reppenhagen, S., Reichert, J. C., Jakob, F., Walles, H., et al. (2012). Stem Cell- and Growth Factor-Based Regenerative Therapies for Avascular Necrosis of the Femoral Head. *Stem Cel Res. Ther.* 3, 7. doi:10.1186/scrt98

Reed, M. C., Schiffer, C., Heales, S., Mehta, A. B., and Hughes, D. A. (2018). Impact of Sphingolipids on Osteoblast and Osteoclast Activity in Gaucher Disease. *Mol. Genet. Metab.* 124 (4), 278–286. doi:10.1016/j.ymgme.2018.06.007

Rezaeeyazdi, M., Colombani, T., Memic, A., and Bencherif, S. (2018). Injectable Hyaluronic Acid-Co-Gelatin Cryogels for Tissue-Engineering Applications. *Materials* 11 (8), 1374. doi:10.3390/ma11081374

Salarian, M., Xu, W. Z., Bohay, R., Lui, E. M. K., and Charpentier, P. A. (2017). Angiogenic Rg1/Sr-Doped TiO2Nanowire/Poly(Propylene Fumarate) Bone Cement Composites. *Macromol. Biosci.* 17 (2), 1600156. doi:10.1002/mabi.201600156

Severyns, M., and Gayet, L. E. (2021). Aseptic Osteonecrosis of the Femoral Head in Patients with Sickle Cell Anemia. *Morphologie* 105 (349), 94–101. doi:10.1016/j.morpho.2020.08.002

Sheikh, F. A., Ju, H. W., Moon, B. M., Lee, O. J., Kim, J.-H., Park, H. J., et al. (2016). Hybrid Scaffolds Based on PLGA and Silk for Bone Tissue Engineering. *J. Tissue Eng. Regen. Med.* 10 (3), 209–221. doi:10.1002/term.1989

Shi, L., Sun, W., Gao, F., Cheng, L., and Li, Z. (2017). Heterotopic Ossification Related to the Use of Recombinant Human BMP-2 in Osteonecrosis of Femoral Head. *Medicine* 96 (27), e7413. doi:10.1097/md.0000000000007413

Shrivats, A. R., McDermott, M. C., and Hollinger, J. O. (2014). Bone Tissue Engineering: State of the union. *Drug Discov. Today* 19 (6), 781–786. doi:10.1016/j.drudis.2014.04.010

Solomon, D. H., Finkelstein, J. S., Wang, P. S., and Avorn, J. (2005). Statin Lipid-Lowering Drugs and Bone mineral Density. *Pharmacoepidem. Drug Safe.* 14 (4), 219–226. doi:10.1002/pds.984

Song, C., Guo, Z., Ma, Q., Chen, Z., Liu, Z., Jia, H., et al. (2003). Simvastatin Induces Osteoblastic Differentiation and Inhibits Adipocytic Differentiation in Mouse Bone Marrow Stromal Cells. *Biochem. Biophysical Res. Commun.* 308 (3), 458–462. doi:10.1016/s0006-291x(03)01408-6

Song, J. E., Tian, J., Kook, Y. J., Thangavelu, M., Choi, J. H., and Khang, G. (2020). A BMSCs-laden Quercetin/duck's Feet Collagen/hydroxyapatite Sponge for Enhanced Bone Regeneration. *J. Biomed. Mater. Res.* 108 (3), 784–794. doi:10.1002/jbm.a.36857

Song, L., Zhao, J., Zhang, X., Li, H., and Zhou, Y. (2013). Icariin Induces Osteoblast Proliferation, Differentiation and Mineralization through Estrogen Receptor-Mediated ERK and JNK Signal Activation. *Eur. J. Pharmacol.* 714 (1), 15–22. doi:10.1016/j.ejphar.2013.05.039

Stevenson, S., Shaffer, J. W., and Goldberg, V. M. (1996). The Humoral Response to Vascular and Nonvascular Allografts of Bone. *Clin. Orthop. Relat. Res.*, 86–95. doi:10.1097/00003086-199605000-00011

Sui, B.-D., Hu, C.-H., Liu, A.-Q., Zheng, C.-X., Xuan, K., and Jin, Y. (2019). Stem Cell-Based Bone Regeneration in Diseased Microenvironments: Challenges and Solutions. *Biomaterials* 196, 18–30. doi:10.1016/j.biomaterials.2017.10.046

Sung, H.-J., Meredith, C., Johnson, C., and Galis, Z. S. (2004). The Effect of Scaffold Degradation Rate on Three-Dimensional Cell Growth and Angiogenesis. *Biomaterials* 25 (26), 5735–5742. doi:10.1016/j.biomaterials.2004.01.066

Tang, L., Chen, Y., Pei, F., and Zhang, H. (2015a). Lithium Chloride Modulates Adipogenesis and Osteogenesis of Human Bone Marrow-Derived Mesenchymal Stem Cells. *Cel Physiol Biochem* 37 (1), 143–152. doi:10.1159/000430340

Tang, Y., Jacobi, A., Vater, C., Zou, L., Zou, X., and Stiehler, M. (2015b). Icariin Promotes Angiogenic Differentiation and Prevents Oxidative Stress-Induced Autophagy in Endothelial Progenitor Cells. *Stem Cells* 33 (6), 1863–1877. doi:10.1002/stem.2005

Tsai, C. C., Yew, T. L., Yang, D. C., Huang, W. H., and Hung, S. C. (2012). Benefits of Hypoxic Culture on Bone Marrow Multipotent Stromal Cells. *Am. J. Blood Res.* 2 (3), 148–159. doi:10.1186/1479-5876-9-10

Vandermeer, J. S., Kamiya, N., Aya-ay, J., Garces, A., Browne, R., and Kim, H. K. (2011). Local Administration of Ibandronate and Bone Morphogenetic Protein-2 after Ischemic Osteonecrosis of the Immature Femoral Head. *The J. Bone Jt. Surgery-American Volume* 93 (10), 905–913. doi:10.2106/JBJS.J.00716

Wang, C.-K., Ho, M.-L., Wang, G.-J., Chang, J.-K., Chen, C.-H., Fu, Y.-C., et al. (2009). Controlled-release of rhBMP-2 Carriers in the Regeneration of Osteonecrotic Bone. *Biomaterials* 30 (25), 4178–4186. doi:10.1016/j.biomaterials.2009.04.029

Wang, L., Xu, L., Peng, C., Teng, G., Wang, Y., Xie, X., et al. (2019a). The Effect of Bone Marrow Mesenchymal Stem Cell and Nano-hydroxyapatite/collagen I/poly-L-lactic A-cid S-caffold I-mplantation on the T-reatment of A-vascular N-ecrosis of the F-emoral H-ead in R-abbits. *Exp. Ther. Med.* 18 (3), 2021–2028. doi:10.3892/etm.2019.7800

Wang, P., Li, G., Qin, W., Shi, B., Liu, F.-J., Wang, L.-L., et al. (2019b). Repair of Osteonecrosis of the Femoral Head. *Orthopäde* 48, 213–223. doi:10.1007/s00132-018-03678-2

Wang, X., Lin, M., and Kang, Y. (2019c). Engineering Porous β-Tricalcium Phosphate (β-TCP) Scaffolds with Multiple Channels to Promote Cell Migration, Proliferation, and Angiogenesis. *ACS Appl. Mater. Inter.* 11 (9), 9223–9232. doi:10.1021/acsami.8b22041

Wang, Y., Zhu, W., Xiao, K., Li, Z., Ma, Q., Li, W., et al. (2019). Self-healing and Injectable Hybrid Hydrogel for Bone Regeneration of Femoral Head Necrosis and Defect. *Biochem. biophysical Res. Commun.* 508, 25–30. doi:10.1016/j.bbrc.2018.11.097

Williams, D. F. (2008). On the Mechanisms of Biocompatibility. *Biomaterials* 29 (20), 2941–2953. doi:10.1016/j.biomaterials.2008.04.023

Wu, S., Deng, L., Hsia, H., Xu, K., He, Y., Huang, Q., et al. (2017). Evaluation of Gelatin-Hyaluronic Acid Composite Hydrogels for Accelerating Wound Healing. *J. Biomater. Appl.* 31 (10), 1380–1390. doi:10.1177/0885328217702526

Xu, H., Wang, C., Liu, C., Peng, Z., Li, J., Jin, Y., et al. (2021). Cotransplantation of Mesenchymal Stem Cells and Endothelial Progenitor Cells for Treating Steroid-induced Osteonecrosis of the Femoral Head. *Stem Cell Transl Med* 10 (5), 781–796. doi:10.1002/sctm.20-0346

Yan, Y., Chen, H., Zhang, H., Guo, C., Yang, K., Chen, K., et al. (2019). Vascularized 3D Printed Scaffolds for Promoting Bone Regeneration. *Biomaterials* 190-191, 97–110. doi:10.1016/j.biomaterials.2018.10.033

Yang, F., Xue, F., Guan, J., Zhang, Z., Yin, J., and Kang, Q. (2018). Stromal-Cell-Derived Factor (SDF) 1-Alpha Overexpression Promotes Bone Regeneration by Osteogenesis and Angiogenesis in Osteonecrosis of the Femoral Head. *Cel Physiol Biochem* 46 (6), 2561–2575. doi:10.1159/000489684

Yao, D., Xie, X.-H., Wang, X.-L., Wan, C., Lee, Y.-W., Chen, S.-H., et al. (2012). Icaritin, an Exogenous Phytomolecule, Enhances Osteogenesis but Not Angiogenesis-An *In Vitro* Efficacy Study. *PLOS ONE* 7 (8), e41264. doi:10.1371/journal.pone.0041264

Yokoi, H., Kinoshita, T., and Zhang, S. (2005). Dynamic Reassembly of Peptide RADA16 Nanofiber Scaffold. *Proc. Natl. Acad. Sci.* 102 (24), 8414–8419. doi:10.1073/pnas.0407843102

Yue, P. Y. K., Mak, N. K., Cheng, Y. K., Leung, K. W., Ng, T. B., Fan, D. T. P., et al. (2007). Pharmacogenomics and the Yin/Yang Actions of Ginseng: Anti-tumor, Angiomodulating and Steroid-like Activities of Ginsenosides. *Chin. Med.* 2 (1), 6. doi:10.1186/1749-8546-2-6

Zhang, H.-X., Zhang, X.-P., Xiao, G.-Y., Hou, Y., Cheng, L., Si, M., et al. (2016). *In Vitro* and *In Vivo* Evaluation of Calcium Phosphate Composite Scaffolds Containing BMP-VEGF Loaded PLGA Microspheres for the Treatment of

Avascular Necrosis of the Femoral Head. *Mater. Sci. Eng. C* 60, 298–307. doi:10.1016/j.msec.2015.11.055

Zhang, J., Neoh, K. G., and Kang, E. T. (2018b). Electrical Stimulation of Adipose-derived Mesenchymal Stem Cells and Endothelial Cells Co-cultured in a Conductive Scaffold for Potential Orthopaedic Applications. *J. Tissue Eng. Regen. Med.* 12 (4), 878–889. doi:10.1002/term.2441

Zhang, L., Yang, G., Johnson, B. N., and Jia, X. (2019a). Three-dimensional (3D) Printed Scaffold and Material Selection for Bone Repair. *Acta Biomater.* 84, 16–33. doi:10.1016/j.actbio.2018.11.039

Zhang, S., Holmes, T., Lockshin, C., and Rich, A. (1993). Spontaneous Assembly of a Self-Complementary Oligopeptide to Form a Stable Macroscopic Membrane. *Proc. Natl. Acad. Sci.* 90 (8), 3334–3338. doi:10.1073/pnas.90.8.3334

Zhang, Y., Liu, X., Zeng, L., Zhang, J., Zuo, J., Zou, J., et al. (2019b). Polymer Fiber Scaffolds for Bone and Cartilage Tissue Engineering. *Adv. Funct. Mater.* 29 (36), 1903279. doi:10.1002/adfm.201903279

Zhao, C., Qazvini, N. T., Sadati, M., Zeng, Z., Huang, S., De La Lastra, A. L., et al. (2019a). A pH-Triggered, Self-Assembled, and Bioprintable Hybrid Hydrogel Scaffold for Mesenchymal Stem Cell Based Bone Tissue Engineering. *ACS Appl. Mater. Inter.* 11 (9), 8749–8762. doi:10.1021/acsami.8b19094

Zhao, D., Zhu, T., Li, J., Cui, L., Zhang, Z., Zhuang, X., et al. (2021). Poly(lactic-co-glycolic Acid)-Based Composite Bone-Substitute Materials. *Bioactive Mater.* 6 (2), 346–360. doi:10.1016/j.bioactmat.2020.08.016

Zhao, F., Lei, B., Li, X., Mo, Y., Wang, R., Chen, D., et al. (2018a). Promoting *In Vivo* Early Angiogenesis with Sub-micrometer Strontium-Contained Bioactive Microspheres through Modulating Macrophage Phenotypes. *Biomaterials* 178, 36–47. doi:10.1016/j.biomaterials.2018.06.004

Zhao, L., Kaye, A. D., Kaye, A. J., and Abd-Elsayed, A. (2018b). Stem Cell Therapy for Osteonecrosis of the Femoral Head: Current Trends and Comprehensive Review. *Curr. Pain Headache Rep.* 22 (6), 9. doi:10.1007/s11916-018-0700-x

Zhao, X., Han, Y., Zhu, T., Feng, N., Sun, Y., Song, Z., et al. (2019b). Electrospun Polylactide-Nano-HydroxyapatiteVancomycin Composite Scaffolds for Advanced Osteomyelitis Therapy. *J Biomed. Nanotechnol* 15 (6), 1213–1222. doi:10.1166/jbn.2019.2773

Zheng, L.-z., Cao, H.-j., Chen, S.-h., Tang, T., Fu, W.-m., Huang, L., et al. (2015). Blockage of Src by Specific siRNA as a Novel Therapeutic Strategy to Prevent Destructive Repair in Steroid-Associated Osteonecrosis in Rabbits. *J. Bone Miner Res.* 30 (11), 2044–2057. doi:10.1002/jbmr.2542

Zhou, C.-h., Meng, J.-h., Zhao, C.-c., Ye, C.-y., Zhu, H.-x., Hu, B., et al. (2017). PTH [1-34] Improves the Effects of Core Decompression in Early-Stage Steroid-Associated Osteonecrosis Model by Enhancing Bone Repair and Revascularization. *Plos One* 12 (5), e0178781. doi:10.1371/journal.pone.0178781

Zhou, Z., Pan, C., Wang, N., Zhou, L., Shan, H., Gao, Y., et al. (2019). A High-Fat Diet Aggravates Osteonecrosis through a Macrophage-Derived IL-6 Pathway. *Int. Immunol.* 31, 263–273. doi:10.1093/intimm/dxz002

Zhu, T., Cui, Y., Zhang, M., Zhao, D., Liu, G., and Ding, J. (2020). Engineered Three-Dimensional Scaffolds for Enhanced Bone Regeneration in Osteonecrosis. *Bioactive Mater.* 5 (3), 584–601. doi:10.1016/j.bioactmat.2020.04.008

Zhu, W., Zhao, Y., Ma, Q., Wang, Y., Wu, Z., and Weng, X. (2017). 3D-printed Porous Titanium Changed Femoral Head Repair Growth Patterns: Osteogenesis and Vascularisation in Porous Titanium. *J. Mater. Sci. Mater. Med.* 28 (4), 11. doi:10.1007/s10856-017-5862-2

Zuo, S., and Gong, Y. (2012). Application and Prospects of Bone Marrow Mesenchymal Stem Cells and Cytokines in the Treatment of Femoral Head Necrosis. *Chin. J. Tissue Eng. Res.* 16 (14), 2621–2624. doi:10.3969/j.issn.1673-8225.2012.14.030

**Conflict of Interest:** The authors declare that the research was conducted in the absence of any commercial or financial relationships that could be construed as a potential conflict of interest.

**Publisher's Note:** All claims expressed in this article are solely those of the authors and do not necessarily represent those of their affiliated organizations, or those of the publisher, the editors and the reviewers. Any product that may be evaluated in this article, or claim that may be made by its manufacturer, is not guaranteed or endorsed by the publisher.

frontiers in Bioengineering and Biotechnology

ORIGINAL RESEARCH
published: 11 October 2021
doi: 10.3389/fbioe.2021.752506

# A Rapid and Convenient Approach to Construct Porous Collagen Membranes *via* Bioskiving and Sonication-Feasible for Mineralization to Induce Bone Regeneration

*Zhenzhen Wu*[1], *Juan Zhong*[2], *Yingjie Yu*[3], *Mingdeng Rong*[1]* *and Tao Yang*[2]*

[1]Department of Periodontology and Implantology, Stomatological Hospital, Southern Medical University, Guangzhou, China, [2]Hospital of Stomatology, Guangdong Provincial Key Laboratory of Stomatology, Institute of Stomatological Research, Guanghua School of Stomatology, Sun Yat-sen University, Guangzhou, China, [3]Department of Biomedical Engineering, Tufts University, Boston, MA, United States

OPEN ACCESS

**Edited by:**
Guicai Li,
Nantong University, China

**Reviewed by:**
Xibo Pei,
Sichuan University, China
Lin Wang,
Jilin University, China
Xiangning Liu,
Jinan University, China

***Correspondence:**
Mingdeng Rong
rmdeng@smu.edu.cn
Tao Yang
ytdentist@outlook.com

**Specialty section:**
This article was submitted to Biomaterials, a section of the journal Frontiers in Bioengineering and Biotechnology

**Received:** 03 August 2021
**Accepted:** 08 September 2021
**Published:** 11 October 2021

**Citation:**
Wu Z, Zhong J, Yu Y, Rong M and Yang T (2021) A Rapid and Convenient Approach to Construct Porous Collagen Membranes via Bioskiving and Sonication-Feasible for Mineralization to Induce Bone Regeneration. Front. Bioeng. Biotechnol. 9:752506. doi: 10.3389/fbioe.2021.752506

Porous mineralized collagen membranes efficiently promote bone regeneration. To generate them, we need to fabricate collagen membranes that are porous. However, the current fabrication method is primarily based on a bottom-up strategy, with certain limitations, such as a long manufacturing process, collagen denaturation, and failure to control fibril orientation. Using a top-down approach, we explore a novel method for constructing porous collagen membranes *via* the combined application of bioskiving and sonication. Numerous collagen membranes with well-aligned fibril structures were rapidly fabricated by bioskiving and then sonicated at 30, 60, 90, and 120 W for 20 min. This treatment allowed us to study the effect of power intensity on the physicochemical traits of collagen membranes. Subsequently, the prepared collagen membranes were immersed in amorphous calcium phosphate to evaluate the feasibility of mineralization. Additionally, the bioactivities of the membranes were assessed using preosteoblast cells. Tuning the power intensity was shown to modulate fibril orientation, and the porous membrane without denatured collagen could be obtained by a 20-min sonication treatment at 90 W. The prepared collagen membrane could also be further mineralized to enhance osteogenesis. Overall, this study offers a rapid and convenient approach for fabricating porous collagen membranes *via* bioskiving and sonication.

**Keywords: porous collagen membrane, bioskiving, sonication, mineralization, bone regeneration**

## INTRODUCTION

The clinical treatment of alveolar bone defects caused by periodontitis and trauma has advanced considerably with the use of the guided bone regeneration (GBR) technique. Despite various issues associated with the GBR technique, the GBR membrane has a crucial function (Turri et al., 2016; Wu et al., 2020; Farnezi Bassi et al., 2021; Zhang et al., 2021). Historically, the GBR membrane has aided in stabilizing the blood coagulum and secluding the rapidly proliferating tissue, including the gingival epithelium and connective tissue, thereby creating a suitable environment for osteogenesis (Elgali et al., 2017). Collagen, which has proven biocompatibility and excellent tissue integration (Pei et al., 2021), has received much attention regarding its use in GBR membrane construction (Dacache Neto

et al., 2020; Kapogianni et al., 2021). Currently, the GBR membrane is designed with a dual-layered structure, including the layer facing the mucosa and the layer facing the bone defect (Li P. et al., 2021). Notably, driven by the requirement for superior osteogenic performance, there is an urgent need for a bone defect–faced layer to induce and promote bone regeneration. However, premature biodegradation, poor space maintenance ability, undesirable mechanical properties, and insufficient osteogenic capacity make the collagen membrane imperfect. Moreover, the layer facing the bone defect should provide a favorable microenvironment for regulating the fate of osteogenic-related cells (Chuang et al., 2019). In addition, a suitably porous structure of the membrane is also required to facilitate the new bone formation, which guarantees a good supplement of nutrients and enables osteogenic-related cells to grow (Zhang et al., 2017).

The mineralized collagen fibril is the fundamental building block of natural bone (Liu et al., 2016b; Yang et al., 2020b). Compared with pure collagen, it is characterized by advanced biomechanical properties, desirable biodegradation, and superior bone regeneration ability (Pereira et al., 2020). Therefore, the fabrication of porous architecture based on mineralized collagen fibril has generated increased interest (Qiu et al., 2015; Li Z. et al., 2021), and the resulting membrane has been demonstrated to enhance GBR (Li J. et al., 2021). At present, the fabrication procedure for a porous mineralized collagen membrane mainly involves two key processes. The porous collagen membrane is first manufactured and then subjected to mineralization (Wang et al., 2018). Notably, with an increased understanding of natural mineralization, amorphous calcium phosphate (ACP) has been extensively and successfully employed to mineralize collagen fibril (Liu et al., 2016a; Yang et al., 2020a). As demonstrated previously, the physicochemical and biological properties of the resulting mineralized collagen fibril were highly similar to those of the bone (Liu et al., 2016b). Therefore, a significant requirement for the construction of porous mineralized collagen membranes is the fabrication of a porous collagen membrane.

To date, the porous collagen membrane is constructed *via* a bottom-up strategy. In brief, the collagen-rich tissues (such as the rat tail and bovine tendon) are dissolved in a collagen molecule solution using acid, salt, or enzyme extraction (Ferraro et al., 2017). Subsequently, the collagen molecules are assembled and organized into porous collagen membranes using various techniques like freeze-drying, pH adjustment, or electrospinning (Marelli et al., 2015; Zhang et al., 2018; Salvatore et al., 2021; Zhou et al., 2021). Unfortunately, several drawbacks exist during the preparation of porous collagen membranes. First, the collagen extraction process is relatively slow. It usually takes several days to even a week, and the resulting collagen has a low yield and purity (Ferraro et al., 2017). Second, the enzyme removes telopeptides and the acid partially breaks interchain cross-linkages of collagen during the extraction. This technique partially impairs the stability of subsequently assembled collagen fibrils and leads to the loss of topographical cues (Wan et al., 2021). Third, the electrospinning process can severely denature collagen (Zeugolis et al., 2008). Additionally, the pore size, collagen fibril orientation, and membrane thickness cannot be precisely controlled during the pH adjustment or freeze-drying process, impairing new bone formation and clinical application. The aforementioned deficiencies can be mainly attributed to the bottom-up strategy. Altering this fabrication strategy may provide a feasible approach for addressing this challenge.

Bioskiving is a sectioning-based fabrication approach based on a top-down strategy (Alberti and Xu, 2013; Ghazanfari et al., 2019). Instead of employing collagen molecules as the raw material, bioskiving directly utilizes the bovine tendon to construct the collagen membrane (Alberti and Xu, 2016). Therefore, the problems associated with collagen extraction can be avoided. Moreover, the thickness of the collagen membrane can be precisely controlled using a cryomicrotome (Alberti et al., 2014). In addition, as the tendon is composed of highly aligned collagen bundles, numerous collagen membranes with unidirectional fibril architecture can be rapidly fabricated through bioskiving (Alberti and Xu, 2013). Interestingly, as shown using previous studies, the collagen fibril orientation in the meniscus was mildly disrupted after gentle sonication treatment (Yusof et al., 2019), while disordered organization and denatured collagen fibrils were observed in the semitendinosus muscle following a high-power sonication process (Chang et al., 2012). Thus, we hypothesized that proper sonication treatment could alter the unidirectional pattern of the collagen membrane into a randomly organized pattern without collagen denaturation, resulting in the production of a porous collagen membrane that was appropriate for mineralization.

The present study describes our attempt to explore a novel method to construct porous collagen membranes *via* a combined bioskiving and sonication treatment approach and verify the feasibility of mineralizing the prepared porous collagen membrane (**Figure 1**). A series of collagen membranes were first manufactured *via* bioskiving and subsequently sonicated at various power intensities. Using a systematic characterization approach, the influence of sonication power intensity on the physicochemical properties of the collagen membrane was elucidated. Next, porous mineralized collagen membranes were produced using ACP mineralization, and the physicochemical traits (such as microstructure, crystallinity, and inorganic mass) and bioactivity (using preosteoblast cells) were investigated. We expect that from this study, a promising and feasible approach to fabricate the GBR membrane will be developed.

# MATERIALS AND METHODS

## Fabrication and Characterization of Porous Collagen Membranes

### Construction of Porous Collagen Membranes *via* Bioskiving and Sonication

Collagen membranes with a unidirectional fibril structure were fabricated through bioskiving (Alberti et al., 2015; Yang et al., 2020a). In brief, the bovine Achilles tendons were purchased from

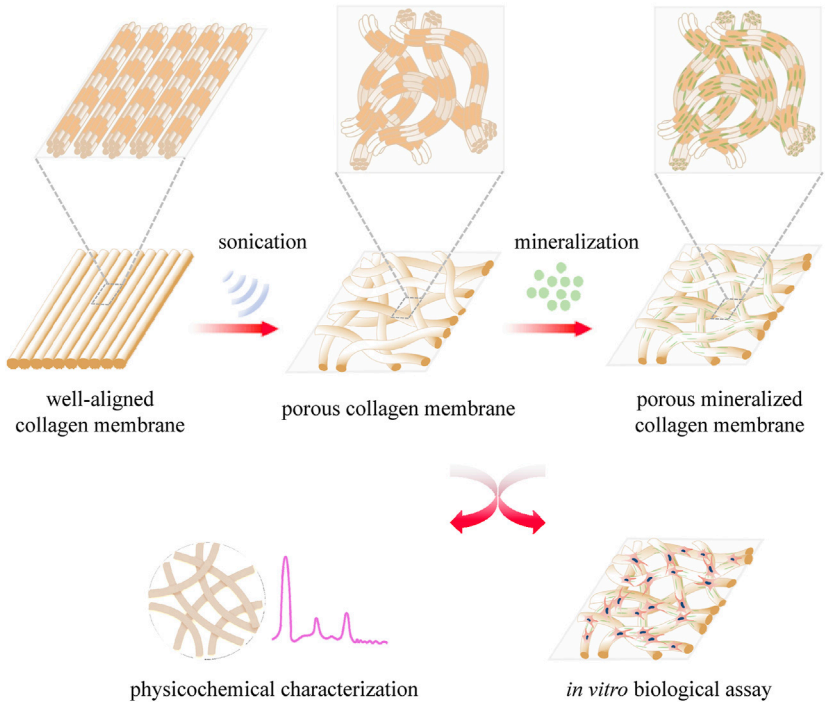


**FIGURE 1 |** Schematic illustration of the construction of porous collagen membranes *via* bioskiving combined with sonication and mineralization treatment.

a slaughter house and trimmed into blocks (approximately 10 mm × 10 mm × 2 mm) before immersion in a decellularization solution, containing sodium dodecyl sulfate (1% w/v), ethylenediaminetetraacetic acid (0.1 mM), and Tris buffer (1 mM). The tendon blocks were vigorously shaken in the decellularization solution for 36 h, and the solution was refreshed every 18 h. After a thorough wash with deionized water, the tendon blocks were sectioned into collagen membranes using a cryomicrotome, and the thickness was precisely maintained at 100 μm. Following repeated washes, the bovine tendon membranes were treated at different sonication powers (30, 60, 90, and 120 W) for 20 min using a sonicator (Lifeng Co., China). During the sonication treatment, the collagen membranes were placed on a polytetrafluoroethylene (PTFE) plate and covered with a glass slide to avoid membrane folding. Ice was supplied to the sonic bath to keep the temperature at around 25°C. Next, the prepared porous collagen membranes were cross-linked by 1-ethyl-3-(3-dimethylaminopropyl)-carbodiimide (0.25 M)/ N-hydroxysuccinimide (0.1 M) for 2 h. The prepared collagen membranes were labeled according to the power intensity of the sonication treatment: 30 W collagen membrane (WCM), 60, 90, and 120 WCM. All the chemical reagents mentioned before were purchased from Xiya (Xiya Reagent Co., Shangdong, China). In addition, gelatin was used as the control to evaluate whether the sonication treatment denatured the collagen and was obtained by placing bioskiving-fabricated bovine tendon membranes into an 80°C water bath for 20 min.

## Scanning Electron Microscopy

A SEM (Quanta 400F) was utilized to evaluate the surface and lateral micromorphology of prepared collagen membranes at an accelerating voltage of 15 kV. The 30, 60, 90, and 120 WCMs were dehydrated in a gradient ethanol solution (50–100%), mounted on a stub, and sputter-coated with gold particles. The diameter and orientation of the collagen fibrils were measured and analyzed by ImageJ software.

## Differential Scanning Calorimetry

DSC (DSC-204 F1) analyses of the 30, 60, 90, and 120 WCMs and gelatin were conducted in a nitrogen atmosphere with temperatures ranging between 100 and 120°C. The heating rate was 5°C/ min.

## Circular Dichroism

CD measurements were conducted by using a Chirascan Plus spectropolarimeter (Applied Photophysics). The samples were prepared by dissolving the porous collagen membrane into hydrochloric acid (pH = 1), and the concentration was 0.4 mg/ ml. The samples were equilibrated for 1 h before the test, and CD spectra were collected from 190 to 240 nm.

## Attenuated Total Reflectance–Fourier Transform Infrared Spectroscopy

The functional group and integrity of the triple helix of the collagen fibril were investigated by the ATR-FTIR

spectrophotometer (Nicolet iN10). The 30, 60, 90, and 120 WCMs were scanned in the range between 400 and 4,000 $cm^{-1}$. The peak ratio of the amide band III to 1,448 $cm^{-1}$ was calculated to evaluate the integrity of the triple helix.

### Atomic Force Microscope

The elasticity modulus of the untreated membrane, 30, 60, 90, and 120 WCMs, and gelatin were characterized by using an AFM (MFP-3D-S). The AFM was tested in an AC mode (tapping mode) at room temperature and atmospheric pressure.

### Surface Wettability Characterization

The water contact angles of membranes were measured by using a contact angle goniometer (Model JY-82). The untreated membrane, 30, 60, 90, and 120 WCMs, and gelatin were stuck to the glass slide. Water droplets dripped at a rate of 2.00 μL/ s onto the membranes.

## Fabrication and Characterization of Porous Mineralized Collagen Membranes

### Construction of Porous Collagen Membranes

A mineralized solution was prepared based on the previously reported method (Yang et al., 2016; Yang et al., 2020b). One gram of carboxymethyl chitosan (CMCS, Xiya Reagent Co.) was dissolved in Tris buffer containing 2,742 mg of $K_2HPO_4$, followed by addition of (drop-by-drop) 2000 mg of $CaCl_2$. The porous collagen membranes were immersed in the mineralized solution and shaken (60 rpm) at room temperature, and the mineralized solution was refreshed every 2 days. After 8 days, the porous mineralized collagen membranes were collected and named according to the power intensity of sonication: 30, 60, 90, and 120 WMCM. Mineralized collagen membranes were washed with deionized water to eliminate the loosely attached minerals and freeze-dried before the physicochemical characterization.

### SEM and Element Analysis

SEM was employed to investigate the microstructure of mineralized collagen membranes at an accelerating voltage of 15 kV. The samples were prepared according to the aforementioned method. The chemical elements were detected by the energy-dispersive spectrum (EDS).

### Transmission Electron Microscopy

TEM (FEI Tecnai G2 Spirit) was used to evaluate the intra- and extrafibrillar mineralization of the 30, 60, 90, and 120 WMCMs. Sample powders were prepared by pulverizing porous mineralized collagen membranes in liquid nitrogen and dispersed in ethanol before dropping onto the 300-mesh copper grid.

### X-Ray Diffractometer and Thermogravimetric Analysis

The crystal structure of 30, 60, 90, and 120 WMCMs was determined by XRD (Empyrean), which was operated at 40 kV and 35 mA. The mineral content of the porous mineralized collagen membranes was investigated using a TGA (TG 209 F1 Libra) under an air atmosphere. The TGA was conducted at a temperature ranging from room temperature to 800°C at a heating rate of 10°C/ min.

## *In Vitro* Biological Assays

### Cell Culture and Proliferation Assay

MC3T3-E1 preosteoblasts were purchased from Procell Life Science and Technology Co., Ltd (Wuhan, China). The cells were cultured in an alpha modified Eagle's medium (αMEM, Gibco, NY, United States) in the presence of 10% fetal bovine serum (FBS, Gibco) and 1% penicillin/streptomycin (Gibco) at 37°C and 5% $CO_2$. The culture medium was refreshed every 2 days. As cells reached approximately 90% confluence, the MC3T3-E1 cells were passaged at a ratio of 1:3 or seeded onto membranes to conduct biological assays. Both collagen membranes (30, 60, 90, and 120 WCM) and mineralized collagen membranes (30, 60, 90, and 120 WMCM) were cut into 6-mm × 6-mm sections before placing in 96-well plates. The membranes were sterilized with 75% ethanol for 1 day and thoroughly washed with PBS.

As for the cell proliferation assay, MC3T3-E1 cells were seeded on the membrane surface (at a density of $1 \times 10^4$) with 100 μL of culture medium. The culture medium was changed every 2 days. On days 1, 3, and 5, cell proliferation was evaluated using the CCK-8 assay kit (Dojindo, Kumamoto, Japan). The culture medium was removed at the determined time, and the membranes were gently rinsed three times with PBS. Subsequently, 90 μL culture medium supplied with 10 μL of CCK-8 reagent was added and incubated for 1 h. Next, the medium was removed, and the optical density (OD) value at 450 nm was observed using the plate reader (Beckman Coulter AD 340). Live/dead cell double staining was performed using the Live/Dead kit (BestBio Science, Shanghai, China) according to the manufacturer's instructions to investigate the morphology and distribution of cells that grew on the membrane. On day 5, the culture medium was aspirated entirely, and the membrane was seeded with MC3T3-E1 cells and carefully washed with PBS. Subsequently, the membranes were subjected to the calcein-AM staining for 30 min, washed with PBS, stained with PI for 30 min, and last washed with PBS. Finally, the membranes were observed using a fluorescence microscope (Leica DM2500 LED). The percentage of live cells and the cell cover area were measured by ImageJ software.

## Osteogenic Differentiation Assay

Membranes were cut into 8-mm × 8-mm sections and placed in 48-well plates, followed by ethanol (75%) sterilization and PBS washing. MC3T3-E1 cells were seeded at a density of $2 \times 10^4$ cells per membrane with 200 μL culture medium. After 2 days, the osteogenic culture medium (MC3T3-E1 culture medium supplemented with 50 μg/ ml ascorbic acid, 10 mM β-glycerol phosphate, and 10 nM dexamethasone) was added and refreshed every 2 days. On day 7, ALP staining was performed. The membranes seeded with cells were rinsed with PBS, fixed by 4% paraformaldehyde, and stained with a BCIP/NBT Alkaline Phosphatase Color Development Kit (Beyotime, Shanghai,

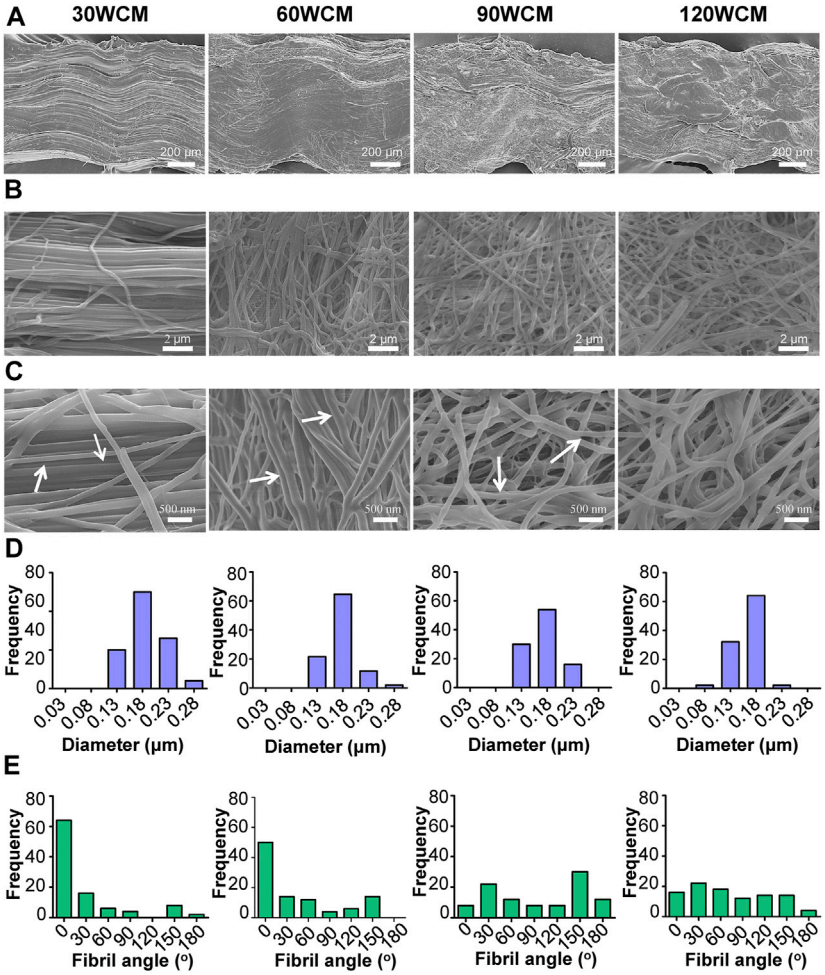


**FIGURE 2 |** Microstructures of prepared collagen membranes. **(A)** SEM images of lateral view. **(B)** Low-magnification SEM images of surface **(C)** High-magnification SEM images of surface (the arrows represent the cross-band structure of collagen fibrils). Corresponding **(D)** fibril diameter distributions and **(E)** fibril orientation distributions of 30, 60, 90, and 120 WCM.

China) for 2 h. Then membranes were observed using a stereomicroscope (Leica S9i). Meanwhile, ALP activity was tested on days 7 and 14. The cells that grew on the membranes were washed three times with PBS and then 100 μL of lysate (Beyotime) was added and kept on ice for 1 h . The ALP activity was further tested using the Alkaline Phosphatase Assay Kit (Beyotime). The results were normalized to the total intracellular protein content determined by the Bicinchoninic Acid Protein Assay Kit (Beyotime). The culture medium was collected on days 14 and 21, and OCN levels were measured using the Osteocalcin ELISA kit (Shanghai Enzyme-linked Biotechnology Co., Ltd, Shanghai, China).

## Statistical Analysis

All the experiments were repeated in triplicate. Data are expressed as mean ± standard deviation. One-way ANOVA and a post hoc Bonferroni t-test were employed to evaluate statistical significance. The significance level was set as $p < 0.05$.

# RESULTS

## Synthesis and Characterization of Porous Collagen Membranes

The microstructure of prepared collagen membranes was investigated by SEM (**Figure 2**). As the sonic power increased, the lateral section view of the collagen membrane changed from the tightly packed orientated pattern to the loosely packed disordered pattern, indicating that fiber orientations inside the membrane could be altered following the sonication treatment (**Figure 2A**). Compared with the well-aligned fibril structure of the untreated bovine tendon membrane (**Supplementary Figure S1B**), only a mild alteration of fibril orientation was observed in the 30 WCM group, and a majority of the fibrils still had a unidirectional organization (**Figure 2B**). Additionally, the periodic cross-band structure was not affected (**Figure 2C**). As the sonic power was increased to 60 W, the pattern of parallel alignment was disrupted to some extent (**Figure 2E**), and several

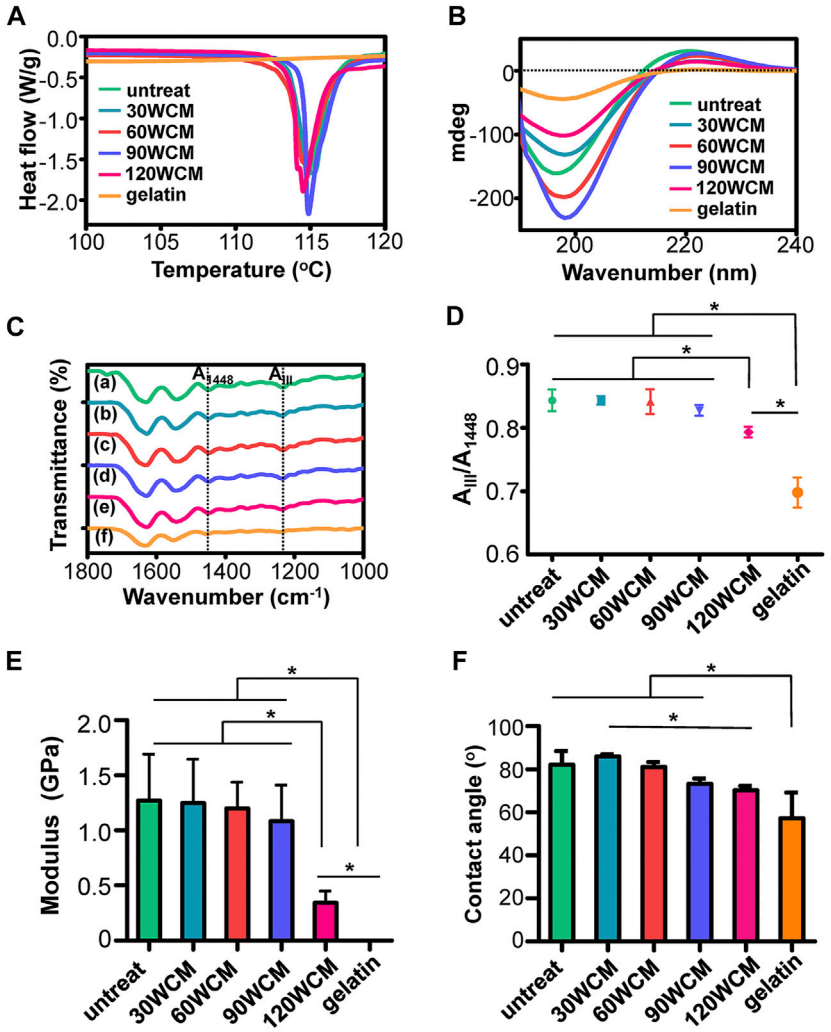


**FIGURE 3 | (A)** DSC and **(B)** CD results of prepared collagen membranes. **(C)** ATR-FTIR spectra, the dotted lines in the ATR-FTIR spectra indicated the peaks at 1,448 $cm^{-1}$ and amide band III, respectively. **(D)** Peak ratio of $A_{III}/A_{1448}$ **(A)** untreated collagen membrane, **(B–E)** 30, 60, 90, and 120 WCM, respectively, and **(F)** gelatin. **(E)** Young's modulus of the prepared collagen membranes. **(F)** The contact angles of water on prepared collagen membranes. The asterisk on top of the bar indicated a statistically significant difference between groups ($p < 0.05$).

micropores were detected. The cross-band structure was also distinctly found in the collagen fibrils. Notably, the alignment of collagen fibrils was disrupted entirely in the 90 WCM. Numerous micropores emerged in this collagen network, and the cross-band structure could also be found in the fibrils. In the 120 WCM group, the collagen membrane still exhibited a porous architecture combined with disordered organization patterns, and the fibril diameter (approximately 0.18 μm) was comparable to that of the 30, 60, and 90 WCM groups (**Figure 2D**). However, the cross-band structure became obscure, which was almost similar to the gelatin group (**Supplementary Figure S1C**).

The thermal stability of prepared collagen membranes was tested by DSC (**Figure 3A**). Contrary to the gelatin group, the endothermic peak, associated with the denaturation from a triple helix to the random coil of collagen (He et al., 2011), could be found in the sonication-treated collagen membranes. **Figure 3B** demonstrates the results of the CD spectra. The gelatin exhibited a single negative peak of lower molar ellipticity, revealing the random conformation of collagen α-chains (Zeugolis et al., 2008). Conversely, the characteristic sinusoidal spectra could be found in the sonication-treated collagen membranes. Notably, the peak intensity of both negative and positive peaks was reduced in the 120 WCM group compared with other groups. To further investigate the influence of sonication power on the collagen fibril structure, ATR-FTIR was conducted to assess the integrity of the triple helix (**Figure 3C**); (He et al., 2011; Marelli et al., 2015). Three typical amide bands associated with collagen could be detected in the untreated bovine tendon membrane. The amide I band at 1,631 $cm^{-1}$ was assigned to the C=O stretching vibration. The amide II band at 1,541 $cm^{-1}$ was related to the N–H bending vibration coupled with the C–N

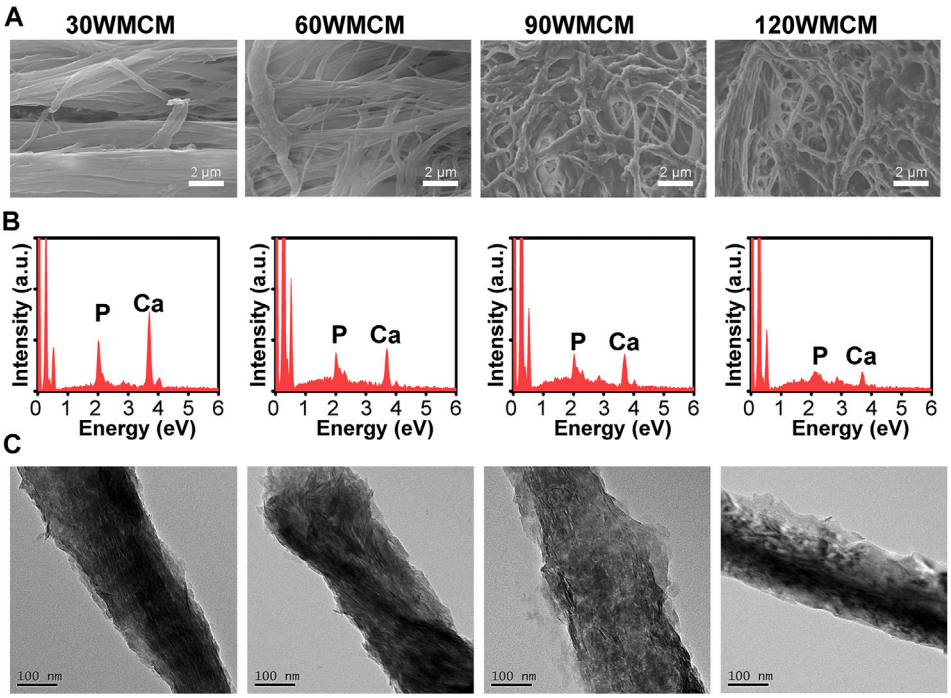


**FIGURE 4 | (A)** SEM images, **(B)** EDS, and **(C)** TEM images of the prepared mineralized collagen membranes.

stretching vibration. The amide III bands at 1,238 $cm^{-1}$ were attributed to N–H bending vibration and C–N stretching. The position and intensity of these amide bands were maintained in the 30, 60, and 90 WCM groups. As reported, the peak ratio of amide band III to 1,448 $cm^{-1}$ was a crucial parameter used to evaluate the integrity of the triple helix (He et al., 2011). **Figure 3D** shows no significant difference among the untreated, 30, 60, and 90 WCM groups, indicating that sonic power (30, 60, and 90 W) could tune the fibril orientation without destroying the triple helix. Although the peak ratio of the 120 WCM group was significantly higher than that of gelatin, this peak ratio was remarkably lower than that of other sonication-treated collagen membranes. The triple helix of the collagen fibril was partially damaged following the 120 W sonication treatment, and this was confirmed using an AFM. **Figure 3E** shows that Young's modulus of the 30, 60, and 90 WCM groups was similar to that of the untreated bovine tendon membrane (approximately 1.2 ± 0.38 GPa). Nevertheless, Young's modulus of the 120 WCM was dramatically reduced to 0.34 ± 0.10 GPa, while Young's modulus of gelatin only reached 0.001 ± 0.0002 GPa. All the prepared collagen membranes exhibited a hydrophilic interface. As the sonic power increased, the water contact angle of prepared collagen membranes gradually decreased (**Figure 3F**).

## Synthesis and Characterization of Porous Mineralized Collagen Membranes

The micromorphology of mineralized collagen membranes was characterized by SEM (**Figure 4A**). Compared with an unmineralized collagen membrane, the pattern of fibril organization was not tremendously altered. The 90 and 120 WMCMs still had a porous network architecture. After mineralization, the periodic cross-band structure almost disappeared, and a rougher collagen fibril surface was obtained. The EDS analyses (**Figure 4B**) verified that these membranes were rich in calcium and phosphate elements, showing that calcium and phosphate were efficiently deposited in the collagen fibril following mineralization. Furthermore, TEM images displayed numerous plate-shaped minerals, intrafibrillarly and extrafibrillarly distributed along the collagen fibril axis in the 30, 60, and 90 WMCM groups. However, minerals were also present in the 120 WMCM group, and the micromorphology of the fibrils was quite different. The fibril contours were indistinct, and this may be ascribed to the partial denaturing of collagen fibrils because of the potent sonication treatment.

To determine the crystallinity of the mineral, an XRD analysis was conducted. **Figure 5A** shows that the typical peaks of hydroxyapatite (32.2° and 25.8°) were detected in the 30, 60, and 90 WMCM groups, suggesting that the minerals deposited inside the collagen fibril were hydroxyapatite and the constructed mineralized collagen fibril was very similar to the bone tissue. The relevant peaks could also be found in the 120 WMCM group. However, the peak intensity was significantly diminished, revealing that the damaged collagen fibrils may not provide sufficient nucleation sites. The inorganic content of the mineralized collagen membranes was determined by TGA (**Figure 5B**). This analysis found that the mineral mass of the 30, 60, and 90 WMCM was 21.10, 21.03, and 19.35%, respectively, whereas the 120 WMCM contained a mineral mass of 12.37%.

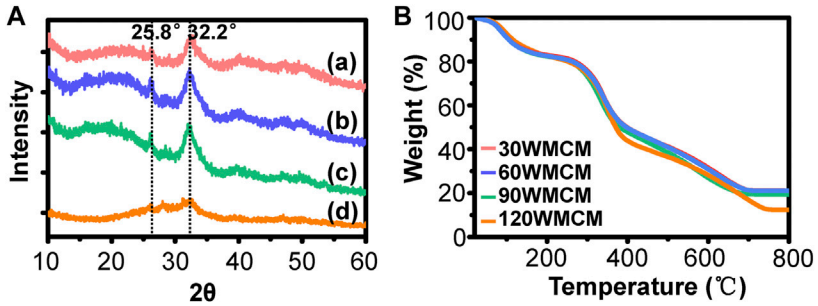


**FIGURE 5 | (A)** XRD and **(B)** TGA results of the prepared mineralized collagen membranes. (a–d) 30, 60, 90, and 120 WMCM, respectively.

## *In Vitro* Biological Assay

To monitor the distribution and viability of cells seeded on the membranes, live/dead cell double staining was conducted (**Figure 6A**). Most cells were viable, and only a few dead cells were observed. The percentage of live cells on each membrane was higher than 90% of all the cells (**Figure 6B**), demonstrating that all the membranes exhibited a desirable cytocompatibility. Meanwhile, the preosteoblasts spread, and growth was linked to the fibril orientation. As the sonication power increased from 30 to 120 W, the cell arrangement changed from almost unidirectional to random distribution. Notably, the cell density and cell cover area (**Figure 6C**) were significantly higher in mineralized collagen membranes than in unmineralized collagen membranes. The proliferation of preosteoblasts on membranes is shown in **Figure 6D**. The number of preosteoblasts from each group increased as the culture time prolonged, demonstrating that the constructed membranes allowed for cell proliferation. On days 3 and 5, the number of preosteoblasts on mineralized collagen membranes was significantly higher than unmineralized collagen membranes, which was consistent with the live/dead cell double staining images.

To analyze the osteogenic differentiation, ALP staining was conducted. **Figure 7A** shows that the ALP expression was significantly enhanced in mineralized collagen membranes compared with unmineralized collagen membranes, revealing that mineralization improved the osteoinduction ability of membranes. Additionally, similar to the live/dead cell double staining, we observed that the cells were arranged in the direction of the fibril orientation. To further qualitatively compare the osteogenic differentiation ability of mineralized and unmineralized collagen membranes, ALP activity and OCN content were measured. Similarly, we observed that mineralized collagen membranes could significantly enhance the ALP activity and promote OCN expression at predetermined time intervals (**Figures 7B,C**).

# DISCUSSION

A disordered architecture of type I collagen, for example, the collagen matrix of the woven bone and the cambium layer of the periosteum, was widely found in humans (Reznikov et al., 2014; Chen et al., 2015). Constructing the disordered architecture of collagen is vitally essential for engineering the biomimetic organ. Type I collagen is abundant in humans, and the triple helix is the primary structure of type I collagen. Under the packing arrangement rule, the triple helices are self-assembled into collagen fibrils that have a periodically banded structure, containing alternating overlap and gap zones (Reznikov et al., 2014; Luo et al., 2021). These topological features are vital for collagen fibrils to give biological cues to cells and provide the templates for mineralization (Liu et al., 2016a). However, the current porous collagen membrane is fabricated using the bottom-up strategy that involves collagen extraction and assembly. Both procedures can damage the topological features of the collagen fibril (Alberti and Xu, 2013). To address this, the top-down strategy, which involves the bioskiving approach, can be used to fabricate the collagen membrane with a well-aligned fibril morphology that avoids potential topological damage to the collagen fibril. The thorough decellularization process could remove the majority of original resident cells, and the collagen membranes fabricated by bioskiving exhibited excellent bioactivities without immunological reaction *in vivo* (Alberti et al., 2014; Alberti et al., 2016). After implantation, the collagen membranes can be degraded by collagenase-1, which belonged to the matrix metalloproteinase family and primarily secreted by fibroblasts, neutrophils, monocytes, macrophages, and endothelial cells. During the tissue healing and under the regulation of growth factors, cytokines, and hormones, the expression of collagenase-1 was enhanced and the collagen membranes were gradually degraded (Alberti and Xu, 2016; Helling et al., 2017). In addition, the acid environment under the inflammation condition could also contribute to the degradation of the collagen membrane. Therefore, the collagen membranes fabricated by bioskiving can be eventually replaced by the regenerated tissue. An increased alteration of this well-aligned fibril organization into a randomly distributed orientation without damaging the collagen fibril topology represents a feasible approach to manufacture the porous collagen membrane. Inspired by the previous study that demonstrated that sonication could change the cellulose pattern arrangement (Wang and Cheng, 2009), the power intensity of sonication was shown to be the crucial factor regulating the collagen fibril orientation. Therefore, we combined bioskiving and sonication treatment to fabricate the porous collagen membrane and

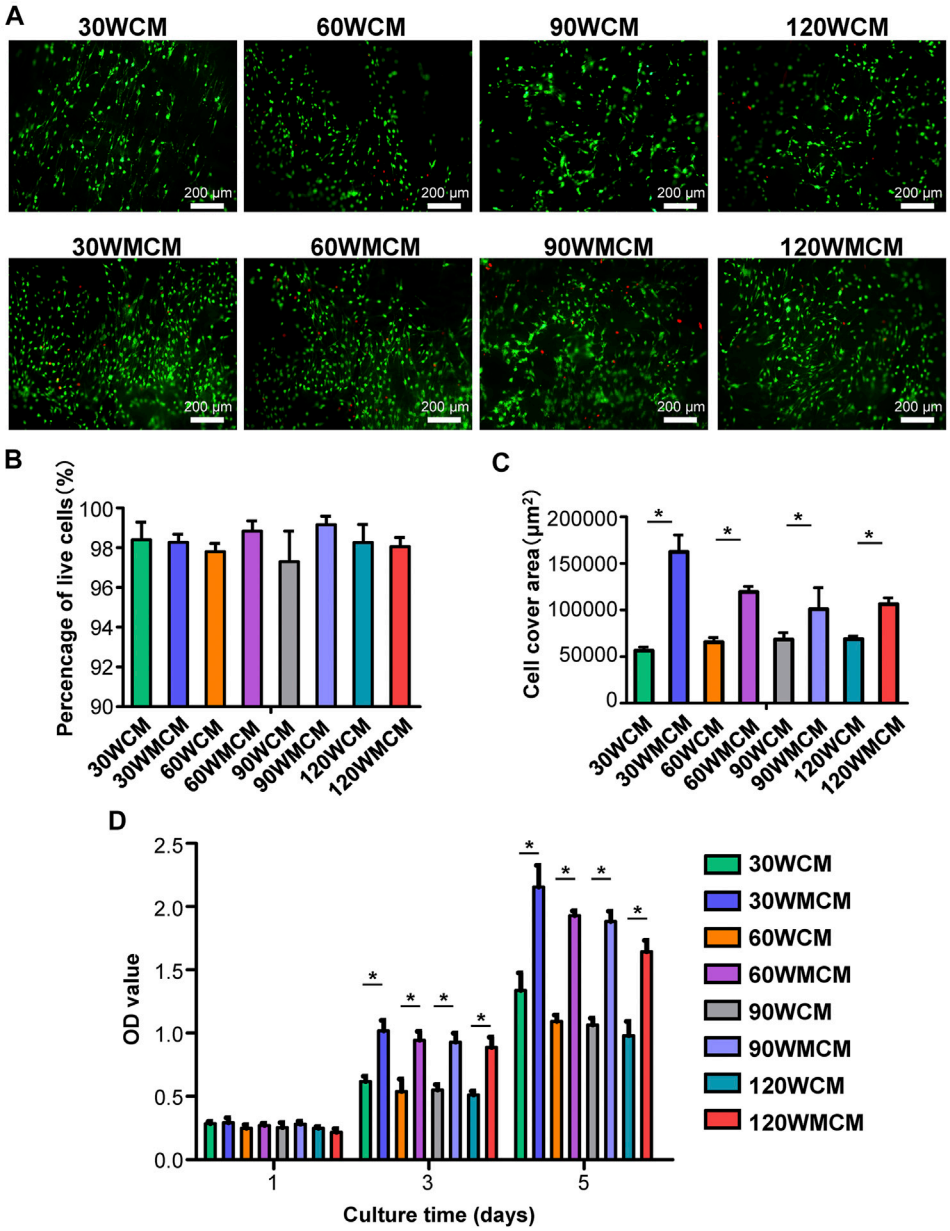


**FIGURE 6 | (A)** Representative live/dead images of cells cultured for 5 days on the unmineralized and mineralized collagen membranes. The live cells were stained green and dead cells were stained red. **(B)** The percentage of live cells and **(C)** cell cover area calculated from live/dead images of cells. **(D)** The CCK-8 results of cell proliferation on days 1, 3, and 5. The asterisk on top of the bar indicates a statistically significant difference between groups ($p < 0.05$).

investigated the effect of power intensity on the physicochemical properties of the collagen membrane.

As the power intensity of sonication increased from 30 to 90 W, the alignment pattern of the collagen fibrils was gradually disrupted, and micropores were also detected in the collagen membrane (**Figure 2B**). The average diameter of the collagen fibril was not significantly altered, whereas the fibril angle was dramatically changed (**Figures 2D,E**). As the power intensity reached 120 W, the collagen membrane still had a disordered pattern, and the fibril angle remained unchanged compared with the 90 W collagen membrane. Based on the previous results, we verified that tuning the power intensity of sonication could regulate the fibril orientation of the collagen membrane, and the porous structure could be rapidly fabricated following a 20-min sonication treatment at 90 W. Notably, high-intensity sonication denatured and destroyed the collagen tissue (Cheng et al., 2010). Therefore, the topological integrity of the collagen fibril was further evaluated. **Figure 2C** shows that a periodic cross-band structure was detected in the 30, 60, and 90 W groups, indicating that the collagen fibril's triple helices were well-

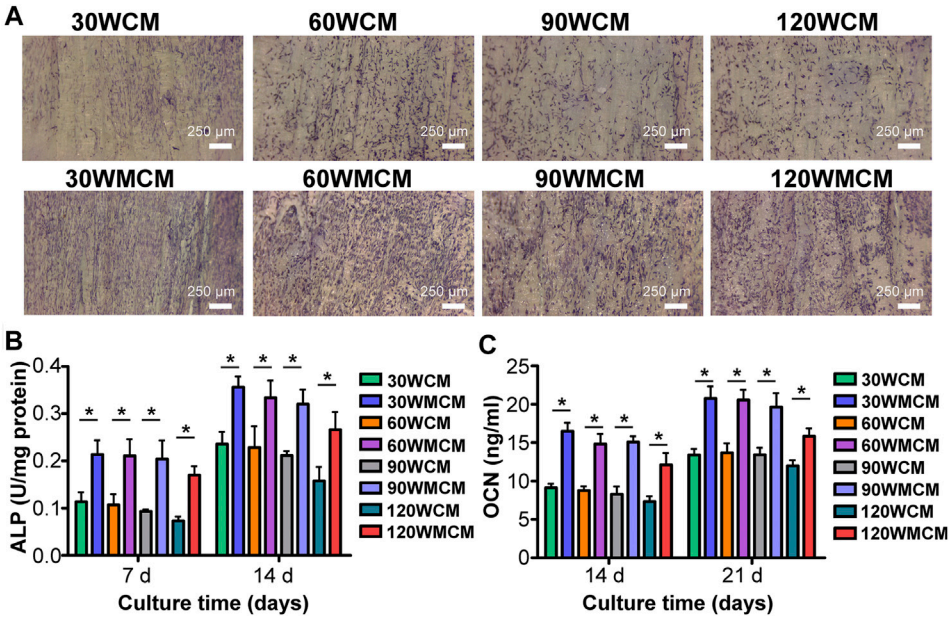


**FIGURE 7 | (A)** Representative images (on day 7) of ALP staining of cells cultured on the unmineralized and mineralized collagen membranes. **(B)** ALP activity and **(C)** OCN content of cells. The asterisk on top of the bar indicated a statistically significant difference between groups ($p < 0.05$).

preserved. However, the cross-band structure became indistinct in the 120 W group. Similarly, the CD and ATR-FTIR results also indicated that the triple helix of the 120 WCM was somewhat damaged (**Figures 3B–D**). Moreover, Young's moduli of the 30 W, 60 W, 90 W, and the untreated groups were significantly higher than those of the 120 W group (**Figure 3E**), demonstrating that the collagen fibril was partially denatured following the 120 W sonication treatment.

The results mentioned before prove that the combined application of bioskiving and adequate sonication treatment is a feasible approach for preparing the porous collagen membrane. Recently, synchronous self-assembly/mineralization (SSM) is an emerging novel approach to fabricate mineralized porous collagen membranes (Lin et al., 2019; Liu et al., 2020). In brief, collagen molecules and amorphous mineral nanoparticles stabilized by the polyampholytes were mixed in the acidic solution. As the pH gradually increased, the mineralized collagen fibrils were generated *via* a self-adaptive interaction. Through this approach, both the construction of a disordered architecture and mineralization can be achieved simultaneously. SSM stands as an innovative and convenient avenue to obtaining a disordered structure of mineralized collagen fibril. Its essence however is still based on the bottom-up strategy. The potential collagen denature cannot be avoided, and the orientation of the fibril cannot be precisely controlled *via* SSM. On the contrary, the combined application of bioskiving and sonication treatment, directed by the top-down strategy, could address the aforementioned deficiencies and represent an alternative method to fabricate the mineralized porous collagen membranes. Using this novel approach, the topological structure of the collagen fibril can be highly preserved. Unlike the collagen extraction and assembly procedures that usually take several days to even a week, bioskiving to fabricate collagen membranes can be completed within 2 days. The porous structure is then obtained by the sonication treatment for an additional 20 min. This approach, which features a rapid and straightforward operation, is particularly appropriate for large-scale production. Additionally, this technique does not require the freeze-drying and pH adjustment technique, and the orientation of the collagen fibril can be easily manipulated by regulating the power intensity of sonication. Overall, these adjustments allow for the various collagen membranes to meet diverse needs.

Porous mineralized collagen membranes are perceived to be promising materials that can promote GBR. Therefore, mineralizing prepared porous collagen membranes is an essential aspect of this study. After immersing porous collagen membranes in ACP, the calcium and phosphate elements were detected in all the groups (**Figure 4B**). Both intra- and extrafibrillar mineralization structures were observed in the 30, 60, and 90 WMCM groups (**Figure 4C**). This experiment demonstrated that collagen membranes fabricated *via* bioskiving and sonication treatment could be mineralized. The porous mineralized collagen membrane could be obtained by mineralizing the 90 W sonication-treated collagen membrane. Although the 120 WMCM exhibited a porous architecture, its mineralization was impaired. As indicated by TEM, XRD, and TGA results (**Figures 4C, 5A,B**), the hierarchy of the mineralized fibril was partially damaged, and the inorganic mass was reduced, confirming that the denatured collagen fibril could not provide a template for crystallization. Furthermore, the porous mineralized collagen membrane was shown to efficiently induce the spread and ingrowth of cells (**Figure 6**). Meanwhile, mineralized collagen membranes significantly promoted the proliferation and osteogenic

differentiation of preosteoblasts (**Figure 7**), which was attributed to the favorable microenvironment (mechanical properties, topographical structures, and released $Ca^{2+}$) provided by mineralized collagen fibrils (Wang et al., 2018). The *in vitro* biological results indicated that our prepared porous mineralized collagen membranes could promote efficient GBR *in vivo*.

## CONCLUSION

Recognizing the drawbacks of porous collagen membranes manufactured using the bottom-up strategy, the present study explored a novel fabrication approach using the combined application of bioskiving and sonication treatment. Using this method, numerous porous collagen membranes were rapidly and easily manufactured, where the collagen fibril orientation was controlled without damaging its topological structure. These porous collagen membranes were further mineralized *via* ACP, and an enhanced osteogenic performance was observed. In this study, we offered an alternative approach for fabricating the porous mineralized collagen membrane for GBR. This fabrication approach could also be employed to build various fundamental structures of the bone (mimicking bone hierarchy), such as the ordered bone (lamellar bone) and the disordered bone (woven bone).

## DATA AVAILABILITY STATEMENT

The raw data supporting the conclusions of this article will be made available by the authors, without undue reservation.

## AUTHOR CONTRIBUTIONS

ZW, MR, and TY contributed substantially to the conception and design of the experiments. ZW and TY conducted experiments and wrote the manuscript. JZ, YY, and MR conducted data analyses. YY and MR revised and modified the draft.

## FUNDING

This research was funded by the Science Research Cultivation Program of Stomatological Hospital, Southern Medical University (PY2018039), Scientific Research Talent Cultivation Project of Stomatological Hospital, Southern Medical University (RC202009), Guangzhou Science and Technology Program (202102020519), and National Natural Science Foundation of China (82001094).

## ACKNOWLEDGMENTS

We would like to thank Zhichao Hao for technical assistance with Photoshop software.

## SUPPLEMENTARY MATERIAL

The Supplementary Material for this article can be found online at: https://www.frontiersin.org/articles/10.3389/fbioe.2021.752506/full#supplementary-material

## REFERENCES

Alberti, K. A., and Xu, Q. (2013). Slicing, Stacking and Rolling: Fabrication of Nanostructured Collagen Constructs from Tendon Sections. *Adv. Healthc. Mater.* 2 (6), 817–821. doi:10.1002/adhm.201200319

Alberti, K. A., and Xu, Q. (2016). Biocompatibility and Degradation of Tendon-Derived Scaffolds. *Regen. Biomater.* 3 (1), 1–11. doi:10.1093/rb/rbv023

Alberti, K. A., Hopkins, A. M., Tang-Schomer, M. D., Kaplan, D. L., and Xu, Q. (2014). The Behavior of Neuronal Cells on Tendon-Derived Collagen Sheets as Potential Substrates for Nerve Regeneration. *Biomaterials* 35 (11), 3551–3557. doi:10.1016/j.biomaterials.2013.12.082

Alberti, K. A., Sun, J.-Y., Illeperuma, W. R., Suo, Z., and Xu, Q. (2015). Laminar Tendon Composites with Enhanced Mechanical Properties. *J. Mater. Sci.* 50 (6), 2616–2625. doi:10.1007/s10853-015-8842-2

Alberti, K. A., Neufeld, C. I., Wang, J., and Xu, Q. (2016). *In Vivo* Peripheral Nerve Repair Using Tendon-Derived Nerve Guidance Conduits. *ACS Biomater. Sci. Eng.* 2 (6), 937–945. doi:10.1021/acsbiomaterials.6b00034

Chang, H.-J., Xu, X.-L., Zhou, G.-H., Li, C.-B., and Huang, M. (2012). Effects of Characteristics Changes of Collagen on Meat Physicochemical Properties of Beef Semitendinosus Muscle during Ultrasonic Processing. *Food Bioproc. Technol.* 5 (1), 285–297. doi:10.1007/s11947-009-0269-9

Chen, K., Lin, X., Zhang, Q., Ni, J., Li, J., Xiao, J., et al. (2015). Decellularized Periosteum as a Potential Biologic Scaffold for Bone Tissue Engineering. *Acta Biomater.* 19, 46–55. doi:10.1016/j.actbio.2015.02.020

Cheng, Q., Wang, S., and Han, Q. (2010). Novel Process for Isolating Fibrils from Cellulose Fibers by High-Intensity Ultrasonication. II. Fibril Characterization. *J. Appl. Polym. Sci.* 115 (5), 2756–2762. doi:10.1002/app.30160

Chuang, Y.-C., Yu, Y., Wei, M.-T., Chang, C.-C., Ricotta, V., Feng, K.-C., et al. (2019). Regulating Substrate Mechanics to Achieve Odontogenic Differentiation for Dental Pulp Stem Cells on TiO2 Filled and Unfilled Polyisoprene. *Acta Biomater.* 89, 60–72. doi:10.1016/j.actbio.2019.02.040

Neto, A. M. D., Sartoretto, S. C., Duarte, I. M., Resende, R. F. d. B., Neves Novellino Alves, A. T., Mourão, C. F. d. A. B., et al. (2020). *In Vivo* Comparative Evaluation of Biocompatibility and Biodegradation of Bovine and Porcine Collagen Membranes. *Membranes* 10 (12), 423. doi:10.3390/membranes10120423

Elgali, I., Omar, O., Dahlin, C., and Thomsen, P. (2017). Guided Bone Regeneration: Materials and Biological Mechanisms Revisited. *Eur. J. Oral Sci.* 125 (5), 315–337. doi:10.1111/eos.12364

Bassi, A., Bizelli, V., Francatti, T., Rezende de Moares Ferreira, A., Carvalho Pereira, J., Al-Sharani, H., et al. (2021). Bone Regeneration Assessment of Polycaprolactone Membrane on Critical-Size Defects in Rat Calvaria. *Membranes* 11 (2), 124. doi:10.3390/membranes11020124

Ferraro, V., Gaillard-Martinie, B., Sayd, T., Chambon, C., Anton, M., and Santé-Lhoutellier, V. (2017). Collagen Type I from Bovine Bone. Effect of Animal Age, Bone Anatomy and Drying Methodology on Extraction Yield, Self-Assembly, thermal Behaviour and Electrokinetic Potential. *Int. J. Biol. Macromol.* 97, 55–66. doi:10.1016/j.ijbiomac.2016.12.068

Ghazanfari, S., Alberti, K. A., Xu, Q., and Khademhosseini, A. (2019). Evaluation of an Elastic Decellularized Tendon-derived Scaffold for the Vascular Tissue Engineering Application. *J. Biomed. Mater. Res.* 107, 1225–1234. doi:10.1002/jbm.a.36622

He, L., Mu, C., Shi, J., Zhang, Q., Shi, B., and Lin, W. (2011). Modification of Collagen with a Natural Cross-Linker, Procyanidin. *Int. J. Biol. Macromol.* 48 (2), 354–359. doi:10.1016/j.ijbiomac.2010.12.012

Helling, A. L., Tsekoura, E. K., Biggs, M., Bayon, Y., Pandit, A., and Zeugolis, D. I. (2017). *In Vitro* Enzymatic Degradation of Tissue Grafts and Collagen Biomaterials by Matrix Metalloproteinases: Improving the Collagenase Assay. *ACS Biomater. Sci. Eng.* 3 (9), 1922–1932. doi:10.1021/acsbiomaterials.5b00563

Kapogianni, E., Alkildani, S., Radenkovic, M., Xiong, X., Krastev, R., Stöwe, I., et al. (2021). The Early Fragmentation of a Bovine Dermis-Derived Collagen Barrier Membrane Contributes to Transmembraneous Vascularization-A Possible Paradigm Shift for Guided Bone Regeneration. *Membranes* 11 (3), 185. doi:10.3390/membranes11030185

Li, J., Yan, J.-F., Wan, Q.-Q., Shen, M.-J., Ma, Y.-X., Gu, J.-T., et al. (2021a). Matrix Stiffening by Self-Mineralizable Guided Bone Regeneration. *Acta Biomater.* 125, 112–125. doi:10.1016/j.actbio.2021.02.012

Li, P., Li, Y., Kwok, T., Yang, T., Liu, C., Li, W., et al. (2021b). A Bi-layered Membrane with Micro-nano Bioactive Glass for Guided Bone Regeneration. *Colloids Surf. B: Biointerfaces* 205, 111886. doi:10.1016/j.colsurfb.2021.111886

Li, Z., Du, T., Ruan, C., and Niu, X. (2021c). Bioinspired Mineralized Collagen Scaffolds for Bone Tissue Engineering. *Bioactive Mater.* 6 (5), 1491–1511. doi:10.1016/j.bioactmat.2020.11.004

Lin, M., Liu, H., Deng, J., An, R., Shen, M., Li, Y., et al. (2019). Carboxymethyl Chitosan as a Polyampholyte Mediating Intrafibrillar Mineralization of Collagen *via* Collagen/ACP Self-Assembly. *J. Mater. Sci. Technol.* 35 (9), 1894–1905. doi:10.1016/j.jmst.2019.05.010

Liu, Y., Liu, S., Luo, D., Xue, Z., Yang, X., Gu, L., et al. (2016a). Hierarchically Staggered Nanostructure of Mineralized Collagen as a Bone-Grafting Scaffold. *Adv. Mater.* 28 (39), 8740–8748. doi:10.1002/adma.201602628

Liu, Y., Luo, D., and Wang, T. (2016b). Hierarchical Structures of Bone and Bioinspired Bone Tissue Engineering. *Small* 12 (34), 4611–4632. doi:10.1002/smll.201600626

Liu, H., Lin, M., Liu, X., Zhang, Y., Luo, Y., Pang, Y., et al. (2020). Doping Bioactive Elements into a Collagen Scaffold Based on Synchronous Self-Assembly/mineralization for Bone Tissue Engineering. *Bioact. Mater.* 5 (4), 844–858. doi:10.1016/j.bioactmat.2020.06.005

Luo, X., Zhang, S., Luo, B., and Li, H. (2021). Engineering Collagen Fiber Templates with Oriented Nanoarchitecture and Concerns on Osteoblast Behaviors. *Int. J. Biol. Macromol.* 185, 77–86. doi:10.1016/j.ijbiomac.2021.06.072

Marelli, B., Ghezzi, C. E., Zhang, Y. L., Rouiller, I., Barralet, J. E., and Nazhat, S. N. (2015). Fibril Formation pH Controls Intrafibrillar Collagen Biomineralization *In Vitro* and *In Vivo*. *Biomaterials* 37, 252–259. doi:10.1016/j.biomaterials.2014.10.008

Pei, Y., Jordan, K. E., Xiang, N., Parker, R. N., Mu, X., Zhang, L., et al. (2021). Liquid-Exfoliated Mesostructured Collagen from the Bovine Achilles Tendon as Building Blocks of Collagen Membranes. *ACS Appl. Mater. Inter.* 13 (2), 3186–3198. doi:10.1021/acsami.0c20330

de Melo Pereira, D., Eischen-Loges, M., Birgani, Z. T., and Habibovic, P. (2020). Proliferation and Osteogenic Differentiation of hMSCs on Biomineralized Collagen. *Front. Bioeng. Biotechnol.* 8, 554565. doi:10.3389/fbioe.2020.554565

Qiu, Z.-Y., Cui, Y., Tao, C.-S., Zhang, Z.-Q., Tang, P.-F., Mao, K.-Y., et al. (2015). Mineralized Collagen: Rationale, Current Status, and Clinical Applications. *Materials* 8 (8), 4733–4750. doi:10.3390/ma8084733

Reznikov, N., Shahar, R., and Weiner, S. (2014). Bone Hierarchical Structure in Three Dimensions. *Acta Biomater.* 10 (9), 3815–3826. doi:10.1016/j.actbio.2014.05.024

Salvatore, L., Gallo, N., Natali, M. L., Terzi, A., Sannino, A., and Madaghiele, M. (2021). Mimicking the Hierarchical Organization of Natural Collagen: Toward the Development of Ideal Scaffolding Material for Tissue Regeneration. *Front. Bioeng. Biotechnol.* 9, 644595. doi:10.3389/fbioe.2021.644595

Turri, A., Elgali, I., Vazirisani, F., Johansson, A., Emanuelsson, L., Dahlin, C., et al. (2016). Guided Bone Regeneration Is Promoted by the Molecular Events in the Membrane Compartment. *Biomaterials* 84, 167–183. doi:10.1016/j.biomaterials.2016.01.034

Wan, Y., Gao, Y., Shao, J., Tumarbekova, A., Zhang, D., and Zhu, J. (2021). Effects of Ultrasound and thermal Treatment on the Ultrastructure of Collagen Fibers from Bovine Tendon Using Atomic Force Microscopy. *Food Chem.* 347, 128985. doi:10.1016/j.foodchem.2020.128985

Wang, S., and Cheng, Q. (2009). A Novel Process to Isolate Fibrils from Cellulose Fibers by High-Intensity Ultrasonication, Part 1: Process Optimization. *J. Appl. Polym. Sci.* 113 (2), 1270–1275. doi:10.1002/app.30072

Wang, Y., Hua, Y., Zhang, Q., Yang, J., Li, H., Li, Y., et al. (2018). Using Biomimetically Mineralized Collagen Membranes with Different Surface Stiffness to Guide Regeneration of Bone Defects. *J. Tissue Eng. Regener. Med.* doi:10.1002/term.2670

Wu, Z., Bao, C., Zhou, S., Yang, T., Wang, L., Li, M., et al. (2020). The Synergetic Effect of Bioactive Molecule-Loaded Electrospun Core-shell Fibres for Reconstruction of Critical-sized Calvarial Bone Defect-The Effect of Synergetic Release on Bone Formation. *Cell Prolif* 53 (4), e12796. doi:10.1111/cpr.12796

Yang, T., Xiao, W., Chen, W., Li, L., Zhu, Z., and Sui, L. (2016). Effect of Carboxymethyl Chitosan and Aging Time on Synthesis and Storage of Amorphous Calcium Phosphate. *j nanosci Nanotechnol.* 16 (12), 12582–12589. doi:10.1166/jnn.2016.12982

Yang, T., Li, Y., Hong, Y., Chi, L., Liu, C., Lan, Y., et al. (2020a). The Construction of Biomimetic Cementum through a Combination of Bioskiving and Fluorine-Containing Biomineralization. *Front. Bioeng. Biotechnol.* 8, 341. doi:10.3389/fbioe.2020.00341

Yang, T., Xie, P., Wu, Z., Liao, Y., Chen, W., Hao, Z., et al. (2020b). The Injectable Woven Bone-like Hydrogel to Perform Alveolar ridge Preservation with Adapted Remodeling Performance after Tooth Extraction. *Front. Bioeng. Biotechnol.* 8, 11901–11915. doi:10.3389/fbioe.2020.00119

Yusof, F., Sha'ban, M., and Azhim, A. (2019). Development of Decellularized Meniscus Using Closed Sonication Treatment System: Potential Scaffolds for Orthopedics Tissue Engineering Applications. *Ijn* 14, 5491–5502. doi:10.2147/ijn.S207270

Zeugolis, D. I., Khew, S. T., Yew, E. S. Y., Ekaputra, A. K., Tong, Y. W., Yung, L.-Y. L., et al. (2008). Electro-spinning of Pure Collagen Nano-Fibres - Just an Expensive Way to Make Gelatin? *Biomaterials* 29 (15), 2293–2305. doi:10.1016/j.biomaterials.2008.02.009

Zhang, J., Ma, S., Liu, Z., Geng, H., Lu, X., Zhang, X., et al. (2017). Guided Bone Regeneration with Asymmetric Collagen-Chitosan Membranes Containing Aspirin-Loaded Chitosan Nanoparticles. *Ijn* 12, 8855–8866. doi:10.2147/ijn.s148179

Zhang, L., Yu, Y., Feng, K.-c., Chuang, Y.-c., Zuo, X., Zhou, Y., et al. (2018). Templated Dentin Formation by Dental Pulp Stem Cells on Banded Collagen Bundles Nucleated on Electrospun Poly (4-vinyl Pyridine) Fibers *In Vitro*. *Acta Biomater.* 76, 80–88. doi:10.1016/j.actbio.2018.06.028

Zhang, W., Li, P., Shen, G., Mo, X., Zhou, C., Alexander, D., et al. (2021). Appropriately Adapted Properties of Hot-Extruded Zn-0.5Cu-xFe Alloys Aimed for Biodegradable Guided Bone Regeneration Membrane Application. *Bioact. Mater.* 6 (4), 975–989. doi:10.1016/j.bioactmat.2020.09.019

Zhou, T., Chen, S., Ding, X., Hu, Z., Cen, L., and Zhang, X. (2021). Fabrication and Characterization of Collagen/PVA Dual-Layer Membranes for Periodontal Bone Regeneration. *Front. Bioeng. Biotechnol.* 9, 630977. doi:10.3389/fbioe.2021.630977

**Conflict of Interest:** The authors declare that the research was conducted in the absence of any commercial or financial relationships that could be construed as a potential conflict of interest.

**Publisher's Note:** All claims expressed in this article are solely those of the authors and do not necessarily represent those of their affiliated organizations, or those of the publisher, the editors, and the reviewers. Any product that may be evaluated in this article, or claim that may be made by its manufacturer, is not guaranteed or endorsed by the publisher.

frontiers in Bioengineering and Biotechnology

ORIGINAL RESEARCH
published: 04 November 2021
doi: 10.3389/fbioe.2021.784838

# A Rapid Dual-Responsive Releasing Nano-Carrier by Decomposing the Copolymer and Reversing the Core Dissolution

*Sen Liu[1], Can Shen[1], Cheng Qian[1], Jianquan Wang[2], Zhihao Wang[1], Xuecong Tang[1], Qiuyang Zhang[1], Changjiang Pan[1]* and Wei Ye[1]**

[1]*Jiangsu Provincial Engineering Research Center for Biomedical Materials and Advanced Medical Devices, Faculty of Mechanical and Material Engineering, Huaiyin Institute of Technology, Huaian, China,* [2]*College of Engineering and Applied Sciences, Institute of Materials Engineering, Collaborative Innovation Center of Chemistry for Life Sciences, Nanjing University, Nanjing, China*

The accumulation of nanotechnology-based drugs has been realized in various ways. However, the concentration of drugs encapsulated by nanomaterials is not equal to the concentration of effective drugs; often, the drugs become effective only when they are released from the nanomaterials as free drugs. This means only when the drugs are rapidly released after the accumulated drug-encapsulating nanomaterials can they truly achieve the purpose of increasing the concentration of drugs in the tumor. Therefore, we herein report a dual-response nano-carrier of glutathione and acid to achieve the rapid release of encapsulated drug and increase the effective drug concentration in the tumor. The nano-carrier was constructed using a dual-responsive amphiphilic copolymer, composed of polyethylene glycol and hydrophobic acetylated dextran and connected by a disulfide bond. In the tumor microenvironment, disulfide bonds could be biodegraded by glutathione that is overexpressed in the tumor, exposing the core of nano-carrier composed of acetylated dextran. Then the acidic environment would induce the deacetylation of acetylated dextran into water-soluble dextran. In this way, the nano-carrier will degrade quickly, realizing the purpose of rapid drug release. The results showed that the drug release rate of dual-responsive nano-carrier was much higher than that of glutathione or acid-responsive nano-carrier alone. Furthermore, both *in vitro* and *in vivo* experiments confirmed that dual-responsive nano-carrier possessed more efficient anti-tumor effects. Therefore, we believe that dual-responsive nano-carriers have better clinical application prospects.

**Keywords: dual-responsive, nano-carrier, dissolution reversing, rapid drug release, tumor chemotherapy**

OPEN ACCESS

***Edited by:***
*Guicai Li,*
*Nantong University, China*

***Reviewed by:***
*Da Huo,*
*Nanjing Medical University, China*
*Luzhong Zhang,*
*Nantong University, China*

****Correspondence:***
*Changjiang Pan*
*panchangjiang@hyit.edu.cn*
*Wei Ye*
*weiye@hyit.edu.cn*

***Specialty section:***
*This article was submitted to Biomaterials, a section of the journal Frontiers in Bioengineering and Biotechnology*

***Received:*** *28 September 2021*
***Accepted:*** *21 October 2021*
***Published:*** *04 November 2021*

***Citation:***
*Liu S, Shen C, Qian C, Wang J, Wang Z, Tang X, Zhang Q, Pan C and Ye W (2021) A Rapid Dual-Responsive Releasing Nano-Carrier by Decomposing the Copolymer and Reversing the Core Dissolution. Front. Bioeng. Biotechnol. 9:784838. doi: 10.3389/fbioe.2021.784838*

## INTRODUCTION

Nano-carriers have played significant roles in improving the therapeutic effects of tumor chemotherapy in the past decades (Petros and Desimone, 2010; Shi et al., 2016). Therefore, currently, it is one of the most interesting research directions to explore more effective drug carriers to overcome tumors (Sun et al., 2017; Yao et al., 2020; Zhang et al., 2021). The rapid release of nano-carriers at the lesion site is an important property of ideal nano-carriers (Hou et al., 2019). Drugs exhibit their therapeutic activity only after being liberated from their carrier (Luck and Mason,

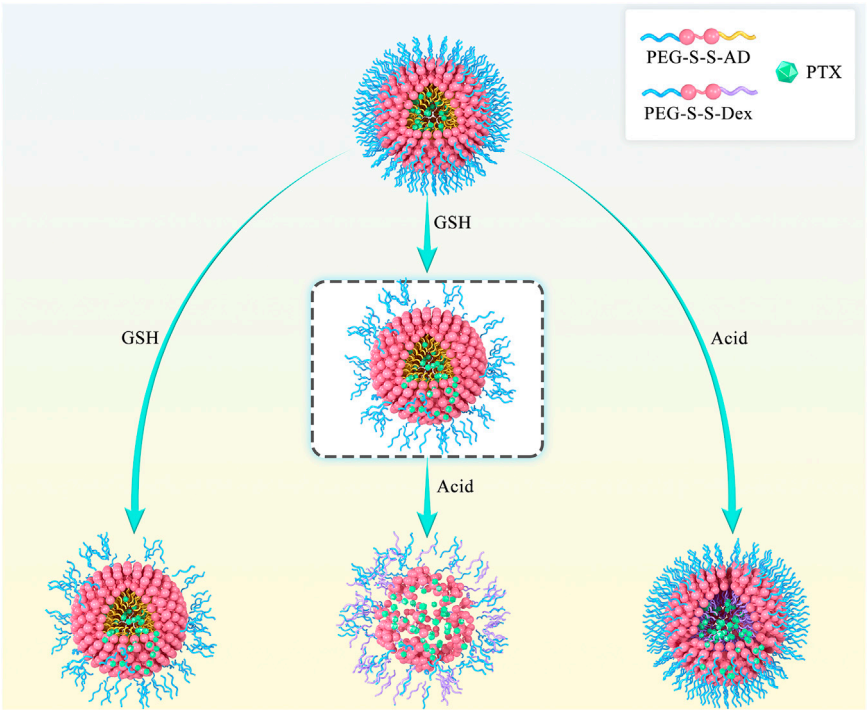


**FIGURE 1 |** Scheme of rapid cleavage of dual-responsive nano-medicine (PTX@PSA NPs) in the presence of glutathione and acid. Compared to the shedding of the outer PEG layer induced by the breaking of disulfide bond in the presence of glutathione alone and the internal expansion induced by the change of hydrophobic AD to hydrophilic Dex in the presence of acid alone, dual-responsive PTX@PSA NPs possess a faster drug release rate.

2013), and cancer cells have multiple mechanisms of multi-drug resistance to protect them from drugs, such as drug efflux (Ye et al., 2017; Liu et al., 2019), cell-intrinsic drug metabolism (Colombo et al., 1999), or detoxification (Wegiel et al., 2013). Thus, the drug release rate should be rapid enough to achieve a sufficiently high concentration in tumor cells, allowing the drugs to reach their targets and kill cancer cells.

Usually, the drugs are released from the carrier to become free drugs through the drug diffusion (Colombo et al., 1999) or carrier disintegration (Colombo et al., 1999; Yu et al., 2015a; Liu et al., 2019; Zhang et al., 2019; Cao et al., 2021) mechanisms. However, the rate of drug diffusion is relatively slow, usually with a half-life of several hours or days after release (Sun et al., 2012). Therefore, the carrier can be designed with the characteristics of rapid response dissociation so that they can quickly become free drugs at the lesion site to play their role in tumor inhibition.

Herein, we report a dual-responsive amphiphilic copolymer (PEG-SS-AD), composed of polyethylene glycol (PEG) and acetylated dextran (AD) linked by a disulfide bond (-S-S-). The rapid dual-responsive releasing nano-carrier (PSA NPs) was formed by the self-assembly of PEG-SS-AD. It is well-established that tumor cells overexpress glutathione (GSH) (Yan et al., 1991; Hou et al., 2019), which could act on -S-S- through biodegrading (Lappi and Ruddock, 2011; Hou et al., 2019). Therefore, the nano-carrier would degrade at the tumor site, and the water-soluble outer shell would be separated and dissolved in the -S-S- biodegrading process. The hydrophobic part was functionalized with acid-induced solubility reversible ability to accelerate the disintegration of the exposed hydrophobic core. Hydrophobic acetylated dextran (Dex) can be converted into hydrophilic Dex in the tumor's acidic microenvironment (Dai et al., 2019). Hence, the dual-responsive nano-carrier is capable of rapid cleavage in the tumor (**Figure 1**). Once loaded with chemotherapeutic drugs, these nano-carriers can quickly release the coated drugs at the tumor site, increasing the concentration of the drug at the tumor site to enhance the effectiveness of chemotherapy.

## EXPERIMENTAL SECTION

### Materials

Methoxy-terminated polyethylene glycol (mPEG, Mw ≈ 2 KDa), carboxylic acid functionalized methoxyl polyethylene glycol (mPEG-COOH, Mw ≈ 2 KDa) were purchased from Ruixi Biological Technology Co., Ltd,. (Xi'an, China). N,N′-carbonyldiimidazole (CDI), 2,2-dithiodiethanol (DIT), succinic anhydride, dextran (Mw ≈ 2 KDa), 1-(3-Dimethylaminopropyl)-3-ethylcarbodiimide hydrochloride (EDC), N-Hydroxy succinimide (NHS), 2-methoxy propylene, pyridine p-toluene sulfonate, propionic anhydride, and dimethylaminopyridine (DMAP) were purchased from Energy Chemical (Shanghai, China). Water used in all the experiments was deionized (DI) water depurated by a Millipore ultrapure water system (Billerica,

MA, United States) with a resistivity of 18.2 MΩ cm. High-glucose DMEM containing 1% penicillin/streptomycin, phosphate-buffered saline (PBS), and trypsin were obtained from KeyGen BioTech Co., Ltd,. (Jiangsu, China). Fetal bovine serum (FBS) was purchased from Absin Bioscience Inc (Shanghai, China).

## Synthesis of PEG-SS-AD (PSA)

Briefly, 4.0 g of mPEG and 0.162 g of CDI were dissolved in 50 ml of N,N-dimethyl formamide (DMF) and stirred for 24 h at room temperature. Then, 0.26 g of DIT was added and reacted at room temperature for another 12 h. The byproduct was then dialyzed and lyophilized to obtain disulfide bond-functionalized PEG (mPEG-SS, polymer 2).

Then, 2.2 g of mPEG-SS, dissolved in 50 ml DMF, was dissolved in 20 ml of DMF. Next, excess succinic anhydride was added and stirred at room temperature for 24 h. The byproduct was then dialyzed and lyophilized to obtain carboxyl-functionalized mPEG-SS (mPEG-SS-COOH, polymer 3).

In the next stage, 1.0 g of mPEG-SS-COOH and 1.0 g of Dex were dissolved in 20 ml of DMF, and 0.1 g of EDC and 0.06 g of NHS were added as catalysts. After 24 h of reaction, the byproduct was dialyzed and lyophilized to obtain PEG-SS-Dex (polymer 4).

Subsequently, 0.1 g of PEG-SS-Dex, 10 ml of 2-methoxy propylene, and 50 mg of pyridine p-toluene sulfonate were dissolved in 20 ml of dimethyl sulfoxide (DMSO). Then, the reactions were carried out at room temperature for 3 h. The byproduct was dialyzed and lyophilized to obtain PEG-SS-AD (polymer 5).

$^1$H-NMR of the polymers was performed on a Bruker 400M (JNM-ECZS) with the $CDCl_3$ solvent.

## Synthesis of PEG-propionic anhydride-modified dextran (PPD)

To synthesize PDP as a non-responsive control group, 1.2 g of mPEG-COOH, 1.0 g of Dex, and 97.5 mg of CDI were dissolved in 20 ml of DMSO, and the reactions were allowed to continue under stirring at 80°C overnight. Then, 5 ml of propionic anhydride, 100 mg of DMAP, and 1 ml of triethylamine were mixed and stirred at room temperature for 8 h. PPD was then obtained by dialysis and lyophilization.

## Preparation of Nano-Carriers (PSA NPs) and Nano-Medicine (PTX@PSA NPs)

PSA NPs were prepared by the self-assembly of PEG-SS-AD in the selective solvent of dichloromethane (DCM) in DI water, as reported previously (Hu et al., 2007; Yu et al., 2015b). Briefly, 10 mg of PEG-SS-AD was dissolved in 1 ml of DCM, and the mixture was slowly added to 10 ml of DI water. The mixture was then emulsified by ultra-sonication for 10 min. Finally, the emulsion was evaporated to remove DCM, followed by filtration and lyophilization. PTX@PSA NPs were obtained by adding 10 mg of PEG-SS-AD and 2 mg of PTX in 1 ml of DCM, and then the steps above were followed. Non-responsive PTX@PPD NPs were obtained by adding 10 mg of PEG-PD and 2 mg of PTX to 1 ml of DCM. Then the steps above were followed.

## Characterization of PSA NPs

To this end, 10 mg of PSA NPs was dissolved in 10 ml of alkalescent (pH ≈ 7.3) phosphate-buffered saline (PBS) solution, 0.2 μmol/L GSH alkalescent (pH ≈ 7.3) solution, acidic (pH ≈ 6.0) PBS solution, and 0.2 μmol/L GSH (pH ≈ 6.0) PBS solution, respectively, and incubated for 2 h. In addition, transmission electron microscopic (TEM, JEM-2100F) images were obtained to analyze changes in the morphology of PSA NPs under different conditions.

## Drug Loading Content and Encapsulation Efficiency

Standard solutions of PTX at concentrations of 0.001, 0.005, 0.01, 0.05, 0.1, 0.5, and 1 mg/ml were prepared to measure their ultraviolet absorption spectrum and evaluate the relationship between concentration and absorbance at 273 nm.

Then 10 mg of PTX@PSA NPs ($W_{PTX@PSA\ NPs}$ = 10 mg) was dissolved in 4 ml of acetonitrile and PBS (pH = 7.4) (V/V = 2:3) mixed solvent and the supernatant was centrifuged. Then the concentration of PTX ($C_{PTX}$) was measured by absorption photometry. The PTX loading content and encapsulation efficiency were calculated by (**Eqs. 1**, **2**)

$$\text{PTX loading content} = \frac{C_{PTX} \times 4\,mL}{W_{PTX@PSA\ NPs}} \times 100\% \quad (1)$$

$$\text{PTX encapsulation efficiency} = \frac{C_{PTX} \times 4\,mL}{\text{total amount of PTX}} \times 100\% \quad (2)$$

where the total amount of PTX = $W_{PTX@PSA\ NPs}/6$ = 1.67 mg, according to the feeding ratio.

## *In Vitro* Controlled Release Ability

First, 5 ml of PTX@PSA NPs aqueous solutions (2 mg/ml) were sealed into dialysis tubes (MWCO 2 kDa) for four copies, and then immersed in 45 ml of alkalescent (pH ≈ 7.3) phosphate-buffered saline (PBS) solution, 0.2 μmol/L GSH alkalescent (pH ≈ 7.3) PBS solution, acidic (pH ≈ 6.0) PBS solution, and 0.2 μmol/L GSH acidic (pH ≈ 6.0) PBS solution, respectively. The drug release experiment was performed at 37°C, and three 1-ml solutions were taken from each group at 10 min and 0.5, 1, 3, 5, 8, 12, and 24 h, respectively. The concentration of PTX was measured by ultraviolet absorption spectrum, and the cumulative released PTX was calculated.

## *In vitro* cytotoxicity assay and anti-tumor effect

The cytotoxicity of 4T1 cells was tested using an MTT (3-(4,5-dimethylthiazol-2-yl)-2,5-diphenyltetrazolium bromide) assay. The cells were inoculated in 96-well plates, and when the cells covered approximately 80% of the total area, the medium was

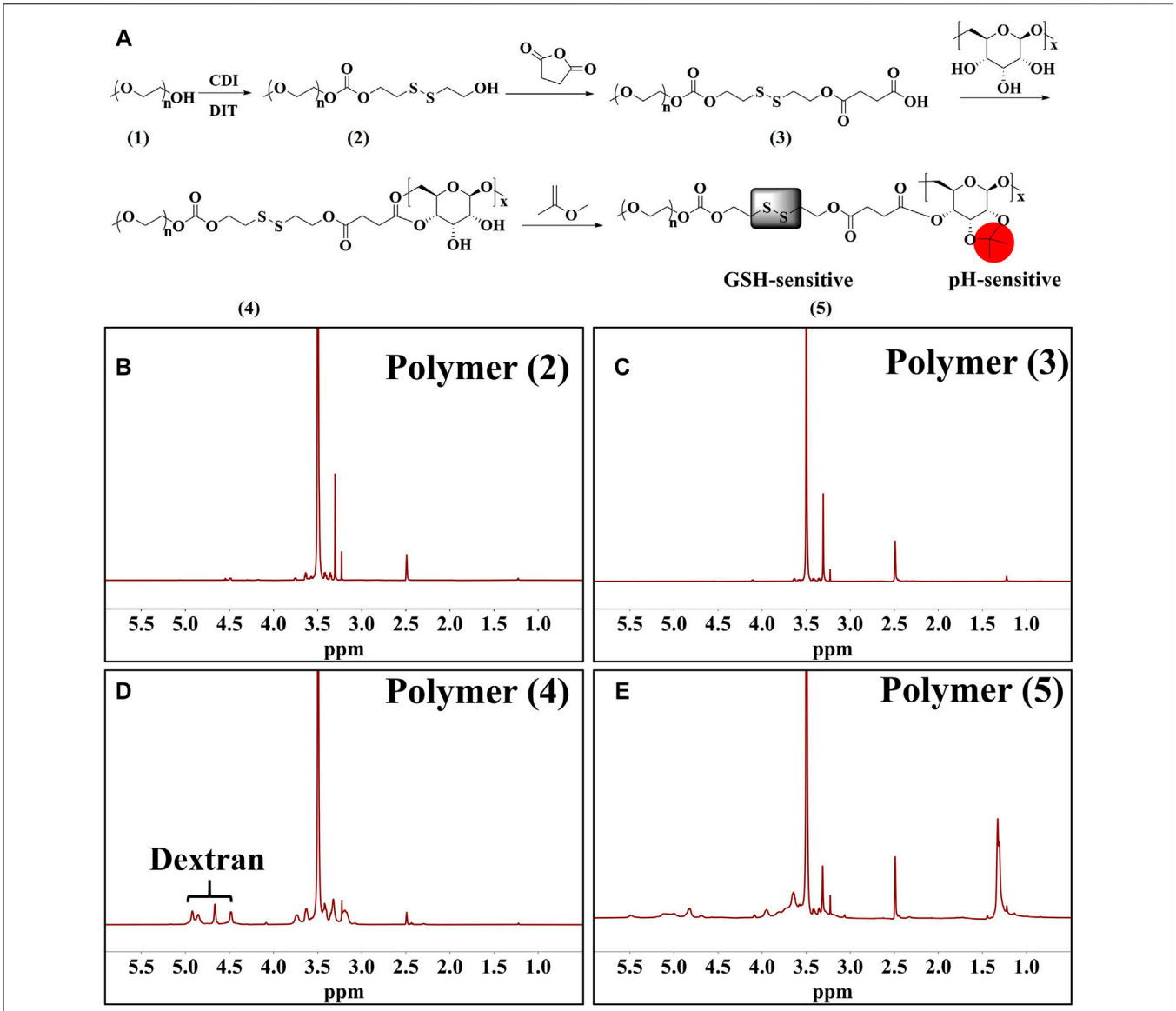


**FIGURE 2 | (A)** Synthetic route of dual-responsive amphiphilic polymer; 1H NMR spectrum of polymers 2 to 5 **(B–E)**.

removed, and 100 μl of PSA NPs medium solution was added at concentrations of 0, 10, $10^2$, $10^3$, $10^4$, $10^5$, and $10^6$ ng/ml. After incubation for 24 h, the medium was removed, and the cells were washed three times with saline solution. Then 20 μl of MTT solution (2.5 mg $ml^{-1}$ in saline solution) and 80 μl of culture medium were added per well, and the cells were incubated for another 4 h. Subsequently, the medium was aspirated, and 200 μl of DMSO solution was added to each well. After 15 min, the absorbance was measured at 490 nm using an iMark Enzyme mark instrument (Biotek Eon$^{TM}$). The cell viability was calculated according to a previously reported approach.

The anti-tumor effects of PTX@PSA NPs and PTX@PPD NPs were tested using MTT assay by following the above method.

## *In vivo* Anti-Tumor Effects

A tumor-bearing mouse model was constructed by injecting 4T1 into the back of the mouse. When the tumor grew to approximately 100 $mm^3$, they were divided into three groups ($n$ = 10). Each mouse was intravenously injected with saline solution (100 μl) (group 1), PTX@PPD NPs (100 μl, 0.5 mg/ml) (group 2), and PTX@PSA NPs (100 μl, 0.5 mg/ml) (group 1). The treatment was performed twice a week for two weeks. Then the length (L, longest diameter) and width (W, shortest diameter) of the tumor were measured with vernier calipers every 3 days from the beginning of treatment, and the tumor volume was calculated using this **Eq. (3)**:

$$V = (L \times W^2)/2 \quad (3)$$

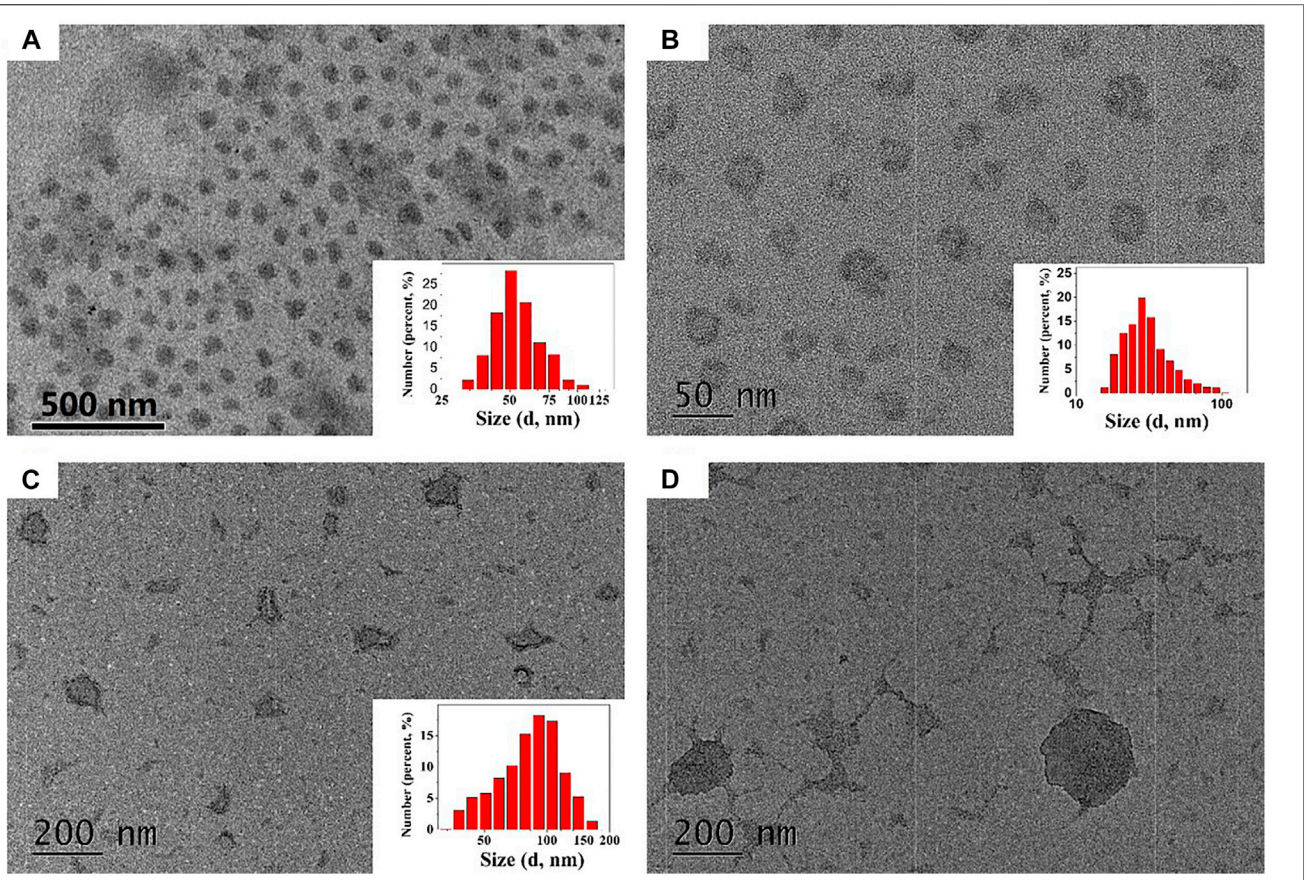


**FIGURE 3 | (A)** The TEM images of PEG-SS-AD NPs (PSA NPs). **(B)** The TEM images of PEG-SS-AD NPs incubated in 0.2 μmol/L GSH alkalescent (pH ≈ 7.3) phosphate-buffered saline (PBS) solution. **(C)** The TEM images of PEG-SS-AD NPs incubated in acidic (pH ≈ 6.0) PBS solution. **(D)** The TEM images of PEG-SS-AD NPs incubated in 0.2 μmol/L GSH acidic (pH ≈ 6.0) PBS solution.

Three of the tumors in each group were harvested, and their optical pictures were obtained. The survival of the mice was determined every 3 days.

Three tumor-bearing mice were randomly selected and treated according to the above procedures. Tumors were harvested, isolated, immobilized, embedded into paraffin, cut into sections, stained with H&E, and observed under a microscope on the 14th day.

## Pathological Analysis

The tumor-bearing mice were intravenously injected with PSA NPs and PTX@PSA NPs, and then sacrificed on the 14th day. The main organs (heart, liver, spleen, lungs, kidneys) were harvested, isolated, fixed, embedded into paraffin, cut into sections, stained by H&E, and observed under a microscope.

# RESULTS AND DISCUSSION

## Synthesis and Characterization of Dual-Responsive Amphiphilic Copolymers

**Figure 2A** shows the synthesis pathway of GSH and pH dual-responsive PEG-SS-AD (Polymer 5). The GSH response was achieved by incorporating disulfide bonds between polyethylene glycol (PEG, Mw ≈ 2 KDa) and Dex (Mw ≈ 2 KDa) copolymer, while the pH response was achieved by acetylated dextran, which could be converted into hydrophilic dextran in the tumor's acidic microenvironment. The products of polymers 2–5 were confirmed at each step by $^1$H NMR (**Figures 2B–E**). The absorption peak at 3.50 ppm represents the presence of PEG. The absorption peak of Dex at 4.48–4.92 ppm, which could be attributed to H atoms in -OH in each monomer of Dex, was detected in polymer 4, indicating that Dex was attached to PEG. In addition, after the acetylated dextran, the absorption peak of methyl (-$CH_3$, the red part of polymer five in **Figure 2A**) appeared at 1.33 ppm, and the absorption peaks of -OH in Dex weakened, indicating the successful preparation of AD. These findings showed that the GSH and pH dual-responsive PEG-SS-AD were successfully synthesized according to the synthetic route.

## Characterization of Dual-Responsive Nano-Carriers

Then the nano-carriers were formed by the self-assembly of PEG-SS-AD in a selective solvent (PSA NPs), using the solvent evaporation method as we reported previously (Hu et al., 2007; Yu et al., 2015b). As shown in **Figure 3A**, PSA NPs have good water dispersion with

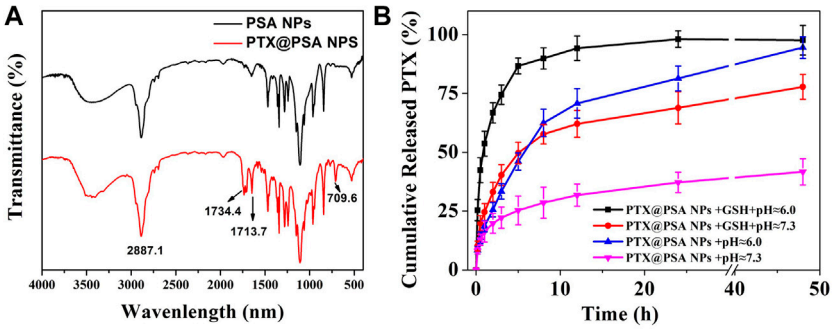


**FIGURE 4 | (A)** FT-IR spectra of the nano-carriers (PSA NPs) and PTX encapsulation nano-medicine (PTX@PSA NPs). **(B)** *In vitro* release of CO from PTX@PSA NPs under stimulation without GSH and acid (PTX@PSA NPs + pH ≈ 7.3), acid (PTX@PSA NPs + pH ≈ 6.0), GSH (PTX@PSA NPs + GSH + pH ≈ 7.3), GSH and acid (PTX@PSA NPs + GSH + pH ≈ 6.0).

**TABLE 1 |** The PTX loading content and encapsulation efficiency of PTX@PSA NPs.

| Weight of the PTX@PSA NPs (mg) | Concentration of PTX (μg/ml) | PTX loading content (wt%) | PTX encapsulation efficiency (wt%) |
|---|---|---|---|
| 10 | 292.5 | 11.7 | 70.2 |

relatively uniform size, i.e., approximately 40 nm. The mean hydrodynamic diameter of these PSA NPs was measured by dynamic light scattering (DLS), which was 55 nm with a polydispersity index (PdI) of 0.068 (inset). Then, PSA NPs were incubated in different solutions for 30 min, and their morphologies were observed under TEM, and mean hydrodynamic diameter was measured by DLS (**Figure 3B–D**). After incubating in 0.2 μmol/L GSH alkalescence (pH ≈ 7.3) phosphate-buffered saline (PBS) solution, the morphology of the PSA NPs was no longer regular, and some PSA NPs were worn out, and others were shrunk in size, with a mean hydrodynamic diameter of 41 nm and a higher PdI of 0.238 (**Figure 3B**). This might be due to the cleavage of -S-S- in PEG-SS-AD by GSH and the dissolution of the PEG shell. In addition, after incubating in acidic (pH ≈ 6.0) PBS solution without GSH, significant changes were observed in the morphology of PSA NPs, and more organic debris appeared, with a mean hydrodynamic diameter of 82.7 nm and a much higher PdI of 0.452 (**Figure 3C**). This might be attributed to the transition from hydrophobic AD to hydrophilic Dex in the acidic environment and the nano-carriers dissolved by the solvent. However, after incubating in 0.2 μmol/L GSH acidic (pH ≈ 6.0) PBS solution, there were no nano-carriers anymore, and all the nano-carriers degraded to organic fragments (**Figure 3D**). These findings indicated that PSA NPs possess the dual-responsive characteristics of GSH and acid and could disintegrate rapidly under the dual action of GSH and acid compared to GSH or acid alone. Encapsulation and controlled release properties of PTX@PSA NPs.

As PSA NPs possess dual-responsive characteristics of GSH and acid, PSA NPs encapsulating paclitaxel (PTX) (PTX@PSA NPs) were prepared, and the encapsulation and controlled release properties of PTX@PSA NPs were evaluated.

To prove the successful encapsulation of PTX by PSA NPs, the as-prepared PTX@PSA NPs were centrifuged and re-dispersed three times to fully remove the free PTX. FT-IR of PTX@PSA NPs and PSA NPs were then carried out, as shown in **Figure 4A**. The appearance of vibration peaks of the carbonyl group (1734.4, 1713.7 $cm^{-1}$) and aromatic ring peak (709.6 $cm^{-1}$) of PTX indicates that PTX was successfully encapsulated in PTX@PSA NPs. Through further testing, the PTX loading content and encapsulation efficiency of PTX@PSA NPs were calculated at 11.7 and 70.6%, according to **Eqs. 1**, **2** (**Table 1**).

The cumulative *in vitro* release of PTX from PTX@PSA NPs was then measured under different conditions (**Figure 4B**). The release rate of PTX from PTX@PSA NPs was relatively slow in the absence of GSH and acid (pH ≈ 7.3); 19.8 ± 4.2% of the total amount was released in the first 2 h, most of which were probably the PTX adhering to the surface of PTX@PSA NPs, and only 41.7 ± 5.6% of the total amount was released at 48 h. Under the stimulation of GSH (GSH + pH ≈ 7.3) or acid (pH ≈ 6.0) alone, the PTX release rate increased, with 25.6 ± 3.1% and 33.1 ± 4.1% being released within 2 h, and 94.5 ± 4.6% and 77.8 ± 5.3% being released at 48 h, respectively. In contrast, under the combined action of GSH and acid (GSH + pH ≈ 6.0), the release rate of PTX increased significantly; 66.8 ± 4.3% of the total amount was released within 2 h, and almost all the drug was released after 12 h (94.2 ± 5.2%). The results were consistent with the morphologies of the nano-carriers under different conditions in **Figure 3**. The nano-carriers remained relatively stable under the weak alkaline condition without GSH, and the drug release rate was slow. Part of the nano-carriers degraded under the stimulation of GSH or acid, resulting in an increased PTX release rate. Under the dual stimulation of GSH and acid, the nano-carriers degraded rapidly, and the corresponding controlled release rate of drugs was very fast, releasing the coated PTX in a short time.

It is well-established that the tumor microenvironment is acidic, and overexpressed GSH, the dual-responsive nano-carriers designed here can rapidly degrade and release the encapsulated drugs into the tumor.

## *In vitro* Analysis

Although PEG and dextran have good biocompatibility, (Mura et al., 2013; Zhang et al., 2014) the safety of nano-carriers should

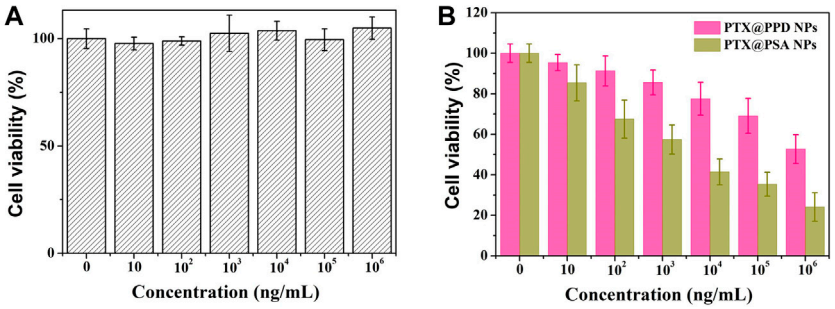


**FIGURE 5 | (A)** Cytotoxicity profiles of 4T1 cells. **(B)** *In vitro* cell proliferation-inhibiting efficiency of PTX@PPD NPs and PTX@PSA NPs on 4T1 cells.

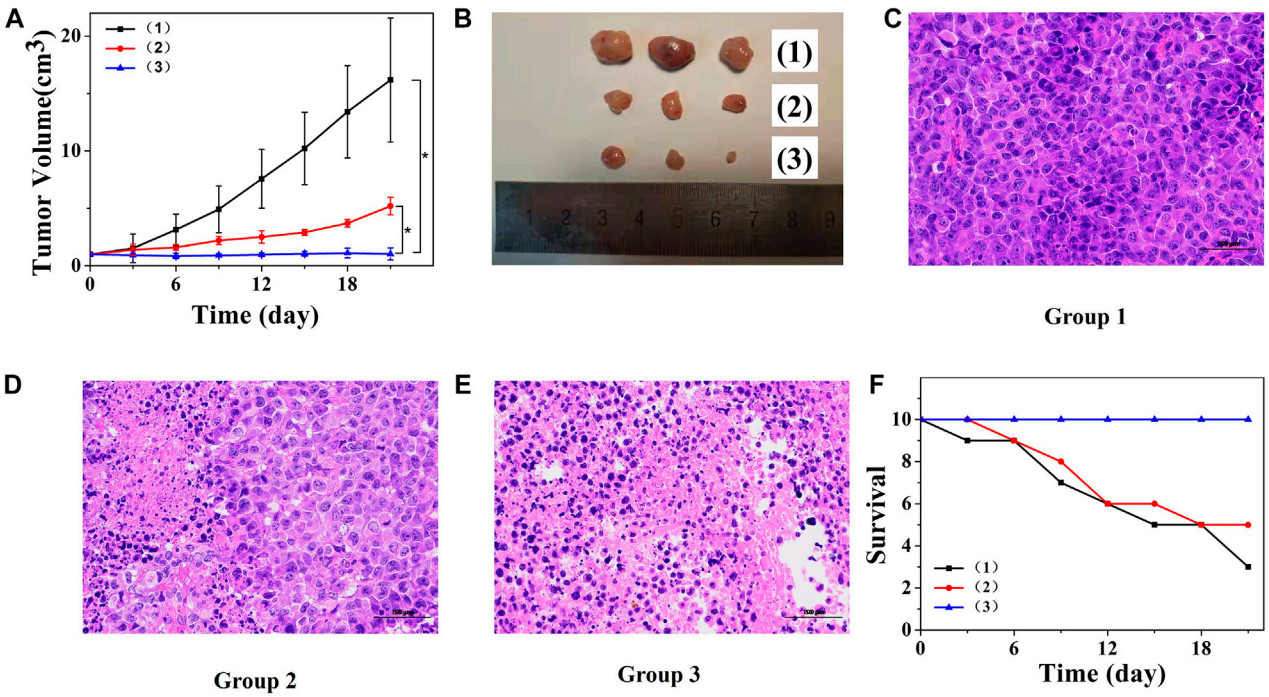


**FIGURE 6 | (A)** Changes in tumor volumes of mice receiving different treatments. *$p < 0.01$. **(B)** Tumor images after treatment and observation period. **(C)** Pathological section of tumor tissue from group 1 via H&E staining. **(D)** Pathological section of tumor tissue from group 2 via H&E staining. **(E)** Pathological section of tumor tissue from group 3 via H&E staining. Scale bars: 100 μm. **(F)** Survival curves of mice in each group ($n = 10$ each group). Each mouse was intravenously injected with saline solution (100 μl) (1), PTX@PPD NPs (100 μl, 0.5 mg/ml) (2), and PTX@PSA NPs (100 μl, 0.5 mg/ml) (3).

be evaluated. The cytotoxicity of the PSA NPs was evaluated at different concentrations through the MTT assay using 4T1 cells. As shown in **Figure 5A**, PSA NPs showed no cytotoxicity. After co-culturing PSA NPs with 4T1 cells, cell proliferation was almost not inhibited under various concentrations of PSA NPs solution, and the cell's survival rate was 104.9 ± 5.2% at a relatively high concentration of 1 mg/ml.

Then, propionic anhydride-modified dextran (PD), with no acid response characteristics, was successfully synthesized and directly connected to PEG without -S-S- to form a non-responsive amphiphilic copolymer (PEG-PD). Then non-responsive nano-medicine was prepared by PEG-PD encapsulating PTX (PTX@PPD NPs). Then the *in vitro* cell proliferation-inhibiting efficiency of PTX@PPD NPs and PTX@PSA NPs was evaluated. As shown in **Figure 5B**, both PTX@PPD NPs and PTX@PSA NPs showed cytotoxicity, but PTX@PSA NPs exhibited higher inhibitory efficiency on the proliferation of tumor cells. This might be because PTX@PSA NPs has a faster controlled release rate, forming a higher concentration of PTX, with a better tumor cell inhibition efficiency.

## *In vivo* Anti-Tumor Effects

Due to the EPR effect of solid tumors, nanoparticles measuring approximately 100 nm would accumulate in tumors (Lammers et al., 2012; Maeda et al., 2013; Wu, 2021). As the rapid, controlled

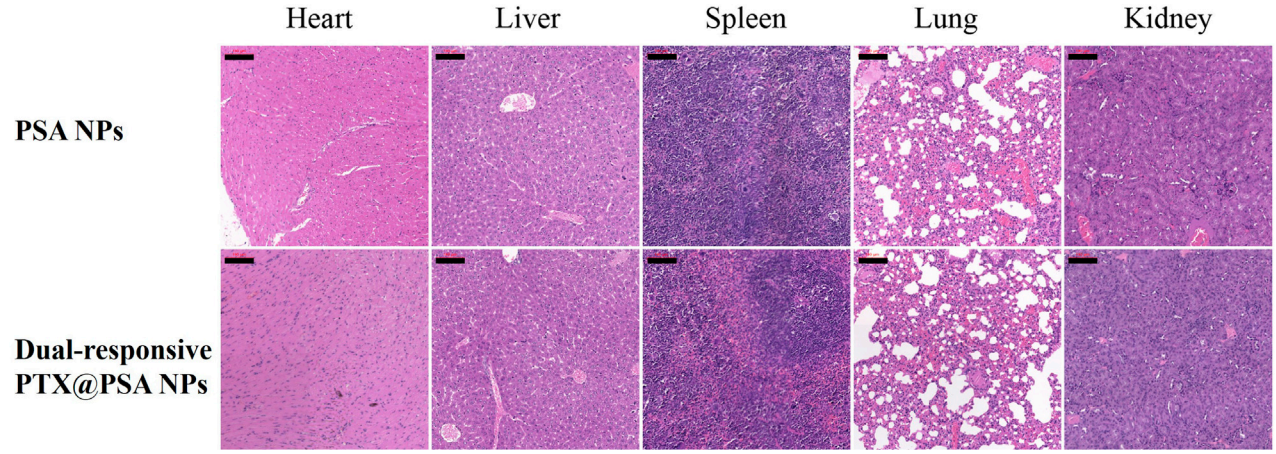


**FIGURE 7 |** The cytotoxic effect caused by PSA NPs and PTX@PSA NPs in major organs via H&E staining (heart, liver, spleen, lungs, and kidneys). Scale bars: 100 μm.

release of PTX, PTX@PSA NPs showed could rapidly increase drug concentration and enhancing tumor cell inhibition *in vitro*. Thus, we speculated that PTX@PSA NPs would also show a significant anti-tumor effect *in vivo*. When the tumor size reached ~100 $mm^3$, tumor-bearing mice were equally divided into three groups ($n = 10$) and injected with normal saline solution (100 μl), PTX@PPD NPs, and PTX@PSA NPs, twice a week for 2 weeks.

The tumor volume was measured and calculated every 3 days, and the statistical results are presented in **Figure 6A**. The tumor volume in mice injected with saline solution increased rapidly. The tumor volume in mice injected with non-responsive PTX@PPD NPs was suppressed but still grew to 520 ± 76 $mm^3$ on day 21. Dual-responsive PTX@PSA NPs showed promising tumor inhibition, and the tumor volume did not increase; it even decreased during the statistical period within 21 days. On day 21, optical camera images of three randomly selected tumors, presented in **Figure 6B**, showed the therapeutic effect. To further illustrate the effect of treatment on the tumor, three tumor-bearing mice were treated according to the above groups, and the tumoral sections of mice were harvested on the 14th day to observe the pathological changes (**Figure 6C**). The morphology of tumor cells in group 1 was almost unaffected. However, after treatment with non-responsive PTX@PPD NPs, the nuclei of some tumor cells were damaged, indicating the apoptosis of tumor cells (**Figure 6D**). However, after treatment with dual-responsive PTX@PSA NPs, tumor cells were significantly affected, and an extensive range of apoptosis appeared, indicating that dual-responsive PTX@PSA NPs have excellent *in vivo* tumor inhibition effect (**Figure 6E**).

**Figure 6F** presents the changes in the number of mice surviving after different treatments. Mice treated with saline solution died on day 3; seven of them died on day 21. However, the mice in the dual-responsive PTX@PSA NPs treatment did not die during the treatment and observation period, indicating that the dual-responsive PTX@PSA NPs can prolong the lifespan of mice by inhibiting tumor proliferation.

## Long-Term Pathological Study

The long-term *in vivo* safety of PSA NPs and PTX@PSA NPs were then further evaluated (**Figure 7**). Tumor-bearing mice received i.v., injections of 100-μl PSA NPs (0.5 mg/ml) and PTX@PSA NPs (0.5 mg/ml), respectively. Then, they were sacrificed on the 14th day after treatment, and their five major organs (heart, liver, spleen, lungs, and kidneys) were resected. H&E staining test was performed to evaluate the pathological condition. No apparent pathological changes, such as inflammatory lesions or abnormalities, were observed in the tissue sections of mice.

## CONCLUSION

In conclusion, we reported a dual-responsive nano-carrier constructed from an amphiphilic copolymer composed of -S-S- linked PEG and AD. The nano-carrier exhibited dual-responsive characteristics of GSH and acid and could quickly degrade and achieve rapid, controlled release of the drug under the interaction of GSH and acid, which was faster than the response of GSH or acid alone. Therefore, the dual-responsive PTX@PSA NPs possess a good tumor inhibition effect *in vivo* and *in vitro*. Furthermore, through the rapid, controlled release of PTX induced by the dual-responsive performance, the inhibitory effect was significantly better than that of non-responsive PTX@PPD NPs. Based on these conclusions, we believe that the rapid, controlled release of dual-responsive nano-carrier has more potential for clinical applications (Michael and Doherty, 2005).

## DATA AVAILABILITY STATEMENT

The original contributions presented in the study are included in the article/Supplementary Material, further inquiries can be directed to the corresponding authors.

## ETHICS STATEMENT

The animal study was reviewed and approved by the committee on animals in Nanjing University.

## AUTHOR CONTRIBUTIONS

SL, CP, and YW contributed to conception and design of the study. CS, CQ, and JW organized the database. ZW, XT, and QZ performed the statistical analysis. SL wrote the first draft of the article. CS, CQ, JW, and ZW wrote sections of the article. All authors contributed to article revision, read, and approved the submitted version.

## FUNDING

This work was supported by the National Natural Science Foundation of China (Nos. 52103162, 52073111, and 31870952), the Natural Science Foundation of Jiangsu Province (BK20201070), Natural Science Foundation of Jiangsu Higher Education Institution of China (19KJB430013).

## REFERENCES

Cao, X. T., Vu-Quang, H., Doan, V. D., and Nguyen, V. C. (2021). One-step Approach of Dual-Responsive Prodrug Nanogels via Diels-Alder Reaction for Drug Delivery. *Colloid Polym. Sci.* 10, 1–9. doi:10.1007/s00396-020-04789-z

Colombo, P., Bettini, R., and Peppas, N. A. (1999). Observation of Swelling Process and Diffusion Front Position during Swelling in Hydroxypropyl Methyl Cellulose (HPMC) Matrices Containing a Soluble Drug. *J. Control. Release* 61 (1-2), 83–91. doi:10.1016/s0168-3659(99)00104-2

Dai, B., Wu, X., Butch, C. J., Wang, J., Wang, Z. T. S., Wang, Y., et al. (2019). Encapsulating Maytansinoid in pH-Sensitive Nanocarriers: The Importance of Using Extremely Potent Cytotoxic Agents and Fast Release for Nanomedicine to Achieve Tumor Elimination. *Nano Res.* 12, 1959–1966. doi:10.1007/s12274-019-2464-y

Hou, S.-L., Chen, S.-S., Huang, Z.-J., and Lu, Q.-H. (2019). Dual-responsive Polyphosphazene as a Common Platform for Highly Efficient Drug Self-Delivery. *J. Mater. Chem. B* 7, 4319–4327. doi:10.1039/c9tb00801b

Hu, Y., Xie, J., Tong, Y. W., and Wang, C.-H. (2007). Effect of PEG Conformation and Particle Size on the Cellular Uptake Efficiency of Nanoparticles with the HepG2 Cells. *J. Controlled Release* 118 (1), 7–17. doi:10.1016/j.jconrel.2006.11.028

Lammers, T., Kiessling, F., Hennink, W. E., and Storm, G. (2012). Drug Targeting to Tumors: Principles, Pitfalls and (Pre-) Clinical Progress. *J. Controlled Release* 161 (2), 175–187. doi:10.1016/j.jconrel.2011.09.063

Lappi, A.-K., and Ruddock, L. W. (2011). Reexamination of the Role of Interplay between Glutathione and Protein Disulfide Isomerase. *J. Mol. Biol.* 409 (2), 238–249. doi:10.1016/j.jmb.2011.03.024

Liu, S., Luo, X., Liu, S., Xu, P., Wang, J., and Hu, Y. (2019). Acetazolamide-Loaded pH-Responsive Nanoparticles Alleviating Tumor Acidosis to Enhance Chemotherapy Effects. *Macromol. Biosci.* 19 (2), 1800366. doi:10.1002/mabi.201800366

Luck, A. N., and Mason, A. B. (2013). Structure and Dynamics of Drug Carriers and Their Interaction with Cellular Receptors: Focus on Serum Transferrin. *Adv. Drug Deliv. Rev.* 65 (8), 1012–1019. doi:10.1016/j.addr.2012.11.001

Maeda, H., Nakamura, H., and Fang, J. (2013). The Epr Effect for Macromolecular Drug Delivery to Solid Tumors: Improvement of Tumor Uptake, Lowering of Systemic Toxicity, and Distinct Tumor Imaging *In Vivo*. *Adv. Drug Deliv. Rev.* 65 (1), 71–79. doi:10.1016/j.addr.2012.10.002

Michael, M., and Doherty, M. M. (2005). Tumoral Drug Metabolism: Overview and its Implications for Cancer Therapy. *Jco* 23 (1), 205–229. doi:10.1200/jco.2005.02.120

Mura, S., Nicolas, J., and Couvreur, P. (2013). Stimuli-responsive Nanocarriers for Drug Delivery. *Nat. Mater* 12 (11), 991–1003. doi:10.1038/nmat3776

Petros, R. A., and Desimone, J. M. (2010). Strategies in the Design of Nanoparticles for Therapeutic Applications. *Nat. Rev. Drug Discov.* 9 (8), 615–627. doi:10.1038/nrd2591

Shi, J., Kantoff, P. W., Wooster, R., and Farokhzad, O. C. (2016). Cancer Nanomedicine: Progress, Challenges and Opportunities. *Nat. Rev. Cancer* 17, 20–37. doi:10.1038/nrc.2016.108

Sun, Q., Radosz, M., and Shen, Y. (2012). Challenges in Design of Translational Nanocarriers. *J. Controlled Release* 164 (2), 156–169. doi:10.1016/j.jconrel.2012.05.042

Sun, Q., Zhou, Z., Qiu, N., and Shen, Y. (2017). Rational Design of Cancer Nanomedicine: Nanoproperty Integration and Synchronization. *Adv. Mater.* 29 (14), 1606628. doi:10.1002/adma.201606628

Wegiel, B., Gallo, D., Csizmadia, E., Harris, C., Belcher, J., Vercellotti, G. M., et al. (2013). Carbon Monoxide Expedites Metabolic Exhaustion to Inhibit Tumor Growth. *Cancer Res.* 73 (23), 7009–7021. doi:10.1158/0008-5472.can-13-1075

Wu, J. (2021). The Enhanced Permeability and Retention (EPR) Effect: The Significance of the Concept and Methods to Enhance its Application. *Jpm* 11 (8), 771. doi:10.3390/jpm11080771

Yan, L., Yee, J. A., Boylan, M., and Spallholz, J. E. (1991). Effect of Selenium Compounds and Thiols on Human Mammary Tumor Cells. *Biol. Trace Elem. Res.* 30 (2), 145–162. doi:10.1007/bf02990350

Yao, K., Gong, G., Fu, Z., Wang, Y., Zhang, L., Li, G., et al. (2020). Synthesis and Evaluation of Cytocompatible Alkyne-Containing Poly(β-Amino Ester)-Based Hydrogels Functionalized via Click Reaction. *ACS Macro Lett.* 9 (9), 1391–1397. doi:10.1021/acsmacrolett.0c00545

Ye, M., Han, Y., Tang, J., Piao, Y., Liu, X., Zhou, Z., et al. (2017). A Tumor-specific Cascade Amplification Drug Release Nanoparticle for Overcoming Multidrug Resistance in Cancers. *Adv. Mater.* 29, 1702342. doi:10.1002/adma.201702342

Yu, H., Chen, J., Liu, S., Lu, Q., He, J., Zhou, Z., et al. (2015). Enzyme Sensitive, Surface Engineered Nanoparticles for Enhanced Delivery of Camptothecin. *J. Controlled Release* 216, 111–120. doi:10.1016/j.jconrel.2015.08.021

Yu, M., Guo, F., Tan, F., and Li, N. (2015). Dual-targeting Nanocarrier System Based on Thermosensitive Liposomes and Gold Nanorods for Cancer Thermo-Chemotherapy. *J. Controlled Release* 215, 91–100. doi:10.1016/j.jconrel.2015.08.003

Zhang, L., Yao, K., Wang, Y., Zhou, Y. L., Fu, Z., Li, G., et al. (2021). Brain-Targeted Dual Site-Selective Functionalized Poly(β-Amino Esters) Delivery Platform for Nerve Regeneration. *Nano Lett.* 21 (7), 3007–3015. doi:10.1021/acs.nanolett.1c00175

Zhang, X., Yang, Y., Yao, J., Shao, Z., and Chen, X. (2014). Strong Collagen Hydrogels by Oxidized Dextran Modification. *ACS Sustainable Chem. Eng.* 2 (5), 1318–1324. doi:10.1021/sc500154t

Zhang, Z., Zhang, X., Ding, Y., Long, P., Guo, J., and Wang, C. (2019). NIR-Induced Disintegration of CuS-Loaded Nanogels for Improved Tumor Penetration and Enhanced Anticancer Therapy. *Macromol. Biosci.* 19 (4), 1800416. doi:10.1002/mabi.201800416

**Conflict of Interest:** The authors declare that the research was conducted in the absence of any commercial or financial relationships that could be construed as a potential conflict of interest.

**Publisher's Note:** All claims expressed in this article are solely those of the authors and do not necessarily represent those of their affiliated organizations, or those of the publisher, the editors and the reviewers. Any product that may be evaluated in this article, or claim that may be made by its manufacturer, is not guaranteed or endorsed by the publisher.

frontiers in Bioengineering and Biotechnology

ORIGINAL RESEARCH
published: 24 November 2021
doi: 10.3389/fbioe.2021.780609

# Bioclickable Mussel-Derived Peptides With Immunoregulation for Osseointegration of PEEK

*Huan Zhao[1†], Xiaokang Wang[1,2†], Wen Zhang[1†], Lin Wang[1], Can Zhu[1], Yingkang Huang[1], Rongrong Chen[3], Xu Chen[4], Miao Wang[4], Guoqing Pan[4]*, Qin Shi[1]* and Xichao Zhou[1]**

[1]Department of Orthopaedics, The First Affiliated Hospital of Soochow University, Orthopaedic Institute of Soochow University, Suzhou, China, [2]Department of Orthopaedics, The Affiliated Maternity and Child Health Care Hospital of Nantong University, Nantong University, Nantong, China, [3]Department of Pediatrics, The Affiliated Maternity and Child Health Care Hospital of Nantong University, Nantong University, Nantong, China, [4]Institute for Advanced Materials, School of Materials Science and Engineering, Jiangsu University, Zhenjiang, China

Polyether ether ketone (PEEK)–based biomaterials have been widely used in the field of spine and joint surgery. However, lack of biological activity limits their further clinical application. In this study, we synthesized a bioclickable mussel-derived peptide Azide-$DOPA_4$ as a PEEK surface coating modifier and further combined bone morphogenetic protein 2 functional peptides (BMP2p) with a dibenzylcyclooctyne (DBCO) motif through bio-orthogonal reactions to obtain $DOPA_4$@BMP2p-PEEK. As expected, more BMP2p can be conjugated on PEEK after Azide-$DOPA_4$ coating. The surface roughness and hydrophilicity of $DOPA_4$@BMP2p-PEEK were obviously increased. Then, we optimized the osteogenic capacity of PEEK substrates. *In vitro*, compared with the BMP2p-coating PEEK material, $DOPA_4$@BMP2p-PEEK showed significantly higher osteogenic induction capability of rat bone marrow mesenchymal stem cells. *In vivo*, we constructed a rat calvarial bone defect model and implanted PEEK materials with a differently modified surface. Micro-computed tomography scanning displayed that the $DOPA_4$@BMP2p-PEEK implant group had significantly higher new bone volume and bone mineral density than the BMP2p-PEEK group. Histological staining of hard tissue further confirmed that the $DOPA_4$@BMP2p-PEEK group revealed a better osseointegrative effect than the BMP2p-PEEK group. More importantly, we also found that $DOPA_4$@BMP2p coating has a synergistic effect with induced Foxp3+ regulatory T (iTreg) cells to promote osteogenesis. In summary, with an easy-to-perform, two-step surface bioengineering approach, the $DOPA_4$@BMP2p-PEEK material reported here displayed excellent biocompatibility and osteogenic functions. It will, moreover, offer insights to engineering surfaces of orthopedic implants.

**Keywords: PEEK, clickable mussel-biomimetic peptide, bone morphogenetic protein 2 functional peptides, bio-orthogonal reaction, osseointegration, FOXP3+ regulatory T cells**

OPEN ACCESS

***Edited by:***
*Jingan Li,*
*Zhengzhou University, China*

***Reviewed by:***
*Zhilu Yang,*
*Southwest Jiaotong University, China*
*Wenguo Cui,*
*Shanghai Jiao Tong University, China*
*Hengwei Zhang,*
*University of Rochester, United States*

****Correspondence:***
*Guoqing Pan*
*panguoqing@ujs.edu.cn*
*Qin Shi*
*shiqin@suda.edu.cn*
*Xichao Zhou*
*zhouxichao@suda.edu.cn*

*[†]These authors have contributed equally to this work*

***Specialty section:***
*This article was submitted to Biomaterials, a section of the journal Frontiers in Bioengineering and Biotechnology*

***Received:*** *21 September 2021*
***Accepted:*** *25 October 2021*
***Published:*** *24 November 2021*

***Citation:***
*Zhao H, Wang X, Zhang W, Wang L, Zhu C, Huang Y, Chen R, Chen X, Wang M, Pan G, Shi Q and Zhou X (2021) Bioclickable Mussel-Derived Peptides With Immunoregulation for Osseointegration of PEEK. Front. Bioeng. Biotechnol. 9:780609. doi: 10.3389/fbioe.2021.780609*

## INTRODUCTION

With extended life expectancy worldwide, the number of people suffering from bone and joint diseases and injuries is increasing year by year. Most of the patients need to receive internal fixation implants to restore the structure and function of damaged bones or joints (Dhawan et al., 2012; Chamoli et al., 2014). Polyether ether ketone (PEEK) is a colorless organic thermoplastic polymer in the polyaryletherketone series. Because of its high mechanical strength, high temperature resistance, chemical resistance, abrasion resistance and excellent biocompatibility, PEEK has been widely used in medical treatments, such as spinal implants, joint reconstruction, and dental and craniomaxillofacial procedures (Ghosh and Abanteriba, 2016). In the last few years, PEEK implants have been widely accepted in the human body over other traditional plastics and metals. By 2017, PEEK cages accounted for 68% of inter-body devices, representing a market of over 1 billion US$ in the United States alone. However, the common problem of PEEK implants is lack of biological induction capacity, and the biological inertness of PEEK may hinder specific cell adhesion and tissue response (for example, adhesion, signal conduction, and stimulation) during bone regeneration at the bone-implant interface, which in turn affects the osseointegration of PEEK.

Osseointegration is the early stage of the implant to form a direct and stable bone-implant connection, and it plays a very vital role in the biological and clinical success of the implants (Asri et al., 2017). Therefore, more and more clinicians and researchers have modified PEEK and its composite materials through physical, chemical, and biological methods to improve its biological activity and osteogenic properties, including blending modification, direct surface modification, and surface coating modification (Kurtz and Devine, 2007). At present, the modification methods of physical technology require a variety of complex technical procedures, such as thermal spraying, pulsed laser, ion sputtering, sandblasting, electrochemical method, and ion implantation, which require a lot of optimization experiments and complex facilities. Some biologically active molecules, such as peptides, proteins, growth factors, and even inorganic ions ($Ca^{2+}$), can be used to modify PEEK materials through physical adsorption or covalent access. However, the current physical adsorption method can cause serious molecular leakage, while the chemical method requires complex chemical means and non-biologically compatible chemical molecules to bridge the active molecules. Thus, surface coating modification of PEEK simply and conveniently is of great clinical significance in orthopedics and dentistry (Shah et al., 2019).

Marine mussel organisms have recently attraction attention because of their adsorption capacity. The adhesion plaques formed by them are composed of six kinds of foot proteins (*Mytilus edulis* foot proteins, Mfps) (Minati et al., 2017). Mfps are rich in a variety of catechol amino acids (3,4-dihydroxy-L-phenylalanine, DOPA). DOPA and its substrate can easily form covalent and non-covalent bonding, coupled with the interaction

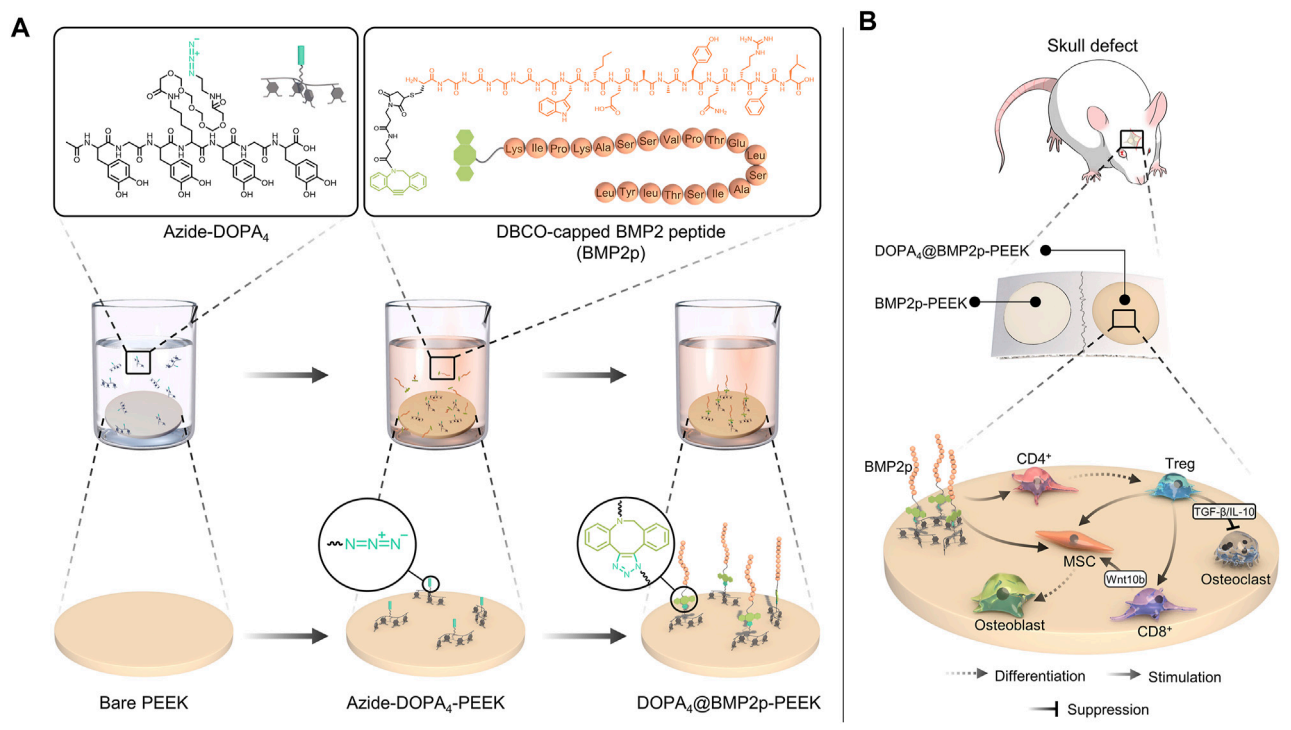


**SCHEME 1 |** Schematic diagram of the two-step surface bioengineering of PEEK implants. **(A)** Upper: molecular formula of Azide-$DOPA_4$ and bio-orthogonal conjugation of BMP2p and lower: schematic diagram of the surface modification of PEEK implants by bioclickable mussel-inspired Azide-$DOPA_4$ and BMP2p. **(B)** Schematic diagram of osteogenic and immunoregulatory effects of the $DOPA_4$@BMP2p PEEK material.

between various catechu groups, enabling marine mussel organisms to be able to adsorb to the surface of almost all solid objects under moist conditions, such as rocks, ship bottoms, and cement (Lee et al., 2006; Zhao and Waite, 2006). DOPA can provide strong adhesion on both inorganic and organic surfaces (Saiz-Poseu et al., 2013; Wei et al., 2014), which shows a huge prospect for surface modification of medical materials (Ejima et al., 2013; Yang et al., 2020a).

Bioclickable conjugation is a novel and simple attachment method, which is based on the reaction of a diarylcyclooctyne moiety (DBCO) with an Azide-labeled reaction partner. Unlike conventional click chemistry (copper-catalyzed alkyne-azide cycloaddition, CuAAC), its reaction is rapid at room temperature and does not require copper ions, which is toxic to most organisms and can cause protein denaturation. The DBCO-azide copper-free click method has been widely used in antibody-peptide preparation, labeling, and conjugation between biomolecules and cells and cell tracking (Gong et al., 2016; Yoon et al., 2016; Xiao et al., 2020).

In this study, we developed a biomimetic peptide Azide-$DOPA_4$ which is derived from mussel foot protein. With a strong and widely applicable catechol group adhesion effect, $DOPA_4$ can form an adhesion layer on the surface of PEEK, which can effectively improve the cell adhesion ability of PEEK. Due to the terminal azide groups on $DOPA_4$, this would enable subsequent integration of the biofunctional module by a second-step conjugation of the DBCO-capping biomolecules through the DBCO-Azide bioclick reaction. Bone morphogenetic protein-2 (BMP-2) is a well-characterized growth factor in that it can induce osteoblast differentiation and bone formation, which are also widely used in biomaterial tissue engineering (Khan and Lane, 2004). Therefore, we further combined typical DBCO-bearing BMP-2 functional peptides (BMP2p) through the DBCO-Azide bioclick reaction to generate $DOPA_4$@BMP2p PEEK and enhance the biological activity of PEEK. We anticipate that this improved surface strategy based on mussel adhesion and bio-orthogonal conjugation would provide a means for surface bioengineering of PEEK with optional functions.

# MATERIALS AND METHODS

## Materials

According to a previously reported method (Pan et al., 2016; Liu et al., 2018; Ma et al., 2019), Azide-$DOPA_4$ (**Scheme 1A**), BMP2p (Lys-Ile-Pro-Lys-Ala-Ser-Ser-Val-Pro-Thr-Glu-Leu-Ser-Ala-Ile-Ser-Thr- Leu-Tyr-Leu, **Scheme 1A**), and BMP2p-FITC peptides were synthesized based on the standard Fmoc-mediated solid-phase peptide synthesis strategy, with assistance from ChinaPeptides Co. Ltd. (Shanghai, China). Reserved-phase high-performance liquid chromatography (HPLC) was performed to purify the peptides on an Agilent system by using a Kromasil 100-5C18 column (5 μm, 4.6 mm × 250 mm, column temperature 25°C). The peptides were dissolved in dimethyl sulfoxide (DMSO) at 1 mg/10 μl for stocking. The phosphate-buffered saline solution (PBS, 0.02 mM, pH 7.2) was prepared in ultra-purified water (purified with a Merck Millipore pure water system to yield a minimum resistivity of 18.2 MΩ cm) and a purchased phosphate buffer salt (Beyotime Biotechnology, China). PEEK substrates were purchased from Weigao Group Medical Polymer Co., Ltd. (Shandong, China), and their diameter is 15.5 mm. Trypsin/EDTA solution (0.25%), streptomycin, and penicillin were purchased from Gibco BRL (United States). DMEM (Dulbecco's modified eagle medium) and FBS (fetal bovine serum) were purchased from HyClone (United States). DBCO-Cy5 (#A130) was purchased from Click Chemistry Tools (United States). PEEK was first washed with ultrapure water, ethanol, and hydrogen peroxide/ammonia (1:1) three times, then dried, and treated with oxygen plasma. All other common biochemical reagents were used as received.

## Azide-$DOPA_4$ or BMP2p Peptide Coating and Bio-Orthogonal BMP2p Grafting

After plasma treatment, the PEEK substrates were then immersed in the PBS solution of Azide-$DOPA_4$ (0.01 mg/ml, pre-purged with nitrogen for 15 min) or BMP2p (0.1 mg/ml). After 12 h, the coated substrates were named Azide-$DOPA_4$-PEEK and BMP2p-PEEK. Some Azide-$DOPA_4$-PEEK substrates were further incubated with BMP2p (0.1 mg/ml) for another 12 h at room temperature and named as $DOPA_4$@BMP2p-PEEK (**Scheme 1A**). All PEEK substrates were rinsed thoroughly using ultrapure water to wash away the unbounded peptides and then dried with nitrogen for further use. The PBS-immersed PEEK substrates were named PBS-PEEK and set as the control group.

## BMP2p Binding Efficiency on PEEK After Azide-$DOPA_4$ Coating

The binding efficiency of Azide-$DOPA_4$ coating on PEEK was examined by using a DBCO-Cy5 fluorescent dye. The PEEK substrates were first immersed in 0.01 mg/ml Azide-$DOPA_4$ for 12 h at room temperature and then immersed in 10 μmol/L DBCO-Cy5 PBS solution for another 12 h. The samples were denoted as Cy5-labeled Azide-$DOPA_4$-PEEK. To measure the bonding efficiency of BMP2p on PEEK, the Azide-$DOPA_4$ coating PEEK substrates were then immersed in BMP2p-FITC PBS solution for 24 h to obtain Azide-$DOPA_4$@BMP2p-FITC-PEEK. All PEEK substrates were rinsed using sterile deionized water three times before testing, and the fluorescence intensity was observed under a fluorescence microscope (Carl Zeiss, Germany).

## Characterization of the Surface of PEEK

Electrospray ionization mass spectrometry (ESI-MS) spectra were recorded on a Sciex API 150EX LC/MS with Agilent 1100 HPLC. Surface chemical compositions of the substrates were determined by using an X-ray photoelectron spectroscopy (XPS) instrument (ESCALAB MK II X-ray photoelectron spectrometer, VG Scientific). The static water contact angle (WCA) of PEEK at room temperature was evaluated with a KRÜSS DSA25 contact angle equipment (Germany). The surface morphology of the

substrates was examined using atomic force microscopy (AFM, Dimension ICON, Bruker, United States). The morphologies of all samples were observed using a scanning electron microscope (SEM) (S-4800, Hitachi, Japan).

## Osteogenic Induction

Rat bone marrow–derived mesenchymal stem cells (rBMSCs) from the bone marrow of male rats were isolated and cultured in a growth medium (DMEM supplemented with 10% FBS, 100 U/ml of penicillin, and 100 μg/ml of streptomycin) as described in the previous study (Zhao et al., 2018; Huang et al., 2020). For osteogenic differentiation of rBMSCs, the cells (passage 3) were seeded on different surface-modified PEEK substrates and cultured in an osteogenic induction (OB) medium, which was prepared from a growth medium supplemented with 50 μg/ml of ascorbic acid and 10 mM of β-glycerol phosphate. In order to test the dose and osteogenic effects of BMP2p, rBMSCs were cultured in the OB medium complement with different doses of BMP2p (10/50/100/200 ng/ml) or 10 ng/ml recombinant human BMP-2 (rhBMP-2, PeproTech, United States); the medium was changed twice a week. All cells were cultured at 37°C with 5% $CO_2$ atmosphere.

## Alkaline Phosphatase Staining and Activity Assay

To test the osteogenic activity, the ALP activity of rBMSCs cultured in the OB medium for 7 days was detected by ALP staining and ALP assay (24-well plate, $3\times10^4$ cells per well). ALP staining of the cells was performed by using the BCIP/NBT ALP Color Development Kit (Beyotime Biotech, China) according to the manufacturer's protocol. The images were acquired using a microscope (Carl Zeiss, Germany). In the ALP assay, the cells were washed with PBS 3 times and then lysed. ALP activity was determined colorimetrically using the ALP Assay Kit (Beyotime Biotech, China) and standardized on the total protein concentration calculated with the bicinchoninic acid (BCA) protein assay reagent (Beyotime Biotech, China).

## Alizarin Red Staining

Alizarin red staining was performed when rBMSCs were cultured in the OB medium for 2 weeks. The cells were fixed in 4% paraformaldehyde for 30 min at room temperature, rinsed with PBS 3 times each for 5 min, and then stained using Alizarin Red S (Solarbio, China), pH 4.2, for 30 min. The mineralized nodules containing calcium were stained as red spots and were photographed. The Alizarin red dye was subsequently extracted with 5% perchloric acid at room temperature for 20 min. Absorbance was then measured at 490 nm using a microplate spectrophotometer (BioTek, United States).

## Real-Time Quantitative RT-PCR

Messenger RNA (mRNA) of the cells was extracted according to the instructions of the TRIzol kit (Beyotime, China) after being cultured in the OB medium for 7 days. MRNA of the samples was reverse transcribed and qPCR was carried out (Bio-rad, United States). The relative gene expressions were calculated by the $2^{-\Delta\Delta Ct}$ method. GAPDH was selected to normalize the expression levels of the target genes. The results were presented in fold increase relative to the PBS-PEEK group. The primer sequences of the osteogenic-related genes, including ALP, Runt-related transcription factor 2 (Runx2), and type I collagen (Collagen I), are listed in **Supplementary Table S1**.

## Cytotoxicity Assay

The lactate dehydrogenase (LDH) activity assay was used in the cytotoxicity study. rBMSCs were cultured on different surface modified PEEK substrates for 3 days, the supernatant was collected, and the LDH content released from cultured rBMSCs was determined using an LDH assay kit (Beyotime Biotechnology, China) according to the manufacturer's instructions. The LDH release from the PBS-pretreated PEEK group was set as 100%.

## Cell Adhesion

$5\times10^4$ rBMSCs were seeded on the different modified substrates placed in a 24-well cell plate with serum-free medium. After incubation at 37°C for 6 h, all the substrates were washed with PBS and fixed in 4% paraformaldehyde. After 30 min, the substrates were washed 3 times with PBS and incubated for 5 min with 0.4% Triton-X and 1 mM $CaCl_2$ in PBS to punch the cell membrane at room temperature, and then stained with FITC-conjugated phalloidin (for staining F-actin stress fibers) and 4′-6-diamidino-2-phenylindole (DAPI, for staining nuclei) for 15 min. After staining, the substrates were washed three times with PBS and then examined under a fluorescence microscope.

## Foxp3+ Regulatory T Cell (Treg) Induction

All animal procedures were approved by the Soochow University Animal Care Committee and in accordance with the National Institute of Health's Guide for the Care and Use of Laboratory Animals. C57BL/6 mice (male, 6–8 weeks) were used for T cell isolation. Mouse spleens were passed through a 70-μm nylon mesh to produce single-cell suspensions. $CD4^+$ T cells were further magnetically enriched by negative selection according to the manufacturer's instructions (Miltenyi Biotec, Germany), resulting in a purity ≥ 96%. Anti-CD3/CD28 antibodies were coated on a 24-well-plate to generate the activation plate, and isolated $CD4^+$ spleen cells were cultured on the activation plate for 24 h to get the activating $CD4^+$ spleen cells for further Treg-generated experiments (**Supplementary Scheme S1A**).

To assess the effects of Treg induction under different conditions, activated $CD4^+$ spleen cells were cultured in a growth medium or stimulated with TGF-β (2 ng/ml) in the presence of IL-2 (20 units/ml) in AIM-V serum-free medium with or without BMP2p. Activated $CD4^+$ spleen cells were also cultured in $DOPA_4$@BMP2p–coated 24-well plate with or without stimulation with TGF-β and IL-2 (**Supplementary Scheme S1B**). After 24 h of stimulation, all the cells were collected, and the percentage of induced-Treg (iTreg, $CD4^+$CD25 + Foxp3+) cells was analyzed by flow cytometry

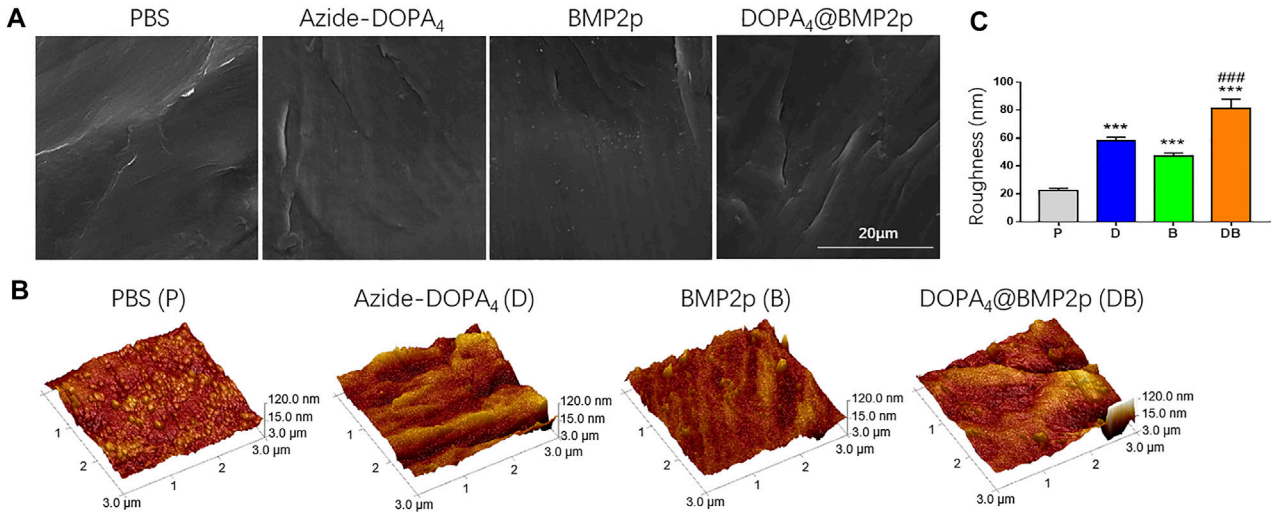


**FIGURE 1 |** Surface morphology of PEEK after different modifications. **(A)** SEM images of the PEEK substrates with different treatment methods, **(B,C)** AFM images and the surface roughness measure of the PEEK substrates after different treatment methods. Statistically significant differences are indicated by $^{***}p < 0.001$ compared with the PBS-PEEK group and $^{###}p < 0.001$ compared with the BMP2p group. Abbreviations: P (PBS), D (Azide-$DOPA_4$), B (BMP2p), and DB ($DOPA_4$@BMP2p).

assay (FCA, Merck Millipore, Germany). As shown in **Supplementary Scheme S1B**, the culture supernatant from the Treg induction (T), $DOPA_4$@BMP2p (DB), and Treg induction plus $DOPA_4$@BMP2p groups (DB + T) were collected for further experiments.

## Osteogenic Effects of Conditional Medium From iTreg Cells

RBMSCs were cultured in the growth medium and OB medium with or without 50 ng/ml BMP2p, or different conditional mediums (70% OB medium with 30% supernatant). In order to test the osteogenic activity, ALP activity of rBMSCs cultured in a different medium for 7 days was detected by ALP staining. The positive area of ALP staining was analyzed through ImageJ, and five images for each sample and three samples for each group were chosen to perform the analysis.

## *In vivo* Rat Calvarial Bone Defect Model

A total of 18 healthy male SD (Sprague–Dawley) rats, weighing around 300 g, were used to construct the 5-mm critical calvarial bone defect model. In brief, all the rats were anesthetized by intraperitoneal injection of 2% sodium pentobarbital, and a 5-mm electric drill was used to drill holes on both sides of the calvarial suture to remove the entire calvarial bone. The PEEK substrates with a differently modified surface were randomly placed in the defect holes, and the holes without the implant were set as the control group. Then, the muscles and skin were sequentially sutured with absorbable 4-0 surgical sutures. After the operation, the rats were reared in separate cages, and penicillin (150,000 Units) was injected intramuscularly once a day after the operation for 3 days. Eight weeks after the surgery, all rats were killed by an overdose of anesthesia and calvarial bones were harvested.

## Micro-CT Analysis and Histological Staining

The bone samples were fixed with neutral formalin for 48 h and then micro-computed tomography (SkyScan 1176, SkyScan, Belgium) scanning was performed. The parameters are as follows: 65 kV, 385 mA, and 1-mm aluminum filter. Three-dimensional images were reconstructed by using Mimics, and new bone volume/tissue volume (BV/TV) and bone mineral density (BMD) of the defect area were analyzed by CTAn. All bone samples were embedded in neutral resin and then were sliced with a hard tissue microtome according to the previously reported method (Zhao et al., 2018). The sections were stained with hematoxylin and eosin (H&E and Masson). The images were acquired by using a microscope (Carl Zeiss, Germany), and the bone-to-implant contact ratio (BIC, %) was calculated as the percentage of PEEK's circumference that was in direct contact with bone mineral in histological sections.

## Statistical Analysis

All quantitative data were expressed as mean ± standard deviation (*S.D.*) with no less than three replicates for each experimental condition. Statistical differences between two groups were analyzed by Student's t-test, and significant differences between more than two groups were analyzed by one-way analysis of variance (ANOVA), followed by Tukey's post hoc test. Differences between the two groups were considered statistically significant when the *p*-value was less than 0.05.

# RESULTS

## Peptide Synthesis

The mussel-inspired $DOPA_4$ peptide was prepared according to previously reported methods via a standard Fmoc-mediated solid-phase synthesis strategy (Pan et al., 2016; Liu et al., 2018; Ma et al.,

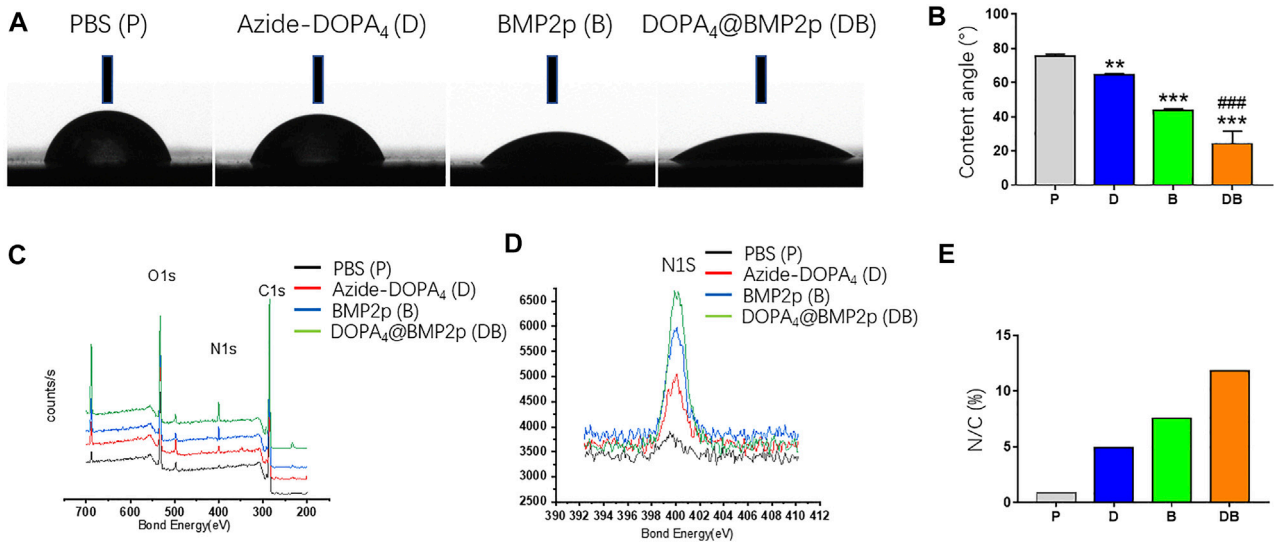


**FIGURE 2 |** Surface characterization of PEEK after different modifications. **(A)** Images of corresponding water contact angles. **(B)** Quantitative results of water contact angles. **(C–E)** XPS spectra and the surface N/C elemental ratios of PEEK substrates after different modifications. Statistically significant differences are indicated by $^{**}p < 0.01$ or $^{***}p < 0.001$ compared with the PBS-PEEK group and $^{\#\#\#}p < 0.001$ compared with the BMP2p group. Abbreviations: P (PBS), D (Azide-DOPA$_4$), B (BMP2p), and DB (DOPA$_4$@BMP2p).

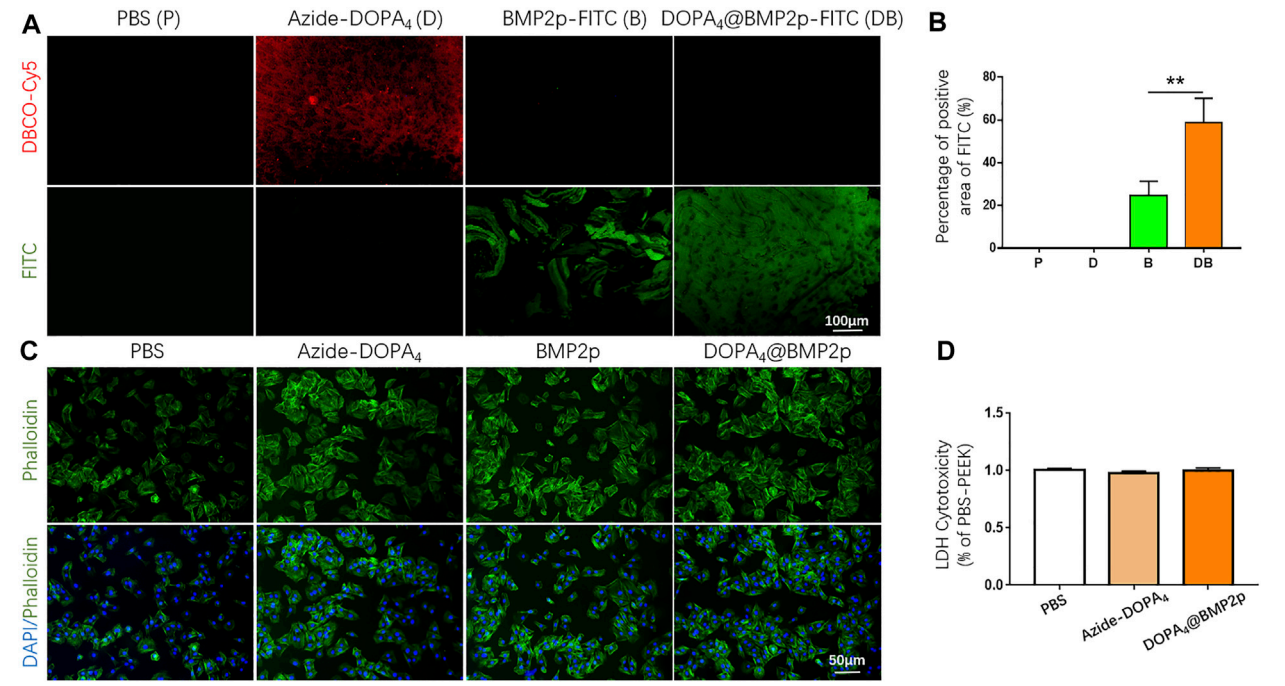


**FIGURE 3 |** Biocompatibility of different modified substrates, and bioclickable BMP2p binding on PEEK after Azide-DOPA$_4$ coating. **(A)** Fluorescence images of PEEK substrates treated with fluorescent dyes labeled Azide-DOPA$_4$ and BMP2p-FITC. **(B)** Percentage of FITC positive areas of PEEK after different treatment methods, **(C)** Morphologies of adherent rBMSCs after 6 h of culture. The cells were stained with DAPI (nuclei, blue) and Alexa Fluor 488–conjugated phalloidin (actin filaments, green). **(D)** Quantification of LDH. Abbreviations: P (PBS), D (Azide-DOPA$_4$), B (BMP2p-FITC), and DB (DOPA$_4$@BMP2p-FITC).

2019). To form mussel-like molecular binding, acetonide and Fmoc-protected DOPA (Fmoc-DOPA (acetone)-OH) was used for peptide synthesis. The amino acid sequence of this peptide was primarily designed with tetravalent DOPA units. To facilitate the molecular twist of the multiple catecholic groups and enhance the mussel-like surface binding, the DOPA units were further

improved by alternately inserting two glycine (G) and one lysine (K) molecule as spacers. In this case, the amino group of the K spacer could also be functionalized with carboxylated and azide-bearing polyethylene glycol (PEG), finally leading to the Azide-$DOPA_4$ peptide (Ac-(DOPA)-G-(DOPA)-K(PEG5-Azido)-(DOPA)-G-(DOPA)) (N→C) (**Scheme 1A**). BMP-2 functional peptides were conjugated with DBCO by N-hydroxysuccinimide and maleimidethiol coupling (**Scheme 1A**).

After being purified by HPLC (**Supplementary Figures S1A,B**), ESI-MS was then used to characterize the synthesized peptides according to the measured molecular weight. The monoisotopic mass $[M + H]^+$ of Azide-$DOPA_4$ and $[M+2H]^{2+}$ of BMP2p were measured at 1,336.79 and 1,439.8 Da, respectively, consisting with their theoretical molecular weight 1,336.4 and 2,877.3, respectively (**Supplementary Figures S1C,D**). These results confirmed the successful synthesis of the azide-capped mussel-inspired peptide (Azide-$DOPA_4$) and DBCO-conjugated BMP-2 functional peptides (BMP2p).

## Peptide Coating and Surface Characteristics

In order to study the surface characteristics after different peptide coatings on PEEK, we first observed the surface changes of materials by SEM, and no apparent differences could be found (**Figure 1A**). AFM was then employed to characterize the surface topography. Compared with the PBS-PEEK group, the roughness of the Azide-$DOPA_4$ and BMP2p groups was significantly increased, while there were many nano-sized embosses unevenly deposited on the $DOPA_4$@BMP2p group surface, and the roughness measure was also the highest (**Figures 1B,C**). Furthermore, WCA test results demonstrated that the surface of PBS-PEEK was strongly hydrophobic, and the surface wettability of the substrates showed significant improvement after peptide coating (**Figure 2A**). According to the calculation of the corresponding WCA profile on the surface of the material, we found that the $DOPA_4$@BMP2p-PEEK material had the best hydrophilicity (**Figure 2B**). Therefore, these results primarily indicated the feasibility of our $DOPA_4$ peptide combined with BMP2p for surface modification of PEEK.

Following that, we used XPS to confirm the changes of surface elemental compositions of PEEK after different surface modifications. Due to the high nitrogen (N) content of Azide-$DOPA_4$ and BMP2p, all peptide-treated substrates showed a remarkably enhanced N1s signal (400.12 eV) compared with that of the PBS-PEEK group, which suggested that the peptide was successfully loaded onto the surface of PEEK. Compared with the BMP2p-PEEK group, $DOPA_4$@BMP2p-PEEK showed a higher N1s signal. Since this peak corresponds to the amide in the peptide bond, it reminds us that Azide-$DOPA_4$ coating can significantly increase the binding of BMP2p on the surface of the PEEK (**Figures 2C,D**). The quantitative results further revealed that the N/C atomic ratios significantly increased in all the peptide-treated groups, especially in the $DOPA_4$@BMP2p-PEEK group (**Figure 2E**).

In order to detect the coating condition of Azide-$DOPA_4$ on PEEK, we used DBCO-Cy5 fluorescent dye to label Azide-$DOPA_4$ on PEEK through a bio-orthogonal reaction. As observed in the images given in **Figure 3A**, red fluorescence can be observed on the surface of DBCO-Cy5-Azide-$DOPA_4$-PEEK (group D) and this confirmed the successful embedding of Azide-$DOPA_4$ on PEEK. We also synthesized FITC-labeled BMP2p (BMP2p-FITC) to further confirm the efficiency of BMP2p conjugating on PEEK, especially after Azide-$DOPA_4$ coating. As we expected, specific fluorescence can be observed on the surface of DBCO-Cy5-Azide-$DOPA_4$-PEEK (group D) and BMP2p-FITC-PEEK (group B) under the fluorescence microscope after 12 h of immersion at room temperature. Scattered green fluorescence can be seen on the surface of the group B material, while uniformly distributed green fluorescence can be seen on the surface of the $DOPA_4$@BMP2p-FITC-PEEK (group DB) material (**Figure 3A**). The FITC fluorescence positive area was significantly increased in group DB compared to group B, which further verified that the PEEK material could bind more with BMP2p after Azide-$DOPA_4$ surface coating (**Figure 3B**).

We further performed a cell adhesion experiment of rBMSCs cultured on the different modified substrates, and the effects of cell adhesion were investigated by F-actin cytoskeleton staining (phalloidin, green). As shown in **Figure 3C**, rBMSCs could adhere on all the substrates after 6 h of culture, while the organization of F-actin networks for cells adhered on the group of $DOPA_4$@BMP2p exhibited larger amount and improved spreading shape compared with other three groups. However, there was also an enhancement of rBMSC adhesion in the Azide-$DOPA_4$ and BMP2p-modified groups compared with the PBS group, which is consistent with the surface characterization results of different modified PEEK substrates. Besides, the interaction between BMP-2 and BMPRs could also enhance cell adhesion. LDH assay provides a simple and reliable method for determining cellular cytotoxicity, especially in finding the damage inflicted on the plasma membrane. We assessed the biocompatibility of different modified PEEK surfaces via LDH assay after we synthesized the peptides. As shown in **Figure 3D**, there was no statistical difference of LDH content released from cells cultured on peptide-grafted substrates compared to the PBS-pretreated PEEK substrates, indicating that peptide modification of PEEK displayed no cytotoxicity. Through the abovementioned analysis of the surface characteristics of the material, we have confirmed that the $DOPA_4$@BMP2p surface modification significantly improves the characteristics of PEEK. The surface roughness was obviously increased and the hydrophilicity was improved after coating, which is better for cell adhesion on PEEK. Besides, PEEK can bind more with BMP2p after Azide-$DOPA_4$ coating by bioclickable conjugation. More importantly, compared with other physical and chemical methods, this combination method is convenient and stable.

## Osteogenesis Induction Capability of PEEK Materials With $DOPA_4$-BMP2p Modified Surface *in vitro*

In order to test the dose and osteogenic effects of our BMP2p, rBMSCs were cultured in the OB medium with different doses of BMP2p (10/50/100/200 ng/ml) or 10 ng/ml rhBMP-2, and the cells

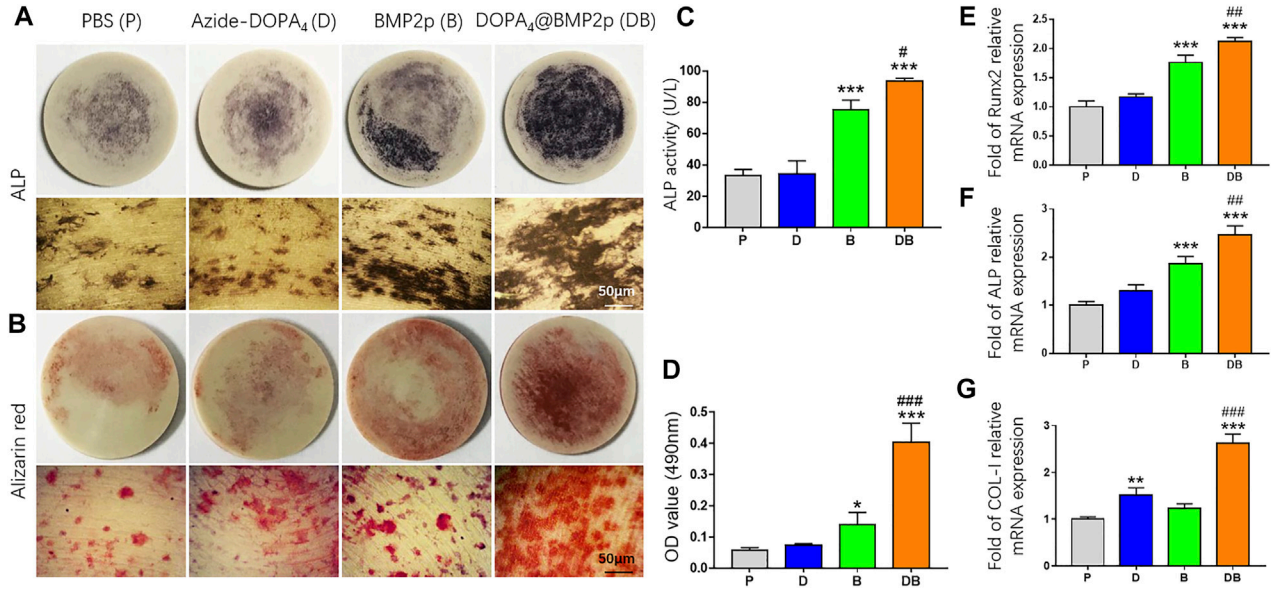


**FIGURE 4 |** *In vitro* osteogenesis induction capability of PEEK after different surface modifications. **(A)** Representative images of ALP staining of rBMSCs on different PEEK substrates after 7 days of culture in the osteogenic induction medium (upper: general photo of whole PEEK and lower: images under the microscope). **(B)** Representative images of Alizarin red S staining after 14 days of osteogenic differentiation (upper: general photo of whole PEEK and lower: images under the microscope). **(C,D)** Quantitative analysis of ALP activity and Alizarin red–stained mineral layer. **(E–G)** QPCR analysis of osteogenic differentiation genes of rBMSCs on different PEEK substrates after 5 days of culture in the osteogenic induction medium. Statistically significant differences are indicated by $^{*}p < 0.05$, $^{**}p < 0.01$, or $^{***}p < 0.001$ compared with the PBS-PEEK group (P) and $^{\#}p < 0.05$ and $^{\#\#\#}p < 0.001$ compared with the BMP2p-PEEK group (B). Abbreviations: P (PBS), D (Azide-DOPA$_4$), B (BMP2p), and DB (DOPA$_4$@BMP2p).

cultured in the OB medium were set as the control. We first performed ALP staining after 7 days of cell culture, which is an early marker for evaluating the metabolic activity of osteoblasts. Compared with the control group, the number of ALP staining positive cells increased significantly when cultured with exogenous 10 ng/ml rhBMP-2 or 100 ng/ml BMP2p (**Supplementary Figure S1A**), and the results of ALP activity were consistent with those of the staining (**Supplementary Figure S1C**). Matrix mineralization is an indicator in the later stage of osteogenesis, which is also an important index of enhanced osteogenesis. We further performed Alizarin red staining to observe its effect on cell mineralization after 14 days of culture, and the mineralization of rBMSCs was significantly enhanced when cultured with exogenous 50/100/200 ng/ml BMP2p (**Supplementary Figures S1B,D**). From the results mentioned above, we identified the osteogenic activity of our BMP2p, and 100 ng/ml BMP2p even displayed better osteogenic promoting effects than 10 ng/ml rhBMP-2 (**Supplementary Figure S1D**).

We then characterized osteogenic differentiation of rBMSCs on different surface-modified PEEK substrates by testing the activity of ALP. After being cultured in the OB medium for 7 days, ALP staining positive cells can be found in all PEEK groups. There were more ALP-positive cells in the BMP2p and DOPA$_4$@BMP2p groups (**Figure 4A**). By normalizing the ALP protein contents, the BMP2p-PEEK group showed 2.26-fold higher ALP activity, and the DOPA$_4$@BMP2p group showed 2.81-fold higher ALP activity than the PBS group. More importantly, the DOPA$_4$@BMP2p group had significantly higher ALP activity than that of the BMP2p group (**Figure 4C**). This result indicated early enhancement of osteogenicity. We further stained the rBMSCs with Alizarin red after 14 days of culture in the OB medium, and positive staining can also be found in all PEEK groups (**Figure 4B**). The quantitative analysis results of Alizarin red were consistent with those of the ALP. The BMP2p-PEEK group showed 2.43-fold higher Alizarin red content, and the DOPA$_4$@BMP2p group showed 6.95-fold higher Alizarin red content than the PBS group. Moreover, the DOPA$_4$@BMP2p group showed 2.86-fold higher mineralization effects than the BMP2p group (**Figure 4D**). Then, we examined the expression of the osteogenic-related genes of rBMSCs cultured on different PEEK materials. Compared with the PBS-PEEK, gene expression level of Runx2, ALP and COL-I were also significantly upregulated in the DOPA$_4$@BMP2p group after 7 days of osteogenic induction (**Figures 4E–G**). Collectively, the osteogenetic capability of PEEK is significantly enhanced in the DOPA$_4$@BMP2p group through bioclickable conjugation.

## Bone Defect Repairing Effects of PEEK Materials With the DOPA$_4$@BMP2p Modified Surface *in vivo*

In order to examine the osteogenic induction of PEEK after different surface modifications *in vivo*, we constructed a rat

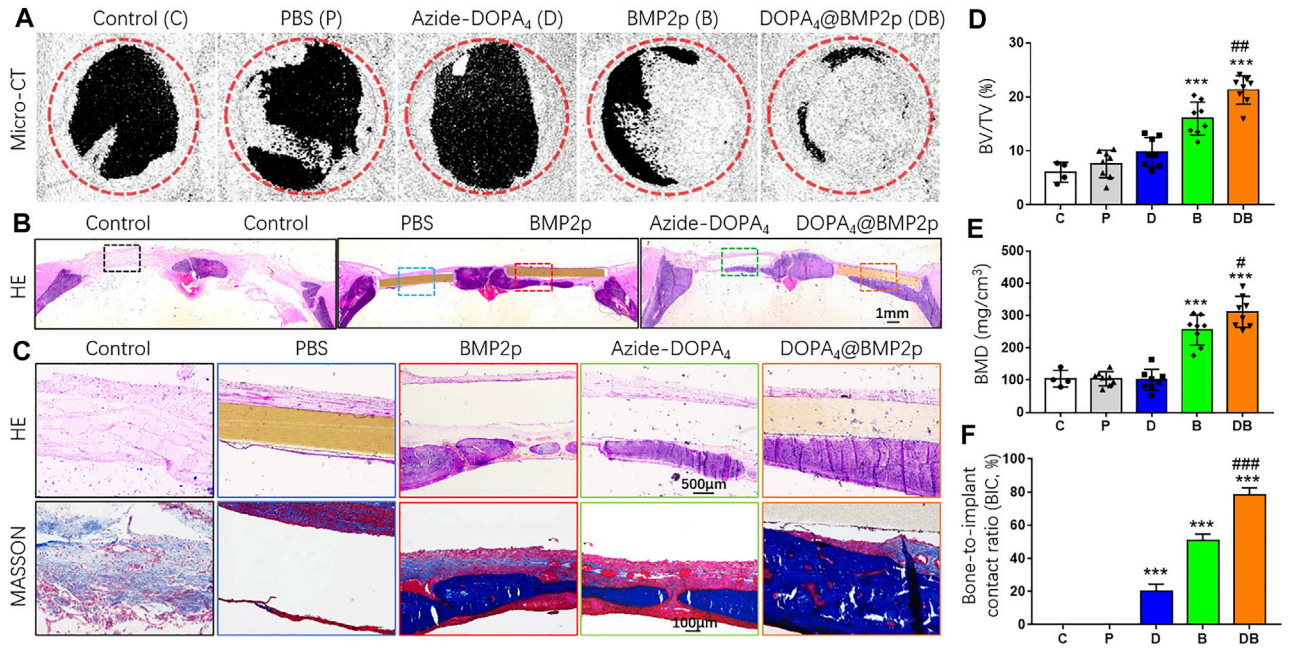


**FIGURE 5 |** *In vivo* bone defect repairing effects of PEEK after different surface modifications. **(A)** Micro-CT 3D-reconstructed images and **(D,E)** quantitatively evaluating the peri-implant bone generation according to the percentage bone volume (BV) among tissue volume (TV) (BV/TV) and bone mineral density (BMD). **(B)** H&E histological section staining images of the *in vivo* osseointegration of different surface-modified PEEK implants at low magnification and **(C)** high magnification. **(D)** Masson's staining images of the different surface-modified PEEK implants. **(G)** Histomorphometric analysis of bone-implant contact (BIC) percentage of different surface-modified PEEK implants. Data are presented as the mean ± SD, $n = 4–8$. Statistically significant differences are indicated by $^{***}p < 0.001$ compared with the sham control group (group C) and $^{\#}p < 0.05$, $^{\#\#}p < 0.01$, or $^{\#\#\#}p < 0.001$ compared with the BMP2p-PEEK group (group B). Abbreviations: C (control), P (PBS), D (Azide-$DOPA_4$), B (BMP2p), and DB ($DOPA_4$@BMP2p).

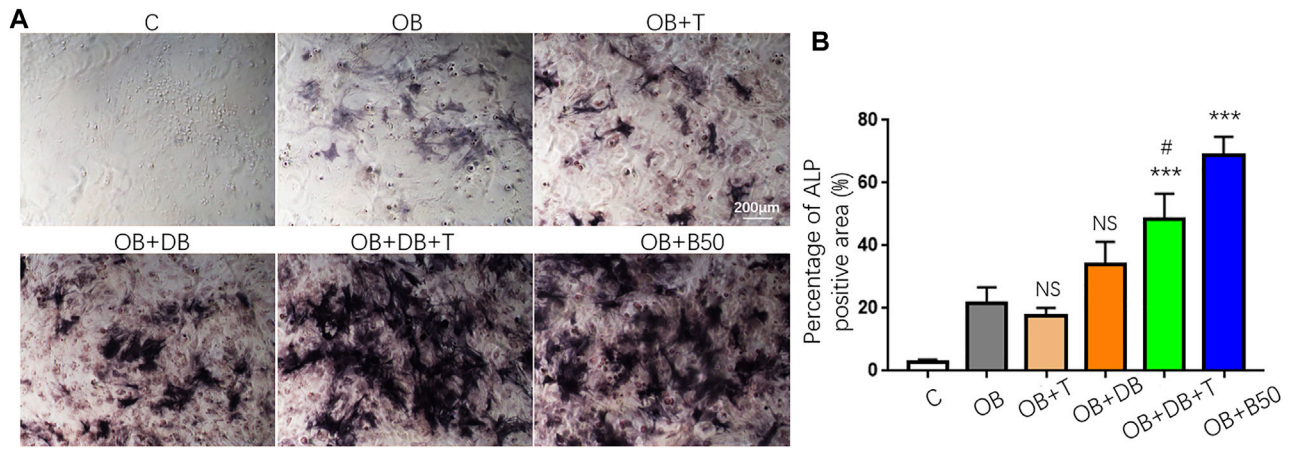


**FIGURE 6 |** Synergistic osteogenesis effect of $DOPA_4$@BMP2p coating and Treg cells. **(A)** Representative images of ALP staining of rBMSCs cultured in a different medium. **(B)** Percentage of ALP staining positive area (%). Data are presented as the mean ± SD, $n = 4$. Statistically significant differences are indicated by $^{***}p < 0.001$ compared with the OB group (OB), and NS means not statistically significant. $^{\#}p < 0.05$ compared with the OB + DB group. Abbreviations: C (control), OB (osteogenic induction medium), OB + T (conditional medium consist of OB medium and supernatant from Treg induction group), OB + DB (conditional medium consist of OB medium and supernatant from $DOPA_4$@BMP2p group), OB + DB + T (conditional medium consist of OB medium and supernatant from Treg induction + $DOPA_4$@BMP2p group), and OB + B (OB medium plus 50 ng/ml BMP2p).

model with the 5-mm critical calvarial bone defects and implanted them with surface-modified PEEK. The rat calvarial bone samples were collected 8 weeks after the surgery. Micro-CT scanning and histological staining of hard tissue sections were used to determine the bone defect repairing effect of different surface-modified PEEK

materials. Three-dimensional reconstruction images of Micro-CT scanning showed that there was no obvious new bone formation in the bone defect area of the control group (C). Compared with group C, there were several scattered new bone formations in the PBS-PEEK (P) group, and some new bone formations around the edge of the bone defect area were found in the Azide-$DOPA_4$-PEEK (D) group. Both the BMP2p-PEEK group (B) and $DOPA_4$@BMP2p-PEEK (DB) group showed apparent new bone formation, and the group DB grew more new bones, which almost covered the bone defect area (**Figure 5A**). We further analyzed the new bone volume (BV/TV) and bone mineral density (BMD) of the defect area. Compared with group C, the BV/TV and BMD in groups P and D were slightly increased, but the difference had no significance, while in groups B (2.65-fold) and DB (3.53-fold), they were significantly increased. BMD results showed no difference in groups P and D compared with group C, that is, there was a 2.44-fold increase in group B and a 2.97-fold increase in group DB. Compared with group B, the BV/TV and BMD were significantly higher in group DB (**Figures 5D,E**).

Furthermore, we performed H&E and Masson's staining of the hard tissue slices of the calvarial bone samples. No foreign body giant cells or fibrous capsules were found around the bone-implant interface in each surface-modified PEEK group. There was no apparent new bone formation in the bone defect area in groups C and P; a small amount of new bone formation was found under the PEEK material in the group D, and some new bone and new blood vessels were seen in group B, but the bonding interface between the PEEK material and the new bone was not good. In group DB, a large number of new bones were continuously distributed along the bottom of PEEK (**Figures 5B,C**). The bone-to-implant contact ratio (BIC, %) was calculated, and group DB had the best bone-to-implant contact (**Figure 5F**). These *in vivo* data indicated that, compared with the single-peptide surface modification, Azide-$DOPA_4$ combined with BMP2p surface modification could effectively enhance the osteogenicity and osseointegration ability of PEEK. To the best of our knowledge, our study is the first one to improve the osseointegration and osteoinduction capacity of PEEK through the DBCO-Azide copper-free click method.

## Synergistic Osteogenesis Effect of $DOPA_4$@BMP2p With Anti-Inflammation of iTreg

Numerous studies have implicated the immunomodulatory properties of BMP-2, which also plays an indispensable role in bone regeneration (Shu et al., 2018; Wei et al., 2018; Pajarinen et al., 2019). Consequently, we examined whether our BMP2p also retains these immune regulatory effects. CD4+Foxp3- conventional T cells could be induced to Foxp3+ Treg (iTreg) cells in the presence of TGF-β and IL-2 *in vitro* (Joetham et al., 2020). As shown in **Supplementary Scheme S1**, we cultured activated $CD4^+$ spleen cells under different conditions and collected the supernatant. The number of iTreg cells ($CD4^+$CD25 + Foxp3+) was determined by flow cytometry. Unexpectedly, the exogenous addition of 50 ng/ml BMP2p or $DOPA_4$@BMP2p coating did not promote the generation of iTreg cells (**Supplementary Figure S3**). However, the conditional medium from $DOPA_4$@BMP2p coating iTreg cells (OB + DB + T) showed better osteogenic activity than $DOPA_4$@BMP2p coating activated $CD4^+$ T cells (OB + DB) and classical iTreg cells (OB + T). These results suggested that $DOPA_4$@BMP2p coating may have a synergistic effect with iTreg cells to promote osteogenesis (**Figure 6**).

# DISCUSSION

It is believed that the surface characteristics of the material (the composition of the surface, the roughness morphology, and the hydrophilicity) are very essential for its osseointegration, and the medium roughness and strong hydrophilic surface is more conducive to cell activity and osseointegration (Stach and Kohles, 2003; Feller et al., 2014). Compared with traditional metallic bone tissue implantation materials, such as stainless steel, titanium, and its alloys, PEEK has excellent properties, such as stable chemical structure, good biocompatibility, wear-resistance, and transmittable X-rays. PEEK also has an elastic modulus closer to the cortical bone, which can effectively reduce or eliminate the stress-shielding effect, thereby reducing or avoiding bone resorption (Kurtz and Devine, 2007). However, surface hydrophobicity, lack of bone conduction, and osseointegration capabilities limit its further clinical application. Over the past decades, surface modification has been widely used to improve its biological activity and osteogenic properties (Ouyang et al., 2016; Chen et al., 2017; Wang et al., 2019). Nonetheless, these methods mostly involve tedious chemical reactions and complicated surface treatments, which may also compromise the controllability, operability, and reproducibility of a multicomponent bioactive surface.

Like Mfps, our mussel-inspired peptide (DOPA) could stably bind to the Ti implants via a facile self-organized multivalent coordinative interaction (Guo et al., 2019), and further improved the osseointegration of Ti screws in osteoporotic conditions by combining with two bioactive peptides (cell adhesive peptide RGD and osteogenic growth peptide OGP) (Zhao et al., 2018). Here, we developed a biomimetic method for introducing an osteogenic bioactive coating onto PEEK surfaces by combining bio-orthogonal conjugation with mussel-inspired adhesive chemistry. A mussel-inspired peptide with a clickable azide group (Azide-$DOPA_4$) was synthesized for the first-step grafting via mussel adhesion mechanism, and the osteogenic moiety BMP2p spontaneously binds onto the mussel-inspired peptide layer through bio-orthogonal click chemistry. According to the analysis of the surface characteristics of the $DOPA_4$@BMP2p-modified PEEK material, we confirmed that the surface roughness was obviously increased, and the hydrophilicity was improved after coating, which is better for cell adhesion on PEEK. Compared to traditional chemical methods, the combination of mussel adhesion and bio-orthogonal chemistry features simplicity, rapidness, and high efficiency.

BMP is a member of the TGF-β (transforming growth factor-β) superfamily and plays an influential regulatory role in embryogenesis, skeletal growth, remodeling, and repair. A large number of studies have shown that BMP-2 can increase the expression of osteoblast functional proteins, enhance the activity of ALP, and promote the osteogenic-related cells to form mineralized nodules *in vitro*. Besides, rhBMP-2 is currently available for orthopedic usage (Khan and Lane, 2004). However, rhBMP-2 still has some limitations, such as easy decomposition, short half-life, and high cost. BMP-2 is also widely used in biomaterial tissue engineering (Liu et al., 2007). Nevertheless, the material-loaded BMP-2 may be released in large quantities in a short period of time, which has certain risks, such as swelling, seroma, and even an increased risk of cancer (Carreira et al., 2014). The polypeptide is a chain of more than 20 and less than 50 amino acids bound together via covalent peptide bonds. Polypeptides can be synthesized using various chemical means, and the cost is low. Moreover, compared with high molecular proteins, the biological function of the polypeptide is more stable and durable. In our study, Azide-$DOPA_4$ and BMP2p can be easily and safely combined on PEEK. Moreover, compared with immersion in the BMP2p-FITC solution, we verified that PEEK material could bind more with BMP2p after Azide-$DOPA_4$ surface coating through bio-orthogonal chemistry. Likewise, the osteogenesis induction capability of $DOPA_4$@BMP2p PEEK is significantly enhanced *in vitro*. Interestingly, we also found the synergistic effect of Azide-$DOPA_4$ and BMP2p on osteogenesis *in vivo*, which also appeared in other materials with dual or multiple biological activity or surface modification materials (Naskar et al., 2017; Yang et al., 2020b). The Azide-$DOPA_4$ peptide might provide a site for cells to attach to the matrix, thereby enhancing the interaction between the BMP2p and transmembrane protein receptors of the cell and further increasing bone formation. Besides, the potential immune regulatory functions of BMP2p may also play an important role in this synergistic osteogenesis effect.

Immune-bone crosstalk is thought to play a crucial role in implant integration in bone tissue. After trauma caused by the surgical implant procedure (Anderson et al., 2008), the immune response runs not only in parallel but also resulting in a complex network of reactions that dictate the long-term fate of the implant (Jones, 2008). Many types of immune cells play a notable role in such a process, including monocyte–macrophage cells, lymphocytes (T, B cells), and NK cells (Smith et al., 2009). The critical role of macrophages in the inflammatory balance has been well established. They can polarize two main different phenotypes that depend on local conditions, while the classical (M1) phenotype is favorable for proinflammation and alternative (M2) for anti-inflammation and tissue regeneration (Gu et al., 2017). Lymphocytes interact with macrophages and bone cells, thus eliciting their participation in the osseointegration process (Chen et al., 2014).

It is becoming increasingly clear that a balanced immune response is an essential condition for successful bone regeneration (Mountziaris et al., 2011). $CD4^+$CD25 + Foxp3+ Treg cells play a crucial role in the maintenance of immune and bone homeostasis. Bone homeostasis is mostly mediated by the interaction between osteoblastic bone formation and osteoblastic bone resorption. The protective role of Treg cells in bone loss is mainly by inhibiting the formation of osteoclasts *in vitro* and *in vivo* (Zaiss et al., 2007; Zaiss et al., 2010a). For example, Treg cells inhibit the osteoclasts' differentiation through paracrine signaling of TGF-β and IL-4 *in vitro* (Kim et al., 2007). Treg cells also protect TNF-α–induced bone destruction and ovariectomy-induced bone loss *in vivo* (Zaiss et al., 2010a; Zaiss et al., 2010b). The interplay between Treg cells and osteoblasts has not been completely understood. It has been demonstrated that Treg cells may directly promote osteoblast differentiation from progenitors (MSC) by inhibiting $CD4^+$ conventional T-cells and decrease their secretion of IFN-$\gamma$ and TNF-α (Liu et al., 2011; Liu et al., 2015). On the other hand, Treg cells have also been implicated in promoting the differentiation of osteoblasts directly (Lei et al., 2015). Research on intermittent PTH–induced bone anabolism found that Treg cells are involved in the upregulation of the expression of wnt10b, an osteogenic factor secreted by the $CD8^+$ T cells, which was also demonstrated in the stimulation of bone formation by oral supplementation with *Lactobacillus rhamnosus* GG (LGG) (Li et al., 2014; Tyagi et al., 2018). Additionally, bone healing and repair also can be promoted by Treg cells by enhancing bone formation and suppressing osteoclastic bone resorption (Fischer et al., 2019). More and more research studies suggest immune modulation as a novel therapeutic strategy to enhance implant osseointegration.

Recently, several studies found the immunomodulatory properties of BMP-2 to manipulate the osteoimmune environment for favorable bone regeneration (Shu et al., 2018). BMP-2 can increase the recruitment and migration of macrophages *in vitro* and increased the infiltration of macrophage populations of M2 phenotypes in the subcutaneous implants (Wei et al., 2018). The addition of BMP-2 also significantly increases the ability of TGF-β to promote the generation of Foxp3+ induced Treg cells (Lu et al., 2010). In our study, we did not find apparent promotion of the generation of iTreg cells by exogenous addition of 50 ng/ml BMP2p or $DOPA_4$@BMP2p coating. We speculated that one of the possible reasons is that the spatial structure of rhBMP2 and BMP2p is different, and the function and effect on the generation of iTreg cells of BMP2p may decrease or even be lost. On the other hand, the dosage of BMP2p we used may not be enough. However, the conditional mediums from $DOPA_4$@BMP2p coating–induced Treg cells showed better osteogenic activity than $DOPA_4$@BMP2p coating–activated $CD4^+$ T cells and classical-induced Treg cells. This suggested that $DOPA_4$@BMP2p coating may have a synergistic effect with iTreg cells to promote osteogenesis, which may also be the reason for the synergistic effect of Azide-$DOPA_4$ and BMP2p on the osteogenesis we found *in vivo*. The PEEK material cannot be decalcified, and we do not have a good way to carry out immunofluorescence staining on the tissue embedded in the neutral resin to further verify the effects of Treg cells in the bone defect area *in vivo*. The effects and mechanism of the synergistic effect of $DOPA_4$@BMP2p coating material with Treg cells *in vivo* still need to be further explored in future.

## CONCLUSION

In summary, we reported here an improved mussel-inspired surface engineering strategy for PEEK by the combination of mussel-inspired peptide and bio-orthogonal click chemistry. The main

idea of this improved strategy is to synthesize an Azide-bearing mussel-inspired peptide. With the Azide residues on the $DOPA_4$-modified surface, this strategy enables a second-step bio-orthogonal conjugation of DBCO-capping BMP2p via DBCO-Azide clicking. *In vivo* results demonstrated that our Azide-$DOPA_4$ combined with the BMP2p surface modification method can increase new bone formation around the PEEK implant and also significantly improve the integration ability of PEEK, which will reduce the possibility of implant loosening after surgery. Importantly, we also found that $DOPA_4$@BMP2p coating has a synergistic effect with induced Foxp3+ regulatory T (iTreg) cells to promote osteogenesis. This research provides a theoretical and experimental basis for the further application of PEEK materials in trauma and tissue engineering scaffolds. In addition, the molecular specificity of bio-orthogonal conjugation and the universality of the mussel adhesion mechanism reflected in our strategy may provide a versatile surface bioengineering method for a broader range of biomedical implants.

## DATA AVAILABILITY STATEMENT

The original contributions presented in the study are included in the article/**Supplementary Material**; further inquiries can be directed to the corresponding authors.

## ETHICS STATEMENT

The animal study was reviewed and approved by the Animal Care Committee of Soochow University.

## AUTHOR CONTRIBUTIONS

GP and QS conceived the project; XZ, QS, and GP designed the experiments; HZ, XW, and WZ performed the experiments and collected the data; XZ, HZ, and WZ carried out most of the data analysis; all of the other co-authors partially contributed to data collection/analysis. All authors discussed the results, contributed to the writing of the manuscript, and approved the final version.

## FUNDING

We gratefully acknowledge financial support from the National Natural Science Foundation of China (81772312 and 81972059), the Social Development Project of Jiangsu Province (BK2019668), the Natural Science Foundation of Jiangsu Province (BK20160056), Jiangsu Provincial Clinical Orthopedic Center, the Priority Academic Program Development of Jiangsu Higher Education Institutions (PAPD), National Natural Science Foundation of China (21875092) and the "Six Talent Peaks" program of Jiangsu Province (2018-XCL-013).

## SUPPLEMENTARY MATERIAL

The Supplementary Material for this article can be found online at: https://www.frontiersin.org/articles/10.3389/fbioe.2021.780609/full#supplementary-material

## REFERENCES

Anderson, J. M., Rodriguez, A., and Chang, D. T. (2008). Foreign Body Reaction to Biomaterials. *Semin. Immunol.* 20 (2), 86–100. doi:10.1016/j.smim.2007.11.004

Asri, R. I. M., Harun, W. S. W., Samykano, M., Lah, N. A. C., Ghani, S. A. C., Tarlochan, F., et al. (2017). Corrosion and Surface Modification on Biocompatible Metals: A Review. *Mater. Sci. Eng. C.* 77, 1261–1274. doi:10.1016/j.msec.2017.04.102

Carreira, A. C., Lojudice, F. H., Halcsik, E., Navarro, R. D., Sogayar, M. C., and Granjeiro, J. M. (2014). Bone morphogenetic proteins: facts, challenges, and future perspectives. *J. Dent Res.* 93 (4), 335–345. doi:10.1177/0022034513518561

Chamoli, U., Diwan, A. D., and Tsafnat, N. (2014). Pedicle Screw-Based Posterior Dynamic Stabilizers for Degenerative spine:In Vitrobiomechanical Testing and Clinical Outcomes. *J. Biomed. Mater. Res.* 102 (9), 3324–3340. doi:10.1002/jbm.a.34986

Chen, Z., Wu, C., Gu, W., Klein, T., Crawford, R., and Xiao, Y. (2014). Osteogenic Differentiation of Bone Marrow MSCs by β-Tricalcium Phosphate Stimulating Macrophages via BMP2 Signalling Pathway. *Biomaterials* 35 (5), 1507–1518. doi:10.1016/j.biomaterials.2013.11.014

Chen, M., Ouyang, L., Lu, T., Wang, H., Meng, F., Yang, Y., et al. (2017). Enhanced Bioactivity and Bacteriostasis of Surface Fluorinated Polyetheretherketone. *ACS Appl. Mater. Inter.* 9 (20), 16824–16833. doi:10.1021/acsami.7b02521

Dhawan, A., Ghodadra, N., Karas, V., Salata, M. J., and Cole, B. J. (2012). Complications of Bioabsorbable Suture Anchors in the Shoulder. *Am. J. Sports Med.* 40 (6), 1424–1430. doi:10.1177/0363546511417573

Ejima, H., Richardson, J. J., Liang, K., Best, J. P., van Koeverden, M. P., Such, G. K., et al. (2013). One-step Assembly of Coordination Complexes for Versatile Film and Particle Engineering. *Science* 341 (6142), 154–157. doi:10.1126/science.1237265

Feller, L., Chandran, R., Khammissa, R. A., Meyerov, R., Jadwat, Y., Bouckaert, M., et al. (2014). Osseointegration: Biological Events in Relation to Characteristics of the Implant Surface. *SADJ* 69112 (3), 112–117.

Fischer, L., Herkner, C., Kitte, R., Dohnke, S., Riewaldt, J., Kretschmer, K., et al. (2019). Foxp3+ Regulatory T Cells in Bone and Hematopoietic Homeostasis. *Front. Endocrinol.* 10, 578. doi:10.3389/fendo.2019.00578

Ghosh, S., and Abanteriba, S. (2016). Status of Surface Modification Techniques for Artificial Hip Implants. *Sci. Technol. Adv. Mater.* 17 (1), 715–735. doi:10.1080/14686996.2016.1240575

Gong, H., Holcomb, I., Ooi, A., Wang, X., Majonis, D., Unger, M. A., et al. (2016). Simple Method to Prepare Oligonucleotide-Conjugated Antibodies and its Application in Multiplex Protein Detection in Single Cells. *Bioconjug. Chem.* 27 (1), 217–225. doi:10.1021/acs.bioconjchem.5b00613

Gu, Q., Yang, H., and Shi, Q. (2017). Macrophages and Bone Inflammation. *J. Orthop. Transl.* 10, 86–93. doi:10.1016/j.jot.2017.05.002

Guo, X., Liu, Y., Bai, J., Yu, B., Xu, M., Sun, H., et al. (2019). Efficient Inhibition of Wear-Debris-Induced Osteolysis by Surface Biomimetic Engineering of Titanium Implant with a Mussel-Derived Integrin-Targeting Peptide. *Adv. Biosys.* 3 (2), 1800253. doi:10.1002/adbi.201800253

Huang, Y., Yin, Y., Gu, Y., Gu, Q., Yang, H., Zhou, Z., et al. (2020). Characterization and Immunogenicity of Bone Marrow-Derived Mesenchymal Stem Cells under Osteoporotic Conditions. *Sci. China Life Sci.* 63 (3), 429–442. doi:10.1007/s11427-019-1555-9

Joetham, A., Schedel, M., Ning, F., Wang, M., Takeda, K., and Gelfand, E. W. (2020). Dichotomous Role of TGF-β Controls Inducible Regulatory T-Cell Fate in Allergic Airway Disease through Smad3 and TGF-β-Activated Kinase 1. *J. Allergy Clin. Immunol.* 145 (3), 933–946.e4. doi:10.1016/j.jaci.2019.09.032

Jones, K. S. (2008). Effects of Biomaterial-Induced Inflammation on Fibrosis and Rejection. *Semin. Immunol.* 20 (2), 130–136. doi:10.1016/j.smim.2007.11.005

Khan, S. N., and Lane, J. M. (2004). The Use of Recombinant Human Bone Morphogenetic Protein-2 (rhBMP-2) in Orthopaedic Applications. *Expert Opin. Biol. Ther.* 4 (5), 741–748. doi:10.1517/14712598.4.5.741

Kim, Y. G., Lee, C.-K., Nah, S.-S., Mun, S. H., Yoo, B., and Moon, H.-B. (2007). Human CD4+CD25+ Regulatory T Cells Inhibit the Differentiation of Osteoclasts from Peripheral Blood Mononuclear Cells. *Biochem. Biophys. Res. Commun.* 357 (4), 1046–1052. doi:10.1016/j.bbrc.2007.04.042

Kurtz, S. M., and Devine, J. N. (2007). PEEK Biomaterials in Trauma, Orthopedic, and Spinal Implants. *Biomaterials* 28 (32), 4845–4869. doi:10.1016/j.biomaterials.2007.07.013

Lee, H., Scherer, N. F., and Messersmith, P. B. (2006). Single-Molecule Mechanics of Mussel Adhesion. *Proc. Natl. Acad. Sci.* 103 (35), 12999–13003. doi:10.1073/pnas.0605552103

Lei, H., Schmidt-Bleek, K., Dienelt, A., Reinke, P., and Volk, H.-D. (2015). Regulatory T Cell-Mediated Anti-Inflammatory Effects Promote Successful Tissue Repair in Both Indirect and Direct Manners. *Front. Pharmacol.* 6, 184. doi:10.3389/fphar.2015.00184

Li, J.-Y., Walker, L. D., Tyagi, A. M., Adams, J., Weitzmann, M. N., and Pacifici, R. (2014). The Sclerostin-Independent Bone Anabolic Activity of Intermittent PTH Treatment Is Mediated by T-Cell-Produced Wnt10b. *J. Bone Miner Res.* 29 (1), 43–54. doi:10.1002/jbmr.2044

Liu, Y., Enggist, L., Kuffer, A. F., Buser, D., and Hunziker, E. B. (2007). The Influence of BMP-2 and its Mode of Delivery on the Osteoconductivity of Implant Surfaces during the Early Phase of Osseointegration. *Biomaterials* 28 (16), 2677–2686. doi:10.1016/j.biomaterials.2007.02.003

Liu, Y., Wang, L., Kikuiri, T., Akiyama, K., Chen, C., Xu, X., et al. (2011). Mesenchymal Stem Cell-Based Tissue Regeneration Is Governed by Recipient T Lymphocytes via IFN-γ and TNF-α. *Nat. Med.* 17 (12), 1594–1601. doi:10.1038/nm.2542

Liu, Y., Yang, R., and Shi, S. (2015). Systemic Infusion of Mesenchymal Stem Cells Improves Cell-Based Bone Regeneration via Upregulation of Regulatory T Cells. *Tissue Eng. A* 21 (3-4), 498–509. doi:10.1089/ten.TEA.2013.0673

Liu, L., Tian, X., Ma, Y., Duan, Y., Zhao, X., and Pan, G. (2018). A Versatile Dynamic Mussel-Inspired Biointerface: From Specific Cell Behavior Modulation to Selective Cell Isolation. *Angew. Chem. Int. Ed.* 57 (26), 7878–7882. doi:10.1002/anie.201804802

Lu, L., Ma, J., Wang, X., Wang, J., Zhang, F., Yu, J., et al. (2010). Synergistic Effect of TGF-β Superfamily Members on the Induction of Foxp3+ Treg. *Eur. J. Immunol.* 40 (1), 142–152. doi:10.1002/eji.200939618

Ma, Y., He, P., Tian, X., Liu, G., Zeng, X., and Pan, G. (2019). Mussel-Derived, Cancer-Targeting Peptide as pH-Sensitive Prodrug Nanocarrier. *ACS Appl. Mater. Inter.* 11 (27), 23948–23956. doi:10.1021/acsami.9b09031

Minati, L., Migliaresi, C., Lunelli, L., Viero, G., Dalla Serra, M., and Speranza, G. (2017). Plasma Assisted Surface Treatments of Biomaterials. *Biophysical Chem.* 229, 151–164. doi:10.1016/j.bpc.2017.07.003

Mountziaris, P. M., Spicer, P. P., Kasper, F. K., and Mikos, A. G. (2011). Harnessing and Modulating Inflammation in Strategies for Bone Regeneration. *Tissue Eng. B: Rev.* 17 (6), 393–402. doi:10.1089/ten.TEB.2011.0182

Naskar, D., Ghosh, A. K., Mandal, M., Das, P., Nandi, S. K., and Kundu, S. C. (2017). Dual Growth Factor Loaded Nonmulberry Silk Fibroin/carbon Nanofiber Composite 3D Scaffolds for *In Vitro* and *In Vivo* Bone Regeneration. *Biomaterials* 136, 67–85. doi:10.1016/j.biomaterials.2017.05.014

Ouyang, L., Zhao, Y., Jin, G., Lu, T., Li, J., Qiao, Y., et al. (2016). Influence of Sulfur Content on Bone Formation and Antibacterial Ability of Sulfonated PEEK. *Biomaterials* 83, 115–126. doi:10.1016/j.biomaterials.2016.01.017

Pajarinen, J., Lin, T., Gibon, E., Kohno, Y., Maruyama, M., Nathan, K., et al. (2019). Mesenchymal Stem Cell-Macrophage Crosstalk and Bone Healing. *Biomaterials* 196, 80–89. doi:10.1016/j.biomaterials.2017.12.025

Pan, G., Sun, S., Zhang, W., Zhao, R., Cui, W., He, F., et al. (2016). Biomimetic Design of Mussel-Derived Bioactive Peptides for Dual-Functionalization of Titanium-Based Biomaterials. *J. Am. Chem. Soc.* 138 (45), 15078–15086. doi:10.1021/jacs.6b09770

Saiz-Poseu, J., Sedó, J., García, B., Benaiges, C., Parella, T., Alibés, R., et al. (2013). Versatile Nanostructured Materials via Direct Reaction of Functionalized Catechols. *Adv. Mater.* 25 (14), 2066–2070. doi:10.1002/adma.201204383

Shah, F. A., Thomsen, P., and Palmquist, A. (2019). Osseointegration and Current Interpretations of the Bone-Implant Interface. *Acta Biomater.* 84, 1–15. doi:10.1016/j.actbio.2018.11.018

Shu, Y., Yu, Y., Zhang, S., Wang, J., Xiao, Y., and Liu, C. (2018). The Immunomodulatory Role of Sulfated Chitosan in BMP-2-Mediated Bone Regeneration. *Biomater. Sci.* 6 (9), 2496–2507. doi:10.1039/c8bm00701b

Smith, M. J., White, K. L., Jr., Smith, D. C., and Bowlin, G. L. (2009). *In Vitro* evaluations of Innate and Acquired Immune Responses to Electrospun Polydioxanone-Elastin Blends. *Biomaterials* 30 (2), 149–159. doi:10.1016/j.biomaterials.2008.09.019

Stach, R. M., and Kohles, S. S. (2003). A Meta-Analysis Examining the Clinical Survivability of Machined-Surfaced and Osseotite Implants in Poor-Quality Bone. *Implant Dent.* 12 (1), 87–96. doi:10.1097/01.id.0000042507.37401.6f

Tyagi, A. M., Yu, M., Darby, T. M., Vaccaro, C., Li, J.-Y., Owens, J. A., et al. (2018). The Microbial Metabolite Butyrate Stimulates Bone Formation via T Regulatory Cell-Mediated Regulation of WNT10B Expression. *Immunity* 49 (6), 1116–1131.e7. doi:10.1016/j.immuni.2018.10.013

Wang, H., Lin, C., Zhang, X., Lin, K., Wang, X., and Shen, S. G. (2019). Mussel-Inspired Polydopamine Coating: A General Strategy to Enhance Osteogenic Differentiation and Osseointegration for Diverse Implants. *ACS Appl. Mater. Inter.* 11 (7), 7615–7625. doi:10.1021/acsami.8b21558

Wei, Q., Becherer, T., Noeske, P.-L. M., Grunwald, I., and Haag, R. (2014). A Universal Approach to Crosslinked Hierarchical Polymer Multilayers as Stable and Highly Effective Antifouling Coatings. *Adv. Mater.* 26 (17), 2688–2693. 2615. doi:10.1002/adma.201304737

Wei, F., Zhou, Y., Wang, J., Liu, C., and Xiao, Y. (2018). The Immunomodulatory Role of BMP-2 on Macrophages to Accelerate Osteogenesis. *Tissue Eng. Part A* 24 (7-8), 584–594. doi:10.1089/ten.TEA.2017.0232

Xiao, Y., Wang, W., Tian, X., Tan, X., Yang, T., Gao, P., et al. (2020). A Versatile Surface Bioengineering Strategy Based on Mussel-Inspired and Bioclickable Peptide Mimic. *Research* 2020, 7236946. doi:10.34133/2020/7236946

Yang, Z., Zhao, X., Hao, R., Tu, Q., Tian, X., Xiao, Y., et al. (2020). Bioclickable and Mussel Adhesive Peptide Mimics for Engineering Vascular Stent Surfaces. *Proc. Natl. Acad. Sci. USA* 117 (28), 16127–16137. doi:10.1073/pnas.2003732117

Yang, Y., Gao, P., Wang, J., Tu, Q., Bai, L., Xiong, K., et al. (2020). Endothelium-Mimicking Multifunctional Coating Modified Cardiovascular Stents via a Stepwise Metal-Catechol-(Amine) Surface Engineering Strategy. *Research* 2020, 9203906. doi:10.34133/2020/9203906

Yoon, H. I., Yhee, J. Y., Na, J. H., Lee, S., Lee, H., Kang, S.-W., et al. (2016). Bioorthogonal Copper Free Click Chemistry for Labeling and Tracking of Chondrocytes *In Vivo*. *Bioconjug. Chem.* 27 (4), 927–936. doi:10.1021/acs.bioconjchem.6b00010

Zaiss, M. M., Axmann, R., Zwerina, J., Polzer, K., Gückel, E., Skapenko, A., et al. (2007). Treg Cells Suppress Osteoclast Formation: a New Link between the Immune System and Bone. *Arthritis Rheum.* 56 (12), 4104–4112. doi:10.1002/art.23138

Zaiss, M. M., Frey, B., Hess, A., Zwerina, J., Luther, J., Nimmerjahn, F., et al. (2010). Regulatory T Cells Protect from Local and Systemic Bone Destruction in Arthritis. *J. Immunol.* 184 (12), 7238–7246. doi:10.4049/jimmunol.0903841

Zaiss, M. M., Sarter, K., Hess, A., Engelke, K., Böhm, C., Nimmerjahn, F., et al. (2010). Increased Bone Density and Resistance to Ovariectomy-Induced Bone Loss in FoxP3-Transgenic Mice Based on Impaired Osteoclast Differentiation. *Arthritis Rheum.* 62 (8), 2328–2338. doi:10.1002/art.27535

Zhao, H., and Waite, J. H. (2006). Linking Adhesive and Structural Proteins in the Attachment Plaque of *Mytilus californianus*. *J. Biol. Chem.* 281 (36), 26150–26158. doi:10.1074/jbc.M604357200

Zhao, H., Huang, Y., Zhang, W., Guo, Q., Cui, W., Sun, Z., et al. (2018). Mussel-Inspired Peptide Coatings on Titanium Implant to Improve Osseointegration in Osteoporotic Condition. *ACS Biomater. Sci. Eng.* 4 (7), 2505–2515. doi:10.1021/acsbiomaterials.8b00261

**Conflict of Interest:** The authors declare that the research was conducted in the absence of any commercial or financial relationships that could be construed as a potential conflict of interest.

**Publisher's Note:** All claims expressed in this article are solely those of the authors and do not necessarily represent those of their affiliated organizations, or those of the publisher, the editors, and the reviewers. Any product that may be evaluated in this article, or claim that may be made by its manufacturer, is not guaranteed or endorsed by the publisher.

frontiers in Bioengineering and Biotechnology

ORIGINAL RESEARCH
published: 25 November 2021
doi: 10.3389/fbioe.2021.755692

# The Feasibility of Targeted Magnetic Iron Oxide Nanoagent for Noninvasive IgA Nephropathy Diagnosis

*Yaoyao Wu[1], Qiang Huang[1], Junli Wang[2], Yuhua Dai[3], Ming Xiao[4], Yangyang Li[5]*, Hongbo Zhang[6]* and Wenbo Xiao[1]**

*[1]Department of Radiology, First Affiliated Hospital, School of Medicine, Zhejiang University, Hangzhou, China, [2]Department of Radiology, Fourth Affiliated Hospital, School of Medicine, Zhejiang University, Hangzhou, China, [3]Clinical Medical Research Center, Fourth Affiliated Hospital, School of Medicine, Zhejiang University, Hangzhou, China, [4]Department of Pathology, First Affiliated Hospital, School of Medicine, Zhejiang University, Hangzhou, China, [5]Zhejiang Provincial Key Laboratory for Precision Diagnosis and Treatment of Major Gynecological Diseases, Women's Hospital, Zhejiang University School of Medicine, Hangzhou, China, [6]Pharmaceutical Sciences Laboratory, Åbo Akademi University, Turku Bioscience Centre, University of Turku, Åbo Akademi University, Turku, Finland*

OPEN ACCESS

**Edited by:**
*Tairong Kuang, Zhejiang University of Technology, China*

**Reviewed by:**
*Jingchao Li, Donghua University, China*
*Feng Chen, Zhejiang University of Technology, China*

***Correspondence:**
*Wenbo Xiao*
*xiaowenbo@zju.edu.cn*
*Hongbo Zhang*
*hongbo.zhang@abo.fi*
*Yangyang Li*
*11526010@zju.edu.cn*

**Specialty section:**
*This article was submitted to Biomaterials, a section of the journal Frontiers in Bioengineering and Biotechnology*

**Received:** *09 August 2021*
**Accepted:** *20 October 2021*
**Published:** *25 November 2021*

**Citation:**
*Wu Y, Huang Q, Wang J, Dai Y, Xiao M, Li Y, Zhang H and Xiao W (2021) The Feasibility of Targeted Magnetic Iron Oxide Nanoagent for Noninvasive IgA Nephropathy Diagnosis. Front. Bioeng. Biotechnol. 9:755692. doi: 10.3389/fbioe.2021.755692*

IgA nephropathy is the most common glomerular disease in the world and has become a serious threat to human health. Accurate and non-invasive molecular imaging to detect and recognize the IgA nephropathy is critical for the subsequent timely treatment; otherwise, it may progress to end-stage renal disease and lead to glomerular dysfunction. In this study, we have developed a sensitive, specific, and biocompatible integrin αvβ3-targeted superparamagnetic $Fe_3O_4$ nanoparticles (NPs) for the noninvasive magnetic resonance imaging (MRI) of integrin αvβ3, which is overexpressed in glomerular mesangial region of IgA nephropathy. The rat model of IgA nephropathy was successfully established and verified by biochemical tests and histological staining. Meanwhile, the clinical $^{18}$F-AlF-NOTA-PRGD2 probe molecule was utilized to visualize and further confirmed the IgA nephropathy *in vivo via* positron emission computed tomography. Subsequently, the $Fe_3O_4$ NPs were conjugated with arginine–glycine–aspartic acid (RGD) molecules ($Fe_3O_4$-RGD), and their integrin αvβ3-targeted T2-weighted imaging (T2WI) potential has been carefully evaluated. The $Fe_3O_4$-RGD demonstrated great relaxation *in vivo*. The T2WI signal of renal layers in the targeted group at 3 h after intravenous injection of $Fe_3O_4$-RGD was distinctly lower than baseline, indicating MRI signal decreased in the established IgA nephropathy rat model. Moreover, the TEM characterization and Prussian blue staining confirmed that the $Fe_3O_4$-RGD was located at the region of glomerulus and tubular interstitium. Moreover, no obvious signal decreased was detected in the untargeted $Fe_3O_4$ treated and normal groups. Collectively, our results establish the possibility of $Fe_3O_4$-RGD serving as a feasible MRI agent for the noninvasive diagnosis of IgA nephropathy.

**Keywords: IgA nephropathy (IgAN), Fe3O4-RGD, αvβ3-targeted, noninvasively diagnosis, T2 weighted MR imaging**

## INTRODUCTION

IgA nephropathy is the most common glomerular disease in the world, and approximately 50% of IgA nephropathy will progress to end-stage renal disease within 30 years regardless of treatment (Moriyama et al., 2014). The gold standard for the diagnosis of IgA nephropathy is renal biopsy, clinically (Caliskan and Kiryluk, 2014). However, renal biopsy suffers from many disadvantages, for example, as an invasive examination, renal biopsy may cause various complications, such as perirenal hematoma and pain (Marek-Bukowiec et al., 2018). Moreover, biopsy can only reflect the short-term status of the disease, and multiple biopsies cannot be carried out generally. Hence, the dynamic pathological changes of the disease cannot be evaluated at real time (Suzuki, 2019). Besides, biopsy may not be performed normally due to physical factors, such as hypertension, anatomical variation, and pregnancy. Thus, non-invasive detection of IgA nephropathy has become an urgent issue. Previous studies have tried to find biomarkers of IgA nephropathy from serum and urine samples, such as increasing galactose-deficient IgA1 (Gd-IgA1) in serum (Caliskan and Kiryluk, 2014), decreasing mRNA level of IFI27 protein in peripheral blood mononuclear cells (Nagasawa et al., 2016), and combination of seven urinary markers (Neprasova et al., 2016). However, those markers are not widely used in clinic due to the lack of more experiments to validate effectiveness. Therefore, non-invasive and dynamic diagnostic approaches of IgA nephropathy is still urgent.

Integrins are heterodimer transmembrane glycoprotein receptors composed of two subunits a and $\beta$ (Jin et al., 1996; Pozzi and Zent, 2013), which can activate intracellular and extracellular signal pathways by combining with extracellular matrix such as fibronectin, collagen, laminin, or receptors on other cell surface, and participate in cellular proliferation, differentiation, adhesion, as well as migration (Takada et al., 2007; Anthis and Campbell, 2011). Integrin αvβ3, as a vitronectin receptor, is rarely expressed in normal tissues, and a little expression can be observed around glomerular capillary loops, mesangial regions, and podocytes (Jin et al., 1996; Gauer et al., 1997; Amann et al., 2012). Several studies demonstrated the high expression of integrin αvβ3 in IgA nephropathy, which can be mainly observed in the expanded mesangial region (Peruzzi et al., 2000; Du et al., 2012). It well known that arginine–glycine–aspartic acid (RGD) is a small molecular peptide and has a high affinity for integrin αvβ3 (Ruoslahti, 1996). Targeted RGD peptides can be used to estimate the expression of integrin αvβ3 quantitatively or semi-quantitatively, which has been widely used in cancer research about evaluating angiogenesis, early detection, and assessment of therapeutic response (Lang et al., 2011; Chen et al., 2020).

Magnetic resonance imaging (MRI), as a common examination for clinical disease diagnosis, possesses high spatial resolution and good tissue contrast and is not radioactive (Ye et al., 2002; Jiang et al., 2009). Nevertheless, the shortcoming of MRI is relative low sensitivity (Jiang et al., 2009). Superparamagnetic iron oxide (SPIO), as a commonly used T2 contrast agent, is able to make a rapid response to an external magnetic field, and can significantly reduce the tissue signal intensity in T2-weighted imaging and achieve more signal changes, which can overcome low sensitivity of MRI at some degree (Ye et al., 2002; Sargsyan et al., 2012; Wen et al., 2014). Furthermore, SPIO conjugating with special molecules can target specific receptors *in vivo* and demonstrated great biocompatibility (Sargsyan et al., 2012). At present, a series of studies have investigated the feasibility of targeting molecules to detect renal diseases, such as anti-C59-b-SPIO was used for the detection of Heymann nephritis (Huang et al., 2015) and CR2-SPIO was designed for the detection of lupus nephritis (Serkova et al., 2010; Sargsyan et al., 2012). However, there are few studies to investigate the feasibility of SPIO-RGD nanoprobe for detecting and monitoring IgA nephropathy in a non-invasive way.

Meanwhile, as an important molecular imaging technique, positron emission computed tomography (PET) possesses superior sensitivity and can be used to observe the distribution of specific tracers as well as quantitatively measure the transport rates *in vivo* (Glaser et al., 2008; Guo et al., 2012a) $^{18}$F is a popular PET radioisotope owing to its short half-life (109.8 min) and low positron energy (0.64 MeV) (Cheng et al., 2015). The application of $^{18}$F in the detection of renal disease involves not only neoplastic lesions, but also non-neoplastic lesions. Patients with drug-related acute renal interstitial nephritis showed higher $^{18}$F-FDG uptake in the renal cortex than baseline (Katagiri et al., 2010; Qualls et al., 2019). Moreover, $^{18}$F-labeled RGD tracers can be utilized to target integrin αvβ3 for specific targeting diagnosis (Cheng et al., 2015; Zhang et al., 2016; Jin et al., 2017; Li et al., 2019). Particularly, $^{18}$F-AlF-NOTA-PRGD2 has become an important PET tracer to measure the expression of integrin αvβ3 (Gao et al., 2012; Guo et al., 2012b). However, the short physical half-life of $^{18}$F PET probe requires experiment in a short time; otherwise, the image quality may be poor due to the rapid attenuation of $^{18}$F. In addition, the ionizing radiation of $^{18}$F may cause the body damage in the process used. Besides, an inherent limitation of PET imaging is that the spatial resolution is lower compared with MRI. The renal tissue such as cortex and medulla cannot be revealed distinctly. Nevertheless, in this work, $^{18}$F-AlF-NOTA-PRGD2 probe may be used to auxiliary confirm the successful establishment of the mouse model of IgA nephropathy.

In our work, a facile method was used to prepare the uniform BSA-modified $Fe_3O_4$ nanoparticles (NPs). Subsequently, these paramagnetic NPs were functionalized with RGD molecules (RGD-$Fe_3O_4$) as an integrin αvβ3-targeting MRI nanoprobe to specifically recognize the glomerular mesangial region of IgA nephropathy (**Scheme 1**). At first, the rat model of IgA nephropathy was successfully established and verified by biochemical tests and histological staining. Furthermore, the clinical $^{18}$F-AlF-NOTA-PRGD2 probe molecule was utilized to confirm the successful establishment of the IgA nephropathy rat model. Then, the synthesized RGD-$Fe_3O_4$ NPs were injected intravenously into rats and the integrin αvβ3-targeted T2-weighted imaging (T2WI) RGD-$Fe_3O_4$ NPs have been carefully evaluated in the IgA nephropathy rat model.

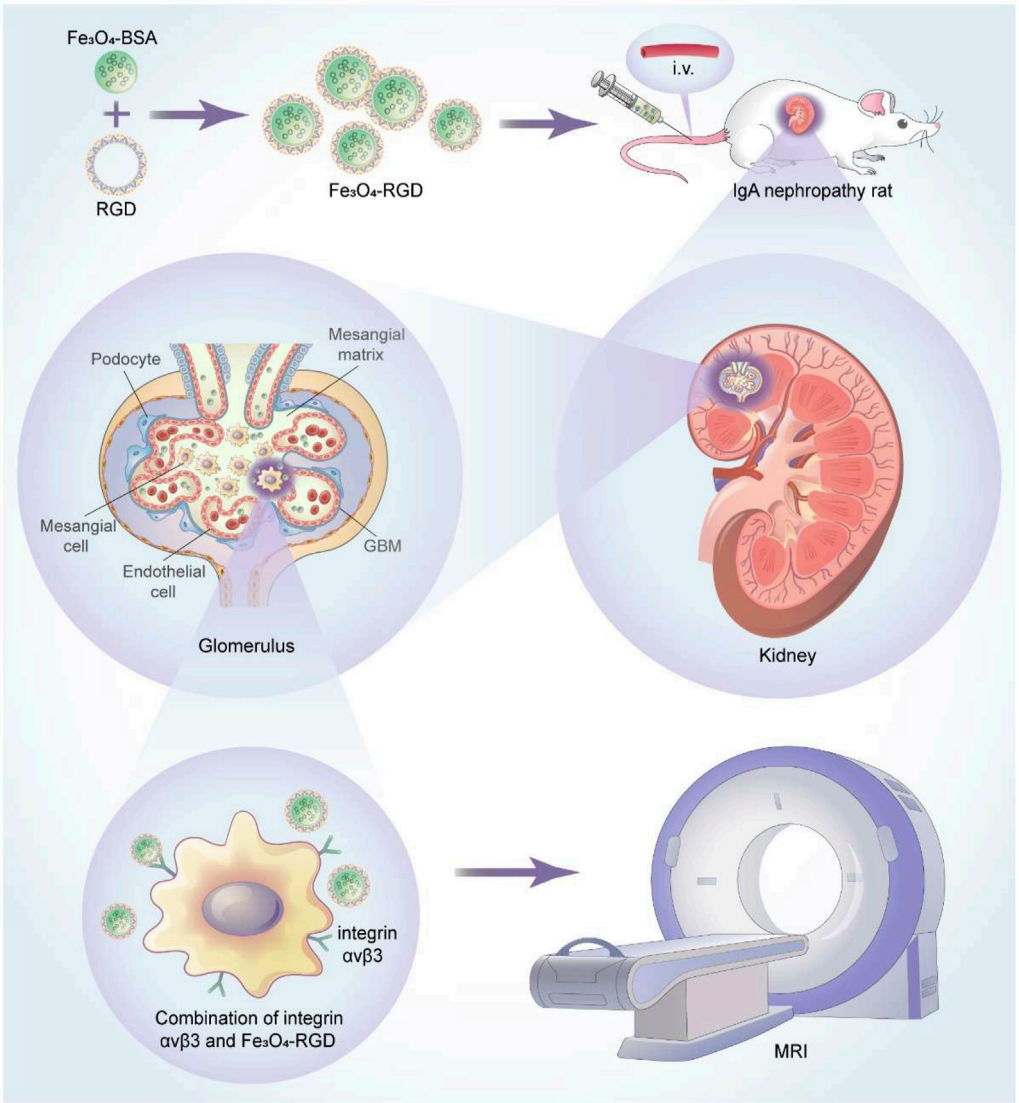


**SCHEME 1 |** Schematic illustration of the application of $Fe_3O_4$-RGD NPs for diagnosis of IgA nephropathy.

Therefore, our study provided a foundation into the development of safe and effective T2WI for molecular imaging of detecting IgA nephropathy noninvasively.

## MATERIALS AND METHODS

### Synthesis and RGD Surface Modification

$Fe_3O_4$ NPs were firstly synthesized by a simple wet chemistry method. Briefly, 200 ml of 0.18 mol/L Fe $(NO_3)_3$ solution and 200 ml of 0.12 mol/L $FeSO_4$ were mixed homogeneously. The above mixed solution was kept stirred at 40°C under the protection of $N_2$ atmosphere. Subsequently, 48 ml of $NH_3.H_2O$ solution was added and stirred for 15 min and then aged at 40°C for 5 min. Finally, $Fe_3O_4$ magnetic NPs were obtained by centrifugation and washing process. $Fe_3O_4$ magnetic NPs were then modified with BSA molecules. Specifically, an appropriate amount of $Fe_3O_4$ NP solution was added to 30 ml of BSA (10 mg/ml) solution and stirred for 24 h, mechanically. The $Fe_3O_4$-BSA NPs were obtained by separating and washing processes.

Twenty milliliters of $Fe_3O_4$-BSA NP solution (2 mg/ml) was uniformly dispersed in 28 ml of ultra-pure water, and then followed by adding 2 ml of PBS (pH 7.4) solution. The above solution was subjected to further ultrasonic dispersion for 10 min. Subsequently, 230 mg of EDC was added to the above mixed solution and stirred for 0.5 h in the dark. One hundred fifty milligrams of NHS was further added and vigorously stirred for 1 h under dark conditions. Fifteen milliliters of RGD (1 mg/ml) was then added and stirred for 24 h under dark conditions, continually. Finally, the above solution was centrifuged through an ultrafiltration tube at a speed of 5,500 RPM and washed three times with ultra-pure water. $Fe_3O_4$-BSA-RGD

NPs were further dispersed in 20 ml of ultra-pure water for further use.

## Establishment of Animal Models

For animal model construction about IgA nephropathy, 40 male SD rats (6 to 8 weeks old) were purchased from Zhejiang Academy of Medical Sciences and fed at 22.8°C (room temperature) and 59.6% relative humidity in the SPF degree animal laboratory of the First Affiliated Hospital, School of Medicine, Zhejiang University. All rats were divided into two groups randomly (model group and control group). The rats of the model group were administrated with 100 g/L BSA solution every other day in a dose of 800 mg/kg by gavage. Besides, the model group also received 0.4 ml mixed solution of CCl4 and castor oil weekly by subcutaneous injection, and 0.05 mg of LPS every other week by tail vein injection. Simultaneously, isodose saline was administered to the control group in the same way.

After 6 weeks' feeding, biochemical and pathological examinations were conducted to verify histopathological changes of IgA nephropathy and investigate renal functions in the above two groups. The samples were harvested repeatedly every 2 weeks until the model group got a significant difference in histology compared with the control group.

## Biochemical Tests and Histological Staining

To detect renal functions, blood samples were taken from the tail vein and 24-h urine was collected to determine creatinine (CRE), blood urea nitrogen (BUN), and albumin (ALB) levels by automatic biochemical analyzers (LW C400, LANDWIND, Shenzhen, China and Chemray240, Rayto, Shenzhen, China).

To compare the changes of mesangial cells and matrix in two groups, two rats from the model and control group were sacrificed, and one part of sagittal renal tissue slices was fixed in formalin, embedded in paraffin, sliced, and dewaxed to water for HE, PAS, and MASSON staining. Subsequently, staining images were acquired from the light microscope (Eclipse Ci, NIKON, Tokyo, Japan).

## Micro-PET Imaging *In Vivo*

In order to further confirm successful establishment of the IgA nephropathy rat model, the $^{18}$F-AlF-NOTA-PRGD2 probe molecule for micro-PET technology was used. The difference in renal radioactivity uptake between IgA nephropathy rat and the normal group was compared after intravenous application of $^{18}$F-ALF-NOTA-PRGD2 *in vivo*. Rats ($n$ = 1/group) were weighed and anesthetized with 4% chloral hydrate by intraperitoneal injection. Micro-PET was performed at 30, 40, 50, 60, 70, 80, and 90 min after injection of $^{18}$F-AlF-NOTA-PRGD2 (about 37 mBq) *via* tail vein. The images were reconstructed according to a two-dimensional Ordered Subsets Expectation Maximum (OSEM) algorithm and then were processed by the Inveon Research Workspace (IRW). The regions of interest (ROIs) of the entire renal parenchyma were drawn manually, and maximum percent injected dose per gram of body weight (%ID/g) was obtained on the workstation directly.

## Fluorescence Staining

To confirm the increased expression of integrin avβ3 in model rat kidney, integrin avβ3 fluorescence staining was performed. Firstly, renal tissue was fixed, embedded, sliced, and dewaxed to water conventionally, and then soaked into 3% $H_2O_2$ solution for 10–20 min. Subsequently, renal sections were treated with citric acid buffer for 15–20 min and sealed with 10% normal serum for 30 min at 37°C. After that, the diluted primary antibody (anti-Integrin alpha V beta three antibody, ab7166) was added and incubated at 37°C for 60 min. The fluorescent second antibody was added and incubated at 37°C for 30 min. DAPI was added for core staining and section sealing. In the end, the fluorescence images were shot under a fluorescence microscope (Eclipse Ti, NIKON, Tokyo, Japan). It is worth mentioning that quantitative analysis of immunofluorescence intensity was performed by Image-Pro Plus 6.0 (Media Cybernetics, Inc. Rockville, United States). Briefly, the mean density, which was the ratio of integrated option density to area, was acquired to estimate the fluorescence intensity.

## MRI Evaluation *In Vitro* and *In Vivo*

For the purpose of evaluating relativity r2 of $Fe_3O_4$-RGD *in vitro*, a series of $Fe_3O_4$-RGD solutions with different Fe concentrations (0, 0.034, 0.067, 0.135, 0.270, 0.540, 1.080) were prepared. Then, T2-weighted imaging and T2*mapping were performed on the clinical GE 3.0-T MRI (DiscoveryMR750, GE Medical System, Boston, United States). Subsequently, the value of R2 was measured by READ Y View (AW VolumeShore7, GE Medical System, Boston, United States) based on the T2* mapping. Finally, the relative curve between R2 value and $Fe_3O_4$-RGD gradient concentration was fitted by GraphPad Prism 8 (GraphPad Software Inc., San Diego, CA, United States).

In order to explore the feasibility for the early noninvasive diagnosis of IgA nephropathy through identifying the increased expression of integrin avβ3 early, the relative rat MRI experiment was performed. The rats were divided into three groups: Group 1 (targeted group) received intravenous tail injection of $Fe_3O_4$-RGD solution at a dose of 15 mg Fe/kg. Group 2 (untargeted group) received intravenous tail injection of $Fe_3O_4$-BSA solution at a dose of 15 mg Fe/kg. Group 3 (normal) group received intravenous tail injection of $Fe_3O_4$-RGD solution at a dose of 15 mg Fe/kg.

Subsequently, the above three group's rats were weighted and anesthetized with 4% chloral hydrate at a dose of 0.8 ml/kg; T2-weighted imaging and T2* mapping were performed at baseline and 3 h after administering $Fe_3O_4$-RGD or $Fe_3O_4$-BSA solution through the tail vein on the clinical GE 3.0-T MRI (DiscoveryMR750, GE Medical System, Boston, United States). T2-weighted imaging was acquired with the following parameters: repetition time (TR), 3,000 ms; echo time (TE), 68 ms; flip angle, 142°; field of view (FOV), 8 cm × 8 cm; matrix size, 128 × 128; number of sections, 16; slice thickness, 1.0 mm; total acquisition time, 4 min. The parameters of T2* mapping were as follows: repetition time (TR), 110 ms; echo time (TE), 2.0 to 16.1 ms; flip angle, 20°; field of view (FOV), 9 cm × 9 cm; matrix size, 64 × 64; number of sections, eight; slice

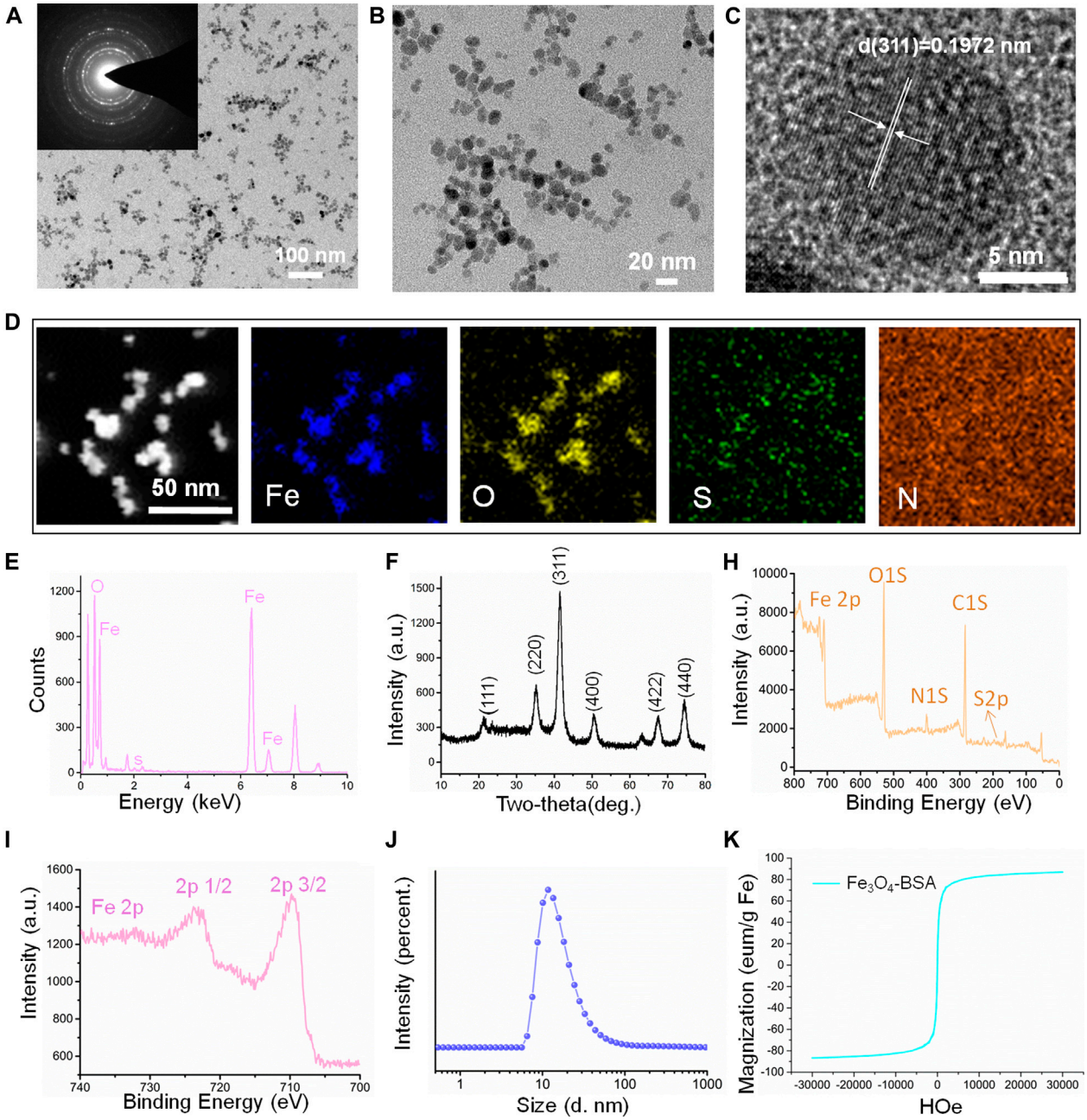


**FIGURE 1 |** Characterization of the magnetic nanoparticles ($Fe_3O_4$-BSA NPs). **(A, B)** TEM and magnified TEM images of $Fe_3O_4$-BSA NPs (the inset image is the corresponding SAED pattern). **(C)** HRTEM image. **(D, E)** HAADF-STEM elemental mapping images and EDX patterns of $Fe_3O_4$-BSA NPs. **(F)** X-ray diffraction pattern. **(H, I)** XPS spectrum of $Fe_3O_4$-BSA NPs and spectra of Fe2p orbits for the binding energy curve. **(J)** Size distribution of $Fe_3O_4$-BSA NPs in ultrapure aqueous solution. **(K)** The MH hysteresis curve of $Fe_3O_4$-BSA NPs.

thickness, 2.2 mm; total acquisition time, 30 s; the R2 values of renal different layers between groups were measured and statistical analysis were conducted by SPSS 26 (IBM Corp, Armonk, NY).

After MRI scan, those rats were sacrificed through cervical dislocation. Kidney samples were harvested rapidly and fixed in formalin for Prussian blue staining, as well fixed in 2.5% glutaraldehyde for TEM tests, respectively.

# RESULTS AND DISCUSSION

## Synthesis and Characterization of $Fe_3O_4$-BSA NPs

The $Fe_3O_4$ magnetic NPs were initially prepared and then modified with BSA molecule ($Fe_3O_4$-BSA) for further RGD grafting process. The morphology and structure were investigated by transmission electron microscopy (TEM).

**Figures 1A, B** demonstrated that the $Fe_3O_4$-BSA NPs exhibited a regularly spherical morphology with the uniform diameters in the range ~20 nm. Meanwhile, the insert selected area electron diffraction (SAED) pattern demonstrated the defined diffraction rings, implying the polycrystalline nature of $Fe_3O_4$-BSA. Furthermore, the HRTEM images of $Fe_3O_4$-BSA NPs revealed that the distance between the adjacent lattice fringes is ~0.1972 nm (**Figure 1C**), which agrees well with the crystal face of (311). The elemental mappings indicated that Fe, O, S and N elements distributed homogeneously within the $Fe_3O_4$-BSA matrix (**Figure 1D**). All expected essential chemical elements (Fe, O, and S) were verified by the energy dispersive x-ray (EDX) spectrum (**Figure 1E**). The crystalline nature $Fe_3O_4$-BSA NPs were further determined by x-ray diffraction (XRD). As presented in **Figure 1F,** the characteristic peaks of $Fe_3O_4$-BSA are related to the crystal planes of $Fe_3O_4$ crystal (JCPDS Card No. 19–0629) (Atila Dincer et al., 2019), indicating that the crystal structures of $Fe_3O_4$ remained unchanged after modification. Subsequently, the chemical composition and the surface states of $Fe_3O_4$-BSA were investigated by x-ray photoelectron spectroscopy (XPS). As displayed, the XPS spectrum of $Fe_3O_4$-BSA contains C1s, O1s, N 1s, S 2p and Fe 2p peaks (**Figure 1H**). In the Fe 2p spectrum (**Figure 1I**), the main peaks are at approximately 710.4 and 723.6 eV (Lian et al., 2019). One notable fact is that the hydrodynamic dimensions of $Fe_3O_4$-BSA is ~20 nm and the NP solution possessed narrow size distribution and good dispersion (**Figure 1J**), indicating the good dispersity and uniform size of the $Fe_3O_4$-BSA NPs. The room-temperature hysteresis loop of the $Fe_3O_4$-BSA NPs was further measured. The magnetization curves of the samples are exhibited in **Figure 1K**; the $Fe_3O_4$-BSA NPs demonstrated remarkable superparamagnetic properties and saturation magnetization was 86.8 emu/g. To investigate the targeting performance of $Fe_3O_4$-BSA NPs for IgA nephropathy detection, RGD peptide, a targetable molecule for integrin αvβ3 molecule, was modified onto $Fe_3O_4$-BSA NPs ($Fe_3O_4$-RGD), which were determined by TEM and EDS mapping observed results. As demonstrated in **Supplementary Figure S1**, the $Fe_3O_4$-RGD NPs possess a well-defined spherical morphology with a diameter of approximately 20 nm and contains Fe, O, S, and N elements. A more interesting phenomenon is that the N element signal intensity was enhanced compared with the $Fe_3O_4$-BSA, which may be due to the successful grafting of the RGD molecules. The hydrodynamic dimensions of $Fe_3O_4$-RGD NPs increased from ~20 to ~50 nm (**Supplementary Figure S2A**). Meanwhile, the zeta potential changed from ~−30.3 to ~22.9 mV after the RGD modification due to the mildly positive charged RGD molecule (**Supplementary Figure S2B, C**). Moreover, the $Fe_3O_4$-RGD NPs can be well dispersed in pure water, PBS, FBS, and DMEM solution (Figure S3). Furthermore, the cytotoxicity of $Fe_3O_4$-RGD on normal cells (293T cells) was assessed by CCK-8 test *in vitro*. The result showed that the cells' viability slightly decreased with the increase in concentrations after 24-h incubation. All groups demonstrated low cytotoxicity compared with the control group ($p > 0.05$). About 74% cell viability was still observed at the highest concentration (80 μg/ml) of $Fe_3O_4$-RGD (**Supplementary Figure S4**). This result suggested that $Fe_3O_4$-RGD NPs possess relative biocompatibility. Finally, the hemolysis assay exhibited obvious red color of positive control compared with the faint-yellow liquid of $Fe_3O_4$-RGD sample groups and negative control (**Supplementary Figure S5**), which indicated that the hemolysis of positive control was more significant than $Fe_3O_4$-RGD groups and negative control. The quantitative results of absorbance confirmed the result again. The mean values of hemolysis ratio for all $Fe_3O_4$-RGD samples were lower than 5%, which reached the standard of national biological safety for medical materials. These results suggested the blood biocompatibility of $Fe_3O_4$-RGD and is feasible to conduct animal experiments.

## Establishment of the Animal Model

### Biochemical Tests

To compare the discrepancy in renal function between the model group and control group, a series of renal functional indexes were detected. The detailed experimental process is presented in **Figure 2A**. The results demonstrated that there were no significant differences in serum creatinine (Cr), blood urea nitrogen (BUN), serum albumin (Alb), and 24-h urinary protein ($p > 0.05$) among two groups (**Figures 2B–E**). In contrast, the ratio of urinary albumin and creatinine was higher in the model group compared with the control group ($p < 0.05$) (**Figure 2F**). This result suggested that the pathological changes of model rats was in the primary stage and showed mild impairment of renal function.

## Histological Tests

To determine the histopathological changes of IgA nephropathy in the model group, various histological tests were conducted. H&E staining revealed that lots of mesangial cells were observed among expanded mesangial matrix with slightly compressed capillary loop in the model group, which was not obvious in the normal group (**Figure 3A**). Meanwhile, compared with the control group, the red and blue stained region means the mesangial area was widened and deepened in the model group on PAS staining (**Figure 3A**) and Masson staining (**Figure 3A**), respectively. There were electron-dense deposits (yellow arrow) in the glomerular mesangial area in the model group under TEM image, while no electron-dense deposits were seen in the normal group. These results indicated that model rats presented an increase in glomerular mesangial cells, mesangial matrix, and immune deposits, corresponding to the pathological changes of IgA nephropathy depicted in the literature (Caliskan and Kiryluk, 2014), and preliminarily demonstrated that the animal model was successfully constructed.

## Immunofluorescence Staining

Relevant immunofluorescence staining experiment was performed to investigate the expression of integrin αvβ3 in renal tissues between the model and normal group. The results illustrated that there was a large amount of spotted green fluorescence presented in the glomerular mesangial area in the model group, and only little green fluorescence in the mesangial region in the normal group (**Figure 3B**). The semi-quantitative analysis of fluorescence intensity demonstrated that the mean

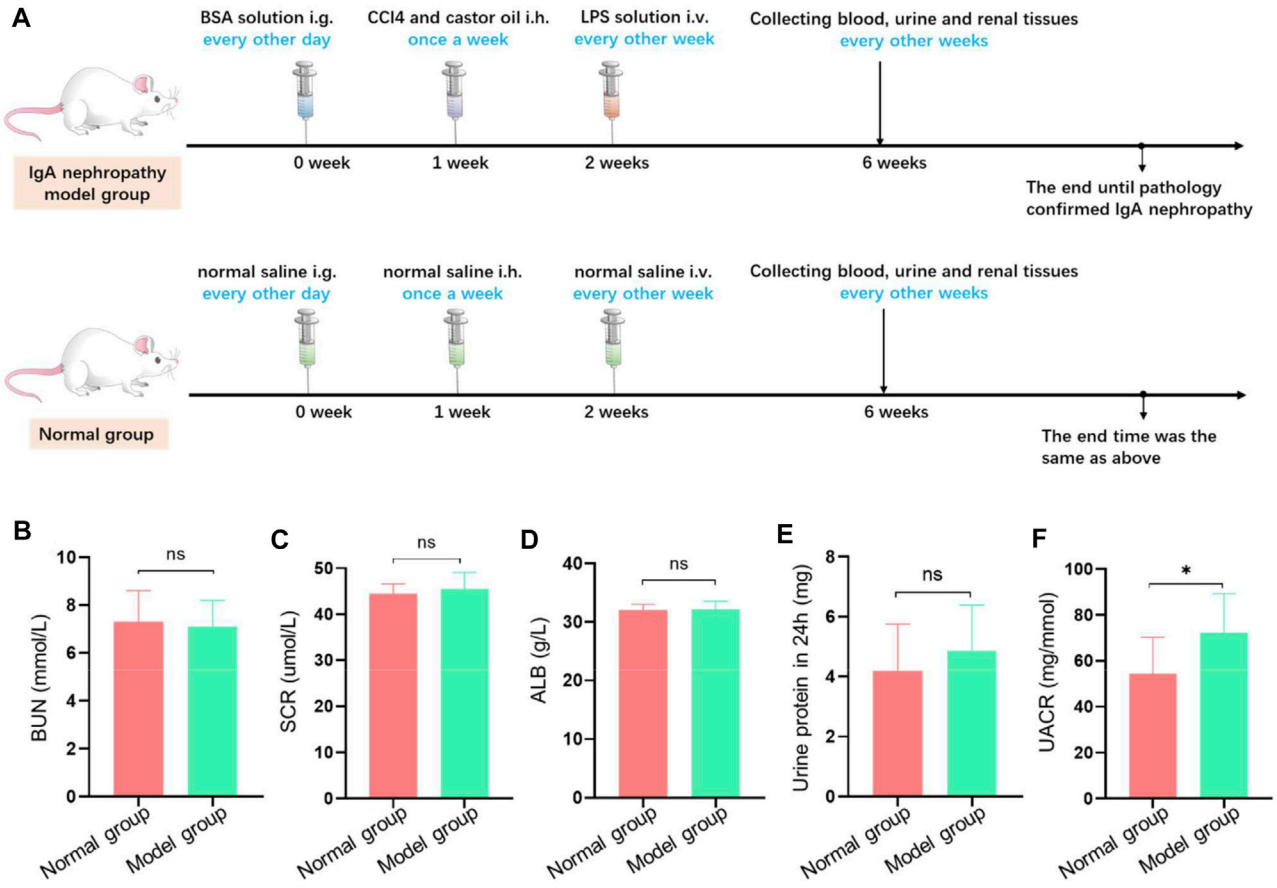


**FIGURE 2 |** The establishment of IgA nephropathy rat. **(A)** The scheme of dosing process to establish IgA nephropathy rat. **(B–F)** Biochemical test examination of rats with different treatment groups. There was no significant difference in blood bun **(B)**, blood Cr **(C)**, blood ALB **(D)**, and total 24-h urinary protein **(E)** between the model group and the normal group. Meanwhile, there was significant difference in the ratio of urinary albumin to creatinine concentration **(F)** between the model group and the normal group (*$p < 0.05$).

optical density in the model group was higher than that of the normal group ($p < 0.05$) (**Figure 3C**). This indicated that the expression of integrin αvβ3 in model rat kidney was higher than that in the normal group. Moreover, the IgA immunofluorescence staining of renal tissue in the model group or normal group was also investigated. There was a large amount of IgA immune complex deposition in the glomerular mesangial area of the model group. Contrarily, a small amount of IgA immune complex deposition in the glomerular mesangial area of the normal group was found (**Supplementary Figure S6**). Therefore, the above immunofluorescence staining results could be the basis for the later study of targeting renal integrin αvβ3 by special contrast agent to achieve imaging diagnosis of IgA nephropathy disease.

## Micro-PET Imaging

In this study, the $^{18}$F-AlF-NOTA-PRGD2 probe was then used to confirm the successful establishment of the IgA nephropathy model. The chemical structure of $^{18}$F-ALF-NOTA-PRGD2 is shown in **Supplementary Figure S7A**. The entire radiosynthesis process took about 30 min with a yield range from 48.99% to 97.33%, which mainly depended on the volume of reaction and the added amount of $^{18}$F-flouride. The radiochemical purity of the sample could reach 98% (**Supplementary Figure S7B**). Based on previous reports (Lang et al., 2011; Gao et al., 2012; Chen et al., 2020), the synthesis process of $^{18}$F-ALF-NOTA-PRGD2 is simple and time-saving.

Subsequently, the$^{18}$F-ALF-NOTA-PRGD2 probe was injected into rats of the IgA nephropathy group and normal group *via* tail vein, and PET imaging was performed (**Figures 4A,B**). The renal uptakes (%ID/g) of $^{18}$F-ALF-NOTA-PRGD2 in IgA nephropathy rats were 0.33 ± 0.03, 0.52 ± 0.07, 0.35 ± 0.03, 0.26 ± 0.02, 0.24 ± 0.01, 0.22 ± 0.01, and 0.21 ± 0.01, while those in the normal group were 0.49 ± 0.21, 0.56 ± 0.22, 0.28 ± 0.07, 0.17 ± 0.03, 0.16 ± 0.02, 0.17 ± 0.02, and 0.16 ± 0.01 at 30, 40, 50, 60, 70, 80, and 90 min after injection, respectively. The statistical analysis showed that the mean uptake values in the control group were higher than that in the IgA nephropathy group at 30 and 40 min, while these values were lower in the control group compared with the IgA nephropathy group at 50, 60, 70, 80, and 90 min. There was

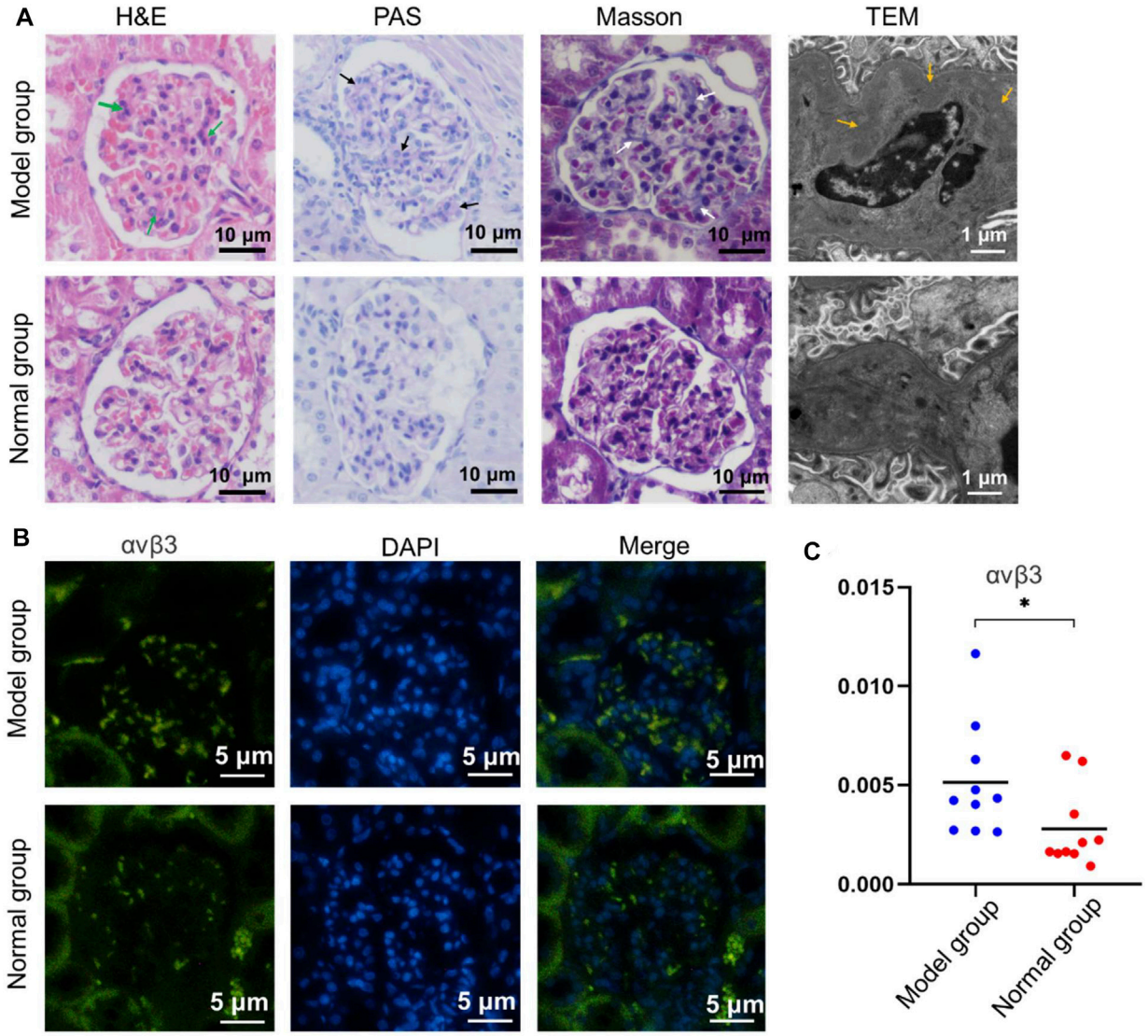


**FIGURE 3 |** Pathological staining of renal tissue in the model group and normal group. **(A)** The H&E staining, PAS staining, Masson staining, and TEM investigation were studied, respectively. **(B)** αvβ3 Immunofluorescence of renal tissue with different treatment. **(C)** The corresponding quantitative analysis of the expressed αvβ3 in (b) (*$p < 0.05$).

significant statistical difference of renal radioactive uptake between two groups at 30, 50, 60, 70, 80, and 90 min ($p < 0.05$) (**Figure 4C**). The former tumor research demonstrated that the uptake of radiotracer depended on the overexpression of integrin αvβ3 (Lee et al., 2013); therefore, IgA nephropathy rats had a higher renal uptake than the control group from 50 to 90 min; the possible reason is that the main factor affecting renal radioactive uptake in the later stage was the expression of integrin αvβ3 after early renal metabolism, which was based on our former study of the overexpression of integrin αvβ3 in IgA nephropathy. This also indicated that the detection of IgA nephropathy through specific molecules targeted to integrin αvβ3 needs a delay phase due to various interferential factors in the early stage. Therefore, the above results further prove the successful establishment of the IgA nephropathy model and provides guidance and recommendations for subsequent MRI.

## MRI Detection of IgA Nephropathy

Next, we studied the MRI of feasibility of $Fe_3O_4$-RGD for IgA nephropathy detection (**Figure 5A**). First of all, the relaxation efficiency of $Fe_3O_4$-RGD was explored *in vitro*. $Fe_3O_4$-RGD NPs solutions with different Fe concentrations (0, 0.034, 0.067, 0.135, 0.270, 0.540, 1.080) were added into tubes, respectively. Subsequently, the above tubes were performed on the clinical GE 3.0-T MRI for T2-weighted imaging. With the $Fe_3O_4$-RGD concentration increased, the T2WI signal decreased more (**Figure 5B**), and the R2 value increased as well (**Figure 5C**). The R2 value of each hole was measured

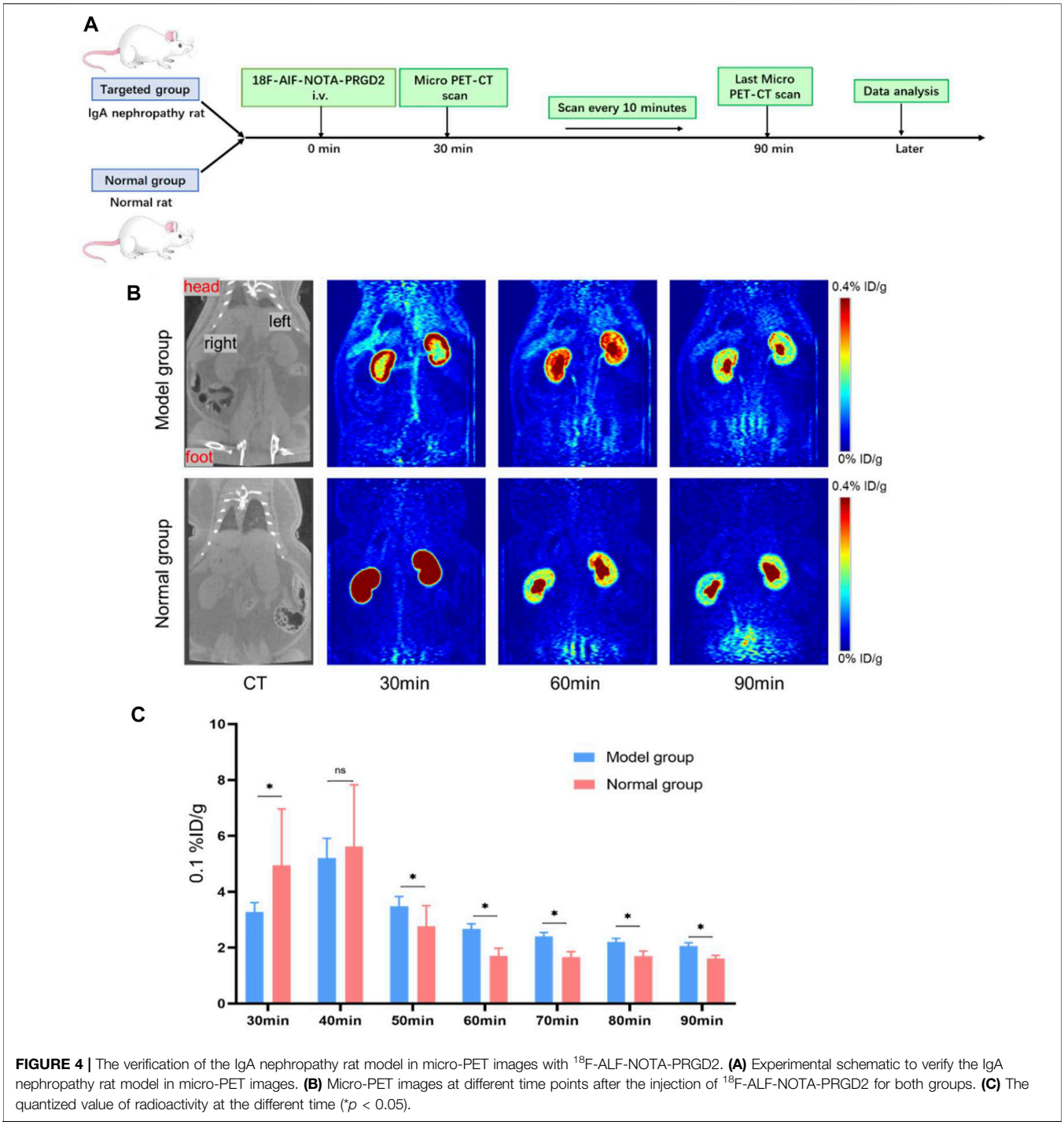


**FIGURE 4 |** The verification of the IgA nephropathy rat model in micro-PET images with $^{18}$F-ALF-NOTA-PRGD2. **(A)** Experimental schematic to verify the IgA nephropathy rat model in micro-PET images. **(B)** Micro-PET images at different time points after the injection of $^{18}$F-ALF-NOTA-PRGD2 for both groups. **(C)** The quantized value of radioactivity at the different time (*$p < 0.05$).

accurately with the READ Y View tool; subsequently, the relevant scatter diagram was drawn and the line was fitted. We could find a linear relationship between the concentration of $Fe_3O_4$-RGD solution and R2 value with r2 value equal to 245.1 $mM^{-1}$ $s^{-1}$. Such remarkable MRI performance indicated the ability of $Fe_3O_4$-RGD as a promising T2WI contrast agent for the exact detection of IgA nephropathy. Furthermore, the circulation time of $Fe_3O_4$-RGD *in vivo* was conducted before performing animal experiments. Our results demonstrated that the blood concentration of $Fe_3O_4$-RGD after intravenous injection decreased slowly over time (**Supplementary Figure S8**). The ratio of Fe content per gram of blood samples was relatively stable from 0.5 h (0.448 ± 0.028 mg/g) to 6 h (0.399 ± 0.031 mg/g). The ratio for 24 h after injection was 0.366 ± 0.033 mg/g. These results indicated that $Fe_3O_4$-RGD was suitable to apply *in vivo*.

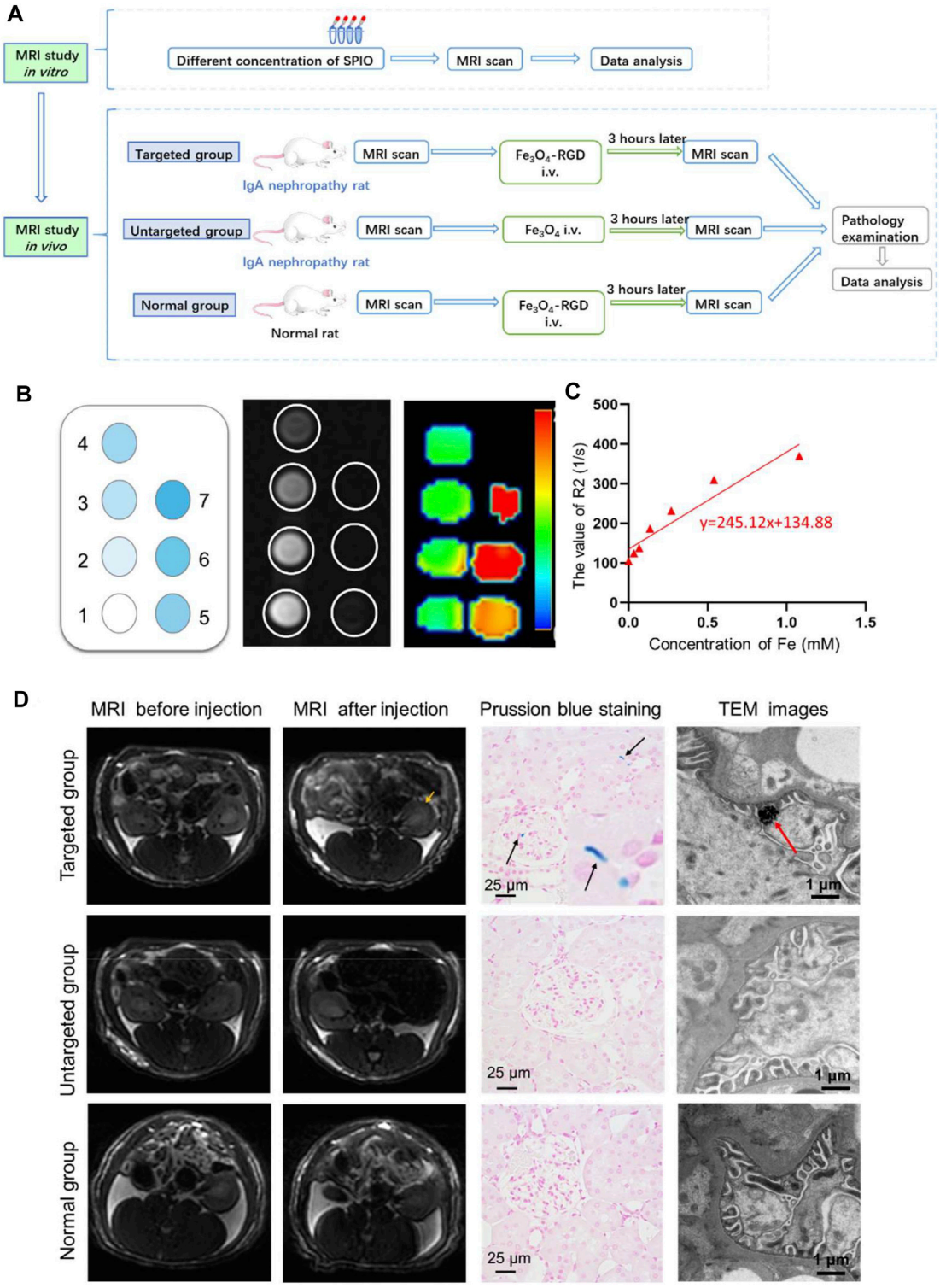


**FIGURE 5 |** *In vivo* diagnosis of IgA nephropathy by $Fe_3O_4$-RGD NPs. **(A)** Suggested workflow of $Fe_3O_4$-RGD NPs for detecting the IgA nephropathy disease by MRI technology. **(B)** *In vitro* MRI scan of $Fe_3O_4$-RGD with different concentration. **(C)** R2 value variation with the increased concentration of $Fe_3O_4$-RGD. **(D)** The targeting performance of $Fe_3O_4$-RGD for diagnosis of IgA nephropathy. Specifically, T2WI images, kidney Prussian blue staining, and TEM images of rats in each group were carefully investigated.

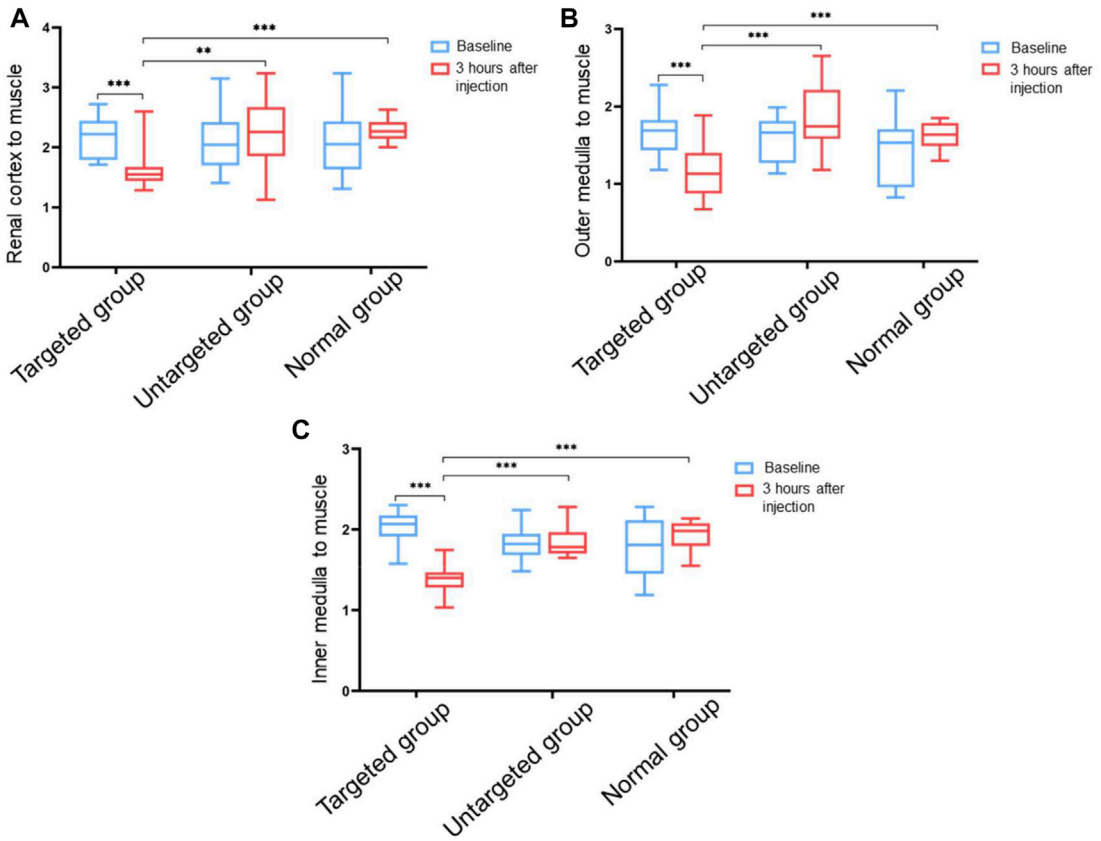


**FIGURE 6 |** Ratio value of T2WI signals in different tissues of rat kidney to muscle tissue before and after injection of $Fe_3O_4$-RGD for 3 h. **(A)** Ratio value of signal intensity from renal cortex to muscle tissue. **(B)** Ratio value of signal intensity from the outer medulla of the kidney to the muscle tissue. **(C)** Ratio value of signal intensity from the inner medulla of the kidney to the muscle tissue (**$p < 0.01$, ***$p < 0.001$).

In order to explore the feasibility of non-invasive diagnosis of IgA nephropathy by MRI through detecting the increased expression of integrin αvβ3 in IgA nephropathy, the experimental rats were divided into three groups (**Figure 5A**). Group 1 (targeted group) model rats received intravenous tail injection of $Fe_3O_4$-RGD solution with a dose of 15 mg Fe/kg. Group 2 (untargeted group) model rats received intravenous tail injection of $Fe_3O_4$-BSA solution at a dose of 15 mg Fe/kg. Group 3 (normal group) received intravenous tail injection of $Fe_3O_4$-RGD solution at a dose of 15 mg Fe/kg. The results indicated that the T2WI signal of renal parenchyma in the targeted group was lower than baseline after injection of $Fe_3O_4$-RGD for 3 h (**Figure 5D**). However, compared with baseline signal intensity, no significant decrease of T2WI signal was observed after 3-h injection of $Fe_3O_4$-BSA or $Fe_3O_4$-RGD in the untargeted model group or normal group, respectively (**Figure 5D**). Furthermore, the quantitative analysis of MRI images was carried out. READ Y View tool was used to measure the T2WI signal intensity of kidney tissues and muscle in each group, and the signal intensity ratio was calculated and analyzed. The signal ratio of renal cortex to muscle, renal outer medulla to muscle, and inner medulla to muscle in the targeted group were significantly lower at 3 h after $Fe_3O_4$-RGD injection than baseline signal intensity ($p < 0.001$) (**Figure 6**). These results demonstrated that $Fe_3O_4$-RGD NPs were expected to be located in each layer of kidney tissue in the targeted group. Due to the high expression of glomerular integrin αvβ3 in the model rat, confirmed by our experiment (**Figure 3B**), and anatomical basis of glomerulus and renal tubules mainly distributed in the renal cortex and medulla, respectively (Huang et al., 2015), we can infer that the abundant deposition of $Fe_3O_4$-RGD in the renal cortex is related to the high expression of integrin αvβ3 in glomerulus. Simultaneously, the deposition of $Fe_3O_4$-RGD in the inner and outer medulla may indicate the expression of integrin αvβ3 in renal tubules, which is similar to other integrin molecules such as integrin α3β1 (Pozzi and Zent, 2013). The signal ratios of renal layers to muscle in the targeted group were lower than those in the untargeted group ($p < 0.05$) and in the normal group ($p < 0.001$). All of these indicated that the targeted binding of $Fe_3O_4$-RGD with integrin αvβ3 achieves T2WI signal reduction. One notable fact is that compared with baseline, the mean value of untargeted group and normal group showed a higher signal ratio after the injection of $Fe_3O_4$-RGD NPs; the reason for this is not clear. Because the main metabolism of $Fe_3O_4$-RGD NPs is through liver, spleen, and kidney (Laurent et al., 2008), we infer that the slow muscle metabolism of iron NPs may induce more muscle signal reduction and make the ratio rise

after injection; however, this needs to be verified by more experiments.

After the MRI detection process, Prussian blue staining and TEM investigation of renal tissue were further performed to explore the targeted location of iron element in the renal tissue. Prussian blue staining demonstrated that the blue dots were scattered in the glomerulus and tubular interstitium in the targeted group. However, no apparent blue dots were found in the untargeted group and normal group (**Figure 5D**). The renal expression of integrin αvβ3 in the IgA model group was higher than the normal group. The $Fe_3O_4$-RGD NPs can be well combined with renal integrin αvβ3 in the targeted group. Thus, no iron element was observed in the untargeted group and normal group for Prussian blue staining. Moreover, the deposition of black iron oxide NPs was observed in the foot process of the targeted group by TEM, while no black iron oxide NPs were detected in the untargeted group and normal group. Finally, we have used the ICP to quantify iron content. This result exhibited that the ratio of Fe content to kidney was 0.240 ± 0.002 mg/g for the administration group after injection of $Fe_3O_4$-RGD for 3 h, and the ratio was 0.130 ± 0.010 mg/g for the normal group. These results indicated that the deposition of $Fe_3O_4$-RGD in kidney for the administration group was higher than that for the normal group (**Supplementary Figure S9**). Besides, the ratio difference was statistically significant ($p < 0.05$). Therefore, the above data further illustrated the dominant location of $Fe_3O_4$-RGD in the glomerular podocytes' reduced kidney T2WI signal of the rats with IgA nephropathy.

## CONCLUSION

In this study, we have developed a sensitive, specific, and biocompatible integrin αvβ3-targeted superparamagnetic $Fe_3O_4$ NPs for the noninvasive MR imaging of integrin αvβ3 in IgA nephropathy disease. The rat model was successfully established and verified by biochemical tests and histological staining. Furthermore, the micro-PET $^{18}$F-AlF-NOTA-PRGD2 probe molecule was utilized to confirm the successful establishment of the IgA nephropathy in the rat model. Subsequently, the synthesized RGD-$Fe_3O_4$ NPs were injected intravenously into model rats and the integrin αvβ3-targeted T2WI RGD-$Fe_3O_4$ NPs proved the accurate detection of the IgA nephropathy disease. Therefore, our study demonstrated the clinical possibility of utilizing the safe and effective $Fe_3O_4$-RGD for accurate MR imaging to diagnose IgA nephropathy noninvasively.

## DATA AVAILABILITY STATEMENT

The raw data supporting the conclusions of this article will be made available by the authors, without undue reservation.

## ETHICS STATEMENT

The animal study was reviewed, approved, and conducted according to the guidelines of the Declaration of Helsinki, and approved by the Research Ethics Committee of the First Affiliated Hospital, College of Medicine, Zhejiang University (ID: 2018–64–1; Date: February 13, 2018).

## AUTHOR CONTRIBUTIONS

WX, HZ, and QH designed and instructed the experiments. JW contributed to the construction of the animal model. YD and MX were responsible for the histopathological detection. YW and YL were responsible for imaging scan experiments, data analyzing, preparing figures, and manuscript writing. YL and HZ played an important role in manuscript editing. HZ and WX supervised the whole study. All authors contributed to the article and approved the submitted version.

## FUNDING

This research was supported by the Natural Science Foundation of Zhejiang province (grant number LZ16H180001) and the General Program of the National Natural Science Foundation of China (grant number 81171388).

## SUPPLEMENTARY MATERIAL

The Supplementary Material for this article can be found online at: https://www.frontiersin.org/articles/10.3389/fbioe.2021.755692/full#supplementary-material.

## REFERENCES

Amann, K., Haas, C. S., Schüssler, J., Daniel, C., Hartner, A., and Schöcklmann, H. O. (2012). Beneficial Effects of Integrin V 3-blocking RGD Peptides in Early but Not Late Phase of Experimental Glomerulonephritis. *Nephrol. Dial. Transplant.* 27 (5), 1755–1768. doi:10.1093/ndt/gfr603

Anthis, N. J., and Campbell, I. D. (2011). The Tail of Integrin Activation. *Trends Biochem. Sci.* 36 (4), 191–198. doi:10.1016/j.tibs.2010.11.002

Atila Dinçer, C., Erdek, A. M., Karakeçili, A., and Yıldız, N. (2019). Preparation of Chitosan and Glycol Chitosan Coated Magnetic Nanoparticles Loaded with Carboplatin as Anticancer Drug. *J. Polytechnic-Politeknik Dergisi* 22 (4), 1017–1022. doi:10.2339/politeknik.501694

Caliskan, Y., and Kiryluk, K. (2014). Novel Biomarkers in Glomerular Disease. *Adv. Chronic Kidney Dis.* 21 (2), 205–216. doi:10.1053/j.ackd.2013.12.002

Chen, Z., Fu, H., Wu, H., Huang, J., Yao, L., Zhang, X., et al. (2020). Syntheses and Preliminary Evaluation of Dual Target PET Probe [18F]-NOTA-Gly3- E (2PEG4-RGD-Wh701) for PET Imaging of Breast Cancer. *Acamc.* 20 (13), 1548–1557. doi:10.2174/1871520620666200424101936

Cheng, Z., Wei, R., Wu, C., Qing, H., Jiang, X., Lu, H., et al. (2015). *Ex-vivo* Biodistribution and Micro-PET/CT Imaging of 18F-FDG, 18F-FLT, 18F-FMISO, and 18F-AlF-NOTA-PRGD2 in a Prostate Tumor-Bearing Nude Mouse Model. *Nucl. Med. Commun.* 36 (9), 914–921. doi:10.1097/mnm.0000000000000339

Du, Y., An, S., Liu, L., Li, L., Zhou, X. J., Mason, R. P., et al. (2012). Serial Non-invasive Monitoring of Renal Disease Following Immune-Mediated Injury

Using Near-Infrared Optical Imaging. *PLoS One* 7 (9), e43941. doi:10.1371/journal.pone.0043941

Gao, H., Lang, L., Guo, N., Cao, F., Quan, Q., Hu, S., et al. (2012). PET Imaging of Angiogenesis after Myocardial Infarction/reperfusion Using a One-step Labeled Integrin-Targeted Tracer 18F-AlF-NOTA-PRGD2. *Eur. J. Nucl. Med. Mol. Imaging* 39 (4), 683–692. doi:10.1007/s00259-011-2052-1

Gauer, S., Yao, J., Schoecklmann, H. O., and Bernd Sterzel, R. (1997). Adhesion Molecules in the Glomerular Mesangium. *Kidney Int.* 51 (5), 1447–1453. doi:10.1038/ki.1997.198

Glaser, M., Morrison, M., Solbakken, M., Arukwe, J., Karlsen, H., Wiggen, U., et al. (2008). Radiosynthesis and Biodistribution of Cyclic RGD Peptides Conjugated with Novel [18F]fluorinated Aldehyde-Containing Prosthetic Groups. *Bioconjug. Chem.* 19 (4), 951–957. doi:10.1021/bc700472w

Guo, J., Lang, L., Hu, S., Guo, N., Zhu, L., Sun, Z., et al. (2014). Comparison of Three Dimeric 18F-AlF-NOTA-RGD Tracers. *Mol. Imaging Biol.* 16 (2), 274–283. doi:10.1007/s11307-013-0668-1

Guo, N., Lang, L., Gao, H., Niu, G., Kiesewetter, D. O., Xie, Q., et al. (2012a). Quantitative Analysis and Parametric Imaging of 18F-Labeled Monomeric and Dimeric RGD Peptides Using Compartment Model. *Mol. Imaging Biol.* 14 (6), 743–752. doi:10.1007/s11307-012-0541-7

Guo, N., Lang, L., Li, W., Kiesewetter, D. O., Gao, H., Niu, G., et al. (2012b). Quantitative Analysis and Comparison Study of [18F]AlF-NOTA-PRGD2, [18F]FPPRGD2 and [68Ga]Ga-NOTA-PRGD2 Using a Reference Tissue Model. *PLoS One* 7 (5), e37506. doi:10.1371/journal.pone.0037506

Huang, Q., Wen, S., Wang, B., Wang, Q., Guo, C., Wu, X., et al. (2015). C5b-9-targeted Molecular MR Imaging in Rats with Heymann Nephritis: a New Approach in the Evaluation of Nephrotic Syndrome. *PLoS One* 10 (3), e0121244. doi:10.1371/journal.pone.0121244

Jin, C., Zhang, B.-N., Wei, Z., Ma, B., Pan, Q., and Hu, P. (2017). Effects of WD-3 on Tumor Growth and the Expression of Integrin αvβ3 and ERK1/2 in Mice Bearing Human Gastric Cancer Using the 18F-RGD PET/CT Imaging System. *Mol. Med. Rep.* 16 (6), 9295–9300. doi:10.3892/mmr.2017.7827

Jin, D. K., Fish, A. J., Wayner, E. A., Mauer, M., Setty, S., Tsilibary, E., et al. (1996). Distribution of Integrin Subunits in Human Diabetic Kidneys. *Jasn* 7 (12), 2636–2645. doi:10.1681/asn.V7122636

Katagiri, D., Masumoto, S., Katsuma, A., Minami, E., Hoshino, T., Inoue, T., et al. (2010). Positron Emission Tomography Combined with Computed Tomography (PET-CT) as a New Diagnostic Tool for Acute Tubulointerstitial Nephritis (AIN) in Oliguric or Haemodialysed Patients. *Clin. Kidney J.* 3 (2), 155–159. doi:10.1093/ndtplus/sfp188

Lang, L., Li, W., Guo, N., Ma, Y., Zhu, L., Kiesewetter, D. O., et al. (2011). Comparison Study of [18F]FAl-NOTA-PRGD2, [18F]FPPRGD2, and [68Ga]Ga-NOTA-PRGD2 for PET Imaging of U87MG Tumors in Mice. *Bioconjug. Chem.* 22 (12), 2415–2422. doi:10.1021/bc200197h

Laurent, S., Forge, D., Port, M., Roch, A., Robic, C., Vander Elst, L., et al. (2008). Magnetic Iron Oxide Nanoparticles: Synthesis, Stabilization, Vectorization, Physicochemical Characterizations, and Biological Applications. *Chem. Rev.* 108 (6), 2064–2110. doi:10.1021/cr068445e

Lee, B. C., Moon, B. S., Ji, S. K., Jung, J. H., Park, H. S., Katzenellenbogen, J. A., et al. (2013). Synthesis and Biological Evaluation of RGD Peptides with the 99mTc/188Re Chelated Iminodiacetate Core: Highly Enhanced Uptake and Excretion Kinetics of Theranostics against Tumor Angiogenesis. *RSC Adv.* doi:10.1039/c2ra22460g

Li, L., Ma, L., Shang, D., Liu, Z., Yu, Q., Wang, S., et al. (2019). Pretreatment PET/CT Imaging of Angiogenesis Based on 18F-RGD Tracer Uptake May Predict Antiangiogenic Response. *Eur. J. Nucl. Med. Mol. Imaging* 46 (4), 940–947. doi:10.1007/s00259-018-4143-8

Lian, T., Huang, C., Liang, F., Li, X., and Xi, J. (2019). Simultaneously Providing Iron Source toward Electro-Fenton Process and Enhancing Hydrogen Peroxide Production via a Fe3O4 Nanoparticles Embedded Graphite Felt Electrode. *ACS Appl. Mater. Inter.* 11 (49), 45692–45701. doi:10.1021/acsami.9b16236

Marek-Bukowiec, K., Konieczny, A., Ratajczyk, K., and Witkiewicz, W. (2018). Candidate Urine Peptide Biomarkers for IgA Nephropathy: Where Are We Now? *Dis. Markers* 2018, 1–7. doi:10.1155/2018/5205831

Moriyama, T., Tanaka, K., Iwasaki, C., Oshima, Y., Ochi, A., Kataoka, H., et al. (2014). Prognosis in IgA Nephropathy: 30-year Analysis of 1,012 Patients at a Single center in Japan. *PLoS One* 9 (3), e91756. doi:10.1371/journal.pone.0091756

Nagasawa, Y., Okuzaki, D., Muso, E., Yamamoto, R., Shinzawa, M., Iwasaki, Y., et al. (2016). IFI27 Is a Useful Genetic Marker for Diagnosis of Immunoglobulin A Nephropathy and Membranous Nephropathy Using Peripheral Blood. *PLoS One* 11 (4), e0153252. doi:10.1371/journal.pone.0153252

Neprasova, M., Maixnerova, D., Novak, J., Reily, C., Julian, B. A., and Boron, J., (2016). Toward Noninvasive Diagnosis of IgA Nephropathy: A Pilot Urinary Metabolomic and Proteomic Study. *Dis. Markers* 2016, 3650909. doi:10.1155/2016/3650909

Peruzzi, L., Amore, A., Cirina, P., Trusolino, L., Basso, G., Ricotti, E., et al. (2000). Integrin Expression and IgA Nephropathy: *In Vitro* Modulation by IgA with Altered Glycosylation and Macromolecular IgA. *Kidney Int.* 58 (6), 2331–2340. doi:10.1046/j.1523-1755.2000.00417.x

Pozzi, A., and Zent, R. (2013). Integrins in Kidney Disease. *J. Am. Soc. Nephrol.* 24 (7), 1034–1039. doi:10.1681/asn.2013010012

Qualls, D., Seethapathy, H., Bates, H., Tajmir, S., Heidari, P., Endres, P., et al. (2019). Positron Emission Tomography as an Adjuvant Diagnostic Test in the Evaluation of Checkpoint Inhibitor-Associated Acute Interstitial Nephritis. *J. Immunother. Cancer* 7 (1), 356. doi:10.1186/s40425-019-0820-9

Ruoslahti, E. (1996). RGD and Other Recognition Sequences for Integrins. *Annu. Rev. Cel Dev Biol* 12, 697–715. doi:10.1146/annurev.cellbio.12.1.697

Sargsyan, S. A., Serkova, N. J., Renner, B., Hasebroock, K. M., Larsen, B., Stoldt, C., et al. (2012). Detection of Glomerular Complement C3 Fragments by Magnetic Resonance Imaging in Murine Lupus Nephritis. *Kidney Int.* 81 (2), 152–159. doi:10.1038/ki.2011.332

Serkova, N. J., Renner, B., Larsen, B. A., Stoldt, C. R., Hasebroock, K. M., Bradshaw-Pierce, E. L., et al. (2010). Renal Inflammation: Targeted Iron Oxide Nanoparticles for Molecular MR Imaging in Mice. *Radiology* 255 (2), 517–526. doi:10.1148/radiol.09091134

Suzuki, H. (2019). Biomarkers for IgA Nephropathy on the Basis of Multi-Hit Pathogenesis. *Clin. Exp. Nephrol.* 23 (1), 26–31. doi:10.1007/s10157-018-1582-2

Takada, Y., Ye, X., and Simon, S. (2007). The Integrins. *Genome Biol.* 8 (5), 215. doi:10.1186/gb-2007-8-5-215

Tao Jiang, T., Zhang, C., Liu, S., Xu, X., Xie, X., Liu, H., et al. (2009). Noninvasively Characterizing the Different αvβ3 Expression Patterns in Lung Cancers with RGD-USPIO Using a Clinical 3.0T MR Scanner. *Ijn* 4, 241–249. doi:10.2147/ijn.s7519

Wen, S., Liu, D. F., Cui, Y., Harris, S. S., Chen, Y. C., Li, K. C., et al. (2014). *In Vivo* MRI Detection of Carotid Atherosclerotic Lesions and Kidney Inflammation in ApoE-Deficient Mice by Using LOX-1 Targeted Iron Nanoparticles. *Nanomedicine* 10 (3), 639–649. doi:10.1016/j.nano.2013.09.009

Ye, Q., Yang, D., Williams, M., Williams, D. S., Pluempitiwiriyawej, C., Moura, J. M., et al. (2002). *In Vivo* detection of Acute Rat Renal Allograft Rejection by MRI with USPIO Particles. *Kidney Int.* 61 (3), 1124–1135. doi:10.1046/j.1523-1755.2002.00195.x

Zhang, H., Liu, N., Gao, S., Hu, X., Zhao, W., Tao, R., et al. (2016). Can an $^{18}$F-ALF-NOTA-PRGD2 PET/CT Scan Predict Treatment Sensitivity to Concurrent Chemoradiotherapy in Patients with Newly Diagnosed Glioblastoma? *J. Nucl. Med.* 57 (4), 524–529. doi:10.2967/jnumed.115.165514

**Conflict of Interest:** The authors declare that the research was conducted in the absence of any commercial or financial relationships that could be construed as a potential conflict of interest.

**Publisher's Note:** All claims expressed in this article are solely those of the authors and do not necessarily represent those of their affiliated organizations, or those of the publisher, the editors, and the reviewers. Any product that may be evaluated in this article, or claim that may be made by its manufacturer, is not guaranteed or endorsed by the publisher.

frontiers in Bioengineering and Biotechnology

REVIEW
published: 06 December 2021
doi: 10.3389/fbioe.2021.788461

# Functional Hydrogel Dressings for Treatment of Burn Wounds

*Wentao Shu*[1†], *Yinan Wang*[1,2†], *Xi Zhang*[3], *Chaoyang Li*[4], *Hanxiang Le*[4] *and Fei Chang*[4*]

[1]Department of Biobank, Division of Clinical Research, The First Hospital of Jilin University, Changchun, China, [2]Key Laboratory of Organ Regeneration and Transplantation of the Ministry of Education, The First Hospital of Jilin University, Changchun, China, [3]Department of Burn Surgery, The First Hospital of Jilin University, Changchun, China, [4]Department of Orthopedics, The Second Hospital of Jilin University, Changchun, China

The therapy of burns is a challenging clinical issue. Burns are long-term injuries, and numerous patients suffer from chronic pain. Burn treatment includes management, infection control, wound debridement and escharotomy, dressing coverage, skin transplantation, and the use of skin substitutes. The future of advanced care of burn wounds lies in the development of "active dressings". Hydrogel dressings have been employed universally to accelerate wound healing based on their unique properties to overcome the limitations of existing treatment methods. This review briefly introduces the advantages of hydrogel dressings and discusses the development of new hydrogel dressings for wound healing along with skin regeneration. Further, the treatment strategies for burns, ranging from external to clinical, are reviewed, and the functional classifications of hydrogel dressings along with their clinical value for burns are discussed.

**Keywords: burn wound, hydrogel dressing, emergency temporary coverage, antibacterial, stem cells, factors promoting wound healing**

OPEN ACCESS

***Edited by:***
*Guicai Li,*
*Nantong University, China*

***Reviewed by:***
*Enbo Ma,*
*Fukushima Medical University, Japan*
*Baolin Guo,*
*Xi'an Jiaotong University, China*
*Jingxiao Chen,*
*Jiangnan University, China*

***Correspondence:**
*Fei Chang*
*changfei@jlu.edu.cn*

[†]*These authors have contributed equally to this work*

***Specialty section:***
*This article was submitted to Biomaterials, a section of the journal Frontiers in Bioengineering and Biotechnology*

***Received:*** *02 October 2021*
***Accepted:*** *11 November 2021*
***Published:*** *06 December 2021*

***Citation:***
*Shu W, Wang Y, Zhang X, Li C, Le H and Chang F (2021) Functional Hydrogel Dressings for Treatment of Burn Wounds. Front. Bioeng. Biotechnol. 9:788461. doi: 10.3389/fbioe.2021.788461*

## 1 INTRODUCTION

Between 2015 and 2019, 550,000 people worldwide died from fire, heat and hot substances, and 37 million people were disabled and requiring medical treatment (World Health Organization., 2019). Unfortunately, >95% of these burn injuries occur in low- and middle-income countries (Peck, 2011). Severe burns continue to pose a major challenge in regions with limited medical resources, especially developing countries. With the continuous improvement of burn care, development of new burn dressings is crucial.

## 2 CLINICAL THERAPIES FOR BURN WOUNDS

Thermal injury is one of the most severe and complex forms of trauma, and one of the main causes of disability. Thermal injury can be caused by heat, high-voltage electricity, or chemicals. People who suffer severe burns may suffer from severe emotional distress, which can lead to mental illness. Severe burns necessitate long-term hospitalization, which results in enormous nursing costs, and can be accompanied by a series of fatal complications (e.g., shock, electrolyte imbalance, respiratory failure, and wound infection). The three main risk factors of death for burn patients are old age, a non-superficial burn accounting for >40% of the total burn surface area (TBSA), and inhalation injury (American Burn Association Burn, 2016).

Evaluation of burn patients involves two crucial parameters: wound depth and TBSA (Burd and Yuen, 2005) (**Figure 1**). First-degree burns affect the superficial layer of the epidermis. Superficial second-degree burns affect the epidermis and dermis. Deep second-degree burns affect the entire


**FIGURE 1 |** Burn wounds. **(A)** First degree. **(B)** Superficial second degree. **(C)** Deep second degree. **(D)** Third degree.

epidermis and dermis. Third-degree burns affect the epidermis, dermis, and subcutaneous tissue (Mertens et al., 1997). Burns can also be evaluated based on TBSA by the nine-point method, and the Lund–Browder table can be used to measure the injured body surface area of the patient accurately (Hettiaratchy and Dziewulski, 2004). In general, large-area burns include mixed burns of different depths, and the depth of burns may change after the initial injury (Hettiaratchy and Papini, 2004). Clinically, it is difficult to judge the wounds of deep second- and third-degree burns. Laser Doppler imaging is expected to be a powerful tool for evaluating burn depth (Jaskille et al., 2009; Jaskille et al., 2010).

The systemic treatment of burn patients is divided into preliminary assessment, emergency treatment, fluid resuscitation, severe management, and infection prevention.

Initial assessment comprises: identification of respiratory distress and smoke-inhalation injury; assessment of cardiovascular status and signs of shock; identification of injury complications; determination of burn severity. Emergency treatment of burns involves stabilizing the airway and supporting breathing. An essential component of systemic therapy is fluid resuscitation, which should be started <2 h after the burn has been sustained (Barrow et al., 2000). Management of severe burns involves meeting the high metabolic and nutritional needs of burn patients, provision of analgesia, sedation, and relieving anxiety; the early use of enteral nutrition and proton-pump inhibitors is important to prevent acute gastric ulcers (Raff et al., 1997). Sepsis prevention is critical in treating patients with severe burns, and systemic antibacterial drugs must be used cautiously to prevent the emergence of drug-resistant bacteria (Salick et al., 2007). The death of patients with large burn areas (>30% TBSA) is related to fungal infection of wounds, which requires additional fungal examination and use of antifungal drugs (Horvath et al., 2007).

## 2.1 Surgical Treatments

### 2.1.1 Debridement and Escharotomy

Debridement and escharotomy are the main means to control wound infection. The debridement and excision of contaminated necrotic tissue and eschar improve the visibility of the wound surface (Latenser, 2009; Sen et al., 2009), prevent fragile eschar from being stretched and causing pain in damaged skin areas, and improve the limb ischemia caused by large-area eschar contraction (Dries, 2005). Most importantly, necrotic tissue and eschar are “hotbeds” for the growth and reproduction of bacteria. Removing them minimizes the hidden danger of wound infection and facilitates direct treatment of the wound with therapeutic drugs (Bishop, 2004; DeSanti, 2005).

### 2.1.2 Skin Transplantation

Skin transplantation is a common method for closing burn wounds. For stable patients with small burn areas and a sufficient source of

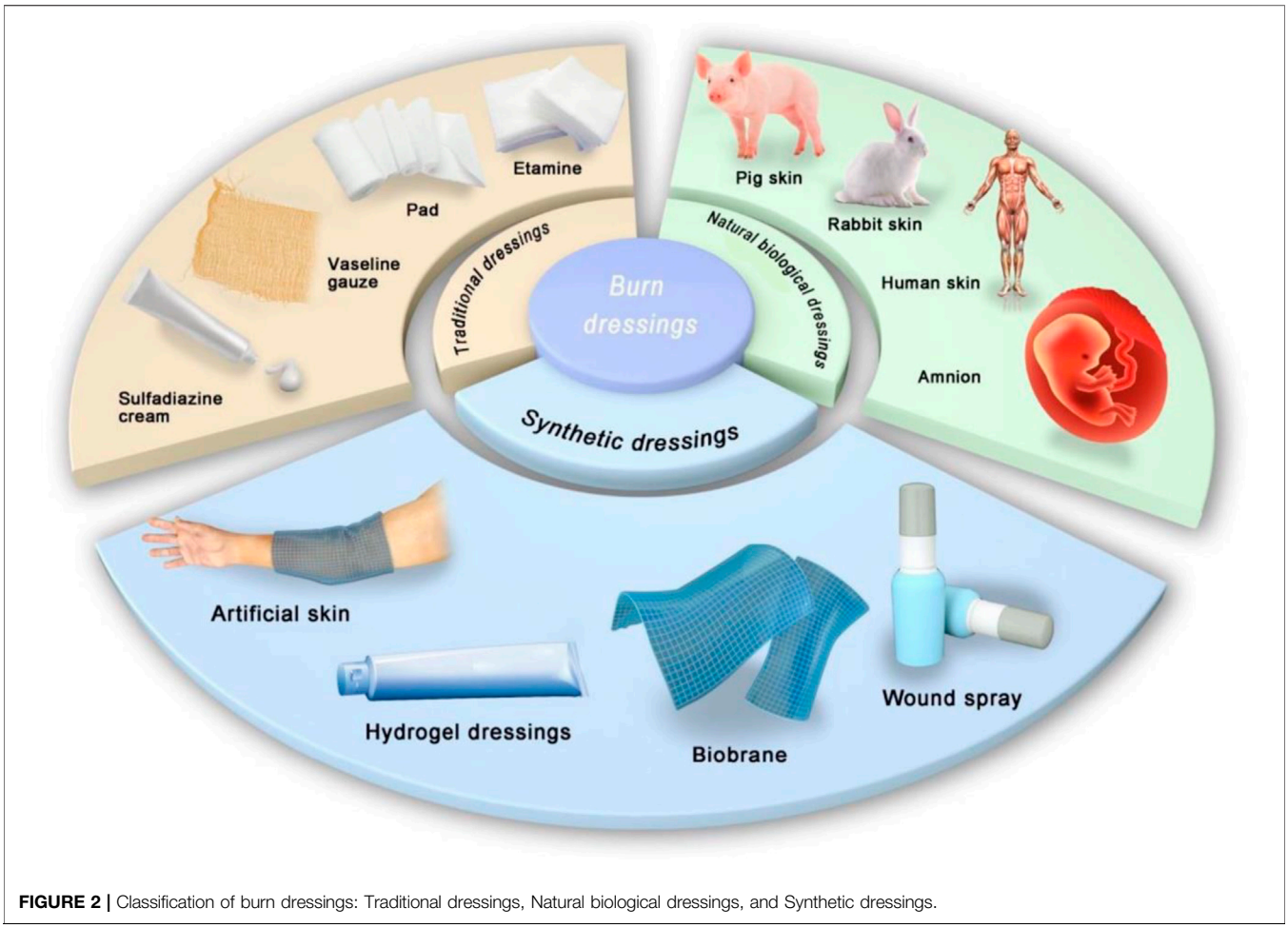


**FIGURE 2 |** Classification of burn dressings: Traditional dressings, Natural biological dressings, and Synthetic dressings.

skin, autologous skin grafts of medium thickness are often used (Hermans, 2014). For burn patients with large burn areas and/or insufficient donor skin, temporary covering with allografts, xenografts, or skin substitutes is needed. Allografts are the optimum substance for the temporary sealing of large, life-threatening burns in cases with insufficient donor skin (American Association of Tissue Bank, 2016). However, cadaveric skin grafts have disadvantages: a serious risk of transmission of infectious disease, rejection, as well as difficulties in obtaining and storing cadavers. Xenotransplantation has a larger application space than that using autotransplantation, with more donors and larger available sizes. Xenografts are available from frogs, rabbits, dogs, and pigs. Nevertheless, natural xenografts often result in hypersensitivity, can spread zoonotic diseases, and are often rejected by the host. The development of specially treated xenografts needs major research.

## 2.2 Non-surgical Treatments

### 2.2.1 Wound Dressings

Dressings are applied to cover burn wounds, promote epithelialization, prevent infection and mechanical trauma, keep wounds moist, and reduce pain. Various types of dressings are available (**Figure 2**). The dressing materials can be made into films, foams, composites, sprays, and gels depending on the requirement. Traditional dressings such as Vaseline™ gauze, silicone tablets, and paraffin dressings (e.g., Mepitel®) are used commonly for daily care of burns. Silver-containing dressings such as Acticoat®, Mepilex Ag®, and Aquacel® Ag have stronger antibacterial activity than silver sulfadiazine (SSD) cream, along with fewer adverse reactions and lower cost. Thus, these silver-containing dressings aid in the fight against wound infections (Tredget et al., 1998; Cuttle et al., 2007; Abboud et al., 2014). Biological dressings such as human amnion and processed products of dehydrated amnion chorionic villi overcome the shortcomings of acquisition of fresh amnion: inconvenience of processing and storage, high cost, and transmission of infectious diseases (Wasiak et al., 2013). Various synthetic dressings, alginate dressings, hydrocolloid dressings, hydrogel dressings, and polyurethane films (e.g., Mepilex®, DuoDERM®, Omniderm®) are used widely to cover the wound surface during re-epithelialization.

### 2.2.2 Skin Substitutes

Biosynthetic skin and bioengineered skin substitutes, both self-cultivated and non-self-cultivated, are used for physiological wound closure until the epidermal layer is repaired. Biosynthetic skin, such as Biobrane® (Smith & Nephew,

London, United Kingdom), is a semi-synthetic double-layered material comprising a dermal analog (porcine collagen) and an epidermal analog (silicone resin), which is used to seal superficial burns temporarily. The wound surface and skin donor area are covered temporarily. Biological skin substitutes include GraftJacket® (KCI, San Antonio, TX, United States), Alloderm® (LifeCell, Bridgewater, NJ, United States), and Integra® (Integra LifeSciences, Plainsboro, NJ, United States). Integra® is a biosynthetic skin scaffold composed of a dermal layer (bovine collagen) and an epidermal layer (silicone membrane). Integra® can reduce the size of the donor area, improve skin elasticity, and improve the appearance of burn wounds (Danin et al., 2012). However, skin substitutes are fragile, expensive, and exhibit poor anti-infection ability. Only experienced and highly trained surgeons can apply these products to patients with severe burns (Purdue et al., 1997). In recent years, the development of a new type of high-efficiency "compound skin" has been a research focus; scholars are eager to find a skin substitute with a similar appearance and texture to normal skin, good tissue elasticity, and friction resistance.

## 3 ADVANTAGES OF HYDROGEL DRESSINGS

Wound healing involves numerous physiological processes. Burn dressings must have biocompatibility, biodegradability, a porous structure, and appropriate mechanical properties (Quinn et al., 1985). The characteristics of an ideal burn dressing are: 1) good adhesion to the wound surface (while not adhering to the wound surface) and remaining accessible for removal (Thomas et al., 1995); 2) transparent, visible, and non-enclosed with a reasonable rate of water-vapor transmission to prevent wound immersion; 3) provide a good barrier against bacterial invasion to prevent infection (Reithofer et al., 2014); 4) good biocompatibility, wide availability, and low cost. Although no material is perfect, hydrogel dressings have shown considerable advantages over traditional dressings (Selig et al., 2012).

Wound healing is a complex physiological process broadly divided into four phases: hemostasis, inflammation, proliferation, and degeneration. Compared with other wounds, the burn wound healing process is more complicated and affected by many factors. A large amount of devitalized tissue in the burn wound bed is caused by high temperature, which leads to a massive proliferation of pathogenic bacteria at the wound site and finally causes local or systemic infection. Considering the characteristics of burn wounds, the primary strategies for their treatment focus on restoring skin barrier function, reducing infection, and inhibiting scar formation and skin contracture. In clinical treatment, the autologous skin graft is generally considered the gold standard for burn treatment. But in cases of extensive severe burns, the source of autografts may be limited due to the unavailability of donor areas, skin contractures. Therefore, wound dressings have broad application prospects in the treatment of burn wounds. An ideal wound dressing should have suitable tack, absorbable rows, antimicrobial capacity, ease of replacement, and individually tailored size. In the process of burn treatment, hydrogel dressings have higher advantages. The modification of hydrogels can enable them to possess a variety of biological functions to fit the different needs that make the wound healing. The hydrogel dressing can control wound infection and perform autolytic debridement of necrotic tissue by piggybacking on antibiotics or anti-inflammatory drugs during the inflammatory phase. In the proliferative phase, hydrogel dressings can promote vascular regeneration and fibroblast proliferation by releasing growth factors and degradation of bioactive materials. In addition, hydrogel dressings can also be used as tissue engineering scaffolds to piggyback on seeded cells or induce factors to promote tissue generation. The porous structure possessed by the hydrogel can absorb wound exudates, maintain the excellent permeability and moist wound environment around the wound, and reduce the pain of patients to a certain extent. Therefore, the hydrogel dressing may serve as a new strategy for burn wound management and play an essential role in wound healing.

Hydrogel is a kind of water-rich polymer network, which is composed of natural or synthetic polymers. Hydrogel polymers are combined by various cross-linking methods to produce different functions and properties. The cross-linking methods are mainly divided into physical cross-linking and chemical cross-linking. Physical cross-linking mainly includes intermolecular interactions, such as hydrogen bonding, ion interaction, crystallization cross-linking, hydrophobic association and so on. The main characteristics of physically crosslinked hydrogels are low molecular toxicity and high biocompatibility. Chemical crosslinking is usually connected by covalent bonds between polymers, such as free radical polymerization crosslinking, radiation crosslinking and so on. Therefore, chemically crosslinked hydrogels have better mechanical properties.

Hydrogels have hydrophilic and soft tissue-like properties. They exhibit mixing behavior with mechanical properties similar to solids but diffusion characteristics resembling those of liquids. Thus, hydrogels can absorb and release water in a reversible manner in response to specific environmental stimuli (e.g., temperature, pH, ionic strength). This intelligent response to physiological variables determines how hydrogel dressings can be applied in the treatment of burn wounds.

Application of hydrogel dressings to treat burn wounds has three advantages. First, hydrogel dressings can absorb wound exudate; the amount of water absorbed by a hydrogel is thousands of times its dry weight (Hoffman, 2002). Moreover, the liquid-supply characteristics of hydrogels also help maintain a moist environment during wound healing, which is particularly important when treating dry wounds. Second, hydrogel dressings can be customized into any shape according to the wound condition. Third, hydrogel dressings can adhere to wounds without adhesion, as well as reduce the temperature and pain of the wound. They are also transparent, allowing the wound to be observed. Research on hydrogel dressings for burns is booming worldwide, and many achievements have been made (**Figure 2**). Hydrogel dressings account for most of the global market for dressings (USD 3 billion) (Kamoun et al., 2017).

# 4 HYDROGEL DRESSINGS FOR BURN WOUNDS

Multiple influencing factors need to be considered during the clinical treatment of burn injuries. First, the breakdown of the skin barrier and coverage of necrotic tissue after burn injuries make the burned tissue vulnerable to infection. Second, hyperthermic injuries often cause increased capillary permeability at the wound site, resulting in massive tissue fluid leakage from the damaged area. Depending on the deep part of the burn, the damage can spread to the dermal tissue, and resulting in several complications.

Burn wound healing is a complex dynamic physiological process that involves several factors, including the regulation of inflammatory factors, cell migration and proliferation, and extracellular matrix deposition. Hydrogels with high hydrophilicity, good biocompatibility, and suitable pore structure can meet the demand in the burn wound healing process. Especially in treating irregular wounds, hydrogel dressings can form a good coverage and filling of the wounds. According to the clinical demand for burn wounds in different periods, hydrogel dressings are designed and play therapeutic roles mainly from three aspects: preventing infections, promoting repair, and constructing scaffolds for skin tissue engineering. In preventing infections, hydrogel dressings can provide better coverage of the wound surface and insulate the wound from the external environment. Second, the functionalized modification on the hydrogel can possess a specific antibacterial function to inhibit bacterial proliferation at the local site of damage. In the process of wound tissue regeneration, hydrogels can be used as a carrier of growth factors to achieve sustained release of growth factors in the wound bed, which is more conducive to tissue repair. In the study of constructing engineered skin tissue *in vitro*, the hydrogel can also serve as a template for tissue regeneration, providing a method to repair full-thickness burn wounds.

The biocompatibility, biodegradability, and bioactivity of natural biopolymers (e.g., collagen, chitosan, cellulose acetate, gelatin, fibrin, hyaluronic acid (HA) and its salts, alginate) determine their potential value as dressings for burns. Sodium alginate has been shown to promote the proliferation of mouse fibroblasts. Collagen and polyose materials can also be used for the healing of burns. Collagen protein is one of the main components of extracellular matrix (ECM). It has been used widely in wound healing and is beneficial for treating severe burn wounds, pressure sores, and diabetic foot ulcers (Mozalewska et al., 2017). Hydrogel dressings made from several natural polymers have also been commercialized (Teodorescu et al., 2010). Compared with natural polymers, hydrogels from synthetic polymers have excellent controllable mechanical properties and biodegradability, along with lower cost and more abundant sources of raw materials. They can also be produced by various manufacturing technologies to provide a wide range of properties (Ekenseair et al., 2012). The combination of natural and synthetic materials can reduce their respective limitations and improve the efficacy of the resulting hydrogel dressing. Several types of hydrogel dressings are available, some of which contain additional drugs with anesthetic, anti-inflammatory, or nutritional properties (**Figure 3**).

Numerous hydrogel-based products are available for burn care, but research and development of hydrogel dressings continue unabated. *In situ*-molded gels and radiation-crosslinked gels have been introduced as new types of burn dressings (Sinko et al., 2015; Mohd Zohdi et al., 2012). In the future, hydrogel dressings for burns will consider the characteristics of wounds in various stages as part of a systematic, multifunctional strategy for the diagnosis and treatment of burns (Yan et al., 2012; Dargaville et al., 2013; Boonkaew et al., 2014) (**Table 1**).

## 4.1 First Aid Hydrogel Dressings

Several studies have reported new wound dressings for pre-hospital emergency treatment, and there is a large market demand for these dressings. In recent years, there has been a rapid increase in the use of alternative emergency cooling and dressings for burn patients in pre-hospital settings. In the United Kingdom, 39% of emergency medical services use burn dressings as first-aid coolants (Walker et al., 2005). Nearly 80% of British fire departments use hydrogels as cooling dressings (Cuttle et al., 2009). One study in Australia found that 13% of pediatric patients received first aid involving burn dressings (Hyland and Harvey., 2014). In a cohort study of 455 people, Hyland and colleagues (Hayati et al., 2018) found that >50% of patients were treated with hydrogel products by non-professional first-aid personnel. In the pre-hospital environment, the lack of skin coverage is the greatest threat to severely burned patients. To reduce fluid loss and prevent bacterial infection, hydrogel dressings are needed urgently to cover burn wounds.

Carbomer 940 hydrogel is a simple, low-cost dressing for burns that can improve tissue perfusion and decrease the area of necrotic tissue in burn wounds (Chouhan et al., 2018). *In situ*-formed hydrogels generated from natural silk fibroin separated from *Bombyx mori* along with *Antheraea assama* support the proliferation of primary human dermal fibroblasts and keratinocyte migration. They also provide support for full-thickness, third-degree burn wounds (Dang et al., 2018). The novel hydrogel HA-az-F127 is formed by the reaction between hydrazide-modified HA and benzaldehyde-terminated F127 triblock copolymer. HA-az-F127 exhibits rapid gelation and shear-thinning behavior (Li et al., 2018). It also exhibits high adaptability with regard to mechanical strength, good self-healing, and the ability to promote wound-tissue repair on a deep partial-thickness-burn model. Bacterial cellulose hydrogels are becoming increasing popular due to their biocompatibility. Bacterial cellulose/acrylic acid (BC/AA) hydrogels can improve the healing rate of burn wounds, accelerate fibroblast proliferation significantly, and promote wound epithelialization (Uppuluri and Shanmugarajan, 2019; Lei et al., 2020). Oxygen-free radicals are considered important factors for inhibiting wound healing, whereas curcumin is an effective antioxidant and anti-inflammatory agent. Liang et al. (Liang et al., 2019) used curcumin and amphiphilic chitosan-g-pluronic copolymer to create an injectable nanocomposite

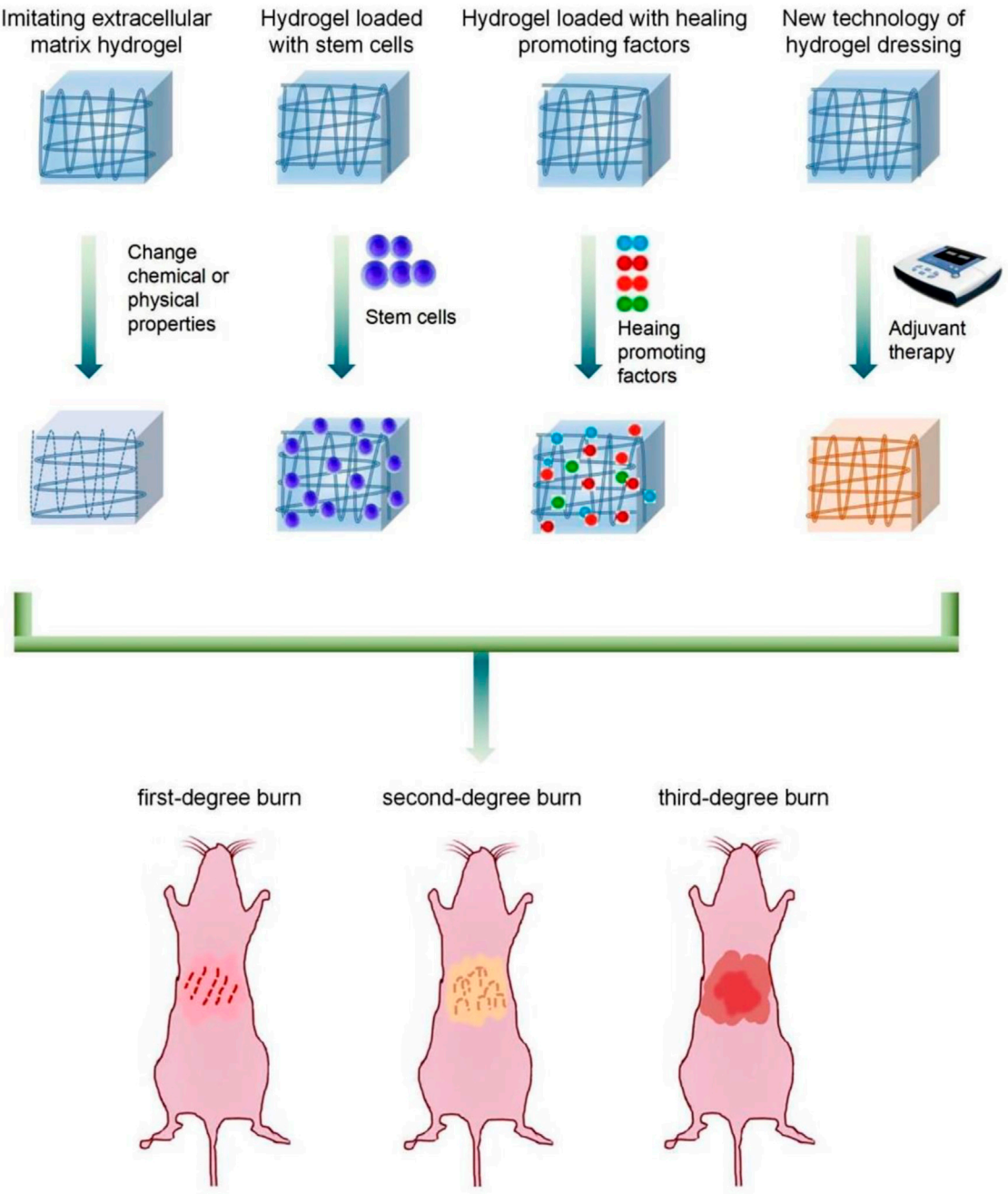


**FIGURE 3 |** Functional classification of hydrogel dressings for burns: Imitating extracellular matrix hydrogel, Hydrogel loaded with stem cells, Hydrogel loaded with healing promoting factors, and New technology of hydrogel dressing.

hydrogel (nCur-CP hydrogel). When applied to burn wounds, nCur-CP hydrogel showed higher collagen content, better granulation, and higher wound maturity in models of second- and third-degree burn wounds.

Neovascularization is an important factor affecting wound healing after severe burns. Sun and coworkers (Sun et al., 2011; Stubbe et al., 2019) found that dextran (Dex)-based hydrogels can be used in third-degree burn wounds, and promote the regeneration of blood vessels and skin in the wound. Conversely, in a model of alkali burns to the cornea, loss of vision along with graft rejection are closely related to corneal neovascularization. Huang and collaborators (Huang et al., 2018) prepared a supramolecular hydrogel comprising MPEG-PCL micelles and α-cyclodextrin that can co-deliver dexamethasone and Avastin® in a burn model in rats. Corneal inflammation significantly inhibits the formation of corneal neovascularization.

**TABLE 1 |** Summary of commonly employed polymers in hydrogel dressings and their functions in wound management.

| Function | Main polymer | Bioactive agent | Burn depth | Function in wounds | Ref. |
|---|---|---|---|---|---|
| First aid | Carbomer 940 | | Full-thickness burn wounds | Nontoxic, improves tissue perfusion, reduces area of necrotic tissue in burn wounds | Chouhan, Lohe, Samudrala and Mandal, (2018) |
| | Natural silk fibroin | | Full-thickness burn wounds | Promotes wound healing, facilitates the transition from the inflammation stage to the proliferation stage | Dang, Nguyen, Tran, Doan and Tran, (2018) |
| | Hydrazidemodified hyaluronic acid (HAAD)/benzaldehyde-terminated F127 triblock copolymer | | Deep partial-thickness burn models | Adaptable mechanical strength, self-healing, liquid absorption/drainage, tissue adhesion, promotes repair of burn wounds | Li, Zhou, Li, Lin, Chen, Liu and Chen, (2018) |
| | Bacterial cellulose/acrylic acid (BC/AA) | | Skin-burn wounds | Non-toxic, promotes wound-healing, enhances epithelialization, accelerates fibroblast proliferation | (Uppuluri and Shanmugarajan, 2019; Lei et al., 2020) |
| | Amphiphilic chitosan-g-pluronic copolymer | Curcumin | Second- and third-degree burn-wound models | Enhances regenerated collagen density, results in the formation of a thicker epidermis layer, increases collagen content, improves granulation, increases wound maturity, and enhances wound closure | Liang, Chen, Wang, Liu, Wei and Zhang, (2019) |
| | Dextran | | Full-thickness burn wounds | Promotes neovascularization and skin regeneration | (Shen, Song, Papa, Burke, Volk and Gerecht, 2015; Stubbe, Mignon, Declercq, Van Vlierberghe and Dubruel, 2019) |
| | MPEG-PCL micelles/α-cyclodextrin | Dexamethasone sodium phosphate/Avastin® | Alkali-burn models in rats | High ocular biocompatibility and non-irritating after topical instillation, attenuates alkali burn-induced corneal inflammation, suppresses corneal neovascularization | Zhai, Xu, Zhou and Jing, (2018) |
| | Polyvinyl alcohol/agar | Icariin | Full-thickness burn wounds | Promotes new translucent skin tissue, repairs the ECM, enhances wound healing | Mohamad et al. (2014) |
| | HA/CCS/HLC | | Skin burns on the backs of rabbits | Prevents bacterial infection effectively, promotes burn-wound healing better than a commercial film (DuoDERM®) | Pandey et al. (2017) |
| | CMC-Na/SA/CS | | Second-degree burn wounds | Excellent self-regulatory and anti-adhesive properties that promote the healing of burn wounds synergistically | Dang, Nguyen, Tran, Doan and Tran, (2018) |
| | Gelatin/alginate | | Burn wounds on skin | Good biocompatibility and cell-attachment properties | Sun, Zhang, Shen, Sebastian, Dickinson, Fox-Talbot, Reinblatt, Steenbergen, Harmon and Gerecht, (2011) |
| | Lysine-based dendron/PEG | | Wounds from second-degree burns | Dissolves "on demand" through the thiol–thioester exchange reaction, allowing the burn dressing to be removed readily | Konieczynska, Villa-Camacho, Ghobril, Perez-Viloria, Tevis, Blessing, Nazarian, Rodriguez and Grinstaff, (2016) |
| | CMC/rigid rod-like dialdehyde-modified cellulose nanocrystal | | Skin-burn wounds | Injected into an irregular deep burn wound, it reforms rapidly into an integrated piece, completely filling the wound area. Amino-acid solution can be used to dissolve the hydrogel, allowing painless dressing removal | Huang, Wang, Huang, Wang, Chen, Zhang and Zhang, (2018) |
| | Keratin-chitosan | Nano-ZnO | Skin-burn wounds | Increases swelling, exhibits bactericidal activity | Huang, Wang, Yu, Yu, Zheng, Peng, He, Zhao, Zhang, Li and Wang, (2017) |

(Continued on following page)

**TABLE 1 |** (*Continued*) Summary of commonly employed polymers in hydrogel dressings and their functions in wound management.

| Function | Main polymer | Bioactive agent | Burn depth | Function in wounds | Ref. |
|---|---|---|---|---|---|
| Anti-bacterial | Silver sulfadiazine-bFGF | | Partial-thickness burn wounds(Zhu, Jiang, Liu, Yan, Feng, Lan, Shan, Xue and Guo, 2018) | Non-toxic and safe | Chakrabarti, Islam, Hazarika, Mazumder, Raju and Chattopadhyay, (2018) |
| | MC | Silver oxide NPs | Second-degree burns | Excellent antimicrobial activity and healing of burn wounds | Dang, Nguyen, Tran, Doan and Tran, (2018) |
| | Agarose | Minocycline/gentamicin | Porcine burn models | Reduces burn depth and the number of bacteria | Grolman, Singh, Mooney, Eriksson and Nuutila, (2019) |
| | Poloxamer (F68/F127) | Boron | Second-degree burn wounds | Increases wound closure *via* fibroblast activity, induces vascularization, exhibits antimicrobial effects against bacteria | Demirci, Dogan, Karakus, Halici, Topcu, Demirci and Sahin, (2015) |
| | Chitosan | Moxiflfloxacin | Animals with bacterial loads | Shows better efficacy than conventional gels in *S. aureus*-infected burn wounds | Chhibber et al. (2020) |
| | Dextran-hyaluronic acid | Sanguinarine | Full-thickness burn infection model (MRSA, *E. coli*) | Improves re-epithelialization, enhances ECM remodeling | Zhu, Jiang, Liu, Yan, Feng, Lan, Shan, Xue and Guo, (2018) |
| | Hyaluronic acid/chondroitin sulfate/asiatic acid | Zinc oxide/copper oxide | Second-degree burn wounds | Non-toxic; exhibits significant antibacterial activity, promotes re-epithelization, collagen-fiber arrangement, and angiogenesis; shows significant wound-healing activity | Thanusha et al. (2018) |
| | Glycol chitosan | Colistin | Burn-infection model in animals *in vivo* | Performs almost as well as native colistin against colistin-sensitive and colistin-resistant *P. aeruginosa* strains | Zhu, Zhao, Kempe, Wilson, Wang, Velkov, Li, Davis, Whittaker and Haddleton, (2017) |
| | Carbomer | Ciprofloxacin and lidocaine | Models of second-degree burns | Reduces the wound-healing period, increases the number of fibroblasts, increases the rates of epithelialization and dermis reconstruction, has an immediate anesthetic effect | Sanchez, Breda, Soria, Tartara, Manzo and Olivera, (2018) |
| | Collagen | *Saccharomyces cerevisiae* | Full-thickness burn wounds | Improves the morphological and biomechanical characteristics of burn wounds | Oryan, Jalili, Kamali and Nikahval, (2018) |
| | Chiosan | Marine peptides | Burn wounds on the backs of rabbits | Enhances cell migration and promotes skin regeneration | Ouyang, Hu, Lin, Quan, Deng, Li, Li and Chen, (2018) |
| Loading with stem cells | BC/AA | Human epidermal keratinocytes/human dermal fibroblasts | Burn wounds in thymic-free mice | Has significant collagen deposition | Badiavas, (2004) |
| | Polysaccharide | MSCs | Alkali burns to the corneas of rats | Enhances the migration rate of primarily cultured corneal epithelial cells; improves the recovery of the corneal epithelium; reduces inflammation, neovascularization, and opacity of the healed cornea | Ke, Wu, Cui, Liu, Yu, Yang and Li, (2015) |
| | UArg-PEA (chitosan derivative) | MSCs | Wounds from third-degree burns | Promotes wound closure, re-epithelialization, granulation-tissue formation, and vascularization | Alapure, Lu, He, Chu, Peng, Muhale, Brewerton, Bunnell and Hong, (2018) |
| | Chitosan/collagen/ β-glycerophosphate | MSCs | Wounds from third-degree burns | Shortens healing time, limits the inflammation area, enhances re-epithelialization, promotes formation of high-quality, well-vascularized granulation tissue, attenuates formation of fibrotic, and hypertrophic scar tissue | Zhou, Li, Zhang, Shi, Li and Ju, (2019) |
| | PEGylated fibrin chitosan/ microspheres (SSD-CSM-FPEG) | Silver sulfadiazine | Burn wounds on rats infected with *P. aeruginosa* | Reduces bacterial infection and promotes neo-vascularization with improved matrix remodeling | Banerjee, Seetharaman, Wrice, Christy and Natesan, (2019) |

(Continued on following page)

**TABLE 1 |** (*Continued*) Summary of commonly employed polymers in hydrogel dressings and their functions in wound management.

| Function | Main polymer | Bioactive agent | Burn depth | Function in wounds | Ref. |
|---|---|---|---|---|---|
| Loading with wound healing-promoting factors | Hyaluronic acid, dextran, and β-cyclodextrin | Resveratrol/VEGF plasmid | Model of splinted excisional wounds in rats | Inhibits the inflammatory response and promotes microvascular formation while being biocompatible | Wang, Huang, Hu, Yang, Lan, Zhu, Hancharou, Guo and Tang, (2019) |
| | | Recombinant human granulocyte/ macrophage colony-stimulating factor | Deep partial-thickness burn wounds | Promotes healing effectively | Yan et al. (2012) |
| Others | Rabbit collagen | Human amnion | Second-degree burns in rats | Non-cytotoxic, accelerates wound healing based on complete re-epithelialization and closure by wound contraction | Rana, Rahman, Ullah, Siddika, Hossain, Akhter, Hasan and Asaduzzaman, (2020) |
| | Honey | | Burn-induced wounds in mice | 75% honey–chitosan hydrogel possesses greater wound healing activity compared with that of commercial treatment and can be used safely as an effective natural treatment for topical wound healing | Mohd Zohdi et al. (2012) |
| | Sea cucumber | | Burn-induced wounds in mice | Stimulates tissue regeneration and regulation of pro-inflammatory cytokines | Zohdi et al. (2011) |
| | Alginate | PWD | Burn-induced wounds in pigs | Safely delivers high concentrations of antibiotics in a hydrogel and treats burn infections | Nuutila, Grolman, Yang, Broomhead, Lipsitz, Onderdonk, Mooney and Eriksson, (2020) |

The supramolecular hydrogel was also found to have a significant prolongation effect on Avastin®.

To deal with the destruction of local-skin function after burns and the loss of a large amount of water and electrolytes from the wound surface, hydrogel dressings have been explored to repair the ECM. Some scholars believe that icariin can repair the ECM after burn injury. When an icariin-loaded polyvinyl alcohol/agar hydrogel was used for burn treatment, new translucent skin tissue appeared on the wound surface and the ECM was repaired (Mohamad et al., 2014). Pandey et al. (2017) mixed HA, carboxylated chitosan, and human-like collagen to simulate the ECM and used glutamine transaminase as a crosslinking agent to optimize the mechanical properties and pore size of the hydrogel. The resulting hydrogel was more conducive to burn wounds compared with the film (DuoDERM®). Few dressings used for burns can regulate humidity to optimize recovery. Liang et al. (2018) constructed a water-soluble carboxymethylcellulose sodium/sodium alginate/chitosan composite hydrogel with excellent self-regulatory ability and anti-adhesive properties that synergistically promoted the healing of burn wounds in rats. Sun et al. (2011) combined photocrosslinkable functionalities with hydrogel films to modify gelatin and alginate. The resulting products showed better cell adhesion and superior mechanical properties. Hydrogels that can be dissolved "on demand" are also needed in clinical settings. A dissolvable gel dressing does not need to be removed from the wound, alleviates pain and avoids the destruction of new tissues.

Researchers have crosslinked lysine-based dendron and a polyethylene glycol (PEG)-based crosslinker to develop a dissolvable dendritic thioester hydrogel dressing for second-degree burns (Konieczynska et al., 2016). This hydrogel is unique because it can be removed readily through a thiol–thioester exchange reaction when needed. Other researchers have combined water-soluble carboxymethyl chitosan (a natural polymer) with rigid dialdehyde-modified cellulose nanocrystal to form self-healing nanocomposite hydrogels (Huang et al., 2018). When the hydrogel was injected into an irregular burn wound, it reformed instantly into an integrated piece, filling the wound area. When the dressing must be changed or removed, an amino-acid solution can be used to dissolve the hydrogel, allowing painless dressing removal (**Figure 4**). Wound bandages are very rigid, lack porosity, have low mechanical strength, poor affinity, and cannot resist bacterial invasion. Some researchers have prepared a composite bandage by combining nano-ZnO with keratin–chitosan hydrogels. These nano-ZnO-containing bandages have been shown to accelerate the construction of skin cells and collagen formation in Sprague–Dawley rats, thereby enhancing wound healing and overcoming the shortcomings of medical bandages (Huang et al., 2017).

## 4.2 Antibacterial Hydrogel Dressings

Wounds have been treated with local antibiotics since the 1960s (Heggers et al., 1991) and, subsequently, silver sulfadiazine(SSD) (Moyer et al., 1965; Fox, 1968). Early resection and transplantation have reduced the prevalence of infection and mortality of burn patients. However, the sepsis caused by infection with Gram-positive and Gram-negative bacteria is a prevalent trigger of death after a burn (Bang et al., 2002; Church et al., 2006). Given that bacterial resistance is widespread and it is difficult for systemic antibiotics to reach local wounds, control of local infection is the key to reducing the mortality from burns.

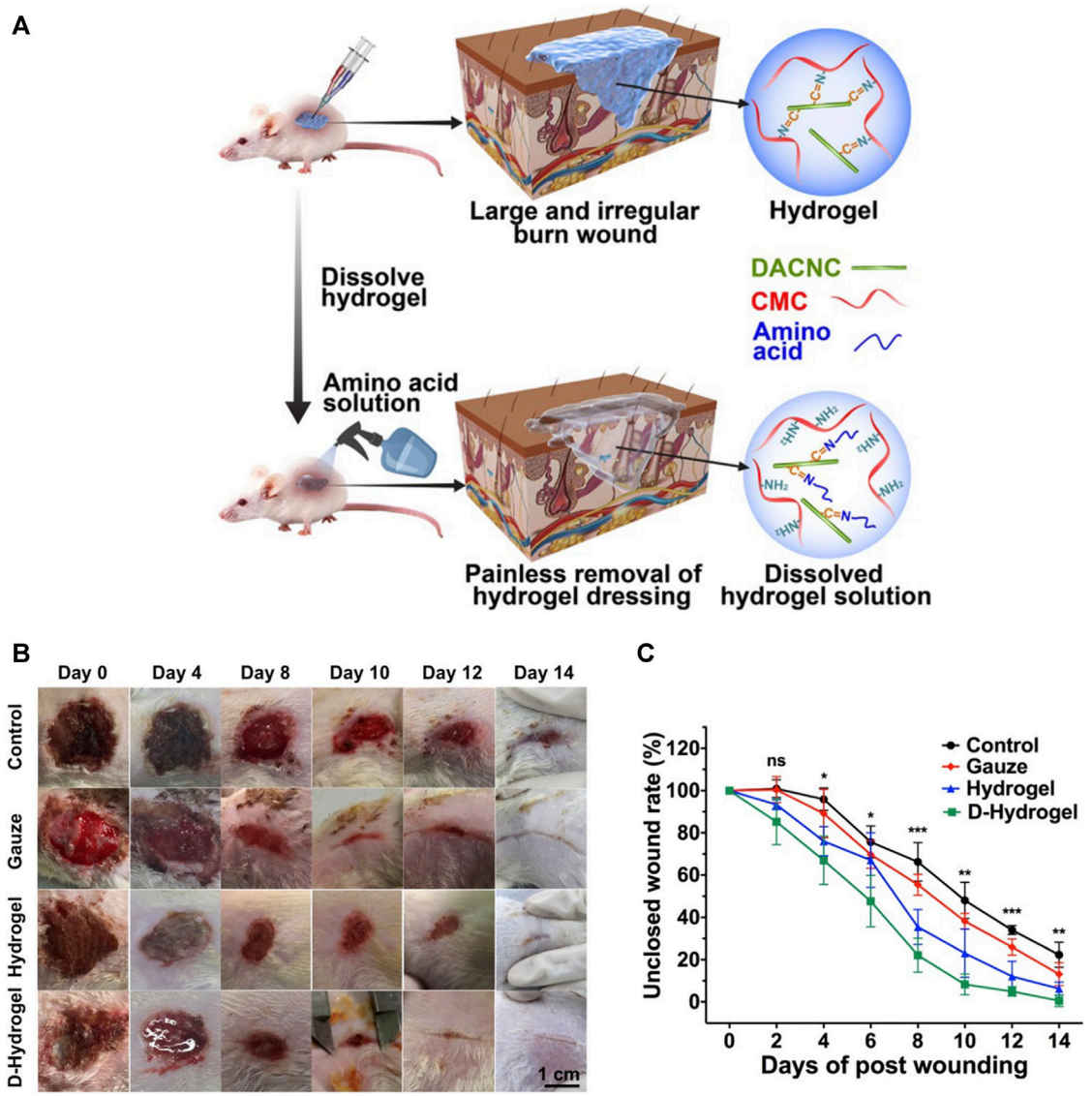


**FIGURE 4 |** "On demand" dissolvable hydrogels for the healing of deep partial-thickness burns. **(A)** How on-demand dissolvable self-healing hydrogels are used to treat wounds (schematic). **(B)** Representative images of wound sites in each treatment group over time. **(C)** Unclosed wound area rate of initial wound as a function of time. ns $p > 0.05$, $^{*}p \leq 0.05$, $^{**}p \geq 0.01$, $^{***}p \leq 0.001$. Reproduced with permission from (Huang et al., 2018).

Often, burn-related deaths are closely related to burn infection. The latter occurs primarily through wound infection, and carries a mortality prevalence of 75–85%. Antibacterial hydrogel burn dressings can not only absorb wound fluid and maintain the moist environment of the wound, but also isolate the external pollution and prevent the wound from direct contact with the external environment. More importantly, antibacterial hydrogel burn dressings effectively reduce wound bacterial colonization and infection and speed up the healing process. Antimicrobial therapy of wounds is a critical component of burn treatment, and the development of antimicrobial hydrogel dressings is an ongoing research focus. A new type of hydrogel loaded with SSD and essential fibroblast growth factor and optimized based on SSD cream was found to not irritate skin or eyes (Chakrabarti et al., 2018). A thermo-sensitive methylcellulose hydrogel containing silver oxide nanoparticles (NPs) was also prepared as an injectable hydrogel and demonstrated an excellent antibacterial effect on the wound surface (Kim et al., 2018). Grolman and colleagues (Grolman et al., 2019) prepared agarose hydrogels containing high concentrations of minocycline or gentamicin. They demonstrated the stability of the two antibiotics in the hydrogels for ≥7 days in a porcine model of burns. The agarose minocycline hydrogel was as effective as the commonly used SSD cream in reducing burn depth and the number of bacteria. Demirci and coworkers (Demirci et al., 2015) prepared a novel antimicrobial carbopol hydrogel composed of boron and multiblock copolymers. This hydrogel not only

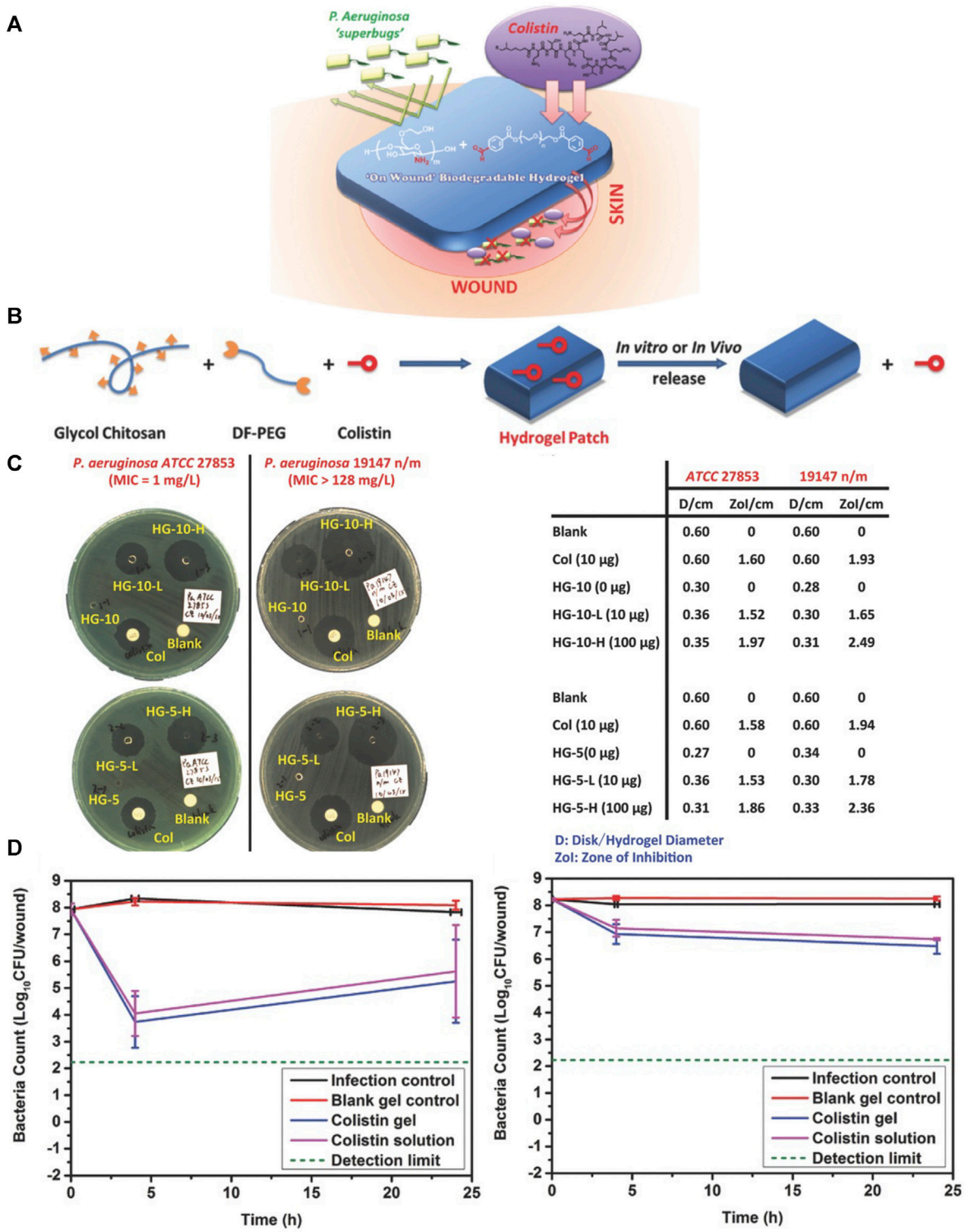


| | ATCC 27853 | | 19147 n/m | |
|---|---|---|---|---|
| | D/cm | ZoI/cm | D/cm | ZoI/cm |
| Blank | 0.60 | 0 | 0.60 | 0 |
| Col (10 μg) | 0.60 | 1.60 | 0.60 | 1.93 |
| HG-10 (0 μg) | 0.30 | 0 | 0.28 | 0 |
| HG-10-L (10 μg) | 0.36 | 1.52 | 0.30 | 1.65 |
| HG-10-H (100 μg) | 0.35 | 1.97 | 0.31 | 2.49 |
| Blank | 0.60 | 0 | 0.60 | 0 |
| Col (10 μg) | 0.60 | 1.58 | 0.60 | 1.94 |
| HG-5(0 μg) | 0.27 | 0 | 0.34 | 0 |
| HG-5-L (10 μg) | 0.36 | 1.53 | 0.30 | 1.78 |
| HG-5-H (100 μg) | 0.31 | 1.86 | 0.33 | 2.36 |

D: Disk/Hydrogel Diameter
ZoI: Zone of Inhibition

**FIGURE 5 |** Hydrogel-based localized release of colistin for antimicrobial treatment of infections from burn wounds. **(A)** Treatment of a burn wound with a colistin-loaded hydrogel (schematic). **(B)** Synthesis of a colistin-containing hydrogel (schematic). **(C)** Disk diffusion assay of a colistin-loaded hydrogel against colistin-sensitive (left) and colistin-resistant (right) *P. aeruginosa* strains **(D)** Test of colistin-loaded hydrogel against colistin-sensitive (left) and colistin-resistant (right) strains of *P. aeruginosa* in a model of burn infection. Reproduced with permission from (Zhu et al., 2017).

increased wound healing through fibroblast activity but also induced angiogenesis and showed significant antimicrobial effects on bacteria, yeasts, and fungi. That study was the first to show that boron-containing hydrogels could treat burn wounds effectively.

Methicillin-resistant *Staphylococcus aureus* (MRSA) is a common colonizing bacterium in burn wounds worldwide, and is associated with high morbidity and mortality. Compared with systemic antibiotic treatment, antimicrobial hydrogel dressings avoid the effects on the whole body and maintain a higher drug concentration at the infection site. Chhibber and collaborators Chhibber et al. (2020) developed a chitosan-based hydrogel antibiofilm agent for local administration of moxifloxacin to wounds. Zhu et al. (2018) prepared heme-rich Dex-HA hydrogels that inhibited MRSA and *Escherichia coli*. Dex-HA promoted cell re-epithelialization and enhanced ECM remodeling in a full-thickness burn-infection model in rats, and reflected a highly effective scar-inhibition effect. Thanusha et al. (2018) prepared a hydrogel platform comprising biopolymer gelatin, glycosaminoglycans (HA and chondroitin sulfate), asiatic acid (a triterpenoid), and NPs (zinc oxide and copper oxide). The resulting hydrogel could resist *E. coli* and *S. aureus* in second-degree burn wounds in rats, and promote wound re-epithelialization, collagen-fiber arrangement, and angiogenesis. New treatments are needed urgently for *Pseudomonas aeruginosa* infections of burn wounds caused by multidrug-resistant Gram-negative "superbugs". Zhu and coworkers (Zhu et al., 2017) chemically reacted the amine groups in glycol chitosan and aldehyde-PEG and combined them with colistin (potent lipopeptide) to form self-healing hydrogels (**Figure 5**). This process increased the storage modulus of the colistin hydrogel from 1.3 to 5.3 kPa, enabled sustained release of colistin from the hydrogel, and maintained wound activity, colistin susceptibility, and microbial resistance. *P. aeruginosa* has almost the same lethality as that of natural colistin.

Numerous attempts have been made to develop new antimicrobial materials and ways of delivering antibiotics to develop innovative antimicrobial hydrogels. Sanchez and colleagues Sanchez et al. (2018) developed a transparent carbomer hydrogel (CbCipLid) that combines ciprofloxacin and lidocaine at neutral pH in a manner higher than its solubility to treat second-degree burns. CbCipLid hydrogel also provides immediate anesthesia for wounds. Oryan and coworkers (Oryan et al., 2018) explored the effect of type-I collagen hydrogel scaffolds carrying *Saccharomyces cerevisiae* on the healing of burn wounds. Topical application of probiotics has been shown to antagonize *Klebsiella pneumonia*, *P. aeruginosa*, *S. aureus*, and *Bacillus subtilis*. More importantly, probiotics have a positive effect on the severe inflammatory response to burns through immunomodulation. Ouyang and collaborators (Ouyang et al., 2018) demonstrated that chitosan-conjugated hydrogels containing peptides extracted from mariculture of tilapia exhibited antibacterial activity and promoted the proliferation and migration of cells, skin regeneration, and accelerated burn healing.

## 4.3 Tissue Regeneration Dressings

### 4.3.1 Stem Cells-Loaded Hydrogel Dressings

Tissue engineering has entered the era of "regenerative medicine" (Auxenfans et al., 2015). Tissue engineering and regenerative medicine can be employed to promote healing and provide templates for the reconstruction of burn wounds. Use of stem cells to replace or repair severely damaged tissues (Auxenfans et al., 2014) and a combination of stem-cell technology and biomaterial engineering are keys to developing new dressings to treat burns (Hermans, 2011). Keratinocytes are essential for wound closure. Cytokine activation leads to keratinocyte migration, which leads to the closure and recovery of a vascular network (Bisson et al., 2013). Thus, hydrogel dressings containing keratinocytes may be clinically viable treatment options for burns (Idrus et al., 2014). Mohamad et al. (2019) introduced human epidermal keratinocytes and human dermal fibroblasts into thymic-free mice. After loading with hydrogel, collagen deposition on the treated burn wound was more obvious, which suggested an expanded application scope of BC/AA hydrogel.

Application of adult stem cells represents a major advance in treating severe burns (Lewis, 2013). Bone-marrow stem cells added to hydrogels can promote healing of burn wounds because they can transform into various types of skin cell (Badiavas, 2004). Ke et al. (2015) extracted polysaccharides from cold-tolerant orchids and the mesenchymal stem cells (MSCs) of Sprague–Dawley rats and used them to prepare hydrogels. When used for treating alkali burns to eyes in rats, the resulting hydrogels were found to significantly improve corneal epithelial recovery and reduce inflammation, neovascularization, and opacity after corneal healing. Alapure and coworkers (Alapure et al., 2018) implanted MSCs into biodegradable composite hydrogels made of unsaturated arginine-based polyesteramide and chitosan derivatives. When applied to treat third-degree burn wounds in mice, the composite hydrogels promoted re-epithelialization, formation of granulation tissue, and vascularization of wounds. Thus, these hydrogels can be used to supplement commonly used skin grafts and overcome some of the shortcomings of transplantation. Zhou and collaborators (Zhou et al., 2019) prepared a thermosensitive hydrogel consisting of human umbilical-cord MSC-conditioned medium, chitosan, collagen, and glycerophosphate (beta-oleophosphate). This hydrogel shortened the healing time of third-degree burn wounds, promoted the regeneration of granulation tissue, and inhibited the proliferation of scar tissue.

Stem cells from hair follicles have also been incorporated into products that can generate a stratified epidermis on human burn wounds (Kim et al., 2007; Trottier et al., 2008). The possibility of making epidermal skin grafts with hair-follicle stem cells is under development. Adipose stem cells promote paracrine activation of host cells by secreting growth factors, producing epidermal, dermal, and subcutaneous layers, and accelerating re-epithelialization (Bey et al., 2010; Natesan et al., 2011). Usually, discarded human adipose stem cells can be separated from tissues and produce a three-layer vascularized structure (Chan et al., 2012). Banerjee et al. (2019) prepared a PEGylated fibrin hydrogel containing SSD chitosan microspheres (SSD-CSM-FPEG) and implanted adipose stem cells into this hydrogel (**Figure 6**). SSD-CSM-FPEG has been shown to reduce infections in a *P. aeruginosa* model of contact burns on

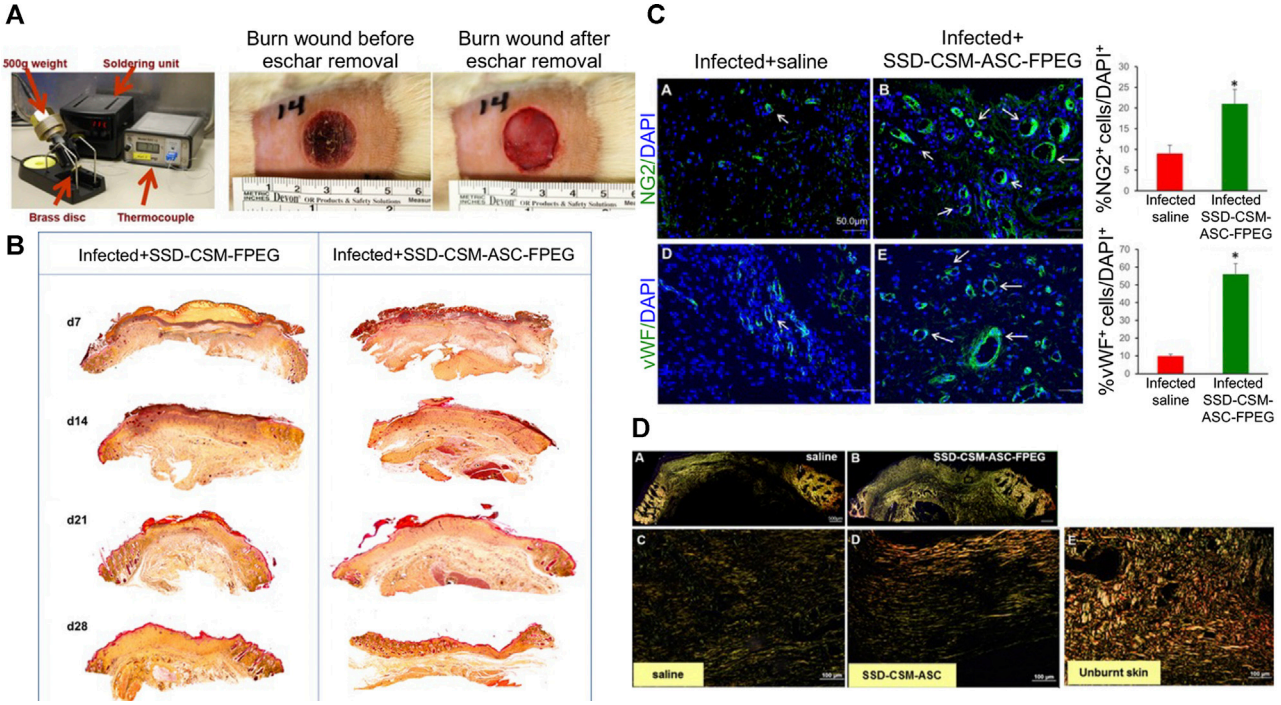


**FIGURE 6 |** Delivery of silver sulfadiazine and adipose-derived stem cells using fibrin hydrogel improves infected burn wounds. **(A)** Photographs of the burn device and burn wound. **(B)** Burn wounds treated with SSD-CSM-ASC-FPEG had significantly thicker granulation tissue than those treated with SSD-CSM-FPEG. **(C)** SSD-CSM-ASC-FPEG facilitates neo-vascularization on day-21. $p < 0.05$. **(D)** Maturation of collagen. Picrosirius staining images on day-28. Reproduced with permission from (Banerjee et al., 2019).

the backs of rats as well as promote angiogenesis and improve matrix remodeling.

Treatment of burn wounds aims to achieve wound closure through skin regeneration rather than skin repair. Therefore, temporary wound dressings for skin healing are being replaced by temporary scaffolds or regenerative templates. The exciting results obtained from using non-embryonic stem cells have stimulated interest in the application and exploration of hydrogel dressings carrying stem cells.

### 4.3.2 Wound Healing-Promoting Hydrogel Dressings

New treatments are being developed thanks to deepening understanding of wound-healing mechanisms. The epidermal growth factor (EGF) receptor is a target during burn healing. Exogenous application of EGF can accelerate re-epithelialization. Understanding of the EGF-mediated pathway during burn healing represents a breakthrough in exogenous treatment. Wang et al. (2019) produced a composite hydrogel composed of modified HA, Dex, beta-cyclodextrin, resveratrol, and vascular EGF plasmids (**Figure 7**). The resulting hydrogel significantly inhibited the inflammatory response, promoted microvessel formation, and accelerated the healing of burn wounds. Yan and coworkers (Yan et al., 2012) explored the effect of recombinant human granulocyte/macrophage colony-stimulating factor (rhGM-CSF) hydrogel on wound healing in 93 patients with a deep partial-thickness burn. The rhGM-CSF hydrogel was better than the control group in terms of wound-healing rate, healing time, wound exudation, pus score, and secretion score. Those findings suggested that rhGM-CSF hydrogel could support burn healing effectively. Thus, molecules or genes can be manipulated in hydrogel dressings to enhance the desired effects (i.e., introduce "positive" cytokines and suppress "negative" factors) (Atiyeh et al., 2005). Development of hydrogel dressings containing pro-wound-healing characteristics for burns is an active area of research.

## 4.4 Other Types of Hydrogel Dressings

The human amniotic membrane avoids large-area dressings, reduces the pain associated with dressing changes, and accelerates epithelial-cell regeneration when treating burn wounds, especially if religious sensitivities hinder application of bovine, porcine, or cadaveric skin (Gajiwala and Lobo Gajiwala, 2003). Rana and colleagues Rana et al. (2020) prepared an acellular hydrogel composed of human amniotic membrane and rabbit collagen that significantly promoted wound healing and re-epithelialization in a model of second-degree burns. Amniotic membranes and collagen-based hybrid hydrogels are inexpensive and easy to manufacture.

Honey is a natural material with excellent biocompatibility. It has shown promising results in treatment of burn wounds. Zohdi and collaborators (Mohd Zohdi et al., 2012) fabricated a crosslinked hydrogel containing Malaysian honey and demonstrated that it had a significant inhibitory effect on wound inflammation. Some scholars have found that

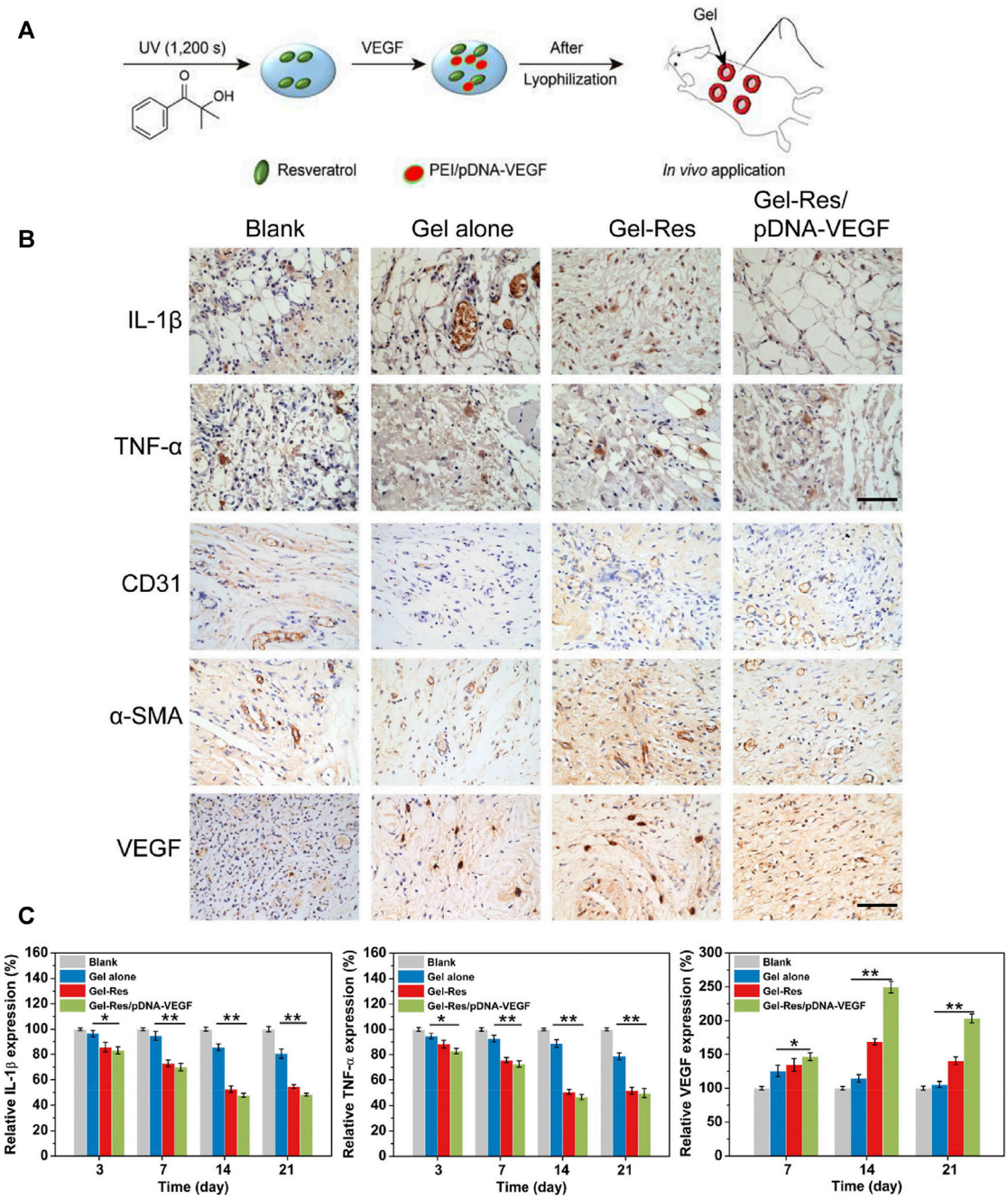


**FIGURE 7 |** *In situ*-formed anti-inflammatory hydrogel loaded with plasmid DNA encoding VEGF for healing of burn wounds. **(A)** Application of this hydrogel in a model of a splinted excisional wound (schematic). **(B)** Immunohistochemical staining showing expression of the proinflammatory cytokines IL-1$\beta$ and TNF-$\alpha$. **(C)** Immunohistochemical staining showing expressions of the angiogenic factors VEGF, CD31, and $\alpha$-SMA. Scale bar = 100 μm. **(D)** RT-qPCR of mRNA expression for inflammatory and angiogenic factors (IL-1β, TNF-α, VEGF). $^{**}p \leq 0.01$, $^{*}p \leq 0.05$. Reproduced with permission from (Wang et al., 2019).

hydrogels prepared with 75% honey had high activity against wound infections caused by *P. aeruginosa*, *S. aureus*, or *Klebsiella pneumoniae* (Mohd Zohdi et al., 2012). Some researchers have introduced sea cucumber (Zohdi et al., 2011) into hydrogels to develop a new crosslinked Gamat hydrogel dressing. The latter was shown to regulate the inflammatory response, stimulate the activation and proliferation of fibroblasts, significantly promote wound contraction and the rapid generation of a collagen-fiber network, and shorten the healing time effectively.

Nuutila and coworkers (Nuutila et al., 2020) combined a platform wound device (PWD) with a sodium-alginate hydrogel

containing a high concentration of antibiotics. When wounds infected by *S. aureus*, *P. aeruginosa*, or *Acinetobacter baumannii* were covered with the hydrogel/PWD device, the covered wound had less bacteria along with less necrotic depth. The hydrogel/PWD could be used safely at high concentrations and applied effectively to burn infections of any size. In future management of burn wounds, auxiliary treatment devices will be developed to help monitor wound conditions, quantify micro-administration in real time, extract tissue fluid for biochemical examination, improve the labor cost of burn-wound care, and prevent nosocomial wound infection.

## 5 CONCLUSION AND OUTLOOK

Targeting many problems faced in the repair process of burn wounds, the functionalities of dressings can be specifically designed during the construction of hydrogel dressings. Burn injuries present many necrotic tissues, so guaranteeing wound debridement is a crucial prerequisite to promote burn wound healing. The hydrogel dressing itself has a particular debridement ability. However, autolytic debridement hydrogel and enzyme debridement hydrogel improved the debridement effect in burn treatment. Autolytic debridement hydrogels achieve the purpose of debridement by removing devitalized or necrotic tissues through many ways, such as softening, hydrolysis, and autolysis. But the disadvantage is the long debridement period. Selective enzyme debridement hydrogels can retain undamaged dermal tissue on the wound bed, accelerate the wound's healing rate, and reduce scar formation, which has the disadvantage of higher fabrication cost.

Wound infection is another critical factor affecting wound healing, and the proliferation of bacteria and the secretion of enzymes can interfere with re-epithelialization and collagen synthesis. Therefore, hydrogel dressings must possess a particular antibacterial ability. Hydrogel dressings can achieve physical barrier sequestration of microorganisms after coverage of the wound, but sometimes this barrier is insufficient to control the extent of wound infection. The antibacterial properties of hydrogels can be further improved with the addition of antibiotics, antimicrobial agents, and the use of materials with antibacterial activity, reducing the risk of wound infection. Currently, the addition of broad-spectrum antibiotics or silver ions with antibacterial ability into hydrogel dressings is mostly adopted. But the application of broad-spectrum antibiotics increases the possibility of developing drug-resistant bacteria. In addition, the potential toxicity of silver ions limits its applications to some extent. Therefore, developing materials with antibacterial activity will be an important area of future research on hydrogel dressings.

Based on adequate debridement and limiting local inflammation, wound healing, and tissue regeneration, especially angiogenesis at the injury site. The introduction of growth factors and functional peptides with specific functions improves the tissue repair ability of hydrogel dressings and plays an essential role in promoting cell proliferation, differentiation, and angiogenesis, but has disadvantages such as higher cost and difficult to mass-produce.

During the nursing process of the burn wound, considering that burn injuries dermis stimulates nerve endings, the pain reaction brought during dressing change is much greater than other wounds. During the clinical dressing change, the replacement of conventional dressings often caused damage to the newly formed skin and tissues, increasing the suffering of patients. While the development of on-demand dissolving hydrogel brings a milder method of dressing replacement and avoids the secondary damage of newly formed tissues during the process of dressing change, which can relieve patient's pain to a more considerable extent.

The limitations of traditional dressings, technological advances, and understanding of burn-wound healing have led to a massive expansion of the range of available burn dressings and promoted the development of new burn dressings (Zhang et al., 2020). Future research on hydrogel dressings for burns is expected to focus on inflammation regulation, infection control, stem cells, transplantation, biomarkers, factors affecting wound healing, and individualized treatment. The way to achieve this goal is to develop hydrogel dressings of multifunctional composite materials. Such materials will improve wound management (e.g., through infection control and dressing elasticity) and wound healing (e.g., epithelialization, collagen synthesis, vascularization, contraction) systematically, deliver active molecules to the sites of interest, and monitor healing to meet the different needs of all the processes involved in wound healing.

The future development trend of hydrogel dressing should be considered according to the clinical need for burn wound treatment. In the early stages of burn wound treatment, emphasis should be placed on considering the anti-infection properties of the hydrogel dressing, mainly to limit bacterial proliferation and control inflammatory factor levels. In the stage of wound repair, hydrogel dressings are required to provide a suitable microenvironment for granulation tissue, which should have the ability to promote skin tissue repair and consider the possibility of inhibiting scar formation.

Furthermore, combining hydrogel dressings with skin tissue engineering concepts can lead to better optimization of hydrogel dressings from a tissue repair perspective. Hydrogel dressings provide a network structure for tissue regeneration and act as a delivery system for cells and biochemical factors. During the repair process, better deposition of ECM around the scaffolds can be achieved through the gradual degradation of the hydrogel, ultimately achieving good integration of the newly formed tissue with the surrounding tissue, preventing scar formation and skin hypofunction.

Most studies on hydrogel dressings for wounds have focused on accelerating the rate of wound healing. However, rapid wound closure would lead to disordered deposition of collagen into the injury site, which is not beneficial for alleviating scar formation or restoring the inherent glands, hair follicles, nerve tissue of skin tissue. Therefore, in the treatment of burn wounds, it is essential to construct different functional hydrogel dressings according

to the different stages of wound healing and ensure that the appropriate therapy is administered when appropriate.

## AUTHOR CONTRIBUTIONS

WS: Methodology, validation, data analyses, resources, and writing (original draft). XZ: Writing (review and editing) and supervision. CL: Writing (review and editing) and supervision. HL: Writing (review and editing) and supervision. YW: Conceptualization, writing (review and editing), supervision, funding acquisition. FC: Conceptualization, writing (review and editing), supervision, funding acquisition.

## FUNDING

This work was supported financially by the Scientific Research Planning Project of the Education Department of Jilin Province (Grant Nos. JJKH20190047KJ and JJKH20201075KJ), the Industrial Technology Research and Development Project of the Development and Reform Commission of Jilin Province (Grant No. 2021C042-3), the Science and Technology Department Program of Jilin Province (Grant No.20190304121YY), the Finance Department of Jilin Province (Grant No. ZXWSTZXEY001), and the Interdisciplinary Research Funding Program for Doctoral Students of Jilin University (Grant No. 101832020DJX049).

## REFERENCES

Abboud, E. C., Legare, T. B., Settle, J. C., Boubekri, A. M., Barillo, D. J., Marcet, J. E., et al. (2014). Do silver-based Wound Dressings Reduce Pain? A Prospective Study and Review of the Literature. *Burns* 40 (Suppl. 1), S40–S47. doi:10.1016/j.burns.2014.09.012

Alapure, B. V., Lu, Y., He, M., Chu, C.-C., Peng, H., Muhale, F., et al. (2018). Accelerate Healing of Severe Burn Wounds by Mouse Bone Marrow Mesenchymal Stem Cell-Seeded Biodegradable Hydrogel Scaffold Synthesized from Arginine-Based Poly(ester Amide) and Chitosan. *Stem Cells Development* 27, 1605–1620. doi:10.1089/scd.2018.0106

American Association of Tissue Bank (2016). Accredited Tissue Banks. Available at: http://www.aatb.org/Accredited-Bank-Search.

American Burn Association Burn (2016). Burn Incidence and Treatment in the United States: 2016. Available at: http://www.ameriburn.org/resources_factsheet.php.

Atiyeh, B. S., Gunn, S. W., and Hayek, S. N. (2005). State of the Art in Burn Treatment. *World J. Surg.* 29, 131–148. doi:10.1007/s00268-004-1082-2

Auxenfans, C., Menet, V., Catherine, Z., Shipkov, H., Lacroix, P., Bertin-Maghit, M., et al. (2015). Cultured Autologous Keratinocytes in the Treatment of Large and Deep burns: a Retrospective Study over 15 Years. *Burns* 41, 71–79. doi:10.1016/j.burns.2014.05.019

Auxenfans, C., Shipkov, H., Bach, C., Catherine, Z., Lacroix, P., Bertin-Maghit, M., et al. (2014). Cultured Allogenic Keratinocytes for Extensive burns: a Retrospective Study over 15 Years. *Burns* 40, 82–88. doi:10.1016/j.burns.2013.05.005

Badiavas, E. (2004). The Potential of Bone Marrow Cells to Orchestrate Homeostasis and Healing in Skin. *Blood Cell Mol. Dis.* 32, 21–23. doi:10.1016/j.bcmd.2003.09.011

Banerjee, J., Seetharaman, S., Wrice, N. L., Christy, R. J., and Natesan, S. (2019). Delivery of Silver Sulfadiazine and Adipose Derived Stem Cells Using Fibrin Hydrogel Improves Infected Burn Wound Regeneration. *PLoS One* 14, e0217965. doi:10.1371/journal.pone.0217965

Bang, R. L., Sharma, P. N., Sanyal, S. C., and Najjadah, I. A. (2002). Septicaemia after Burn Injury: a Comparative Study. *Burns* 28, 746–751. doi:10.1016/s0305-4179(02)00183-3

Barrow, R. E., Jeschke, M. G., and Herndon, D. N. (2000). Early Fluid Resuscitation Improves Outcomes in Severely Burned Children. *Resuscitation* 45, 91–96. doi:10.1016/s0300-9572(00)00175-1

Bey, E., Prat, M., Duhamel, P., Benderitter, M., Brachet, M., Trompier, F. o., et al. (2010). Emerging Therapy for Improving Wound Repair of Severe Radiation burns Using Local Bone Marrow-Derived Stem Cell Administrations. *Wound Repair Regen.* 18, 50–58. doi:10.1111/j.1524-475X.2009.00562.x

Bishop, J. F. (2004). Burn Wound Assessment and Surgical Management. *Crit. Care Nurs. Clin. North America* 16, 145–177. doi:10.1016/j.ccell.2003.09.003

Bisson, F., Rochefort, É., Lavoie, A., Larouche, D., Zaniolo, K., Simard-Bisson, C., et al. (2013). Irradiated Human Dermal Fibroblasts Are as Efficient as Mouse Fibroblasts as a Feeder Layer to Improve Human Epidermal Cell Culture Lifespan. *Ijms* 14, 4684–4704. doi:10.3390/ijms14034684

Boonkaew, B., Kempf, M., Kimble, R., and Cuttle, L. (2014). Cytotoxicity Testing of Silver-Containing Burn Treatments Using Primary and Immortal Skin Cells. *Burns* 40, 1562–1569. doi:10.1016/j.burns.2014.02.009

Burd, A., and Yuen, C. (2005). A Global Study of Hospitalized Paediatric Burn Patients. *Burns* 31, 432–438. doi:10.1016/j.burns.2005.02.016

Chakrabarti, S., Islam, J., Hazarika, H., Mazumder, B., Raju, P. S., and Chattopadhyay, P. (2018). Safety Profile of Silver Sulfadiazine-bFGF-Loaded Hydrogel for Partial Thickness Burn Wounds. *Cutan. Ocul. Toxicol.* 37, 258–266. doi:10.1080/15569527.2018.1442843

Chan, R. K., Zamora, D. O., Wrice, N. L., Baer, D. G., Renz, E. M., Christy, R. J., et al. (20122012). Development of a Vascularized Skin Construct Using Adipose-Derived Stem Cells from Debrided Burned Skin. *Stem Cells Int.* 2012, 1–11. doi:10.1155/2012/841203

Chhibber, T., Gondil, V. S., and Sinha, V. R. (2020). Development of Chitosan-Based Hydrogel Containing Antibiofilm Agents for the Treatment of Staphylococcus Aureus-Infected Burn Wound in Mice. *AAPS PharmSciTech* 21, 43. doi:10.1208/s12249-019-1537-2

Chouhan, D., Lohe, T. U., Samudrala, P. K., and Mandal, B. B. (2018). *In Situ* Forming Injectable Silk Fibroin Hydrogel Promotes Skin Regeneration in Full Thickness Burn Wounds. *Adv. Healthc. Mater.* 7, e1801092. doi:10.1002/adhm.201801092

Church, D., Elsayed, S., Reid, O., Winston, B., and Lindsay, R. (2006). Burn Wound Infections. *Clin. Microbiol. Rev.* 19, 403–434. doi:10.1128/CMR.19.2.403-434.2006

Cuttle, L., Kravchuk, O., Wallis, B., and Kimble, R. M. (2009). An Audit of First-Aid Treatment of Pediatric burns Patients and Their Clinical Outcome. *J. Burn Care Res.* 30, 1028–1034. doi:10.1097/BCR.0b013e3181bfb7d1

Cuttle, L., Naidu, S., Mill, J., Hoskins, W., Das, K., and Kimble, R. M. (2007). A Retrospective Cohort Study of Acticoat versus Silvazine in a Paediatric Population. *Burns* 33, 701–707. doi:10.1016/j.burns.2007.02.012

Dang, L. H., Nguyen, T. H., Tran, H. L. B., Doan, V. N., and Tran, N. Q. (2018). Injectable Nanocurcumin-Formulated Chitosan-G-Pluronic Hydrogel Exhibiting a Great Potential for Burn Treatment. *J. Healthc. Eng.* 2018, 5754890. doi:10.1155/2018/5754890

Danin, A., Georgesco, G., Le Touze, A., Penaud, A., Quignon, R., and Zakine, G. (2012). Assessment of Burned Hands Reconstructed with Integra by Ultrasonography and Elastometry. *Burns* 38, 998–1004. doi:10.1016/j.burns.2012.02.017

Dargaville, T. R., Farrugia, B. L., Broadbent, J. A., Pace, S., Upton, Z., and Voelcker, N. H. (2013). Sensors and Imaging for Wound Healing: a Review. *Biosens. Bioelectron.* 41, 30–42. doi:10.1016/j.bios.2012.09.029

Demirci, S., Doğan, A., Karakuş, E., Halıcı, Z., Topçu, A., Demirci, E., et al. (2015). Boron and Poloxamer (F68 and F127) Containing Hydrogel Formulation for Burn Wound Healing. *Biol. Trace Elem. Res.* 168, 169–180. doi:10.1007/s12011-015-0338-z

DeSanti, L. (2005). Pathophysiology and Current Management of Burn Injury. *Adv. Skin Wound Care* 18, 323–332. doi:10.1097/00129334-200507000-00013

Dries, David. J. (2005). *Textbook of Critical Care*. Editors P. F. Mitchell, A. Edward, J-L. Vincent, and P. M. Kochanek. 5th Ed. (Minneapolis & Duluth , Minnesota , United States: University of Minnesota Medical School).

Ekenseair, A. K., Boere, K. W. M., Tzouanas, S. N., Vo, T. N., Kasper, F. K., and Mikos, A. G. (2012). Structure-property Evaluation of Thermally and Chemically Gelling Injectable Hydrogels for Tissue Engineering. *Biomacromolecules* 13, 2821–2830. doi:10.1021/bm300797m

Fox, C. L. (1968). Silver Sulfadiazine-A New Topical Therapy for Pseudomonas in Burns. *Arch. Surg.* 96, 184–188. doi:10.1001/archsurg.1968.01330200022004

Gajiwala, K., and Lobo Gajiwala, A. (2003). Use of Banked Tissue in Plastic Surgery. *Cell Tissue Banking* 4, 141–146. doi:10.1023/B:CATB.0000007023.85139.c5

Grolman, J. M., Singh, M., Mooney, D. J., Eriksson, E., and Nuutila, K. (2019). Antibiotic-Containing Agarose Hydrogel for Wound and Burn Care. *J. Burn Care Res.* 40, 900–906. doi:10.1093/jbcr/irz113

Hayati, F., Ghamsari, S. M., Dehghan, M. M., and Oryan, A. (2018). Effects of Carbomer 940 Hydrogel on Burn Wounds: an *In Vitro* and *In Vivo* Study. *J. Dermatol. Treat.* 29, 593–599. doi:10.1080/09546634.2018.1426823

Heggers, J. P., Sazy, J. A., Stenberg, B. D., Strock, L. L., McCauley, R. L., Herndon, D. N., et al. (1991). Bactericidal and Wound-Healing Properties of Sodium Hypochlorite Solutions: the 1991 Lindberg Award. *J. Burn Care Rehabil.* 12, 420–424. doi:10.1097/00004630-199109000-00005

Hermans, M. H. E. (2014). Porcine Xenografts vs. (Cryopreserved) Allografts in the Management of Partial Thickness burns: Is There a Clinical Difference? *Burns* 40, 408–415. doi:10.1016/j.burns.2013.08.020

Hermans, M. H. E. (2011). Preservation Methods of Allografts and Their (Lack of) Influence on Clinical Results in Partial Thickness burns. *Burns* 37, 873–881. doi:10.1016/j.burns.2011.01.007

Hettiaratchy, S., and Dziewulski, P. (2004). Pathophysiology and Types of burns. *BMJ* 328, 1427–1429. doi:10.1136/bmj.328.7453.1427

Hettiaratchy, S., and Papini, R. (2004). Initial Management of a Major Burn: II-Assessment and Resuscitation. *BMJ* 329, 101–103. doi:10.1136/bmj.329.7457.101

Hoffman, A. S. (2002). Hydrogels for Biomedical Applications. *Adv. Drug Deliv. Rev.* 54, 3–12. doi:10.1016/s0169-409x(01)00239-3

Horvath, E. E., Murray, C. K., Vaughan, G. M., Chung, K. K., Hospenthal, D. R., Wade, C. E., et al. (2007). Fungal Wound Infection (Not Colonization) Is Independently Associated with Mortality in Burn Patients. *Ann. Surg.* 245, 978–985. doi:10.1097/01.sla.0000256914.16754.80

Huang, J., Wang, W., Yu, J., Yu, X., Zheng, Q., Peng, F., et al. (2017). Combination of Dexamethasone and Avastin by Supramolecular Hydrogel Attenuates the Inflammatory Corneal Neovascularization in Rat Alkali Burn Model. *Colloids Surf. B: Biointerfaces* 159, 241–250. doi:10.1016/j.colsurfb.2017.07.057

Huang, W., Wang, Y., Huang, Z., Wang, X., Chen, L., Zhang, Y., et al. (2018). On-Demand Dissolvable Self-Healing Hydrogel Based on Carboxymethyl Chitosan and Cellulose Nanocrystal for Deep Partial Thickness Burn Wound Healing. *ACS Appl. Mater. Inter.* 10, 41076–41088. doi:10.1021/acsami.8b14526

Hyland, E. L., and Harvey, J. G. (2014). *Burn First Aid – the Weird and Wonderful.* Fremantle, Australia: ANZBA Burns Conference.

Idrus, R. H., Rameli, M. A. b. P., Low, K. C., Law, J. X., Chua, K. H., Latiff, M. B. A., et al. (2014). Full-Thickness Skin Wound Healing Using Autologous Keratinocytes and Dermal Fibroblasts with Fibrin. *Adv. Skin Wound Care* 27, 171–180. doi:10.1097/01.ASW.0000445199.26874.9d

Jaskille, A. D., Ramella-Roman, J. C., Shupp, J. W., Jordan, M. H., and Jeng, J. C. (2010). Critical Review of Burn Depth Assessment Techniques: Part II. Review of Laser Doppler Technology. *J. Burn Care Res.* 31, 151–157. doi:10.1097/BCR.0b013e3181c7ed60

Jaskille, A. D., Shupp, J. W., Jordan, M. H., and Jeng, J. C. (2009). Critical Review of Burn Depth Assessment Techniques: Part I. Historical Review. *J. Burn Care Res.* 30, 937–947. doi:10.1097/BCR.0b013e3181c07f21

Kamoun, E. A., Kenawy, E.-R. S., and Chen, X. (2017). A Review on Polymeric Hydrogel Membranes for Wound Dressing Applications: PVA-Based Hydrogel Dressings. *J. Adv. Res.* 8, 217–233. doi:10.1016/j.jare.2017.01.005

Ke, Y., Wu, Y., Cui, X., Liu, X., Yu, M., Yang, C., et al. (2015). Polysaccharide Hydrogel Combined with Mesenchymal Stem Cells Promotes the Healing of Corneal Alkali Burn in Rats. *PLoS One* 10, e0119725. doi:10.1371/journal.pone.0119725

Kim, M. H., Park, H., Nam, H. C., Park, S. R., Jung, J.-Y., and Park, W. H. (2018). Injectable Methylcellulose Hydrogel Containing Silver Oxide Nanoparticles for Burn Wound Healing. *Carbohydr. Polym.* 181, 579–586. doi:10.1016/j.carbpol.2017.11.109

Kim, W.-S., Park, B.-S., Sung, J.-H., Yang, J.-M., Park, S.-B., Kwak, S.-J., et al. (2007). Wound Healing Effect of Adipose-Derived Stem Cells: a Critical Role of Secretory Factors on Human Dermal Fibroblasts. *J. Dermatol. Sci.* 48, 15–24. doi:10.1016/j.jdermsci.2007.05.018

Konieczynska, M. D., Villa-CamachoPerez-Viloria, J. C., Ghobril, C., Perez-Viloria, M., Tevis, K. M., Blessing, W. A., et al. (2016). On-Demand Dissolution of a Dendritic Hydrogel-Based Dressing for Second-Degree Burn Wounds through Thiol-Thioester Exchange Reaction. *Angew. Chem. Int. Ed.* 55, 9984–9987. doi:10.1002/anie.201604827

Latenser, B. A. (2009). Critical Care of the Burn Patient: the First 48 hours. *Crit. Care Med.* 37, 2819–2826. doi:10.1097/CCM.0b013e3181b3a08f10.1097/00003246-200910000-00021

Lei, H., Zhu, C., and Fan, D. (2020). Optimization of Human-like Collagen Composite Polysaccharide Hydrogel Dressing Preparation Using Response Surface for Burn Repair. *Carbohydr. Polym.* 239, 116249. doi:10.1016/j.carbpol.2020.116249

Lewis, C. J. (2013). Stem Cell Application in Acute Burn Care and Reconstruction. *J. Wound Care* 22, 7–8. doi:10.12968/jowc.2013.22.1.7

Li, Z., Zhou, F., Li, Z., Lin, S., Chen, L., Liu, L., et al. (2018). Hydrogel Cross-Linked with Dynamic Covalent Bonding and Micellization for Promoting Burn Wound Healing. *ACS Appl. Mater. Inter.* 10, 25194–25202. doi:10.1021/acsami.8b08165

Liang, M., Chen, Z., Wang, F., Liu, L., Wei, R., and Zhang, M. (2019). Preparation of Self-regulating/anti-adhesive Hydrogels and Their Ability to Promote Healing in Burn Wounds. *J. Biomed. Mater. Res.* 107, 1471–1482. doi:10.1002/jbm.b.34239

Mertens, D. M., Jenkins, M. E., and Warden, G. D. (1997). Outpatient Burn Management. *Nurs. Clin. North. Am.* 32, 343–364.

Mohamad, N., Loh, E. Y. X., Fauzi, M. B., Ng, M. H., and Mohd Amin, M. C. I. (2019). *In Vivo* evaluation of Bacterial Cellulose/acrylic Acid Wound Dressing Hydrogel Containing Keratinocytes and Fibroblasts for Burn Wounds. *Drug Deliv. Transl. Res.* 9, 444–452. doi:10.1007/s13346-017-0475-3

Mohamad, N., Mohd Amin, M. C. I., Pandey, M., Ahmad, N., and Rajab, N. F. (2014). Bacterial Cellulose/acrylic Acid Hydrogel Synthesized via Electron Beam Irradiation: Accelerated Burn Wound Healing in an Animal Model. *Carbohydr. Polym.* 114, 312–320. doi:10.1016/j.carbpol.2014.08.025

Mohd Zohdi, R., Abu Bakar Zakaria, Z., Yusof, N., Mohamed Mustapha, N., and Abdullah, M. N. H. (2012). Gelam (Melaleucaspp.) Honey-Based Hydrogel as Burn Wound Dressing. *Evidence-Based Complement. Altern. Med.* 2012, 1–7. doi:10.1155/2012/843025

Moyer, C. A., Brentano, L., Gravens, D. L., Margraf, H. W., and Monafo, W. W. (1965). Treatment of Large Human Burns with 0.5% Silver Nitrate Solution. *Arch. Surg.* 90, 812–867. doi:10.1001/archsurg.1965.01320120014002

Mozalewska, W., Czechowska-Biskup, R., Olejnik, A. K., Wach, R. A., Ulański, P., and Rosiak, J. M. (2017). Chitosan-containing Hydrogel Wound Dressings Prepared by Radiation Technique. *Radiat. Phys. Chem.* 134, 1–7. doi:10.1016/j.radphyschem.2017.01.003

Natesan, S., Wrice, N. L., Baer, D. G., and Christy, R. J. (2011). Debrided Skin as a Source of Autologous Stem Cells for Wound Repair. *Stem Cells* 29, 1219–1230. doi:10.1002/stem.677

Nuutila, K., Grolman, J., Yang, L., Broomhead, M., Lipsitz, S., Onderdonk, A., et al. (2020). Immediate Treatment of Burn Wounds with High Concentrations of Topical Antibiotics in an Alginate Hydrogel Using a Platform Wound Device. *Adv. Wound Care* 9, 48–60. doi:10.1089/wound.2019.1018

Oryan, A., Jalili, M., Kamali, A., and Nikahval, B. (2018). The Concurrent Use of Probiotic Microorganism and Collagen Hydrogel/scaffold Enhances Burn Wound Healing: An *In Vivo* Evaluation. *Burns* 44, 1775–1786. doi:10.1016/j.burns.2018.05.016

Ouyang, Q.-Q., Hu, Z., Lin, Z.-P., Quan, W.-Y., Deng, Y.-F., Li, S.-D., et al. (2018). Chitosan Hydrogel in Combination with marine Peptides from tilapia for burns Healing. *Int. J. Biol. Macromolecules* 112, 1191–1198. doi:10.1016/j.ijbiomac.2018.01.217

Pandey, M., Mohamad, N., Low, W.-L., Martin, C., and Mohd Amin, M. C. I. (2017). Microwaved Bacterial Cellulose-Based Hydrogel Microparticles for the Healing of Partial Thickness Burn Wounds. *Drug Deliv. Transl. Res.* 7, 89–99. doi:10.1007/s13346-016-0341-8

Peck, M. D. (2011). Epidemiology of burns throughout the World. Part I: Distribution and Risk Factors. *Burns* 37, 1087–1100. doi:10.1016/j.burns.2011.06.005

Purdue, G. F., Hunt, J. L., Still, J. M., Law, E. J., Herndon, D. N., Goldfarb, I. W., et al. (1997). A Multicenter Clinical Trial of a Biosynthetic Skin Replacement,

Dermagraft-TC, Compared with Cryopreserved Human Cadaver Skin for Temporary Coverage of Excised Burn Wounds. *J. Burn Care Rehabil.* 18, 52–57. doi:10.1097/00004630-199701000-00009

Quinn, K. J., Courtney, J. M., Evans, J. H., Gaylor, J. D. S., and Reid, W. H. (1985). Principles of Burn Dressings. *Biomaterials* 6, 369–377. doi:10.1016/0142-9612(85)90095-x

Raff, T., Germann, G., and Hartmann, B. (1997). The Value of Early Enteral Nutrition in the Prophylaxis of Stress Ulceration in the Severely Burned Patient. *Burns* 23, 313–318. doi:10.1016/s0305-4179(97)89875-0

Rana, M. M., Rahman, M. S., Ullah, M. A., Siddika, A., Hossain, M. L., Akhter, M. S., et al. (2020). Amnion and Collagen-Based Blended Hydrogel Improves Burn Healing Efficacy on a Rat Skin Wound Model in the Presence of Wound Dressing Biomembrane. *Bme* 31, 1–17. doi:10.3233/BME-201076

Reithofer, M. R., Lakshmanan, A., Ping, A. T. K., Chin, J. M., and Hauser, C. A. E. (2014). *In Situ* synthesis of Size-Controlled, Stable Silver Nanoparticles within Ultrashort Peptide Hydrogels and Their Anti-bacterial Properties. *Biomaterials* 35, 7535–7542. doi:10.1016/j.biomaterials.2014.04.102

Salick, D. A., Kretsinger, J. K., Pochan, D. J., and Schneider, J. P. (2007). Inherent Antibacterial Activity of a Peptide-Based β-Hairpin Hydrogel. *J. Am. Chem. Soc.* 129, 14793–14799. doi:10.1021/ja076300z

Sanchez, M. F., Breda, S. A., Soria, E. A., Tártara, L. I., Manzo, R. H., and Olivera, M. E. (2018). Ciprofloxacin-lidocaine-based Hydrogel: Development, Characterization, and *In Vivo* Evaluation in a Second-Degree Burn Model. *Drug Deliv. Transl. Res.* 8, 1000–1013. doi:10.1007/s13346-018-0523-7

Selig, H. F., Lumenta, D. B., Giretzlehner, M., Jeschke, M. G., Upton, D., and Kamolz, L. P. (2012). The Properties of an "ideal" Burn Wound Dressing - what Do We Need in Daily Clinical Practice? Results of a Worldwide Online Survey Among Burn Care Specialists. *Burns* 38, 960–966. doi:10.1016/j.burns.2012.04.007

Sen, C. K., Gordillo, G. M., Roy, S., Kirsner, R., Lambert, L., Hunt, T. K., et al. (2009). Human Skin Wounds: a Major and Snowballing Threat to Public Health and the Economy. *Wound Repair Regen.* 17, 763–771. doi:10.1111/j.1524-475X.2009.00543.x

Shen, Y.-I., Song, H.-H. G., Papa, A. E., Burke, J. A., Volk, S. W., and Gerecht, S. (2015). Acellular Hydrogels for Regenerative Burn Wound Healing: Translation from a Porcine Model. *J. Invest. Dermatol.* 135, 2519–2529. doi:10.1038/jid.2015.182

Sinko, P. J., Stein, S., Menjoge, A. R., Gunaseelan, S., Anumolu, S. N. S. R., and Navath, R. (2015). *Dressing Compositions and Methods*. United States Patent, USOO921 1358B2.

Stubbe, B., Mignon, A., Declercq, H., Vlierberghe, S., and Dubruel, P. (2019). Development of Gelatin-Alginate Hydrogels for Burn Wound Treatment. *Macromol. Biosci.* 19, 1900123. doi:10.1002/mabi.201900123

Sun, G., Zhang, X., Shen, Y.-I., Sebastian, R., Dickinson, L. E., Fox-Talbot, K., et al. (2011). Dextran Hydrogel Scaffolds Enhance Angiogenic Responses and Promote Complete Skin Regeneration during Burn Wound Healing. *Proc. Natl. Acad. Sci.* 108, 20976–20981. doi:10.1073/pnas.1115973108

Teodorescu, M., Negru, I., Stanescu, P. O., Drăghici, C., Lungu, A., and Sârbu, A. (2010). Thermogelation Properties of poly(N-Isopropylacrylamide) - Block - Poly(ethylene Glycol) - Block - poly(N-Isopropylacrylamide) Triblock Copolymer Aqueous Solutions. *Reactive Funct. Polym.* 70, 790–797. doi:10.1016/j.reactfunctpolym.2010.07.015

Thanusha, A. V., Dinda, A. K., and Koul, V. (2018). Evaluation of Nano Hydrogel Composite Based on gelatin/HA/CS Suffused with Asiatic acid/ZnO and CuO Nanoparticles for Second Degree burns. *Mater. Sci. Eng. C* 89, 378–386. doi:10.1016/j.msec.2018.03.034

Thomas, S. S., Lawrence, J. C., and Thomas, A. (1995). Evaluation of Hydrocolloids and Topical Medication in Minor burns. *J. Wound Care* 4, 218–220. doi:10.12968/jowc.1995.4.5.218

Tredget, E. E., Shankowsky, H. A., Groeneveld, A., and Burrell, R. (1998). A Matched-Pair, Randomized Study Evaluating the Efficacy and Safety of Acticoat* Silver-Coated Dressing for the Treatment of Burn Wounds. *J. Burn Care Rehabil.* 19, 531–537. doi:10.1097/00004630-199811000-00013

Trottier, V., Marceau-Fortier, G., Germain, L., Vincent, C., and Fradette, J. (2008). IFATS Collection: Using Human Adipose-Derived Stem/stromal Cells for the Production of New Skin Substitutes. *Stem Cells* 26, 2713–2723. doi:10.1634/stemcells.2008-0031

Uppuluri, V. N. V. A., and Shanmugarajan, T. S. (2019). Icariin-Loaded Polyvinyl Alcohol/Agar Hydrogel: Development, Characterization, and *In Vivo* Evaluation in a Full-Thickness Burn Model. *The Int. J. Lower Extremity Wounds* 18, 323–335. doi:10.1177/1534734619849982

Walker, A., Baumber, R., and Robson, B. (2005). Pre-hospital Management of burns by the UK Fire Service. *Emerg. Med. J.* 22, 205–208. doi:10.1136/emj.2004.015784

Wang, P., Huang, S., Hu, Z., Yang, W., Lan, Y., Zhu, J., et al. (2019). *In Situ* formed Anti-inflammatory Hydrogel Loading Plasmid DNA Encoding VEGF for Burn Wound Healing. *Acta Biomater.* 100, 191–201. doi:10.1016/j.actbio.2019.10.004

Wasiak, J., Cleland, H., Campbell, F., and Spinks, A. (2013). Dressings for Superficial and Partial Thickness burns. *Cochrane Database Syst. Rev.CD002106* 2013, CD002106. doi:10.1002/14651858.CD002106.pub4

World Health Organization.(2019). Burns. Available at: http://www.who.int/mediacentre/factsheets/fs365/en/.

Yan, H., Chen, J., and Peng, X. (2012). Recombinant Human Granulocyte-Macrophage colony-stimulating Factor Hydrogel Promotes Healing of Deep Partial Thickness Burn Wounds. *Burns* 38, 877–881. doi:10.1016/j.burns.2012.02.001

Zhai, M., Xu, Y., Zhou, B., and Jing, W. (2018). Keratin-chitosan/n-ZnO Nanocomposite Hydrogel for Antimicrobial Treatment of Burn Wound Healing: Characterization and Biomedical Application. *J. Photochem. Photobiol. B: Biol.* 180, 253–258. doi:10.1016/j.jphotobiol.2018.02.018

Zhang, X., Shu, W., Yu, Q., Qu, W., Wang, Y., and Li, R. (2020). Functional Biomaterials for Treatment of Chronic Wound. *Front. Bioeng. Biotechnol.* 8, 516. doi:10.3389/fbioe.2020.00516

Zhou, P., Li, X., Zhang, B., Shi, Q., Li, D., and Ju, X. (2019). A Human Umbilical Cord Mesenchymal Stem Cell-Conditioned Medium/Chitosan/Collagen/β-Glycerophosphate Thermosensitive Hydrogel Promotes Burn Injury Healing in Mice. *Biomed. Res. Int.* 2019, 1–14. doi:10.1155/2019/5768285

Zhu, C., Zhao, J., Kempe, K., Wilson, P., Wang, J., Velkov, T., et al. (2017). A Hydrogel-Based Localized Release of Colistin for Antimicrobial Treatment of Burn Wound Infection. *Macromol. Biosci.* 17, 1600320. doi:10.1002/mabi.201600320

Zhu, Q., Jiang, M., Liu, Q., Yan, S., Feng, L., Lan, Y., et al. (2018). Enhanced Healing Activity of Burn Wound Infection by a Dextran-HA Hydrogel Enriched with Sanguinarine. *Biomater. Sci.* 6, 2472–2486. doi:10.1039/c8bm00478a

Zohdi, R. M., Zakaria, Z. A. B., Yusof, N., Mustapha, N. M., and Abdullah, M. N. H. (2011). Sea Cucumber (Stichopus Hermanii) Based Hydrogel to Treat Burn Wounds in Rats. *J. Biomed. Mater. Res.* 98B, 30–37. doi:10.1002/jbm.b.31828

**Conflict of Interest:** The authors declare that they have no known competing financial interests or personal relationships that could have influenced this work.

**Publisher's Note:** All claims expressed in this article are solely those of the authors and do not necessarily represent those of their affiliated organizations, or those of the publisher, the editors and the reviewers. Any product that may be evaluated in this article, or claim that may be made by its manufacturer, is not guaranteed or endorsed by the publisher.

frontiers in Bioengineering and Biotechnology

REVIEW
published: 07 December 2021
doi: 10.3389/fbioe.2021.783816

# Multifunctional Coatings of Titanium Implants Toward Promoting Osseointegration and Preventing Infection: Recent Developments

*Xiaoxuan Lu†, Zichen Wu†, Kehui Xu†, Xiaowei Wang, Shuang Wang, Hua Qiu, Xiangyang Li* and Jialong Chen**

*Key Laboratory of Oral Diseases Research of Anhui Province, Stomatologic Hospital and College, Anhui Medical University, Hefei, China*

OPEN ACCESS

**Edited by:**
*Jingan Li,*
*Zhengzhou University, China*

**Reviewed by:**
*Tao Liu,*
*Guangzhou University of Chinese Medicine, China*
*Jin Wang,*
*Southwest Jiaotong University, China*
*Lumei Liu,*
*Abigail Wexner Research Institute, United States*

***Correspondence:**
*Jialong Chen*
*jialong_dt@126.com*
*Xiangyang Li*
*hlxiangyang@163.com*

†*These authors have contributed equally to this work*

**Specialty section:**
*This article was submitted to Biomaterials, a section of the journal* Frontiers in Bioengineering and Biotechnology

**Received:** *27 September 2021*
**Accepted:** *25 October 2021*
**Published:** *07 December 2021*

**Citation:**
*Lu X, Wu Z, Xu K, Wang X, Wang S, Qiu H, Li X and Chen J (2021) Multifunctional Coatings of Titanium Implants Toward Promoting Osseointegration and Preventing Infection: Recent Developments. Front. Bioeng. Biotechnol. 9:783816. doi: 10.3389/fbioe.2021.783816*

Titanium and its alloys are dominant material for orthopedic/dental implants due to their stable chemical properties and good biocompatibility. However, aseptic loosening and peri-implant infection remain problems that may lead to implant removal eventually. The ideal orthopedic implant should possess both osteogenic and antibacterial properties and do proper assistance to *in situ* inflammatory cells for anti-microbe and tissue repair. Recent advances in surface modification have provided various strategies to procure the harmonious relationship between implant and its microenvironment. In this review, we provide an overview of the latest strategies to endow titanium implants with bio-function and anti-infection properties. We state the methods they use to preparing these efficient surfaces and offer further insight into the interaction between these devices and the local biological environment. Finally, we discuss the unmet needs and current challenges in the development of ideal materials for bone implantation.

**Keywords: orthopedic titanium implants, titanium implants, osseointegration, anti-infection, functional coatings**

## INTRODUCTION

With the aging of the population, the incidence of orthopedic diseases has increased, and the use of orthopedic implants has increased rapidly. Titanium and its alloys, exhibiting stable chemical properties and excellent biocompatibility, are often used as materials for orthopedic implants. However, approximately 10% of implants need to be renovated due to their undesirable properties (Kurtz et al., 2005), among which aseptic loosening and infection of the implant are the main reasons for the failure. A study shows that in 337,597 procedures of knee revision, the infectious factors accounted for approximately 20.3% of implant failures, while aseptic loosening accounted for 20.4% (Delanois et al., 2017).

Aseptic loosening is mainly caused by the tiny gaps of prosthesisbone interface (Goodman, 1994; Sundfeldt et al., 2006). In effect of the gravity and pressure, the tiny gap increased and the wear particles will accumulate at the interface and hinder the direct contact between the implant and bone (Schmalzried et al., 1992; Sundfeldt et al., 2006). Accompanied with local inflammation and cascade reactions activated by immune cells, the osteoclast was enriched and bone resorption (Amstutz et al., 1992) occurred, which lead to implant loosening (Valstar et al., 2002). Besides, this process may also cause the transfer of bacteria from oral cavity to implant through the loosened gaps (Zhang, 2014). With the formation of bacteria colonization and biofilm, the undesirable milieu emerged, and even

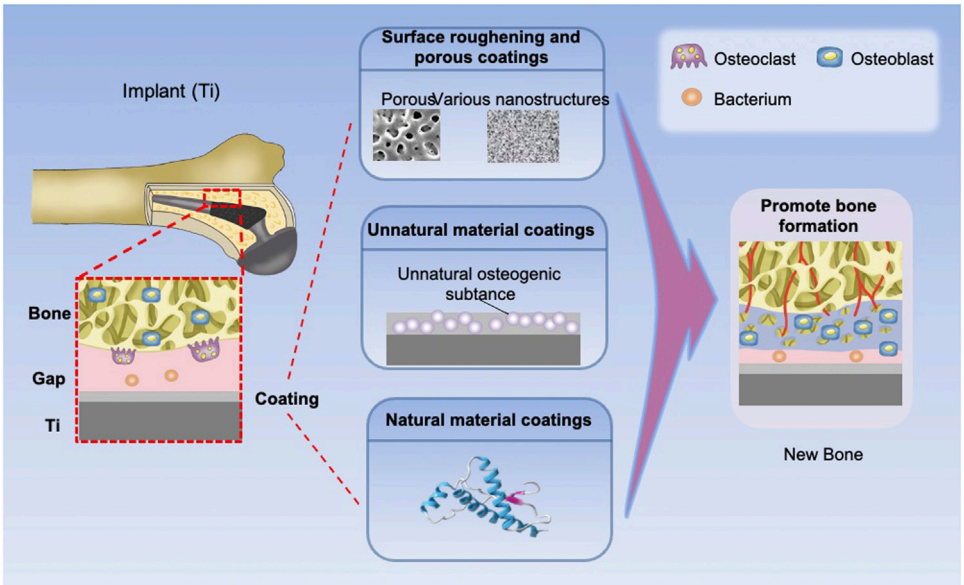


**FIGURE 1 |** Types and effects of osteogenic coatings on titanium implants. The elastic coating can fill the interface gap by expansion. The implants with surface morphology coatings, inactive coatings, and bioactive coatings can promote new bone formation.

the local immune environment was destroyed, thus making antibiotics invalid to bacteria in the biofilm (Kaestner, 2016). Ultimately, implant failure would happen.

Therefore, aseptic loosening and infection are key risks to orthopedic implants. Long-term stability of orthopedic or orthodontic implants lies on the excellent osseointegration and antibacterial performance, which would do favor to establish a stable microenvironment and in turn restrain biofilm formation. Furthermore, the immune system, which is the first responder to the external microorganism and device, cannot be ignored. Xue et al. reviewed the surface modification of Ti and its alloys with the deep sight on physical and chemical techniques, including plasma spray, chemical vapor deposition, and microarc oxidation (MAO) (Xue et al., 2020). While taking more attention to the service environment of implants, this article mainly focuses on the latest report about how materials interact with the local biological milieu, especially with the microbe, osteocyte, and immune cells.

## PREVENTION OF ASEPTIC IMPLANT LOOSENING

Osseointegration is a dynamic process during which the cells around implant secrete various cytokines to promote osteoblast recruitment and induce osteogenic differentiation to achieve bone formation (Sims and Martin, 2014). The osseointegration rate determines the bone remodeling and the sealing speed of the interface between bone and implant. A primary strategy is to construct a functional coating with osteoconduction or osteoinduction to promote osseointegration. In this section, three main categories of coatings for promoting osseointegration are introduced (**Figure 1**; **Table 1**).

### Surface Morphology Coatings

Osseointegration rate of orthopedic/dental implants may be attributed to their biochemical property and surface roughness, among which constructing a rough surface on Ti implant that does favor to bone anchoring and provides primary stability is a relatively mature strategy. In clinical trials, the roughened surface could increase the amount of translocated bone particles and provide greater contact area, both leading to outstanding osteogenic responses (Bencharit et al., 2014; Lou et al., 2015). Roughened surfaces were fabricated by various methods. In this section, we classify rough coatings into three categories from the different surface morphologies: porous, various nanostructures, and biomimetic coatings.

#### Porous Coatings

Porous coatings are one of the most common modifications of titanium surface morphology with a facilitative effect on osseointegration. Novel methods of preparing porous coatings include MAO, dealloying, and 3D printing. MAO can form closely bound porous structures on the titanium surface to promote osteoblast adhesion and proliferation (Zhao et al., 2020a). It was originally used for constructing in-grow oxidation ceramic layers on nonferrous metals (Van et al., 1977). By means of the approved mechanical and anticorrosion properties (Vovna et al., 1998; Gnedenkov et al., 2000), MAO was considered an outstanding method for implant modification to improve their bioactivity (Zhou et al., 2014). However, the sub-microscale pores on the MAO coating limits

**TABLE 1 |** Recent development of osteogenic coatings on titanium implants

| Category | Main methods or substances | Species of cell | Osseointegration function | References |
|---|---|---|---|---|
| Surface morphology coatings | Microarc oxidation (MAO) | MC3T3-E1 pre-osteoblasts | ↑Adhesion, proliferation, differentiation, and mineralization | Zhao et al. (2020a) |
| | Dealloying | EA.hy926 | ↑Early osseointegration *in vivo* | Bai et al. (2017), Bai et al. (2018a), Bai et al. (2018b) |
| | 3D printing | RAW 264.7 | ↑Biological activity of Ti implants | Wang et al. (2021a) |
| | Selective laser melting | BMSCs | ↓Inflammatory response of macrophages | Ma et al. (2018) |
| | Porous/nanoporous | Human 1.19 fetal osteoblast-like (hFOB) | ↑Osteoimmunomodulation to facilitate osteo/angiogenesis | Yu et al. (2020a), MacBarb et al. (2017) |
| | | | ↑Angiogenesis, osteogenesis, and osteointegration | Song et al. (2019) |
| | Electrochemical anodizationNanotubes | MC3T3-E1 | ↑Proliferation of the osteoblast cells | Yao et al. (2020) |
| | | HMSCs | ↑Cell differentiation | Hu et al. (2020) |
| | | BMSCsMice bone marrow-derived macrophages (BMDMs) | Nanotubes with different nanostructure of 80–100 nm were more likely to induce macrophages to the M1 phenotype, while nanotubes with smaller diameters of 30 nm were prone to induce macrophages to the M2 phenotype | Wang et al. (2018b) |
| | Alkali treatment nanonetwork structures (TNS) | rBMMSCs MG63 cell | ↑Early cell adhesion and proliferation | Zeng et al. (2019) |
| | | | ↑Osteogenesis and osseointegration | Yin et al. (2019) |
| | | | ↑Osteogenic gene expression and mineralization | Huang et al. (2019b) |
| | | | ↑Osteoprotegerin secretion | |
| | Vacuum diffusion bonding of titanium meshes | rBMMSCs | ↑Cell adhesion, proliferation, and differentiation | Chang et al. (2016) |
| | Porous scaffolds with a variety of pore size and porosity | | | |
| | Template-assisted plasma spraying technique | BMSCs RAW 264.7 | ↑Polarization of macrophage to anti-inflammatory type M2 | Zhang et al. (2018c) |
| | Patterned surface | | ↑Mineralization | |
| | | | ↑Osteogenesis | |
| | | | ↑Osteoimmunomodulatory properties | |
| | Microsecond laser direct writing and femtosecond laser-induced methods | MC3T3-E1 | ↑Cell adherence, alignment, and proliferation | Li et al. (2020a) |
| | Micro-hexagons and nano-ripples | | ↑Osteointegration | |
| | Acid etching and anodization | BMSCs | Nanotubes with different nanostructure of 80–100 nm were more likely to induce macrophages to the M1 phenotype, while nanotubes with smaller diameters of 30 nm were prone to induce macrophages to the M2 phenotype | Wang et al. (2018b) |
| | Nanotubes with different nanostructure | Mice bone marrow-derived macrophages (BMDMs) | | |
| Inactive coatings | Mg/Ag/HA | Primary human osteoblasts | ↑Adhesion, proliferation, and differentiation | Huang et al. (2018b) |
| | | Human osteoblastic SaOS-2 cells | ↑Osteogenic | Yao et al. (2021) |
| | | Murine C3H10T1/2 cells | | Ke et al. (2019) |
| | MPs-Sr | MC3T3-E1 | ↑Attachment and spreading of preosteoblast MC3T3-E1 cells | Zhang et al., 2018a |
| | | | ↑Collagen secretion and matrix mineralization levels of cells | |
| | | | ↑Osteogenic properties | |
| | Cu | RAW 264.7 Human osteoblastic SaOS-2 cells | ↑Polarize to M1 phenotype | Huang et al. (2018a) |
| | | | ↑Pro-inflammatory cytokines | |
| | | | ↑Macrophage-mediated osteogenesis | |
| | Reduced graphene oxide | hMSCs | ↑Proliferation and osteogenic differentiation of hMSCs | Jin et al. (2015), Kang et al. (2021) |
| | | | ↑Cell adhesion and protein adsorption | |
| | | | ↑Matrix mineralization | |
| | Glutamic acid/dopamine methacrylamide | MC3T3-E1 | ↑Calcium phosphate (CaP) formation with a Ca/P ratio close to that of natural hydroxyapatite | Long et al. (2020) |
| | | | ↑Mineral deposition | |
| | | | ↑Adhesion and proliferation of osteoblasts | |
| Bioactive coatings | BMSCs/BMP-2 | rBMSCs | ↑Biocompatibility and osteogenic differentiation ability | Bai et al. (2020) |
| | | | ↑Osseointegration efficacy | |
| | Physisorption of fibronectin | MG63 cell | ↑Osteoblast compatibility | Chen et al. (2020a) |
| | ADSC-EV | | ↑Osteoinductive activity | |
| | CaP-BMP2 | | ↑Osteogenesis and angiogenesis | Teng et al. (2019) |

(Continued on following page)

**TABLE 1 |** (*Continued*) Recent development of osteogenic coatings on titanium implants

| Category | Main methods or substances | Species of cell | Osseointegration function | References |
|---|---|---|---|---|
| | | Murine bone marrow mesenchymal stem cell line D1 | ↑Bone formation | |
| | BMP-9 | MC3T3-E1 | ↑Osteoblast proliferation and differentiation | Souza et al. (2018) |
| | | BMSCs | ↑Osseointegration | Zhu et al. (2021) |
| | Nerve growth factor (NGF) | — | ↑Osseointegration<br>↑Nerve regeneration of peri-implant tissues | Lee et al. (2015)<br>Ye et al. (2021) |
| | GO/IL-4 | BMSCs<br>RAW 264.7 | ↑Biocompatibility<br>↑Macrophages polarization to the M2 phenotype *in vitro*<br>↑Proliferation, migration, and osteogenic differentiation of BMSCs | Li et al. (2020b) |
| | OGP-NAC | RAW 264.7 | ↓Important transcription factors for osteoclastogenesis<br>↑Osteoblast proliferation and differentiation | Liu et al. (2019) |

the in-growth of mature bone tissue (Liu et al., 2011). Some researchers proposed a hybrid treatment of MAO followed with hydrothermal synthesis to form a uniform apatite crystal layer on titanium surface, which promoted the interlocking between implant and bone (Huang et al., 2004). After that, Zhou et al. fabricated double-level porous coatings on Ti plates by three-step MAO (Zhou et al., 2015). Compared with the MAO coating treated with post-heat treatment, this strategy possessed better osseointegration and mineralization ability owing to the OH functional group, which promotes the synostosis between new bone and the implant (Bai et al., 2017). Furthermore, grafting metal ions and compounds is also a common method to improve the osteogenic ability of MAO coating. Some researchers used MAO to prepare manganesetitanium dioxide (Mn-$TiO_2$) microporous coatings on titanium surface, which showed good biocompatibility and osteogenic property (Zhao et al., 2020a). Meanwhile, the $Mn^{2+}$ release from the coating promotes surface mineralization, which would also favor osteogenesis. Bai et al. prepared a microporous $TiO_2$ coating with MAO and modified with hydroxyapatite (HA) nanoparticles (Bai et al., 2018a). The microarc oxidation coating annealed at 650°C (MAO-650) had excellent physical and chemical properties. The resultant porous coating significantly promoted the proliferation and differentiation of osteoblasts and additionally inhibited the inflammatory reaction, realizing the dual function of immune regulation and bone formation. However, producing the homogeneous and crack-free coatings by MAO is still challenging (Yu et al., 2020b). Dealloying creates porous structures on alloy through a selective corrosion, preferentially dissolving the active alloying elements to form mono or hierarchical porous structures (Song et al., 2018). Wang et al. formed nanoporous structures on Ti-3Zr-2Sn-3Mo-25Nb (TLM) Ti alloy surfaces via dealloying (Wang et al., 2021a). Compared with hierarchical micro/nanoporous surface, mono structure has a higher hydrophilic and protein adsorption capacity, which is more conducive to the early adhesion of osteoblasts.

3D printing is the construction of a three-dimensional object from a digital 3D model, which can accurately control the surface morphology and integrate calcium phosphate, cytokines, and other osteogenic substances on the implant surface. Ma et al. prepared porous titanium alloy scaffolds customized to bone defects by 3D printing (Ma et al., 2018). The HA nanocrystals and collagen fibers induced by the 3D printed porous structure significantly promoted vascularized bone tissue formation in rabbit radius defect models, and the new bone formed a stable combination with the implant. However, in the process of 3D printing, the unmelted or partially melted particles will inevitably attach to the titanium surface to form rigid residues, which can cause chronic inflammation and osteolysis (Zhao et al., 2016). Therefore, removing residual powders on the substrate of 3D printing needs to obtain better biocompatibility. For example, Yu et al. fabricated micro/nanostructures on the surface of 3D-printed Ti-6Al-4V via acid etching and hydrothermal treatment, which played a positive role on promoting the cell proliferation and adhesion (Yu et al., 2020a). In addition, some researchers used a porous titanium scaffold printed by selective laser melting (SLM), which is similar to 3D printing, to modulate the surface topology of the scaffold and then improve the osseointegration (Song et al., 2019).

## Coatings of Various Nanostructures

Coatings with different nanostructures, including nanoparticles, nanorods, and nanotubes, were prepared on the titanium surface by techniques such as alkali heat treatment and electrochemical anodization (EA), improving the surface roughness and promoting osseointegration. Some researchers found that the $TiO_2$ nanotubes (TNTs) could increase the adsorption of major proteins involved in osteoblast adhesion, thus enhancing osteogenesis (Grimes and Mor, 2009). Due to the larger surface area, TNTs were used in various osteogenic materials. EA is a surface modification approach that applied

an external voltage to the metal plate in the electrolyte to grow a specific structure orderly. Yao et al. fabricated anodic oxide nanotubes and deposited calcium phosphate (CaP) on the surface of Ti and Ti-6Al-4V (Yao et al., 2020). The cell experiment showed that the nanotubes with a higher HA content were suitable for cell adhesion. It should be noted that the fluoride ions and internal stress would cause weak adhesion between TNTs and Ti substrates (Zhang et al., 2015; Cao et al., 2018). Hu et al. performed grain refinement in Ti substrate by high-pressure torsion processing, improving the adhesion between nanotubes and Ti. This strategy also increased the elastic modulus of TNTs and further improved osseointegration (Hu et al., 2020). Moreover, TNTs have also been used as carrier for drug release in recent years because of their simple preparation, controllable size, and high loading capacity (Wang et al., 2017a).

The alkali treatment can produce a homogeneous nanonetwork structure (TNS) on the titanium surface. The study by Zeng et al. showed that this nanostructure enhanced the wettability of Ti to blood and binding to fibrin, which facilitated cell attachment and tissue healing (Zeng et al., 2019). The significant increase in the amount of new bone around the implant also exhibited a greater ability to promote osseointegration. To further improve the adhesion of the surface, Yin et al. coated mussel adhesive protein (MAP) on the TNS, resulting in promotion of new bone growth (Yin et al., 2019). This novel structure has great potential for clinical applications in the dental and orthopedic fields.

Some researchers compared the biological characteristics of different nanostructure coatings. By controlling the duration of the steam-hydrothermal treatment, the researchers prepared HA nanoparticles and nanorods in different sizes on the surface of the MAO micropores of titanium (Bai et al., 2018b). By contrast, the nanoparticles were more conducive to osteogenesis due to the closer resemblance to the structure of natural bone and their larger specific surface area. Huang et al. prepared nanowire-like and nanometal-like topography on the titanium surface using different concentrations of NaOH, both of which showed good biocompatibility compared with untreated titanium, with Ti-5 showing the best osteogenic differentiation ability (Huang et al., 2019b).

## Other Morphology Coatings

Recently, some researchers have found that surfaces with well-defined patterns exhibit higher levels of cell adhesion, proliferation, and differentiation (Chang et al., 2016). Zhang et al. fabricated patterned titanium coatings using a template-assisted plasma spraying technique (Zhang et al., 2018d). The surface was more conducive to the polarization of macrophage to anti-inflammatory type M2 and induced osteoblasts to exhibit more mineralization nodules. Inspired by the skin structures of the tree frog toe pads and the adhesion of the corrugated ridges on the scales of Morpho butterfly wings, Li et al. generated micro-hexagons and nano-ripples on titanium surface by microsecond laser (Li et al., 2020a). This structure provided microscale space for cell behaviors, enhancing mechanical interlocking at the boneimplant interface. Similarly, some researchers have designed biomimetic coatings inspired by bone structure. MacBarb et al. compared the response of osteoblasts on the 3D-printed trabecular-like titanium implant surface, the titanium plasma spray-coated surface with and without nanocrystalline HA coating (MacBarb et al., 2017). The results showed that 3D-printed trabecular-like surface could promote the earlier proliferation of osteoblasts and higher calcium production than other surfaces, holding promise for improving the osseointegration of orthopedic implants.

## Unnatural Material Coatings

Since the composition of HA is similar to bone, it is widely used in bone tissue engineering (LeGeros, 2002). However, due to the mismatch in coefficients of thermal expansion between metal and HA (Sun et al., 2001), there are potential concerns about the low strength of the bond between implant and coating. Ke et al. prepared gradient HA coatings on a titanium surface by Laser Engineered Net Shaping (LENS) and plasma spray deposition technology (Ke et al., 2019). The gradient coating solved the problem of weak interfacial bond, prevented the diffusion of metal ions effectively, and improved the surface osteoconductivity. Besides HA, various metal ions ($Ca^{2+}$, $Sr^{2+}$, $Mg^{2+}$) have been demonstrated to possess the property to promote osseointegration (Xu et al., 2020). One example of these coatings is a biomimetic mesoporous coating doped with strontium (MPs-Sr), proposed by Zhang et al. (2018a). The mesoporous structure and the doped Sr significantly upregulated the attachment and spreading of preosteoblasts, indicating their ability to promote osseointegration and new bone formation. Huang et al. doped Mg elements with osteogenic ability into micro/nanoporous coatings by MAO and hydrothermal treatment to form MgO nanorods, which were later heat treated to convert the nanorods into nanoparticles, further improving the biological properties of the coatings (Huang et al., 2018b). Others reported the nanostructured $Mg(OH)_2$ films on Ti surface fabricated by hydrothermal treatment (Yao et al., 2021). The animal experimental results and genome expression analysis indicated that the coating with Mg ion release could activate BMP-4-related signaling pathways, thus promoting bone formation and regeneration. At the same time, the alkaline environment has also been shown to favor the deposition of HA, leading to further osteogenesis, which has been proved by various studies (Chen et al., 2020b; Zhao et al., 2020b). Furthermore, researchers prepared the Cu-containing surface to induce macrophages to polarize to M1 phenotype, which could release appropriate pro-inflammatory cytokines to form an inflammatory microenvironment, thereby promoting osteogenic differentiation of MSCs (Huang et al., 2018a).

Besides, non-metallic substances have also been explored for promoting osseointegration. Graphene is a novel nanomaterial with excellent mechanical properties. It is increasingly used in the biomedical field owning to their excellent electronic, optical, mechanical, and chemical properties. Moreover, graphene derivatives such as reduced graphene oxide (rGO) can enhance protein adsorption and cellcell interactions, and have extraordinary osteoinductive ability (Jin et al., 2015). Kang et al.

used meniscus-dragging deposition technology to coat rGO on the titanium surface to fabricate an rGO-Ti substrate (Kang et al., 2021). *In vitro* experimental results showed that the coating enhanced cell proliferation and significantly promoted matrix mineralization. Inspired by the physiological function of bone sialoprotein during osteogenesis, Long et al. synthesized a polymer from glutamic acid and dopamine methacrylamide via reversible addition-fragmentation chain transfer polymerization and immobilized it on a titanium base by means of catechol pendants on the polymer chain (Long et al., 2020). The coating could induce calcium phosphate (CaP) formation with a Ca/P ratio close to that of natural hydroxyapatite, thus effectively promoting mineral deposition. In addition, the coating could promote the adhesion and proliferation of osteoblasts.

## Natural Material Coatings

Cellular active substances such as extracellular matrix proteins, growth factors, and chemokines are hotspots of research for osseointegration, and their application on the surface of orthopedic prostheses can effectively improve the biocompatibility of the surface and promote osseointegration. These bioactive coatings could be classified into two parts: 1) directly loaded with osteogenic factors; 2) loaded with immunomodulatory factors. In this part, we will introduce the new progress of bioactive coating in recent years and discuss their application in detail.

### Coatings Loaded with Osteogenic Factors

Stem cell encapsulation and extracellular vesicle loading that endow surfaces with bioactive property for rapid osteogenesis are two main strategies in constructing bioactive surfaces. Mesenchymal stem cells (MSCs) have been widely used in research and clinic because of their self-renewal potential and multilineage differentiation (Mushahary et al., 2018). Bone marrow is the prevailing source of MSCs and bone marrow mesenchymal stem cells (BMSCs) have a potential to differentiate into osteoblasts (Pittenger et al., 1999). Bai et al. encapsulated BMSCs, bone morphogenetic protein-2 (BMP2), and other bioactive substances in hydrogels and formed a three-dimensional inorganicorganic supramolecular bioactive interface on a porous titanium alloy scaffold (Bai et al., 2020). Osteogenic differentiation of BMSCs was induced by the continuous release of BMP2. With the degradation of the hydrogel, bone tissue grew into the pores of the scaffold to achieve good bone integration. However, since the harvesting procedure with general anesthesia limits the supply of BMSCs (Li et al., 2016), adipose tissue stem cells (ADSCs), another candidate for bone engineering that is easy be obtained, are attracting more attention (Kolaparthy et al., 2015). The main way to exert the benefit of MSC is to secrete extracellular vesicles (EVs) to promote tissue repair and regeneration (Vizoso et al., 2017; Mushahary et al., 2018). On one hand, MSC-EVs can carry and transfer various cargo such as regulatory miRNAs, growth factors, and cytokines. On the other hand, the membrane of EVs contains bioactive signaling molecules to obtain protection (Malda et al., 2016; Tsiapalis and O'Driscoll, 2020). Based on physisorption of fibronectin, Chen et al. immobilized adipose-derived stem cell-derived extracellular vesicles (ADSC-EVs) onto the titanium surface, which enhanced osteoblast compatibility and osteoinduction activity (Chen et al., 2020a).

Osteogenesis-related molecular loading is another strategy for constructing bioactive surface. Growth factors and cytokines could promote osteogenesis by upregulating the level of osteogenic differentiation-related genes or activating osteogenic-related signal pathways. Bone morphogenetic proteins (BMPs) are the widely used cytokines to confer osteoinductivity (Carson and Bostrom, 2007). However, a burst release will decrease the osteogenic effect (Haidar et al., 2009a; Haidar et al., 2009b). Teng et al. prepared a porous structure on the titanium surface by 3D printing and MAO to endow the coating with osteogenic property, calcium, phosphate, and BMP-2 that was grafted onto the surface (Teng et al., 2019). The results showed that the continuous BMP-2 release sustained for more than 35 days, and enhanced the osseointegration between the implant and surrounding bones. Compared with BMP-2, BMP-9 has higher osteoinductive differentiation ability (Kang et al., 2004; Souza et al., 2018). Zhu et al. implanted thermosensitive collagen and BMP-9 into porous titanium, which could release BMP-9 via temperature-controlled sustained release (Zhu et al., 2021). The thermosensitive collagen degraded slowly at 37°C and the released BMP-9 significantly promoted osteogenesis around the implant. Besides, sympathetic nerves are also widely distributed in bone tissue and can regulate bone formation. Nerve growth factor (NGF) has been shown to enhance the activity of osteoblasts and promote and mineralization after implantation (Lee et al., 2015). The NGFchondroitin sulfate/hydroxyapatite coating (NGF-CS/HA-coating) prepared by modified biomimetic method was placed in the mandible of beagles (Ye et al., 2021). The results showed that the coating significantly upregulated the level of osteogenesis differentiation-related genes in the mandible, promoting the differentiation of osteoblasts and nerve cells in the early bone binding and the bone healing around the implant.

### Coatings Loaded with Immunomodulatory Factors

As a foreign body, the implant inevitably leads to a series of immune responses, which mainly arise from the macrophage activation that would reduce the service life of implants. In addition, as mentioned previously, the wear particles produced in the gap of implant and bones can also aggravate inflammatory reaction, and cause a dynamic imbalance between osteoblasts and osteoclasts, which eventually lead to bone resorption and implant loosening (Zhou et al., 2021). Therefore, tuning immunoreaction to keep an appropriate immune environment is beneficial to improve osseointegration and reduce loosening. There are many ways to regulate immune microenvironment. Previous studies have shown that different nanostructured Ti can induce different macrophage responses, which can affect the osseointegration (Wang et al., 2018b). Alternatively, some coatings loaded with immune factors can also regulate the immune response, such as interleukin 4 (IL-4) (Li et al., 2020b) and complement activating immunoglobulin (Harmankaya et al., 2012). Li et al. sprayed

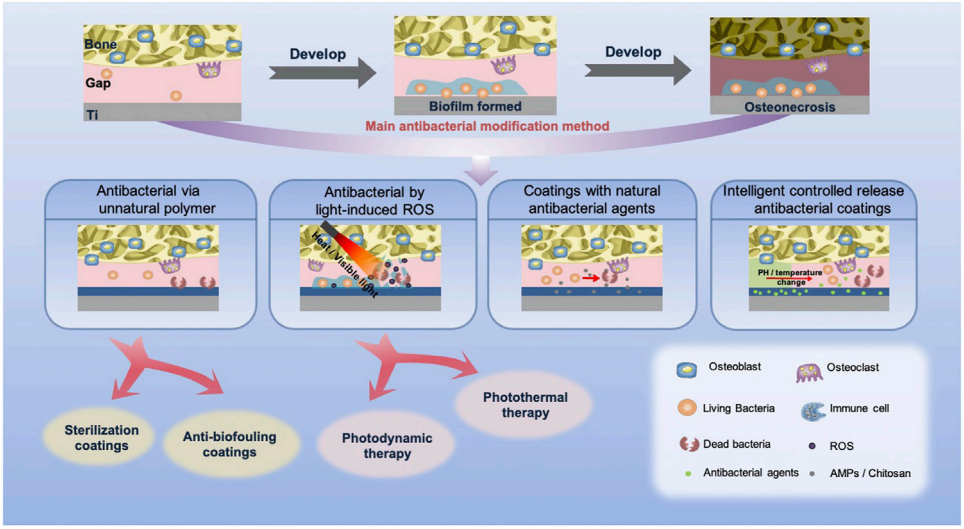


**FIGURE 2 |** Types and effects of antibacterial coatings of titanium implants. After implantation, biofilm may be formed, leading to osteonecrosis in general. At present, to avoid infection, the coatings with inactive polymers, light-induced ROS and bioactive antibacterial agents, and the intelligent controlled release antibacterial coatings are the main antibacterial methods.

graphene oxide (GO) on Ti and loaded IL-4 to construct a GO/IL-4 coating for regulating macrophage-related inflammation (Li et al., 2020b). In the process of acute inflammation, type 1 macrophages (M1) can produce fibers to protect the host, while type 2 macrophages (M2) can inhibit the development of inflammation and promote the growth of osteogenic factors (Franz et al., 2011). The release of IL-4 from GO/IL-4 coating induced the macrophage polarization to the M2 phenotype, weakened the inflammatory response, and promoted osteogenesis. Another method for immune regulation is to regulate the balance between osteoblasts and osteoclasts. Liu et al. conjugated an osteogenic growth peptide (OGP) with N-acetylcysteine (NAC) to synthesize a multifunctional peptide OGP-NAC and then employed OGP-NAC to titanium (Liu et al., 2019). Such an OGP-NAC coating could inhibit the important transcription factors for osteoclastogenesis, such as MAPK, NF-κB, and NFAT c1, and promote osteoblast proliferation and differentiation.

## Prevention of Implant Infection

Infections within 3 months are considered as early postoperative infection, while delayed (or subacute) infection occurs after 3–24 months and late infection more than 24 months later (Montanaro et al., 2011; Zimmerli, 2014). Early infection is usually caused by pathogens such as *Staphylococcus aureus* at the surgical site (Trampuz and Widmer, 2006). After operation, patients need systemic antibiotic treatment to prevent infections, but the rising antibiotic resistance of bacteria can make the existing antibiotics noneffective (Park et al., 2019). Also, the concentration of antibiotics in the focus site is insufficient, resulting in the rapid proliferation and secretion of extracellular polymers to form a biofilm after some pathogens gather and adhere to the implant surface (Gristina and Costerton, 1985). Exopolysaccharides of the biofilm can hinder and delay the penetration of antibiotics, and the quorum sensing of bacteria in the biofilm regulates the development of the biofilm to resist the host immune defense, thus making the biofilm a barrier to antibiotics (Kaestner, 2016). Therefore, the ideal antibacterial coating is supposed to remove or kill the pathogens once the primary contact occurs, thus preventing the formation of the biofilm. Orthopedic implants would maintain for a long time in the organism, so late infections would happen if no defensive measures were taken (Del Pozo and Patel, 2009). At this stage, the biofilm formed, resulting in poor antibiotic treatment (van de Belt et al., 2001), so it is necessary for the implant surface to provide long-term antibacterial properties.

The key to preventing infection is to inhibit the adhesion of microorganisms, but long-term infection can still be a risk to the implant because of continuous pathogens. Therefore, the anti-infective implants should target early infection and long-lasting antibacterial agents. This section introduces preventive and treatment strategies of infections (**Figure 2**; **Table 2**).

## Antibacterial *via* Unnatural Polymers

Some metal ions and polymers are widely used as antimicrobial agents coating the implants. In this section, we divide these unnatural antimicrobial agents, such as metal ions, non-metallic ions, and other synthetic polymers, into sterilization coatings and anti-biofouling coatings to describe them in detail.

## Sterilization Coating

### *Antibacterial Metal Ions*

Clinically, antibiotics have been widely used in the treatment of implant infection, but its clinical effect is limited due to the drug resistance of bacteria and the narrow antibacterial spectrum of single antibiotics. Therefore, metal ions with broad-spectrum

**TABLE 2 |** Recent development of antibacterial coatings on titanium implants

| Categories | Main anti-infection agent | Mentioned synthesis method | Included bacteria species | Antibacterial effects | References |
|---|---|---|---|---|---|
| Metal ions | AgNPs | Physical vapor deposition (PVD) | *S. aureus*, *S. mutans*, *S. epidermidis*, *E. coli*, *P. aeruginosa* | ↑Antibacterial effect | Lampé et al. (2019) |
| | | Electron cyclotron resonance (ECR) | | | Chen et al. (2016) |
| | | *In situ* dopamine reduction | | | Guo et al. (2020) |
| | | Layer-by-layer assembly | | | Wang et al. (2021b) |
| | | Electrodeposition | | | Ren et al. (2021) |
| | | Thermochemical treatment | | | Rodríguez-Contreras et al. (2021) |
| | Zn | MAO | *S. aureus* | ↑Antibacterial effect | Ye et al. (2020) |
| | | Electrodeposition | *E. coli* | | Shahmohammadi and Khazaei (2021) |
| | | Hydrothermal method | *P. gingivalis* | | Chen et al. (2021b) |
| | Cu | — | MRSA | ↓Biofilm formation, virulence<br>↓Antibiotic resistance of MRSA | Zhuang et al. (2021) |
| | Ga | Hydrothermal method | *S. aureus*<br>*E. coli* | Strong antibacterial ability | Li et al. (2021b) |
| | AgNPs<br>$Zn^{2+}$ | Laser cladding | *S. aureus*<br>*E. coli* | Long-term synergistic antibacterial activity of $Zn^{2+}$ and $Ag^{+}$ | Zhang et al. (2018b) |
| | AgNPs<br>CuNPs | Plasma electrolytic oxidation | MRSA | Synergistic antibacterial activity of Ag and Cu | van Hengel et al. (2020b) |
| Non-metallic antibacterial substances | Iodine | Anodization | *S. aureus*<br>*E. coli* | ↓Bacterial colonization | Shirai et al. (2011) |
| | Chlorhexidine | Organosilane chemistry | *S. aureus* | ↓Bacteria adhesion and growth | Wang et al. (2019) |
| Anti-fouling coatings | PEG | Simultaneous deposition; electrodeposition | *S. aureus*<br>*E. coli*<br>*S. sanguinis* | ↓Protein absorption<br>↓Bacterial and platelet adhesion<br>↓Biofilm formation | Guo et al. (2021)<br>Hoyos-Nogués et al. (2018) |
| | Zwitterionic copolymer | Free radical polymerization<br>RAFT polymerization | *E. coli* | ↓Protein adsorption, platelet adhesion<br>↓Bacteria adhesion | Huang et al. (2017) |
| Light-induced ROS | Photodynamic-induced ROS | Plasma electrolytic oxidation | *S. sanguinis*, *A. naeslundii* | ↑Antibacterial effect in light conditions | Nagay et al. (2019) |
| | | | | ↑Degradation efficiency of lipopolysaccharide | Wu et al. (2019) |
| | Photothermal-induced ROS | π-π stacking | *S. aureus*, MRSA | ↑Bacteria killing | Yuan et al. (2019) |
| | | Hydrothermal method<br>EDC-NHS chemistry | | ↓Biofilm formation | (Song et al., 2020) |
| | | Sulfur doping | | | Su et al. (2020) |
| Bioactive antibacterial agent | AMP | Organosilane chemistry, click chemistry | *S. gordonii*, *S. aureus* | ↑Antibiofilm activity | Acosta et al. (2020) |
| | | Layer-by-layer assembly | | | Rodríguez López et al. (2019) |
| Intelligent controlled release antibacterial coating | Gentamicin | — | *S. aureus*<br>*E. coli* | ↓Bacteria growth and adhesion<br>↑Bacteria killing in a slightly acidic environment | Sang et al. (2021) |
| | Glycerin | Anodization | *S. aureus*<br>*E. coli* | ↑Immunoregulatory antibacterial activities at 40°C | Li et al. (2021a) |

antimicrobial effects that do not lead to severe resistance are deemed potential antibiotic substitutes for implant surface modification, such as $Ag^{+}$, $Cu^{2+}$, and $Zn^{2+}$ (Sundfeldt et al., 2006). Chen et al. integrated silver nanoparticles on the surface of titanium by *in situ* reduction of dopamine (Chen et al., 2016). The results showed that the surface had excellent antibacterial activity, but Ag also showed strong cytotoxicity. To reduce the cytotoxicity, Guo et al. prepared a poly-L-lysine (PLL)/sodium alginated (SA)/PLL self-assembled coating on the surface of Ti, then loaded nano-silver and induced mineralization in simulated body fluid (Guo et al., 2020). The antibacterial results showed the coating effectively inhibited the adhesion of bacteria. At the same time, PLL/SA/PLL coating can greatly improve the cytocompatibility and reduce the cytotoxicity. Another potential idea is to decrease the cell cytotoxicity *via* adjusting the concentration of antimicrobial agents. Wang et al. systematically determined the osteogenesis of dopamine silver-loaded coatings prepared at different pH (4, 7, 10) and different $Ag^{+}$ concentrations (0.01, 0.1 mg/ml) (Wang et al., 2021b). The results showed that the pH 10/0.1 group had obvious osteogenesis

in bacterial environment, which may be due to its strong antibacterial properties to kill the surrounding bacteria and then promote mineralization to achieve good osseointegration. Also, other researches incorporated zinc-doped coating on titanium surface (Ye et al., 2020). The amorphous coating with ZnO bond acts as the $Zn^{2+}$ donor and generator of reactive oxygen species (ROS), which could trigger the *S. aureus* killing. In addition, although $Zn^{2+}$ and ROS can cause osteoblast damage, the surface did not show noteworthy cytotoxicity.

Since the antibacterial and cytotoxicity of $Ag^{+}$ are both dose dependent, many researches focus on doping adjuvant antibacterial substance. Zhang et al. deposited HA nano-powder mixed with Ag and ZnO on a titanium surface by laser cladding (Zhang et al., 2018c). The combined release of $Ag^{+}$ and $Zn^{2+}$ for more than 5 weeks showed a long-term effective antibacterial activity. Moreover, with the assistance of $Zn^{+}$, the antibacterial efficiency was significantly increased and cytotoxicity of the $Ag^{+}$ contained coating was reduced. To reduce the negative performance of $Ag^{+}$, Xie et al. prepared a hybrid coating containing chitosan (CS), dopamine (PDA), HA, and nano-silver. The double chelation of PDA and CS achieved long-term release of silver and a continuous bacteriostatic effect. It is worth noting that this coating exhibits significantly osteogenic potential in both *in vitro* and *in vivo* tests (Xie et al., 2019). However, the antibacterial substances released by this kind of coating gradually decrease over time, and with the adhesion of proteins and host cells, the antibacterial property will decrease. Therefore, the long-term and stable antibacterial effect is still a challenge in the development of antimicrobial coatings.

### *Non-Metallic Antibacterial Substances*

In addition to antimicrobial metal ions, some non-metallic compounds and biomolecules are also prominent candidates for fabricating antibacterial coatings, among which iodine is found to have a wide antibacterial spectrum and do not develop drug resistance (Tsuchiya et al., 2012). Shirai et al. described the novel use of povidone-iodine as the electrolyte to form the iodine coating on the Ti surface (Shirai et al., 2011). After implanting into the femora of rabbits, the implants significantly inhibited the formation of biofilm. Meanwhile, since iodine is an important component of the thyroid hormone, the coating has important biological safety. Since then, Kabata et al. treated 28 patients with iodine-supported implants (Kabata et al., 2015). None of the patients showed infection after 1-year follow-up, indicating that the coating could effectively prevent postoperative infections. Others used the same method to prepare iodine coatings and investigated temporal changes in iodine for implants using animal models for 1 year (Kato and Shirai, 2016). The results showed that the implants retained 30% of the iodine content after 1 year, which proved to have sufficient antibacterial properties. Similarly, chlorhexidine is a commonly used clinical antibacterial agent (Kim et al., 2019), which can be adsorbed on the surface of bacteria to destroy membrane permeability, thus sterilizing. Wang et al. covalently grafted chlorhexidine onto porous titanium through the coupling ability of aminosilane and glutaraldehyde (Wang et al., 2019). The results showed that chlorhexidine could inhibit the adhesion and proliferation of bacteria. What is more, in the cell-bacterial competition environment, this surface is of great help to osteoblast adhesion.

### *Anti-Biofouling Coatings*

The anti-biofouling coatings can change the hydrophilicity of the surface, thus repelling the adhesion of bacteria and proteins. Polyethylene glycol (PEG) is the most common anti-biofouling material that is highly hydrophilic, which can constitute a wide exclusion volume that repels bacterial contamination (Tanaka et al., 2010). Guo et al. deposited both polyphenol tannic acid and PEG on the titanium surface, providing good inhibition of non-specific adsorption of proteins, adhesion of bacteria and platelets, and prevented biofilm formation (Guo et al., 2021). However, since its rejection is non-specific, the coating repels contamination while also inhibiting cell adhesion (Tanaka et al., 2010). The researchers introduced RGD sequence and antimicrobial peptides onto the PEG layer to obtain both cell adhesion and antimicrobial properties (Hoyos-Nogués et al., 2018).

It should be noted that PEG is easily oxidized in biological environment due to its poor stability (Guo et al., 2021). Zwitterionic copolymer is a hydration layer that can form a close bond on the surface of the material, and it is an ideal substitute for PEG (Xie et al., 2012). Huang et al. prepared a phosphonatezwitterionic block copolymer from sulfobetaine methacrylate and phosphonate/phosphonic methyl methacrylate, and immobilized it on titanium sheets (Huang et al., 2017). The results showed that this copolymer effectively inhibited protein adsorption, platelet adhesion, and bacterial adhesion, significantly improving the anti-biofouling ability of the titanium base. In addition, Salvagni et al. applied elastin-like recombinamer to modify the titanium base (Salvagni et al., 2014). The coating was capable of reducing serum-protein adsorption and was biologically active compared with the untreated titanium base, laying the groundwork for future medical applications. However, non-specific anti-biofouling still needs to be addressed.

## Antibacterial by Light-Induced ROS

Reactive oxygen species (ROS) can destroy the polysaccharides, which is the main component of the external surface of biofilm, thus representing bactericidal effect to drug-resistant bacteria (Konopka and Goslinski, 2007). Photosensitizers such as $TiO_2$ and ICG can produce ROS when exposed to light. This section introduces the new progress in antimicrobial activity through light-induced ROS.

### Photodynamic Therapy

Photodynamic therapy can destroy the biofilm by creating free radicals and then disrupting the biofilm (Konopka and Goslinski, 2007). Sharab et al. combined this therapy with physical methods and applied it to the combating with biofilm of *Streptococcus mutans*, showing that photodynamic therapy can weaken biofilms of different maturity levels (Sharab et al., 2020). Titanium dioxide ($TiO_2$) is a stable photocatalyst, which can produce ROS to kill bacteria under ultraviolet (UV) irradiation (Carp, 2004), but UV is harmful to the human body. To solve this

problem, Nagay et al. prepared nitrogen and bismuth doped $TiO_2$ coatings by plasma electrolytic oxidation of titanium (PEO), which produces ROS to kill bacteria under visible light (Nagay et al., 2019). Others used PEO to prepare $TiO_2$ nano-ceramic coating on titanium surface to kill bacteria and decompose organic residues under visible light irradiation, and effectively prevent the occurrence of peri-implant inflammation (Wu et al., 2019). However, since this strategy is light dependent, they are only fit for oral implants.

### Photothermal Therapy

In recent years, photothermal therapy (PTT) based on near infrared radiation has become a hot spot in the field of nanomedicine because it is less traumatic than UV light, allows deep tissue penetration, and has high selectivity (Cheng et al., 2014). PTT can destroy bacterial integrity or biofilm structure through local warming (Hu et al., 2017; Wang et al., 2018a; Li et al., 2018; Qiao et al., 2019), but its unselective heating may adversely affect the surrounding tissue (Lei et al., 2016; Tan et al., 2018). Therefore, PTT has a higher application potential in combination with other antibacterial strategies. Zhang et al. combined indocyanine green (ICG) with mesoporous polydopamine (mPDA) to form a multi-functional coating on titanium surface, using mPDA to convert light energy into heat for microorganism killing, and the ICG can also produce ROS under light radiation to destroy the bacterial cell wall (Yuan et al., 2019). This strategy can be remotely controlled to eradicate the biofilm formed on the surface of implants *in vivo*, avoiding debridement surgery or invasive treatment, and does not cause side effect to surrounding tissue. Song et al. used dopamine and ferrocene (PDA-Fc) to modify $TiO_2$ nanorods as an antibacterial coating on titanium surface (Song et al., 2020). Local high temperature was attained by photothermal transformation of PDA, and ROS were produced by PDA-Fc redox reactions, which achieve a synergistic and more efficient bactericidal performance.

Photodynamic $TiO_2$ is not only a typical photosensitizer but also sound sensitizers, so ROS can be produced by ultrasound-triggered electron hole separation (Harada et al., 2011). Su et al. proposed a photoacoustic therapy, which produced oxygen defects on titanium implants by sulfur doping (Ti-S-$TiO_{2-x}$), to endow the implants with good sonodynamic and photothermal properties (Su et al., 2020). The killing rate of *S. aureus* was as high as 99.995% after 15 min of exposure to near-infrared light and ultrasound. In addition, the implant showed good stability, and the structure and properties did not change after soaking in water for 6 months.

## Antibacterial *via* Natural Antibacterial Agents

Antimicrobial peptides (AMPs) are the most widely studied antibacterial agents in recent years, which are natural anti-infective agents. AMPs are general constituted by two parts: one part is composed of positively charged residues like arginine and lysine, which will do favor to the initial contact; another are hydrophobic residues that may penetrate into the cell to bind intracellular molecules, thus killing the microorganism (Hancock and Sahl, 2006). Shi et al. loaded AMP, Tet213, on titanium via layer-by-layer technique, which effectively inhibited the early *S. aureus* biofilm formation (Shi et al., 2015). Furthermore, this multilayer coating could release AMP continuously for up to a month. Since the function of the AMP is closely related to their conformation, the surface grafting based on covalent bond would inevitably reduce their antibacterial efficiency (Steckbeck et al., 2014). Therefore, mild methods were developed to prepare AMP-loaded coatings without reducing their activity. The antimicrobial peptide GL13K extracted from parotid secretory protein also showed potent antimicrobial activity. To improve the stability, the researchers replaced the lysine residues in GL13K with D-amino acids, generating an all-D-amino acid version of GL13K (D-GL13K), which reduced the solubility of the peptide (Hirt and Gorr, 2013). Based on this, Acosta et al. developed an extracellular matrix system based on elastin-like recombinant (ELR), an extracellular matrixinspired polymer, to attach the D-GL13K to a titanium surface (Acosta et al., 2020). On the one hand, ELR coating could reduce the adsorption of non-specific proteins (Salvagni et al., 2014), thereby giving the surface antifouling performance. On the other hand, D-GL3K has good bactericidal activity and can reduce the adhesion of bacteria and the formation of biofilm.

Similarly, chitosan, a natural polymer, is widely used in tissue engineering due to its good biocompatibility (Ordikhani and Simchi, 2014). Chitosan is a cationic macromolecule that can bind negatively to cell membrane of bacteria that exhibit antibacterial property (Raafat and Sahl, 2009), but the antibacterial activity is too weak that limits its use on implants. To construct the appropriate antibacterial coatings, other antibacterial agents like AMPs are used to develop an antibacterial composite (Raghavendra et al., 2017; Tabesh et al., 2019). López et al. use chitosan (CH) and hyaluronic acid (HA) polyelectrolyte multilayers (PEM) loaded with β-peptide (a kind of antimicrobial peptide), prepared by layer-by-layer electrostatic assembly technology (Rodríguez López et al., 2019). By the strong chemical cross-link of CH/hyaluronic acid thin films, a prolonged β-peptide retention about 8 weeks was obtained and significant inhibition of *S. aureus* biofilm was achieved. In addition, the multilayer film retained its antibacterial activity after five attacks by five separate bacterial over 18 days. Such a strategy that can maintain a long-term antibacterial property is critical for the viability of the Ti implants.

## Intelligent Controlled Release Antibacterial Coatings

As mentioned previously, despite the potent antibacterial activities, certain cytoxicities of antimicrobial agents remain a concern. Since the cytoxicity is dose dependent, the control release that can tune local concentration of the antimicrobial agents and prolong the effect time is a significant direction. At present, the control release behavior mainly relies on pH and temperature to realize the intelligent release of antibacterial

**TABLE 3 |** Recent development of multifunctional coatings on titanium implants

| Categories | Composition of surface coating | Associated coating strategy | Osteogenesis and antibacterial function | References |
|---|---|---|---|---|
| Osteogenic antibacterial polymer coatings | DMADDM/HA | Covalent immobilization by PDA | ↑*In vivo* osteogenic differentiation and new bone formation<br>↓Adherence and growth of pathogens | Zhou et al. (2020) |
| | ALN/QPEI | Covalent immobilization by PGED brushes | ↑Osteointegration and biomechanical properties<br>↓Bacterial infection | Sun et al. (2019) |
| | NCS/AMP | MAO<br>Hydrothermal treatment<br>Covalent immobilization | ↑Osseointegration<br>↑Antimicrobial effect | Zhang et al. (2021) |
| | TNT/ZIF-67/OGP | EPD | ↑Differentiation of MSCs<br>↓Inflammatory response<br>↑Antimicrobial effect | Tao et al. (2021) |
| Roughening/porous surface loaded with antibacterial substance | Mg/Zn-MOF74 | Alkali-heat treatment<br>Thermal oxidation | Leading to alkaline microenvironment<br>↑New bone formation<br>↑*In vivo* antibacterial and anti-inflammatory properties | Shen et al. (2019) |
| | TNPC | Alkali-heat treatment<br>Coordination bonds between catechol and $TiO_2$ | ↑The formation of HA<br>↓Pathogenic bacteria and biofilm formation | Gao et al. (2020) |
| | AgNP/ZnNP | SLM<br>PEO | ↑Metabolic activity of pre-osteoblasts<br>↑Antibacterial leaching activity against MRSA | van Hengel et al. (2020a) |
| | PDA/LL-37/POPC | MAO | ↑Cytocompatibility to MSCs and osteoblasts<br>↑Antibacterial activity against *S. aureus* and *E. coli* | He et al. (2018) |
| Photoantibacterial and osteogenic coatings | Collagen/PDA/$MoS_2$-$TiO_2$ | MAO<br>Hydrothermal treatment<br>Covalent immobilization | ↑Proliferation, adhesion, and spreading of osteoblasts<br>↓*In vivo* bacterial infection and *S. aureus* biofilm | Han et al. (2021) |
| | TiO2/UCN/Qr/LA | Hydrothermal in TMAOH<br>Covalent immobilization<br>Electrostatical | ↑Angiogenesis and osseointegration<br>↑Antimicrobial effect | Zhang et al. (2022) |
| | $TiO_2$/GDY | Electrostatic force | ↑Bone tissue regeneration<br>↑Antimicrobial effect | Wang et al. (2020) |
| | RP/IR780/RGDC | Covalent immobilization by PDA | ↑*In vivo* biostability and biocompatibility<br>↑Antibiofilm property | Huang et al. (2019a) |
| Multifunctional coatings with single material | Flavonoid quercitrin | Wet chemistry | ↑Biocompatibility, cell adhesion, and osteocalcin production<br>↓Adhesion and viability of *S. epidermidis* | Llopis-Grimalt et al. (2020) |
| | *L. casei* | Culturing | ↑Osteogenic differentiation<br>↑Antimicrobial effect | Tan et al. (2020) |
| | TiBP/AMPA | Binding by titanium-binding domain | ↓Adverse host inflammatory immune response | Wisdom et al. (2020) |
| | TiBP/GL13K | | ↓Bacterial colonization and biofilm formation | |
| | HBPL | Silane coupling | Creating an alkaline microenvironment<br>↑Osseointegration<br>↑Damaging DNA of bacterial | Yang et al. (2021) |
| | FP | Cycloaddition<br>Silane coupling | ↑Vascularization and osseointegration<br>↑Antimicrobial effect | Chen et al. (2021a) |

agents (Li et al., 2021a; Sang et al., 2021). As mentioned earlier, antibiotics not only cause drug resistance of bacteria but their rapid release can also produce cytotoxicity. In this regard, some researchers prepared controlled release antibiotic coatings to selectively release drugs when the microenvironment was changed. Silk fibroin that can respond to slightly acidic environment is regarded as a new candidate for drug loading and release (Hassani Besheli et al., 2017). Sang et al. coated a layer of silk protein on the surface of Ti, and then loaded gentamicin (Sang et al., 2021) on it. Bacteriostatic ring tests *in vitro* and *in vivo* showed that the coating exhibits a stable release behavior of gentamicin, and the release rate of gentamicin in acidic environment was faster than that in alkaline environment, which achieved the

intelligent release. Another mechanism for intelligent controlled release is to use the heating effect caused by infection. Li et al. layered a thermosensitive chitosan-glycerol-hydroxypropyl methyl hydrogel (CGHH) on $TiO_2$ nanotubes (Li et al., 2021b). *In vitro* antibacterial test showed that CGHH had almost no antibacterial activity against *E. coli* and *S. aureus*. However, the results of subcutaneous infection animal models showed that under the high temperature caused by an infection *in vivo*, CGHH could release a large amount of glycerin, thus suggesting excellent antibacterial properties.

## Strategies of Both Preventing Aseptic Loosening and Infection

Promoting osseointegration along with the prevention of infections is the key factor of the orthopedic implants, but most of the current implant coatings exhibit only one of the properties. Since many antibacterial surfaces not only inhibit bacterial colonization but also do damage to mammalian cells, strategies to prepare host-friendly devices was the main direction of the orthopedic implants. In this review, several approaches that address the two properties at one surface were displayed, and we classify the coatings into four categories based on their characteristics (**Table 3**): 1) rough surface coating loaded with antibacterial substance; 2) osteogenic antibacterial polymer coatings; 3) photoantibacterial and osteogenic coatings; 4) multifunctional coatings with single material.

### Roughening/Porous Surface Loaded with Antibacterial Substance

The roughening surface facilitates the attachment of osteoblasts; therefore, the combination of antibacterial agents with porous surface is another general strategy to construct a dual-functional coating. As mentioned previously, we introduced the controlled release antibacterial coating. Some researchers doped osteogenic material into the controlled release antibacterial coating to achieve the multifunction surface. Shen et al. deposited magnesium/zinc on the surface of porous titanium and coordinated with 2,5-dihydroxyterephthalic acid (DHTA) to form a hybrid magnesium/zinc-metal organic framework (Mg/Zn-MOF74) coating (Shen et al., 2019). The dissolution of MOF74 coating was accelerated in an acidic environment. The gradual release of DHTA and $Zn^{2+}$ formed an alkaline microenvironment around the implant to kill bacteria and promote osteoblast proliferation. $Mg^{2+}$ improves osteoblast activity and anti-inflammatory gene expression. *In vivo* results showed that the coating had high antibacterial and anti-inflammatory properties at the initial stage of implantation, and greatly improved the new bone formation around the implant. Gao et al. fabricated a titanium dioxide nanospike coating on the titanium surface and immobilized cationic polypeptides on the surface by coordination (Gao et al., 2020). The results showed that this coating was able to rapidly kill pathogenic bacteria, inhibit biofilm formation for up to 2 weeks, and promote the formation of HA.

3D printing was introduced previously as a method to construct a given morphology on implant that promotes osseointegration. Embedding antibacterial ions into 3D-printed coatings is one of the methods to construct multi-functional coatings. Hengel et al. closely embedded silver and zinc nanoparticles into a 3D-printed porous titanium oxide layer. The porous structure could promote the adhesion and the released $Zn^{2+}$ and $Ag^{+}$, which would do favor to promote osteogenesis and achieve an antibacterial effect, respectively (van Hengel et al., 2020a). In addition, this synergistic mechanism apparently reduced the toxicity of Ag to host cells.

To achieve better bone-promoting properties, researchers combined other bone-promoting substances with antibacterial agents on the modified surface. Antibacterial agents that can be directly combined with these bone-promoting surfaces can be utilized to achieve multifunctional coatings. He et al. coated polydopamine, cationic antimicrobial peptide LL-37, and phospholipids on a MAO modified titanium surface, which showed good cytocompatibility to mesenchymal stem cells and osteoblasts (He et al., 2018). LL-37 killed bacteria by blocking the expression of bacterial related genes and enhancing immune response under the controlled release of phospholipids. Others hydrothermally grew ZnO nanorod arrays on titanium and modified them by autopolymerization of dopamine and covalent immobilization of RGDC peptides (Li et al., 2017). The results showed that ZnO nanorod arrays could kill bacteria by producing ROS to destroy the cell membrane, and $Zn^{2+}$ that penetrate the cell membrane could inhibit their metabolism. What is more, $Zn^{2+}$ bound with dopamine could promote cytocompatibility and minimize possible cytotoxicity *via* an antioxidant effect to scavenge ROS.

### Osteogenic Antibacterial Polymer Coatings

A direct approach to fabricate dual-functional orthopedic implants is to co-immobilize antibacterial agents and bone-promoting substances on Ti implants. The most common strategy is to load osseointegration coating and then graft antibacterial agents on the modified surface. For instance, dimethylaminododecyl methacrylate (DMADDM) is a new antibacterial agent whose amino group and long alkyl chain can destroy the bacterial membrane, thus exerting a strong inhibitory effect to bacteria and fungi, including drug-resistant strains (Wang et al., 2017b; Cheng et al., 2017; Rego et al., 2017). To endow a HA modified surface with antibacterial property, DMADDM was introduced with the aid of polydopamine (PDA) (Zhou et al., 2020). DMADDM was gradually released in the first 4 weeks after implantation, exhibiting strong inhibition to the adhesion and proliferation of pathogenic bacteria. After 4 weeks, the samples induced osteogenic differentiation attributed to the bone-like HA. With the aid of an alternative approach, antimicrobial agents and osteogenic materials can be combined and loaded on Ti. Sung et al. functionalized titanium implants with poly(glycidyl methacrylate) (PGED) polymer brushes, and covalently coupled quaternized polyethyleneimine QPEI, an efficient cationic antibacterial agent rich in amino groups, and alendronate, which has a high affinity for bone minerals, to the polymer brushes (Sun et al., 2019). The coating did inhibit bacterial infection in the early stage and enhanced osseointegration in the later stage. Zhang

et al. prepared Ca- and Si-based ceramic (CS) nanorod coatings on Ti using MAO technique, and loaded AMP onto CS coatings with the aid of fluorous-cured collagen scaffolds (Zhang et al., 2021). The release of $Ca^{2+}$ and $Si^{2+}$ enhanced osseointegration and the collagen scaffold loaded with AMP had a good antimicrobial effect while promoting cell adhesion.

It is worth noting that some researchers have achieved antibacterial and osseointegration by modulating the microenvironment around the implant. Tao et al. prepared a multifunctional hybrid coating through depositing the zeolitic imidazolate frameworks-67 (ZIF-67) and an osteogenic growth peptide (OGP) on nanotubes (Tao et al., 2021). Under the acidic environment, the coating gradually decomposed, releasing cobalt ions and forming an alkaline microenvironment to kill bacteria. At the same time, OGP inhibited the inflammatory response and promoted differentiation of MSCs, facilitating osseointegration during the late implantation phase.

### Photoantibacterial and Osteogenic Coatings

Photosterilization includes photodynamic therapy and photothermal therapy mentioned earlier, which can effectively eradicate bacteria in the biofilm. The application of photosensitizer and osteogenic material on the surface of titanium can promote osseointegration after sterilization. Typical types of materials have been explored for multifunction surfaces, including $TiO_2$. To the best of our knowledge, $TiO_2$ has great photocatalytic properties. After surface treatment, $TiO_2$ can not only be used as a photosensitizer but also promote osseointegration. However, $TiO_2$ can generate ROS to eradicate bacteria under ultraviolet light irradiation, but it cannot be triggered by near-infrared light (Zhang et al., 2020). Han et al. chose photosensitizer $MoS_2$ with broader spectral responses to modify the surface of $TiO_2$ and used MAO and hydrothermal treatment to construct the composite collagen/polydopamine/$MoS_2$-$TiO_2$ (CPM-$TiO_2$) coating on the surface of titanium (Han et al., 2021). Under the combined action of photodynamic and photothermal therapy, *S. aureus* in biofilm could be quickly eradicated both *in vivo* and *in vitro*. The collagen in the coating was shown to promote the adhesion and proliferation of osteoblasts. Zhang et al. prepared a titanium dioxide nano-shovel/quercetin/L-arginine coating and doped ytterbium (Yb) and erbium (Er) on the $TiO_2$ nano-shovel array (Zhang et al., 2022). Under near-infrared II light irradiation, Yb and Er promoted the production of ROS, which could kill bacteria. Meanwhile, ROS catalyzed the release of nitric oxide (NO) free radicals from L-arginine, promoting angiogenesis and osseointegration. The nano-shovel structure and quercetin coupled to the surface via organosilanes promoted osteogenic differentiation of BMSCs while NO promoted angiogenesis and osseointegration. In addition, the complex of generated electrons and holes by $TiO_2$ reduces its photocatalytic properties and limits the antibacterial effect (Anandan et al., 2013). Graphdiyne enhances the catalytic effects of metals and possesses osteoinductive potential (Gu et al., 2014). Based on this, the researchers synthesized $TiO_2$/GDY nanofibers by electrostatic force (Wang et al., 2020). The combination of the two increased the production of photocatalytic ROS and prolonged the antibacterial effect, inhibiting the formation of methicillin-resistant *S. aureus* biofilms, while also promoting bone tissue regeneration. Red phosphorus (RP) can also be used for photoantibacterial coatings, which have efficient photothermal properties and biodegradability, and can exist for a long time in human body with no toxicity (Latiff et al., 2015). Huang et al. used IR780 as photosensitizer preparing a RP/IR780/RGDC coating on titanium surface (Huang et al., 2019a). In the experiment, IR780 produced ROS under irradiation of 808 nm laser and improved the temperature sensitivity of bacterial biofilm; RP produced photothermal effect by near-infrared (808 nm) radiation of 50°C, which cooperated with ROS sterilization without causing tissue damage; the existence of RGDC promoted osteogenesis.

## Multifunctional Coatings with Single Material

It is worth noting that, in addition to combining antibacterial agents and osteotropic substances on titanium surface, some researchers have achieved multifunctional effects by using only one substance. Flavonoids from plants have been shown to have the ability to inhibit the formation of biofilm and bacterial toxicity, and to enhance the efficacy of antibiotics by blocking the efflux pump to reverse the antibiotic resistance of bacteria (Górniak et al., 2019). Among them, the flavonoid quercitrin not only had antibacterial properties but also promoted bone and anti-fibrosis (Córdoba et al., 2015; Gomez-Florit et al., 2016). The researchers prepared quercitrin coating on the surface of porous titanium alloy, and it turned out that the quercitrin coating was able to prevent bacterial adhesion, inhibit bacterial activity, and improve the efficiency of surface osteogenesis (Llopis-Grimalt et al., 2020). Another novel method is to culture *Lactobacillus casei* on the surface of a heat-treated Ti to form an inactivated probiotic modified coating (Tan et al., 2020). This *L. casei* biofilm showed an excellent 99.98% antibacterial effectiveness against methicillin-resistant *S. aureus*. Furthermore, the polysaccharides in the biofilm could promote osteogenic differentiation through stimulating macrophages to secrete osteogenic factors.

Synthetic multifunctional peptides can be used as a single material for multifunctional coatings. Antimicrobial sequences are combined with bone-promoting sequences to form multifunctional peptides for immobilization on titanium surfaces to achieve multifunctional coatings (Zhang et al., 2018b; Liu et al., 2018; Wisdom et al., 2020). The RGD peptide is derived from extracellular matrix proteins, promoting mammalian cell adhesion as an integrin ligand (Atefyekta et al., 2019). Based on this, RGD was linked to the antimicrobial sequence from human β-defensin-3 as a multifunctional chimeric peptide (Zhang et al., 2018b). This chimeric peptide effectively prevented the formation of biofilms by inhibiting bacterial gene expression and induced osteoblast differentiation and mineral deposition. Some studies reported that antimicrobial peptides were covalently immobilized onto titanium surfaces, but direct conjugation of these peptides abolishes their antimicrobial activity (Chouirfa et al., 2019).

Wisdom et al. developed high-affinity inorganic binding peptides (TiBP) containing a Ti-binding domain to recognize Ti surfaces (Wisdom et al., 2020). Then, they combined RGD and antibacterial peptides with TiBP, and proved that this biofunctional peptide has antibacterial and bone-promoting properties with good stability and durability. Another method of surface immobilization is silanization of the Ti surface, immobilizing organic molecules by covalent stabilization (Kucharíková et al., 2016). Yang et al. immobilized hyperbranched poly-L-lysine (HBPL) polymers in Ti *via* silane coupling agents (Yang et al., 2021). The poly-L-lysine was able to interfere with the integrity of bacterial membranes and produce ROS to damage DNA of bacterial, exhibiting efficient sterilization properties *in vivo* and *in vitro*. Furthermore, the degradation of the coating *in vivo* created an alkaline microenvironment around the implant, which promotes osseointegration compared with the control group. Chen et al. synthesized a fusion peptide (FP) containing the antimicrobial sequence and the angiogenic sequence by a cycloaddition and introduced an alkyl group on the Ti surface to immobilize FP (Chen et al., 2021a). *In vivo* tests proved that the fusion peptide was able to kill 99.63% of *S. aureus*, as well as promote vascularization and osseointegration.

## DISCUSSION

Aseptic loosening and infection are still challenges in fabricating coatings for orthopedic and orthodontic implants, so we introduce the current strategies combating the aseptic loosening and infection of titanium-based implants in this review. Antibacterial metal ions combined with porous structure to achieve antibacterial properties and promote osseointegration are most widely used. However, burst release, cytotoxicity, short half-life, and limited stability are ongoing problems of metal ionbased strategies. These problems are addressed by coatings with controlled release properties and synergistic effects between the substances. It is worth mentioning that smart release coatings have become research hotspots recently but most of them do not exhibit sufficient capacity to promote osteogenesis. In the future, dual-function smart release coatings may become the focus of research. On the one hand, the coating can release antibacterial agents to kill bacteria in a slightly acidic environment suitable for bacteria; on the other hand, it can release osteogenic factors in a slightly alkaline environment that is conducive to osteogenesis. In addition, strategies to regulate the microenvironment around the implant also have to be mentioned, including the regulation to tissue and the local inflammatory system. Proper inflammation milieu will do facilitative effect to osseointegration, but excessive inflammation will cause serious tissue damage. Therefore, the search for an appropriate inflammatory microenvironment by modulating the polarization of macrophages is a new method to promote osteogenesis. Multifunctional coatings on titanium surfaces are formed based on biomolecules with good cytocompatibility; coatings designed by these strategies promote bone formation and provide antibacterial effects at the same time. Four main strategies are currently followed: the direct binding of antibacterial and bone-promoting substances to the surface of titanium, integrating antibacterial substances into roughening/porous surface modified coatings, photoantibacterial and osteogenic coatings, and multifunctional coatings with single material. Among them, multifunctional peptides have better bone-forming properties and avoid resistance formation, which are the shortcomings of traditional antibacterial agents. However, they still face challenges in terms of stability and long-term performance. New substances or surface modification methods with antibacterial and bone-promoting properties need to be explored, and will become the focus of research to simplify surgery, reduce costs, and provide more safety for the patient.

## AUTHOR CONTRIBUTIONS

XL, ZW, and KX contributed equally to this work. XL: conceptualization, investigation, writing—original draft. ZW: investigation, writing—review and editing. KX: investigation, writing—review and editing. XW: writing—review and editing. SW: writing—review and editing. HQ: supervision. XLi: supervision, resources, funding acquisition. JC: conceptualization, project administration, funding acquisition.

## FUNDING

This work was supported by the National Natural Science Foundation of China (nos. 31670967 and 32000932), the Key Research and Development Projects in Anhui Province (no. 202104j07020039), the Scientific Research Foundation of the Institute for Translational Medicine of Anhui Province (no. 2017zhyx19), and research improvement program in Stomatologic Hospital and College of Anhui Medical University (no. 2020kqkyT01).

## REFERENCES

Acosta, S., Ibañez-Fonseca, A., Aparicio, C., and Rodríguez-Cabello, J. C. (2020). Antibiofilm Coatings Based on Protein-Engineered Polymers and Antimicrobial Peptides for Preventing Implant-Associated Infections. *Biomater. Sci.* 8 (10), 2866–2877. doi:10.1039/D0BM00155D

Amstutz, H. C., Campbell, P., Kossovsky, N., and Clarke, I. C. (1992). Mechanism and Clinical Significance of Wear Debris-Induced Osteolysis. *Clin. Orthop. Relat. Res.* 276, 7–18. doi:10.1097/00003086-199203000-00003

Anandan, S., Narasinga Rao, T., Sathish, M., Rangappa, D., Honma, I., and Miyauchi, M. (2013). Superhydrophilic Graphene-Loaded TiO2 Thin Film for Self-Cleaning Applications. *ACS Appl. Mater. Inter.* 5 (1), 207–212. doi:10.1021/am302557z

Atefyekta, S., Pihl, M., Lindsay, C., Heilshorn, S. C., and Andersson, M. (2019). Antibiofilm Elastin-like Polypeptide Coatings: Functionality, Stability, and Selectivity. *Acta Biomater.* 83, 245–256. doi:10.1016/j.actbio.2018.10.039

Bai, Y., Zhou, R., Cao, J., Wei, D., Du, Q., Li, B., et al. (2017). Microarc Oxidation Coating Covered Ti Implants with Micro-scale Gouges Formed by a Multi-step Treatment for Improving Osseointegration. *Mater. Sci. Eng. C.* 76, 908–917. doi:10.1016/j.msec.2017.03.071

Bai, L., Du, Z., Du, J., Yao, W., Zhang, J., Weng, Z., et al. (2018a). A Multifaceted Coating on Titanium Dictates Osteoimmunomodulation and Osteo/angio-Genesis towards Ameliorative Osseointegration. *Biomaterials* 162, 154–169. doi:10.1016/j.biomaterials.2018.02.010

Bai, L., Liu, Y., Du, Z., Weng, Z., Yao, W., Zhang, X., et al. (2018b). Differential Effect of Hydroxyapatite Nano-Particle versus Nano-Rod Decorated Titanium Micro-surface on Osseointegration. *Acta Biomater.* 76, 344–358. doi:10.1016/j.actbio.2018.06.023

Bai, H., Zhao, Y., Wang, C., Wang, Z., Wang, J., Liu, H., et al. (2020). Enhanced Osseointegration of Three-Dimensional Supramolecular Bioactive Interface through Osteoporotic Microenvironment Regulation. *Theranostics* 10 (11), 4779–4794. doi:10.7150/thno.43736

Bencharit, S., Byrd, W. C., Altarawneh, S., Hosseini, B., Leong, A., Reside, G., et al. (2014). Development and Applications of Porous Tantalum Trabecular Metal-Enhanced Titanium Dental Implants. *Clin. Implant Dent. Relat. Res.* 16 (6), 817–826. doi:10.1111/cid.12059

Cao, S., Huang, W., Wu, L., Tian, M., and Song, Y. (2018). On the Interfacial Adhesion between TiO2 Nanotube Array Layer and Ti Substrate. *Langmuir* 34 (46), 13888–13896. doi:10.1021/acs.langmuir.8b03408

Carp, O. (2004). Photoinduced Reactivity of Titanium Dioxide. *Prog. Solid State. Chem.* 32 (1-2), 33–177. doi:10.1016/j.progsolidstchem.2004.08.001

Carson, J. S., and Bostrom, M. P. G. (2007). Synthetic Bone Scaffolds and Fracture Repair. *Injury* 38 (1), S33–S37. doi:10.1016/j.injury.2007.02.008

Chang, B., Song, W., Han, T., Yan, J., Li, F., Zhao, L., et al. (2016). Influence of Pore Size of Porous Titanium Fabricated by Vacuum Diffusion Bonding of Titanium Meshes on Cell Penetration and Bone Ingrowth. *Acta Biomater.* 33, 311–321. doi:10.1016/j.actbio.2016.01.022

Chen, J., Mei, M. L., Li, Q.-L., and Chu, C.-H. (2016). Mussel-inspired Silver-Nanoparticle Coating on Porous Titanium Surfaces to Promote Mineralization. *RSC Adv.* 6 (106), 104025–104035. doi:10.1039/c6ra20673e

Chen, L., Mou, S., Hou, J., Fang, H., Zeng, Y., Sun, J., et al. (2020a). Simple Application of Adipose-Derived Stem Cell-Derived Extracellular Vesicles Coating Enhances Cytocompatibility and Osteoinductivity of Titanium Implant. *Regenerative Biomater.* 8 (1), rbaa038. doi:10.1093/rb/rbaa038

Chen, X., Zhu, R.-f., Gao, H., Xu, W.-l., Xiao, G.-y., Chen, C.-z., et al. (2020b). A High Bioactive Alkali-Treated Titanium Surface Induced by Induction Heat Treatment. *Surf. Coat. Technol.* 385, 125362. doi:10.1016/j.surfcoat.2020.125362

Chen, J., Hu, G., Li, T., Chen, Y., Gao, M., Li, Q., et al. (2021a). Fusion Peptide Engineered "Statically-Versatile" Titanium Implant Simultaneously Enhancing Anti-infection, Vascularization and Osseointegration. *Biomaterials* 264, 120446. doi:10.1016/j.biomaterials.2020.120446

Chen, Y., Zhou, C., Xie, Y., Xu, A., Guan, Y., Lu, W., et al. (2021b). Zinc- and Strontium- Co-incorporated Nanorods on Titanium Surfaces with Favorable Material Property, Osteogenesis, and Enhanced Antibacterial Activity. *J. Biomed. Mater. Res.* 109 (11), 1754–1767. doi:10.1002/jbm.b.34834

Cheng, L., Wang, C., Feng, L., Yang, K., and Liu, Z. (2014). Functional Nanomaterials for Phototherapies of Cancer. *Chem. Rev.* 114 (21), 10869–10939. doi:10.1021/cr400532z

Cheng, L., Zhang, K., Zhang, N., Melo, M. A. S., Weir, M. D., Zhou, X. D., et al. (2017). Developing a New Generation of Antimicrobial and Bioactive Dental Resins. *J. Dent Res.* 96 (8), 855–863. doi:10.1177/0022034517709739

Chouirfa, H., Bouloussa, H., Migonney, V., and Falentin-Daudré, C. (2019). Review of Titanium Surface Modification Techniques and Coatings for Antibacterial Applications. *Acta Biomater.* 83, 37–54. doi:10.1016/j.actbio.2018.10.036

Córdoba, A., Satué, M., Gómez-Florit, M., Hierro-Oliva, M., Petzold, C., Lyngstadaas, S. P., et al. (2015). Flavonoid-Modified Surfaces: Multifunctional Bioactive Biomaterials with Osteopromotive, Anti-inflammatory, and Anti-fibrotic Potential. *Adv. Healthc. Mater.* 4 (4), 540–549. doi:10.1002/adhm.201400587

Del Pozo, J. L., and Patel, R. (2009). Clinical Practice. Infection Associated with Prosthetic Joints. *N. Engl. J. Med.* 361 (8), 787–794. doi:10.1056/NEJMcp0905029

Delanois, R. E., Mistry, J. B., Gwam, C. U., Mohamed, N. S., Choksi, U. S., and Mont, M. A. (2017). Current Epidemiology of Revision Total Knee Arthroplasty in the United States. *The J. Arthroplasty* 32 (9), 2663–2668. doi:10.1016/j.arth.2017.03.066

Franz, S., Rammelt, S., Scharnweber, D., and Simon, J. C. (2011). Immune Responses to Implants - a Review of the Implications for the Design of Immunomodulatory Biomaterials. *Biomaterials* 32 (28), 6692–6709. doi:10.1016/j.biomaterials.2011.05.078

Gao, Q., Feng, T., Huang, D., Liu, P., Lin, P., Wu, Y., et al. (2020). Antibacterial and Hydroxyapatite-Forming Coating for Biomedical Implants Based on Polypeptide-Functionalized Titania Nanospikes. *Biomater. Sci.* 8 (1), 278–289. doi:10.1039/C9BM01396B

Gnedenkov, S. V., Gordienko, P. S., Sinebryukhov, S. L., Kovryanov, A. N., and Khromushkin, K. D. (2000). Antiscuff Coatings Obtained by Microarc Oxidation of Titanium Alloys. *Russ. J. Appl. Chem.* 73 (1), 6–9. doi:10.1023/A:1008117010991

Górniak, I., Bartoszewski, R., and Króliczewski, J. (2019). Comprehensive Review of Antimicrobial Activities of Plant Flavonoids. *Phytochem. Rev.* 18 (1), 241–272. doi:10.1007/s11101-018-9591-z

Gomez-Florit, M., Pacha-Olivenza, M. A., Fernández-Calderón, M. C., Córdoba, A., González-Martín, M. L., Monjo, M., et al. (2016). Quercitrin-nanocoated Titanium Surfaces Favour Gingival Cells against Oral Bacteria. *Sci. Rep.* 6 (1), 22444. doi:10.1038/srep22444

Goodman, S. B. (1994). The Effects of Micromotion and Particulate Materials on Tissue Differentiation. Bone Chamber Studies in Rabbits. *Acta Orthop. Scand. Suppl.* 258, 1–43. doi:10.3109/17453679409155227

Grimes, C. A., and Mor, G. K. (2009). *Tio2 Nanotube Arrays: Synthesis, Properties, and Applications*. New York, NY: Springer Science and Business Media.

Gristina, A. G., and Costerton, J. W. (1985). Bacterial Adherence to Biomaterials and Tissue. The Significance of its Role in Clinical Sepsis. *J. Bone Jt. Surg.* 67 (2), 264–273. doi:10.2106/00004623-198567020-00014

Gu, M., Liu, Y., Chen, T., Du, F., Zhao, X., Xiong, C., et al. (2014). Is Graphene a Promising Nano-Material for Promoting Surface Modification of Implants or Scaffold Materials in Bone Tissue Engineering? *Tissue Eng. B: Rev.* 20 (5), 477–491. doi:10.1089/ten.teb.2013.0638

Guo, C., Cui, W., Wang, X., Lu, X., Zhang, L., Li, X., et al. (2020). Poly-l-lysine/Sodium Alginate Coating Loading Nanosilver for Improving the Antibacterial Effect and Inducing Mineralization of Dental Implants. *ACS Omega* 5 (18), 10562–10571. doi:10.1021/acsomega.0c00986

Guo, L. L., Cheng, Y. F., Ren, X., Gopinath, K., Lu, Z. S., Li, C. M., et al. (2021). Simultaneous Deposition of Tannic Acid and Poly(ethylene Glycol) to Construct the Antifouling Polymeric Coating on Titanium Surface. *Colloids Surf. B: Biointerf.* 200, 111592. doi:10.1016/j.colsurfb.2021.111592

Haidar, Z. S., Hamdy, R. C., and Tabrizian, M. (2009a). Delivery of Recombinant Bone Morphogenetic Proteins for Bone Regeneration and Repair. Part A: Current Challenges in BMP Delivery. *Biotechnol. Lett.* 31 (12), 1817–1824. doi:10.1007/s10529-009-0099-x

Haidar, Z. S., Hamdy, R. C., and Tabrizian, M. (2009b). Delivery of Recombinant Bone Morphogenetic Proteins for Bone Regeneration and Repair. Part B: Delivery Systems for BMPs in Orthopaedic and Craniofacial Tissue Engineering. *Biotechnol. Lett.* 31 (12), 1825–1835. doi:10.1007/s10529-009-0100-8

Han, X., Zhang, G., Chai, M., and Zhang, X. (2021). Light-assisted Therapy for Biofilm Infected Micro-arc Oxidation TiO2 Coating on Bone Implants. *Biomed. Mater.* 16 (2), 025018. doi:10.1088/1748-605x/abdb72

Hancock, R. E. W., and Sahl, H.-G. (2006). Antimicrobial and Host-Defense Peptides as New Anti-Infective Therapeutic Strategies. *Nat. Biotechnol.* 24 (12), 1551–1557. doi:10.1038/nbt1267

Harada, Y., Ogawa, K., Irie, Y., Endo, H., Feril, L. B., Uemura, T., et al. (2011). Ultrasound Activation of TiO2 in Melanoma Tumors. *J. Controlled Release* 149 (2), 190–195. doi:10.1016/j.jconrel.2010.10.012

Harmankaya, N., Igawa, K., Stenlund, P., Palmquist, A., and Tengvall, P. (2012). Healing of Complement Activating Ti Implants Compared with Non-activating Ti in Rat Tibia. *Acta Biomater.* 8 (9), 3532–3540. doi:10.1016/j.actbio.2012.05.017

Hassani Besheli, N., Mottaghitalab, F., Eslami, M., Gholami, M., Kundu, S. C., Kaplan, D. L., et al. (2017). Sustainable Release of Vancomycin from Silk Fibroin Nanoparticles for Treating Severe Bone Infection in Rat Tibia

Osteomyelitis Model. *ACS Appl. Mater. Inter.* 9 (6), 5128–5138. doi:10.1021/acsami.6b14912

He, Y., Zhang, Y., Shen, X., Tao, B., Liu, J., Yuan, Z., et al. (2018). The Fabrication and *In Vitro* Properties of Antibacterial Polydopamine-LL-37-POPC Coatings on Micro-arc Oxidized Titanium. *Colloids Surf. B: Biointerf.* 170, 54–63. doi:10.1016/j.colsurfb.2018.05.070

Hirt, H., and Gorr, S.-U. (2013). Antimicrobial Peptide GL13K Is Effective in Reducing Biofilms of Pseudomonas aeruginosa. *Antimicrob. Agents Chemother.* 57 (10), 4903–4910. doi:10.1128/AAC.00311-13

Hoyos-Nogués, M., Buxadera-Palomero, J., Ginebra, M.-P., Manero, J. M., Gil, F. J., and Mas-Moruno, C. (2018). All-in-one Trifunctional Strategy: A Cell Adhesive, Bacteriostatic and Bactericidal Coating for Titanium Implants. *Colloids Surf. B: Biointerf.* 169, 30–40. doi:10.1016/j.colsurfb.2018.04.050

Hu, D., Li, H., Wang, B., Ye, Z., Lei, W., Jia, F., et al. (2017). Surface-Adaptive Gold Nanoparticles with Effective Adherence and Enhanced Photothermal Ablation of Methicillin-Resistant Staphylococcus aureus Biofilm. *ACS Nano* 11 (9), 9330–9339. doi:10.1021/acsnano.7b04731

Hu, N., Wu, Y., Xie, L., Yusuf, S. M., Gao, N., Starink, M. J., et al. (2020). Enhanced Interfacial Adhesion and Osseointegration of Anodic TiO2 Nanotube Arrays on ultra-fine-grained Titanium and Underlying Mechanisms. *Acta Biomater.* 106, 360–375. doi:10.1016/j.actbio.2020.02.009

Huang, P., Zhang, Y., Xu, K., and Han, Y. (2004). Surface Modification of Titanium Implant by Microarc Oxidation and Hydrothermal Treatment. *J. Biomed. Mater. Res.* 70B (2), 187–190. doi:10.1002/jbm.b.30009

Huang, T., Liu, H., Liu, P., Liu, P., Li, L., and Shen, J. (2017). Zwitterionic Copolymers Bearing Phosphonate or Phosphonic Motifs as Novel Metal-Anchorable Anti-fouling Coatings. *J. Mater. Chem. B* 5 (27), 5380–5389. doi:10.1039/C7TB01017F

Huang, Q., Li, X., Elkhooly, T. A., Liu, X., Zhang, R., Wu, H., et al. (2018a). The Cu-Containing TiO2 Coatings with Modulatory Effects on Macrophage Polarization and Bactericidal Capacity Prepared by Micro-arc Oxidation on Titanium Substrates. *Colloids Surf. B: Biointerf.* 170, 242–250. doi:10.1016/j.colsurfb.2018.06.020

Huang, Q., Li, X., Liu, T., Wu, H., Liu, X., Feng, Q., et al. (2018b). Enhanced SaOS-2 Cell Adhesion, Proliferation and Differentiation on Mg-Incorporated Micro/nano-Topographical TiO2 Coatings. *Appl. Surf. Sci.* 447, 767–776. doi:10.1016/j.apsusc.2018.04.095

Huang, B., Tan, L., Liu, X., Li, J., and Wu, S. (2019a). A Facile Fabrication of Novel Stuff with Antibacterial Property and Osteogenic Promotion Utilizing Red Phosphorus and Near-Infrared Light. *Bioactive Mater.* 4 (1), 17–21. doi:10.1016/j.bioactmat.2018.11.002

Huang, Y.-Z., He, S.-K., Guo, Z.-J., Pi, J.-K., Deng, L., Dong, L., et al. (2019b). Nanostructured Titanium Surfaces Fabricated by Hydrothermal Method: Influence of Alkali Conditions on the Osteogenic Performance of Implants. *Mater. Sci. Eng. C.* 94, 1–10. doi:10.1016/j.msec.2018.08.069

Jin, L., Lee, J. H., Jin, O. S., Shin, Y. C., Kim, M. J., Hong, S. W., et al. (2015). Stimulated Osteogenic Differentiation of Human Mesenchymal Stem Cells by Reduced Graphene Oxide. *J. Nanosci. Nanotechnol.* 15 (10), 7966–7970. doi:10.1166/jnn.2015.11223

Kabata, T., Maeda, T., Kajino, Y., Hasegawa, K., Inoue, D., Yamamoto, T., et al. (2015). Iodine-Supported Hip Implants: Short Term Clinical Results. *Biomed. Res. Int.* 2015, 1–6. doi:10.1155/2015/368124

Kaestner, K. (2016). Microbial Biofilm Inhibits Wound Healing. Available at https://microbewiki.kenyon.edu/index.php/Microbial_biofilm_inhibits_wound_healing" (Accessed October 4, 2017).

Kang, Q., Sun, M. H., Cheng, H., Peng, Y., Montag, A. G., Deyrup, A. T., et al. (2004). Characterization of the Distinct Orthotopic Bone-Forming Activity of 14 BMPs Using Recombinant Adenovirus-Mediated Gene Delivery. *Gene Ther.* 11 (17), 1312–1320. doi:10.1038/sj.gt.3302298

Kang, M. S., Jeong, S. J., Lee, S. H., Kim, B., Hong, S. W., Lee, J. H., et al. (2021). Reduced Graphene Oxide Coating Enhances Osteogenic Differentiation of Human Mesenchymal Stem Cells on Ti Surfaces. *Biomater. Res.* 25 (1), 4. doi:10.1186/s40824-021-00205-x

Kato, T., and Shirai, T. (2016). Temporal Attenuation of Iodine Content and its Effect on the Antibacterial Activity of Iodine-Supported Titanium Implants. *J. Microb. Biochem. Technol.* 8 (4), 285–289. doi:10.4172/1948-5948.1000298

Ke, D., Vu, A. A., Bandyopadhyay, A., and Bose, S. (2019). Compositionally Graded Doped Hydroxyapatite Coating on Titanium Using Laser and Plasma spray Deposition for Bone Implants. *Acta Biomater.* 84, 414–423. doi:10.1016/j.actbio.2018.11.041

Kim, T.-S., Park, S.-H., Park, D., Lee, J.-H., and Kang, S. (2019). Surface Immobilization of Chlorhexidine on a Reverse Osmosis Membrane for *In-Situ* Biofouling Control. *J. Membr. Sci.* 576, 17–25. doi:10.1016/j.memsci.2019.01.030

Kolaparthy, L. K., Sanivarapu, S., Moogla, S., and Kutcham, R. S. (2015). Adipose Tissue - Adequate, Accessible Regenerative Material. *Ijsc* 8 (2), 121–127. doi:10.15283/ijsc.2015.8.2.121

Konopka, K., and Goslinski, T. (2007). Photodynamic Therapy in Dentistry. *J. Dent Res.* 86 (8), 694–707. doi:10.1177/154405910708600803

Kucharíková, S., Gerits, E., De Brucker, K., Braem, A., Ceh, K., Majdič, G., et al. (2016). Covalent Immobilization of Antimicrobial Agents on Titanium prevents Staphylococcus aureus and Candida Albicans colonization and Biofilm Formation. *J. Antimicrob. Chemother.* 71 (4), 936–945. doi:10.1093/jac/dkv437

Kurtz, S., Mowat, F., Ong, K., Chan, N., Lau, E., and Halpern, M. (2005). Prevalence of Primary and Revision Total Hip and Knee Arthroplasty in the United States from 1990 through 2002. *J. Bone Jt. Surg. Am. Vol.* 87 (7), 1487–1497. doi:10.2106/JBJS.D.02441

Lampé, I., Beke, D., Biri, S., Csarnovics, I., Csík, A., Dombrádi, Z., et al. (2019). Investigation of Silver Nanoparticles on Titanium Surface Created by Ion Implantation Technology. *Int. J. Nanomed.* 14, 4709–4721. doi:10.2147/IJN.S197782

Latiff, N. M., Teo, W. Z., Sofer, Z., Fisher, A. C., and Pumera, M. (2015). The Cytotoxicity of Layered Black Phosphorus. *Chem. Eur. J.* 21 (40), 13991–13995. doi:10.1002/chem.201502006

Lee, J.-Y., Jahng, J.-W., Kim, S.-M., Kim, M.-J., and Lee, J.-H. (2015). Simultaneous Inferior Alveolar Nerve Regeneration and Osseointegration with a Nerve Growth Factor-Supplying Implant: a Preliminary Study. *J. Oral Maxillofac. Surg.* 73 (3), 410–423. doi:10.1016/j.joms.2014.07.009

LeGeros, R. Z. (2002). Properties of Osteoconductive Biomaterials: Calcium Phosphates. *Clin. Orthop. Relat. Res.* 395 (395), 81–98. doi:10.1097/00003086-200202000-00009

Lei, W., Ren, K., Chen, T., Chen, X., Li, B., Chang, H., et al. (2016). Polydopamine Nanocoating for Effective Photothermal Killing of Bacteria and Fungus upon Near-Infrared Irradiation. *Adv. Mater. Inter.* 3 (22), 1600767. doi:10.1002/admi.201600767

Li, H., Ghazanfari, R., Zacharaki, D., Lim, H. C., and Scheding, S. (2016). Isolation and Characterization of Primary Bone Marrow Mesenchymal Stromal Cells. *Ann. N.Y. Acad. Sci.* 1370 (1), 109–118. doi:10.1111/nyas.13102

Li, J., Tan, L., Liu, X., Cui, Z., Yang, X., Yeung, K. W. K., et al. (2017). Balancing Bacteria-Osteoblast Competition through Selective Physical Puncture and Biofunctionalization of ZnO/Polydopamine/Arginine-Glycine-Aspartic Acid-Cysteine Nanorods. *ACS nano* 11 (11), 11250–11263. doi:10.1021/acsnano.7b05620

Li, Y., Liu, X., Tan, L., Cui, Z., Yang, X., Zheng, Y., et al. (2018). Rapid Sterilization and Accelerated Wound Healing Using Zn2+ and Graphene Oxide Modified G-C3 N4 under Dual Light Irradiation. *Adv. Funct. Mater.* 28 (30), 1800299. doi:10.1002/adfm.201800299

Li, C., Yang, Y., Yang, L., Shi, Z., Yang, P., and Cheng, G. (2020a). *In Vitro* Bioactivity and Biocompatibility of Bio-Inspired Ti-6Al-4V Alloy Surfaces Modified by Combined Laser Micro/Nano Structuring. *Molecules* 25 (7), 1494. doi:10.3390/molecules25071494

Li, Q., Liang, B., Wang, F., and Wang, Z. (2020b). Delivery of Interleukin 4 from a Titanium Substrate Coated with Graphene Oxide for Enhanced Osseointegration by Regulating Macrophage Polarization. *ACS Biomater. Sci. Eng.* 6 (9), 5215–5229. doi:10.1021/acsbiomaterials.0c01011

Li, B., Zhang, L., Wang, D., Peng, F., Zhao, X., Liang, C., et al. (2021a). Thermosensitive -Hydrogel-Coated Titania Nanotubes with Controlled Drug Release and Immunoregulatory Characteristics for Orthopedic Applications. *Mater. Sci. Eng. C.* 122, 111878. doi:10.1016/j.msec.2021.111878

Li, K., Tian, H., Guo, A., Jin, L., Chen, W., and Tao, B. (2021b). Gallium (Ga)–strontium (Sr) Layered Double Hydroxide Composite Coating on Titanium Substrates for Enhanced Osteogenic and Antibacterial Abilities. *J. Biomed. Mater. Res. A*. doi:10.1002/jbm.a.37284

Liu, X., Wu, S., Yeung, K. W. K., Chan, Y. L., Hu, T., Xu, Z., et al. (2011). Relationship between Osseointegration and Superelastic Biomechanics in Porous NiTi Scaffolds. *Biomaterials* 32 (2), 330–338. doi:10.1016/j.biomaterials.2010.08.102

Liu, J., Zhu, L., Xiang, S., Wei, Y., Xie, M., Liu, H., et al. (2018). Growing High-Quality CsPbBr3 by Using Porous CsPb2Br5 as an Intermediate: a Promising Light Absorber in Carbon-Based Perovskite Solar Cells. *Sustain. Energ. Fuels* 3 (1), 184–194.

Liu, J., Tang, Y., Yang, W., Tao, B., He, Y., Shen, X., et al. (2019). Functionalization of Titanium Substrate with Multifunctional Peptide OGP-NAC for the Regulation of Osteoimmunology. *Biomater. Sci.* 7 (4), 1463–1476. doi:10.1039/c8bm01611a

Llopis-Grimalt, M. A., Arbós, A., Gil-Mir, M., Mosur, A., Kulkarni, P., Salito, A., et al. (2020). Multifunctional Properties of Quercitrin-Coated Porous Ti-6Al-4V Implants for Orthopaedic Applications Assessed *In Vitro*. *J. Clin.Med.* 9 (3), 855. doi:10.3390/jcm9030855

Long, X., Xu, H., Zhang, D., and Li, J. (2020). Bioinspired by Both Mussel Foot Protein and Bone Sialoprotein: Universal Adhesive Coatings for the Promotion of Mineralization and Osteogenic Differentiation. *Polym. Chem.* 11 (31), 4995–5004. doi:10.1039/D0PY00774A

Lou, W., Dong, Y., Zhang, H., Jin, Y., Hu, X., Ma, J., et al. (2015). Preparation and Characterization of Lanthanum-Incorporated Hydroxyapatite Coatings on Titanium Substrates. *Int. J. Mol.Sci.* 16 (9), 21070–21086. doi:10.3390/ijms160921070

Ma, L., Wang, X., Zhao, N., Zhu, Y., Qiu, Z., Li, Q., et al. (2018). Integrating 3D Printing and Biomimetic Mineralization for Personalized Enhanced Osteogenesis, Angiogenesis, and Osteointegration. *ACS Appl. Mater. Inter.* 10 (49), 42146–42154. doi:10.1021/acsami.8b17495

MacBarb, R. F., Lindsey, D. P., Bahney, C. S., Woods, S. A., Wolfe, M. L., and Yerby, S. A. (2017). Fortifying the Bone-Implant Interface Part 1: An *In Vitro* Evaluation of 3D-Printed and TPS Porous Surfaces. *Int. J. Spine Surg.* 11 (3), 15. doi:10.14444/4015

Malda, J., Boere, J., van de Lest, C. H. A., van Weeren, P. R., and Wauben, M. H. M. (2016). Extracellular Vesicles - New Tool for Joint Repair and Regeneration. *Nat. Rev. Rheumatol.* 12 (4), 243–249. doi:10.1038/nrrheum.2015.170

Montanaro, L., Speziale, P., Campoccia, D., Ravaioli, S., Cangini, I., Pietrocola, G., et al. (2011). Scenery of Staphylococcus Implant Infections in Orthopedics. *Future Microbiol.* 6 (11), 1329–1349. doi:10.2217/fmb.11.117

Mushahary, D., Spittler, A., Kasper, C., Weber, V., and Charwat, V. (2018). Isolation, Cultivation, and Characterization of Human Mesenchymal Stem Cells. *Cytometry* 93 (1), 19–31. doi:10.1002/cyto.a.23242

Nagay, B. E., Dini, C., Cordeiro, J. M., Ricomini-Filho, A. P., de Avila, E. D., Rangel, E. C., et al. (2019). Visible-Light-Induced Photocatalytic and Antibacterial Activity of TiO2 Codoped with Nitrogen and Bismuth: New Perspectives to Control Implant-Biofilm-Related Diseases. *ACS Appl. Mater. Inter.* 11 (20), 18186–18202. doi:10.1021/acsami.9b03311

Ordikhani, F., and Simchi, A. (2014). Long-term Antibiotic Delivery by Chitosan-Based Composite Coatings with Bone Regenerative Potential. *Appl. Surf. Sci.* 317, 56–66. doi:10.1016/j.apsusc.2014.07.197

Park, C., Seong, Y.-J., Kang, I.-G., Song, E.-H., Lee, H., Kim, J., et al. (2019). Enhanced Osseointegration Ability of Poly(lactic Acid) via Tantalum Sputtering-Based Plasma Immersion Ion Implantation. *ACS Appl. Mater. Inter.* 11 (11), 10492–10504. doi:10.1021/acsami.8b21363

Pittenger, M. F., Mackay, A. M., Beck, S. C., Jaiswal, R. K., Douglas, R, Mosca, J. D., et al. (1999). Multilineage Potential of Adult Human Mesenchymal Stem Cells. *Science* 284 (5411), 143–147. doi:10.1126/science.284.5411.143

Qiao, Y., Ping, Y., Zhang, H., Zhou, B., Liu, F., Yu, Y., et al. (2019). Laser-Activatable CuS Nanodots to Treat Multidrug-Resistant Bacteria and Release Copper Ion to Accelerate Healing of Infected Chronic Nonhealing Wounds. *ACS Appl. Mater. Inter.* 11 (4), 3809–3822. doi:10.1021/acsami.8b21766

Raafat, D., and Sahl, H. (2009). Chitosan and its Antimicrobial Potential-Aa Critical Literature Survey. *Microb. Biotechnol.* 2 (2), 186–201. doi:10.1111/j.1751-7915.2008.00080.x

Raghavendra, G. M., Jung, J., Kim, D., and Seo, J. (2017). Effect of Chitosan Silver Nanoparticle Coating on Functional Properties of Korean Traditional Paper. *Prog. Org. Coat.* 110, 16–23. doi:10.1016/j.porgcoat.2017.04.040

Rego, G. F., Vidal, M. L., Viana, G. M., Cabral, L. M., Schneider, L. F. J., Portela, M. B., et al. (2017). Antibiofilm Properties of Model Composites Containing Quaternary Ammonium Methacrylates after Surface Texture Modification. *Dental Mater. : Official Publ. Acad. Dental Mater.* 33 (10), 1149–1156. doi:10.1016/j.dental.2017.07.010

Ren, L., Zhao, Y., Yang, L., Cao, W., Wang, H., Lian, X., et al. (2021). Preparation and Characterization of the Catechol Functionalized Chitosan-Ag NPs Deposited onto Titanium Surface. *Surf. Coat. Technol.* 420, 127319. doi:10.1016/j.surfcoat.2021.127319

Rodríguez López, A. d. L., Lee, M.-R., Ortiz, B. J., Gastfriend, B. D., Whitehead, R., Lynn, D. M., et al. (2019). Preventing S. aureus Biofilm Formation on Titanium Surfaces by the Release of Antimicrobial β-Peptides from Polyelectrolyte Multilayers. *Acta Biomater.* 93, 50–62. doi:10.1016/j.actbio.2019.02.047

Rodríguez-Contreras, A., Torres, D., Rafik, B., Ortiz-Hernandez, M., Ginebra, M. P., Calero, J. A., et al. (2021). Bioactivity and Antibacterial Properties of Calcium- and Silver-Doped Coatings on 3D Printed Titanium Scaffolds. *Surf. Coat. Technol.* 421, 127476. doi:10.1016/j.surfcoat.2021.127476

Salvagni, E., Berguig, G., Engel, E., Rodriguez-Cabello, J. C., Coullerez, G., Textor, M., et al. (2014). A Bioactive Elastin-like Recombinamer Reduces Unspecific Protein Adsorption and Enhances Cell Response on Titanium Surfaces. *Colloids Surf. B: Biointerf.* 114, 225–233. doi:10.1016/j.colsurfb.2013.10.008

Sang, S., Guo, G., Yu, J., and Zhang, X. (2021). Antibacterial Application of Gentamicin-Silk Protein Coating with Smart Release Function on Titanium, Polyethylene, and Al2O3 Materials. *Mater. Sci. Eng. C, Mater. Biol. Appl.* 124, 112069. doi:10.1016/j.msec.2021.112069

Schmalzried, T. P., Jasty, M., and Harris, W. H. (1992). Periprosthetic Bone Loss in Total Hip Arthroplasty. Polyethylene Wear Debris and the Concept of the Effective Joint Space. *The J. bone Jt. Surg. Am. vol.* 74 (6), 849–863. doi:10.2106/00004623-199274060-00006

Shahmohammadi, P., and Khazaei, B. A. (2021). Characterization of Zn/Mg-Enriched Calcium Phosphate Coating Produced by the Two-step Pulsed Electrodeposition Method on Titanium Substrate. *Surf. Inter.* 22, 100819. doi:10.1016/j.surfin.2020.100819

Sharab, L., Baier, R., Ciancio, S., and Mang, T. (2020). Influence of Photodynamic Therapy on Bacterial Attachment to Titanium Surface. *J. Oral Implantol.* 47 (5), 427–435. doi:10.1563/aaid-joi-D-19-00344

Shen, X., Zhang, Y., Ma, P., Sutrisno, L., Luo, Z., Hu, Y., et al. (2019). Fabrication of Magnesium/zinc-Metal Organic Framework on Titanium Implants to Inhibit Bacterial Infection and Promote Bone Regeneration. *Biomaterials* 212, 1–16. doi:10.1016/j.biomaterials.2019.05.008

Shi, J., Liu, Y., Wang, Y., Zhang, J., Zhao, S., and Yang, G. (2015). Biological and Immunotoxicity Evaluation of Antimicrobial Peptide-Loaded Coatings Using a Layer-By-Layer Process on Titanium. *Sci. Rep.* 5, 16336. doi:10.1038/srep16336

Shirai, T., Shimizu, T., Ohtani, K., Zen, Y., Takaya, M., and Tsuchiya, H. (2011). Antibacterial Iodine-Supported Titanium Implants. *Acta Biomater.* 7 (4), 1928–1933. doi:10.1016/j.actbio.2010.11.036

Sims, N. A., and Martin, T. J. (2014). Coupling the Activities of Bone Formation and Resorption: a Multitude of Signals within the Basic Multicellular Unit. *BoneKEy Rep.* 3, 481. doi:10.1038/bonekey.2013.215

Song, T., Yan, M., and Qian, M. (2018). The Enabling Role of Dealloying in the Creation of Specific Hierarchical Porous Metal Structures—A Review. *Corrosion Sci.* 134, 78–98. doi:10.1016/j.corsci.2018.02.013

Song, P., Hu, C., Pei, X., Sun, J., Sun, H., Wu, L., et al. (2019). Dual Modulation of Crystallinity and Macro-/microstructures of 3D Printed Porous Titanium Implants to Enhance Stability and Osseointegration. *J. Mater. Chem. B* 7 (17), 2865–2877. doi:10.1039/c9tb00093c

Song, J., Liu, H., Lei, M., Tan, H., Chen, Z., Antoshin, A., et al. (2020). Redox-Channeling Polydopamine-Ferrocene (PDA-Fc) Coating to Confer Context-dependent and Photothermal Antimicrobial Activities. *ACS Appl. Mater. Inter.* 12 (7), 8915–8928. doi:10.1021/acsami.9b22339

Souza, A. T. P., Bezerra, B. L. S., Oliveira, F. S., Freitas, G. P., Bighetti Trevisan, R. L., Oliveira, P. T., et al. (2018). Effect of Bone Morphogenetic Protein 9 on Osteoblast Differentiation of Cells Grown on Titanium with Nanotopography. *J. Cell Biochem.* 119 (10), 8441–8449. doi:10.1002/jcb.27060

Steckbeck, J. D., Deslouches, B., and Montelaro, R. C. (2014). Antimicrobial Peptides: New Drugs for Bad Bugs? *Expert Opin. Biol. Ther.* 14 (1), 11–14. doi:10.1517/14712598.2013.844227

Su, K., Tan, L., Liu, X., Cui, Z., Zheng, Y., Li, B., et al. (2020). Rapid Photo-Sonotherapy for Clinical Treatment of Bacterial Infected Bone Implants by Creating Oxygen Deficiency Using Sulfur Doping. *ACS nano* 14 (2), 2077–2089. doi:10.1021/acsnano.9b08686

Sun, L., Berndt, C. C., Gross, K. A., and Kucuk, A. (2001). Material Fundamentals and Clinical Performance of Plasma-Sprayed

Hydroxyapatite Coatings: A Review. *J. Biomed. Mater. Res.* 58 (5), 570–592. doi:10.1002/jbm.1056

Sun, Y., Zhao, Y.-Q., Zeng, Q., Wu, Y.-W., Hu, Y., Duan, S., et al. (2019). Dual-Functional Implants with Antibacterial and Osteointegration-Promoting Performances. *ACS Appl. Mater. Inter.* 11 (40), 36449–36457. doi:10.1021/acsami.9b14572

Sundfeldt, M., Carlsson, L. V., Johansson, C. B., Thomsen, P., and Gretzer, C. (2006). Aseptic Loosening, Not Only a Question of Wear: a Review of Different Theories. *Acta Orthop.* 77 (2), 177–197. doi:10.1080/17453670610045902

Tabesh, E., Salimijazi, H. R., Kharaziha, M., Mahmoudi, M., and Hejazi, M. (2019). Development of an *In-Situ* Chitosan-Copper Nanoparticle Coating by Electrophoretic Deposition. *Surf. Coat. Technol.* 364, 239–247. doi:10.1016/j.surfcoat.2019.02.040

Tan, L., Li, J., Liu, X., Cui, Z., Yang, X., Zhu, S., et al. (2018). Rapid Biofilm Eradication on Bone Implants Using Red Phosphorus and Near-Infrared Light. *Adv. Mater.* 30 (31), 1801808. doi:10.1002/adma.201801808

Tan, L., Fu, J., Feng, F., Liu, X., Cui, Z., Li, B., et al. (2020). Engineered Probiotics Biofilm Enhances Osseointegration via Immunoregulation and Anti-infection. *Sci. Adv.* 6(46), eaba5723. doi:10.1126/sciadv.aba5723

Tanaka, Y., Matsuo, Y., Komiya, T., Tsutsumi, Y., Doi, H., Yoneyama, T., et al. (2010). Characterization of the Spatial Immobilization Manner of Poly(ethylene Glycol) to a Titanium Surface with Immersion and Electrodeposition and its Effects on Platelet Adhesion. *J. Biomed. Mater. Res. Part A* 92A (1), 350–358. doi:10.1002/jbm.a.32375

Tao, B., Lin, C., He, Y., Yuan, Z., Chen, M., Xu, K., et al. (2021). Osteoimmunomodulation Mediating Improved Osteointegration by OGP-Loaded Cobalt-Metal Organic Framework on Titanium Implants with Antibacterial Property. *Chem. Eng. J.* 423, 130176. doi:10.1016/j.cej.2021.130176

Teng, F.-Y., Tai, I. C., Ho, M.-L., Wang, J.-W., Weng, L. W., Wang, Y. J., et al. (2019). Controlled Release of BMP-2 from Titanium with Electrodeposition Modification Enhancing Critical Size Bone Formation. *Mater. Sci. Eng. C.* 105, 109879. doi:10.1016/j.msec.2019.109879

Trampuz, A., and Widmer, A. F. (2006). Infections Associated with Orthopedic Implants. *Curr. Opin. Infect. Dis.* 19 (4), 349–356. doi:10.1097/01.qco.0000235161.85925.e8

Tsiapalis, D., and O'Driscoll, L. (2020). Mesenchymal Stem Cell Derived Extracellular Vesicles for Tissue Engineering and Regenerative Medicine Applications. *Cells* 9 (4), 991. doi:10.3390/cells9040991

Tsuchiya, H., Shirai, T., Nishida, H., Murakami, H., Kabata, T., Yamamoto, N., et al. (2012). Innovative Antimicrobial Coating of Titanium Implants with Iodine. *J. Orthopaedic Sci.* 17 (5), 595–604. doi:10.1007/s00776-012-0247-3

Valstar, E. R., Nelissen, R. G. H. H., Reiber, J. H. C., and Rozing, P. M. (2002). The Use of Roentgen Stereophotogrammetry to Study Micromotion of Orthopaedic Implants. *ISPRS J. Photogramm. Remote Sens.* 56 (5), 376–389. doi:10.1016/S0924-2716(02)00064-3

van de Belt, H., Neut, D., Schenk, W., van Horn, J. R., van der Mei, H. C., and Busscher, H. J. (2001). Infection of Orthopedic Implants and the Use of Antibiotic-Loaded Bone Cements. A Review. *Acta Orthop. Scand.* 72 (6), 557–571. doi:10.1080/000164701317268978

Van, T. B., Brown, S. D., and Wirtz, G. P. (1977). Mechanism of Anodic Spark Deposition. *Am. Ceram. Soc. Bull. U. S.*

van Hengel, I. A. J., Putra, N. E., Tierolf, M. W. A. M., Minneboo, M., Fluit, A. C., Fratila-Apachitei, L. E., et al. (2020a). Biofunctionalization of Selective Laser Melted Porous Titanium Using Silver and Zinc Nanoparticles to Prevent Infections by Antibiotic-Resistant Bacteria. *Acta Biomater.* 107, 325–337. doi:10.1016/j.actbio.2020.02.044

van Hengel, I. A. J., Tierolf, M. W. A. M., Valerio, V. P. M., Minneboo, M., Fluit, A. C., Fratila-Apachitei, L. E., et al. (2020b). Self-defending Additively Manufactured Bone Implants Bearing Silver and Copper Nanoparticles. *J. Mater. Chem. B.* 8 (8), 1589–1602. doi:10.1039/C9TB02434D

Vizoso, F., Eiro, N., Cid, S., Schneider, J., and Perez-Fernandez, R. (2017). Mesenchymal Stem Cell Secretome: Toward Cell-free Therapeutic Strategies in Regenerative Medicine. *Int. J. Mol. Sci.* 18 (9), 1852. doi:10.3390/ijms18091852

Vovna, V. I., Gnedenkov, S. V., Gordienko, P. S., Kuznetsov, M. V., and Khrisanfova, O. A. (1998). Surface Layers Produced on Titanium by Microarc Oxidation: An X-ray Diffractometry Study. *Russ. J. Electrochem.* 34 (10), 1090–1093.

Wang, Q., Huang, J., Li, H., Zhao, A., Wang, Y., Zhang, K., et al. (2017a). Recent Advances on Smart TiO Nanotube Platforms for Sustainable Drug Delivery Applications. *Int. J. Nanomed.* 12, 151–165. doi:10.2147/ijn.S117498

Wang, S., Wang, H., Ren, B., Li, H., Weir, M. D., Zhou, X., et al. (2017b). Do quaternary Ammonium Monomers Induce Drug Resistance in Cariogenic, Endodontic and Periodontal Bacterial Species? *Dental Mater. : official Publ. Acad. Dental Mater.* 33 (10), 1127–1138. doi:10.1016/j.dental.2017.07.001

Wang, C., Wang, Y., Zhang, L., Miron, R. J., Liang, J., Shi, M., et al. (2018a). Pretreated Macrophage-Membrane-Coated Gold Nanocages for Precise Drug Delivery for Treatment of Bacterial Infections. *Adv. Mater.* 30 (46), 1804023. doi:10.1002/adma.201804023

Wang, J., Meng, F., Song, W., Jin, J., Ma, Q., Fei, D., et al. (2018b). Nanostructured Titanium Regulates Osseointegration via Influencing Macrophage Polarization in the Osteogenic Environment. *Int. J. Nanomed.* 13, 4029–4043. doi:10.2147/ijn.S163956

Wang, S., Yang, Y., Li, W., Wu, Z., Li, J., Xu, K., et al. (2019). Study of the Relationship between Chlorhexidine-Grafted Amount and Biological Performances of Micro/Nanoporous Titanium Surfaces. *ACS omega* 4 (19), 18370–18380. doi:10.1021/acsomega.9b02614

Wang, R., Shi, M., Xu, F., Qiu, Y., Zhang, P., Shen, K., et al. (2020). Graphdiyne-modified TiO2 Nanofibers with Osteoinductive and Enhanced Photocatalytic Antibacterial Activities to Prevent Implant Infection. *Nat. Commun.* 11 (1), 4465. doi:10.1038/s41467-020-18267-1

Wang, L., Zhou, W., Yu, Z., Yu, S., Zhou, L., Cao, Y., et al. (2021a). An *In Vitro* Evaluation of the Hierarchical Micro/Nanoporous Structure of a Ti3Zr2Sn3Mo25Nb Alloy after Surface Dealloying. *ACS Appl. Mater. Inter.* 13 (13), 15017–15030. doi:10.1021/acsami.1c02140

Wang, X., Xu, K., Cui, W., Yang, X., Maitz, M. F., Li, W., et al. (2021b). Controlled Synthesis of Mussel-Inspired Ag Nanoparticle Coatings with Demonstrated *In Vitro* and *In Vivo* Antibacterial Properties. *Mater. Des.* 208, 109944. doi:10.1016/j.matdes.2021.109944

Wisdom, E., Zhou, Y., Chen, C., Tamerler, C., and Snead, M. (2020). Mitigation of Peri-Implantitis by Rational Design of Bifunctional Peptides with Antimicrobial Properties. *ACS Biomater. Sci. Eng.* 6 (5), 2682–2695. doi:10.1021/acsbiomaterials.9b01213

Wu, H., Xie, L., He, M., Zhang, R., Tian, Y., Liu, S., et al. (2019). A Wear-Resistant TiO Nanoceramic Coating on Titanium Implants for Visible-Light Photocatalytic Removal of Organic Residues. *Acta Biomater.* 97, 597–607. doi:10.1016/j.actbio.2019.08.009

Xie, Y., Liu, M., and Zhou, J. (2012). Molecular Dynamics Simulations of Peptide Adsorption on Self-Assembled Monolayers. *Appl. Surf. Sci.* 258 (20), 8153–8159. doi:10.1016/j.apsusc.2012.05.013

Xie, K., Zhou, Z., Guo, Y., Wang, L., Li, G., Zhao, S., et al. (2019). Long-Term Prevention of Bacterial Infection and Enhanced Osteoinductivity of a Hybrid Coating with Selective Silver Toxicity. *Adv. Healthc. Mater.* 8 (5), e1801465. doi:10.1002/adhm.201801465

Xu, N., Fu, J., Zhao, L., Chu, P. K., and Huo, K. (2020). Biofunctional Elements Incorporated Nano/Microstructured Coatings on Titanium Implants with Enhanced Osteogenic and Antibacterial Performance. *Adv. Healthc. Mater.* 9 (23), 2000681. doi:10.1002/adhm.202000681

Xue, T., Attarilar, S., Liu, S., Liu, J., Song, X., Li, L., et al. (2020). Surface Modification Techniques of Titanium and its Alloys to Functionally Optimize Their Biomedical Properties: Thematic Review. *Front. Bioeng. Biotechnol.* 8 (1261), 603072. doi:10.3389/fbioe.2020.603072

Yang, Z., Xi, Y., Bai, J., Jiang, Z., Wang, S., Zhang, H., et al. (2021). Covalent Grafting of Hyperbranched Poly-L-Lysine on Ti-Based Implants Achieves Dual Functions of Antibacteria and Promoted Osteointegration *In Vivo*. *Biomaterials* 269, 120534. doi:10.1016/j.biomaterials.2020.120534

Yao, Q., Jiang, Y., Tan, S., Fu, X., Li, B., and Liu, L. (2020). Composition and Bioactivity of Calcium Phosphate Coatings on Anodic Oxide Nanotubes Formed on Pure Ti and Ti-6Al-4V alloy Substrates. *Mater. Sci. Eng. C, Mater. Biol. Appl.* 110, 110687. doi:10.1016/j.msec.2020.110687

Yao, M., Cheng, S., Zhong, G., Zhou, J., Shao, H., Ma, L., et al. (2021). Enhanced Osteogenesis of Titanium with nano-Mg(OH) Film and a Mechanism Study via Whole Genome Expression Analysis. *Bioactive Mater.* 6 (9), 2729–2741. doi:10.1016/j.bioactmat.2021.02.003

Ye, J., Li, B., Li, M., Zheng, Y., Wu, S., and Han, Y. (2020). ROS Induced Bactericidal Activity of Amorphous Zn-Doped Titanium Oxide Coatings and Enhanced Osseointegration in Bacteria-Infected Rat Tibias. *Acta Biomater.* 107, 313–324. doi:10.1016/j.actbio.2020.02.036

Ye, J., Huang, B., and Gong, P. (2021). Nerve Growth Factor-Chondroitin Sulfate/hydroxyapatite-Coating Composite Implant Induces Early Osseointegration and Nerve Regeneration of Peri-Implant Tissues in Beagle Dogs. *J. Orthop. Surg. Res.* 16 (1), 51. doi:10.1186/s13018-020-02177-5

Yin, D., Komasa, S., Yoshimine, S., Sekino, T., and Okazaki, J. (2019). Effect of Mussel Adhesive Protein Coating on Osteogenesis *In Vitro* and Osteointegration *In Vivo* to Alkali-Treated Titanium with Nanonetwork Structures. *Int. J. Nanomed.* 14, 3831–3843. doi:10.2147/ijn.S206313

Yu, M., Wan, Y., Ren, B., Wang, H., Zhang, X., Qiu, C., et al. (2020a). 3D Printed Ti-6Al-4V Implant with a Micro/Nanostructured Surface and its Cellular Responses. *ACS omega* 5 (49), 31738–31743. doi:10.1021/acsomega.0c04373

Yu, S., Guo, D., Han, J., Sun, L., Zhu, H., Yu, Z., et al. (2020b). Enhancing Antibacterial Performance and Biocompatibility of Pure Titanium by a Two-step Electrochemical Surface Coating. *ACS Appl. Mater. Inter.* 12 (40), 44433–44446. doi:10.1021/acsami.0c10032

Yuan, Z., Tao, B., He, Y., Mu, C., Liu, G., Zhang, J., et al. (2019). Remote Eradication of Biofilm on Titanium Implant via Near-Infrared Light Triggered Photothermal/photodynamic Therapy Strategy. *Biomaterials* 223, 119479. doi:10.1016/j.biomaterials.2019.119479

Zeng, Y., Yang, Y., Chen, L., Yin, D., Zhang, H., Tashiro, Y., et al. (2019). Optimized Surface Characteristics and Enhanced *In Vivo* Osseointegration of Alkali-Treated Titanium with Nanonetwork Structures. *Int. J. Mol. Sci.* 20 (5), 1127. doi:10.3390/ijms20051127

Zhang, Y., Han, Y., and Zhang, L. (2015). Interfacial Structure of the Firmly Adhered TiO2 Nanotube Films to Titanium Fabricated by a Modified Anodization. *Thin Solid Films* 583, 151–157. doi:10.1016/j.tsf.2015.03.060

Zhang, M., Huang, X., Hang, R., Zhang, X., and Tang, B. (2018a). Effect of a Biomimetic Titania Mesoporous Coating Doped with Sr on the Osteogenic Activity. *Mater. Sci. Eng. C Mater. Biol. Appl.* 91, 153–162. doi:10.1016/j.msec.2018.05.036

Zhang, X., Geng, H., Gong, L., Zhang, Q., Li, H., Zhang, X., et al. (2018b). Modification of the Surface of Titanium with Multifunctional Chimeric Peptides to Prevent Biofilm Formation via Inhibition of Initial Colonizers. *Int. J. Nanomed.* 13, 5361–5375. doi:10.2147/ijn.S170819

Zhang, Y., Liu, X., Li, Z., Zhu, S., Yuan, X., Cui, Z., et al. (2018c). Nano Ag/ZnO-Incorporated Hydroxyapatite Composite Coatings: Highly Effective Infection Prevention and Excellent Osteointegration. *ACS Appl. Mater. Inter.* 10 (1), 1266–1277. doi:10.1021/acsami.7b17351

Zhang, Z., Xie, Y., Pan, H., Huang, L., and Zheng, X. (2018d). Influence of Patterned Titanium Coatings on Polarization of Macrophage and Osteogenic Differentiation of Bone Marrow Stem Cells. *J. Biomater. Appl.* 32 (7), 977–986. doi:10.1177/0885328217746802

Zhang, G., Zhang, X., Yang, Y., Chi, R., Shi, J., Hang, R., et al. (2020). Dual Light-Induced *In Situ* Antibacterial Activities of biocompatibleTiO2/MoS2/PDA/RGD Nanorod Arrays on Titanium. *Biomater. Sci.* 8 (1), 391–404. doi:10.1039/C9BM01507H

Zhang, L., Xue, Y., Gopalakrishnan, S., Li, K., Han, Y., and Rotello, V. M. (2021). Antimicrobial Peptide-Loaded Pectolite Nanorods for Enhancing Wound-Healing and Biocidal Activity of Titanium. *ACS Appl. Mater. Inter.* 13 (24), 28764–28773. doi:10.1021/acsami.1c04895

Zhang, G., Wu, Z., Yang, Y., Shi, J., Lv, J., Fang, Y., et al. (2022). A Multifunctional Antibacterial Coating on Bone Implants for Osteosarcoma Therapy and Enhanced Osteointegration. *Chem. Eng. J.* 428, 131155. doi:10.1016/j.cej.2021.131155

Zhang, J. (2014). Choice of Treatment for Dental Implant Restoration in Patients with Severe Periodontitis. *Chin. J. Stomatol.* 6 (49), 324–327. doi:10.3760/cma.j.issn.1002-0098.2014.06.002

Zhao, Y.-p., Wei, J.-l., Tian, Q.-y., Liu, A. T., Yi, Y.-S., Einhorn, T. A., et al. (2016). Progranulin Suppresses Titanium Particle Induced Inflammatory Osteolysis by Targeting TNFα Signaling. *Sci. Rep.* 6 (1), 20909. doi:10.1038/srep20909

Zhao, Q.-M., Sun, Y.-Y., Wu, C.-S., Yang, J., Bao, G.-F., and Cui, Z.-M. (2020a). Enhanced Osteogenic Activity and Antibacterial Ability of Manganese-Titanium Dioxide Microporous Coating on Titanium Surfaces. *Nanotoxicology* 14 (3), 289–309. doi:10.1080/17435390.2019.1690065

Zhao, X., Ren, X., Wang, C., Huang, B., Ma, J., Ge, B., et al. (2020b). Enhancement of Hydroxyapatite Formation on Titanium Surface by Alkali Heat Treatment Combined with Induction Heating and Acid Etching. *Surf. Coat. Technol.* 399, 126173. doi:10.1016/j.surfcoat.2020.126173

Zhou, R., Wei, D., Feng, W., Cheng, S., Yang, H., Li, B., et al. (2014). Bioactive Coating with Hierarchical Double Porous Structure on Titanium Surface Formed by Two-step Microarc Oxidation Treatment. *Surf. Coat. Technol.* 252, 148–156. doi:10.1016/j.surfcoat.2014.04.061

Zhou, R., Wei, D., Cao, J., Feng, W., Cheng, S., Du, Q., et al. (2015). Conformal Coating Containing Ca, P, Si and Na with Double-Level Porous Surface Structure on Titanium Formed by a Three-step Microarc Oxidation. *RSC Adv.* 5 (37), 28908–28920. doi:10.1039/C4RA14685A

Zhou, W., Peng, X., Ma, Y., Hu, Y., Wu, Y., Lan, F., et al. (2020). Two-staged Time-dependent Materials for the Prevention of Implant-Related Infections. *Acta Biomater.* 101, 128–140. doi:10.1016/j.actbio.2019.10.023

Zhou, Z., Shi, Q., Wang, J., Chen, X., Hao, Y., Zhang, Y., et al. (2021). The Unfavorable Role of Titanium Particles Released from Dental Implants. *Nanotheranostics* 5 (3), 321–332. doi:10.7150/ntno.56401

Zhu, Z., Li, X., Li, Y., Zhu, L., Zhu, C., Che, Z., et al. (2021). Three-dimensionally Printed Porous Biomimetic Composite for Sustained Release of Recombinant Human Bone Morphogenetic Protein 9 to Promote Osteointegration. *Mater. Des.* 208, 109882. doi:10.1016/j.matdes.2021.109882

Zhuang, Y., Ren, L., Zhang, S., Wei, X., Yang, K., and Dai, K. (2021). Antibacterial Effect of a Copper-Containing Titanium alloy against Implant-Associated Infection Induced by Methicillin-Resistant Staphylococcus aureus. *Acta Biomater.* 119, 472–484. doi:10.1016/j.actbio.2020.10.026

Zimmerli, W. (2014). Clinical Presentation and Treatment of Orthopaedic Implant-Associated Infection. *J. Intern. Med.* 276 (2), 111–119. doi:10.1111/joim.12233

**Conflict of Interest:** The authors declare that the research was conducted in the absence of any commercial or financial relationships that could be construed as a potential conflict of interest.

frontiers in Bioengineering and Biotechnology

ORIGINAL RESEARCH
published: 15 December 2021
doi: 10.3389/fbioe.2021.767641

# N-Acetyl-Cysteine-Loaded Biomimetic Nanofibrous Scaffold for Osteogenesis of Induced-Pluripotent-Stem-Cell -Derived Mesenchymal Stem Cells and Bone Regeneration

*Xiaolei Li[1†], Feng Xiong[2†], Shuguang Wang[1], Zhuojun Zhang[2], Jihang Dai[1], Hui Chen[1], Jingcheng Wang[1], Qiang Wang[1]* and Huihua Yuan[2]**

[1]Department of Orthopedics and Orthopedic Institute, Clinical Medical College of Yangzhou University, Subei People's Hospital of Jiangsu Province, Yangzhou, China, [2]School of Life Sciences, Nantong University, Nantong, China

OPEN ACCESS

**Edited by:**
*Hongbo Zhang,*
*Åbo Akademi University, Finland*

**Reviewed by:**
*Jun Fang,*
*Shanghai Jiao Tong University, China*
*Jingyi Zhu,*
*Nanjing Tech University, China*

***Correspondence:**
*Qiang Wang*
*wangqiangyz@sina.com*
*Huihua Yuan*
*yuanhh@ntu.edu.cn*

*†These authors have contributed equally to this work*

**Specialty section:**
*This article was submitted to Biomaterials, a section of the journal Frontiers in Bioengineering and Biotechnology*

**Received:** *31 August 2021*
**Accepted:** *12 November 2021*
**Published:** *15 December 2021*

**Citation:**
*Li X, Xiong F, Wang S, Zhang Z, Dai J, Chen H, Wang J, Wang Q and Yuan H (2021) N-Acetyl-Cysteine-Loaded Biomimetic Nanofibrous Scaffold for Osteogenesis of Induced-Pluripotent-Stem-Cell-Derived Mesenchymal Stem Cells and Bone Regeneration. Front. Bioeng. Biotechnol. 9:767641. doi: 10.3389/fbioe.2021.767641*

To regenerate bone tissues, we investigated the osteogenic differentiation of induced-pluripotent-stem-cell-derived mesenchymal stem cells (iPSC-MSCs) and bone regeneration capacities using N-acetyl cysteine (NAC)-loaded biomimetic nanofibers of hydroxyapatite/silk fibroin (HAp/SF). The addition of HAp and NAC decreased the diameters of the electrospun fibers and enhanced the mechanical properties of the silk scaffold. The release kinetic curve indicated that NAC was released from NAC/HAp/SF nanofibers in a biphasic pattern, with an initial burst release stage and a later sustained release stage. This pattern of release of NAC encapsulated on the NAC/HAp/SF scaffolds prolonged the release of high concentrations of NAC, thereby largely affecting the osteogenic differentiation of iPSC-MSCs and bone regeneration. Thus, a new silk electrospun scaffold was developed. HAp was used as a separate nanocarrier for recharging the NAC concentration, which demonstrated the promising potential for the use of NAC/HAp/SF for bone tissue engineering.

**Keywords: bone tissue engineering, n-acetyl cysteine, HAp/SF nanofibers, drug release, osteogenesis**

## INTRODUCTION

The combination of a pure bone tissue engineering scaffold and seed cells can repair damaged bone tissue to a certain extent. However, it cannot provide close and effective information connection with surrounding natural organs and tissues to accelerate healing of bone tissue damage. The functional bionics of bone tissue engineering scaffolds are based on this signal factor, one of the three elements of bone tissue engineering (Collignon et al., 2017). Bone tissue can produce growth factors during repair (including bone morphogenetic protein-2 (Groeneveld and Burger, 2000), insulin-like growth factor (Koch et al., 2005), basic fibroblast growth factor (Du et al., 2012), transforming growth factor-β (Hong et al., 2000), and vascular endothelial growth factor (Mayr-Wohlfart et al., 2002)). Multiple growth factors coordinately control the behavior of bone cells and accelerate the secretion of extracellular matrix in osteoblasts. Bone tissue engineering can also induce osteoblast proliferation and promote bone regeneration after separation and purification of these growth factors.

The most frequently used functional bionics in bone tissue engineering is to select the growth factor that participates in bone repair as a biological activity factor to prepare the bone scaffold and to

accelerate bone repair by regulating the rate of release of the growth factor. Functional bionics is also referred to as a third generation of bioactive composite material and biological hybrid material, a compound material, combined with the biological activity of cytokines. It can actively stimulate and induce the self-repair and regeneration of the injured tissue. Thus, damaged tissue and organs can eventually be replaced by healthy tissues or organs (Boccaccini and Blaker, 2005). Growth factors cannot be widely used in clinics because of the difficulties in extraction, high price, susceptibility to inactivation, short half-life, and immunogenicity to body tissue (James et al., 2016). Small-molecule drugs have good efficacies and stable pesticide effects. They do not easily become inactive during the preparation of scaffolds and have low molecular weights, high solubilities, and diverse structures and functions. They can also be designed and improved according to the requirements and easily produced in large quantities. They attracted considerable attention because of their known molecular structure, low cost, and simple commercialization (Banaszynski et al., 2006; Ontoria et al., 2009). Accordingly, the use of small-molecule drugs with good properties, instead of growth factors, has become a trend in bone tissue engineering (Xu et al., 2008).

N-acetyl cysteine (NAC), a water-soluble and membrane-permeable small molecule, has various bio-functionalities, including antioxidant activity, ability to improve cytocompatibility, and osteogenic differentiation (Oikawa et al., 1999; Yamada et al., 2013; Zhu et al., 2015). NAC loaded on a collagen sponge scaffold promotes bone regeneration *in vitro* and *in vivo* (Yamada et al., 2013). However, NAC is simply absorbed onto this scaffold, which may result in a burst of release of NAC thereby imposing limitations in biological and clinical applications. Therefore, the enhancement of bone regeneration relies on the effective incorporation and viable release of bioactive molecules in a controlled manner over a comparatively long period of bone regeneration. Recently, an NAC-loaded polylactic-co-glycolic acid electrospun system with mesoporous silica nanoparticle nanocarriers was developed for the promotion of osteogenesis of rBMSCs *in vitro* (Zhu et al., 2019). Although these systems can achieve controlled delivery of NACs *in vitro*, in the clinical settings of bone tissue repair and regeneration, scaffolds as bio-mimetics of the natural bone composition of hydroxyapatite (HAp) and collagen nanofibers are required (Sell et al., 2007). Thus, the fabrication of composite nanofibers consisting of HAp is a rational strategy. HAp-incorporated silk fibroin (HAp/SF) has been considered one of the most attractive biomaterial scaffolding systems for bone tissue engineering (Farokhi et al., 2018).

In this study, HAp/SF composite nanofibers were used as carriers to control the release of NAC and investigate its effect on fiber properties. The effects of HAp/SF composite nanofibers loaded with NAC on the osteogenic differentiation of induced-pluripotent-stem-cell-derived mesenchymal stem cells (iPSC-MSCs) were evaluated at the cellular, protein, and genetic levels. We created a mouse cranial bone defect model and assessed the efficacy of the NAC/HAp/SF nanofibrous scaffold for bone regeneration. This nanofibrous scaffold could maximize the osteogenic ability of iPSC-MSCs in the long term and could be used for personalized and functional bone repair and regeneration applications.

# MATERIALS AND METHODS

## Preparation of NAC/Hydroxyapatite/Silk Fibroin Nanofibers

HAp/SF composite fibers with 10% HAp were selected as drug carriers to prepare drug-loaded fibers with a certain amount of NAC. The blending method was used to disperse NAC evenly in the spinning solution. Drug-loaded fibers were prepared by electrospinning. A solution was prepared by dissolving the required weight of NAC in 10 μl of water and adding it to the spinning solution, followed by stirring, and mixing. 0.4 g of HAp was added to a stirring bottle containing 2 ml of methane acid. The HAp particles were evenly dispersed by ultrasonication for 30 min 0.4 g of SF and 0.0082 g of polyethylene oxide (PEO) were then added to the solution and stirred and dissolved. After stirring for 1 h, 10 μL of an aqueous solution containing NAC (0.78 mg) was added, and the NAC/HAp/SF solution was then prepared by magnetic stirring for 5 h at room temperature. The electrospinning was carried out at a spinning voltage of 7–8 kV, an injection rate of 0.4 ml/h, a receiving distance of 15 cm, at room temperature, and an ambient humidity of 30–40%.

## Characterization of N-Acetyl Cysteine/ Hydroxyapatite/Silk Fibroin Nanofibers

### Morphology of Nanofibers

Morphologies of the different NAC/HAp/SF drug-loaded fiber membranes were observed by scanning electron microscopy (SEM, ZEISS Gemini SEM 300, Germany) and transmission electron microscopy (TEM, Talos F200X, FEI, United States). After a double-sided conductive adhesive was attached to the SEM sample stage, the different electrospun fiber membranes (after evaporation of the solvent) were cut into appropriate sizes and attached to the conductive adhesive. The sample was then sprayed with gold for 40 s under vacuum. Finally, the surface morphology of the electrospun fiber membrane was observed using SEM at an accelerating voltage of 10 kV and imaged as needed. The diameter of the fiber was measured using the ImageJ software (at least 50 times per sample).

## Hydrophilic Performance Test

The contact angles of the different drug-loaded fiber membranes were measured using a contact-angle tester (JCY-1, Shanghai Fangrui Instrument Co., Ltd.). 0.3 μL of deionized water was dropped on the sample. The morphologies of the water droplets on the fiber membrane at different times were imaged. The angle between the water droplet and fiber membrane was measured to obtain the contact angle.

## Test of Drug Release

Ultraviolet spectrophotometry (Thermo Scientific Evolution 300, United States) was used to analyze drug release. Scaffold samples

(20 mg, alcohol gas treated for 1 h) were immersed in 2 ml of distilled deionized water. The samples were then mixed with a 4-chloro-7-nitrobenzofurazan (0.006 wt%) chromogenic agent in a ratio of 1:18. After 30 min of reaction, the NAC concentrations were calculated based on the absorbance at 423 nm.

## *In-vitro* Cyto-Compatibility of the N-Acetyl Cysteine /Hydroxyapatite/Silk Fibroin Nanofibers

The rat iPSC-MSCs was induced by the rat iPS cells (Sidansai Biotechnology, Shanghai, China, China) cultured in MSCs medium and consisted of Dulbecco's Modified Eagle's Medium (Hyclone, United States), 1% penicillin/streptomycin (Tianjin Haoyang Biological Products Technology Co. Ltd., China), L-glutamine (Gibco, United States), and 10% fetal bovine serum (Gibco, United States). The iPSC-MSCs were cultured at 37°C in a 5% $CO_2$ humidified incubator and the culture medium was changed every 2 days.

To prepare nanofiber scaffolds for cell culture, smooth glass sheets (diameter 15 mm) were cleaned, sterilized, and placed on an aluminum foil to collect the fibers. After electrospinning of the 2-ml solution, the prepared HAp/SF membranes were dried in a vacuum-drying chamber for at least 5 days to remove residual solvents. After the solvent was volatilized, the samples were placed in the corresponding cell-culture plate. Four-to-six samples for each structure were utilized, with blank cover slides placed into a plate as a control group. After 10 min of methanol treatment, the SF structure was transformed, methanol was removed, and sample scaffolds were irradiated by ultraviolet light for 2 days after methanol volatilization. The samples were soaked in 75% ethanol for 2 h, and then washed for 10 min with PBS (Phosphate Buffer Saline) three times. Each pore was added to the corresponding cell culture medium. The sample was soaked in an incubator overnight for preculture. The sample was prepared squarely and placed in a cell-culture plate. iPSC-MSCs were planted according to the experimental requirements.

## Effect of Scaffolds on Cell Morphology

Cell spreading on fibers was observed using SEM. To prepare the samples for SEM, the following procedure was used: 1) Cell–scaffold complexes were cultured for 1 and 7 days and then removed from the culture medium and washed with PBS three times; 2) 4% glutaraldehyde was added to the complexes for a period of 2.5 h or longer to immobilize the samples; 3) after the glutaraldehyde was removed, the complexes were washed by PBS three times; 4) samples were washed for 15 min in each of six concentrations of alcohol (10, 30, 50, 70, 90, and 100%) for dehydration; 4) treatment with hexamethyldisiloxane was carried out overnight. After drying, the structures were cut into fragments, sprayed with gold, and observed using SEM.

## Effects of Scaffolds on Cell Proliferation

The effects of the scaffolds on cell proliferation were evaluated by using cell counting kit-8 (CCK-8). At set times (1, 4, and 7 days), an appropriate volume of CCK-8 solution was added to the plates and incubated for 4 h. 200 μl of the culture medium was then extracted and added to a 96-well plate, without bubbles. The absorbance at 450 nm was determined using a microplate reader.

## Osteogenic Differentiation of iPSC-MSCs Induced by N-Acetyl Cysteine /HAp/SF Nanofibers *in vitro*

### Quantitative Analysis of Alkaline Phosphatase (ALP)

A BCIP/NBT color development kit (Nanjing Jiancheng Bioengineering Institute, Nanjing, China) was used to assay ALP activity according to the manufacturer's specifications. A quantitative analysis of ALP was performed using an ALP quantitative kit. The cell supernatant was removed and then 1% Triton X-100 (soluble in PBS) was added and incubated for 30 min to split the cells. 30 ml of the supernatant was distributed among a 96-well plate and then 50 μl of the buffer and matrix solution was added and incubated at 37°C for 15 min 150 μl of the chromogenic reagent was then added to the 96-well plate, shaken gently, and mixed evenly. The absorbance at 520 nm was determined using a microplate reader.

### Quantitative Analysis of Collagen (COL)

Quantitative analysis of collagen was performed using a hydroxyproline testing kit (Nanjing Jiancheng Bioengineering Institute, Nanjing, China) as per the manufacturer's instructions. In summary, the cell supernatant was removed and then 1% Triton X-100 (soluble in PBS) was added and incubated for 30 min to lyse the cells. The resulting solution, after lysis, was collected and pH was adjusted to 6.0–6.8. Reagent was added according to the hydroxyproline test kit and well mixed, followed by incubation at 60 °C in water for 15 min. After cooling and centrifugation for 10 min at 3,500 rpm, absorbance at 550 nm was measured.

## Detection of Osteogenesis-Related Genes

After 14 days incubation, the expressions of osteogenesis-related genes (ALP, COL, OCN (osteocalcin), and OPN (osteopontin)) in iPSC-MSCs cultured in HAp/SF, 10-NAC/HAp/SF, 20-NAC/HAp/SF nanofiber membranes, and the TCP blank control were detected by reverse transcription polymerase chain reaction (RT-PCR). All primer sequences were listed in **Table 1**. The procedure for RT-PCR included three principles processes: ribonucleic acid (RNA) extraction, reverse transcription deoxyribonucleic acid (DNA) synthesis, and RT-PCR gene amplification detection. RNA was rapidly extracted using a Biozol RNA extraction kit. Reverse transcription DNA synthesis was undertaken using a 20 L reactor containing 20–50 ng of RNA. RNA was reverse-transcribed to form complementary DNA (cDNA) using the FastQuant RT Kit (with gDNase). RT-PCR was performed using the SuperReal PreMix Plus (SYBR Green) kit, with the housekeeping gene (GAPDH) as a control. After 40 cycles, the relative expression of each target gene was calculated using the $2^{-\Delta\Delta ct}$ method.

## Bone Regeneration *in vivo*

### Mouse Cranial Defect Model

After the *in vitro* osteogenesis study, we developed a mouse cranial defect model in 6-week-old male Sprague–Dawley (SD)

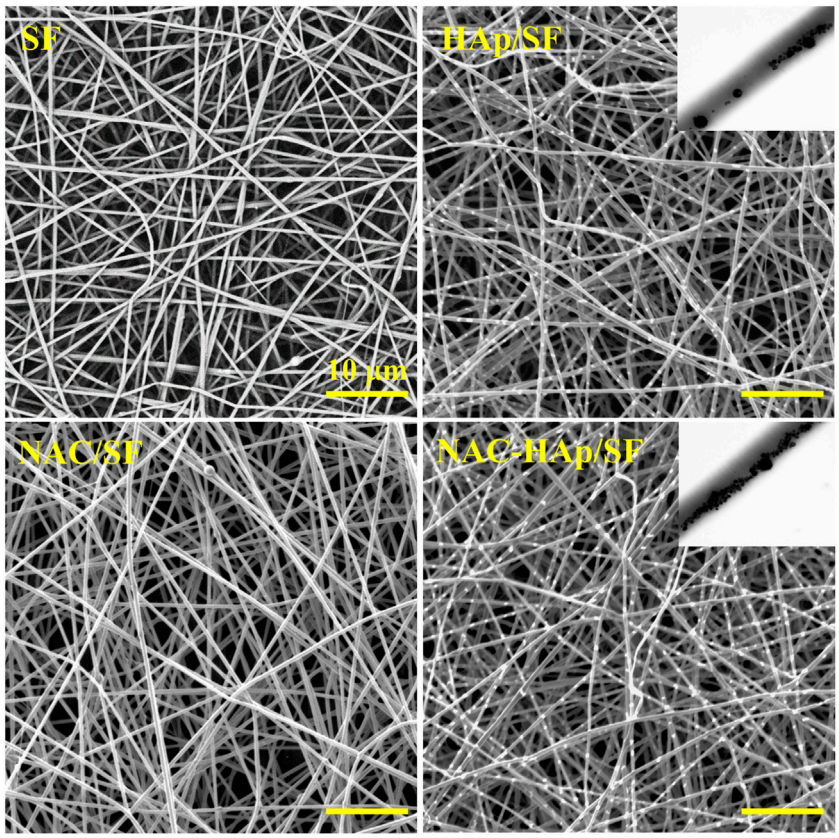


**FIGURE 1 |** SEM images of the pure SF, HAp/SF, NAC/SF, and NAC/HAp/SF scaffolds; the insets are corresponding TEM images.

rats (Shanghai Slac Laboratory Animal Co. Ltd., Shanghai, China) to analyze the efficacy of the nanofibrous HAp/SF scaffold in bone regeneration. Animal care and use protocols were implemented in accordance with the National Institutes of Health (NIH) Guide. The ethical committee of Yangzhou University approved the experimental procedures. Under general anesthesia, the cranium was exposed through a medial incision. The periosteum overlying the calvarial bone was completely resected. A dental bur was used to create a defect with a diameter of 3 mm per mouse. Nanofibrous SF, HAp/SF, NAC/SF, and NAC/HAp/SF scaffolds were implanted in the cranial defects, while the blank group was left untreated. Thirty mice (six in each set) were implanted. The skin was closed with a suture and the defects were analyzed 8 weeks after implantation.

## Computed Tomography (CT) and Bone Mineral Density Analysis

Dual-source CT (SOMATOM Definition, Siemens) was used to detect regeneration and quantify the mineral density of the newly formed bone within the cranial defects. Under general anesthesia, the mouse was fixed and scanned over the entire length at a voxel size of 12 l m and medium resolution of 80 kVp, 110 μA with a 0.5-mm Al filter. The regeneration of bone within the defects was visually identified and the manufacturer's evaluation software was used to separate bone from non-bone and the mineral density of the new bone-like tissue was computed and calibrated to a HAp phantom.

## Statistical Analyses

All quantitative values are expressed as mean ± standard error of at least three replicate samples. An analysis of variance for all quantitative tests was carried out with the software Origin and Tukey's honestly significant difference. *Post hoc* tests were used for pair-wise comparisons between groups. Statistical significance was defined by either $^{*}p < 0.05$ or $^{**}p < 0.01$.

# RESULTS

## Morphology and Physical Properties

Composite fibers were prepared via electrospinning. The morphologies of the different electrospun fibers were observed by SEM (**Figure 1**) and all fibers exhibited a good morphology. White substances appeared on the surface of the fiber because of the aggregation of Hap. The TEM images showed that HAps were encapsulated within the electrospun silk fibers and the diameter of the fibers decreased with the incorporation of NAC and NAC/HAp, which may increase the conductivity and viscosity of the SF fibers,

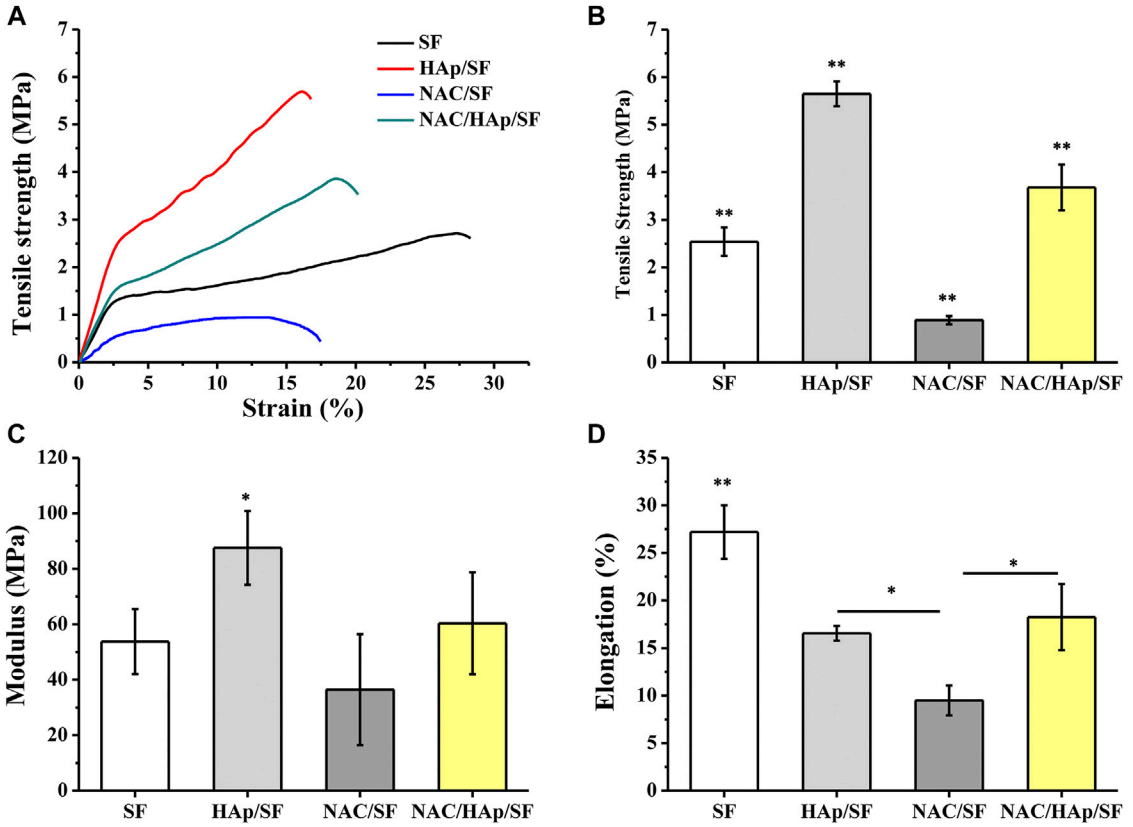


**FIGURE 2 |** Analysis of tensile properties of the composite fibrous scaffolds including typical stress-strain curves **(A)**, tensile strength **(B)**, modulus **(C)** and elongation **(D)**. *$p < 0.05$, **$p < 0.01$, $n = 5$.

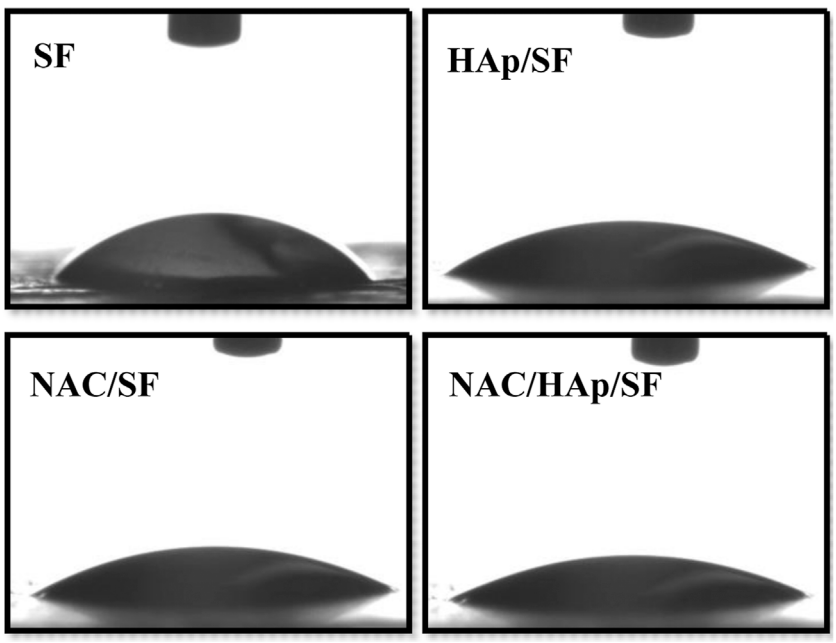


**FIGURE 3 |** Hydrophilic properties of the SF, HAp/SF, NAC/SF, and NAC/HAp/SF composite fiber membranes, $n = 3$.

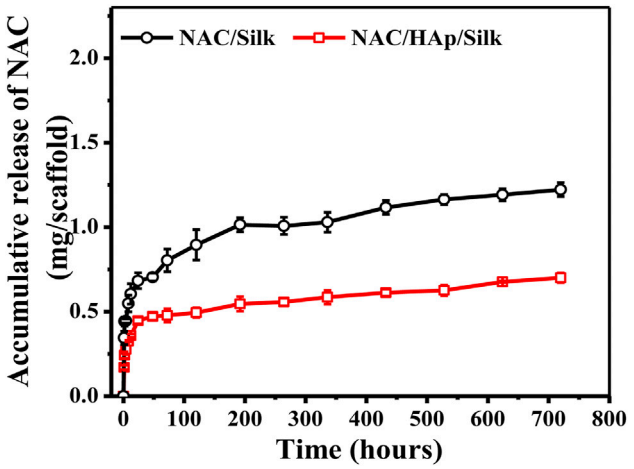


**FIGURE 4 |** NAC release profiles of the NAC/SF and NAC/HAp/SF scaffolds during 0–720 h in a PBS solution, $n = 3$.

consistent with the results of Zhu et al. (2019). Typical tensile stress-strain curves and tensile mechanical properties of composite fiber films are shown in **Figure 2**. The addition of HAp, NAC and NAC/HAp had a significant effect on the mechanical properties of SF fibers. The average Young's modulus and tensile strength of SF fibers were 53.76 ± 11.67 and 2.54 ± 0.30 MPa, respectively. With the addition of HAp, tensile strength and Young's modulus significantly increased. The incorporation of NAC reduced the Young's modulus and the tensile strength to 36.43 ± 19.99 MPa and 0.89 ± 0.09 MPa, respectively. When NAC/HAp were added, the Young's modulus and the tensile strength increases significantly. The rate of elongation rate decreased with the addition of HAp, NAC and NAC/HAp into SF fibers. Generally speaking, the mechanical properties of the fibers were improved by adding NAC/HAp.

## Hydrophilic Properties of Fibers

The hydrophilic angles of the composite fiber membranes were measured to evaluate their hydrophilic properties. Contact angles below 90° are indicative of hydrophilicity, which favors the diffusion of liquid on the materials. In contrast, contact angles exceeding 90° correspond to hydrophobicity (Trinca et al., 2017). The contact angles of NAC/HAp/SF were smaller than those of the other scaffolds (**Figure 3**). Thus the addition of NAC and HAps decreased the contact angle of the material surface through the synergy between NAC, which contains amine and carboxylic functional groups, and HAps, which contain hydroxyl groups.

## Drug Releasing Patterns of the Fiber-Loading Drug

**Figure 4** shows the cumulative release of NAC per Gram of the composite fiber scaffold. The NAC/SF group exhibited an initial burst of release; NAC then became exhausted after a period of time. In contrast, the release of NAC from the NAC/HAp/SF group exhibited a biphasic pattern, characterized by an initial burst of release followed by a long-term, gradual, and continuous release, during which high NAC concentrations were maintained sufficient to promote cell differentiation. In the first stage, the apparent fast release of NAC drugs may have occurred because some of the small NAC molecules dispersed on the surface of the fiber and the inner layer of the fiber *epidermis* during the electrospinning can be released quickly in the PBS buffer solution (Zheng et al., 2013). In the second stage, NAC inside the composite fiber was gradually released. This indicates that HAp exerted an adsorption effect on NAC and also a significant effect on the drug release behavior of NAC.

## Cell Proliferation

The CCK-8 assay was used to detect the proliferation of iPSC-MSCs cultured on composite fiber membranes (**Figure 5**). The cell content in all groups increased with the duration of incubation, which indicates that the cells were in a good state of proliferation. During the process of cell culture, the capacity for cell proliferation of all material groups was higher than that of the coverslip group. Cell proliferation activity was significantly higher in the NAC/SF and NAC/HAp/SF groups than in the control group. This suggests that the addition of NAC and HAps positively affected cell viability.

## Cell Morphology

The proliferation and spreading of iPSC-MSCs on different composite fibers were further observed by SEM (**Figure 6**). After 4 days of culture, the number of adherent cells in the NAC/HAp/SF group was higher than those in the other groups. After 7 days of culture, the number of cells on the fiber increased and the spread of the cells were incorporated with the fiber scaffold. From the perspective of the number of fiber cells, this trend was consistent with the CCK8 results.

## Expression of Osteoblast-Related Genes in Cells

To evaluate the capacity for osteogenic differentiation of iPSC-MSCs on different nanofiber scaffolds, the marker genes of

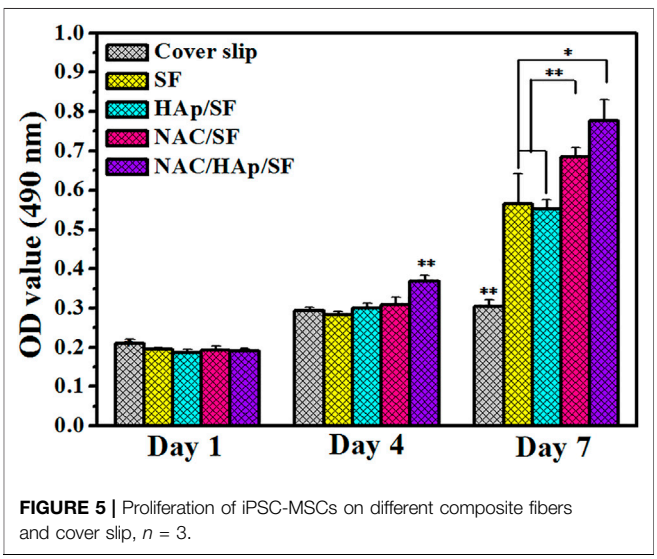


**FIGURE 5 |** Proliferation of iPSC-MSCs on different composite fibers and cover slip, $n = 3$.

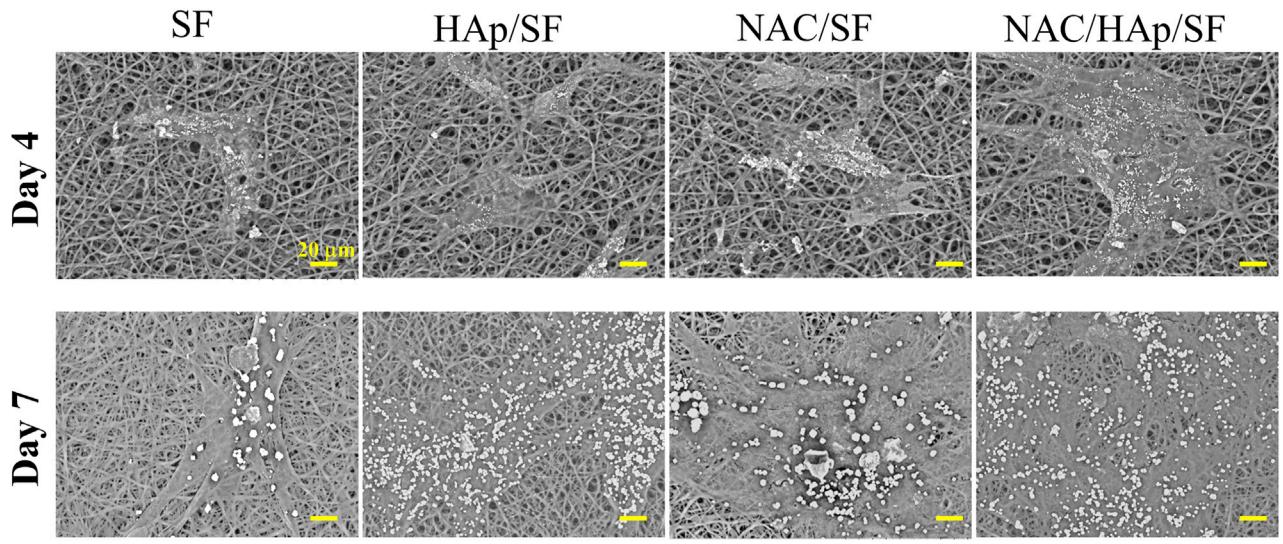


**FIGURE 6 |** Morphological observation of iPSC-MSCs planted on different composite fibers for 4 and 7 days, $n = 3$.

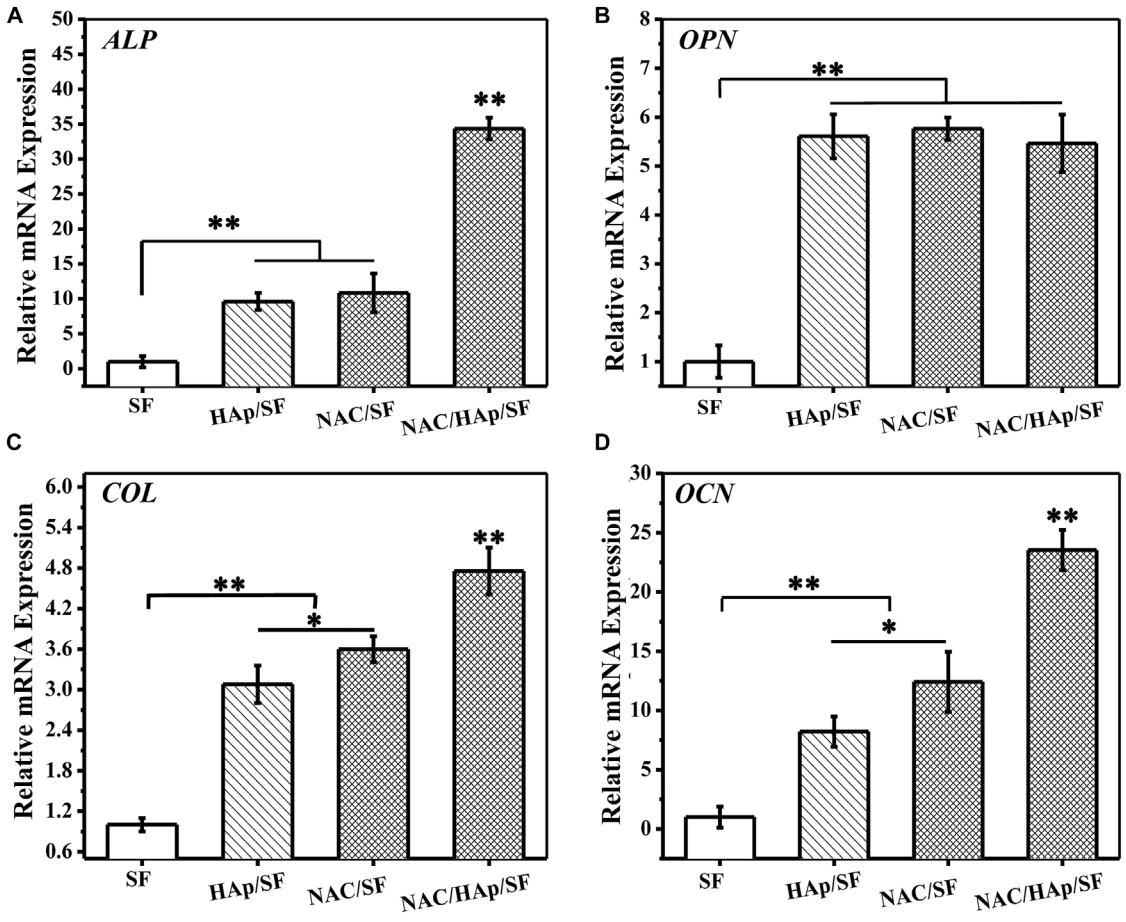


**FIGURE 7 |** Expressions of bone-related genes in iPSC-MSCs on different nanofibers for 14 days, $n = 3$.

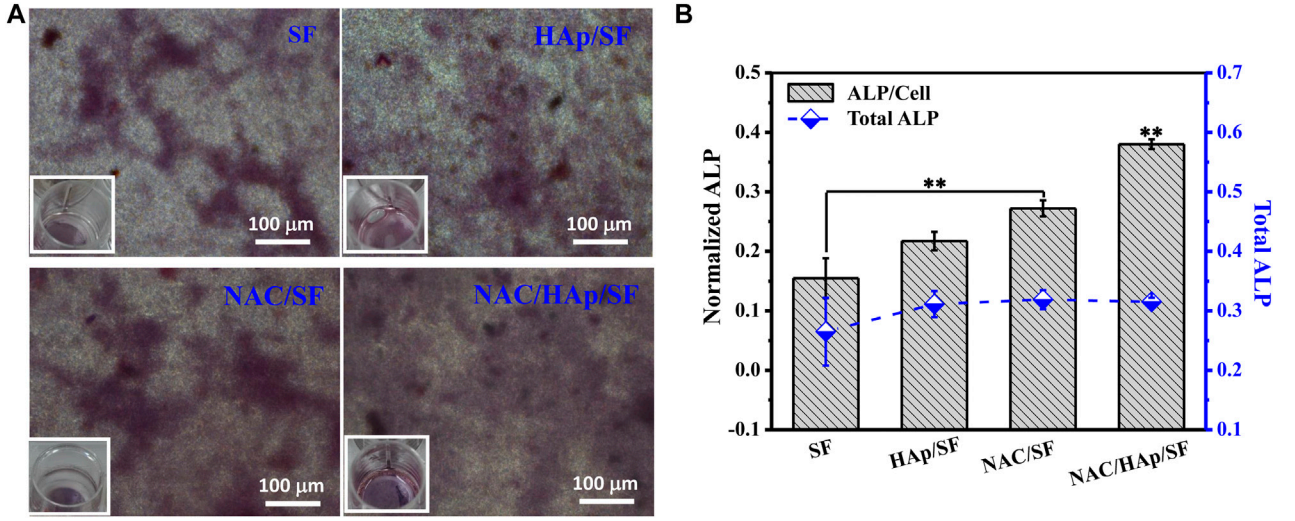


**FIGURE 8 |** ALP staining. **(A)** and quantitative detection of ALP. **(B)** after iPSC-MSC culture on different composite fibers for 14 days, $n = 3$.

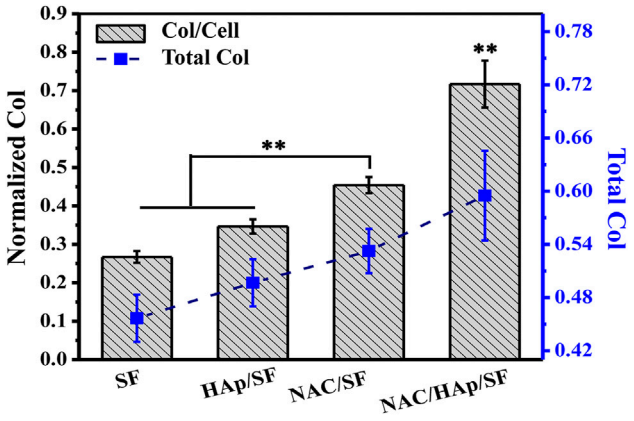


**FIGURE 9 |** Quantitative results of COL after 14 days of culture of iPSC-MSCs on different nanofibers, $n = 3$.

osteogenic differentiation (*ALP*, *COL*, *OCN*, and *OPN*) were detected by RT-PCR. After 14 days of culture, cells in the corresponding culture plate were collected and RNA was extracted for detection. The SF group was used as a control group in this experiment. The expression of *ALP* in the NAC/HAp/SF fibers increased significantly after 14 days (**Figure 7**). This may be explained by the fact that as the fibers promote the osteogenic differentiation of iPSC-MSCs and the cell differentiation process is in the middle and late stages, the content of the early expression product of *ALP* gradually decreases. With the addition of HAp and NAC, the expression levels of *COL* and *OCN* were significantly increased ($p < 0.01$). According to the gene expression level of *OPN*, the addition of HAp increased the level of *OPN* after 14 days of cell culture, while the addition of NAC did not affect the expression of *OPN*. The addition of NAC increased not only the level of expression of *ALP*, but also those of *COL* and *OCN*, the marker genes in the middle and late stages of osteogenesis but had no significant effect on the expression of *OPN*. However, compared to the control group, HAp and NAC complemented each other and promoted the expression of *ALP*, *COL*, *OCN*, and *OPN* genes, thus promoting the osteogenic differentiation of iPSC-MSCs.

## Expression of ALP in Cells

iPSC-MSCs were planted on different composite fibers. After 14 days of culture, ALP staining and quantitative analysis of ALP secreted by cells, including the total amount of ALP and amount of ALP secreted by a single iPSC-MSC, were undertaken. The results are shown in **Figure 8**. The addition of HAp resulted in an increase in the expression of ALP in iPSC-MSCs. The addition of NAC also promoted the expression of ALP in iPSC-MSCs, which indicated that it significantly enhanced the osteogenic differentiation of iPSC-MSCs.

## Expression of COL in Cells

iPSC-MSCs were seeded on composite fibers. After 14 days of culture, collagen was quantitatively examined using a testing kit (**Figure 9**). The detection results were similar to the results of cellular ALP expression. that is, the loading of NAC promoted not only the expression of total cell COL, but also the expression of COL in a single cell. The total COL expression of all cells and expression of COL in single cells on NAC/HAp/SF fibers were significantly higher than those in the other groups. This indicates that the NAC/HAp/SF composite nanofibers had the highest ability to promote collagen production. Thus, the loading of NAC can effectively improve the osteogenic differentiation performance of the fibers.

## *In-vivo* Bone Regeneration

To verify the capability of the biomimetic scaffold of NAC/HAp/SF to regenerate bone *in vivo*, SF, HAp/SF, NAC/SF, and

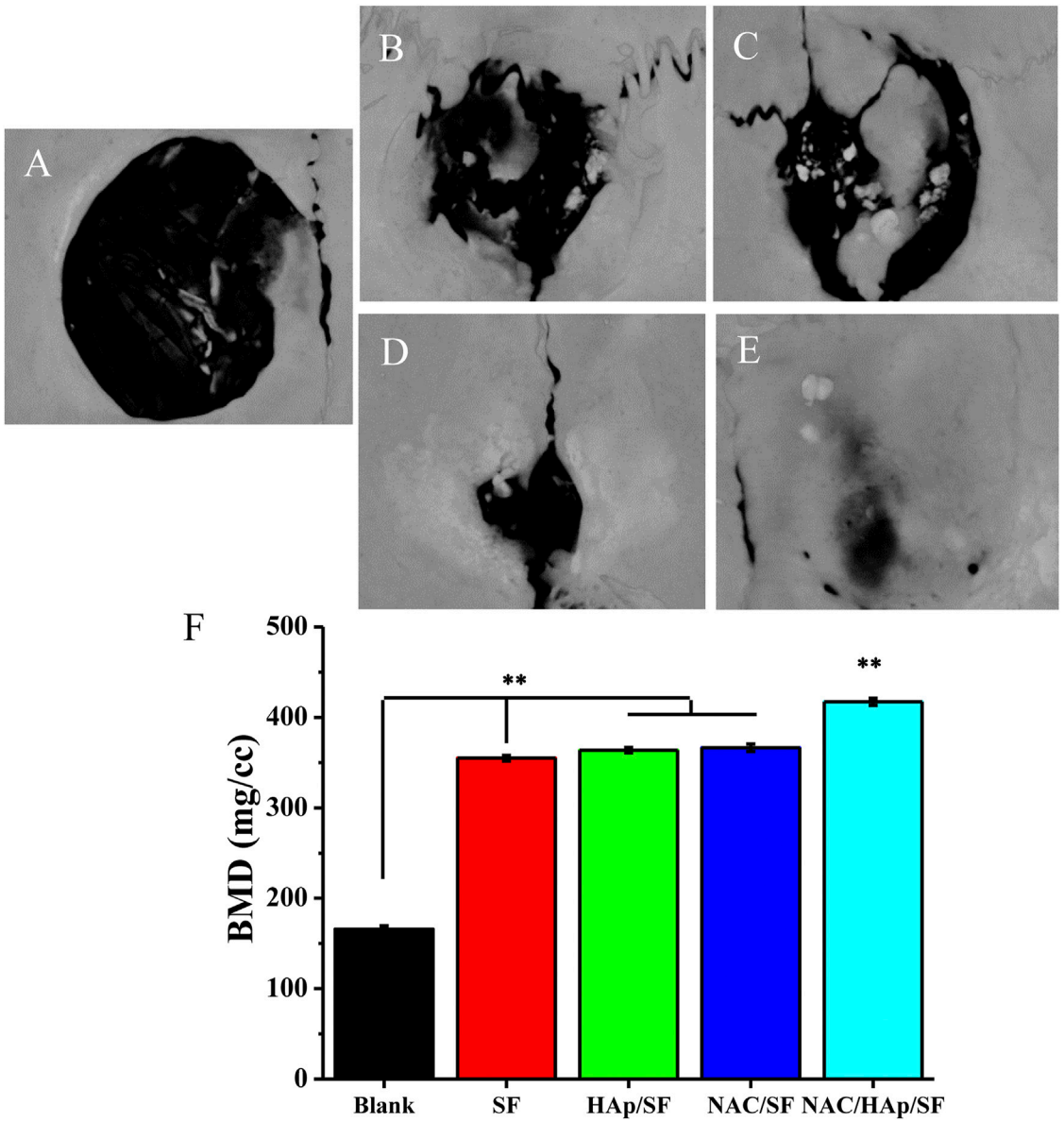


**FIGURE 10 |** CT examination of the whole calvarias **(A–E)** and bone mineral density of the defects **(F)** 8 weeks after implantation *in vivo* **(A)** blank, **(B)** SF, **(C)** HAp/SF, **(D)** NAC/SF, and **(E)** NAC/HAp/SF groups. *$p < 0.05$, **$p < 0.01$, $n = 3$.

NAC/HAp/SF scaffolds were transplanted into calvarial defects in SD rats. After 8 weeks of implantation, CT images demonstrated that the whole defect was almost fully repaired by the formation of bone-like tissues in the NAC/HAp/SF group (**Figure 10**). Moreover, the bone mineral density was significantly increased ($p < 0.01$), peaking at 2.51, 1.18, 1.15, and 1.14 times those of the blank SF, HAp/SF, NAC/SF, and NAC/HAp/SF groups, respectively (**Figure 10F**). Notably, the NAC/HAp/SF scaffold without cells exhibited the highest capacity for repair (**Figures 10A–D**) and highest bone mineral density compared to the other groups (**Figure 10F**). The bone mineral density was higher in the NAC/SF group than in the HAp/SF group, but not significantly. The NAC/HAp/SF led to the best outcomes in regenerating cranial bone defects in rats.

## DISCUSSION

Massive bone defects, defined as critical-size bone defects, can cause delayed union and non-union, and even limb dysfunction. There are several origins of massive bone defects, including trauma, bone tumor resection, and revision arthroplasty (Yamada et al., 2013; Yang et al., 2014).

Numerous small molecules regulate the differentiation and proliferation of various cells (Xu et al., 2008). NAC is a water-

**TABLE 1 |** Primer sequences of bone-related genes.

| Genes | Forward primer sequence (5′-3′) | Reverse primer sequence (5′-3′) |
|---|---|---|
| OCN | CAGTAAGGTGGTGAATAGACTCCG | GGTGCCATAGATGCGCTTG |
| COL | GGTCCCAAAGGTGCTGATGG | GACCAGGCTCACCACGGTCT |
| ALP | GTCCCACAAGAGCCCACAAT | CAACGGCAGAGCCAGGAAT |
| OPN | GCTTCCTGCTCATCAATCGTAAC | TCATCTGCCGACCCTCTTCT |
| GAPDH | GGCAAGTTCAACGGCACAGT | GCCAGTAGACTCCACGACAT |

soluble compound with a low molecular weight. It has antioxidant properties and enhances cytocompatibility (Zafarullah et al., 2003; Watanabe et al., 2018). NAC loaded on a collagenous sponge scaffold can promote bone regeneration by accelerating osteogenesis (Yamada et al., 2013).

SF is a natural biopolymer and promising drug carrier owing to its high biocompatibility, tailorable biodegradability, and low bacterial attachment. SF-based scaffolds have been considered potential carriers for drug delivery (Farokhi et al., 2016; Farokhi et al., 2019; Farokhi et al., 2020). HAp is widely and clinically used to generate bone tissue because of its high-efficiency osteogenesis (He et al., 2012). Scaffolds have an important role in bone tissue generation, particularly electrospun scaffolds, which have good characteristics for applications in drug delivery and bone repair (Xue et al., 2017; Ko et al., 2018).

In this study, we developed an HAp/SF scaffold through electrospinning and NAC was loaded onto the HAP/SF scaffold. We analyzed the optimal amount of NAC in the preparation of fibers and evaluated its physical properties, including the morphology, mechanical properties, and hydrophilic properties. The release of NAC in the NAC/HAp/SF compound scaffold exhibited a biphasic pattern characterized by an initial burst in release followed by a long-term, gradual, and continuous release stage to promote cell differentiation due to high NAC concentrations. In addition, HAp was beneficial to the sustained release of the drug.

The cell compatibility of the NAC/HAp/SF composite fibers was then evaluated. All drug-loaded fibers were beneficial for cell adhesion, spreading, and proliferation. We detected osteogenic differentiation of iPSC-MSCs. At the protein level (ALP and COL) or gene level (*ALP*, *COL*, *OCN*, and *OPN*), the addition of NAC significantly promoted osteogenic differentiation of iPSC-MSCs. NAC and HAp complemented each other and cooperated to promote the expression of *ALP*, *COL*, *OCN*, and *OPN* genes. The NAC/HAp/SF fiber scaffolds exhibited good biocompatibility and safety and induced osteogenic differentiation of iPSC-MSCs.

To further investigate the capacity for osteogenesis of the NAC/HAp/SF scaffold, we implemented cranial bone defects in rats. After 8 weeks, CT imaging confirmed the capacity of the NAC/HAp/SF scaffolds to repair cranial bone defects. The electrospun nanofibrous NAC/HAp/SF scaffold, with an excellent osteo-induction effect, may be ideal for the regulation of osteogenic differentiation of iPSC-MSCs for patient-specific repair and regeneration of bone tissue in the future.

## CONCLUSION

In this study, we formed NAC/HAp/SF scaffolds by electrospinning and analyzed the release of NAC and their ability to promote cell proliferation and osteogenesis. In addition, we detected osteogenesis in NAC/HAp/SF scaffolds in rats. Although satisfactory results were obtained, shortcomings remain. For example, the period of repair of 8 weeks in the rat body is short. Furthermore, the exact mechanism of the effect of the NAC/HAp/SF scaffolds on bone generation is unclear. An extended period of observation and evaluation of the exact mechanism of osteogenesis of the NAC/HAp/SF scaffolds should be performed in further studies.

## DATA AVAILABILITY STATEMENT

The original contributions presented in the study are included in the article/Supplementary Material, further inquiries can be directed to the corresponding authors

## ETHICS STATEMENT

The animal study was reviewed and approved by Yangzhou university.

## AUTHOR CONTRIBUTIONS

XL, FX, SW, QW and HY carried out the concepts, design and manuscript preparation. FX, ZZ and HY carried out the cell experimental and analysis the date. XL, SW, JD, HC, JW and QW carried out the animal experimental and analysis the date. ZZ, JD and HC performed the manuscript review. All authors have read and approved the content of the manuscript.

## FUNDING

This study was supported by National Natural Science Foundation of China (Grants#81801856), Natural Science Foundation of Jiangsu Province (Grants#BK20180949), Jiangsu Provincial Medical Youth Talent (Grants#QNRC2016343), Six Talent Peaks Project of Jiangsu Province (Grants#YY-221, XCL-063) and Key Medical Talent of Yangzhou Public Health Bureau (Grants#2018-6).

## REFERENCES


Banaszynski, L. A., Chen, L.-c., Maynard-Smith, L. A., Ooi, A. G. L., and Wandless, T. J. (2006). A Rapid, Reversible, and Tunable Method to Regulate Protein Function in Living Cells Using Synthetic Small Molecules. *Cell* 126, 995–1004. doi:10.1016/j.cell.2006.07.025

Boccaccini, A. R., and Blaker, J. J. (2005). Bioactive Composite Materials for Tissue Engineering Scaffolds. *Expert Rev. Med. Devices* 2, 303–317. doi:10.1586/17434440.2.3.303

Collignon, A.-M., Lesieur, J., Vacher, C., Chaussain, C., and Rochefort, G. Y. (2017). Strategies Developed to Induce, Direct, and Potentiate Bone Healing. *Front. Physiol.* 8, 927. doi:10.3389/fphys.2017.00927

Du, X., Xie, Y., Xian, C. J., and Chen, L. (2012). Role of FGFs/FGFRs in Skeletal Development and Bone Regeneration. *J. Cel. Physiol.* 227, 3731–3743. doi:10.1002/jcp.24083

Farokhi, M., Mottaghitalab, F., Fatahi, Y., Saeb, M. R., Zarrintaj, P., Kundu, S. C., et al. (2019). Silk Fibroin Scaffolds for Common Cartilage Injuries: Possibilities for Future Clinical Applications. *Eur. Polym. J.* 115, 251–267. doi:10.1016/j.eurpolymj.2019.03.035

Farokhi, M., Mottaghitalab, F., Reis, R. L., Ramakrishna, S., and Kundu, S. C. (2020). Functionalized Silk Fibroin Nanofibers as Drug Carriers: Advantages and Challenges. *J. Controlled Release* 321, 324–347. doi:10.1016/j.jconrel.2020.02.022

Farokhi, M., Mottaghitalab, F., Samani, S., Shokrgozar, M. A., Kundu, S. C., Reis, R. L., et al. (2018). Silk Fibroin/hydroxyapatite Composites for Bone Tissue Engineering. *Biotechnol. Adv.* 36, 68–91. doi:10.1016/j.biotechadv.2017.10.001

Farokhi, M., Mottaghitalab, F., Shokrgozar, M. A., Kaplan, D. L., Kim, H.-W., and Kundu, S. C. (2016). Prospects of Peripheral Nerve Tissue Engineering Using Nerve Guide Conduits Based on Silk Fibroin Protein and Other Biopolymers. *Int. Mater. Rev.* 62, 367–391. doi:10.1080/09506608.2016.1252551

Groeneveld, E., and Burger, E. (2000). Bone Morphogenetic Proteins in Human Bone Regeneration. *Eur. J. Endocrinol.* 142, 9–21. doi:10.1530/eje.0.1420009

He, J., Wang, D., and Cui, S. (2012). Novel Hydroxyapatite/tussah Silk Fibroin/chitosan Bone-like Nanocomposites. *Polym. Bull.* 68, 1765–1776. doi:10.1007/s00289-012-0702-5

Hong, L., Tabata, Y., Miyamoto, S., Yamada, K., Aoyama, I., Tamura, M., et al. (2000). Promoted Bone Healing at a Rabbit Skull Gap between Autologous Bone Fragment and the Surrounding Intact Bone with Biodegradable Microspheres Containing Transforming Growth Factor-B1. *Tissue Eng.* 6, 331–340. doi:10.1089/107632700418056

James, A. W., Lachaud, G., Shen, J., Asatrian, G., Nguyen, V., Zhang, X., et al. (2016). A Review of the Clinical Side Effects of Bone Morphogenetic Protein-2. *Tissue Eng. B: Rev.* 22, 284–297. doi:10.1089/ten.teb.2015.0357

Ko, E., Lee, J. S., Kim, H., Yang, S. Y., Yang, D., Yang, K., et al. (2018). Electrospun Silk Fibroin Nanofibrous Scaffolds with Two-Stage Hydroxyapatite Functionalization for Enhancing the Osteogenic Differentiation of Human Adipose-Derived Mesenchymal Stem Cells. *ACS Appl. Mater. Inter.* 10, 7614–7625. doi:10.1021/acsami.7b03328

Koch, H., Jadlowiec, J. A., and Campbell, P. G. (2005). Insulin-like Growth Factor-I Induces Early Osteoblast Gene Expression in Human Mesenchymal Stem Cells. *Stem Cell Dev.* 14, 621–631. doi:10.1089/scd.2005.14.621

Mayr-Wohlfart, U., Waltenberger, J., Hausser, H., Kessler, S., Günther, K.-P., Dehio, C., et al. (2002). Vascular Endothelial Growth Factor Stimulates Chemotactic Migration of Primary Human Osteoblasts. *Bone* 30, 472–477. doi:10.1016/s8756-3282(01)00690-1

Oikawa, S., Yamada, K., Yamashita, N., Tada-Oikawa, S., and Kawanishi, S. (1999). N-acetylcysteine, a Cancer Chemopreventive Agent, Causes Oxidative Damage to Cellular and Isolated DNA. *Carcinogenesis* 20, 1485–1490. doi:10.1093/carcin/20.8.1485

Ontoria, J. M., Altamura, S., Di Marco, A., Ferrigno, F., Laufer, R., Muraglia, E., et al. (2009). Identification of Novel, Selective, and Stable Inhibitors of Class II Histone Deacetylases. Validation Studies of the Inhibition of the Enzymatic Activity of HDAC4 by Small Molecules as a Novel Approach for Cancer Therapy. *J. Med. Chem.* 52, 6782–6789. doi:10.1021/jm900555u

Sell, S., Barnes, C., Smith, M., Mcclure, M., Madurantakam, P., Grant, J., et al. (2007). Extracellular Matrix Regenerated: Tissue Engineering via Electrospun Biomimetic Nanofibers. *Polym. Int.* 56, 1349–1360. doi:10.1002/pi.2344

Trinca, R. B., Westin, C. B., Da Silva, J. A. F., and Moraes, Â. M. (2017). Electrospun Multilayer Chitosan Scaffolds as Potential Wound Dressings for Skin Lesions. *Eur. Polym. J.* 88, 161–170. doi:10.1016/j.eurpolymj.2017.01.021

Watanabe, J., Yamada, M., Niibe, K., Zhang, M., Kondo, T., Ishibashi, M., et al. (2018). Preconditioning of Bone Marrow-Derived Mesenchymal Stem Cells with N-Acetyl-L-Cysteine Enhances Bone Regeneration via Reinforced Resistance to Oxidative Stress. *Biomaterials* 185, 25–38. doi:10.1016/j.biomaterials.2018.08.055

Xu, Y., Shi, Y., and Ding, S. (2008). A Chemical Approach to Stem-Cell Biology and Regenerative Medicine. *Nature* 453, 338–344. doi:10.1038/nature07042

Xue, J., Xie, J., Liu, W., and Xia, Y. (2017). Electrospun Nanofibers: New Concepts, Materials, and Applications. *Acc. Chem. Res.* 50, 1976–1987. doi:10.1021/acs.accounts.7b00218

Yamada, M., Tsukimura, N., Ikeda, T., Sugita, Y., Att, W., Kojima, N., et al. (2013). N-acetyl Cysteine as an Osteogenesis-Enhancing Molecule for Bone Regeneration. *Biomaterials* 34, 6147–6156. doi:10.1016/j.biomaterials.2013.04.064

Yang, X., Li, E., Wan, Y., Smith, P., Shang, G., and Cui, Q. (2014). Antioxidative Fullerol Promotes Osteogenesis of Human Adipose-Derived Stem Cells. *Int. J. Nanomedicine.* 9, 4023–4031. doi:10.2147/ijn.s66785

Zafarullah, M., Li, W. Q., Sylvester, J., and Ahmad, M. (2003). Molecular Mechanisms of N -acetylcysteine Actions. *Cell Mol. Life Sci. (Cmls)* 60, 6–20. doi:10.1007/s000180300001

Zheng, F., Wang, S., Wen, S., Shen, M., Zhu, M., and Shi, X. (2013). Characterization and Antibacterial Activity of Amoxicillin-Loaded Electrospun Nano-Hydroxyapatite/poly(lactic-Co-Glycolic Acid) Composite Nanofibers. *Biomaterials* 34, 1402–1412. doi:10.1016/j.biomaterials.2012.10.071

Zhu, Y., Gu, Y.-x., Mo, J.-j., Shi, J.-y., Qiao, S.-c., and Lai, H.-c. (2015). N-acetyl Cysteine Protects Human Oral Keratinocytes from Bis-GMA-Induced Apoptosis and Cell Cycle Arrest by Inhibiting Reactive Oxygen Species-Mediated Mitochondrial Dysfunction and the PI3K/Akt Pathway. *Toxicol. Vitro* 29, 2089–2101. doi:10.1016/j.tiv.2015.09.002

Zhu, Y., Song, F., Ju, Y., Huang, L., Zhang, L., Tang, C., et al. (2019). NAC-loaded Electrospun Scaffolding System with Dual Compartments for the Osteogenesis of rBMSCs *In Vitro*. *Nt J. Nanomedicine* 14, 787–798. doi:10.2147/ijn.s183233


**Conflict of Interest:** The authors declare that the research was conducted in the absence of any commercial or financial relationships that could be construed as a potential conflict of interest.

frontiers in Bioengineering and Biotechnology

ORIGINAL RESEARCH
published: 28 January 2022
doi: 10.3389/fbioe.2021.840421

# Nerve Decellularized Matrix Composite Scaffold With High Antibacterial Activity for Nerve Regeneration

*Yan Kong, Di Wang, Qufu Wei* and Yumin Yang**

*Key Laboratory of Eco-Textiles, Ministry of Education, College of Textile Science and Engineering, Jiangnan University, Wuxi, China*

Nerve decellularized matrix (NDM) has received much attention due to its natural composition and structural advantages that had proven to be an excellent candidate for peripheral nerve regeneration. However, NDM with simultaneous biocompatibility, promoting nerve regeneration, as well as resistant to infection was rarely reporter. In this study, a porous NDM-CS scaffold with high antimicrobial activity and high biocompatibility was prepared by combining the advantages of both NDM and chitosan (CS) in a one-step method. The NDM-CS scaffold possessed high porosity and hydrophilicity, exhibited excellent biocompatibility which was suitable for cell growth and nutrient exchange. Meanwhile, NDM-CS scaffold had a significant antibacterial effect on both *Escherichia coli* (*E. coli*) and *Staphylococcus aureus* (*S. aureus*), which could avoid wound infection during the repair process. In addition, the NDM-CS scaffold could support the growth and viability of Schwann cells effectively. Among them, the E2C1 group had the strongest ability to enhance proliferation, polarization and migration of Schwann cells among the three groups. The positive effect on Schwann cells indicated their ability in the process of nerve injury repair. Therefore, this NDM-CS scaffold may have potential prospects for application in neural tissue engineering.

**Keywords: nerve decellularized matrix, chitosan, antibacterial, nerve regeneration, schwann cells**

OPEN ACCESS

***Edited by:***
*Jingan Li,*
*Zhengzhou University, China*

***Reviewed by:***
*Xiao Luo,*
*University of Electronic Science and Technology of China, China*
*Shuo Wang,*
*Northwestern Polytechnical University, China*
*Feng Wu,*
*Xuzhou University of Technology, China*

****Correspondence:***
*Qufu Wei*
*qfwei@jiangnan.edu.cn*
*Yumin Yang*
*yangym702@163.com*

***Specialty section:***
*This article was submitted to Biomaterials, a section of the journal Frontiers in Bioengineering and Biotechnology*

***Received:*** *21 December 2021*
***Accepted:*** *30 December 2021*
***Published:*** *28 January 2022*

***Citation:***
*Kong Y, Wang D, Wei Q and Yang Y (2022) Nerve Decellularized Matrix Composite Scaffold With High Antibacterial Activity for Nerve Regeneration. Front. Bioeng. Biotechnol. 9:840421. doi: 10.3389/fbioe.2021.840421*

## INTRODUCTION

Tissue engineering nerve scaffolds have aroused the interest of researchers because of their potential to replace autologous nerves (Jahromi et al., 2019). The ideal tissue engineering nerve scaffold mainly contains three elements: biomaterials, supporting cells and growth factors (Yi et al., 2019). As the most important factor in nerve scaffolds, suitable biomaterials have always been the key to investigate. Superior biomaterials could provide a suitable microenvironment for cell growth, as well as three-dimensional spatial structure, hydrophilic and antibacterial properties, etc. The three-dimensional structure of the nerve scaffold could provide enough pores and a staggered structure as growth space. The three-dimensional structure simulates the structure of the extracellular matrix, and the appropriate pores are conducive to the exchange of nutrients. Many tissue-engineered neural scaffolds based on natural or synthetic materials were composed of polymer materials (Ghane et al., 2021; Lu et al., 2021). Natural materials are more suitable than synthetic materials due to their biocompatibility, degradability, and potential hazards (Yang et al., 2007; Li et al., 2019). Another major problem after nerve scaffold implantation was bacterial infection (Tang et al., 2021a).

Contamination during the procedure and recovery leads to increased use of antibiotics, which directly affects the outcome of nerve regeneration. Antibiotics or silver nanoparticles have been added to composite scaffolds as a slow-release agent to achieve an antimicrobial effect (Lan et al., 2014; Craciunescu et al., 2021). However, due to the short and unstable antibacterial effect of antibiotics or other antibacterial agents in the body, researchers are more inclined to look for a biological material with good antibacterial effect. Therefore, fabricating a nerve scaffold with good biocompatibility that could reproduce the natural nerve growth microenvironment and also possess natural antimicrobial properties is urgently needed in clinical practice.

The tissue decellularized matrix is an excellent natural material that could retain the natural extracellular matrix components intact. It is non-toxic, non-immunogenic and has reliable regeneration-promoting abilities, and thus was widely studied (Tao et al., 2021a; Rafaeva et al., 2021). Moreover, tissue decellularized matrix was considered as a candidate to replace autologous tissue in future clinical applications. It has been demonstrated that the deuterogenic materials derived from tissue decellularized matrix were used for the repair of bones (Qiu et al., 2020), skin (Xu et al., 2021), retina (Maqueda et al., 2021), nerves (Rao et al., 2021), muscles (Cheng et al., 2020), and other tissues and organs (Tao et al., 2021b; Wu et al., 2022). Moreover, the tissue decellularization matrix could induce direct differentiation of stem cells (Han et al., 2019). However, the decellularized matrix in per se did not have antibacterial properties and its effectiveness against postoperative infection was insufficient.

Chitosan (CS) with antibacterial function was a product of natural chitin deacetylation (Ke et al., 2021). CS has a positive charge, which can adsorb negatively charged bacteria and prevent bacterial transport across the membrane (Li and Zhuang, 2020). In addition, chitosan possesses excellent mechanical properties and provides stable mechanical strength for tissue engineering scaffold materials. CS had been certified as a valuable medical material and was widely used in various fields. The positive effects of chitosan and its degradation products on nerve injury repair have been confirmed (Wang et al., 2016; Boecker et al., 2019).

In this study, a facile method was developed to construct porous NDM-CS scaffolds that simulates the natural neural microenvironment with high antibacterial properties by a freeze-drying technique. The three-dimensional structure of the composite scaffolds were observed by scanning electron microscopy. Infrared spectroscopy and BCA Protein Assay Kit were used to analyze the composition of the scaffolds. The contact angle and porosity of the scaffolds also were tested. In addition, the antimicrobial properties of the scaffolds were evaluated by culturing the growth of *E. coli* and *S. aureus in vitro*. Cell culture experiment also demonstrated the excellent biocompatibility and ability of the NDM-CS scaffolds to promote the growth of Schwann cells. This study may provide a reasonable and reliable solution for future clinical applications of neural scaffolds.

# MATERIALS AND METHODS

## Preparation of NDM

The nerves were decellularized according to the existing method in this study (Lin et al., 2018). Fresh sciatic nerves were decellularized by repeatedly shaking in 4% Triton X-100 for 6 h and in 4% sodium deoxycholate for 12 h at 4°C. Then the decellularized sciatic nerves were rinsed with ethanol for 1 h. Afterward, the nerve was divided into small segments for lyophilization. Finally, the lyophilized decellularized matrix was ground into a powder.

## Preparation of NDM-CS Scaffolds

The NDM-CS hybrid lyophilized scaffold was prepared by the freeze-drying method. NDM and CS were dissolved separately and then mixed well before lyophilization. An 0.01 M hydrochloric acid solution of 2 mg/ml of pepsin was prepared which was used to dissolve the lyophilized neural decellularized matrix powder. The concentration of the decellularized matrix was 20 mg/ml dissolved with the acid solution at 37°C for 48 h. After the decellularization matrix was fully dissolved, 0.1 M sodium hydroxide solution was added to adjust the pH of the decellularization solution to neutral. 5% chitosan was fully dissolved in 2% aqueous acetic acid solution. Then three mass ratios of NDM:CS = 1:2, NDM:CS = 1:1 and NDM:CS = 2:1 (v/v) was prepared to fabricate mixed lyophilized scaffolds respectively. For ease of reference, the NDM:CS = 1:2, NDM:CS = 1:1 and NDM:CS = 2:1 were named as E1C2, E1C1 and E2C1 respectively. 400 μL of the mixed solution of different proportions were added to each well of the 24-well cell culture plate. After freeze-drying for 48 h, the three groups of mixed scaffolds were cross-linked with EDC:NHS = 1:2 ethanol solution for 24 h. And then the scaffolds were rinsed with 2% sodium hydroxide and PBS respectively. Finally, the scaffolds were lyophilized for 48 h again. **Figure 1** shows the summary of the preparation process of the NDM-CS scaffolds and the overall experiment.

## Rheological Analysis

The viscosity properties of the NDM-CS solutions were tested to evaluate the differences in compositional changes between the three groups. The NDM solution and CS solution were mixed adequately at 4°C in different proportions firstly. Then 1 ml of each solution was pipetted out and added to the rheometer test platform. The experiments were conducted on a Rheometer (RheoWin MARS40, Thermo Fisher Scientific, USA) with parallel-plate (35 mm diameter) geometry at 25°C. Dynamic viscosity was tested at a 1 mm gap from 0.1 $s^{-1}$ to 300 $s^{-1}$ for 300 s.

## Morphological Observation

The morphology of the NDM-CS freeze-dried scaffolds was observed by scanning electron microscopy. 400 uL of three ratios of mixed solutions were added to the 24-well plate each well. The scaffolds were cut crosswise after being fully lyophilized. The scaffolds were observed from surface and cross-section

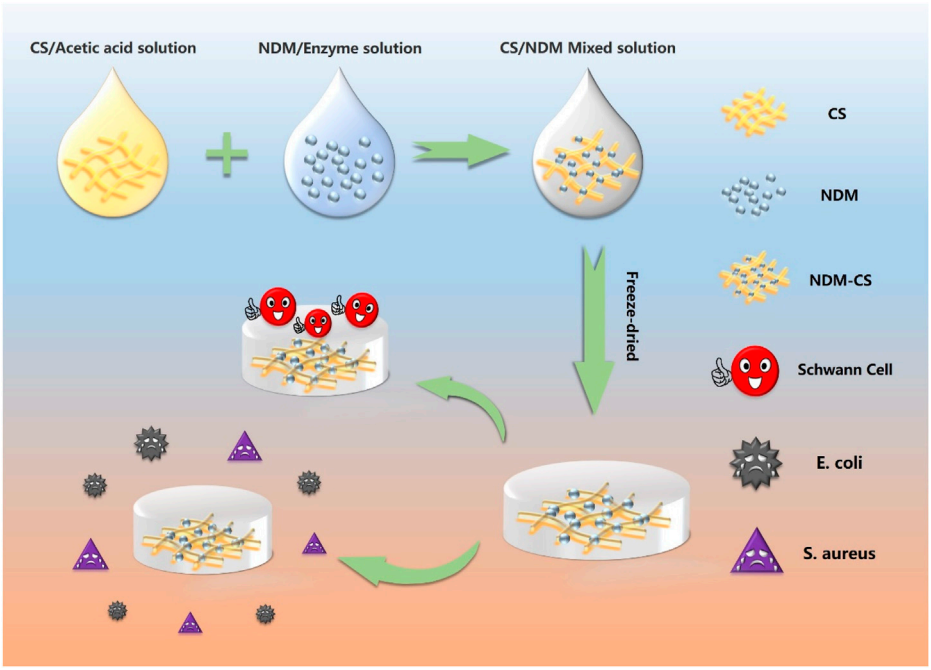


**FIGURE 1 |** Schematic illustration of the preparation of NDM-CS composite scaffold and the experiment.

respectively. The lyophilized scaffolds were fixed on the electron microscope carrier table, and observed after being gold plated on the material surface. Three parallel samples were set up for each group.

## Fourier Transform Infrared Analysis

Fourier transforms infrared (FTIR) spectra was used to analyze composition in scaffolds with tablets containing samples and KBr (KBr/sample ≈ 100). After the three NDM-CS scaffolds were lyophilized, a small portion of each scaffold was taken out and fully crushed with KBr (KBr/sample ≈100). After that, the mixed powder was pressed into slides under high pressure. The FTIR spectra were recorded from 4,000 to 500 $cm^{-1}$. All tests have proceeded with humidity around 65% and at room temperature.

## Protein Content Detection

The BCA method was used to detect the content of NDM in the scaffolds. The NDM-CS solution was lyophilized in a 24-well plate, and then 3 ml of BCA working solution was added to each well. The scaffolds and BCA solution were incubated for 30 min at 37°C. At the end of the reaction, 200 μL of BCA reaction solution was aspirated from each group and the absorbance was measured at 562 nm.

## Porosity Detection

The ethanol substitution method was used to determine the porosity of NDM-CS scaffolds (Chen et al., 2020a). The total volume of ethanol origination was recorded as $V_0$. The scaffolds were freeze-dried in 24-well plate with 400 μL solution, then were immersed into the ethanol and put under the pressure of 0.08 MPa for 1 min. The total volume of ethanol and the scaffolds at this time was recorded as $V_1$. Then the scaffolds were taken out of the ethanol and the remaining ethanol was recorded as $V_2$. The porosity was calculated by the following formula:

$$(V_0 - V_2)/(V_1 - V_2) \times 100\%$$

## Hydrophilic Property

The hydrophilicity of NDM-CS scaffolds was detected by the contact angle. The smaller the contact angle, the better the hydrophilicity of the material. The three groups of NDM-CS composite scaffolds were lyophilized in 24-well plates. Then all the NDM-CS composite scaffolds were taken out from 24-well plates and placed on the test bench of the contact angle instrument (JYPHa, Chengde, China) under the dry conditions. The contact angles of the scaffold were measured by the wetting of the droplets on the scaffolds. Five parallel samples were set for each group of materials. All samples were performed at room temperature and around 65% humidity. In this study, the contact angles of droplets were examined at the beginning of contact with the material and after 30 s of contact respectively.

## *In Vitro* Antibacterial Experiment

The antibacterial experiment *in vitro* was referred to the common experimental methods (Tang et al., 2021b). 100 μL of *E. coli* and *S. aureus* (≈$10^4$ CFU/ml) (China Microbial Culture Collection, China) were incubated with the freeze-dried scaffolds at 37°C for 4 h. Then 900 μL of phosphate-buffered saline (PBS) was added to resuspend *E. coli* and *S. aureus*. 100 μL of the resuspended *E. coli* and *S. aureus* solution were spread on a

solid LB agar medium plate respectively. The colonies formed were counted after culturing for 24 h. The calculation formula of bacterial kill rate was:

$$\text{Kill\%} = C_0 - C/C_0 \times 100\%$$

C indicates the CFU of the scaffolds and $C_0$ indicates the CFU of the control group inoculated on a blank plate.

## Cytotoxicity Test

Firstly, each group of scaffolds was sterilized by ultraviolet light and 75% ethanol for 30 min respectively. The scaffolds were immersed in basal medium for 48 h under 37°C sterile conditions. Then 10% fetal bovine serum (FBS, Gibco, USA) was added into the extraction medium of each group for culturing L929 cells. $1 \times 10^4$ cells/mL were cultured in each well of the 96-well plate with 200 μL. And there were five replicate wells for each group. The normal culture medium group served as the control group. After being cultured for 24 h in a cell incubator, 20 μL MTT was added to each well and then incubated for another 4 h in the dark condition. Then all the culture solution was discarded and 200 μL dimethyl sulfoxide (DMSO, Sigma-Aldrich, USA) was added to incubate for 30 min. Then the absorbance at 570 nm of each well was measured by an enzyme-labeled instrument.

## The Viability and Morphology of Schwann Cells

The RSC96 cells in this experiment were obtained from the Center for Excellence in Molecular Cell Science, Chinese Academy of Sciences. The DMEM infusion of NDM-CS scaffolds was used to culture Schwann cells. Firstly, the DMEM infusion of three scaffolds was added with 10% FBS and 1% penicillin-streptomycin antibiotic to configure the complete culture medium. Then RSC96 cells were resuspended with the complete medium above. 0.5 ml of RSC96 cell suspension was added dropwise to each of the three sets of NDM-CS scaffolds and incubated in a cell incubator.

The viability of RSC96 cells was assayed by the cck-8 method after 1 and 2 days of incubation. The cell culture solution was discarded firstly and 1 ml of cck-8 working solution (cck-8: complete medium = 1:10) was added to each well. Then the incubation was continued for 4 h. Finally, the absorbance value at 450 nm of each group of cck-8 working solution was detected.

The samples were washed once with PBS and the cells were fixed with 4% paraformaldehyde for 4 h subsequently. Fluorescent blocking solution was added overnight for 4 h after PBS rinsing. Afterward, RSC96 was specifically labeled with fluorescent dyes phalloidin and observed under a microscope.

## Migration of Schwann Cells

The study used Ibidi chambers to form stable wounds to study the migration of Schwann cells. Sterile ibidi chambers adhered to the bottom of cell culture plates. Afterwards, 80 μL of RSC96 cell suspension (complete medium) was added to the ibidi chambers. The ibidi chambers were removed after being incubated in a cell culture incubator for 12 h. Then serum-free DMEM was added to the wells. Photographs were taken and recorded as the 0 h at this time. After that, pictures were taken after 6, 12 and 24 h of incubation respectively.

## Statistical Analysis

Statistical analyses of all data (mean ± SEM) were performed using GraphPad prism 8. Comparisons across three groups and two groups used one-way analysis of variance (ANOVA) testing and two-tailed *t*-test where a $p$-value $< 0.05$ was considered significant respectively. Sample sizes are indicated in figure legends.

# RESULTS AND DISCUSSION

## Viscosity of the Mixed Solution

The viscosity of the mixed solutions with different ratios was analyzed by rheometry (**Figures 2A–C**). The results revealed that the viscosity of all mixed solutions showed property of shear-thinning as the shear rate increased. The E1C2 group showed the greatest degree of shear-thinning, while the E2C1 group showed the least degree of shear-thinning. This phenomenon was mainly caused by chitosan. The shear-thinning behavior was more obvious with the increasing amount of chitosan solution. **Figure 2D** shows the average viscosity of the three mixed solutions. It showed that the viscosities of the E1C2, E1C1 and E2C1 groups were 0.047, 0.015 and 0.009 Pa·s respectively. There were significant differences among them. The trend of viscosity changes was consistent with the trend of shear-thinning which indicated that the effect of chitosan solution on viscosity change was significant. Also, the phenomenon reflected the good mechanical properties of chitosan, which played a good role in supporting the stability of the scaffold.

## Morphological Observation

The three groups of mixed scaffolds with different ratios did not differ from each other under the macroscopic and microscopic state (**Figure 3**). **Figure 3A** showed the macroscopic morphology of three groups of NDM-CS scaffold. All groups appeared white spongy. Scanning electron micrographs allowed clearer observation of the morphology of the three groups of scaffolds. Both the surface and the cross-section showed a clear pore structure under the observation of scanning electron microscope (**Figure 3B**). All groups showed a lamellar structure of lyophilized chitosan on the surface which were densely and uniformly distributed. And the cross-section could be observed which possessed a honeycomb-like three-dimensional pore structure. In the magnified SEM photographs, it could be found that there were thin layers or agglomerates with small size and pores between the chitosan lamellar structures or on the surface of each group of scaffolds (pointed by the yellow arrow). This fine structure which was different from chitosan could be observed in the cross-section of the scaffolds too. Moreover, this structure increased with ascending NDM concentration. The agglomerates were supposed to be formed after lyophilization of neural decellular matrix protein. This result indicated that the

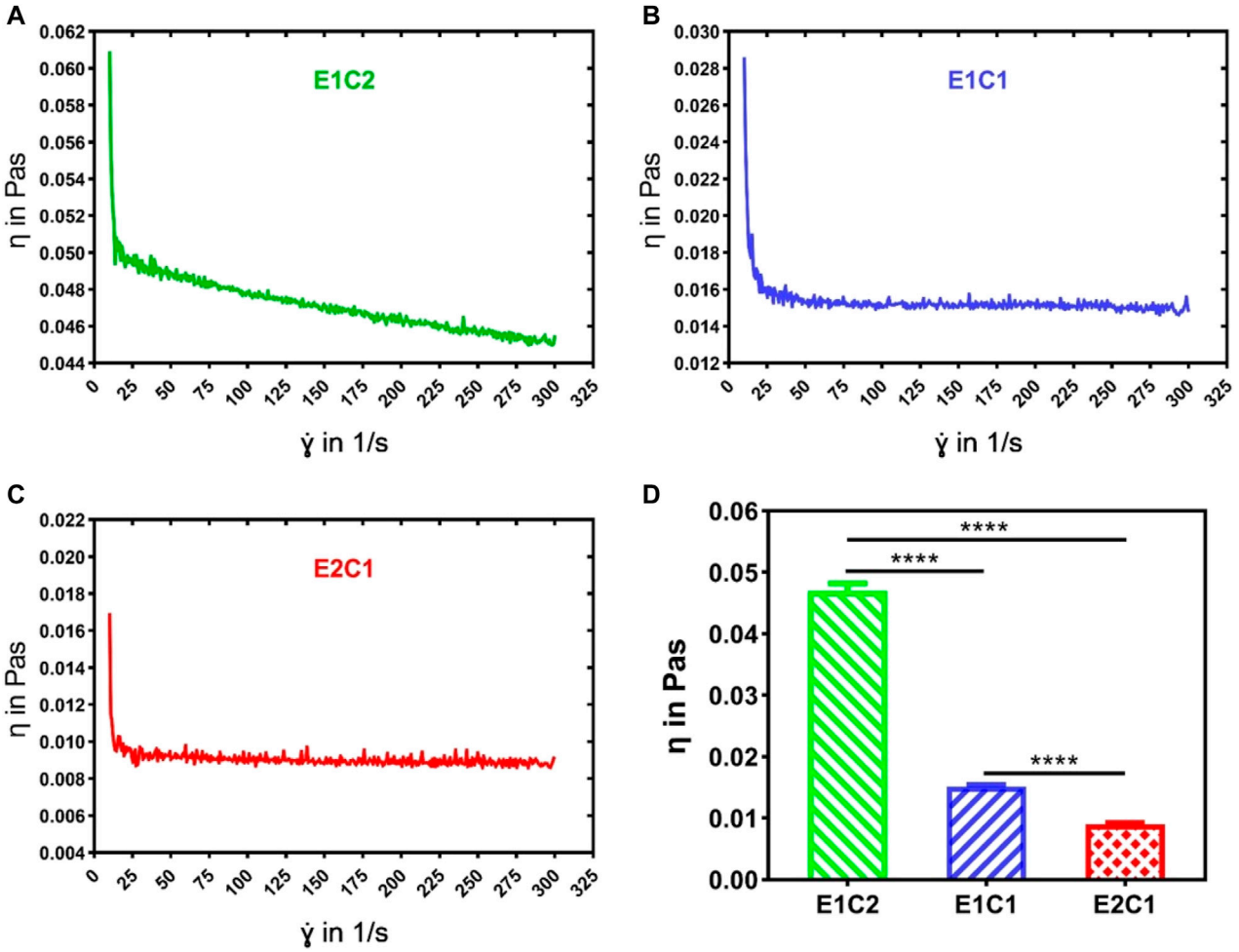


**FIGURE 2 |** The viscosity curves of the three mixed solutions were detected by the rheometer: **(A)** E1C2, **(B)** E1C1, **(C)** E2C1, **(D)** Statistical results of the viscosity of the three mixed solutions. ****$p < 0.0001$.

neural decellular matrix was successfully cross-linked with chitosan.

## FTIR Analysis

The changes in the composition of the hybrid scaffold were analyzed by FTIR detection. **Figure 4A** shows the FTIR curves of the four groups of scaffolds. The pure CS scaffold was used as a control. The FTIR curves of the four materials were almost identical. In all groups, the peak of the stretching vibrations of the O-H and N-H groups could be found near 3,432 $cm^{-1}$. The C-H stretching band and the stretching vibrational band of C-O could also be observed near 2,920 $cm^{-1}$ and 1,080 $cm^{-1}$ respectively. However, besides the CS group, the other three hybrid scaffolds had a typical distinct C=O stretching peak of dECM at around 1745 $cm^{-1}$ (Xu et al., 2021). In addition, the peak area of C=O stretching became more and more obvious as the NDM concentration increased (**Figure 4B**). Such results indicated that the NDM-CS scaffold did contain the NDM protein component. And the change of the characteristic peak of C = O also reflected the change of the concentration of NDM contained in the scaffold. Thus, it was verified that the neural decellularized matrix protein and chitosan were successfully bound together.

## NDM Protein Content

The infrared analysis only gave a qualitative insight into the presence of neural decellular matrix in the hybrid scaffolds. Protein concentration assay was performed to further verify the changes in the NDM ratio in the three sets of scaffolds (Dong et al., 2020). **Figure 5A** demonstrates the formation of purple complexes in the three groups of hybrid scaffolds after adsorption of the protein reaction solution. It was shown that the E1C2 group had the lightest purple color while the E2C1 group had the darkest purple color. In addition, the absorbance comparison results of the protein reaction solution at 562 nm for the three groups of materials showed the same trend (**Figure 5B**). The absorbance value of E1C2 was the smallest at 0.079 while the absorbance of E2C1 group was the largest at 0.17. The absorbance of E1C1 group was 0.12 which was between the other two groups. And there was a significant difference

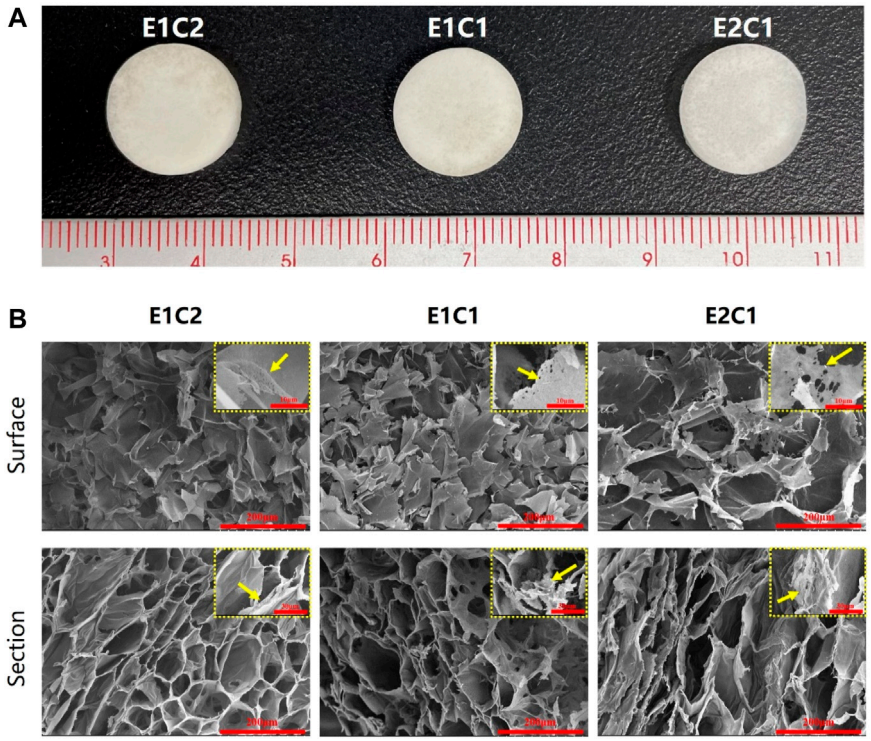


**FIGURE 3 |** Observation of the NDM-CS scaffolds. **(A)** The macroscopic state of NDM-CS composite scaffolds. **(B)** Scanning electron microscope observation of the surface and cross-section of NDM-CS scaffolds.

between all three groups. These results proved that the concentration of NDM was completely different in the three hybrid scaffolds. the amount of NDM in E2C1 was the most and twice as much as that in E1C2. The amount of NDM in E1C1 was 1.5 times more than that in E1C2. This was fully consistent with the ratio change of the three hybrid scaffold designs.

## Porosity of the Scaffolds

Porosity refers to the percentage of the pore volume in the total volume of the material in its natural state. A certain porosity is conducive to the exchange of nutrients and beneficial to cell growth and hyperplasia (Zhu et al., 2015; Ardeshirylajimi et al., 2018).

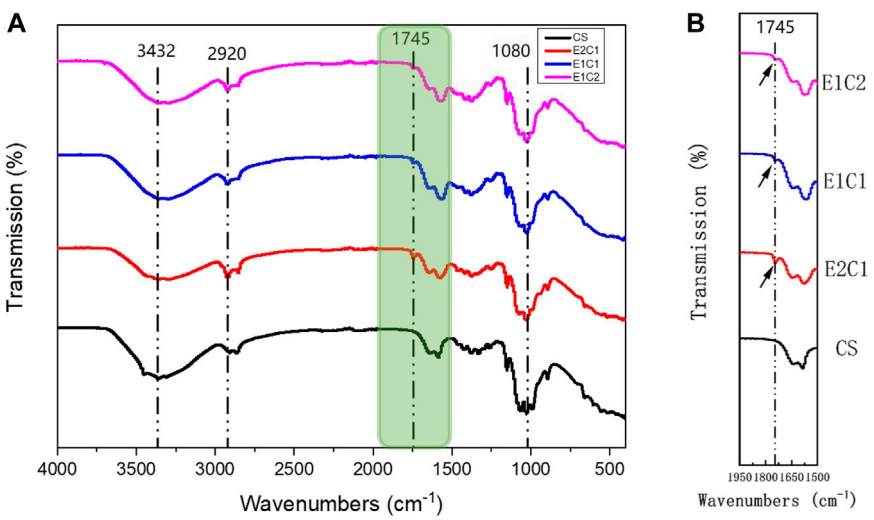


**FIGURE 4 |** FTIR analysis of the scaffolds. **(A)** Detection curve from 500 $cm^{-1}$ to 4,000 $cm^{-1}$. **(B)** Enlarged view of the green area in the FTIR curve.

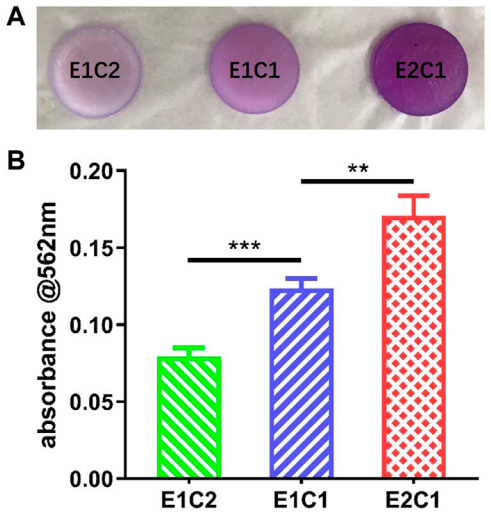


**FIGURE 5 | (A)** Macrophotographs of different scaffolds after BCA reaction. **(B)** The OD value of the BCA reaction solution at 562 nm $^{**}p < 0.01$, $^{***}p < 0.001$.

The results in **Figure 6** shows the porosity of the three groups of hybrid scaffolds. The porosity of all three groups was above 80% and did not differ from each other which indicates that although there were slight differences in the three groups of scaffold components, it did not affect the overall porosity. All groups of scaffolds had enough three-dimensional pores to meet the infiltration and exchange of nutrients and air, which could provide a suitable growth environment for cells.

## Wettability Analysis

The surface hydrophilicity results of the three groups of NDM-CS scaffolds are shown in **Figure 7**. The contact angles of droplets were measured when they touched the surface of the scaffolds at the beginning and 30 s later (**Figure 7A**). When the droplets contacted the surface of the NDM-CS scaffolds, they showed a round spherical shape. However, they were not stable after contact with NDM-CS interestingly. The shape of the droplets changed from round spheres to hemispheres and eventually spreads flat on the scaffold surface. The change in droplet shape indicated that the liquid gradually infiltrated the surface of the material. The contact angle also became significantly smaller during this gradual change. In about 30 s, all droplets on the scaffolds were almost infiltrated into the material, and the contact angle decreased significantly. The contact angle was counted for each of the two states of the droplets. It could be found that the contact angles of all three groups were greatly larger than 90 degrees at the beginning (**Figure 7B**). The contact angles of E1C2, E1C1 and E2C1 were 96.57° ± 7.457°, 103° ± 1.537° and 107.3° ± 2.051° respectively, and there was no difference between the three groups. This indicated that the surfaces of the three NDM-CS scaffolds were hydrophobic at first. However, the contact angle decreased significantly in 30 s which was about 10 degrees in all three groups (**Figure 7C**). At this time, the contact angles of E1C2, E1C1 and E2C1 became 8.3° ± 1.435°, 10.97° ± 1.139° and 9.467° ± 1.048° respectively. This demonstrated that the surfaces of the three scaffolds were hydrophilic at this time. This phenomenon may be caused by the surface microstructure and roughness of the freeze-dried NDM-CS scaffolds. The experimental results showed that the NDM-CS composite material was hydrophilic inherently. However, NDM-CS scaffold became rough and formed a microstructure with multiple voids after freeze-drying, which affected the spread of droplets. As time went by, the droplets gradually infiltrate the scaffolds and the contact angle became smaller. The suitable hydrophilicity of the scaffolds could facilitate cell adhesion, extension, nutrient penetration and factor diffusion, so as to better support the growth of cells (Kang et al., 2021).

## Antibacterial Ability of Scaffolds

Antimicrobial activity is necessary for nerve scaffolds because bacterial infection interferes nerve repair after nerve injury. The antibacterial neural scaffold could promote recovery by avoiding the inflammatory response after infection. The antibacterial activity of NDM-CS hybrid scaffold was tested by Gram-negative *E. coli* and Gram-positive *S. aureus* (**Figure 8**). **Figure 8A** shows the results of colony formation (CFU) on the medium after incubation of *E. coli* and *S. aureus* with the NDM-CS scaffold for 4 h respectively. It was shown that dense and obvious colonies of *E. coli* and *S. aureus* were formed on the plate compared with the blank control group. The number of colonies in the three groups of NDM-CS scaffolds was greatly reduced. **Figures 8B,D** respectively display the number of colonies of *E. coli* and *S. aureus* in different groups. There was an obvious difference between the number of colonies in the NDM-CS scaffold groups and the blank control group. **Figures 8C,E** show statistics of the antibacterial rates of NDM-CS scaffold on *E. coli* and *S. aureus* respectively. Among them, the antibacterial rate of the three NDM-CS scaffolds to *E. coli* could reach more than 90%. In addition, the antibacterial rate of NDM-CS stent to *S. aureus* could reach more than 80%. The above results showed that the NDM scaffolds containing CS had a significant antibacterial activity for both *E. coli* and *S. aureus*. This confirmed that CS has a strong antibacterial effect in the scaffolds. The results were consistent with other related studies (Kong et al.,

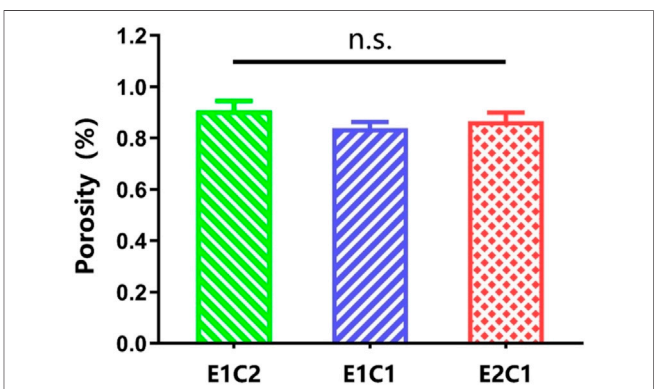


**FIGURE 6 |** The porosity of the scaffolds. n.s.: $p > 0.05$.

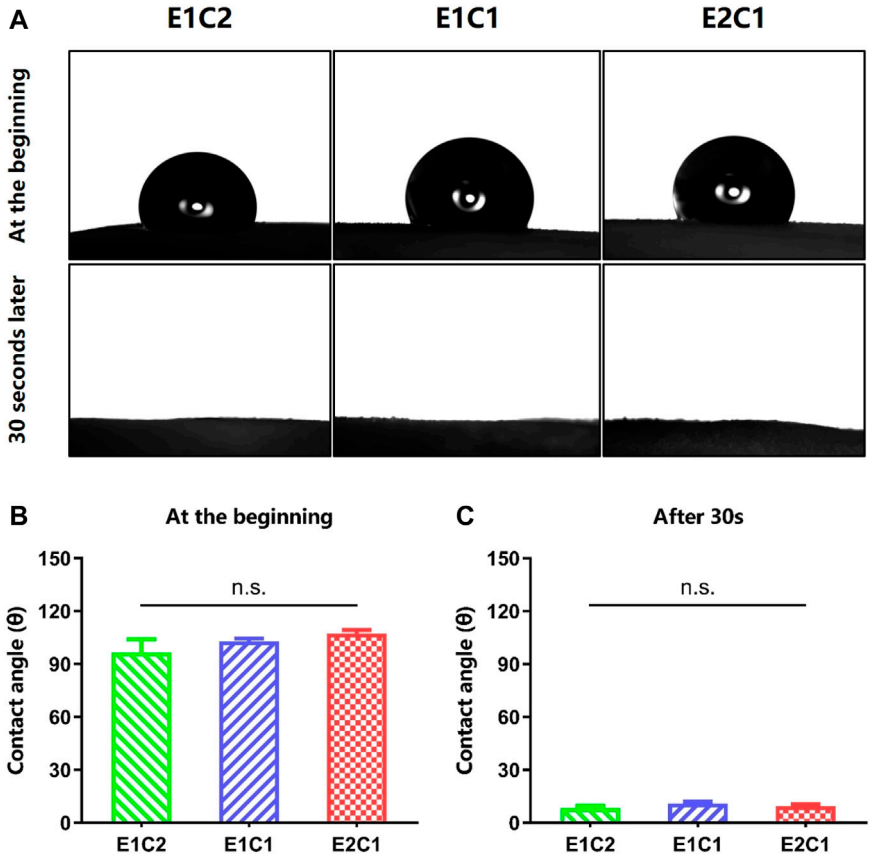


**FIGURE 7 |** Contact angle of the scaffolds. **(A)** The pictures of the contact angle at the beginning and 30 s later. **(B)** The statistical result of the contact angle at the beginning. **(C)** The statistical result of the contact angle 30 s later. n.s.: $p > 0.05$.

2020). And the inhibition effect of NDM-CS scaffold on *E. coli* and *S. aureus* did not decrease with the decrease of CS's concentration.

## Cytotoxicity of Scaffolds

**Figure 9** showed the MTT results for the three NDM-CS scaffold groups 1 day after. The Control group was the normal cell group without material. The absorbance of all three groups of hybrid scaffolds was close to the control group and showed no difference. It also indicated that all the hybrid scaffolds had no toxicity to the cells and could provide a safe growth environment to the cells. The results of the MTT test proved that the NDM-CS scaffolds had excellent biocompatibility.

## Effect of NDM-CS Scaffold on the Growth of Schwann Cells

The effect of NDM-CS scaffolds on nerve repair was evaluated by the morphology of Schwann cells. The Schwann cells were cultured with the extract medium of the NDM-CS scaffolds, and the growth of Schwann cells was observed by immunofluorescence staining (**Figure 10**). **Figures 10A,B** showed the growth of Schwann cells under the influence of different NDM-CS scaffolds for 1 and 2 days respectively. It was shown that Schwann cells grew vigorously in all groups. And the number of Schwann cells labeled by green fluorescently increased after 2 days of cultured compared to that at 1 day. **Figure 10C** presents the number of Schwann cells in all groups. Schwann cells were much more in the E1C1 and E2C1 groups than in the E1C2 group. And the number of Schwann cells in the E2C1 group was significantly higher than in both other groups after 2 days. NDM could promote cell proliferation significantly (Chen et al., 2020b) so that the number of Schwann cells in the experimental group increased. Some of the Schwann cells in the experimental groups also showed polarization during the culture process which was also caused by NDM (Agmon and Christman, 2016). These polarized Schwann cells grew pseudopods to varying degrees (indicated by yellow arrows). The number of polarized Schwann cells in all NDM-CS scaffolds was counted in **Figure 10D**. The trend of Schwann cell polarization was consistent with the change in quantity. The polarized number of Schwann cells was highest in the E2C1 group and was lowest in E1C2. In particular, polarized Schwann cells were much more in the E2C1 group than in the other groups after 2 days. Besides, the viability of Schwann cells was measured under the influence of NDM-CS scaffolds by CCK8 assay. **Figure 10E** showed the activity of Schwann cells on different NDM-CS scaffolds after culture for 1 and 2 days. There was essentially no difference

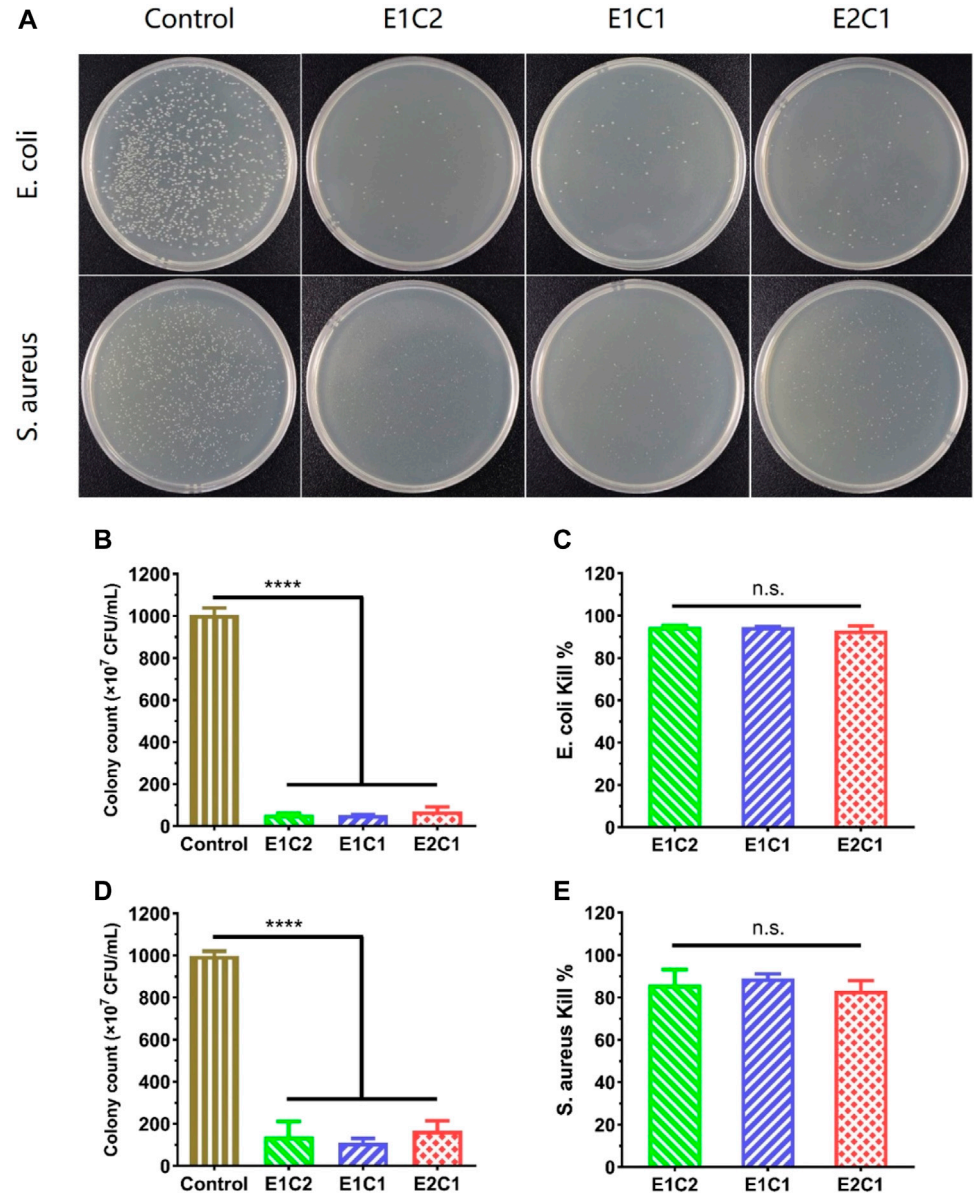


**FIGURE 8 |** The antibacterial activity of the NDM-CS scaffolds. **(A)** Images of colonies of *E. coli* and *S. aureus* derived from the scaffolds. **(B)** The colonies of *E. coli* in different groups. **(C)** *E. coli* inhibition rate of NDM-CS scaffolds. **(D)** The colonies of *S. aureus* in different groups. **(E)** *S. aureus* inhibition rate of NDM-CS scaffolds.****$p <$ 0.0001. n.s.: $p > 0.05$.

between the cell densities in each group of scaffolds either 1 or 2 days. However, the OD values in all scaffolds increased significantly after 2 days of incubation which indicated that all NDM-CS scaffolds promoted the growth and proliferation of Schwann cells. However, there was no difference in cell activity between the three groups of scaffolds as the NDM content increased. Therefore, the NDM-CS scaffold could provide a good growth environment for Schwann cells and is suitable for the growth of Schwann cells. NDM-CS scaffold also has a significant promotion effect on the proliferation and polarization of Schwann cells which enhanced with the increase of NDM content.

## The Effect of NDM-CS Scaffolds on Schwann Cell Migration

It was proved that the NDM-CS hybrid scaffold could promote the migration of Schwann cells in this study. **Figure 11** shows the migration of three groups of Schwann cells at different time. At 0 h, the cell gaps of equal distance were shown in all groups. As time progressed, Schwann cells in all groups migrated toward the center of the gap. The longer the time, the longer distance of Schwann cell migration. The most pronounced migration of Schwann cells was observed in the E2C1 group. The migration distance and migration speed of

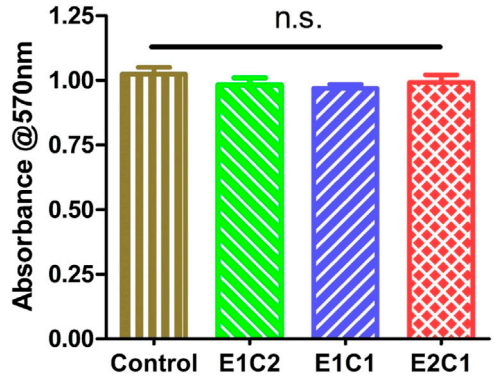


**FIGURE 9 |** The absorbance of the supernatant at 570 nm of the scaffolds. n.s.: $p > 0.05$.

Schwann cells at different time points were counted in **Figures 11A,B** respectively. The results showed that the migration distance of Schwann cells increased obviously in all groups with time elapsing. This indicated that the NDM-CS scaffolds have the ability to promote the migration of Schwann cells regardless of the ratio of NDM and CS. However, the migration rate of Schwann cells in each group at different time points showed an opposite trend to the migration distance. The migration velocity of Schwann cells was decreasing in all groups which indicated that the NDM-CS scaffold had the strongest ability to promote Schwann cell migration in the early stage. Although the migration velocity decreased, the Schwann cells were still able to reach a velocity greater than 5 μm/h after 24 h.

We further compared the differences between the different groups (**Figures 11C,D**). It was found that E1C2 showed the smallest migration distance at all points among the three groups. Meanwhile, the E2C1 group showed the largest cell migration distance at all points. And the migration distance of E2C1 could reach 308.3 μm, which was as twice times as other two groups. In addition, the migration speed of cells in three groups showed a consistent trend. The migration velocity of cells in the E2C1 group was faster than that of E1C1 and E1C2 all the time. The migration velocity of the E2C1 group could reach a maximum value of 23.1 μm/h at 6 h throughout the experiment. Even though the migration velocity was

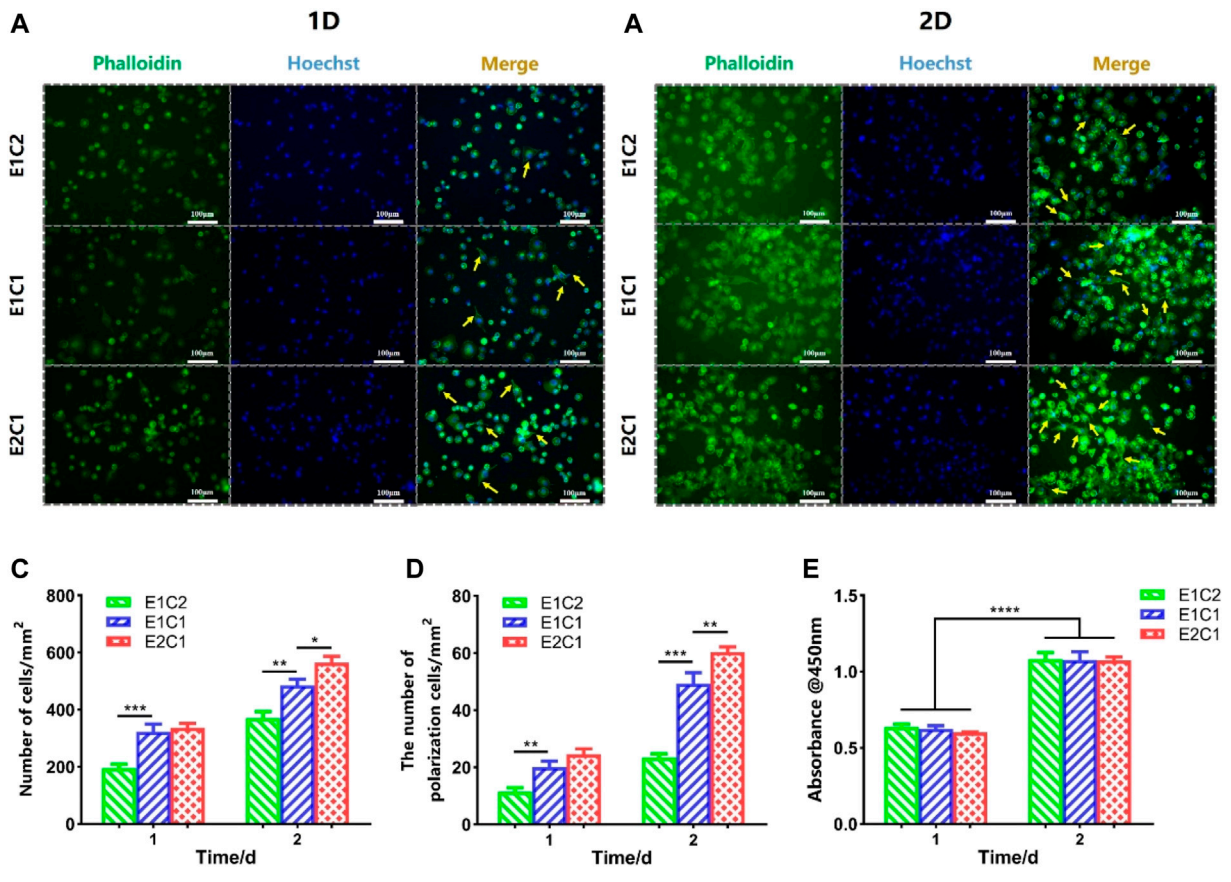


**FIGURE 10 |** Growth of RSC96 cells under the influence of NDM-CS scaffolds. Immunofluorescence staining of RSC96 cells cultured for **(A)** 1 day and **(B)** 2 days. **(C)** The number of Schwann cells in different groups. **(D)** The number of polarized cells in different groups. **(E)** Cell viability of Schwann cells on different scaffolds of 1 and 2 days. Scale bars represent 100 μm*$p < 0.05$, **$p < 0.01$, ***$p < 0.001$, ****$p < 0.0001$.

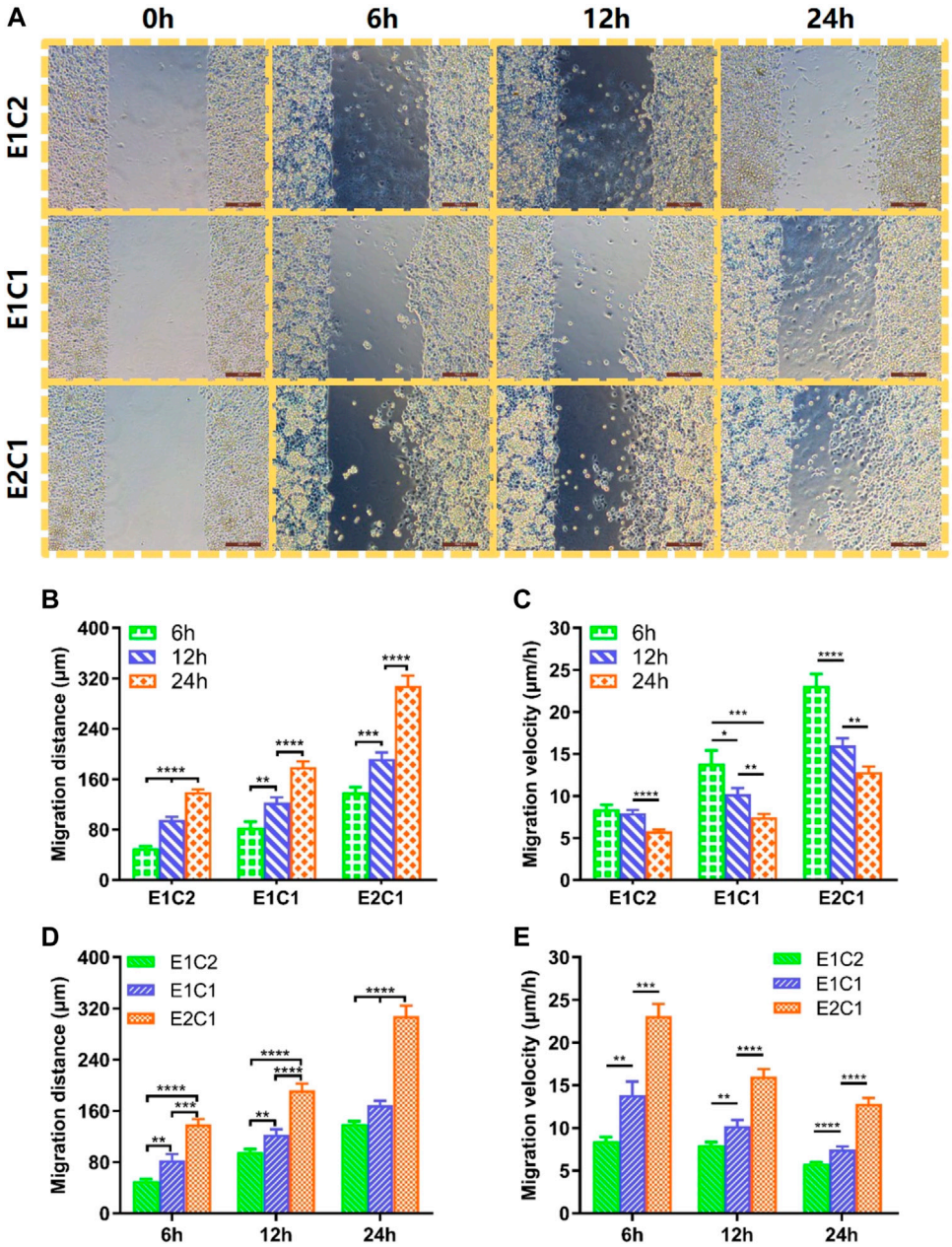


**FIGURE 11 |** Cell migration of RSC96 cells on cell culture plate surface with different scaffolds extract cultures. **(A)** The migration state of Schwann cells of all groups at different time points (scale bar: 200 μm). **(B)** Changes in migration distance of Schwann cells in different groups. **(C)** Changes in migration velocity of Schwann cells in different groups. **(D)** Migration distance statistics of Schwann cells in the three groups at 6, 12 and 24 h. **(E)** Migration velocity statistics of Schwann cells in the three groups at 6, 12 and 24 h $^{*}p < 0.05$, $^{**}p < 0.01$, $^{***}p < 0.001$, $^{****}p < 0.0001$.

decreasing gradually, the migration velocity of E2C1 could still reach 12.8 μm/h at 24 h. Based on the above results, it revealed that the E2C1 scaffold has the strongest ability to promote the migration of Schwann cells in this study which was attributed to the effect of NDM (Mao et al., 2020). Therefore, NDM-CS as a neural scaffold could provide a suitable growth microenvironment for Schwann cells to migrate. It could be predicted that NDM-CS scaffold would promote the migration of Schwann cells after neurological defects, thus establishing connections between the damaged ends more quickly and building a bridge for neuronal cell regeneration.

## CONCLUSION

In this study, a composite scaffold with high antimicrobial properties and high biocompatibility was successfully prepared by combining the advantages of nerve

decellularized matrix and chitosan. The NDM-CS scaffold exhibited excellent three-dimensional pore structure and hydrophilicity. The CS component in the composite scaffold conferred excellent antibacterial properties to the composite scaffold, avoiding cell invasion and infection and providing a clean microenvironment for nerve repair. In addition, the addition of NDM could significantly promoted the proliferation, polarization and migration of Schwann cells. Moreover, this ability of NDM-CS scaffold was enhanced with the increase of NDM content. Among them, the E2C1 group was considered to be the most excellent performer. It has superior antibacterial property against both *E. coli* and *S. aureus* comparable to E1C2 and E1C1. Meanwhile, E2C1 has the best ability to promote Schwann cell proliferation and migration. All these properties of NDM-CS scaffolds provided a more reliable microenvironment for the neural regeneration process and may have potential application prospects for future clinic application.

## DATA AVAILABILITY STATEMENT

The raw data supporting the conclusion of this article will be made available by the authors, without undue reservation.

## AUTHOR CONTRIBUTIONS

YK contributed substantially to the conception and design of the experiments. YK and DW conducted experiments and wrote the manuscript. YK and DW conducted data analyses. QW and YY revised and modified the draft.

## ACKNOWLEDGMENTS

The authors gratefully acknowledge the financial support of the National Natural Science Foundation of China (31830028).

## REFERENCES

Agmon, G., and Christman, K. L. (2016). Controlling Stem Cell Behavior with Decellularized Extracellular Matrix Scaffolds. *Curr. Opin. Solid State. Mater. Sci.* 20, 193–201. doi:10.1016/j.cossms.2016.02.001

Ardeshirylajimi, A., Delgoshaie, M., Mirzaei, S., and Khojasteh, A. (2018). Different Porosities of Chitosan Can Influence the Osteogenic Differentiation Potential of Stem Cells. *J. Cel. Biochem.* 119, 625–633. doi:10.1002/jcb.26223

Boecker, A., Daeschler, S. C., Kneser, U., and Harhaus, L. (2019). Relevance and Recent Developments of Chitosan in Peripheral Nerve Surgery. *Front. Cel. Neurosci.* 13, 104. doi:10.3389/fncel.2019.00104

Chen, L., Yan, D., Wu, N., Zhang, W., Yan, C., Yao, Q., et al. (2020). 3D-Printed Poly-Caprolactone Scaffolds Modified with Biomimetic Extracellular Matrices for Tarsal Plate Tissue Engineering. *Front. Bioeng. Biotechnol.* 8, 219. doi:10.3389/fbioe.2020.00219

Chen, S. Y., Liu, S., Zhang, L. L., Han, Q., Liu, H. Q., Shen, J. H., et al. (2020). Construction of Injectable Silk Fibroin/Polydopamine Hydrogel for Treatment of Spinal Cord Injury. *Chem. Eng. J.* 399, 125795. doi:10.1016/j.cej.2020.125795

Cheng, Y.-W., Shiwarski, D. J., Ball, R. L., Whitehead, K. A., and Feinberg, A. W. (2020). Engineering Aligned Skeletal Muscle Tissue Using Decellularized Plant-Derived Scaffolds. *ACS Biomater. Sci. Eng.* 6, 3046–3054. doi:10.1021/acsbiomaterials.0c00058

Craciunescu, O., Seciu, A.-M., and Zarnescu, O. (2021). *In Vitro* and *In Vivo* Evaluation of a Biomimetic Scaffold Embedding Silver Nanoparticles for Improved Treatment of Oral Lesions. *Mater. Sci. Eng. C* 123, 112015. doi:10.1016/j.msec.2021.112015

Dong, Z., Zhao, W., Li, Y., Wang, X., Ma, T., Wang, Y., et al. (2020). Development and Evaluation of New Methods for Protein Quantification in Dissolving Microneedles Formulations. *J. Pharm. Biomed. Anal.* 189, 113453. doi:10.1016/j.jpba.2020.113453

Ghane, N., Khalili, S., Nouri Khorasani, S., Esmaeely Neisiany, R., Das, O., and Ramakrishna, S. (2021). Regeneration of the Peripheral Nerve via Multifunctional Electrospun Scaffolds. *J. Biomed. Mater. Res.* 109, 437–452. doi:10.1002/jbm.a.37092

Han, W., Singh, N. K., Kim, J. J., Kim, H., Kim, B. S., Park, J. Y., et al. (2019). Directed Differential Behaviors of Multipotent Adult Stem Cells from Decellularized Tissue/Organ Extracellular Matrix Bioinks. *Biomaterials* 224, 119496. doi:10.1016/j.biomaterials.2019.119496

Jahromi, M., Razavi, S., and Bakhtiari, A. (2019). The Advances in Nerve Tissue Engineering: From Fabrication of Nerve Conduit Toin Vivonerve Regeneration Assays. *J. Tissue Eng. Regen. Med.* 13, 2077–2100. doi:10.1002/term.2945

Kang, Z., Li, D., Shu, C., Du, J., Yu, B., Qian, Z., et al. (2021). Polydopamine Coating-Mediated Immobilization of BMP-2 on Polyethylene Terephthalate-Based Artificial Ligaments for Enhanced Bioactivity. *Front. Bioeng. Biotechnol.* 9, 749221. doi:10.3389/fbioe.2021.749221

Ke, C. L., Deng, F. S., Chuang, C. Y., and Lin, C. H. (2021). Antimicrobial Actions and Applications of Chitosan. *Polymers (Basel)* 13, 904. doi:10.3390/polym13060904

Kong, Y., Tang, X., Zhao, Y., Chen, X., Yao, K., Zhang, L., et al. (2020). Degradable Tough Chitosan Dressing for Skin Wound Recovery. *Nanotechnol Rev.* 9, 1576–1585. doi:10.1515/ntrev-2020-0105

Lan, Y., Li, W., Jiao, Y., Guo, R., Zhang, Y., Xue, W., et al. (2014). Therapeutic Efficacy of Antibiotic-Loaded Gelatin Microsphere/Silk Fibroin Scaffolds in Infected Full-Thickness Burns. *Acta Biomater.* 10, 3167–3176. doi:10.1016/j.actbio.2014.03.029

Li, G., Chen, S., Zeng, M., Kong, Y., Zhao, F., Zhang, L., et al. (2019). Hierarchically Aligned Gradient Collagen Micropatterns for Rapidly Screening Schwann Cells Behavior. *Colloids Surf. B: Biointerfaces* 176, 341–351. doi:10.1016/j.colsurfb.2019.01.019

Li, J. H., and Zhuang, S. L. (2020). Antibacterial Activity of Chitosan and its Derivatives and Their Interaction Mechanism with Bacteria: Current State and Perspectives. *Eur. Polym. J.* 138, 109984. doi:10.1016/j.eurpolymj.2020.109984

Lin, T., Liu, S., Chen, S., Qiu, S., Rao, Z., Liu, J., et al. (2018). Hydrogel Derived from Porcine Decellularized Nerve Tissue as a Promising Biomaterial for Repairing Peripheral Nerve Defects. *Acta Biomater.* 73, 326–338. doi:10.1016/j.actbio.2018.04.001

Lu, P. J., Wang, G., Qian, T. M., Cai, X. D., Zhang, P., Li, M. Y., et al. (2021). The Balanced Microenvironment Regulated by the Degradants of Appropriate PLGA Scaffolds and Chitosan Conduit Promotes Peripheral Nerve Regeneration. *Mater. Today Bio* 12, 100158. doi:10.1016/j.mtbio.2021.100158

Mao, Q., Wang, Y., Li, Y., Juengpanich, S., Li, W., Chen, M., et al. (2020). Fabrication of Liver Microtissue with Liver Decellularized Extracellular Matrix (dECM) Bioink by Digital Light Processing (DLP) Bioprinting. *Mater. Sci. Eng. C* 109, 110625. doi:10.1016/j.msec.2020.110625

Maqueda, M., Mosquera, J. L., Garcia-Arumi, J., Veiga, A., and Duarri, A. (2021). Repopulation of Decellularized Retinas with hiPSC-Derived Retinal Pigment Epithelial and Ocular Progenitor Cells Shows Cell Engraftment, Organization and Differentiation. *Biomaterials* 276, 121049. doi:10.1016/j.biomaterials.2021.121049

Qiu, P., Li, M., Chen, K., Fang, B., Chen, P., Tang, Z., et al. (2020). Periosteal Matrix-Derived Hydrogel Promotes Bone Repair through an Early Immune Regulation Coupled with Enhanced Angio- and Osteogenesis. *Biomaterials* 227, 119552. doi:10.1016/j.biomaterials.2019.119552

Rafaeva, M., Horton, E. R., Jensen, A. R. D., Madsen, C. D., Reuten, R., Willacy, O., et al. (2021). Modeling Metastatic Colonization in a Decellularized Organ Scaffold-Based Perfusion Bioreactor. *Adv. Healthc. Mater.*, e2100684. doi:10.1002/adhm.202100684

Rao, Z. L., Lin, T., Qiu, S., Zhou, J., Liu, S., Chen, S. H., et al. (2021). Decellularized Nerve Matrix Hydrogel Scaffolds with Longitudinally Oriented and Size-Tunable Microchannels for Peripheral Nerve Regeneration. *Mat Sci. Eng. C-mater.* 120, 111791. doi:10.1016/j.msec.2020.111791

Tang, N., Zhang, R., Zheng, Y., Wang, J., Khatib, M., Jiang, X., et al. (2021). Highly Efficient Self-Healing Multifunctional Dressing with Antibacterial Activity for Sutureless Wound Closure and Infected Wound Monitoring. *Adv. Mater.*, e2106842. doi:10.1002/adma.202106842

Tang, X. X., Chen, X. L., Zhang, S. M., Gu, X. Y., Wu, R. H., Huang, T. T., et al. (2021). Silk-Inspired *In Situ* Hydrogel with Anti-Tumor Immunity Enhanced Photodynamic Therapy for Melanoma and Infected Wound Healing. *Adv. Funct. Mater.* 31, 2101320. doi:10.1002/adfm.202101320

Tao, C., Jin, M., Yao, H., and Wang, D.-A. (2021). Dopamine Based Adhesive Nano-Coatings on Extracellular Matrix (ECM) Based Grafts for Enhanced Host-Graft Interfacing Affinity. *Nanoscale* 13, 18148–18159. doi:10.1039/d1nr06284k

Tao, M., Liang, F., He, J., Ye, W., Javed, R., Wang, W., et al. (2021). Decellularized Tendon Matrix Membranes Prevent Post-Surgical Tendon Adhesion and Promote Functional Repair. *Acta Biomater.* 134, 160–176. doi:10.1016/j.actbio.2021.07.038

Wang, Y., Zhao, Y., Sun, C., Hu, W., Zhao, J., Li, G., et al. (2016). Chitosan Degradation Products Promote Nerve Regeneration by Stimulating Schwann Cell Proliferation via miR-27a/FOXO1 Axis. *Mol. Neurobiol.* 53, 28–39. doi:10.1007/s12035-014-8968-2

Wu, Q., Li, Y., Yang, Z., Li, L., Yang, J., Zhu, X., et al. (2022). Ectopic Expansion and Vascularization of Engineered Hepatic Tissue Based on Heparinized Acellular Liver Matrix and Mesenchymal Stromal Cell Spheroids. *Acta Biomater.* 137, 79–91. doi:10.1016/j.actbio.2021.10.017

Xu, J., Fang, H., Zheng, S., Li, L., Jiao, Z., Wang, H., et al. (2021). A Biological Functional Hybrid Scaffold Based on Decellularized Extracellular Matrix/Gelatin/Chitosan with High Biocompatibility and Antibacterial Activity for Skin Tissue Engineering. *Int. J. Biol. Macromolecules* 187, 840–849. doi:10.1016/j.ijbiomac.2021.07.162

Yang, Y., Ding, F., Wu, J., Hu, W., Liu, W., Liu, J., et al. (2007). Development and Evaluation of Silk Fibroin-Based Nerve Grafts Used for Peripheral Nerve Regeneration. *Biomaterials* 28, 5526–5535. doi:10.1016/j.biomaterials.2007.09.001

Yi, S., Xu, L., and Gu, X. (2019). Scaffolds for Peripheral Nerve Repair and Reconstruction. *Exp. Neurol.* 319, 112761. doi:10.1016/j.expneurol.2018.05.016

Zhu, Y., Zhu, R., Ma, J., Weng, Z., Wang, Y., Shi, X., et al. (2015). *In Vitro* cell Proliferation Evaluation of Porous Nano-Zirconia Scaffolds with Different Porosity for Bone Tissue Engineering. *Biomed. Mater.* 10, 055009. doi:10.1088/1748-6041/10/5/055009

**Conflict of Interest:** The authors declare that the research was conducted in the absence of any commercial or financial relationships that could be construed as a potential conflict of interest.

**Publisher's Note:** All claims expressed in this article are solely those of the authors and do not necessarily represent those of their affiliated organizations, or those of the publisher, the editors and the reviewers. Any product that may be evaluated in this article, or claim that may be made by its manufacturer, is not guaranteed or endorsed by the publisher.

frontiers in Bioengineering and Biotechnology

ORIGINAL RESEARCH
published: 09 February 2022
doi: 10.3389/fbioe.2022.853487

# Synthesis of Star 6-Arm Polyethylene Glycol-Heparin Copolymer to Construct Anticorrosive and Biocompatible Coating on Magnesium Alloy Surface

*Qingxiang Hong[1†], Hualan Zhou[2†], Yuxin Cheng[1], Minhui Yang[1], Qiuyang Zhang[1], Sen Liu[1], Qingping Xiong[3] and Changjiang Pan[1]**

[1]Faculty of Mechanical and Materials Engineering, Jiangsu Provincial Engineering Research Center for Biomaterials and Advanced Medical Devices, Huaiyin Institute of Technology, Huai'an, China, [2]The Affiliated Huai'an Hospital of Xuzhou Medical University, Huai'an, China, [3]Faculty of Chemical Engineering, Huaiyin Institute of Technology, Huai'an, China

Magnesium alloy has become a research hotspot of the degradable vascular stent materials due to its biodegradability and excellent mechanical properties. However, its rapid degradation rate after implantation and the limited biocompatibility restrict its application in clinic. Constructing a multifunctional bioactive polymer coating on the magnesium alloys represents one of the popular and effective approaches to simultaneously improve the corrosion resistance and biocompatibility. In the present study, the copolymer of 6-arm polyethylene glycol and heparin (PEG-Hep) was successfully synthesized and then immobilized on the surface of chitosan (Chi)-modified magnesium alloy surface through electrostatic interaction to improve the corrosion resistance and biocompatibility. The results of attenuated total reflection Fourier transform infrared spectroscopy (ATR-FTIR), X-ray photoelectron spectroscopy (XPS) and scanning electron microscopy showed that a dense and compact coating was created on the magnesium alloy surface. The coating displayed excellent hydrophilicity. At the same time, the as-prepared coating can significantly not only improve the corrosion potential, reduce the corrosion current and the pH changes of the immersion solution, but also keep a relatively intact surface morphology after immersing in simulated body fluid solution for 14 days, demonstrating that the coating can significantly improve the corrosion resistance of the magnesium alloy. Moreover, the magnesium alloy with PEG-Hep coating exhibited excellent hemocompatibility according to the results of the hemolysis rate and platelet adhesion and activation. In addition, the modified magnesium alloy had a good ability to promote the endothelial cell adhesion and proliferation. Therefore, the PEG-Hep multifunctional coating can be applied in the surface modification of the biodegradable magnesium alloy stent to simultaneously improve the corrosion resistance and biocompatibility.

**Keywords: magnesium alloy, corrosion resistance, biocompatibility, polyethylene glycol, heparin**

OPEN ACCESS

***Edited by:***
*Jingan Li,*
*Zhengzhou University, China*

***Reviewed by:***
*Tao Huang,*
*The University of Melbourne, Australia*
*Feng Wu,*
*Xuzhou University of Technology, China*
*Shuo Wang,*
*Northwestern Polytechnical University, China*

****Correspondence:***
*Changjiang Pan*
*panchangjiang@hyit.edu.cn*

*†These authors share first authorship*

***Specialty section:***
*This article was submitted to Biomaterials, a section of the journal Frontiers in Bioengineering and Biotechnology*

***Received:*** *12 January 2022*
***Accepted:*** *21 January 2022*
***Published:*** *09 February 2022*

***Citation:***
*Hong Q, Zhou H, Cheng Y, Yang M, Zhang Q, Liu S, Xiong Q and Pan C (2022) Synthesis of Star 6-Arm Polyethylene Glycol-Heparin Copolymer to Construct Anticorrosive and Biocompatible Coating on Magnesium Alloy Surface. Front. Bioeng. Biotechnol. 10:853487. doi: 10.3389/fbioe.2022.853487*

## INTRODUCTION

Vascular disease caused by the cardiovascular stenosis has become one of the highest incidences and mortality rates in the world (Lv et al., 2017; He et al., 2019). Although the stent insertion has significantly reduced the mortality rate (Sigwart et al., 1987; Qi et al., 2013), the inferior biocompatibility of the current non-biodegradable stent and the complications of the late thrombosis and the delayed endothelium healing caused by the released drug from the polymer coating on stent often lead to the implantation failure (Torii et al., 2020). In recent years, the biodegradable stent made from the biodegradable polymers and metals has attracted more and more attention thanks to their acceptable biodegradability and biocompatibility (Bowen et al., 2015; Zhou et al., 2019; Shi et al., 2020). Due to its limited toughness and strength, the polymer stent must have a larger stent strut thickness to produce the mechanical properties similar to metal stent. Moreover, the degradation products of the polymer stents often lead to inflammation, resulting in the occurrence of complications such as late thrombosis and delayed endothelial healing and finally leading to in-stent restenosis. Therefore, the biodegradable metal stents have received more and more attention. Due to it good mechanical and biodegradable properties, the magnesium alloy has become the research hotspot of the biodegradable cardiovascular stents (Zhang et al., 2021a; Yang et al., 2021). However, the rapid degradation *in vivo* and the limited biocompatibility are still great challenges for its clinical application.

Because the corrosion resistance and biocompatibility of the magnesium alloys are closely related to their surface properties, surface modification represents one of the basic methods to reduce the corrosion rate and enhance the bioactivities of the magnesium alloys. At present, three strategies have been employed to improve the corrosion resistance of the magnesium alloys. One is to produce a chemical conversion layer on the surface by chemical treatment or electrochemical treatment (Kröger et al., 2018; Jiang et al., 2019; Yan et al., 2019), however, the biological activities of the chemical conversion layers need to be improved. The second strategy is to improve the corrosion resistance of magnesium alloy by changing the surface microstructure (such as ion implantation, surface heat treatment, etc.), but its biocompatibility is still very limited. The third is to construct a covering layer on the surface, such as surface self-assembly (Pan et al., 2016) and layer by layer self-assembly (Zhang et al., 2021b), deposition of inorganic coating (Li et al., 2020a), formation of layered double hydroxide (Guo et al., 2018), preparation of polymer coating, etc. The covering layer not only effectively improves the corrosion resistance, but also enhances the biocompatibility to a certain extent. However, due to the lack of sufficient biological activities on the surface, it may still lead to coagulation and delayed healing of the endothelium.

Among the strategies to improve the corrosion resistance and biocompatibility of the magnesium alloys, the polymer coating does not change the matrix properties, and it not only has good degradation performance and biocompatibility, but also can regulate cell behaviors to some degree and be used for drug loading. It has become one of the most effective methods to improve the corrosion resistance of the magnesium alloys. Generally speaking, the polymer coatings mainly include sol-gel polymers, synthetic polymers and natural polymers. The sol-gel polymer coating is mainly produced by the hydrolysis of organosilicon compounds to form a firmly bonded polymer coating with substrate, which can significantly improve the corrosion resistance and blood compatibility to some degree, as well as promote growth of vascular endothelial cells (Liu and Xi, 2016). Synthetic polymers mainly include polylactic acid (PLA), polyglycol-lactide (PLGA), polycaprolactone (PCL) (Jiang et al., 2017), polyurethane (PU) (Wang et al., 2019), polycarbonate (PC) (Pan et al., 2022) and plasma polymerization coatings (Qi et al., 2016), etc. Although the synthetic polymer coatings can significantly improve the corrosion resistance of the magnesium alloys, the biocompatibility is relatively limited. Therefore, synthetic polymer coatings often need to be further modified by the surface biofunctionalization or drug loading to improve the biocompatibility. Natural polymers mainly include chitosan (Jiang et al., 2016), hyaluronic acid (Li et al., 2020b), silk fibroin (Xu et al., 2019), etc. Natural polymers have better biocompatibility due to their biomimetic properties, but they still cannot fundamentally improve the biocompatibility of the magnesium alloys. Therefore, the biocompatibility of natural polymer coatings still needs to be improved by other surface modification methods.

Heparin is a polysaccharide substance with excellent blood compatibility and it has been widely used for the surface modification of the blood-contacting biomaterials. Heparin can not only improve the blood compatibility, but also promote the growth of endothelial cells to some extent (Pan et al., 2014), even selectively promote endothelial cell growth (Liu et al., 2017; Zhang et al., 2018). 6-arm polyethylene glycol (PEG) is a kind of polymer with excellent hydrophilicity and anti-biofouling ability, which can also provide a good cell growth microenvironment and inhibit nonspecific protein adhesion. Therefore, if 6-arm polyethylene glycol and heparin copolymer (PEG-Hep) is introduced on the magnesium alloy surface, it should not only improve the corrosion resistance, but also enhance the blood compatibility and promote endothelial cell growth. To this end, the copolymer of 6-arm polyethylene glycol and heparin (PEG-Hep) was firstly synthesized. Then, the magnesium alloy was treated by hydrofluoric acid followed by the deposition of a polydopamine layer on the surface. The chitosan was immobilized on the surface via Michael addition reaction between polydopamine coating and amine groups of chitosan to produce the positive-charged surface. Finally, the synthesized copolymer (PEG-Hep) was immobilized on the surface by electrostatic adsorption. The results *in vitro* demonstrated that the coating can significantly improve the corrosion resistance and biocompatibility of the magnesium alloy.

## MATERIALS AND METHODS

### Synthesis of Polyethylene Glycol-Hep

The synthesis route of PEG-Hep was shown in **Scheme 1**. In brief, 50 ml tetrahydrofuran was firstly added into a 100 ml single mouth flask and then 10 g 6-arm polyethylene glycol (PEG,

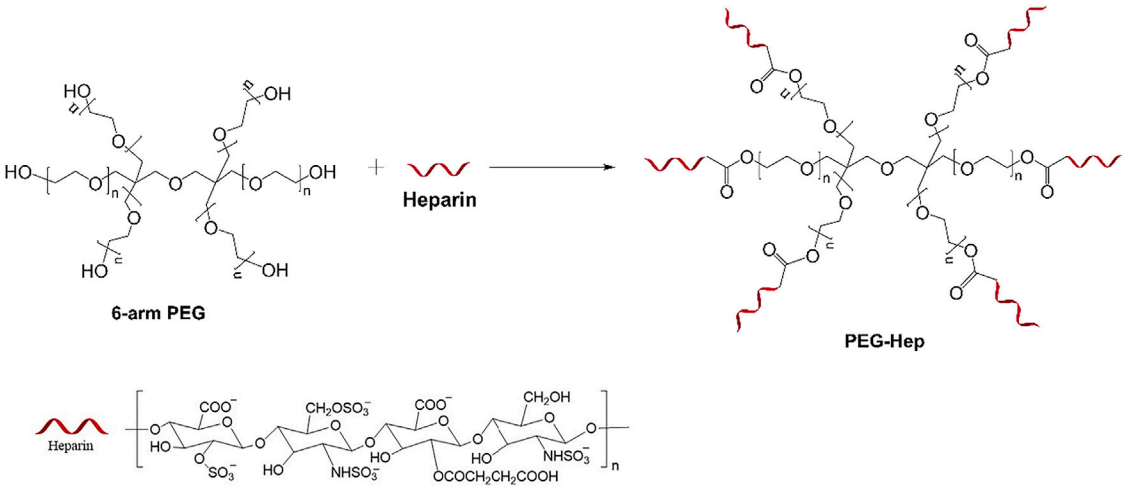


**SCHEME 1 |** The synthesis route of PEG-Hep.

Sigma-Aldrich Shanghai, China) and 0.5 g heparin (Sigma-Aldrich Shanghai, China) were added. After thoroughly stirring in ice bath for 25 min, 0.03 g DMAP (4-dimethylamino-pyridine) and 0.2 g EDC (N-(3-Dimethylaminopropyl)-N′-ethylcarbodiimide hydrochloride, Sigma-Aldrich Shanghai, China) was added to react 12 h at room temperature under stirring. After precipitating by the ice ethanol and filtration, the products were dried in the vacuum oven. The molecular structure of PEG-Hep was determined by nuclear magnetic resonance hydrogen spectrum ($^1$H-NMR) and ATR-FTIR.

## Surface Modification

AZ31B magnesium alloy with the diameter of 12 mm was cut into 3 mm thickness slices, followed by successively polishing using 400#, 800#, 1000#, 1500#, 2000# sandpapers. The polished samples (Mg) were ultrasonically cleaned in acetone, ethanol, deionized water for 5 min, respectively. The sample was immersed in a 12 mol/L hydrofluoric acid (HF) solution for 15 min. After washed and dried, the HF treated sample (Mg-HF) was immersed in 2 mg/ml dopamine solution (Tris buffer, pH8.5) for 12 h at room temperature. The chitosan was then immobilized on the polydopamine-modified sample (Mg-DA) by putting the sample into the chitosan solution (0.2% acetic acid, pH 5) for reacting 2 h. The chitosan-modified sample (Mg-Chi) was immersed into 2 mg/ml PEG-Hep solution to adsorb heparin through electrostatic interaction, and the resulting sample was denoted as Mg-PEG-Hep.

## Surface Characterization

The surface chemical structures of the samples were characterized by ATR-FTIR (TENSOR27, Bruker of Germany) with a scanning range of 4,000–650 $cm^{-1}$ at room temperature, and the elemental analysis were performed by X-ray photoelectron spectroscopy (XPS, Quantum 2000; PHI Co., Chanhassen, MN) with Al Kα source (1486.6 eV). The morphology and surface wettability of the samples were observed by scanning electron microscopy (SEM, FEI, Quata 250, United States) and contact angle meter (KR ü SS GmbH, Germany) at room temperature, respectively. In order to ensure the accuracy of the water contact angle, three parallel samples were measured to calculate the average value.

## Corrosion and Degradation Behaviors

The potentiodynamic polarization curves of the different samples were measured by a CHI660D electrochemical workstation (CHI Instruments, Inc., Shanghai, China) using a standard three-electrode system. The corrosive medium is simulated body fluid (SBF, composition: NaCl 8 g/L; KCl 0.4 g/L; $NaHCO_3$ 0.35 g/L; $CaCl_2$ 0.14 g/L; $Na_2HPO_4$ 0.06 g/L; $KH_2PO_4$ 0.06 g/L; $MgSO_4{\cdot}7H_2O$ 0.01 g/L; glucose 1 g/L). The sample, saturated Ag/AgCl electrode and platinum electrode are working electrode, reference electrode and auxiliary electrode, respectively. Before the test, the sample was sealed with the silicone rubber using a copper wire as the conductor. The exposed area was 1 $cm^2$. The sample was immersed into 100 ml SBF solution for 10 min to achieve a stable open circuit potential before the polarization test. The potentiodynamic polarization test was carried out at a scanning rate of 1 mV/s. The corrosion current and corrosion potential were determined according to the polarization curve.

In order to further determine the corrosion behaviors, the pristine magnesium alloy and the modified samples were immersed in SBF solution at 37°C for 1 day, 3, 7 and 14 days, respectively. Before the experiment, the sample needs to be encapsulated with silicone rubber. The sample was placed in a tube containing 20 ml SBF, and the medium was changed every 2 days. At the predetermined times, the sample was taken out, cleaned and dried, and the surface morphology was observed by a scanning electron microscopy.

At the same time, the degradable behaviors of the different samples were characterized by immersing experiment. Before testing, the samples were all encapsulated and then put them into 20 ml SBF solution with the initial pH of 7.4. The pH values of the

solutions were measured by a pH meter at least three times for each time. Then the average value was obtained.

## Blood Compatibility

### Hemolysis Assay

Fresh whole blood containing sodium citrate as an anticoagulant was legally obtained from a healthy volunteer. The blood was centrifuged at 1500 rev/min for 10 min to obtain the red blood cells. The concentration of the red blood cells was adjusted to 2% by physiological saline, and 2 ml solution was added to each sample to incubate 3 h at 37°C. Distilled water and normal saline were used to prepare 2% erythrocyte suspension as positive control and negative control, respectively. 1 ml red blood cell solution was taken from each sample and centrifuged 5 min at 3,000 r/min. 200 μL of the supernatant was taken and placed into a 96-well plate, the absorbance was measured at 450 nm by a microplate reader (Bio-Tek, Eons). The following formula was used to calculate the hemolysis rate.

$$R = (A - C1)/(C1 - C2) \times 100$$

where, A, C1, C2 are the absorbance of the sample, negative and positive control, respectively.

### Platelet Adhesion

The anticoagulated fresh whole blood was legally obtained from a healthy volunteer and then centrifuged at 1500 rpm for 10 min to collect the platelet rich plasma (PRP). 200 μL platelet-rich plasma was dropped on each sample to incubate 2.5 h at 37°C. The samples were washed twice by saline, followed by fixing 3 h at 4°C using 2.5% glutaraldehyde solution. Finally, the samples were dehydrated with 50, 70, 90, 100% ethanol solutions gradually, each step for 15 min. After dried in air, the attached platelets were observed by scanning electron microscopy.

## Endothelial Cell Behaviors

### Endothelial Cell Adhesion

Before the experiment, the sample was sealed with silicone rubber and sterilized under an ultraviolet light. The samples were placed into 24-well plate and then 0.5 ml of $5\times10^4$ cell/mL endothelial cells (EVC304, Cobioer, Nanjing, China) and 1.5 ml of cell culture medium were added into each sample. After incubating 6 and 24 h at 37°C and 5% $CO_2$, respectively, the samples were rinsed twice by physiological saline. The attached cells were fixed with 2.5% glutaraldehyde at 4°C for 3 h. After rinsing twice with physiological saline, the cells were successively stained by rhodamine (PBS, 10 μg/ml) for 20 min and 4, 6-diamidino-2-phenylindole (DAPI, UP water, 500 ng/ml) for 10 min, respectively. After rinsed and dried, the fluorescent images of the attached endothelial cells were acquired by an inverted fluorescent microscopy (Carl Zeiss A2 inverted).

### CCK-8 Assay

Before the experiment, the sealed samples were placed into 24-well plate to sterilize 24 h under an ultraviolet light. Then 0.5 ml of $5\times10^4$ cell/mL endothelial cells and 1.5 ml of cell culture medium were added into each sample and incubate at 37°C and 5% $CO_2$ for 6 and 24 h, respectively. After that, the samples were transferred into another new plate, and 0.5 ml 10% CCK-8 solution was added into each well for incubating 3.5 h. Finally, 200 μL CCK-8 solution was taken from each well and placed in a 96-well plate, and the absorbance at 450 nm was measured by a microplate reader (Bio-Tek Eons).

## Statistical Analysis

All the data of the water contact angle, pH changes, hemolysis rate and CCK-8 values in this paper were expressed by mean ± SD, and the statistical analyses were performed using SPSS 12.0. Statistically significant differences were determined by one way analysis of variance (ANOVA). A probability value ($p$) of less than 0.05 was considered to be statistically significant.

# RESULTS AND DISCUSSION

## Structural Analysis of Polyethylene Glycol-Hep

The chemical structure of the synthesized PEG-Hep was characterized by ATR-FTIR and hydrogen nuclear magnetic resonance spectroscopy ($^1$H-NMR). The results are shown in **Figures 1A**,**B**, respectively. For ATR-FTIR (**Figure 1A**), a broad absorption band appeared at 3,500 $cm^{-1}$, which is mainly due to the stretching vibration of -OH. The peaks of $CH_2$ and $CH_3$ at 2,980 $cm^{-1}$ and 2,890 $cm^{-1}$ can be clearly observed, and the peaks of C-O-C at 1275–1020 $cm^{-1}$ can also be detected. They are all characteristic peaks of PEG. The peaks of C-O-S at 842 $cm^{-1}$ and C=O at 1700 $cm^{-1}$ suggested that heparin was successfully introduced. In $^1$H-NMR spectra, the integral intensity ratio from low field to high field is 2:3, combined with the results of ATR-FTIR, it can be known that the substance has the chemical structure of $CH_2$-$CH_3$, and the OH peak appeared at 3.42 ppm. The H1 of N-sulfated glucosamine and the methyl of N-acetylglucosamine in heparin appear at 3.27 ppm and 2.05 ppm, respectively. All these results indicated that the PEG-Hep copolymer was successfully obtained.

## Surface Characterization of the Modified Magnesium Alloy

The surface chemical structures of the samples were firstly characterized by ATR-FTIR, and the results are shown in **Figure 2A**. There was no infrared absorption on the pristine magnesium alloy surface, suggesting that there were no chemical groups on the blank magnesium alloy surface. After hydrogen fluoride treatment, a chemical layer of $MgF_2$ was produced on the surface, leading to the occurrence of the sharp peak at 900 $cm^{-1}$ (Pan et al., 2017). The Mg-DA sample had new absorption peaks at 1250 $cm^{-1}$ and 1600 $cm^{-1}$, which are caused by the stretching vibration of the C-O bond and the bending vibration and shearing vibration of the N-H. After chitosan was grafted on the surface, two new absorption peaks appeared at 1670 $cm^{-1}$ and 1415 $cm^{-1}$, namely C=O and C-N, indicating that chitosan was successfully immobilized on the surface of Mg-DA sample. The Mg-PEG-Hep sample showed a sharp peak corresponding to the hydroxyl group at 3,700 $cm^{-1}$, and the peaks at 2,980 $cm^{-1}$ and

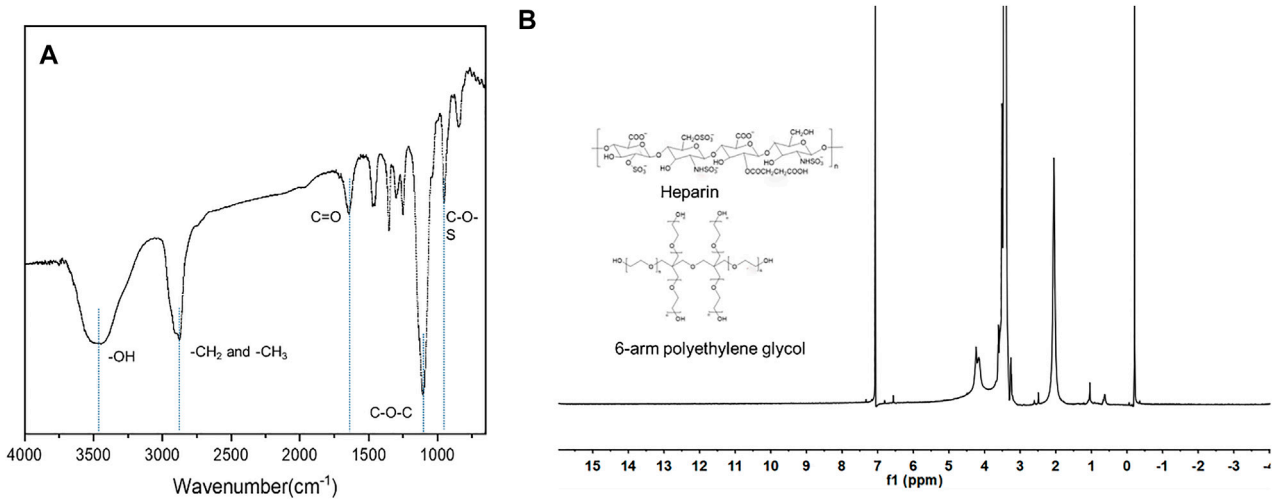


**FIGURE 1 |** The ATR-FTIR **(A)** and $^{1}$H-NMR **(B)** of PEG-Hep.

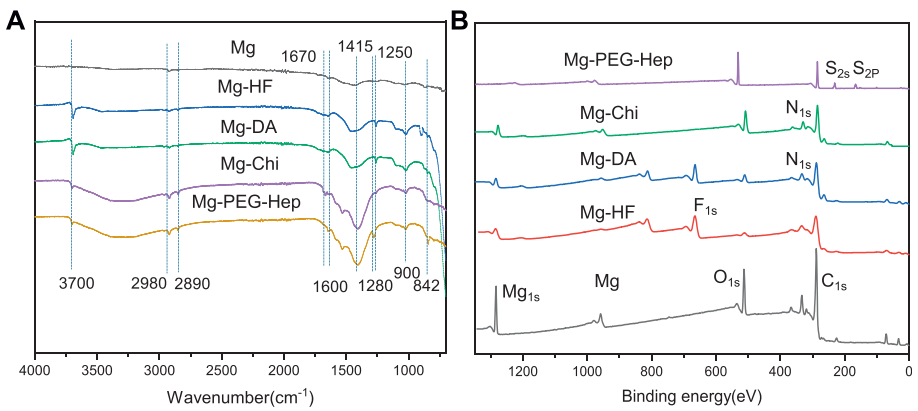


**FIGURE 2 |** The ATR-FTIR **(A)** and XPS **(B)** spectra of the different samples.

**TABLE 1 |** The surface atom percentages (wt%) of the different samples characterized by X-ray photoelectron spectroscopy (XPS).

| Samples | Mg | O | C | S | N | F |
|---|---|---|---|---|---|---|
| Mg | 47.3 | 46.20 | 6.5 | - | - | - |
| Mg-HF | 10.55 | 23.97 | 9.3 | - | - | 56.18 |
| Mg-DA | 7.31 | 35 | 40.25 | - | 5.44 | 12 |
| Mg-Chi | 2.97 | 41.53 | 48.38 | - | 7.12 | - |
| Mg-PEG-Hep | 0.18 | 44.04 | 50.31 | 5.19 | 0.28 | - |

2,890 $cm^{-1}$ were the appearance of $CH_2$ and $CH_3$, respectively. The characteristic peak at 842 $cm^{-1}$ and 1280 $cm^{-1}$ were the appearance of C-O-S and S=O, respectively, indicating that PEG-Hep was successfully introduced on the Mg-Chi surface.

XPS was utilized to further detect the surface atomic concentrations of the different samples, and the results are shown in **Figure 2B** and **Table 1**. In addition to $Mg_{1s}$, the blank magnesium alloy surface had $C_{1s}$ and $O_{1s}$ peaks, indicating that the magnesium surface was oxidized and C contamination appeared. After the hydrogen fluoride treatment, the oxygen concentration was reduced, and $F_{1s}$ peak appeared, suggesting that the $MgF_2$ chemical conversion layer on the surface was produced and replaced the previously oxide layer. The decreased $O_{1s}$ peak and the occurrence of the $N_{1s}$ peak on Mg-DA surface indicated that the polydopamine layer was formed on the surface, which can provide the reaction sites for the subsequent reaction. After grafting chitosan, the $C_{1s}$, $O_{1s}$ and $N_{1s}$ peaks were all significantly enhanced. For Mg-PEG-Hep, the $C_{1s}$ and $O_{1s}$ peaks on the surface were significantly enhanced, the $N_{1s}$ content was reduced, and $S_{2p}$ and $S_{2s}$ appeared, indicating that PEG-Hep was successfully introduced on the surface. In conclusion, it can be inferred that DA, Chi and PEG-Hep were successfully introduced on the magnesium alloy.

The surface morphologies of the samples were characterized by scanning electron microscopy (SEM). As shown in **Figure 3A**,

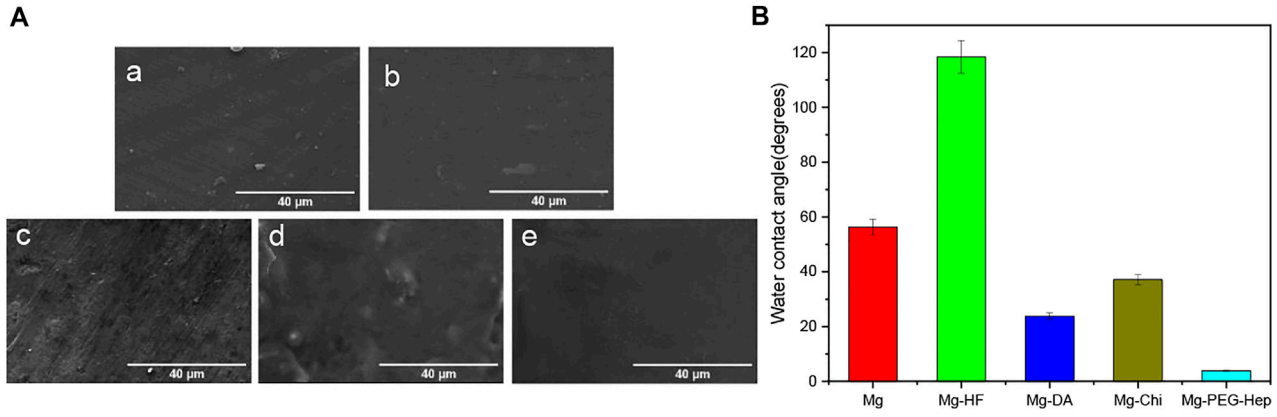


**FIGURE 3 | (A)** SEM images of **(a)** Mg, **(b)** Mg-HF, **(c)** Mg-DA, **(d)** Mg-Chi, **(e)** Mg-PEG-Hep, **(B)** The water contact angles of the different samples.

the surface of the magnesium alloy is relatively flat after polishing. After the hydrogen fluoride treatment, the $MgF_2$ layer was formed on the magnesium alloy according to ATR-FTIR and XPS, which can play protective role to prevent the corrosion of the magnesium alloys (Da Conceicao et al., 2010), and initially improve the corrosion resistance of the magnesium matrix. Dopamine (DA) is a kind of high adhesion protein inspired by mussel foot. The dopamine molecule can self-polymerize to polydopamine (PDA) in air which has a strong binding force with a variety of materials (Waite, 1983; Liu et al., 2014a). Moreover, it can also react with substances containing amino and thiol groups. From the XPS results, it can be known that the polydopamine was successfully immobilized on the Mg-HF sample. Compared with the Mg-HF, the surface of Mg-DA was rougher, which may be caused by the time-consuming immersion process and a large amount of PDA agglomeration (Ball et al., 2012; Wang et al., 2014). After grafting chitosan, white particles appeared on the surface, which is a common feature of chitosan films (Zhai et al., 2018). The positive charges of chitosan can absorb the negative-charged heparin, so that PEG-Hep can be successfully immobilized on the surface of Mg-Chi. The surface of Mg-PEG-Hep was smoother than Mg-Chi, which can protect the magnesium matrix and thus improve the corrosion resistance.

Surface hydrophilicity plays an important role in the biocompatibility of the biomaterials. Good hydrophilicity can prevent the nonspecific protein adhesion and thus improve the blood compatibility and provide good cell compatibility. The hydrophilicity of the magnesium alloy before and after surface modification was evaluated by water contact angle, and the results are shown in **Figure 3B**. The water contact angle of the original magnesium was 56.2°, exhibiting limited hydrophilicity. The original magnesium surface had no hydrophilic groups (as shown in **Figures 2A**,**B**) and the surface was smooth (as shown in **Figure 3A**), resulting in the limited hydrophilicity. After the hydrogen fluoride treatment, the water contact angle increased to 118.4°. Studies have shown that the $MgF_2$ chemical layer formed after the hydrofluoric acid treatment has the characteristics of low water solubility (Makkar et al., 2018), which is the reason for the increase in the water contact angle. After polydopamine deposition, the water contact angle was reduced to 23.8° because of the introduction of hydrophilic amine groups, and the enhanced surface roughness (as shown in **Figure 3A**) also contributed to the better hydrophilicity. Chitosan is a hydrophilic polymer (Ludwiczak and Mucha, 2010), but the Michael addition reaction between the polydopamine coating and the amino groups in chitosan formed a dense layer, resulting in a slight decrease in hydrophilicity, and thus the water contact angle was increased to 37.1°. Heparin is a natural polysaccharide, which has rich hydrophilic groups such as hydroxyl, carboxyl and sulfonic acid groups, therefore, the water contact angle of Mg-PEG-Hep was reduced to 3.9°, displaying the superhydrophilicity.

## Corrosion Behaviors

The potentiodynamic polarization curves of the magnesium alloy before and after modification in the simulated body fluid are shown in **Figure 4A**, and the corresponding corrosion potential and current are summarized in **Table 2**. Generally speaking, a high corrosion potential means that the material is thermodynamically more stable and resistant to corrosion, while a low corrosion potential means that the corrosion tendency is lager and the corrosion resistance could become worse. The surface of the unmodified magnesium alloy is active, therefore, the corrosion potential (-1.57 V) was the lowest and the corrosion current (1.419 × 10-4A·cm$^{-2}$) was the highest among all samples, indicating that the corrosion resistance of unmodified magnesium alloy was the worst. After hydrogen fluoride treatment, a $MgF_2$ layer was formed. Lee et al. proved that the $MgF_2$ layer on the magnesium alloy has the advantages of good compactness and high bonding strength with the substrate (Makkar et al., 2018). The dense film layer is not conducive to the penetration of electrolytes, and the poor hydrophilicity can prevent water adhesion, consequently, it can reduce the corrosion rate of the magnesium alloy. After the polydopamine deposition, the polymer layer on the magnesium alloy can isolate the substrate from the corrosive medium and thus effectively protect the magnesium matrix, and the corrosion current was further reduced to ×3.37010$^{-7}$ A cm$^{-2}$.

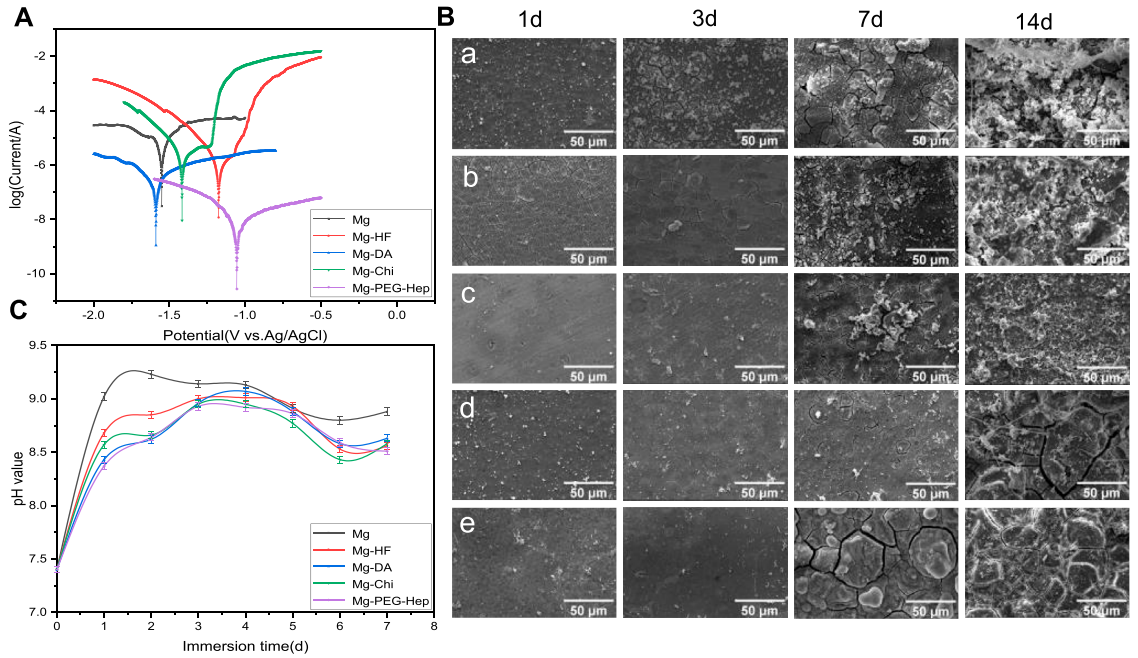


**FIGURE 4 | (A)** Potentiodynamic polarization curves of the different samples. **(B)** Typical SEM images of the samples immersed in SBF for 1, 3, 7, and 14 d **(a)** Mg, **(b)** Mg-HF, **(c)** Mg-DA, **(d)** Mg-Chi, **(e)** Mg-PEG-Hep, **(C)** pH values of the different samples immersed in SBF for 7 days.

**TABLE 2 |** Corrosion potential and corrosion current densities of the different samples.

| Samples | Ecorr/V | Icorr/A·cm$^{-2}$ |
|---|---|---|
| Mg | −1.570 | $1.419 \times 10^{-4}$ |
| Mg-HF | −1.175 | $1.177 \times 10^{-6}$ |
| Mg-DA | −1.589 | $3.370 \times 10^{-7}$ |
| Mg-Chi | −1.417 | $3.071 \times 10^{-6}$ |
| Mg-PEG-Hep | −1.055 | $6.650 \times 10^{-9}$ |

**TABLE 3 |** Surface element contents of the different samples after immersing in SBF for 14 days.

| Samples | Mg | O | C | Ca | P | |
|---|---|---|---|---|---|---|
| Mg | | 7.13 | 40.37 | 22.65 | 26.45 | 3.58 |
| Mg-HF | 5.03 | 42.78 | 42.62 | 5.35 | 4.21 | |
| Mg-DA | 6.12 | 36.69 | 36.47 | 13.65 | 7.07 | |
| Mg-Chi | 5.22 | 53.83 | 24.51 | 9.43 | 7.01 | |
| Mg-PEG-Hep | 9.50 | 20.16 | 65.69 | 0.60 | 4.05 | |

At the same time, the self-polymerized dopamine-coated catechol can also undergo a Michael addition reaction with the amine group of chitosan, thus chitosan was grafted on the magnesium alloy surface. After grafting chitosan, the positive charges of chitosan can adsorb anions and hinder the direct erosion of anions to the magnesium matrix, leading to the improved corrosion resistance. At the same time, the increase of the polymer layer thickness can also improve the corrosion resistance. After PEG-Hep immobilization, the anions of heparin can combine with the positive charges of chitosan, making the surface exhibit electronegativity to prevent the adsorption of anions, so that the corrosion resistance of the magnesium alloy was further improved, and the corrosion potential increased to −1.055 V, the corrosion current was reduced to $6.650 \times 10^{-9}$ A cm$^{-2}$. It can be concluded that the PEG-Hep coating can significantly improve the corrosion resistance of the magnesium alloy. It can be seen from **Figure 3A** that the surface film layer was relatively dense, which made the magnesium alloy difficult to corrode in the SBF and may achieve the purpose of long-term protection of the magnesium alloy.

The corrosion behaviors of the different samples were further evaluated by immersion test. The samples were immersed in SBF solution for 1 day, 3, 7 and 14 days, respectively, and then the surface morphologies of the samples before and after immersion were observed by scanning electron microscopy. The typical surface morphologies of the different samples after immersing different time were shown in **Figure 4B**. Elemental analysis was also performed by EDX after immersion and the results are listed in **Table 3**. It can be seen that the small cracks appeared on the surface of the magnesium alloy after soaking 1 day, because the pristine magnesium alloy had loose magnesium oxide, which cannot resist the erosion of anionic ions in SBF, leading to the poor corrosion resistance. Hydrogen gas was generated during pretreatment with hydrogen fluoride, resulting in a few microcracks on the Mg-HF surface. The released hydrogen during the soaking process and the presence of the corrosive $Cl^-$ can weaken the adhesion between PDA and Mg, resulting in

the appearance of small corrosion pits on the Mg-DA surface. However, no cracks can be observed on the Mg-Chi and Mg-PEG-Hep surfaces, indicating that the introduction of chitosan and PEG-Hep can significantly enhance the corrosion resistance of the magnesium alloy. After 3 days of immersion, the surface cracks of the magnesium alloy increased significantly. Studies have shown that the corrosion rate of the magnesium alloys is faster at 3 days as compared to 14 days (Makkar et al., 2018). On one hand, the initial larger area exposed to the solution could promote the exothermic reaction and increase the corrosion rate; on the other hand, the higher concentration of $Cl^-$ and other salts may also cause the corrosion rate to increase. The surface of other modified samples was basically unchanged at 1 day, and no cracks occurred, indicating that dopamine, chitosan and PEG-Hep coatings were beneficial to improve the corrosion resistance of magnesium alloy to the different degree. On the 7th day, the corrosion on the magnesium surface became serious, and the cracks and corrosion products increased significantly. The corrosion of other samples was also more serious than before. However, there were only microcracks on the Mg-Chi and MG-PEG-Hep surface because they could cover the magnesium alloy surface and protect the magnesium alloy matrix from corrosion. After being immersed 14 days, it can be seen that white granular substances appeared on all sample surfaces (**Figure 4B**), and it was found that the main component may be hydroxyapatite (HA, $Ca_{10}(PO_4)_6(OH)_2$) (Ly and Yang, 2019). As shown in **Table 3**, P and Ca elements appeared on the surfaces of all samples, which may be Ca-P particles formed on the surface. The surface corrosion of Mg was more serious, and the content of Mg decreased, and the content of O and C increased, indicating that these corrosion products may be carbonate. The increase of P element content on the Mg-HF surface indicates that the $MgF_2$ coating on the surface may be damaged. After the fixation of dopamine, the content of P and Mg further increased, and the small pits on the surface of the PDA coating caused serious corrosion of the samples. The changes of elements in other samples were not different from Mg. During the immersion of Mg-Chi, the chitosan film was slightly corroded, and a small amount of corrosion products appeared, so the elements C and Mg basically did not change, and the content of O increased. Mg-PEG-Hep surface coating had the best integrity, less corrosion products and the highest Mg content can be observed, indicating that it had the best corrosion resistance. On one hand, the coating can act as an isolating barrier between magnesium alloy and SBF, and on the other hand, heparin with negative charge properties can inhibit anion erosion.

The pH in the human body is about 7.4, which is weakly alkaline. Too high pH will damage the normal growth microenvironment of cells. The high corrosion rate of magnesium alloy can produce a large amount of $OH^-$, resulting in the increase of pH. Therefore, the pH changes of the different samples soaked in SBF for 7 days were measured and the results are shown in **Figure 4C**. The pH value of all samples increased rapidly on the first day, among which Mg increased the fastest (from the 7.4–9.02), indicating that its corrosion resistance was the worst. After 2 days, the pH value changed slowly and became steady, implying that the degradation rate became slower. During the immersion process, the pH value of Mg was always the highest, so its corrosion resistance was the worst. After hydrogen fluoride treatment, a chemical conversion layer of $MgF_2$ was formed. Yuan et al. proved that the $NaHCO_3$, NaCl and other components in SBF can effectively prevent the dissolution of $MgF_2$ (Mao et al., 2013), so the pH value change tends to be flat. After grafting chitosan, the positive charge of the amine group can prevent the corrosion of $Cl^-$ and other anions, so it can have a long-term protective effect on the magnesium matrix. After 4 days of immersion, a dynamic equilibrium was reached between the dissolution and corrosion products of the samples, and the corrosion rate decreased, so the pH value decreased, which was consistent with the results of the immersion experiment. The pH values of the Mg, Mg-HF, Mg-DA, and Mg-Chi samples increased slightly after being soaked for 6 days. This may be because the corrosion products had no protective effect on the magnesium matrix over time. After immersing 7 days, the pH value of Mg-PEG-Hep was the lowest. The positive charges of chitosan can react with the negative charge of heparin to form a dense protective layer, as shown in **Figure 4B**, which can effectively inhibit the corrosion of the magnesium alloy.

## Blood Compatibility

Human blood is mainly composed of red blood cells, white cells, platelets and so on. When the stent enters the human body, the red blood cells may be damaged and even ruptured, resulting in severe hemolysis. National standards stipulate that the hemolysis rate of biomaterials or devices should be less than 5%. The hemolysis rates of the different samples are shown in **Figure 5A**. Due to the limited corrosion resistance, the blank magnesium alloy can produce a large amount of $OH^-$ during the corrosion process, which will increase the local pH. High pH will increase the binding capacity of hemoglobin and membranes, leading to the increase of hemolysis rate. Severe hemolysis can cause the hemolysis rate of magnesium alloys to reach as high as 40%. After hydrogen fluoride treatment, the hemolysis rate was 10.3%. Studies have shown that the hemolysis rate of $MgF_2$ formed after hydrofluoric acid treatment is 10.1% (Mao et al., 2013). This is because fluoride itself is biocompatible, and the increased corrosion resistance can also reduce the release of $OH^-$. After the deposition of polydopamine, the hemolysis rate increased rapidly to 35%. The research showed that although the polydopamine layer could slow down the corrosion of the material (as shown in **Figure 4A**), however, due to the amine groups on its surface, more platelets and red blood cells adhere to the surface, resulting in the poor blood compatibility (Chen et al., 2018). After grafting chitosan, the hemolysis rate was about 7.9%, the negatively charged glycoprotein on the surface of erythrocytes can combine with the positively charged amino group of chitosan, resulting in the decrease of hemolysis rate, but it is still larger than 5%. After PEG-Hep was introduced, the hemolysis rate decreased to 3.8%. It can be considered that heparin can not only enhance the activity of thrombin III, thereby indirectly exerting anticoagulant effect, but also can improve the activities of protein C and stimulate endothelial cells releasing anticoagulant and fibrinolytic substances (Wu, 1996), so the hemolysis rate of Mg-PEG-Hep can meet the requirement of the national standard for hemolysis rate.

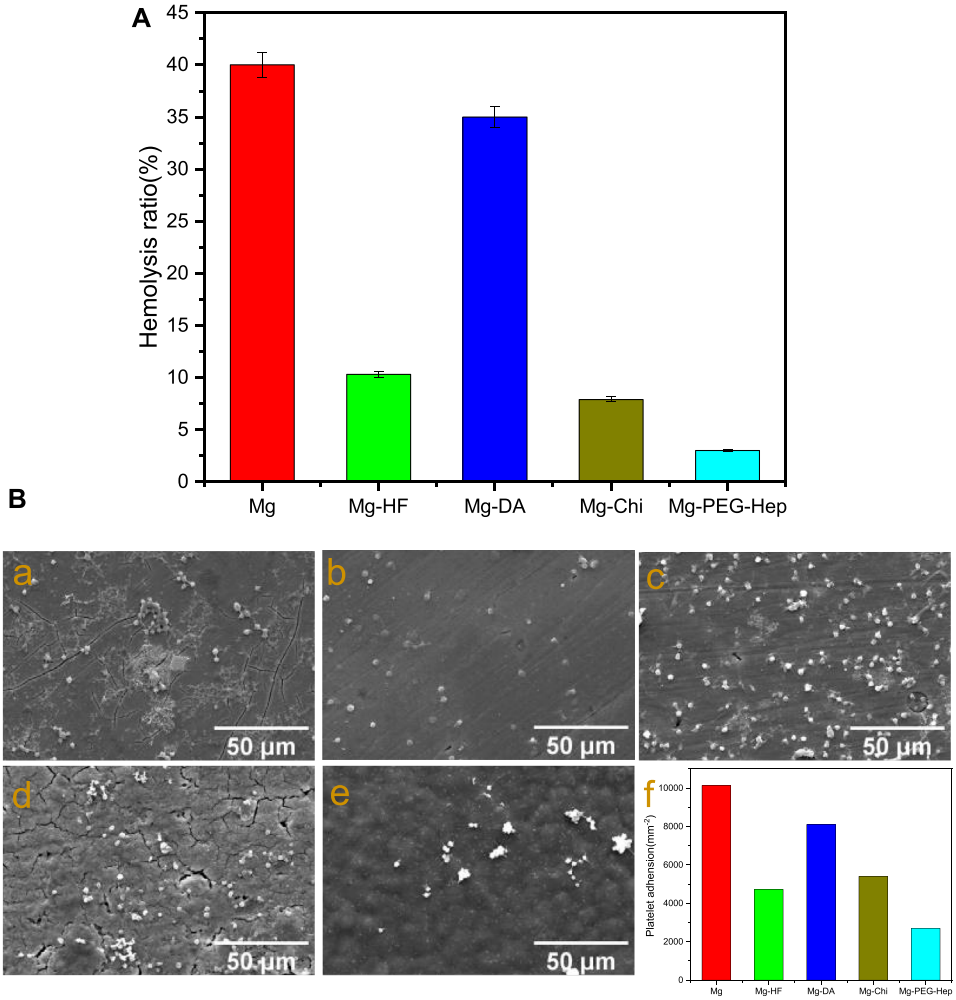


**FIGURE 5 | (A)** Hemolysis rate of the different samples. **(B)** SEM images of platelet adhesion on the different samples. **(a)** Mg, **(b)** Mg-HF, **(c)** Mg-DA, **(d)** Mg-Chi, **(e)** Mg-PEG-Hep, **(f)** The number of the attached platelets on the different samples.

Another way of evaluating blood compatibility is platelet adhesion. When the stent enters the human body, platelet aggregation and activation may occur to promote the production of thrombin, thereby forming a thrombus. Therefore, platelets are considered to be one of the important causes of thrombus formation. The SEM images of platelet adhesion and the amount of platelets on the different samples are shown in **Figure 5B**. The platelets on the magnesium alloy were mostly in an aggregated state, and most of them had pseudopodia exhibiting a spreading state, indicating that the blood compatibility of the magnesium alloy was poor. After hydrogen fluoride treatment, a chemical layer of $MgF_2$ was formed. Mao et al. proved that $MgF_2$ has good anti-platelet adhesion ability (Mao et al., 2013), and the improvement of corrosion resistance (as shown in **Figure 4A**) can also reduce the platelet adhesion. Wei et al. (2011) and Ma et al. (2013) have also proved that the imine and quinine groups in the polydopamine layer can quickly adsorb proteins, leading to platelet adhesion and aggregation, therefore, compared with Mg-HF, the number of platelets adhered to Mg-DA was increased. In general, surfaces with good hydrophilicity have lower surface free energy which can prevent the adhesion of plasma proteins and thus inhibit platelet adhesion (Gao et al., 2019). After chitosan graft, the decreased hydrophilicity (as shown in **Figure 3B**) resulted in platelet aggregation, so the number of platelet adhesion did not decrease significantly. Heparin has excellent anticoagulant effect and can reduce platelet adhesion and thus only several round platelets can be found on Mg-PEG-Hep. Meanwhile, Mg-PEG-Hep had good surface wettability, which can preventthe non-specific protein adsorption, and thus further reduced the platelet adhesion and aggregation, so the number of the attached platelets decreased significantly, which also confirmed that Mg-PEG-Hep had good blood compatibility.

## Endothelial Cell Behavior

### Cell Adhesion

The inner wall of normal human blood vessel is an endothelial layer composed of vascular endothelial cells. Vascular endothelium plays a very important role in maintaining the dynamic balance of human

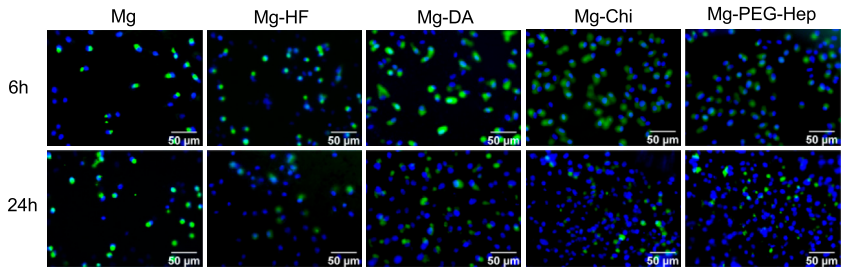


**FIGURE 6 |** SEM images of the endothelial cells adhered on the different samples surfaces for 6 and 24 h, respectively.

blood and preventing excessive proliferation of smooth muscle cells. When cardiovascular materials are implanted into human blood vessels, the surrounding endothelial tissue is damaged, which causes endothelial dysfunction. Therefore, for intravascular implant, the rapid formation of a vascular endothelial layer on the surface after the implantation is one of the important methods to solve the clinical complications of the cardiovascular implants. We first used endothelial cell adhesion to characterize the ability to promote endothelial growth. The fluorescent images of the endothelial cells cultured on the different samples for 6 and 24 h, respectively, are shown in **Figure 6**. Cells are very sensitive to environmental fluctuations, any small physical and chemical changes may lead to bad results (Witte et al., 2008; Xin et al., 2009). Magnesium can produce a large amount of $OH^-$ during the corrosion process to cause local alkalization, and at the same time a large amount of the released $Mg^{2+}$ may damage the cell growth environment. Consequently, with the extension of the culture time, the number of cells did not change significantly for the pristine magnesium alloy. As compared with Mg, Mg-HF had a slight increase in the number of cell adhesion after 6 and 24 h culture. It can be attributed to the improved corrosion resistance and the hydrophobic surface of the $MgF_2$ layer. Studies have shown that endothelial cells can better adhere to hydrophobic surfaces (Dekker et al., 1993). Studies have shown that the polydopamine layer can effectively enhance the adhesion, proliferation and migration of endothelial cells (Yang et al., 2012; Liu et al., 2014b), and the hydrophilicity was also improved, so the number of endothelial cell adhesion was increased on Mg-DA. Chitosan is a natural polysaccharide polymer that can promote cell adhesion and proliferation. Okamoto et al. (2002) demonstrated that chitosan and its derivatives can stimulate endothelial cells to secrete the inflammatory cytokine Interleukin-8 (IL-8). IL-8 has vascular proliferation and chemotactic attraction to endothelial cells, thus can promote endothelial cell migration and proliferation (Koch et al., 1992; Ueno et al., 1999). Therefore, the number of endothelial cells on Mg-Chi was further increased. Heparin is a natural polysaccharide molecule, which can not only improve the blood compatibility of the material, but also promote the growth of endothelial cells (Gao et al., 2019). PEG and its derivatives have excellent inhibition of non-specific adhesion of proteins, platelets and cells, and contain a large number of hydrophilic groups (Banerjee et al., 2011; Alibeik et al., 2012; Kovach et al., 2014). In addition, the PEG-Hep coating can endow magnesium alloys with good corrosion resistance (as shown in **Figure 4**), which can significantly reduce the hydrogen bubbles and local alkalization caused by excessive corrosion of magnesium alloys, thereby improving endothelial cells growth. Therefore, Mg-PEG-Hep shows good biocompatibility, and the number of endothelial cell adhesion was the largest.

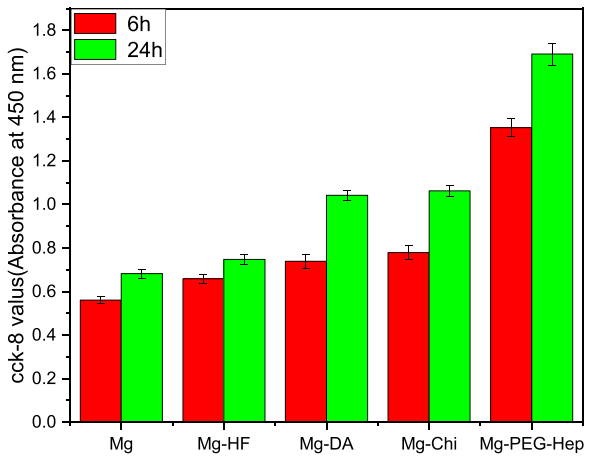


**FIGURE 7 |** The CCK-8 results of the endothelial cells adhered on the different samples for 6 and 24 h.

## Cell Proliferation

The cell proliferation was characterized by CCK-8 assay. Generally speaking, the higher the CCK-8 value, the more the number of cells. The CCK-8 values of the different samples are shown in **Figure 7**. After 6 h incubation, the CCK-8 value of the magnesium alloy was the lowest. This may be due to the poor corrosion resistance of the blank magnesium, and the increase of pH value caused local alkalization, and at the same time it was accompanied by the generation of hydrogen bubbles, which was not conducive to cell growth. After hydrogen fluoride treatment, the hydrophobic Mg-HF surface lacks reactive groups and cannot bind cells through non-receptors, which is not conducive to cell adhesion. However, the hydrophobic surface may adsorb proteins in the culture medium, thereby promoting cell adhesion and proliferation (Pan et al., 2017), resulting in the increased CCK-8 values. After the deposition of the polydopamine, both the corrosion resistance and hydrophilicity increased, and a variety of active groups were also introduced, so the CCK-8 value increased significantly. Chitosan is a natural

polysaccharide polymer, which has good biodegradability and can promote cell adhesion and growth (Adhikari et al., 2016), so the CCK-8 value further increased for Mg-Chi. After continuous surface modification, the surface hydrophilicity was enhanced and more chemical groups (such as–OH, –COOH, $–NH_2$) were introduced, thus cell adhesion can also occur through non-receptor chemical binding, such as electrostatic, ionic–polar interactions, hydrogen binding to surface functional groups (Dekker et al., 1993; Liu et al., 2014b). After the introduction of PEG-Hep, the hydrophilicity became the best, which can provide excellent conditions for the initial growth of cells. Meanwhile, Mg-PEG-Hep has the best corrosion resistance and a non-polluting surface, which can inhibit protein adsorption and cell adhesion (Pan et al., 2016), and heparin can specifically bind to vascular endothelial growth factor to promote endothelial cells grow, so the CCK-8 value was the highest and the number of cells was also the highest. In summary, Mg-PEG-Hep had good cell compatibility, which was conducive to cell adhesion and growth.

## CONCLUSION

In this paper, PEG-Hep polymer was successfully synthesized and immobilized on the magnesium alloy, and its biological properties were evaluated by various methods. The introduction of PEG-Hep on the magnesium alloy can obtain the compact and dense layer, which can effectively enhance the corrosion resistance of the magnesium alloy. At the same time, due to the introduction of PEG-Hep, the blood compatibility of the magnesium alloy was significantly improved. In addition, the modified surface by PEG-Hep displayed good cytocompatibility to endothelial cells, the immobilization of PEG-Hep can significantly improve the adhesion and proliferation of vascular endothelial cells. In conclusion, the method of the present study can be used to modify the magnesium alloy to simultaneously improve the corrosion resistance biocompatibility, which can further enlarge the application of the magnesium alloy implants in the cardiovascular devices such as the stent.

## DATA AVAILABILITY STATEMENT

The original contributions presented in the study are included in the article/Supplementary Material, further inquiries can be directed to the corresponding author.

## AUTHOR CONTRIBUTIONS

QH, HZ and CP contributed substantially to the conception and design of the experiments. QH and YC conducted experiments and wrote the manuscript. MY and QZ conducted data analyses. SL and QX revised and modified the draft.

## FUNDING

This work was financially supported by the National Natural Science Foundation of China (31870952) and Natural Science Foundation of Jiangsu Province of China (BK20181480).

## REFERENCES

Adhikari, U., Rijal, N. P., Khanal, S., Pai, D., Sankar, J., and Bhattarai, N. (2016). Magnesium Incorporated Chitosan Based Scaffolds for Tissue Engineering Applications. *Bioact. Mater.* 1, 132–139. doi:10.1016/j.bioactmat.2016.11.003

Alibeik, S., Zhu, S., Yau, J. W., Weitz, J. I., and Brash, J. L. (2012). Dual Surface Modification with PEG and Corn Trypsin Inhibitor: Effect of PEG:CTI Ratio on Protein Resistance and Anticoagulant Properties. *J. Biomed. Mater. Res.* 100A, 856–862. doi:10.1002/jbm.a.34022

Ball, V., Frari, D. D., Toniazzo, V., and Ruch, D. (2012). Kinetics of Polydopamine Film Deposition as a Function of pH and Dopamine Concentration: Insights in the Polydopamine Deposition Mechanism. *J. Colloid Interf. Sci.* 386, 366–372. doi:10.1016/j.jcis.2012.07.030

Banerjee, I., Pangule, R. C., and Kane, R. S. (2011). Antifouling Coatings: Recent Developments in the Design of Surfaces that Prevent Fouling by Proteins, Bacteria, and Marine Organisms. *Adv. Mater.* 23 (6), 690–718. doi:10.1002/adma.201001215

Bowen, P. K., Guillory, R. J., Shearier, E. R., Seitz, J.-M., Drelich, J., Bocks, M., et al. (2015). Metallic Zinc Exhibits Optimal Biocompatibility for Bioabsorbable Endovascular Stents. *Mater. Sci. Eng. C.* 56, 467–472. doi:10.1016/j.msec.2015.07.022

Chen, L., Li, J., Chang, J., Jin, S., Wu, D., Yan, H., et al. (2018). Mg-Zn-Y-Nd Coated with Citric Acid and Dopamine by Layer-By-Layer Self-Assembly to Improve Surface Biocompatibility. *Sci. China Technol. Sci.* 61, 1228–1237. doi:10.1007/s11431-017-9190-2

Da Conceicao, T. F., Scharnagl, N., Blawert, C., Dietzel, W., and Kainer, K. U. (2010). Surface Modification of Magnesium alloy AZ31 by Hydrofluoric Acid Treatment and its Effect on the Corrosion Behaviour. *Thin Solid Films* 518, 5209–5218. doi:10.1016/j.tsf.2010.04.114

Dekker, A., Beugeling, T., Poot, A., Spijkers, J., van Mourik, J. A., Feijen, J., et al. (1993). The Role of Cellular Fibronectin in the Interaction of Human Endothelial Cells with Polymers. *Clin. Mater.* 13, 101–107. doi:10.1016/0267-6605(93)90096-p

Gao, F., Hu, Y., Gong, Z., Liu, T., Gong, T., Liu, S., et al. (2019). Fabrication of Chitosan/heparinized Graphene Oxide Multilayer Coating to Improve Corrosion Resistance and Biocompatibility of Magnesium Alloys. *Mater. Sci. Eng. C* 104, 109947. doi:10.1016/j.msec.2019.109947

Guo, L., Wu, W., Zhou, Y., Zhang, F., Zeng, R., and Zeng, J. (2018). Layered Double Hydroxide Coatings on Magnesium Alloys: a Review. *J. Mater. Sci. Technol.* 34, 1455–1466. doi:10.1016/j.jmst.2018.03.003

He, Y., Li, Y., Yang, X., Hemler, E. C., Fang, Y., Zhao, L., et al. (2019). The Dietary Transition and its Association with Cardiometabolic Mortality Among Chinese Adults, 1982-2012: a Cross-Sectional Population-Based Study. *Lancet Diabetes Endocrinol.* 7, 540–548. doi:10.1016/s2213-8587(19)30152-4

Jiang, P.-L., Hou, R.-Q., Chen, C.-D., Sun, L., Dong, S.-G., Pan, J.-S., et al. (2016). Controllable Degradation of Medical Magnesium by Electrodeposited Composite Films of Mussel Adhesive Protein (Mefp-1) and Chitosan. *J. Colloid Interf. Sci.* 478, 246–255. doi:10.1016/j.jcis.2016.06.001

Jiang, W., Tian, Q., Vuong, T., Shashaty, M., Gopez, C., Sanders, T., et al. (2017). Comparison Study on Four Biodegradable Polymer Coatings for Controlling Magnesium Degradation and Human Endothelial Cell Adhesion and Spreading. *ACS Biomater. Sci. Eng.* 3, 936–950. doi:10.1021/acsbiomaterials.7b00215

Jiang, S., Cai, S., Lin, Y., Bao, X., Ling, R., Xie, D., et al. (2019). Effect of Alkali/acid Pretreatment on the Topography and Corrosion Resistance of As-Deposited CaP Coating on Magnesium Alloys. *J. Alloys Compd.* 793, 202–211. doi:10.1016/j.jallcom.2019.04.198

Koch, A. E., Polverini, P. J., Kunkel, S. L., Harlow, L. A., DiPietro, L. A., Elner, V. M., et al. (1992). Interleukin-8 as a Macrophage-Derived Mediator of Angiogenesis. *Science* 258, 1798–1801. doi:10.1126/science.1281554

Kovach, K. M., Capadona, J. R., Sen Gupta, A., and Potkay, J. A. (2014). The Effects of PEG-Based Surface Modification of PDMS Microchannels on Long-Term Hemocompatibility. *J. Biomed. Mater. Res.* 102A, 4195–4205. doi:10.1002/jbm.a.35090

Kröger, N., Kopp, A., Staudt, M., Rusu, M., Schuh, A., and Liehn, E. A. (2018). Hemocompatibility of Plasma Electrolytic Oxidation (PEO) Coated Mg-RE and Mg-Zn-Ca Alloys for Vascular Scaffold Applications. *Mater. Sci. Eng. C* 92, 819–826. doi:10.1016/j.msec.2018.07.031

Li, C.-Y., Yu, C., Zeng, R.-C., Zhang, B.-C., Cui, L.-Y., Wan, J., et al. (2020). *In Vitro* corrosion Resistance of a Ta2O5 Nanofilm on MAO Coated Magnesium alloy AZ31 by Atomic Layer Deposition. *Bioactive Mater.* 5, 34–43. doi:10.1016/j.bioactmat.2019.12.001

Li, J.-a., Chen, L., Zhang, X.-q., and Guan, S.-k. (2020). Enhancing Biocompatibility and Corrosion Resistance of Biodegradable Mg-Zn-Y-Nd alloy by Preparing PDA/HA Coating for Potential Application of Cardiovascular Biomaterials. *Mater. Sci. Eng. C* 109, 110607. doi:10.1016/j.msec.2019.110607

Liu, J., and Xi, T. (2016). Enhanced Anti-corrosion Ability and Biocompatibility of PLGA Coatings on MgZnYNd alloy by BTSE-APTES Pre-treatment for Cardiovascular Stent. *J. Mater. Sci. Technol.* 32, 845–857. doi:10.1016/j.jmst.2016.06.021

Liu, Y., Ai, K., and Lu, L. (2014). Polydopamine and its Derivative Materials: Synthesis and Promising Applications in Energy, Environmental, and Biomedical Fields. *Chem. Rev.* 114, 5057–5115. doi:10.1021/cr400407a

Liu, T., Liu, Y., Chen, Y., Liu, S., Maitz, M. F., Wang, X., et al. (2014). Immobilization of Heparin/poly-L-Lysine Nanoparticles on Dopamine-Coated Surface to Create a Heparin Density Gradient for Selective Direction of Platelet and Vascular Cells Behavior. *Acta Biomater.* 10, 1940–1954. doi:10.1016/j.actbio.2013.12.013

Liu, T., Hu, Y., Tan, J., Liu, S., Chen, J., Guo, X., et al. (2017). Surface Biomimetic Modification with Laminin-Loaded Heparin/poly-L-Lysine Nanoparticles for Improving the Biocompatibility. *Mater. Sci. Eng. C.* 71, 929–936. doi:10.1016/j.msec.2016.11.010

Ludwiczak, S., and Mucha, M. (2010). Modeling of Water Sorption Isotherms of Chitosan Blends. *Carbohydr. Polym.* 79, 34–39. doi:10.1016/j.carbpol.2009.07.014

Lv, J., Yu, C., Guo, Y., Bian, Z., Yang, L., Chen, Y., et al. (2017). Adherence to Healthy Lifestyle and Cardiovascular Diseases in the Chinese Population. *J. Am. Coll. Cardiol.* 69, 1116–1125. doi:10.1016/j.jacc.2016.11.076

Ly, X. N., and Yang, S. (2019). Influence of Current Mode on Microstructure and Corrosion Behavior of Micro-arc Oxidation (MAO) Biodegradable Mg-Zn-Ca alloy in Hank's Solution. *Surf. Coat. Technol.* 358, 331–339. doi:10.1016/j.surfcoat.2018.11.040

Ma, L., Qin, H., Cheng, C., Xia, Y., He, C., Nie, C., et al. (2013). Mussel-inspired Self-Coating at Macro-Interface with Improved Biocompatibility and Bioactivity via Dopamine Grafted Heparin-like Polymers and Heparin. *J. Mater. Chem. B* 2, 363–375. doi:10.1039/c3tb21388a

Makkar, P., Kang, H. J., Padalhin, A. R., Park, I., Moon, B.-G., and Lee, B. T. (2018). Development and Properties of Duplex MgF2/PCL Coatings on Biodegradable Magnesium alloy for Biomedical Applications. *PLOS ONE* 13, e0193927. April 2. doi:10.1371/journal.pone.0193927

Mao, L., Yuan, G., Niu, J., Zong, Y., and Ding, W. (2013). *In Vitro* degradation Behavior and Biocompatibility of Mg-Nd-Zn-Zr alloy by Hydrofluoric Acid Treatment. *Mater. Sci. Eng. C* 33, 242–250. doi:10.1016/j.msec.2012.08.036

Okamoto, Y., Watanabe, M., Miyatake, K., Morimoto, M., Shigemasa, Y., and Minami, S. (2002). Effects of Chitin/chitosan and Their Oligomers/monomers on Migrations of Fibroblasts and Vascular Endothelium. *Biomaterials* 23 (9), 1975–1979. doi:10.1016/s0142-9612(01)00324-6

Pan, C.-J., Hou, Y.-H., Zhang, B.-B., Dong, Y.-X., and Ding, H.-Y. (2014). Blood Compatibility and Interaction with Endothelial Cells of Titanium Modified by Sequential Immobilization of Poly (Ethylene Glycol) and Heparin. *J. Mater. Chem. B* 2, 892–902. doi:10.1039/c3tb21403f

Pan, C.-J., Hou, Y., Wang, Y.-N., Gao, F., Liu, T., Hou, Y.-H., et al. (2016). Effects of Self-Assembly of 3-phosphonopropionic Acid, 3-aminopropyltrimethoxysilane and Dopamine on the Corrosion Behaviors and Biocompatibility of a Magnesium alloy. *Mater. Sci. Eng. C* 67, 132–143. doi:10.1016/j.msec.2016.05.038

Pan, C.-J., Pang, L.-Q., Hou, Y., Lin, Y.-B., Gong, T., Liu, T., et al. (2017). Improving Corrosion Resistance and Biocompatibility of Magnesium Alloy by Sodium Hydroxide and Hydrofluoric Acid Treatments. *Appl. Sci.* 7, 33–48. doi:10.3390/app7010033

Pan, K., Li, X., Shi, H., Dai, M., Yang, Z., Chen, M., et al. (2022). Preparation of Photo-Crosslinked Aliphatic Polycarbonate Coatings with Predictable Degradation Behavior on Magnesium-alloy Stents by Electrophoretic Deposition. *Chem. Eng. J.* 427, 131596. doi:10.1016/j.cej.2021.131596

Qi, P., Yang, Y., Maitz, F. M., and Huang, N. (2013). Current Status of Research and Application in Vascular Stents. *Chin. Sci. Bull.* 58, 4362–4370. doi:10.1007/s11434-013-6070-1

Qi, P., Yang, Y., Zhao, S., Wang, J., Li, X., Tu, Q., et al. (2016). Improvement of Corrosion Resistance and Biocompatibility of Biodegradable Metallic Vascular Stent via Plasma Allylamine Polymerized Coating. *Mater. Des.* 96, 341–349. doi:10.1016/j.matdes.2016.02.039

Shi, J., Miao, X., Fu, H., Jiang, A., Liu, Y., Shi, X., et al. (2020). *In Vivo* biological Safety Evaluation of an Iron-Based Bioresorbable Drug-Eluting Stent. *Biometals* 33, 217–228. doi:10.1007/s10534-020-00244-2

Sigwart, U., Puel, J., Mirkovitch, V., Joffre, F., and Kappenberger, L. (1987). Intravascular Stents to Prevent Occlusion and Re-stenosis after Transluminal Angioplasty. *N. Engl. J. Med.* 316, 701–706. doi:10.1056/nejm198703193161201

Torii, S., Jinnouchi, H., Sakamoto, A., Kutyna, M., Cornelissen, A., Kuntz, S., et al. (2020). Drug-eluting Coronary Stents: Insights from Preclinical and Pathology Studies. *Nat. Rev. Cardiol.* 17, 37–51. doi:10.1038/s41569-019-0234-x

Ueno, H., Yamada, H., Tanaka, I., Kaba, N., Matsuura, M., Okumura, M., et al. (1999). Accelerating Effects of Chitosan for Healing at Early Phase of Experimental Open Wound in Dogs. *Biomaterials* 20, 1407–1414. doi:10.1016/s0142-9612(99)00046-0

Waite, J. H. (1983). Adhesion in Byssally Attached Bivalves. *Biol. Rev.* 58, 209–231. doi:10.1111/j.1469-185x.1983.tb00387.x

Wang, J.-l., Li, B.-c., Li, Z.-j., Ren, K.-f., Jin, L.-j., Zhang, S.-m., et al. (2014). Electropolymerization of Dopamine for Surface Modification of Complex-Shaped Cardiovascular Stents. *Biomaterials* 35, 7679–7689. doi:10.1016/j.biomaterials.2014.05.047

Wang, C., Yi, Z., Sheng, Y., Tian, L., Qin, L., Ngai, T., et al. (2019). Development of a Novel Biodegradable and Anti-bacterial Polyurethane Coating for Biomedical Magnesium Rods. *Mater. Sci. Eng. C* 99, 344–356. doi:10.1016/j.msec.2019.01.119

Wei, Q., Li, B., Yi, N., Su, B., Yin, Z., Zhang, F., et al. (2011). Improving the Blood Compatibility of Material Surfaces via Biomolecule-Immobilized Mussel-Inspired Coatings. *J. Biomed. Mater. Res.* 96A, 38–45. doi:10.1002/jbm.a.32956

Witte, F., Hort, N., Vogt, C., Cohen, S., Kainer, K. U., Willumeit, R., et al. (2008). Degradable Biomaterials Based on Magnesium Corrosion. *Curr. Opin. Solid State. Mater. Sci.* 12, 63–72. doi:10.1016/j.cossms.2009.04.001

Wu, K. K. (1996). Platelet Activation Mechanisms and Markers in Arterial Thrombosis. *J. Intern. Med.* 239, 17–34. doi:10.1046/j.1365-2796.1996.331661000.x

Xin, Y., Jiang, J., Huo, K., Tang, G., Tian, X., and Chu, P. K. (2009). Corrosion Resistance and Cytocompatibility of Biodegradable Surgical Magnesium alloy Coated with Hydrogenated Amorphous Silicon. *J. Biomed. Mater. Res.* 89A, 717–726. doi:10.1002/jbm.a.32006

Xu, W., Yagoshi, K., Asakura, T., Sasaki, M., and Niidome, T. (2019). Silk Fibroin as a Coating Polymer for Sirolimus-Eluting Magnesium alloy Stents. *ACS Appl. Bio Mater.* 3, 531–538. doi:10.1021/acsabm.9b00957

Yan, X., Zhao, M.-C., Yang, Y., Tan, L., Zhao, Y.-C., Yin, D.-F., et al. (2019). Improvement of Biodegradable and Antibacterial Properties by Solution Treatment and Micro-arc Oxidation (MAO) of a Magnesium alloy with a Trace of Copper. *Corrosion Sci.* 156, 125–138. doi:10.1016/j.corsci.2019.05.015

Yang, Z., Tu, Q., Zhu, Y., Luo, R., Li, X., Xie, Y., et al. (2012). Mussel-inspired Coating of Polydopamine Directs Endothelial and Smooth Muscle Cell Fate for Re-endothelialization of Vascular Devices. *Adv. Healthc. Mater.* 1, 548–559. doi:10.1002/adhm.201200073

Yang, Y., Xiong, X., Chen, J., Peng, X., Chen, D., and Pan, F. (2021). Research Advances in Magnesium and Magnesium Alloys Worldwide in 2020. *J. Magnesium Alloys* 9, 705–747. doi:10.1016/j.jma.2021.04.001

Zhai, X., Li, K., Guan, F., Sun, C., Duan, J., and Hou, B. (2018). Corrosion Behavior of the Chitosan-Zinc Composite Films in Sulfate-Reducing Bacteria. *Surf. Coat. Technol.* 344, 259–268. doi:10.1016/j.surfcoat.2018.03.032

Zhang, L.-C., Xu, M., Hu, Y.-D., Gao, F., Gong, T., Liu, T., et al. (2018). Biofunctionization of Biodegradable Magnesium alloy to Improve the *In Vitro* Corrosion Resistance and Biocompatibility. *Appl. Surf. Sci.* 451, 20–31. doi:10.1016/j.apsusc.2018.04.235

Zhang, Z.-Q., Yang, Y.-X., Li, J.-A., Zeng, R.-C., and Guan, S.-K. (2021). Advances in Coatings on Magnesium Alloys for Cardiovascular Stents - A Review. *Bioact. Mater.* 6, 4729–4757. doi:10.1016/j.bioactmat.2021.04.044

Zhang, B., Yao, R., Maitz, M. F., Mao, G., Hou, Z., Yu, H., et al. (2021). Poly (Dimethyl Diallyl Ammonium Chloride) Incorporated Multilayer Coating on Biodegradable AZ31 Magnesium alloy with Enhanced Resistance to Chloride Corrosion and Promoted Endothelialization. *Chem. Eng. J.* 421, 127724. doi:10.1016/j.cej.2020.127724

Zhou, C., Li, H.-F., Yin, Y.-X., Shi, Z.-Z., Li, T., Feng, X.-Y., et al. (2019). Long-term *In Vivo* Study of Biodegradable Zn-Cu Stent: a 2-year Implantation Evaluation in Porcine Coronary Artery. *Acta Biomater.* 97, 657–670. doi:10.1016/j.actbio.2019.08.012

**Conflict of Interest:** The authors declare that the research was conducted in the absence of any commercial or financial relationships that could be construed as a potential conflict of interest.

**Publisher's Note:** All claims expressed in this article are solely those of the authors and do not necessarily represent those of their affiliated organizations, or those of the publisher, the editors and the reviewers. Any product that may be evaluated in this article, or claim that may be made by its manufacturer, is not guaranteed or endorsed by the publisher.

frontiers in Bioengineering and Biotechnology

ORIGINAL RESEARCH
published: 06 December 2021
doi: 10.3389/fbioe.2021.792893

# Gelatin/Polycaprolactone Electrospun Nanofibrous Membranes: The Effect of Composition and Physicochemical Properties on Postoperative Cardiac Adhesion

*Xingang Wang[1,2†], Li Xiang[1†], Yongxuan Peng[3], Zihao Dai[2], Yuqing Hu[1], Xiaoting Pan[2], Xingliang Zhou[1], Hao Zhang[2]* and Bei Feng[1]**

[1]Shanghai Institute of Pediatric Congenital Heart Disease, Shanghai Children's Medical Center, School of Medicine, Shanghai Jiao Tong University, Shanghai, China, [2]Children's Heart Center, Institute of Cardiovascular Development and Translational Medicine, The Second Affiliated Hospital and Yuying Children's Hospital, Wenzhou Medical University, Wenzhou, China, [3]Department of Pediatric Cardiology, Xinhua Hospital, Shanghai Jiao Tong University School of Medicine, Shanghai, China

OPEN ACCESS

**Edited by:**
Guicai Li,
Nantong University, China

**Reviewed by:**
Shige Wang,
University of Shanghai for Science and Technology, China
Hui Wang,
Shanghai Advanced Research Institute (CAS), China

***Correspondence:**
Hao Zhang
drzhanghao@126.com
Bei Feng
fengbei04@163.com

[†]These authors have contributed equally to this work

**Specialty section:**
This article was submitted to Biomaterials, a section of the journal Frontiers in Bioengineering and Biotechnology

**Received:** 11 October 2021
**Accepted:** 08 November 2021
**Published:** 06 December 2021

**Citation:**
Wang X, Xiang L, Peng Y, Dai Z, Hu Y, Pan X, Zhou X, Zhang H and Feng B (2021) Gelatin/Polycaprolactone Electrospun Nanofibrous Membranes: The Effect of Composition and Physicochemical Properties on Postoperative Cardiac Adhesion. Front. Bioeng. Biotechnol. 9:792893. doi: 10.3389/fbioe.2021.792893

Cardiovascular diseases have become a major threat to human health. The adhesion formation is an inevitable pathophysiological event after cardiac surgery. We have previously shown that gelatin/polycaprolactone (GT/PCL, mass ratio 50:50) electrospun nanofibrous membranes have high potential in preventing postoperative cardiac adhesion, but the effect of GT:PCL composition on anti-adhesion efficacy was not investigated. Herein, nanofibrous membranes with different GT:PCL mass ratios of 0:100, 30:70, 50:50, and 70:30 were prepared via electrospinning. The 70:30 membrane failed to prevent postoperative cardiac adhesion, overly high GT contents significantly deteriorated the mechanical properties, which complicated the suturing during surgery and hardly maintained the structural integrity after implantation. Unexpectedly, the 0:100 membrane (no gelatin contained) could not effectively prevent either, since its large pore size allowed the penetration of numerous inflammatory cells to elicit a severe inflammatory response. Only the GT:PCL 50:50 membrane exhibited excellent mechanical properties, good biocompatibility and effective anti-cell penetration ability, which could serve as a physical barrier to prevent postoperative cardiac adhesion and might be suitable for other biomedical applications such as wound healing, guided tissue or bone regeneration.

**Keywords: electrospinning, gelatin, polycaprolactone, postoperative adhesion, cardiac surgery**

## HIGHLIGHTS

- The 70:30 membrane (high gelatin contained) failed to prevent postoperative cardiac adhesion in view of its poor mechanical properties.
- The 0:100 membrane (no gelatin contained) was not suitable to prevent postoperative adhesion either because of its large pore size.
- Only the 50:50 membrane effectively prevented postoperative adhesion and showed great potential in wound healing, guided tissue or bone regeneration.

# 1 INTRODUCTION

Cardiovascular diseases have become a major threat to human health, accounting for nearly 31% of deaths worldwide (Leong et al., 2017). The rapid development of interventional therapy and novel drugs has helped a lot to these diseases; nevertheless, surgical treatments still remain essential to many complex heart diseases. Thus, the formation of adhesions between the chest wall and epicardium is an inevitable postoperative pathophysiological event after cardiac surgery. Adhesions caused by the initial surgery make the original anatomical structure disappear or become much more complicated, which increases the risks during reoperations (Shen and Xu, 2014). The prevention of postoperative cardiac adhesion can greatly reduce the reoperative difficulties, intraoperative and postoperative bleeding, surgery time and costs, and even mortality (Lassaletta et al., 2012).

Among the strategies adopted to prevent postoperative cardiac adhesions (e.g., pharmacological intervention (Lopes et al., 2009) or physical barriers (de Oliveira et al., 2014)), using biomaterial-based membranes is believed to be the most promising one. Expanded polytetrafluoroethylene (ePTFE) is possibly the most extensively utilized and evaluated membrane used to prevent postoperative cardiac adhesion (Minale et al., 1988; Jacobs et al., 1996), but it has not been routinely applied in clinic due to certain shortages such as non-degradability, chronic foreign-body reactions, and predispose to infection over time (Ozeren et al., 2002; Tsukihara et al., 2006). Furthermore, several reports have shown that ePTFE membranes may cause severe adhesions and prominent inflammatory reactions as well (Naito et al., 2008; Kaushal et al., 2011).

Electrospinning has become a widely applied method to fabricate nanofibers due to its cost-effectiveness, simplicity, and suitability for mass production (Xue et al., 2019; Keshvardoostchokami et al., 2020; Xu et al., 2021). Owing to its dense fibrous structure, tiny pore size, controllable mechanical properties, and adjustable degradation rate, the electrospun nanofibrous membrane has shown great potential in preventing postoperative adhesions as a physical barrier (Chen et al., 2019; Alimohammadi et al., 2020; Mao et al., 2021). In our pilot study, we have discovered the elelctrospun GT/PCL (mass ratio 50:50) nanofibrous membrane might become a promising barrier to prevent postoperative cardiac adhesion (Feng et al., 2019). However, the GT:PCL composition could affect the mechanical properties, physical structure, biocompatibility, and degradation rate of membranes, and therefore might eventually influence their anti-adhesion efficacy. For instance, Ghasemi et al. reported that compared with GT:PCL 0:100 and 50:50, 30:70 nanofibrous membranes exhibited the most balanced properties to meet all required specifications for nerve regeneration (Ghasemi-Mobarakeh et al., 2008). While Zheng et al. demonstrated that the high PCL content in GT/PCL membranes was unfavorable for 3-D cartilage regeneration and 70:30 might be a relatively suitable ratio (Zheng et al., 2014).

Herein, we fabricated four nanofibrous membranes with different GT:PCL mass ratios of 0:100, 30:70, 50:50, and 70:30 via electrospinning, and comprehensively evaluated their physicochemical properties, biocompatibility, heart/liver/kidney functions, CRP/immunoglobulin levels, and anti-adhesion performance to determine the most optimal composition and provide a strong theoretical basis for the clinical development and applications of these related membranes. Pure GT membrane was not considered since it failed to maintain the structural integrity owing to its poor mechanical properties (Nagarajan et al., 2017).

# 2 MATERIALS AND METHODS

## 2.1 Materials

GT type A (V900863, 300 Bloom from porcine skin), PCL (440744, average $M_w$ = 80,000 Da), acetic acid (HAc; 338826, ≥99.8%), and 2, 2, 2-trifluoroethanol (TFE; T63002, ≥99.0%) were purchased from Sigma Aldrich (United States) and were used as received without further purification. Dulbecco's modified Eagle medium nutrient mix F12 (DMEM/F12, 11330033), fetal bovine serum (FBS; 10099-141C), penicillin-streptomycin (15140-122), and trypsin (25200-056) were purchased from Thermo Fisher Scientific (United States). Anti-cardiac troponin T (ab45932) and anti-vimentin (ab92547) primary antibodies were purchased from Abcam (United Kingdom). Anti-rabbit IgG fluorescent secondary antibody (4412S) was purchased from Cell Signaling Technology (United States). 4′, 6-Diamidino-2-phenylindole (DAPI; C1002) was purchased from Beyotime Biotechnology (China). The neonatal rat/mouse cardiomyocyte isolation kit (nc-6031) was purchased from Cellutron Life Technologies (United States). Live/dead cell viability assay kits (L3224) were purchased from Thermo Fisher Scientific (United States). Cell Counting Kit-8 (CCK-8; CK04) was purchased from Dojindo Laboratories (Kumamoto, Japan). A modified hematoxylin-eosin (H-E) staining kit (G1121) was purchased from Solarbio Technology (China).

## 2.2 Membrane Preparation

GT and PCL with mass ratios of 30:70, 50:50, and 70:30 were dissolved in TFE to produce a total concentration of 10% (w/v), and the solution was supplemented with a small amount of HAc (0.2 vol%) to obtain a transparent GT/PCL solution. In the case of pure-PCL membrane, PCL was dissolved in TFE at a concentration of 12% (w/v) without HAc. After 48-h stirring, the solutions were filled into a 10-ml syringe with a blunt needle (20G) and fed into the electrospinning device at 2 ml/h using a syringe pump (KDS100, KD Scientific, United States). A rotating stainless-steel drum (diameter = 5 cm, rotation speed = 100 rpm) was used as a collector to prepare membranes with uniform thickness. A high voltage (TXR1020N30-30, Teslaman, China) was applied between the needle tip and grounded collector, with the distance between tip and collector maintained at 13 cm. Other detailed electrospinning parameters in fabrication of different GT/PCL nanofibrous membranes were listed in **Table 1**. Aluminum foil was wrapped on the collector before electrospinning to facilitate membrane collection and tailoring. The obtained membranes were placed in a vacuum oven for at least 1 week to remove the residual solvent for subsequent use.

**TABLE 1 |** Parameters used for electrospinning nanofibrous membranes of GT/PCL.

| Membranes (GT:PCL) | Concentration (%) | Applied voltage (KV) | Temperature (°C) | Humidity (%) |
|---|---|---|---|---|
| 0:100 | 12 w/v | 8–9 | 20–25 | 40–60 |
| 30:70 | 10 w/v | 13–14 | 20–25 | 40–60 |
| 50:50 | 10 w/v | 14–15 | 20–25 | 40–60 |
| 70:30 | 10 w/v | 15–16 | 20–25 | 40–60 |

## 2.3 Membrane Characterization

Membrane morphologies were observed by scanning electron microscopy (SEM; JSM-5600LV, JEOL, Japan) at an acceleration voltage of 10 kV. Prior to imaging, the membranes were sputter-coated with Pt for 60 s to increase their conductivity. Fiber diameters and pore sizes were determined from SEM images.

Attenuated total reflection Fourier transform infrared (FT-IR) spectra were recorded on an FT-IR spectrometer (Nicolet-Nexus 670, Thermo Fisher Scientific, United States) using a scan range of 500–4,000 $cm^{-1}$ and a resolution of 2 $cm^{-1}$.

Membrane surface hydrophilicity/hydrophobicity was evaluated by a video contact angle analyzer (Attension Theta, Biolin Scientific AB, Finland). Briefly, deionized water droplets (3 μL) were automatically dispensed onto the membrane surface, and the dynamic changes in their shape were recorded.

Given that the membranes would be applied in a moist environment at 37°C *in vivo*, their post-implantation shrinkage behavior was tested by immersing 1.5 cm × 1.5 cm membrane pieces with attached aluminum foil into physiological saline at 37°C. After 24 h, the membranes were removed and imaged using a high-resolution camera (EOS 6D, Canon, Japan). For post-implantation mechanical property evaluation, the membranes were cut into 5 cm × 1 cm pieces, immersed into physiological saline at 37°C for 24 h as well, loaded on a biomechanical testing machine (Instron-3343, Norwood, United States), and stretched as previously described (Feng et al., 2020).

## 2.4 *In vitro* Evaluation of Membrane Biocompatibility

### 2.4.1 Isolation and Culturing of Neonatal Rat Ventricular Cardiomyocytes and Cardiac Fibroblasts

Given the membranes were designed for implantation *in vivo* as pericardial substitutes, cardiomyocytes and cardiac fibroblasts were selected as seeding cells to evaluate the biocompatibility of membranes. Cells were isolated from neonatal Sprague Dawley (SD) rats within 3 days after birth using a neonatal rat/mouse cardiomyocyte isolation kit. Briefly, neonatal SD rats were sterilized with 75 vol% aqueous ethanol, the chests were opened, hearts were removed, and ventricular tissues were cut and digested in a specific enzyme buffer for 12 min at 37°C. Then, the supernatant was transferred to a new tube, and new enzyme buffer was added to digest the remaining tissues. This step was repeated four to six times until all the tissues have been digested. Finally, the supernatant was collected and centrifuged at 1,200 rpm for 1 min to afford the desired cells as a pellet. After 2-h culturing, most cardiac fibroblasts were attached to the bottom of the plates, and the unattached cells were transferred to new plate and cultured for another 4 h to remove residual cardiac fibroblasts and afford cardiomyocytes suspended in the culture medium. The two types of cells were cultured in DMEM/F-12 medium with 10% FBS and 1% penicillin-streptomycin and ready for further experiments after 48 h.

### 2.4.2 Evaluation of Membrane Cytotoxicity

Nanofibrous membranes were collected on circular cover slices (diameter = 15 mm), exposed to ultraviolet radiation for 30 min in a biological safety cabin, placed at the bottom of a 24-well plate with steel rings, and pre-cultured in DMEM/F-12 medium with 10% FBS and 1% penicillin-streptomycin overnight. In view of the rapid proliferation capacity of cardiac fibroblasts, cardiomyocytes and cardiac fibroblasts were seeded onto the membranes at densities of $5 \times 10^4$ and $2.5 \times 10^4$ cells per well, respectively. Cell viability was determined using the live and dead cell viability/cytotoxicity assay kit after one and 7 days of culturing. Briefly, the cells were incubated in with 2 μM calcein AM and 4 μM ethidium homodimer-1 for 1 h in the dark, washed in Dulbecco's phosphate buffered saline three times, and directly imaged using a laser confocal microscope system (TSC SP8, Leica, Germany).

### 2.4.3 Efficiency of Cell Seeding on Membranes

Cardiomyocytes and cardiac fibroblasts were counted using an automated cell counter (iM1200, Countstar, China) to determine the total cell number and total live cell number prior to seeding. Given their absolutely different adhesion speeds, cardiac fibroblasts were incubated for 6 h, while cardiomyocytes overnight. At predetermined times, the culture medium was collected to determine the total unattached cell number suspended in medium by the automated cell counter again. Hence, the total attached cell number = total cell number − total unattached cell number. The seeding efficiency (%) was calculated as 100% × total attached cell number/total live cell number.

### 2.4.4 Morphology of Cells on Membranes

The morphology of membrane-attached cells was observed using immunostaining. After one- and 5-day incubation on membranes, cells were fixed with 4% paraformaldehyde for 30 min, permeabilized with 0.5% Triton X-100 for 10 min and blocked with 10% goat serum in phosphate-buffered saline (PBS) for 1 h at room temperature. Two primary antibodies (anti-cardiac troponin T and anti-vimentin antibodies for cardiomyocytes and cardiac fibroblasts, respectively) were used according to manufacturer's instructions. Additionally, the antibodies were labeled with fluorescent conjugated secondary

antibodies for another 2 h, and the cell nuclei were stained with DAPI for 30 s in the dark. The samples were washed three times with PBS on a shaker and visualized using a confocal microscope.

#### 2.4.5 Cell Proliferation on Membranes

Cell proliferation on membranes was evaluated using CCK-8 on days one, three, five, and seven. Prior to measurements, the cells were cultured in another medium containing 10% CCK-8 for 2.5 h. Absorbance was measured at 450 nm using a microplate reader (Multiskan MK3, Thermo Electron Corporation, United States).

### 2.5 *In vivo* Evaluation of Membrane Anti-Adhesion Efficacy

#### 2.5.1 Animals

Three-month-old healthy male New Zealand white rabbits weighing 2–2.5 kg were obtained from Shanghai Jiaotong University Agricultural Experimental Practice Field (Shanghai, China), housed in a temperature-controlled room (22°C) and fed a standard laboratory diet and water. All animal experiments were approved by the Animal Care and Experiment Committee of Shanghai Jiaotong University Agricultural Experimental Practice Field. The experiment was set up consisting five groups (positive control, 0:100, 30:70, 50:50, and 70:30) at 1 month after surgery, each group was analyzed for 5 animals. And at another time point of three months, positive control (6 animals), 0:100 (8 animals which considered its strong individual differences one month after surgery), 30:70 (6 animals), and 50:50 (6 animals) were analyzed, while two animals were died after surgery (one positive control group and one 0:100 group). In total, 51 animals were used in this study.

#### 2.5.2 Surgical Procedures

The animals were divided into one positive control group and four experimental groups (GT:PCL = 0:100, 30:70, 50:50, and 70:30). In this study, we optimized our previous experimental procedure (e.g., cut the membranes into 1.5 cm × 1.5 cm pieces) and paid more attention to postoperative treatment and ethical care. Cefuroxime (30 mg/kg) was intramuscularly administered for anti-infection for three consecutive days, while tramadol (50 mg) was intramuscularly administered for analgesia for two consecutive days. Other specific surgical protocols were almost consistent with those used previously (Feng et al., 2019).

#### 2.5.3 Heart Function Evaluation

Echocardiography was used one and 3 months after surgery to determine whether the nanofibrous membranes influenced heart function or induced ventricular remodeling. Briefly, the rabbits were anesthetized by intravenous injection of sodium pentobarbital (30 mg/kg), and transthoracic echocardiography was performed from the right sternum using a 12S probe (Vivid E95, GE, United States) to detect the long axial section of the left ventricle. The left ventricular ejection fraction (LVEF) and fractional shortening (LVFS) required indirect calculation, while the left ventricular posterior wall thickness (LVPWd) and interventricular septal thickness (IVSd) at end-diastole were directly determined using M-mode echocardiography. Six healthy rabbits were randomly selected for detection before surgery as a normal control.

#### 2.5.4 Liver/Kidney Function and CRP/Immunoglobulin Level Assessments

The liver/kidney function and CRP/immunoglobulin levels were evaluated one and 3 months after surgery to assess the biosafety of membranes after implantation. Seven (aspartate transaminase (AST), alanine transaminase (ALT), total bilirubin (TBIL), total protein (TP), albumin (ALB), globulin, albumin/globulin (A/G)) and three (blood urea nitrogen (BUN), creatinine (CREA), and cystatin C (Cys C)) commonly used indices were employed to assess liver and kidney functions (Chen et al., 2015a), respectively. Four immunoglobulins (IgG, IgM, IgA, and total IgE) were selected to evaluate the immune rejection level (Jin et al., 2019). Specifically, ~3 ml of fasting blood was collected from the internal jugular vein after completing the echocardiography. 2-ml blood was placed into a non-coagulated sterile tube and centrifuged at 4,000 rpm for 10 min. The upper serum was analyzed to determine the liver/kidney function and immunoglobulin levels using an automatic biochemical analyzer (C16000, Abbott Architect, United States) and a specific protein analyzer (BN II, Siemens, Germany), respectively. The remaining 1 ml was promptly transferred to an ethylene diamine tetraacetic acid (EDTA) blood collection tube, and the CRP level was determined by an automated specific protein iPOCT workstation (Ottoman-1000, Ottoman, China). All procedures were performed in strict accordance with manufacturer's instructions. Given the short half-life of immunoglobulins (maximal at ~28 days for IgG), their levels were examined only for a period of 1 month after surgery. The basic normal levels of liver/kidney function, CRP and immunoglobulins were determined by six healthy rabbits before surgery as well.

#### 2.5.5 Overall Observation

Following echocardiography and blood collection, each rabbit was euthanized with sufficient sodium pentobarbital and underwent repeated sternotomy. The macroscopic adhesions were scored by an experienced surgeon, who was blinded for the purpose of this study, and the adhesion was scored using a previously reported standardized scale (Malm et al., 1992): 0 = no adhesion between the heart and sternum/material; 1 = mild adhesions, easy to separate by blunt dissection; 2 = moderate adhesions, partially requiring sharp dissection; 3 = severe adhesions, mainly requiring sharp dissection and easy bleeding. Another blinded observer assisted in image acquisition at the same time.

#### 2.5.6 Histological Staining

After overall observation, the membranes were carefully removed from surrounding tissues, fixed in 10% neutral buffered formalin for at least 24 h, dehydrated using alcohol gradients, embedded in paraffin, and sectioned into 5-μm-thick slices for H-E staining to assess the inflammatory reaction and physical barrier function.

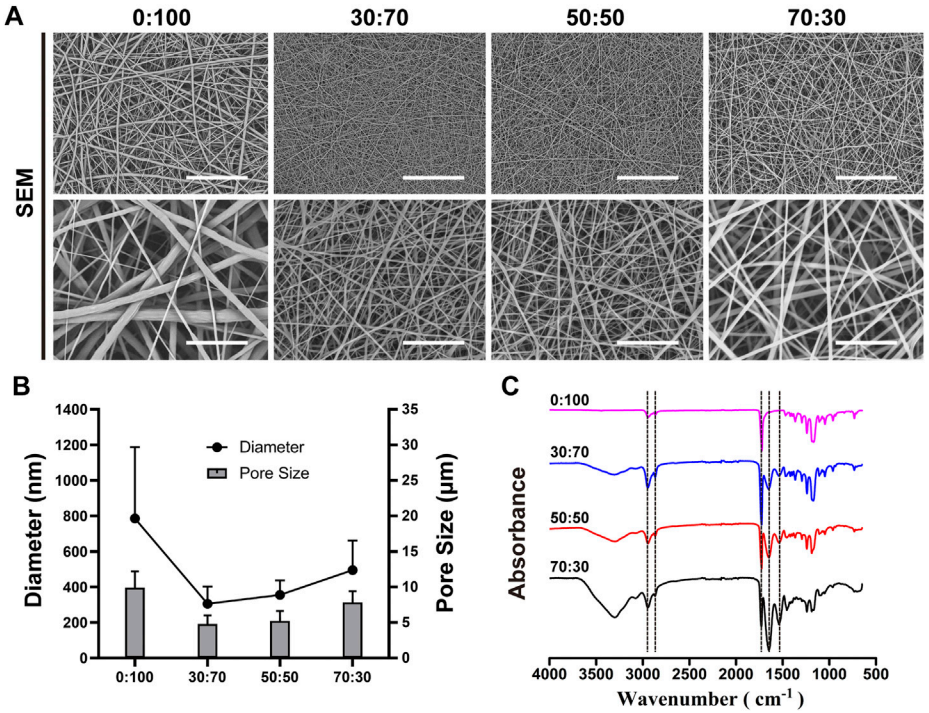


**FIGURE 1 |** Representative **(A)** SEM micrographs [scale bars equal 50 μm (low magnification) and 10 μm (high magnification)], **(B)** fiber diameters and pore sizes, and **(C)** FT-IR spectra of nanofibrous membranes.

## 2.6 Statistical Analysis

All quantitative data were presented as means ± standard deviations. One-way analysis of variance followed by Tukey's post hoc test was used to determine statistically significant differences between groups. Significant difference was considered at $^{*}p < 0.05$; $^{**}p < 0.01$; $^{***}p < 0.001$.

# 3 RESULTS

## 3.1 Preparation and Characterization of GT/PCL Membranes

As shown in **Figure 1A**, all fibers exhibited a smooth surface without beads or bonding. The pure-PCL (0:100) membrane fibers were relatively thick (average diameter = 785.5 ± 401.5 nm), while thinner fibers were present in GT-containing membranes (average diameters = 304.7 ± 98.1 and 355.7 ± 81.0 nm for GT:PCL = 30:70 and 50:50, respectively). However, at a ratio of 70:30, the fiber diameter increased to 494.7 ± 166.6 nm. As for the pore size, which is an important parameter for selection of membranes as barriers to prevent cell penetration, increased with the increasing fiber diameter (**Figure 1B**), equaling 9.9 ± 2.3, 4.8 ± 1.2, 5.2 ± 1.4, and 7.8 ± 1.6 μm for different ratios of 0:100, 30:70, 50:50, and 70:30, respectively. Membrane composition was probed by FT-IR (**Figure 1C**). The characteristic peaks of PCL at 2,943 $cm^{-1}$ (asymmetric $CH_2$ stretch), 2,865 $cm^{-1}$ (symmetric $CH_2$ stretch), and 1,724 $cm^{-1}$ (C=O stretch) were observed for all membranes, while the characteristic peaks of GT at 1,652 $cm^{-1}$ (amide I) and 1,540 $cm^{-1}$ (amide II) were only observed for GT/PCL membranes. The amide I band was attributed to the random coil and α-helix conformations of GT. As expected, the areal fractions of PCL- and GT-specific peaks decreased and increased with increasing GT content, respectively.

The 0:100 membrane was highly hydrophobic, and the water droplets deposited thereon formed a large obtuse contact angle (137.0 ± 7.0°) and remained stable. The incorporation of GT greatly increased hydrophilicity, and all GT/PCL membranes presented hydrophilic surfaces with acute contact angles (**Figure 2**). In the case of the 30:70 membrane, water was rapidly absorbed to afford a contact angle of zero within 30 s. However, the rate of water absorption decreased at higher GT contents, in line with the fact that water absorption by pure-GT membranes is also insufficient (Feng et al., 2012).

As the membranes were implanted *in vivo*, they were immersed into saline held at 37°C to characterize shrinkage under simulated physiological conditions. Compared with their original size (i.e., the size of the underlying aluminum foil), the 0:100 membrane did not shrink, while 30:70, 50:50, and 70:30 membranes slightly contracted, which indicated that all membranes had good thermal stability (**Figure 3A**). However, these membranes showed different mechanical properties (**Figure 3B**; **Table 2**). The introduction of GT

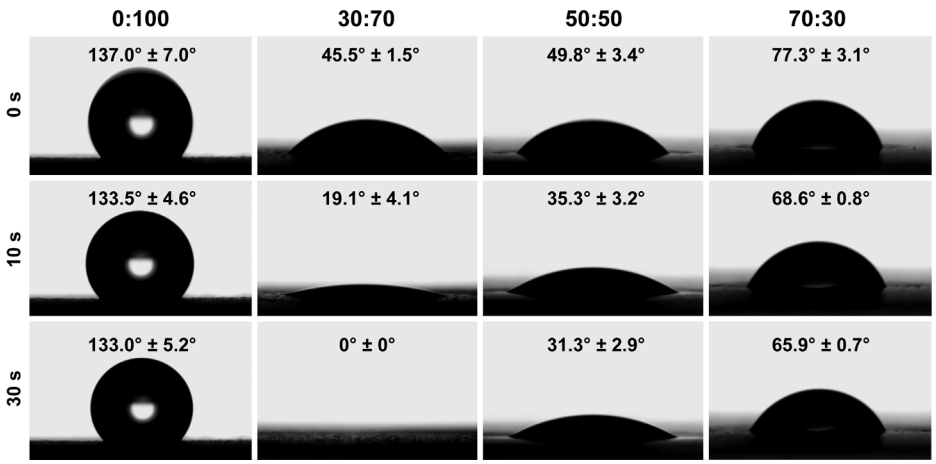


**FIGURE 2 |** Water contact angles of different nanofibrous membranes.

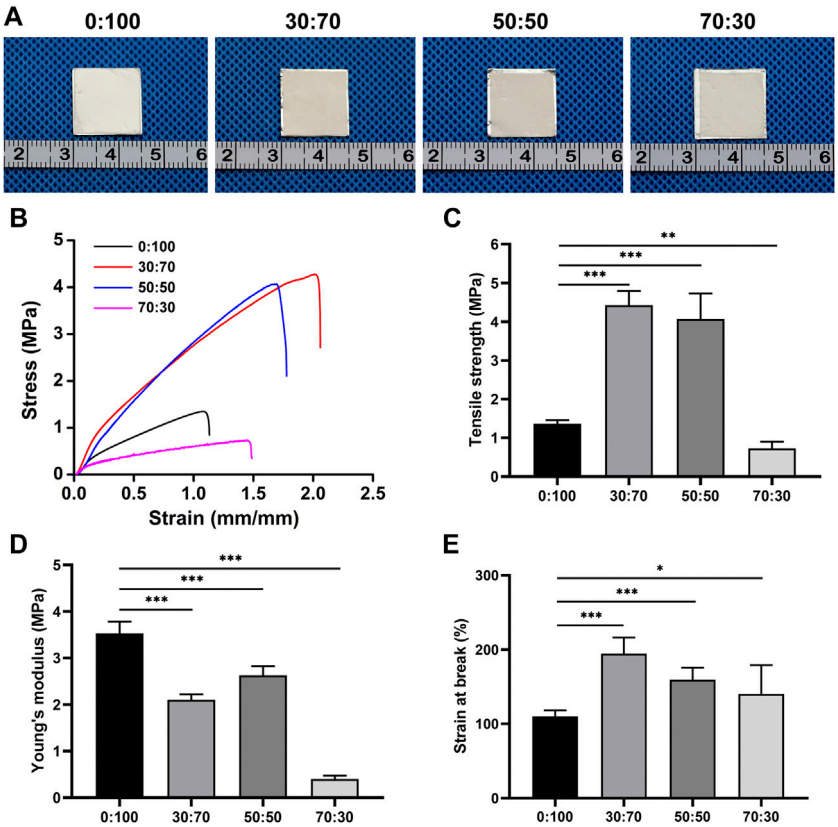


**FIGURE 3 | (A)** Gross views, **(B)** stress-strain curves, **(C)** tensile strengths, **(D)** Young's modulus, and **(E)** strains at break of membranes after 24-h immersion into physiological saline at 37°C (*$p < 0.05$; **$p < 0.01$; ***$p < 0.001$).

greatly improved the mechanical properties of membranes with the increased maximum tensile strength (**Figure 3C**) and strain at break (**Figure 3E**), while significant mechanical property deterioration was observed at a GT content of 70%, as exemplified by the decreased maximum tensile strength (**Figure 3C**) and Young's modulus (**Figure 3D**). In

**TABLE 2 |** Mechanical parameters calculated from the strain-stress curves of wet membranes.

| Membrane | Young's modulus (MPa) | Tensile strength (MPa) | Strain at break (%) |
|---|---|---|---|
| 0:100 | 3.5 ± 0.2 | 1.4 ± 0.1 | 110.0 ± 8.1 |
| 30:70 | 2.1 ± 0.1 | 4.4 ± 0.3 | 194.6 ± 21.4 |
| 50:50 | 2.6 ± 0.2 | 4.1 ± 0.7 | 159.4 ± 16.2 |
| 70:30 | 0.4 ± 0.1 | 0.7 ± 0.2 | 140.3 ± 39.0 |

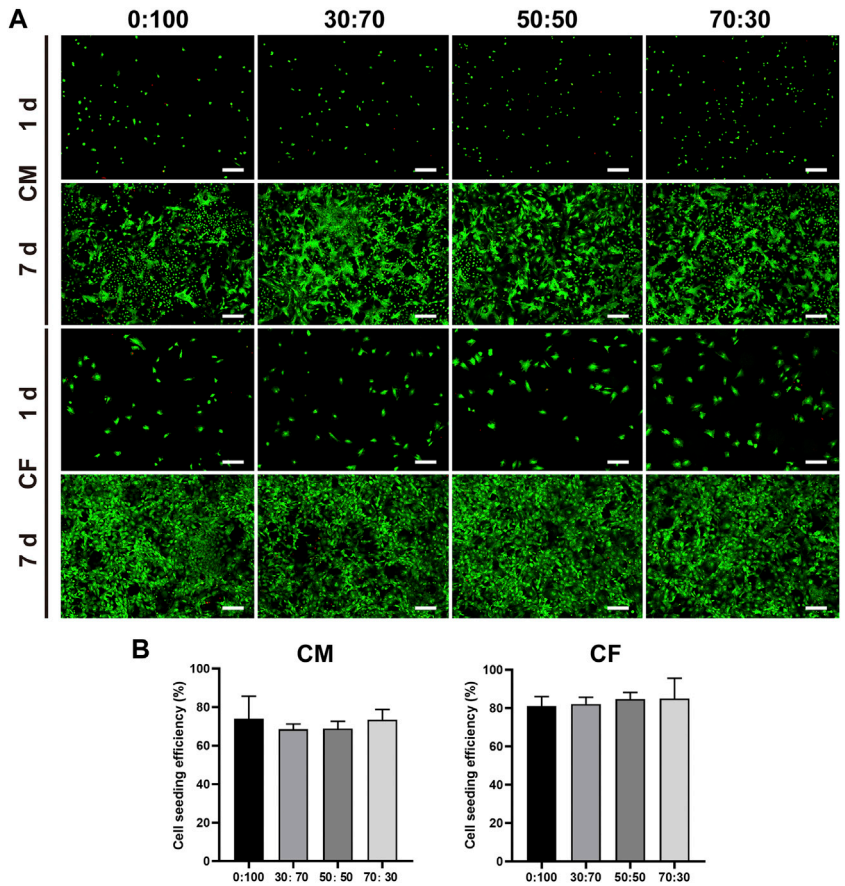


**FIGURE 4 | (A)** Representative live and dead staining images of cardiomyocytes and cardiac fibroblasts cultured on different membranes for one and 7 days. Scale bars = 200 μm. **(B)** Seeding efficiencies of cardiomyocytes and cardiac fibroblasts on different membranes.

particular, the maximum tensile strength decreased in the order of 4.4 ± 0.4 MPa (30:70) > 4.1 ± 0.6 MPa (50:50) > 1.4 ± 0.1 MPa (0:100) > 0.7 ± 0.2 MPa (70:30).

## 3.2 Biocompatibility of GT/PCL Membranes *in vitro*

The viability of cardiomyocytes and cardiac fibroblasts on membranes was assessed using the live/dead cell assay. In the obtained images, green fluorescence represents live cells, while red fluorescence represents the dead. After 1 day of culturing, both cardiomyocytes and cardiac fibroblasts adhered well to all membranes, as exemplified by the numerous green dots (live cells) and few red dots (dead cells) (**Figure 4A**). The cells continued to grow with time, reaching ~90% (cardiomyocytes) and 100% (fibroblasts) confluency on all membranes with bright green fluorescence on day seven. In addition, cell seeding efficiencies reached ~70% (cardiomyocytes) and 80% (fibroblasts) on all membranes without significant differences (**Figure 4B**).

The morphology and proliferation of cells cultured on membranes were evaluated using immunofluorescence staining (**Figure 5A**). Troponin T (cardiomyocytes) and vimentin (fibroblasts) staining showed that both cells well adhered and spread on all membranes on day one, although a larger fibroblast spreading area was observed for the 70:30 group. With increasing cultivation time, cardiomyocytes and fibroblasts rapidly proliferated on all membranes at day five. In line with the results of immunofluorescence staining, those of the CCK-8

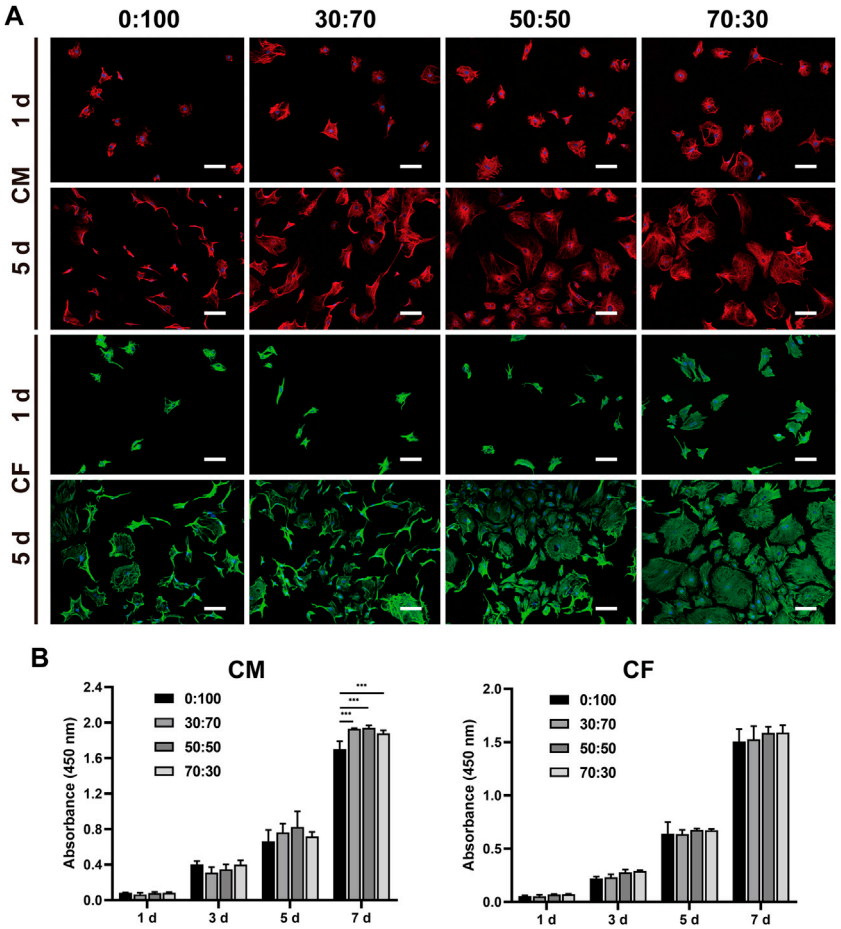


**FIGURE 5 | (A)** Representative immunofluorescence staining images of cardiomyocytes and cardiac fibroblasts cultured on different membranes for one and 5 days. Blue: nucleus. Red: cTNT. Green: vimentin. Scale bars = 100 μm. **(B)** Proliferation of cardiomyocytes and cardiac fibroblasts cultured on different nanofibrous membranes for one, three, five, and 7 days. (***$p < 0.001$).

assay (**Figure 5B**) revealed that cardiomyocytes and fibroblasts exhibited steady and continuous proliferation without significant difference between groups, except for the downward trend in the 0:100 group at day seven for cardiomyocytes.

Collectively, these results indicated that all GT/PCL membranes had good biocompatibility with cardiomyocytes and cardiac fibroblasts and were suitable for applications in cardiac surgery.

## 3.3 Anti-adhesion Efficacies of GT/PCL Membranes One Month After Surgery

One month after surgery, the heart/liver/kidney functions and CRP/immunoglobulin lever assessments were used to detect whether the membranes would cause adverse reactions *in vivo* implantation. Echocardiography (**Figures 6A,B**) showed that compared with the normal group (healthy rabbits that did not undergo surgery), the heart function indicators LVEF and LVFS in the positive control and 70:30 groups were significantly reduced, whereas no significant differences were observed among the 0:100, 30:70, and 50:50 groups. Conversely, there were no significant differences in liver (**Figure 6C**) or kidney (**Figure 6D**) function indicators among all groups, which suggested that the membranes were not toxic to the liver and kidneys. Additionally, the results of CRP and immunoglobulin level evaluation (**Table 3**) were not significantly different among all groups either, indicating that the membranes did not induce strong inflammation reaction and immune rejection response after implantation *in vivo*. Collectively, these results demonstrated that all the membranes exhibited sufficient biosafety for implantation *in vivo*, except for the 70:30 group, in which case a reduction in heart function (i.e., in LVEF and LVFS) was observed.

After echocardiography and blood examination, animals were anesthetized and sacrificed. The thoracic cavity was reopened, and adhesions between the heart and sternum were separated by dissection. In the positive control group, severe adhesions were formed at the injury site of the previous operation (**Figures 7A,E**), and more attention had to be paid during dissection to keep the heart intact. Strong individual differences were observed in the 0:100 group, i.e., some rabbits had no or slight adhesions that could

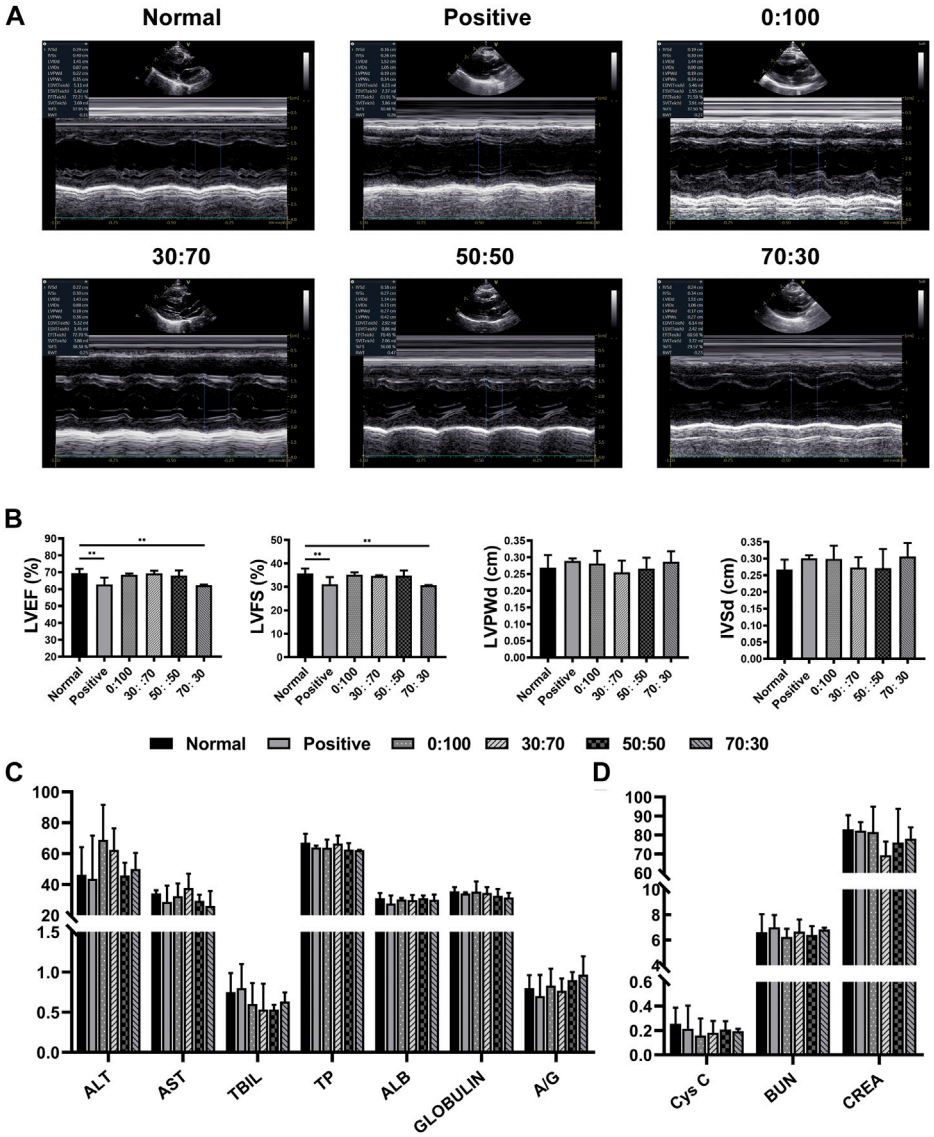


**FIGURE 6 |** One month after surgery **(A)** representative echocardiography images, **(B)** heart function and **(C,D)** liver/kidney function for normal and experimental groups. (**$p < 0.01$).

**TABLE 3 |** CRP and immunoglobulin levels in different groups 1 month after surgery.

| Indicator | Normal | Positive | 0:100 | 30:70 | 50:50 | 70:30 |
|---|---|---|---|---|---|---|
| CRP (mg/L) | <1 | <1 | <1 | <1 | <1 | <1 |
| IgG (g/L) | <0.07 | <0.07 | <0.07 | <0.07 | <0.07 | <0.07 |
| IgA (g/L) | <0.07 | <0.07 | <0.07 | <0.07 | <0.07 | <0.07 |
| IgM (g/L) | <0.18 | <0.18 | <0.18 | <0.18 | <0.18 | <0.18 |
| Total IgE (IU/ml) | <4.23 | <4.23 | <4.23 | <4.23 | <4.23 | <4.23 |

be easily separated by blunt dissection (**Figures 7B,F**); whereas others had thick and heavy adhesions requiring continuous sharp dissection (**Figures 7C,G**). However, mild filamentous adhesions were observed in 30:70 (**Figures 7D,H**) and 50:50 (**Figures 7I,K**) groups, the membranes could be easily separated from the heart and maintained their original shape with a white appearance. In the 70:30 group, intense and solid adhesions were observed, and the original membrane shape was hardly recognizable due to the rapid degradation of GT (**Figure 7J**). Broken holes and bleeding were easily induced upon membrane detachment from the sternum due to the poor mechanical properties of this membrane (**Figure 7L**). Furthermore, according to the results of adhesion grade scoring (**Figure 7M**), the adhesions were severe in the positive control (score = 2.6 ± 0.9) and 70:30 (2.6 ± 0.5) groups. Much lower scores were observed for 30:70 (1.2 ± 0.4) and 50:50 (1.2 ± 0.8) groups, while a very large score fluctuation was observed for the 0:100 group (1.4 ± 1.5).

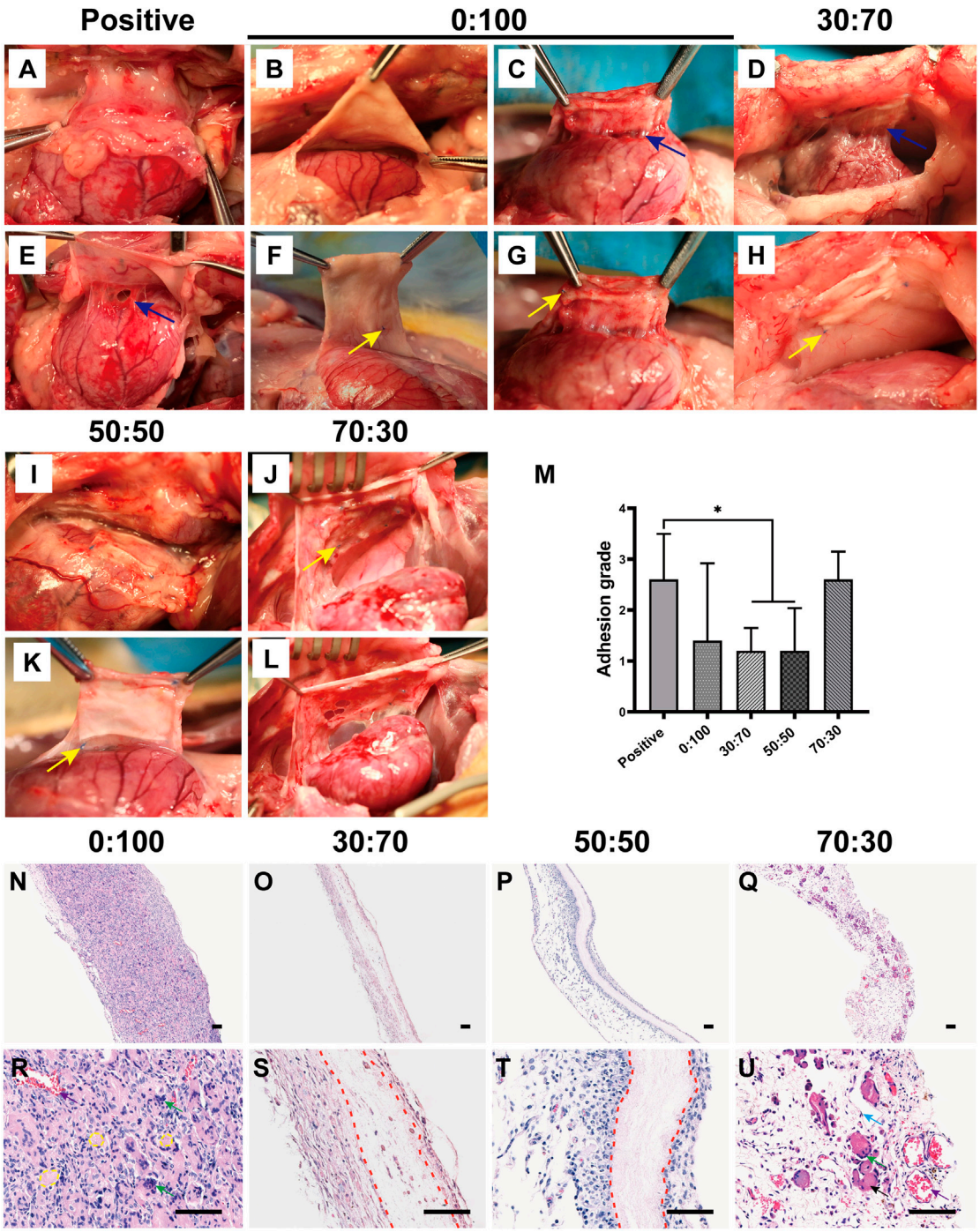


**FIGURE 7 |** One month after surgery representative overall images for **(A,E)** positive control, **(B,C,F,G)** 0:100, **(D,H)** 30:70, **(I,K)** 50:50, and **(J,L)** 70:30 groups, blue arrows indicate adhesion sites, and yellow arrows show sutures positions. **(M)** pericardial adhesion grades, $^{*}p < 0.05$, and representative H-E staining images for **(N,R)** 0:100, **(O,S)** 30:70, **(P,T)** 50:50, and **(Q,U)** 70:30 groups, yellow circles indicate "islands," red dot lines indicate "barriers." Green, blue, black, and purple arrows show multinucleated giant cells, fibroblasts, muscular tissues, and blood vessels, respectively. Scale bars = 80 μm.

After overall observation, the membranes were carefully removed from surrounding tissues. Histological analysis demonstrated that though all the membranes had the same thickness before surgery, the thickness of 0:100 membrane significantly exceeded than others after implantation. Numerous inflammatory cells have entirely infiltrated into the 0:100 membrane regardless of whether adhesions were slight or strong (**Figure 7N**). High-magnification imaging showed that the membrane was divided into masses of small islands, many macrophages gathered and ranged along islands to form

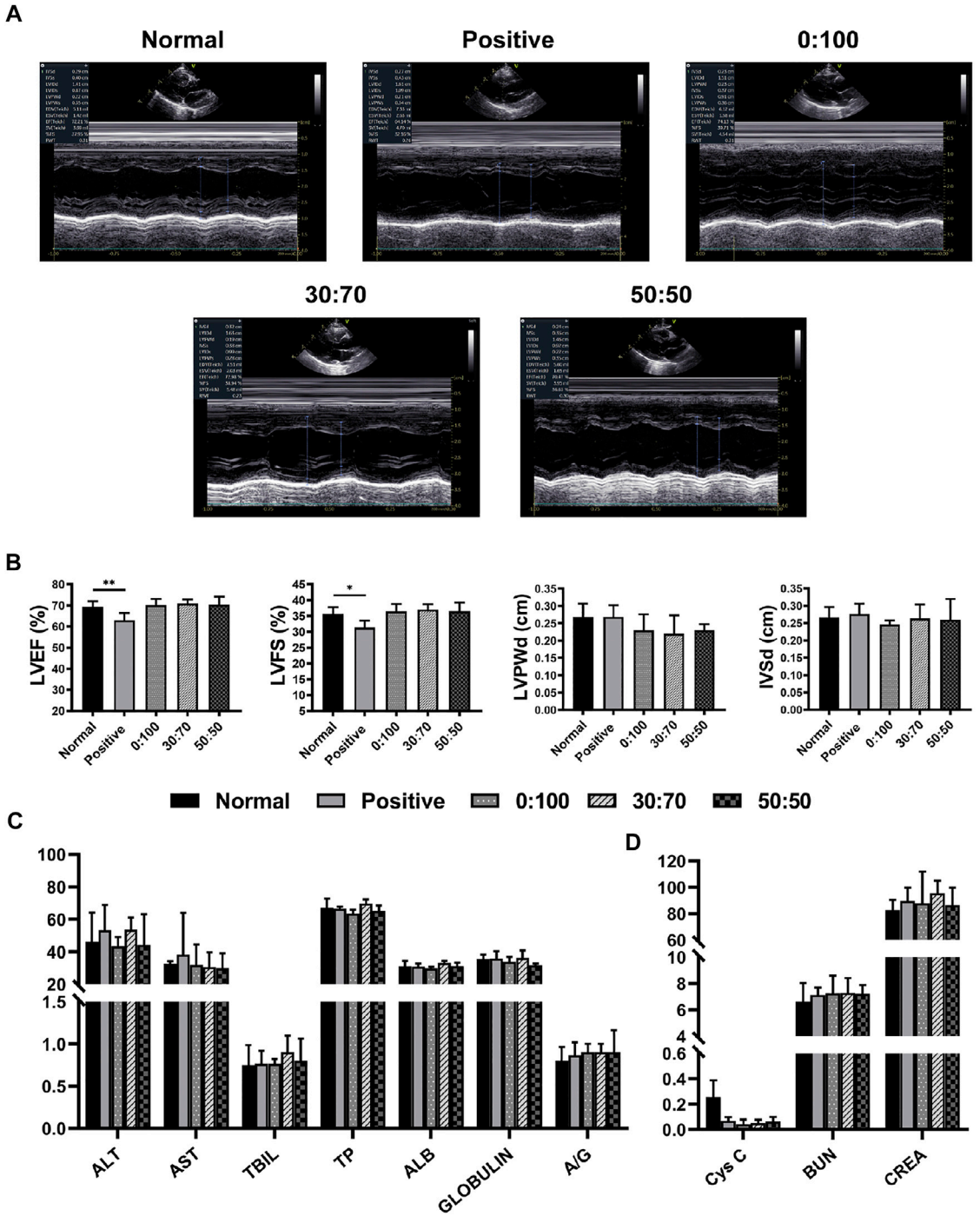


**FIGURE 8 |** Three months after surgery **(A)** representative echocardiography images, **(B)** heart function and **(C,D)** liver/kidney function for normal and experimental groups. (*$p < 0.05$; **$p < 0.01$).

multinucleated giant cells thereby inducing membrane disintegration and phagocytosis (**Figure 7R**). In the 30:70 and 50:50 groups, obvious pink barriers were observed with several (30:70, **Figures 7O,S**) or no (50:50, **Figures 7P,T**) infiltrating cells and a small number of inflammatory cells and sporadic blood capillaries distributed on both sides of barriers. While in the 70:30 group, many monocytes, multinucleated giant cells, fibroblasts, blood vessels and muscular tissues have invaded into the membranes, and no barriers were formed (**Figures 7Q,U**).

Considering the 70:30 membrane was not only difficult to suture during surgery but also could not maintain its structural integrity to prevent cardiac postoperative adhesion after being

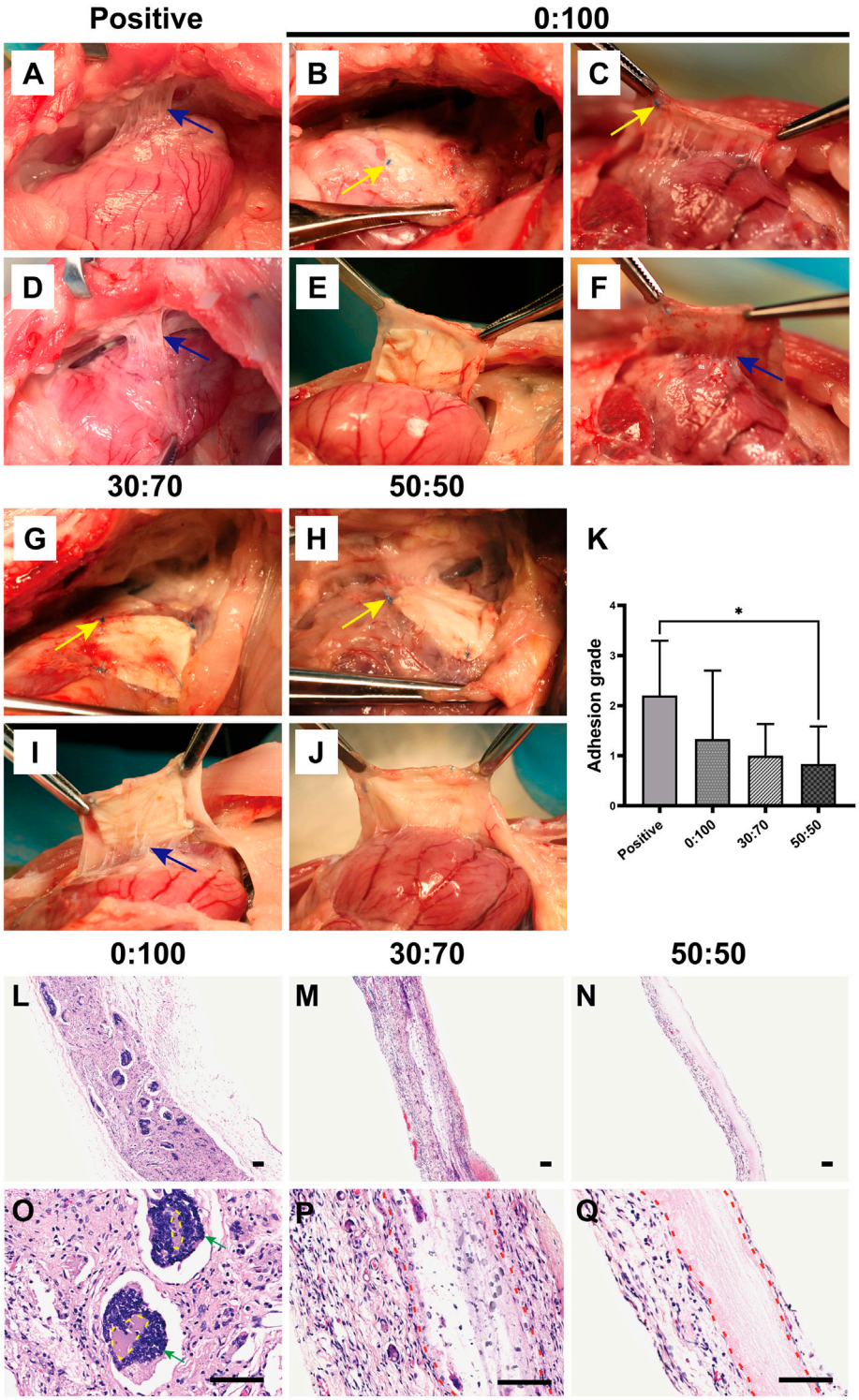


**FIGURE 9 |** Three months after surgery representative overall images for **(A,D)** positive control, **(B,C,E,F)** 0:100, **(G,I)** 30:70, and **(H,J)** 50:50 groups, blue arrows indicate adhesion sites, and yellow arrows show sutures positions. **(K)** Pericardial adhesion grades, $^{*}p < 0.05$, and representative H-E staining images for **(L,O)** 0:100, **(M,P)** 30:70, and **(N,Q)** 50:50 groups, yellow circles indicate "islands," red dot lines indicate "barriers," green arrows indicate multinucleated giant cells. Scale bars = 80 μm.

implanted *in vivo*, and therefore, this membrane was not investigated further.

## 3.4 Anti-adhesion Efficacies of GT/PCL Membranes Three Months After Surgery

Echocardiography (**Figures 8A,B**) showed that compared with the normal group, the heart function (i.e., LVEF and LVFS values) was significantly reduced in the positive control group, while no significant differences were observed for other three groups (0: 100, 30:70, and 50:50). Further blood examination showed that the liver/kidney function indicators (**Figures 8C,D**) of normal group were not significantly different from those of other groups, and CRP levels were still less than 1 mg/L for all groups. These results were consistent with those obtained 1-month after surgery, which illustrated the high biosafety of PCL and GT/PCL (30:70 and 50:50) membranes for long-term *in vivo* implantation.

Overall, dense and solid adhesions were observed between the pericardial defect area and sternum in the positive control group (**Figures 9A,D**). These adhesions were more serious than those formed 1-month after surgery and could only be separated by sharp dissection. And the adhesion conditions still showed large variations between individual animals in the 0:100 group, i.e., some rabbits had no or slight adhesions (**Figures 9B,E**), while the others had severe adhesions (**Figures 9C,F**). However, filamentous and sparse adhesions were observed between the membranes and epicardium in 30:70 (**Figures 9G,I**) and 50:50 (**Figures 9H,J**) groups, which could be easily separated by digital dissection. Specifically, the membrane became blurred and developed a yellow-like appearance similar to that of the native pericardium tissues. The heart was smooth and moist, and the coronary arteries were clearly visible. The related adhesion grade scores were shown in **Figure 9K**. The adhesion was strongest in the positive control group (score = 2.2 ± 1.1), with lower scores observed for 30:70 (1.0 ± 0.6) and 50:50 (0.8 ± 0.8) groups. As in the case of 1 month after surgery, a large standard deviation was observed for the 0:100 group (1.3 ± 1.4).

Histological staining showed that the 0:100 membrane gradually degraded, and most islands have disappeared (**Figure 9L**). Multinucleated giant cells were much bigger and more visible than 1 month after surgery, forming many dark purple (nucleus) bumps (**Figure 9O**). In the 30:70 group, some inflammatory cells together with small arteries and blood capillaries infiltrated the membrane, and the barrier became blurred (**Figures 9M,P**). However, an obvious pink barrier with no cell infiltration was observed in the 50:50 group (**Figures 9N,Q**), indicating that this membrane could act as a perfect barrier to prevent cell infiltration, which was in line with the results obtained 1 month after surgery.

# 4 DISCUSSION

Adhesion is one of the most frequent postoperative complications with many serious consequences. For example, peritoneal adhesions are commonly observed after abdominal and pelvic surgery, leading to chronic abdominal pain, intestinal obstruction, and female infertility (Hol et al., 2019; Tang et al., 2020). And pelvic adhesions resulting from gynecologic surgery may also cause chronic pelvic pain, small bowel obstruction, and female infertility (Al-Jabri and Tulandi, 2011; Dawood and Elgergawy, 2018). Besides, tendon adhesions not only cause dysfunction and pain, but also usually require surgical intervention to loosen (Liu et al., 2013; Cai et al., 2021). In addition, many patients undergoing cardiac surgery require reoperation even multiple operations. Owing to the adhesions generated by the first operation, original anatomical layers and gaps have been disappeared, leaving the reoperation a daunting task. In our pilot study, electrospun membranes with a GT:PCL mass ratio of 50:50 have showed high potential in reducing sternal and epicardial adhesions after cardiac surgery (Feng et al., 2019). However, the GT:PCL ratio can affect the physical structure, mechanical properties, degradation rate, and biocompatibility of membranes, which may eventually lead to changes in anti-adhesion efficacy. Thus, GT/PCL membranes with various compositions were investigated herein.

Good mechanical properties are a primary prerequisite for given materials used as anti-adhesion barriers after cardiac surgery, as the membranes must withstand the stretching during surgical suturing and the forces generated during movements *in vivo*. PCL is a synthetic bioresorbable polymer with excellent mechanical properties, while GT is a natural biodegradable polymer in poor mechanical properties. Surprisingly, in line with our previous findings (Feng et al., 2012), the hybridization of PCL with GT (GT:PCL = 30:70 and 50:50, w/w) did not deteriorate but rather enhance the mechanical properties than pure PCL membranes (**Figures 3C,E**). This behavior was ascribed to the good miscibility of GT and PCL, their good entanglement made the molecular chains difficult to slide under loading. However, at an overly high GT content of 70 wt%, the mechanical properties worsened (**Figures 3C,D**), which complicated the suture during surgery and then resulted in increasing operation time and difficulties. Further animal dissection demonstrated that this membrane was easily broken, hardly maintained its structural integrity (**Figures 7J,L**), and could not act as an effective physical barrier to prevent postoperative cardiac adhesion (**Figures 7Q,U**). It is known that the structural integrity is a critical consideration as a physical barrier. Therefore, the 70:30 membrane was concluded to be unsuitable for preventing postoperative cardiac adhesion because of its poor mechanical properties.

Biocompatibility is another important factor for assessing the suitability of membranes to be implanted *in vivo*. Live/dead staining showed that all the tested membranes had no cytotoxicity to cardiomyocytes and cardiac fibroblasts *in vitro*, and there were no obvious differences on cell seeding efficiencies as well (**Figure 4**). Furthermore, the cells adhered well and experienced rapid proliferation on all membranes, as revealed by immunofluorescence staining and the CCK-8 assay (**Figure 5**). *In vivo* studies have shown that heart/liver/kidney functions (**Figures 6**, **8**) and CRP/immunoglobulin levels (**Table 3**) in 0:100, 30:70, and 50:50 groups were not different from those of normal healthy rabbits. These results indicated that PCL and GT/PCL (30:70 and 50:50) membranes are biosafety enough and did not affect the heart/liver/kidney functions or induce intense

inflammation and immune rejection responses after implantation *in vivo*. Given their good mechanical properties and excellent biocompatibility, the 0:100, 30:70, and 50:50 membranes showed promising potential as barriers in preventing postoperative cardiac adhesion.

Unexpectedly, the overall observation showed inconsistent results after the animals were sacrificed and anatomized (**Figures 7A–L**, **9A–J**). Large differences between individual animals were observed in the 0:100 group, i.e., some animals had no or slight adhesions, while the others were severe. However, mild adhesions were observed in both 30:70 and 50:50 groups. These results suggested that the 0:100 membrane was not suitable for the prevention of adhesions after cardiac surgery either.

Adhesion formation involves a series of complex pathophysiological reactions, such as the tissue damage, inflammatory responses, coagulation, fibrin deposition, fibroblast proliferation, collagen formation, and angiogenesis (Cannata et al., 2013; Kheilnezhad and Hadjizadeh, 2021), but the specific mechanism remains to be elucidated. Previous studies supposed that biomaterials could act as anti-adhesion barriers by blocking fibroblasts penetration (Jiang et al., 2014; Chen et al., 2015b), as the excessive proliferation of fibroblasts resulted in producing abundant collagen fibers to form dense and thick fibrous adhesions. However, in this study, histological staining showed that numerous inflammatory cells instead of fibroblasts infiltrated into the 0:100 membranes. It is known that the inflammatory response plays an important role in adhesion formation, e.g., inflammatory cell aggregation and inflammatory mediator release can promote fibroblast proliferation and thus aggravate adhesion (Pismensky et al., 2011; Hu et al., 2021; Zhang et al., 2021). Therefore, the inflammatory cells infiltration, not fibroblasts penetration, might be the real reason that PCL membranes failed to prevent postoperative cardiac adhesion.

Accumulation of acidic degradation products can elicit a severe inflammatory response. Polymers such as polyglycolic acid, polylactic acid (PLA), and their copolymers [poly (lactic-co-glycolic acid)] contain abundant carboxyl groups and can therefore release many acidic degradation products that trigger severe aseptic inflammatory responses (Lin et al., 2017; Shen et al., 2019; Tu et al., 2020). Unlike PLA, PCL has no carboxyl groups and therefore cannot induce an inflammatory response via the above mechanism. Further analysis showed that the pore size of materials might be the key factor to induce inflammatory responses (Madden et al., 2010; Chiu et al., 2011; Garg et al., 2013; Wang et al., 2014). Inflammatory cells are the smallest cells *in vivo*, the diameter was generally in the range of 6–20 μm, being largest for macrophages (14–20 μm) and smallest for lymphocytes (6–10 μm). And the 0:100 membrane had the largest pore size (9.9 ± 2.3 μm, **Figure 1B**) and was theoretically permeable to most inflammatory cells, whereas the pore sizes of 30:70 and 50:50 membranes were much smaller (4.8 ± 1.2 and 5.2 ± 1.4 μm, respectively, **Figure 1B**) than that of lymphocytes. In addition, the pore size of GT/PCL membranes will decrease further after implanting *in vivo* due to the hydrophilicity of GT (**Figure 2**), as the nanofibers can absorb large amounts of water and swell. Therefore, the small pore size enabled the 30:70 and 50:50 membranes not only block the invasion of fibroblasts (diameter = 20–30 μm), but also prevent the infiltration of inflammatory cells. Furthermore, compared to the 30:70 membrane, the 50:50 membrane might experience a larger pore size reduction due to its higher content of GT, which was strongly supported by the fact that some cells invaded into the 30:70 membrane, while no cells were observed in the 50:50 group 3 months after surgery (**Figures 9L–Q**).

Collectively, in consideration of good mechanical properties, excellent biocompatibility and effective anti-cell penetration ability, the GT/PCL 50:50 membrane is concluded the best one to prevent postoperative cardiac adhesion among all groups. As a physical barrier, it might have great potential in other biomedical applications, such as the prevention of non-cardiac postoperative adhesions, wound healing, and guided tissue or bone regeneration. Nevertheless, it still has some limitations. Though mild adhesions were observed between the GT/PCL 50:50 membrane and epicardium, there were still moderate or severe adhesions between the membrane and sternum, increasing the difficulties of reoperation as well. Loading medicine into the GT/PCL 50:50 membrane to further enhance its anti-adhesion efficacy will be investigated in our future study. In addition, the degradation rate of PCL is pretty slow which will increase the risk of infection and hinder tissue regeneration. Replacing or blending the PCL with easier absorbable materials such as polydioxanone (PDO) (Oh et al., 2011; Kwon et al., 2019) or Poly (glycerol sebacate) (PGS) (Vogt et al., 2019; Fu et al., 2020) might be more preferable.

## 5 CONCLUSION

Pure PCL (0:100) and GT/PCL (30:70, 50:50, 70:30) nanofibrous membranes were successfully fabricated via electrospinning. Through the assessments of physicochemical properties and biocompatibility, as well as evaluations of rabbit heart/liver/kidney functions, CRP/immunoglobulin levels and adhesion degree, we discovered that the 70:30 membrane failed to prevent postoperative cardiac adhesion because of its poor mechanical properties, and the pure PCL membrane could not effectively prevent either, because numerous inflammatory cells have infiltrated into the membrane which induced a serious inflammatory response. Only the GT:PCL 50:50 membrane exhibited excellent mechanical properties, good biocompatibility and effective anti-cell penetration ability, which might be a perfect barrier to prevent postoperative cardiac adhesion and show great potential in other biomedical applications such as the prevention of non-cardiac postoperative adhesions, wound healing, and guided tissue or bone regeneration. In addition, as a physical barrier, the ability to inhibit inflammatory cells infiltration, not fibroblasts penetration, might be the key consideration in design and fabrication of nanofibrous membrane to prevent postoperative adhesion.

## DATA AVAILABILITY STATEMENT

The raw data supporting the conclusion of this article will be made available by the authors, without undue reservation.

## ETHICS STATEMENT

The animal study was reviewed and approved by The Animal Care and Experiment Committee of Shanghai Jiaotong University Agricultural Experimental Practice Field.

## AUTHOR CONTRIBUTIONS

XW: Conceptualization, Methodology, Investigation, Formal analysis, Writing-Original Draft. LX: Methodology, Investigation, Validation. YP: Methodology, Formal analysis. ZD: Investigation, Validation. YH: Investigation, Validation. XP：Data Curation. XZ: Methodology. HZ: Conceptualization, Resources, Project administration, Supervision. BF: Conceptualization, Formal analysis, Writing—Review and editing, Supervision.

## FUNDING

This work was supported by the National Key R&D Program of China (2019YFA0110401 and 2019YFA0110402), the National Natural Science Foundation of China (81601622 and 31971048), the Fund of Transformation Medicine Cross Research of Shanghai Jiao Tong University (YG2019ZDA04), the Leading Medical Talent in Shanghai (2019LJ22), and the Natural Science Foundation of Shanghai (20ZR1434400).

## REFERENCES

Al-Jabri, S., and Tulandi, T. (2011). Management and Prevention of Pelvic Adhesions. *Semin. Reprod. Med.* 29, 130–137. doi:10.1055/s-0031-1272475

Alimohammadi, M., Aghli, Y., Fakhraei, O., Moradi, A., Passandideh-Fard, M., Ebrahimzadeh, M. H., et al. (2020). Electrospun Nanofibrous Membranes for Preventing Tendon Adhesion. *ACS Biomater. Sci. Eng.* 6, 4356–4376. doi:10.1021/acsbiomaterials.0c00201

Cai, C. D., Wang, W., Liang, J., Li, Y. G., Lu, M. K., Cui, W. G., et al. (2021). MMP-2 Responsive Unidirectional Hydrogel-Electrospun Patch Loading TGF-Beta 1 siRNA Polyplexes for Peritendinous Anti-adhesion. *Adv. Funct. Mater.*, 31.

Cannata, A., Petrella, D., Russo, C. F., Bruschi, G., Fratto, P., Gambacorta, M., et al. (2013). Postsurgical Intrapericardial Adhesions: Mechanisms of Formation and Prevention. *Ann. Thorac. Surg.* 95, 1818–1826. doi:10.1016/j.athoracsur.2012.11.020

Chen, C.-H., Chen, S.-H., Shalumon, K. T., and Chen, J.-P. (2015). Prevention of Peritendinous Adhesions with Electrospun Polyethylene Glycol/polycaprolactone Nanofibrous Membranes. *Colloids Surf. B: Biointerfaces* 133, 221–230. doi:10.1016/j.colsurfb.2015.06.012

Chen, S. H., Chou, P. Y., Chen, Z. Y., and Lin, F. H. (2019). Electrospun Water-Borne Polyurethane Nanofibrous Membrane as a Barrier for Preventing Postoperative Peritendinous Adhesion. *Int. J. Mol. Sci.* 20. doi:10.3390/ijms20071625

Chen, Z., Zheng, J., Zhang, J., and Li, S. (2015). A Novel Bioabsorbable Pericardial Membrane Substitute to Reduce Postoperative Pericardial Adhesions in a Rabbit Model. *Interact Cardiovasc. Thorac. Surg.* 21, 565–572. doi:10.1093/icvts/ivv213

Chiu, Y.-C., Cheng, M.-H., Engel, H., Kao, S.-W., Larson, J. C., Gupta, S., et al. (2011). The Role of Pore Size on Vascularization and Tissue Remodeling in PEG Hydrogels. *Biomaterials* 32, 6045–6051. doi:10.1016/j.biomaterials.2011.04.066

Dawood, A. S., and Elgergawy, A. E. (2018). Incidence and Sites of Pelvic Adhesions in Women with post-caesarean Infertility. *J. Obstet. Gynaecol.* 38, 1158–1163. doi:10.1080/01443615.2018.1460583

de Oliveira, P. P. M., Bavaresco, V. P., Silveira-Filho, L. M., Schenka, A. A., Vilarinho, K. A. d. S., Barbosa de Oliveira Severino, E. S., et al. (2014). Use of a Novel Polyvinyl Alcohol Membrane as a Pericardial Substitute Reduces Adhesion Formation and Inflammatory Response after Cardiac Reoperation. *J. Thorac. Cardiovasc. Surg.* 147, 1405–1410. doi:10.1016/j.jtcvs.2013.07.021

Feng, B., Ji, T., Wang, X., Fu, W., Ye, L., Zhang, H., et al. (2020). Engineering Cartilage Tissue Based on Cartilage-Derived Extracellular Matrix cECM/PCL Hybrid Nanofibrous Scaffold. *Mater. Des.*, 193. doi:10.1016/j.matdes.2020.108773

Feng, B., Tu, H., Yuan, H., Peng, H., and Zhang, Y. (2012). Acetic-acid-mediated Miscibility toward Electrospinning Homogeneous Composite Nanofibers of GT/PCL. *Biomacromolecules* 13, 3917–3925. doi:10.1021/bm3009389

Feng, B., Wang, S., Hu, D., Fu, W., Wu, J., Hong, H., et al. (2019). Bioresorbable Electrospun Gelatin/polycaprolactone Nanofibrous Membrane as a Barrier to Prevent Cardiac Postoperative Adhesion. *Acta Biomater.* 83, 211–220. doi:10.1016/j.actbio.2018.10.022

Fu, J., Ding, X., Stowell, C. E. T., Wu, Y.-L., and Wang, Y. (2020). Slow Degrading Poly(glycerol Sebacate) Derivatives Improve Vascular Graft Remodeling in a Rat Carotid Artery Interposition Model. *Biomaterials* 257, 120251. doi:10.1016/j.biomaterials.2020.120251

Garg, K., Pullen, N. A., Oskeritzian, C. A., Ryan, J. J., and Bowlin, G. L. (2013). Macrophage Functional Polarization (M1/M2) in Response to Varying Fiber and Pore Dimensions of Electrospun Scaffolds. *Biomaterials* 34, 4439–4451. doi:10.1016/j.biomaterials.2013.02.065

Ghasemi-Mobarakeh, L., Prabhakaran, M. P., Morshed, M., Nasr-Esfahani, M.-H., and Ramakrishna, S. (2008). Electrospun Poly(ε-Caprolactone)/gelatin Nanofibrous Scaffolds for Nerve Tissue Engineering. *Biomaterials* 29, 4532–4539. doi:10.1016/j.biomaterials.2008.08.007

Hol, J. C., Strik, C., Chaturvedi, A. A., Lomme, R. M. L. M., van Goor, H., Stommel, M. W. J., et al. (2019). The Efficacy of an Ultrapure Alginate Gel in Reducing Adhesion Formation in a Rat Model of Blood Contamination. *J. Surg. Res.* 241, 271–276. doi:10.1016/j.jss.2019.03.035

Hu, Q., Xia, X., Kang, X., Song, P., Liu, Z., Wang, M., et al. (2021). A Review of Physiological and Cellular Mechanisms Underlying Fibrotic Postoperative Adhesion. *Int. J. Biol. Sci.* 17, 298–306. doi:10.7150/ijbs.54403

Jacobs, J. P., Iyer, R. S., Weston, J. S., Amato, J. J., Elliott, M. J., de Leval, M. R., et al. (1996). Expanded PTFE Membrane to Prevent Cardiac Injury during Resternotomy for Congenital Heart Disease. *Ann. Thorac. Surg.* 62, 1778–1782. doi:10.1016/s0003-4975(96)00610-8

Jiang, S., Zhao, X., Chen, S., Pan, G., Song, J., He, N., et al. (2014). Down-regulating ERK1/2 and SMAD2/3 Phosphorylation by Physical Barrier of Celecoxib-Loaded Electrospun Fibrous Membranes Prevents Tendon Adhesions. *Biomaterials* 35, 9920–9929. doi:10.1016/j.biomaterials.2014.08.028

Jin, D., Hu, J., Xia, D., Liu, A. l., Kuang, H., Du, J., et al. (2019). Evaluation of a Simple Off-The-Shelf Bi-layered Vascular Scaffold Based on poly(L-Lactide-Co-ε-Caprolactone)/silk Fibroin *In Vitro* and *In Vivo*. *Ijn* 14, 4261–4276. doi:10.2147/ijn.s205569

Kaushal, S., Patel, S. K., Goh, S.-K., Sood, A., Walker, B. L., Backer, C. L., et al. (2011). A Novel Combination of Bioresorbable Polymeric Film and Expanded Polytetrafluoroethylene Provides a Protective Barrier and Reduces Adhesions. *J. Thorac. Cardiovasc. Surg.* 141, 789–795. doi:10.1016/j.jtcvs.2010.11.043

Keshvardoostchokami, M., Majidi, S. S., Huo, P., Ramachandran, R., Chen, M., and Liu, B. (2020). Electrospun Nanofibers of Natural and Synthetic Polymers as Artificial Extracellular Matrix for Tissue Engineering. *Nanomaterials* 11, 21. doi:10.3390/nano11010021

Kheilnezhad, B., and Hadjizadeh, A. (2021). A Review: Progress in Preventing Tissue Adhesions from a Biomaterial Perspective. *Biomater. Sci.* 9, 2850–2873. doi:10.1039/d0bm02023k

Kwon, T. R., Han, S. W., Yeo, I. K., Kim, J. H., Kim, J. M., Hong, J. Y., et al. (2019). Biostimulatory Effects of Polydioxanone, Poly-D, L Lactic Acid, and Polycaprolactone Fillers in Mouse Model. *J. Cosmet. Dermatol.* 18, 1002–1008. doi:10.1111/jocd.12950

Lassaletta, A. D., Chu, L. M., and Sellke, F. W. (2012). Effects of Alcohol on Pericardial Adhesion Formation in Hypercholesterolemic Swine. *J. Thorac. Cardiovasc. Surg.* 143, 953–959. doi:10.1016/j.jtcvs.2011.12.016

Leong, D. P., Joseph, P. G., McKee, M., Anand, S. S., Teo, K. K., Schwalm, J.-D., et al. (2017). Reducing the Global Burden of Cardiovascular Disease, Part 2. *Circ. Res.* 121, 695–710. doi:10.1161/circresaha.117.311849

Lin, X., Wang, W., Zhang, W., Zhang, Z., Zhou, G., Cao, Y., et al. (2017). Hyaluronic Acid Coating Enhances Biocompatibility of Nonwoven PGA Scaffold and Cartilage Formation. *Tissue Eng. C: Methods* 23, 86–97. doi:10.1089/ten.tec.2016.0373

Liu, S., Qin, M., Hu, C., Wu, F., Cui, W., Jin, T., et al. (2013). Tendon Healing and Anti-adhesion Properties of Electrospun Fibrous Membranes Containing bFGF Loaded Nanoparticles. *Biomaterials* 34, 4690–4701. doi:10.1016/j.biomaterials.2013.03.026

Lopes, J. B., Dallan, L. A. O., Campana-Filho, S. P., Lisboa, L. A. F., Gutierrez, P. S., Moreira, L. F. P., et al. (2009). Keratinocyte Growth Factor: a New Mesothelial Targeted Therapy to Reduce Postoperative Pericardial Adhesions☆. *Eur. J. Cardio-Thoracic Surg.* 35, 313–318. doi:10.1016/j.ejcts.2008.09.046

Madden, L. R., Mortisen, D. J., Sussman, E. M., Dupras, S. K., Fugate, J. A., Cuy, J. L., et al. (2010). Proangiogenic Scaffolds as Functional Templates for Cardiac Tissue Engineering. *Proc. Natl. Acad. Sci.* 107, 15211–15216. doi:10.1073/pnas.1006442107

Malm, T., Bowald, S., Bylock, A., and Busch, C. (1992). Prevention of Postoperative Pericardial Adhesions by Closure of the Pericardium with Absorbable Polymer Patches. *J. Thorac. Cardiovasc. Surg.* 104, 600–607. doi:10.1016/s0022-5223(19)34724-5

Mao, Y., Chen, M., Guidoin, R., Li, Y., Wang, F., Brochu, G., et al. (2021). Potential of a Facile Sandwiched Electrospun Scaffold Loaded with Ibuprofen as an Anti-adhesion Barrier. *Mater. Sci. Eng. C* 118, 111451. doi:10.1016/j.msec.2020.111451

Minale, C., Nikol, S., Hollweg, G., Mittermayer, C., and Messmer, B. J. (1988). Clinical Experience with Expanded Polytetrafluoroethylene Gore-Tex Surgical Membrane for Pericardial Closure: a Study of 110 Cases. *J. Card. Surg.* 3, 193–201. doi:10.1111/j.1540-8191.1988.tb00239.x

Nagarajan, S., Belaid, H., Pochat-Bohatier, C., Teyssier, C., Iatsunskyi, I., Coy, E., et al. (2017). Design of Boron Nitride/Gelatin Electrospun Nanofibers for Bone Tissue Engineering. *ACS Appl. Mater. Inter.* 9, 33695–33706. doi:10.1021/acsami.7b13199

Naito, Y., Shin'oka, T., Hibino, N., Matsumura, G., and Kurosawa, H. (2008). A Novel Method to Reduce Pericardial Adhesion: a Combination Technique with Hyaluronic Acid Biocompatible Membrane. *J. Thorac. Cardiovasc. Surg.* 135, 850–856. doi:10.1016/j.jtcvs.2007.10.062

Oh, S. H., Park, S. C., Kim, H. K., Koh, Y. J., Lee, J.-H., Lee, M. C., et al. (2011). Degradation Behavior of 3D Porous Polydioxanone-B-Polycaprolactone Scaffolds Fabricated Using the Melt-Molding Particulate-Leaching Method. *J. Biomater. Sci. Polym. Edition* 22, 225–237. doi:10.1163/092050609x12597621891620

Ozeren, M., Han, U., Mavioglu, I., Simsek, E., Soyal, M., Guler, G., et al. (2002). Consequences of PTFE Membrane Used for Prevention of Re-entry Injuries in Rheumatic Valve Disease. *Cardiovasc. Surg.* 10, 489–493. doi:10.1016/s0967-2109(02)00061-3

Pismensky, S. V., Kalzhanov, Z. R., Eliseeva, M. Y., Kosmas, I. P., and Mynbaev, O. A. (2011). Severe Inflammatory Reaction Induced by Peritoneal Trauma Is the Key Driving Mechanism of Postoperative Adhesion Formation. *BMC Surg.* 11, 30. doi:10.1186/1471-2482-11-30

Shen, J., and Xu, Z. W. (2014). Combined Application of Acellular Bovine Pericardium and Hyaluronic Acid in Prevention of Postoperative Pericardial Adhesion. *Artif. Organs* 38, 224–230. doi:10.1111/aor.12140

Shen, Y., Tu, T., Yi, B., Wang, X., Tang, H., Liu, W., et al. (2019). Electrospun Acid-Neutralizing Fibers for the Amelioration of Inflammatory Response. *Acta Biomater.* 97, 200–215. doi:10.1016/j.actbio.2019.08.014

Tang, J., Xiang, Z., Bernards, M. T., and Chen, S. (2020). Peritoneal Adhesions: Occurrence, Prevention and Experimental Models. *Acta Biomater.* 116, 84–104. doi:10.1016/j.actbio.2020.08.036

Tsukihara, H., Takamoto, S., Kitahori, K., Matsuda, K., Murakami, A., Novick, R. J., et al. (2006). Prevention of Postoperative Pericardial Adhesions with a Novel Regenerative Collagen Sheet. *Ann. Thorac. Surg.* 81, 650–657. doi:10.1016/j.athoracsur.2005.07.022

Tu, T., Shen, Y. B., Wang, X. S., Zhang, W. J., Zhou, G. D., Zhang, Y. Z., et al. (2020). Tendon ECM Modified Bioactive Electrospun Fibers Promote MSC Tenogenic Differentiation and Tendon Regeneration. *Appl. Mater. Today*, 18. doi:10.1016/j.apmt.2019.100495

Vogt, L., Rivera, L. R., Liverani, L., Piegat, A., El Fray, M., and Boccaccini, A. R. (2019). Poly(ε-caprolactone)/poly(glycerol Sebacate) Electrospun Scaffolds for Cardiac Tissue Engineering Using Benign Solvents. *Mater. Sci. Eng. C* 103, 109712. doi:10.1016/j.msec.2019.04.091

Wang, Z., Cui, Y., Wang, J., Yang, X., Wu, Y., Wang, K., et al. (2014). The Effect of Thick Fibers and Large Pores of Electrospun Poly(ε-Caprolactone) Vascular Grafts on Macrophage Polarization and Arterial Regeneration. *Biomaterials* 35, 5700–5710. doi:10.1016/j.biomaterials.2014.03.078

Xu, X., Wang, S., Wu, H., Liu, Y., Xu, F., and Zhao, J. (2021). A Multimodal Antimicrobial Platform Based on MXene for Treatment of Wound Infection. *Colloids Surf. B: Biointerfaces* 207, 111979. doi:10.1016/j.colsurfb.2021.111979

Xue, J., Wu, T., Dai, Y., and Xia, Y. (2019). Electrospinning and Electrospun Nanofibers: Methods, Materials, and Applications. *Chem. Rev.* 119, 5298–5415. doi:10.1021/acs.chemrev.8b00593

Zhang, Q., Yang, Y., Yildirimer, L., Xu, T., and Zhao, X. (2021). Advanced Technology-Driven Therapeutic Interventions for Prevention of Tendon Adhesion: Design, Intrinsic and Extrinsic Factor Considerations. *Acta Biomater.* 124, 15–32. doi:10.1016/j.actbio.2021.01.027

Zheng, R., Duan, H., Xue, J., Liu, Y., Feng, B., Zhao, S., et al. (2014). The Influence of Gelatin/PCL Ratio and 3-D Construct Shape of Electrospun Membranes on Cartilage Regeneration. *Biomaterials* 35, 152–164. doi:10.1016/j.biomaterials.2013.09.082

**Conflict of Interest:** The authors declare that the research was conducted in the absence of any commercial or financial relationships that could be construed as a potential conflict of interest.

**Publisher's Note:** All claims expressed in this article are solely those of the authors and do not necessarily represent those of their affiliated organizations, or those of the publisher, the editors and the reviewers. Any product that may be evaluated in this article, or claim that may be made by its manufacturer, is not guaranteed or endorsed by the publisher.

frontiers in Bioengineering and Biotechnology

ERRATUM
published: 11 February 2022
doi: 10.3389/fbioe.2022.862276

# Erratum: Gelatin/Polycaprolactone Electrospun Nanofibrous Membranes: The Effect of Composition and Physicochemical Properties on Postoperative Cardiac Adhesion

*Frontiers Production Office* *

*Frontiers Media SA, Lausanne, Switzerland*

**Keywords: electrospinning, gelatin, polycaprolactone, postoperative adhesion, cardiac surgery**

OPEN ACCESS

***Approved by:***
*Frontiers Editorial Office,*
*Frontiers Media SA, Switzerland*

***Correspondence:**
*Frontiers Production Office*
*production.office@frontiersin.org*

***Specialty section:***
*This article was submitted to Biomaterials, a section of the journal Frontiers in Bioengineering and Biotechnology*

***Received:*** *25 January 2022*
***Accepted:*** *25 January 2022*
***Published:*** *11 February 2022*

***Citation:***
*(2022) Erratum: Gelatin/Polycaprolactone Electrospun Nanofibrous Membranes: The Effect of Composition and Physicochemical Properties on Postoperative Cardiac Adhesion. Front. Bioeng. Biotechnol. 10:862276. doi: 10.3389/fbioe.2022.862276*

**An Erratum on**

**Gelatin/Polycaprolactone Electrospun Nanofibrous Membranes: The Effect of Composition and Physicochemical Properties on Postoperative Cardiac Adhesion**
*by Wang, X., Xiang, L., Peng, Y., Dai, Z., Hu, Y., Pan, X., Zhou, X., Zhang, H., and Feng, B. (2021). Front. Bioeng. Biotechnol. 9:792893. doi:10.3389/fbioe.2021.792893*

Due to a production error, the image used for **Figure 8** was incorrect. Figure 6 was mistakenly duplicated and used in place of the correct image for **Figure 8**.
The correct **Figure 8** appears below. The publisher apologizes for this mistake. The original version of this article has been updated.

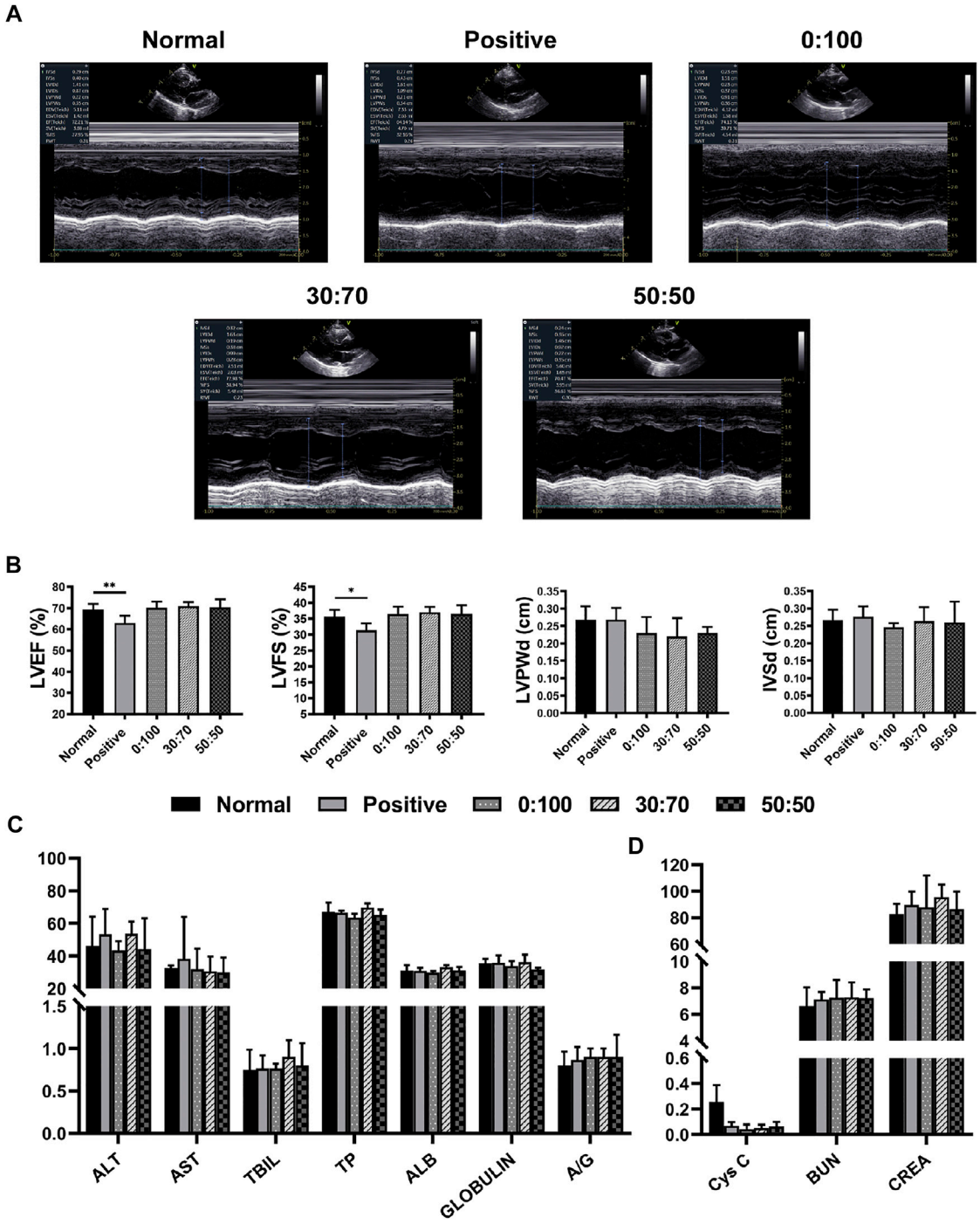


**FIGURE 8 |** Three months after surgery **(A)** representative echocardiography images, **(B)** heart function and **(C,D)** liver/kidney function for normal and experimental groups. (*$p < 0.05$; **$p < 0.01$).

frontiers in Bioengineering and Biotechnology

ORIGINAL RESEARCH
published: 17 February 2022
doi: 10.3389/fbioe.2022.855471

# Enhanced Hemocompatibility of Silver Nanoparticles Using the Photocatalytic Properties of Titanium Dioxide

*Xiao Chen, Sheng Dai, Luying Liu, Peng Liu, Peng Ye, Yuzhen Liao, Ansha Zhao, Ping Yang*, Nan Huang* and Jiang Chen**

*Key Laboratory for Advanced Technologies of Materials, Institute of Biomaterials and Surface Engineering, Ministry of Education, Southwest Jiaotong University, Chengdu, China*

Silver nanoparticles (AgNPs) are widely used because of their excellent antimicrobial properties. However, the poor hemocompatibility limits the application of AgNPs in blood contact materials. General approaches to improve the hemocompatibility of AgNPs-containing surfaces are to construct barrier layers or co-immobilize anticoagulant biomolecules. But such modification strategies are often cumbersome to prepare and have limited applications. Therefore, this study proposes a simple UV-photo-functionalization strategy to improve the hemocompatibility of AgNPs. We loaded AgNPs onto titanium dioxide ($TiO_2$) nanoparticles to form a composite nanoparticles (Ag@$TiO_2$NPs). Then, UV treatment was performed to the Ag@$TiO_2$NPs, utilizing the diffusible photo-induced anticoagulant properties of $TiO_2$ nanoparticles to enhance the hemocompatibility of AgNPs. After being deposited onto the PU surface, the photo-functionalized Ag@$TiO_2$NPs coating showed excellent antibacterial properties against both Gram-positive/Gram-negative bacteria. Besides, *In vitro* and *ex-vivo* experiments demonstrated that the photo-functionalized Ag@$TiO_2$NPs coating had desirable hemocompatibility. This modification strategy can provide a new solution idea to improve the hemocompatibility of metal nanoparticles.

**Keywords: Silver nanoparticles (AgNPs), Titanium dioxide ($TiO_2$), hemocompatibility, antibacterial ability, UV treatment**

OPEN ACCESS

***Edited by:***
*Guicai Li,*
*Nantong University, China*

***Reviewed by:***
*Zhoukun He,*
*Chengdu University, China*
*Tao Gong,*
*University of South China, China*

****Correspondence:***
*Ping Yang*
*yangping8@263.net*
*Nan Huang*
*nhuang@263.net*
*Jiang Chen*
*283876533@qq.com*

***Specialty section:***
*This article was submitted to Biomaterials, a section of the journal Frontiers in Bioengineering and Biotechnology*

***Received:*** *15 January 2022*
***Accepted:*** *01 February 2022*
***Published:*** *17 February 2022*

***Citation:***
*Chen X, Dai S, Liu L, Liu P, Ye P, Liao Y, Zhao A, Yang P, Huang N and Chen J (2022) Enhanced Hemocompatibility of Silver Nanoparticles Using the Photocatalytic Properties of Titanium Dioxide. Front. Bioeng. Biotechnol. 10:855471. doi: 10.3389/fbioe.2022.855471*

## 1 INTRODUCTION

Silver has historically been a commonly used antibacterial material. When silver is oxidized, the free $Ag^+$ released can act as an antibacterial/sterilizing agent by damaging the cell walls of bacteria and entering the bacteria to disrupt their metabolism and proliferation (Möhler et al., 2018). In the new century, various silver nanoparticles (AgNPs) have been developed and widely used in response to new needs. Due to their high specific surface area, AgNPs can release $Ag^+$ efficiently and stably. Also, AgNPs with nanometer size can be directly uptaken by bacteria and thus combine with thiol-containing subcellular structures to kill bacteria synergistically with $Ag^+$ (Zheng et al., 2018).

Due to their broad-spectrum and efficient antibacterial properties, AgNPs have been used in various medical devices and medical materials, such as burn dressing, catheter, and bone cement (Chaloupka et al., 2010). However, reports of AgNPs in blood contact devices are few because of the controversy of AgNPs' hemocompatibility. Many studies have shown that AgNPs can cause adverse

hematological events such as platelet adhesion and thrombosis when exposed to blood (Huang et al., 2016; Tran et al., 2022). This deficiency undoubtedly limits the use of AgNPs in blood-contact devices with antimicrobial needs, such as extracorporeal circuits and indwelling medical devices.

Researchers have tried many methods to improve the hemocompatibility of AgNPs. These approaches can be roughly classified into two categories. One is to construct a barrier layer to avoid direct contact between AgNPs and blood cells by utilizing biopolymer coatings or hydrogels (Fischer et al., 2015; Marulasiddeshwara et al., 2017). The other category involves co-immobilizing AgNPs with anticoagulant biomolecules to enhance hemocompatibility (Le Thi et al., 2017; Wu et al., 2020). However, both strategies are often cumbersome to prepare and do not address the hemocompatibility issue of AgNPs themselves. When the protective layer fails or AgNPs detach from the anticoagulant molecules, the AgNPs will face adverse hematological events again. Therefore, it is important to find a convenient and reliable improvement method to solve the hemocompatibility problem of AgNPs themselves.

$TiO_2$ owns excellent biosafety and has a wide range of applications in the medical field (Jafari et al., 2020). Due to its unique photocatalytic activity, when $TiO_2$ is subjected to UV irradiation, free radicals are generated, which can interact with the surrounding environment, thus making $TiO_2$ exhibit biological activity (Ziental et al., 2020). Therefore, this photo-induced bioactivity of $TiO_2$ has become a hot research topic in the last decade. The preliminary study of our team found that $TiO_2$ after UV irradiation can acquire excellent anticoagulant properties. The changes in the physicochemical properties of the $TiO_2$ surface, which are triggered by the $TiO_2$ photo-generated free radicals, are thought to be responsible for this photo-induced anticoagulant properties (Chen et al., 2014). More importantly, we further revealed that this photo-induced anticoagulant properties could spread to the surface of silicon adjacent to $TiO_2$ due to the diffusion effect of free radicals (Chen et al., 2015).

The mentioned understanding of AgNPs and $TiO_2$ inspired us that it is possible to improve the hemocompatibility of AgNPs by utilizing the diffusible photo-induced anticoagulant properties of $TiO_2$. To realize this idea, in this study, we firstly performed a short time of UV irradiation in seconds, using the $TiO_2$'s photocatalytic reduction property to load AgNPs onto $TiO_2$ nanoparticles ($TiO_2$NPs) (Chen et al., 2021). Subsequently, we performed a one-hour UV irradiation to activate the photo-induced anticoagulant properties of $TiO_2$. By the diffusion effect of the photo-induced anticoagulant properties, the hemocompatibility of AgNPs loaded on the $TiO_2$NPs nanoparticles was enhanced. Finally, we obtained the photo-functionalized composite nanoparticles (UV-Ag@$TiO_2$NPs) with anticoagulation and antibacterial properties.

In this study, microscopic appearance and elemental analysis by transmission electron microscopy (TEM) and energy dispersive spectroscopy (EDS) were used to examine the preparation of Ag@$TiO_2$NPs. Water contact angle (WCA), photocatalytic degradation of methylene blue and silver ion release experiments were used to characterize the physicochemical properties of nanoparticles coating. Gram-positive *Staphylococcus aureus* and Gram-negative *Pseudomonas aeruginosa* were used to examine the antibacterial ability of photo-functionalized composite nanoparticles. *In vitro* platelet adhesion assay and *ex-vivo* antithrombogenicity test were used to examine the hemocompatibility of the photo-functionalized composite nanoparticles.

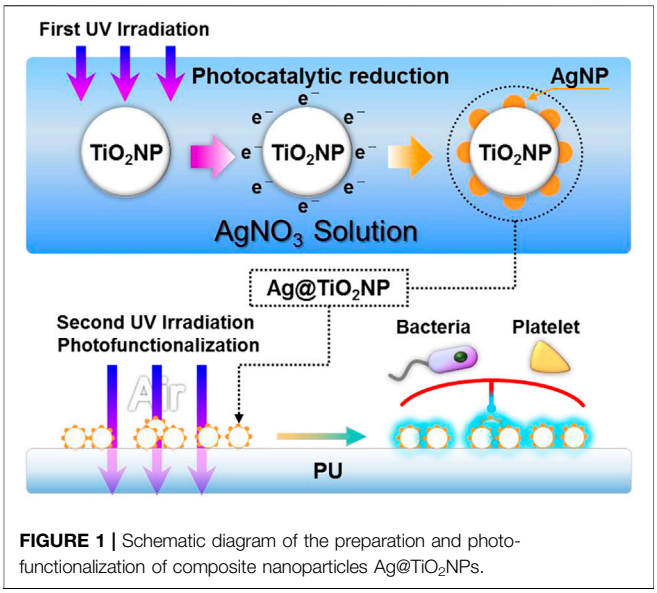


**FIGURE 1 |** Schematic diagram of the preparation and photo-functionalization of composite nanoparticles Ag@$TiO_2$NPs.

## 2 MATERIALS AND METHODS

### 2.1 Preparation of Ag@$TiO_2$NPs

The composite nanoparticles (Ag@$TiO_2$NPs) were obtained by loading AgNPs particles on the surface of $TiO_2$NPs using photocatalytic reduction, as shown in **Figure 1**. Briefly, P25-TiO2NPs (Sigma, United States) were ultrasonically dispersed in 5% alcohol solution to obtain a suspension of 1 mg/ml, and then the $TiO_2$NPs suspension was mixed with 1 mg/ml of silver nitrate solution in equal volume. The $AgNO_3$ & $TiO_2$ suspensions were irradiated with UV light (UV light intensity = 10 mW/cm$^2$, wavelength $\lambda$ = 365 nm) at 2 mm liquid depth to obtain the Ag@$TiO_2$NPs suspensions. Then the suspension was centrifuged, washed, and dried at 60°C, obtaining Ag@$TiO_2$NPs. Photocatalytic reduction times were 1, 5, 20, and 60 s to obtain the composite nanoparticles labeled as "1#", "2#", "3#", and "4#". Samples storage away from light.

### 2.2 Preparation and Photo-Functionalization of Ag@$TiO_2$NPs Coating

Ultrasonically resuspend Ag@$TiO_2$NPs with 5% alcohol in the same volume as the Ag@$TiO_2$NPs suspensions in **Section 2.1**.

subsequently, 1 × 1 $cm^2$ PU sheets were immersed in the suspension and deposited for 3 hours at room temperature to form a coating. Medical-grade silicone rubber (SR) catheters were peristaltic pump circulating with Ag@$TiO_2$NPs suspension for 12 h to obtain the coating for the *ex-vivo* antithrombogenicity test in **Section 2.5.2**. After coating, samples were rinsed with RO water, dried under nitrogen, and stored away from light.

Photo-functionalization of the samples was achieved by UV irradiation (UV light intensity = 10 mW/$cm^2$, wavelength λ = 365 nm) for 1 h.

The untreated coatings of $TiO_2$, 1#, 2#, 3#, and 4# nanoparticles are labeled as "UNT-$TiO_2$C", "UNT-1#C", "UNT-2#C", "UNT-3#C", "UNT-4#C", and the corresponding UV photo-functionalized nanoparticles coatings are labeled as "UV-$TiO_2$C", " UV-1#C", " UV-2#C", " UV-3#C", "UV-4#C".

## 2.3 Physicochemical Characterization of Ag@$TiO_2$NPs and Ag@$TiO_2$NPs Coating

The microstructure and the element distribution of Ag@$TiO_2$NPs were examined by field-emission transmission electron microscopy (TEM, JEM-2100F, JEOL, Japan) and the energy dispersive spectroscopy (EDS, JEM-2100F, JEOL, Japan).

Water contact angles (WCA) of Ag@$TiO_2$NPs coatings were obtained by analyzing images using ImageJ software (National Institutes of Health, United States).

Photocatalytic degradation of methylene blue assay was performed to examine the photocatalytic activity of Ag@$TiO_2$NPs coating. In brief, methylene blue powder was prepared as a 5 mg/L solution in deionized water. A sample was immersed in 1 ml of the solution, and UV irradiated (UV light intensity = 10 mW/$cm^2$, wavelength λ = 365 nm) for 1, 3, and 5 h. 200 μL of the solution was collected at each time point, and the absorbance (A) at a wavelength of 664 nm was determined using a microplate reader (BIO-TEK Instruments, United States). The relationship between A and the degradation rate (G) was calculated as

$$G = [(A_0 - A_t)/A_0] \times 100\% \quad (1)$$

where $A_0$ is the original absorbance of the undegraded methylene blue, and $A_t$ is the absorbance value after t hours of degradation.

In the $Ag^+$ release test, atomic absorption spectroscopy (AAS, TAS-990F, Beijing Purkinje General Instrument Co., Ltd., China) was performed to measure the release of $Ag^+$ from different samples into phosphate-buffered saline (PBS; pH = 7.4). Briefly, PU samples coated with Ag@$TiO_2$NPs were immersed in 1 ml of PBS in the dark. The PBS was collected and replaced with 1 ml of fresh PBS every 2 days. This process was repeated for a total of 14 days. All collected PBS solutions were analyzed for their content of $Ag^+$, and an $Ag^+$ time-release curve was plotted.

## 2.4 Antibacterial Assay

In this study, *Staphylococcus aureus* (*S. aureus*) and *Pseudomonas aeruginosa* (*P. aeruginosa*) were used to evaluate the antibacterial ability of the Ag@$TiO_2$NPs coating. Briefly, *S. aureus* and *P. aeruginosa* obtained from Sichuan Provincial People's Hospital were inoculated onto blood agar plates and cultivated in an incubator at 37°C. After the appearance of multiple colonies, *S. aureus* and *P. aeruginosa* were collected and dispersed in an F12 medium containing 10% fetal bovine serum (FBS, Sigma, United States). The density of *S. aureus* and *P. aeruginosa* was adjusted to 1 × $10^6$ colony forming units (CFU)/mL, and then 1 ml of bacterial suspension was added to the wells of a 24-well plate to soak the samples. After incubation at 37°C for 6 hours, the samples were washed three times and then transferred to a new 24-well plate containing a mixture of F12 FBS medium and cell counting kit-8(CCK-8, APExBIO Ltd., Houston, United States) agent. After 3 h of incubation, the activity of adherent bacteria was tested by detecting the absorbance of the medium at a wavelength of 450 nm using a microplate reader. The samples were then fixed with 2.5% glutaraldehyde for 12 h, after which they were dehydrated, and the adherent bacteria on the samples were observed and analyzed with an optical microscope (OM, DM4000M; Leica, Germany).

## 2.5 Evaluation of Hemocompatibility

### 2.5.1 Platelet Static Adhesion Test

Fresh whole blood was drawn from human healthy adult volunteers and anticoagulated with citric acid dextrose (ACD) (blood to ACD ratio of 9:1), in compliance with the ethical standards of Southwest Jiaotong University. Then, the fresh ACD blood was centrifuged at 1,500 rpm for 15 min, and thus platelet-rich plasma (PRP) was obtained. The PU samples (1 × 1 $cm^2$) deposited with the nanoparticles coatings were placed in 24-well cell culture plates and incubated with PRP (100 μL per sample) at 37°C for 1 hour under static conditions. After incubation, the samples were rinsed carefully three times with 0.9% saline to remove non-adherent platelets. Subsequently, the samples were fixed with 2.5% glutaraldehyde for 2 hours at room temperature. After typical rhodamine staining (Sigma, United States), the number of platelet adhesions in each sample was calculated by ImageJ software with six random fluorescence microscopy (DMRX, Leica, Germany) images (size = 400×). Furthermore, the morphology of the adhered platelets was observed under a scanning electron microscope (SEM, Quanta 200; FEI, Holland).

### 2.5.2 Antithrombogenicity Test by Ex-Vivo Blood Circulation

All succeeding procedures were performed in compliance with the China Council on Animal Care and Southwest Jiaotong University Animal Use protocol, following all the ethical guidelines for experimental animals.

The establishment of *ex-vivo* blood circulation has been described elsewhere (Qiu et al., 2021). Thrombogenicity of the SR catheters was assessed using an *ex-vivo* arteriovenous (AV) shunt model in the rabbit. For the detail of the AV shunt model, a custom-built extracorporeal circulation (ECC) pipeline with three parallel channels was set up. The ECC pipeline was made of medical-grade polyvinyl chloride (PVC) tubing. Samples, including the uncoated SR, UNT-1#C, and UV-1#C catheters, were connected to the ECC system.

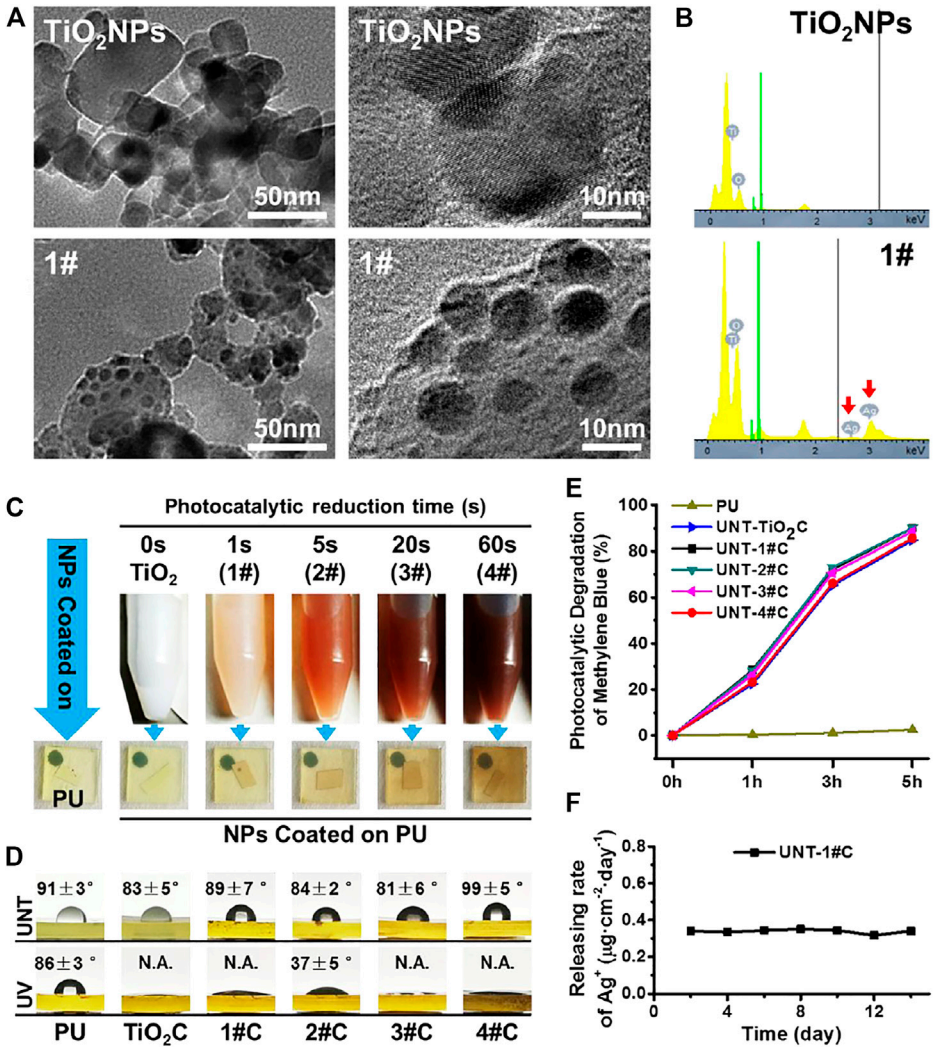


**FIGURE 2 |** TEM microscopic images of $TiO_2$NPs before and after photocatalytic reduction in silver nitrate solution **(A)** and the results of EDS elemental analysis **(B)**; photos of Ag@$TiO_2$NPs suspensions and corresponding coating on PU sheets at different photocatalytic reduction times **(C)**; WCA of Ag@$TiO_2$NPs coatings on PU sheets before and after photo-functionalization **(D)**; Untreated Ag@$TiO_2$NPs coatings photocatalytic degrade of methylene blue **(E)**; $Ag^+$ release from UNT-1# coating **(F)**.

Rabbits (New Zealand white rabbits, 2.5 kg) were anesthetized by intravenous injection of sodium pentobarbital (30 mg/kg). The rabbit left carotid artery and the right external jugular vein were isolated through a midline neck incision. The AV custom-built extracorporeal circulation (ECC) was placed into position by cannulating the left carotid artery for ECC inflow and the right external jugular vein for ECC outflow (**Figure 5A**). The flow through the ECC was started by unclamping the arterial and venous sides of the ECC. Animals had no systemic anticoagulation throughout the experiment.

After 30min on ECC, the circuits were clamped, removed from the animal, rinsed with 0.9% saline (pH 7.4) gently, and drained. The cross-sections of the catheters were photographed for determination of the occlusion rates. Then, the residual thrombosis in the catheters was fixed in 2.5% glutaraldehyde solution overnight at room temperature and dehydrated. After weighing, samples undergo a micromorphological analysis by scanning electron microscopy (SEM, Quanta 200, FEI, Holland).

## 3 RESULTS AND DISCUSSION

### 3.1 Characterization of Ag@$TiO_2$NPs

To confirm that Ag@$TiO_2$NPs were successfully prepared, TEM was used to characterize the microstructure of the nanoparticles, and EDS was used to perform elemental analysis of the nanoparticles. From the TEM results, additional spherical secondary structures with diameters of 5–10 nm were observed on the surface of 1# nanoparticles compared to $TiO_2$NPs (**Figure 2A**). the signal of elemental Ag appeared in the EDS data for 1# nanoparticles (**Figure 2B**), which indicates that the spherical secondary structures appearing on the surface of 1# nanoparticles are

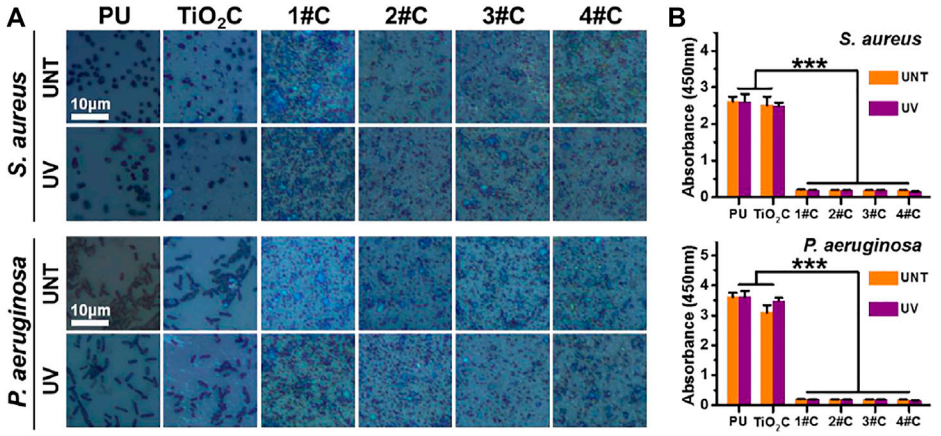


**FIGURE 3 |** Antibacterial activity assay. Optical microscopy images of bacteria cultured on nanoparticles coatings before and after photo-functionalization **(A)** and bacterial activity measured by CCK-8 kit **(B)**.

AgNPs. These AgNPs should be the products of $Ag^+$ reduction by electrons generated on the surface of $TiO_2$NPs during the photocatalytic reduction process (Lu et al., 2013; Chen et al., 2021).

The results of TEM and EDS indicate that Ag@$TiO_2$NPs were successfully prepared. Furthermore, the color of the suspensions of Ag@$TiO_2$NPs deepened with the prolongation of the photocatalytic reduction time, which implied that the AgNPs content in Ag@$TiO_2$NPs might increase with the photocatalytic reduction time prolongation (Lu et al., 2013). The color of the coatings deposited by Ag@$TiO_2$NPs onto the PU sheets also showed the same trend (**Figure 2C**).

## 3.2 Characterization of Ag@$TiO_2$NPs Coating

The photo-induced hydrophilicity of $TiO_2$ has been reported in many pieces of literature (Carp et al., 2004). Excellent hydrophilicity is considered to facilitate biofouling resistance (He et al., 2021). Compared with the non-photo-functionalized UNT-Ag@$TiO_2$NPs coatings, the photo-functionalized UV-Ag@$TiO_2$NPs coatings showed a significant decrease in WCA and exhibited strong photo-induced hydrophilicity (**Figure 2D**), which means that photo-functionalized nanoparticle coatings may be somehow more anticoagulant and antibacterial than their counterparts in the group. Among all UV-Ag@$TiO_2$NPs coatings, 2# coating had the highest water contact angle, perhaps related to the content of AgNPs on the surface of Ag@$TiO_2$NPs, the exact mechanism of which needs to be further investigated.

The photocatalytic oxidation activity of $TiO_2$ is another manifestation of the photocatalytic activity of $TiO_2$, which is closely related to the mechanism of photo-induced anticoagulant properties of $TiO_2$ (Chen et al., 2014; Chen et al., 2015). Although it has been reported in the literature that loading AgNPs on the surface of $TiO_2$ can enhance the photocatalytic activity of $TiO_2$ by forming Schottky energy barriers (Gomathi Devi and Kavitha, 2016). However, in this study, through the photocatalytic oxidation decomposition of methylene blue, we found that the loading of AgNPs did not significantly affect the photocatalytic oxidation activity of Ag@$TiO_2$NPs coating, compared to $TiO_2$NPs coating (**Figure 2E**).

The $Ag^+$ release rate is closely related to AgNPs' biosafety and antimicrobial properties (Marchioni et al., 2018). 1# nanoparticles were used to analyze their $Ag^+$ release in PBS after coating on PU, and it was found that the $Ag^+$ release rate of UNT-1#C was stable around 0.35 $\mu g\ cm^{-2}\ day^{-1}$ (**Figure 2F**), which was considered to be safe (Liu et al., 2018).

## 3.3 Analysis of Antibacterial Property

Here, Gram-positive *Staphylococcus aureus* (*S. aureus*) and Gram-negative *Pseudomonas aeruginosa* (*P. aeruginosa*) were used to examine the broad-spectrum antimicrobial resistance of the Ag@$TiO_2$NPs coatings. The results of optical microscopy showed that morphologically intact *S. aureus* and *P. aeruginosa* could be seen on the surface of all PU and $TiO_2$NPs coatings, in contrast to all Ag@$TiO_2$NPs coatings with a large amount of debris, probably necrotic bacterial fragments (**Figure 3A**).

The results of the cellular activity analysis (**Figure 3B**) were consistent with the observation under optical microscopy, where the bacterial activity on the surface of the $TiO_2$NPs coating was similar to that of the PU. In contrast, all Ag@$TiO_2$NPs coatings exhibited significant antimicrobial activity compared to the PU substrate and the $TiO_2$NPs coating. Notably, there was no significant difference between the antimicrobial properties of UNT-Ag@$TiO_2$NPs coatings and UV-Ag@$TiO_2$NPs coatings, suggesting that the photo-functionalization treatment did not affect the AgNPs portion of Ag@$TiO_2$NPs to perform the antimicrobial function. Another noteworthy point is that the antimicrobial performance of 1# coatings with the lowest AgNPs loading is comparable to that of 4# coaitngs with the highest AgNPs loading, indicating a powerful antimicrobial performance.

## 3.4 Analysis of Anticoagulant Property *in vitro*

*In vitro* platelet adhesion experiments were performed using deposited Ag@$TiO_2$NPs coatings on PU sheets, for PU is widely used in various blood contact devices. The results of fluorescence images (**Figure 4A**) and adhesion density

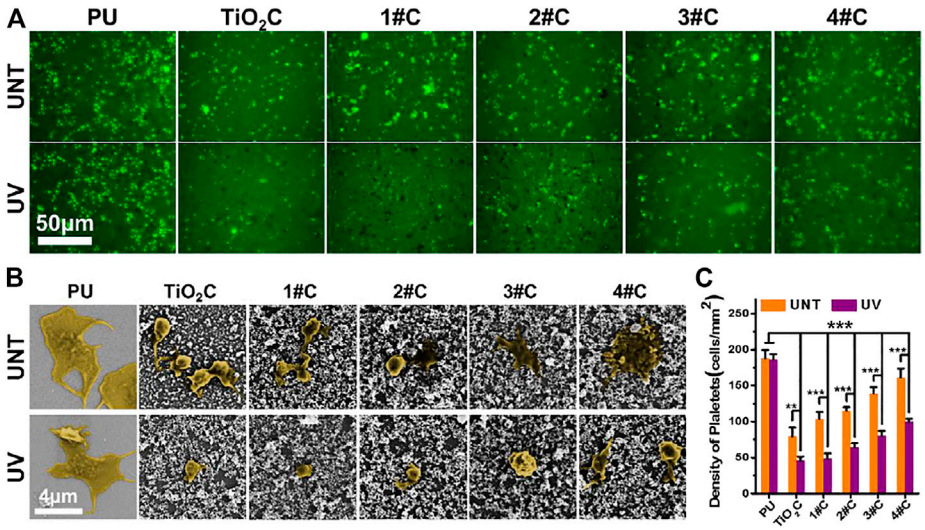


**FIGURE 4 |** *In vitro* platelet adhesion assay. Fluorescence images **(A)**, SEM images **(B)**, and adhesion density **(C)** of adhered platelet on nanoparticles coatings.

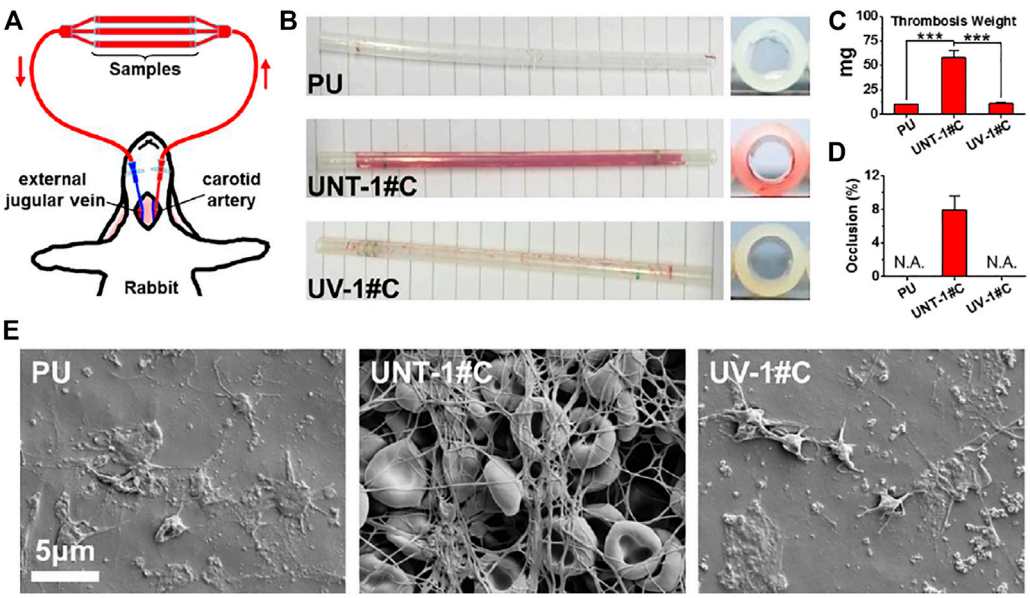


**FIGURE 5 |** Schematic diagram of the *ex-vivo* blood circulation experiment **(A)**; photograph of the catheter after the experiment **(B)**; the weight of the thrombus formed in the catheter **(C)**; catheter occlusion rate **(D)**; microscopic image of the catheter lining by SEM **(E)**.

(**Figure 4C**) showed that all nanoparticles coatings significantly reduced the number of platelet adhesions after photo-functionalization compared with that before treatment. Besides, the platelet adhesions density on the photo-functionalized nanoparticle coatings was significantly lower than that of PU substrates. Notably, the platelet adhesion density of nanoparticles coatings tended to increase with the prolongation of photocatalytic reduction time in the composite nanoparticles preparation stage. Considering the issue of blood compatibility of AgNPs, this result is similar to the phenomenon that the color of Ag@TiO2NPs suspension deepens with increasing photocatalytic reduction time (**Figure 2C**), supporting the idea that the AgNPs content in Ag@TiO2NPs increases with increasing photocatalytic reduction time.The SEM results of platelet adhesion (**Figure 4B**) showed that the platelets on the PU substrate were in a partially spreading dendrites state, with the degree of spread much higher than that of platelets on the UV-photo-functionalized nanoparticles coating, which was between spherical to partially spread. In contrast, the degree of platelet spreading on all nanoparticles coatings showed a

tendency to increase with increasing photocatalytic reduction time at the composite nanoparticles preparation stage. This trend is consistent with the results of platelet adhesion density, which could be similarly influenced by the content of AgNPs in the composite nanoparticles.

The results of platelet adhesion experiments suggested that the Ag@$TiO_2$NPs coatings can acquire anti-platelet adhesion ability after photo-functionalization. However, this photo-induced anticoagulant properties of the UV-Ag@$TiO_2$NPs may be weakened by increasing the content of AgNPs, this implies that the photo-induced anticoagulant properties of $TiO_2$ have a limited or dose-dependent improvement on the hemocompatibility of AgNPs. Therefore, proper loading of AgNPs is essential to impart UV-Ag@TiO2NPs with excellent antimicrobial properties without causing deterioration of hemocompatibility.

Here, combined with the results of the antimicrobial experiments and *in vitro* platelet adhesion assays, the UV-1# sample with the lowest silver loading may be an ideal candidate capable of obtaining balanced antimicrobial and anticoagulant properties.

### 3.5 *Ex-vivo* Antithrombogenicity Test

The Antithrombogenicity test by *ex-vivo* blood circulation provides a more comprehensive test of the anticoagulant capacity of the UV-Ag@$TiO_2$NPs coating compared to the *in vitro* blood test. SR is a material commonly used for central venous catheters, which is a typical medical device that requires both anticoagulation and antimicrobial activity. Considering the *in vitro* platelet adhesion and Antibacterial Assay results, SR catheters deposited with 1# nanoparticles were selected for the *ex-vivo* blood circulation assay. After 30 min of *ex-vivo* blood circulation, the surface of the UNT-1# coating showed patches of sizable thrombus layer that blocked nearly 8% of the catheter lumen compared to the UV-1# coating with only a small amount of thrombus on the surface (**Figures 5B,D**). The analysis of the weight of the formed thrombus showed a significant increase in UNT-1# coating compared to both UV-1# coating and PU substrate (**Figure 5C**). At the same time, there was no significant difference in UV-1# coating compared to PU substrate.

SEM images of the inner wall of the catheter revealed that UNT-1# coating had fully initiated the coagulation mechanism, and the fibrinogen network captured a large number of red blood cells, forming a thrombus layer that completely covered the substrate. In contrast, the UV-1# coating and the PU substrate were similar, with only some platelets adhering to the surface (**Figure 5E**). It is worth noting that most of the erythrocytes in the thrombus layer remain in typical form, and combined with the data on the rate of silver ion release from the coating (**Figure 2F**), hemolysis may not be a problem that the coating would cause.

Here, UV-Ag@$TiO_2$NPs coating did not show significantly better results than PU substrates in the *ex-vivo* blood assay as in the *in vitro* platelet adhesion assay. This may be due to the dynamic environment and more comprehensive blood composition in the *ex-vivo* blood circulation assay (Courtney et al., 1994). Nevertheless, the results of *in vitro* platelet adhesion and *ex-vivo* blood experiments were sufficient to suggest that loading AgNPs onto the surface of $TiO_2$NPs and performing UV-Photo-functionalization treatment was an effective way to improve their hemocompatibility.

## 4 CONCLUSION

This study prepared a composite nanoparticles (Ag@$TiO_2$NPs) by loading AgNPs onto $TiO_2$NPs using a photocatalytic reduction method. Then, we utilized secondary UV irradiation to photo-functionalize Ag@$TiO_2$NPs to improve the hemocompatibility of $TiO_2$NPs and AgNPs. *In vitro* and *ex-vivo* experiments showed that such photo-functionalized UV-Ag@$TiO_2$NPs coatings are endowed with excellent hemocompatibility. When UV-Ag@$TiO_2$NPs were deposited onto the PU and SR to form a coating, they significantly inhibited platelet adhesion and activation, showing anticoagulant properties not inferior to those of medical-grade substrates. In addition, this UV-Ag@$TiO_2$NPs coating exhibited excellent antibacterial properties against both Gram-positive and Gram-negative bacteria. Therefore, these UV-Ag@$TiO_2$NPs could service the medical devices that require both anticoagulant and antibacterial properties, such as central venous catheters. More importantly, this UV- photo-functionalized modification strategy relying on $TiO_2$ could provide a new idea to solve the problem of blood compatibility of functionalized metal nanoparticles similar to AgNPs.

## DATA AVAILABILITY STATEMENT

The original contributions presented in the study are included in the article/Supplementary Material, further inquiries can be directed to the corresponding authors.

## ETHICS STATEMENT

The animal study was reviewed and approved by Ethics Committee of Southwest Jiaotong University.

## AUTHOR CONTRIBUTIONS

XC: Experiment, Writing- Original draft preparation. SD, LL, PL, and PEY: Experiment, Original draft preparation. YL and AZ: Data curation and Writing- Reviewing. PIY: Supervision and language polishment. NH and JC: Conceptualization and manuscript revision.

## FUNDING

This work was supported by the National Natural Science Foundation of China (No. 31870958 (PIY), 31700821 (JC), 81771988 (AZ), and the Sichuan Science and Technology Program (No.20GJHZ0268) (AZ).

## REFERENCES


Carp, O., Huisman, C. L., and Reller, A. (2004). Photoinduced Reactivity of Titanium Dioxide. *Prog. Solid State Chem.* 32 (1-2), 33–177. doi:10.1016/j.progsolidstchem.2004.08.001

Chaloupka, K., Malam, Y., and Seifalian, A. M. (2010). Nanosilver as a New Generation of Nanoproduct in Biomedical Applications. *Trends Biotechnol.* 28 (11), 580–588. doi:10.1016/j.tibtech.2010.07.006

Chen, J., Zhao, A., Chen, H., Liao, Y., Yang, P., Sun, H., et al. (2014). The Effect of Full/partial UV-Irradiation of TiO 2 Films on Altering the Behavior of Fibrinogen and Platelets. *Colloids Surf. B: Biointerfaces* 122, 709–718. doi:10.1016/j.colsurfb.2014.08.004

Chen, J., Yang, P., Liao, Y., Wang, J., Chen, H., Sun, H., et al. (2015). Effect of the Duration of UV Irradiation on the Anticoagulant Properties of Titanium Dioxide Films. *ACS Appl. Mater. Inter.* 7 (7), 4423–4432. doi:10.1021/am509006y

Chen, J., Dai, S., Liu, L., Maitz, M. F., Liao, Y., Cui, J., et al. (2021). Photo-functionalized TiO2 Nanotubes Decorated with Multifunctional Ag Nanoparticles for Enhanced Vascular Biocompatibility. *Bioactive Mater.* 6 (1), 45–54. doi:10.1016/j.bioactmat.2020.07.009

Courtney, J. M., Lamba, N. M. K., Sundaram, S., and Forbes, C. D. (1994). Biomaterials for Blood-Contacting Applications. *Biomaterials* 15 (10), 737–744. doi:10.1016/0142-9612(94)90026-4

Fischer, M., Vahdatzadeh, M., Konradi, R., Friedrichs, J., Maitz, M. F., Freudenberg, U., et al. (2015). Multilayer Hydrogel Coatings to Combine Hemocompatibility and Antimicrobial Activity. *Biomaterials* 56, 198–205. doi:10.1016/j.biomaterials.2015.03.056

Gomathi Devi, L., and Kavitha, R. (2016). A Review on Plasmonic metal□TiO2 Composite for Generation, Trapping, Storing and Dynamic Vectorial Transfer of Photogenerated Electrons across the Schottky junction in a Photocatalytic System. *Appl. Surf. Sci.* 360, 601–622. doi:10.1016/j.apsusc.2015.11.016

He, Z., Yang, X., Wang, N., Mu, L., Pan, J., Lan, X., et al. (2021). Anti-Biofouling Polymers with Special Surface Wettability for Biomedical Applications. *Front. Bioeng. Biotechnol.* 9, 807357. doi:10.3389/fbioe.2021.807357

Huang, H., Lai, W., Cui, M., Liang, L., Lin, Y., Fang, Q., et al. (2016). An Evaluation of Blood Compatibility of Silver Nanoparticles. *Sci. Rep.* 6 (1), 1–15. doi:10.1038/srep25518

Jafari, S., Mahyad, B., Hashemzadeh, H., Janfaza, S., Gholikhani, T., and Tayebi, L. (2020). Biomedical Applications of $TiO_2$ Nanostructures: Recent Advances. *Ijn* 15, 3447–3470. doi:10.2147/ijn.s249441

Le Thi, P., Lee, Y., Kwon, H. J., Park, K. M., Lee, M. H., Park, J.-C., et al. (2017). Tyrosinase-mediated Surface Coimmobilization of Heparin and Silver Nanoparticles for Antithrombotic and Antimicrobial Activities. *ACS Appl. Mater. Inter.* 9 (24), 20376–20384. doi:10.1021/acsami.7b02500

Liu, X., Chen, J., Qu, C., Bo, G., Jiang, L., Zhao, H., et al. (2018). A Mussel-Inspired Facile Method to Prepare Multilayer-AgNP-Loaded Contact Lens for Early Treatment of Bacterial and Fungal Keratitis. *ACS Biomater. Sci. Eng.* 4 (5), 1568–1579. doi:10.1021/acsbiomaterials.7b00977

Lu, Q., Lu, Z., Lu, Y., Lv, L., Ning, Y., Yu, H., et al. (2013). Photocatalytic Synthesis and Photovoltaic Application of Ag-TiO2 Nanorod Composites. *Nano Lett.* 13 (11), 5698–5702. doi:10.1021/nl403430x

Marchioni, M., Jouneau, P.-H., Chevallet, M., Michaud-Soret, I., and Deniaud, A. (2018). Silver Nanoparticle Fate in Mammals: Bridging *In Vitro* and *In Vivo* Studies. *Coord. Chem. Rev.* 364, 118–136. doi:10.1016/j.ccr.2018.03.008

Marulasiddeshwara, M. B., Dakshayani, S. S., Sharath Kumar, M. N., Chethana, R., Raghavendra Kumar, P., and Devaraja, S. (2017). Facile-one Pot-Green Synthesis, Antibacterial, Antifungal, Antioxidant and Antiplatelet Activities of Lignin Capped Silver Nanoparticles: A Promising Therapeutic Agent. *Mater. Sci. Eng. C* 81, 182–190. doi:10.1016/j.msec.2017.07.054

Möhler, J. S., Sim, W., Blaskovich, M. A. T., Cooper, M. A., and Ziora, Z. M. (2018). Silver Bullets: A New Lustre on an Old Antimicrobial Agent. *Biotechnol. Adv.* 36 (5), 1391–1411. doi:10.1016/j.biotechadv.2018.05.004

Qiu, H., Tu, Q., Gao, P., Li, X., Maitz, M. F., Xiong, K., et al. (2021). Phenolic-Amine Chemistry Mediated Synergistic Modification with Polyphenols and Thrombin Inhibitor for Combating the Thrombosis and Inflammation of Cardiovascular Stents. *Biomaterials* 269, 120626. doi:10.1016/j.biomaterials.2020.120626

Tran, H. D., Moonshi, S. S., Xu, Z. P., and Ta, H. T. (2022). Influence of Nanoparticles on the Haemostatic Balance: between Thrombosis and Haemorrhage. *Biomater. Sci.* 10 (1), 10–50. doi:10.1039/d1bm01351c

Wu, H., Su, M., Jin, H., Li, X., Wang, P., Chen, J., et al. (2020). Rutin-Loaded Silver Nanoparticles with Antithrombotic Function. *Front. Bioeng. Biotechnol.* 8, 1356. doi:10.3389/fbioe.2020.598977

Zheng, K., Setyawati, M. I., Leong, D. T., and Xie, J. (2018). Antimicrobial Silver Nanomaterials. *Coord. Chem. Rev.* 357, 1–17. doi:10.1016/j.ccr.2017.11.019

Ziental, D., Czarczynska-Goslinska, B., Mlynarczyk, D. T., Glowacka-Sobotta, A., Stanisz, B., Goslinski, T., et al. (2020). Titanium Dioxide Nanoparticles: Prospects and Applications in Medicine. *Nanomaterials* 10 (2), 387. doi:10.3390/nano10020387


**Conflict of Interest:** The authors declare that the research was conducted in the absence of any commercial or financial relationships that could be construed as a potential conflict of interest.

frontiers in Bioengineering and Biotechnology

REVIEW
published: 17 February 2022
doi: 10.3389/fbioe.2022.853193

# Development and Prospect of Esophageal Tissue Engineering

*Rui Xu[1,2], Xinnan Fang[2], Shengqian Wu[2], Yiyin Wang[2], Yi Zhong[2], Ruixia Hou[1,2]*, Libing Zhang[3], Lei Shao[2], Qian Pang[2], Jian Zhang[4], Xiang Cui[4], Rongyue Zuo[1], Liwei Yao[1] and Yabin Zhu[2]*

[1]The Affiliated Hospital of Medical School, Ningbo University, Ningbo, China, [2]School of Medicine, Ningbo University, Ningbo, China, [3]Ningbo Institute of Materials Technology and Engineering, Chinese Academy of Sciences, Ningbo, China, [4]The Affiliated Lihuili Hospital, Ningbo University, Ningbo, China

Currently, patients with esophageal cancer, especially advanced patients, usually use autologous tissue for esophageal alternative therapy. However, an alternative therapy is often accompanied by serious complications such as ischemia and leakage, which seriously affect the prognosis of patients. Tissue engineering has been widely studied as one of the ideal methods for the treatment of esophageal cancer. In view of the complex multi-layer structure of the natural esophagus, how to use the tissue engineering method to design the scaffold with structure and function matching with the natural tissue is the principle that the tissue engineering method must follow. This article will analyze and summarize the construction methods, with or without cells, and repair effects of single-layer scaffold and multi-layer scaffold. Especially in the repair of full-thickness and circumferential esophageal defects, the flexible design method and the binding force between the layers of the scaffold are very important. In short, esophageal tissue engineering technology has broad prospects and plays a more and more important role in the treatment of esophageal diseases.

**Keywords: esophageal repair, tissue engineering, single-layer scaffold, multi-layer scaffold, stem cells**

OPEN ACCESS

***Edited by:***
*Guicai Li,*
*Nantong University, China*

***Reviewed by:***
*Yifeng Lei,*
*Wuhan University, China*
*Liu Hengquan,*
*Chengdu University of Technology, China*

****Correspondence:***
*Ruixia Hou*
*hourx130@163.com*

***Specialty section:***
*This article was submitted to Biomaterials, a section of the journal Frontiers in Bioengineering and Biotechnology*

***Received:*** *12 January 2022*
***Accepted:*** *31 January 2022*
***Published:*** *17 February 2022*

***Citation:***
*Xu R, Fang X, Wu S, Wang Y, Zhong Y, Hou R, Zhang L, Shao L, Pang Q, Zhang J, Cui X, Zuo R, Yao L and Zhu Y (2022) Development and Prospect of Esophageal Tissue Engineering. Front. Bioeng. Biotechnol. 10:853193. doi: 10.3389/fbioe.2022.853193*

## INTRODUCTION

Esophageal cancer is the seventh most common cancer in the world and ranks sixth in the world in terms of lethality among all malignant tumors. Of the 500,000 new cases worldwide each year, about half occur in China. It is the fifth most commonly diagnosed cancer and the fourth leading cause of cancer death in China. The fatality rate of esophageal cancer remains high, which seriously affects people's lives and health (Pennathur et al., 2013; Chen et al., 2016; Chang et al., 2017; Huang et al., 2018; Uhlenhopp et al., 2020). Surgical alternative therapy requires replacement of the stomach, jejunum, colon, and other autologous tissues, but replacement is likely to cause high morbidity and mortality, and at the cost of normal tissue damage, it seriously affects the quality of life (Dua et al., 2016; Arakelian et al., 2018). In recent years, tissue engineering technology has been used to construct bionic esophageal scaffolds, which avoids taking materials from patients, reduces the risk of high-risk surgery and high mortality and morbidity caused by postoperative surgery, and provides a new method for esophageal repair and reconstruction (Zhu et al., 2017). The esophagus is composed of the mucosa, submucosa, muscularis propria, and adventitia. The muscularis propria is a multi-layer structure with an inner ring and an outer longitudinal shape, called the circular muscle and the longitudinal muscle. The cells mainly include mucosal epithelial cells (ECs) and smooth muscle cells (SMCs) (Peirlinck et al., 2018; Blank et al., 2019; Farhat et al., 2021) (**Figure 1**). Therefore, as an ideal esophageal tissue engineering scaffold and a bionic

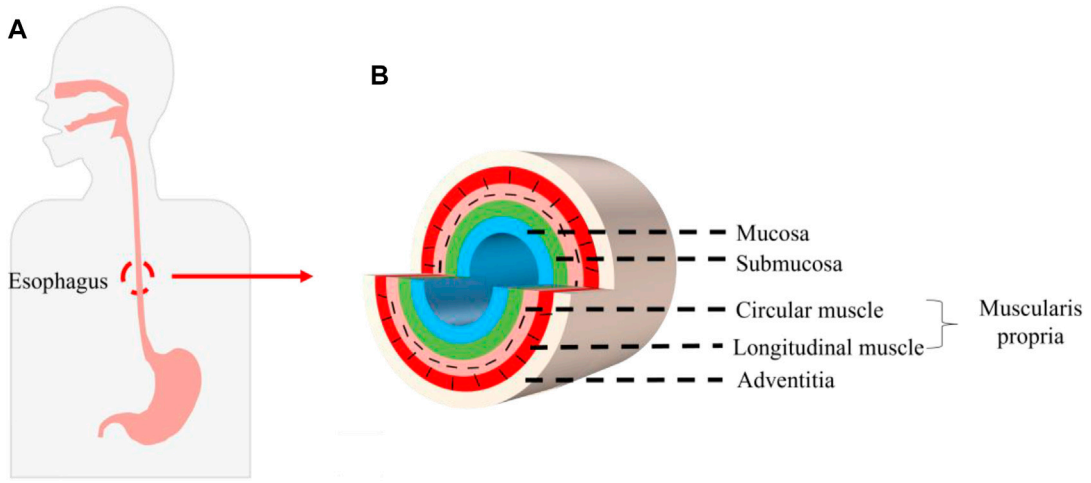


**FIGURE 1 |** Structure of the human esophagus. **(A)** Position of the esophagus in the human body. **(B)** Schematic diagram of cross section of the esophagus.

multi-layer structure of the esophagus, it is endowed with corresponding supporting functions for different parts. How to combine each layer of scaffold effectively is one of the important problems that must be considered when constructing a multi-layer scaffold. In view of this, how to design a bionic multi-layer composite scaffold, which has both multi-layer structure and multi-function and ensures the firm connection between each layer, is a scientific problem of great concern in this field and has important scientific significance and potential application value.

## SINGLE-LAYER ESOPHAGEAL SCAFFOLDS

### Scaffold Material

In the research of esophageal tissue engineering, researchers have conducted a large number of innovative research studies on the construction of single-layer scaffolds to repair the mucosal layer or the muscle layer. Single-layer scaffolds are classified according to the choice of materials, mainly including acellular matrix or (and) polymer scaffolds. The acellular matrix includes the small intestinal submucosa (SIS), urinary bladder submucosa (UBS), esophageal mucosa, etc. Polymer materials include polylactide (PLA), poly (L-lactide-co-ε-caprolactone) (PLGA), poly (3-hydroxybutyrate-co-3-hydroxyvalerate) (PHBV), polylactide-poly (ε-caprolactone) (PLA-PCL), polyurethane (PU), etc. (Badylak et al., 2000; Nieponice et al., 2014; Kuppan et al., 2016; Tan et al., 2016; Dorati et al., 2017; Kuppan et al., 2017; Luc et al., 2018) (**Table 1**).

From the perspective of single-layer scaffold structure, the classification mainly includes acellular matrix, membranes grafted with biomolecules, electrospinning scaffolds, micro-pattern scaffolds, etc. (Hou et al., 2016; Wei et al., 2018; Zhuravleva et al., 2019; Chaitin et al., 2021; Levenson et al., 2021) (**Table 2**). In order to accurately simulate the inner ring and outer longitudinal structure of the muscle layer, electrospinning scaffolds and micro-pattern scaffolds are mainly used (Gong et al., 2013; Kuppan et al., 2017). Our team has conducted a large number of *in vitro* and *in vivo* animal studies on single-layer scaffolds. The original idea was to graft collagen on the surface of polymer materials such as PLGA and poly (L-lactide-co-caprolactone) (PLLC) to improve their biocompatibility (Zhu et al., 2005; Zhu et al., 2006). Then, the polycaprolactone/silk fibroin (PCL/SF) electrospinning scaffold is made by electrospinning technology, and the electrospinning fiber pore size can simulate the structure of the extracellular matrix (ECM) (Lv et al., 2014). At this stage, the micro-pattern membrane technology is used to construct a new type of esophageal bionic scaffold, which has successfully constructed a micro-pattern PU scaffold and double-layer scaffold of the esophageal acellular matrix (Hou et al., 2019; Wang X. et al., 2020).

### Cell Seeding

The abovementioned studies carried out the structural bionic design of single-layer scaffolds from the perspectives of material selection and construction methods and achieved a series of achievements in the damage repair of the esophageal mucosa and muscularis. Studies have shown that if cells are introduced into scaffolds, they will work synergistically with scaffolds in the microenvironment *in vivo* to further enhance functional repair of tissues. For example, Badylak et al. made artificial defects in the dog's esophagus and used ECM derived from SIS or UBS to repair the esophageal defect. After 35 days, the scaffold was partially covered by the squamous epithelium, and only scattered skeletal muscle cells surrounded collagen connective tissue (Badylak et al., 2000). Xie et al. proved that, after implantation in dogs, SIS alone is not completely endothelialized. When bone marrow mesenchymal stem cells (MSCs) are combined with SIS, the results show that the defect site is completely endothelialized, the muscle layer is regenerated, and the new microvessels are dense (Tan et al., 2013) (**Figure 2**).

Therefore, researchers have introduced cells, such as ECs, SMCs, and stem cells, into biomimetic single-layer scaffolds to construct tissue engineering scaffolds. The ECs or SMCs are

**TABLE 1 |** Classification according to materials of single-layer scaffolds.

| Author | References | Scaffolds | Formation method | Loading cell | Study | Biota | Outcomes |
|---|---|---|---|---|---|---|---|
| Badylak et al. | Badylak et al. (2000) | SIS, UBS | Multi-layer esophageal scaffold composed of the ECM | — | Patch and full segmental esophageal implantation | Canine | 89% mortality. Complete and confluent squamous epithelium on the surface of the scaffold |
| Dorati et al. | Luc et al. (2018) | Decellularized esophagus | Matrix of decellularized esophagus | — | Full segmental esophageal implantation | Pig | 16% mortality. Complications are reported in the treatment group |
| Nieponice et al. | Nieponice et al. (2014) | UBS | Multi-layer esophageal scaffold composed of the ECM | — | Patch esophageal implantation | Human | 0% mortality. All patients were able to save their esophagus |
| Kuppan et al. | Kuppan et al. (2017) | PHBV, PCL, gelatin | Aligned nanofibrous scaffold made of PHBV, PHBV-gelatin, PCL, and PCL-gelatin | ECs, SMCs | *In vitro* | — | ECs and SMCs can divide into two different levels |
| Dorati et al. | Dorati et al. (2017) | PCL, PLA, chitosan | Multi-layer patch | FBCs | *In vitro* | — | Cells grow better on multi-layer patches than on single-layer patches |
| Tan et al. | Tan et al. (2016) | PLC | Fusion integrated scaffold made of PLC as the material | FBCs | *In vitro* | — | Good mechanical properties and biocompatibility |
| Lv et al. | Lv et al. (2014) | PCL, SF | Using PCL as the raw material for fiber scaffolding by electrospinning | — | Partial-thickness esophageal implantation and subcutaneous implantation | Rabbit | 0% mortality. The esophageal mucosa has regenerated, while the scaffold has been ruptured |
| Zhu et al. | Zhu et al. (2005) | PLGA, collagen | Using collagen to modify the surface of PLGA | SMCs | *In vitro* | — | Collagen-modified PLGA promotes the growth of SMCs in the esophagus |
| Zhu et al. | Zhu et al. (2006) | PLLC | Cellulose and collagen modified the PLLC surface | SMCs, ECs, FBCs | *In vitro* | — | PLLC with collagen or cellulose supports the cell attachment, growth, and functional forms |
| Gong et al. | Gong et al. (2013) | PU | Making a micro-pattern on the surface of PU | SMCs | Partial-thickness esophageal implantation | Rabbit | 0% mortality. The regenerative tissue is tightly attached to the surface of the scaffold material |
| Tam et al. | Tan et al. (2013) | SIS | Single-layer esophageal scaffold | MSCs | Patch and full segmental esophageal implantation | Pig | 0% mortality. Transplantation of MSCs-SIS appears to promote epidermalization, vascularization, and muscle regeneration |
| Marzaro et al. | Marzaro et al. (2020) | Decellularized esophagus | Acellular matrix of esophageal muscle | MSCs | Partial-thickness esophageal implantation | Pig | 0% mortality. Half of the unvaccinated cell groups have narrow esophagus |

*PLC, poly(L-lactide-co-ε-caprolactone); FBCs, fibroblast cells.*

**TABLE 2 |** Classification according to the construction of single-layer scaffolds.

| Author | References | Scaffolds | Formation method | Loading cell | Study | Biota | Outcomes |
|---|---|---|---|---|---|---|---|
| Wei et al. | Wei et al. (2018) | CPU | SF-modified CPU surface | MSCs | *In vitro* | — | SF can enhance the interaction between cells and the biocompatibility of the material |
| Paolo et al. | Zhuravleva et al. (2019) | Polyamide-6 | Polyamide-6 electrospinning scaffold | HUVEC, MSCs | *In vitro* | — | The electrospinning structure can simulate the acellular structure of the esophagus |
| Hou et al. | Hou et al. (2016) | PU | PU scaffold with a micro-pattern surface | — | Partial-thickness esophageal implantation | Rabbit | 0% mortality. The new muscle layer grows in the direction of the micro-pattern channel |
| Kang et al. | Chaitin et al. (2021) | Esophagus | Matrix of the decellularized esophagus | ESCCs, FBCs | *In vitro* | — | The co-culture of FBS and ESCC could secrete more endometrialin |

*CPU, poly(ester urethane); HUVEC, human umbilical vein endothelial cell; ESCCs, esophageal squamous cell carcinomas.*

difficult to be widely used due to the large damage to the donor when they are acquired and the limited ability of proliferation and differentiation after cell expansion. On the contrary, stem cells have the advantages of large differentiation potential, strong proliferation ability, convenient and easy acquisition from the body, and the ability to differentiate into specific cells in tissue. So, they are widely used as seed cells in the field of tissue engineering. For example, Ivo et al. combined MSCs and decellularized

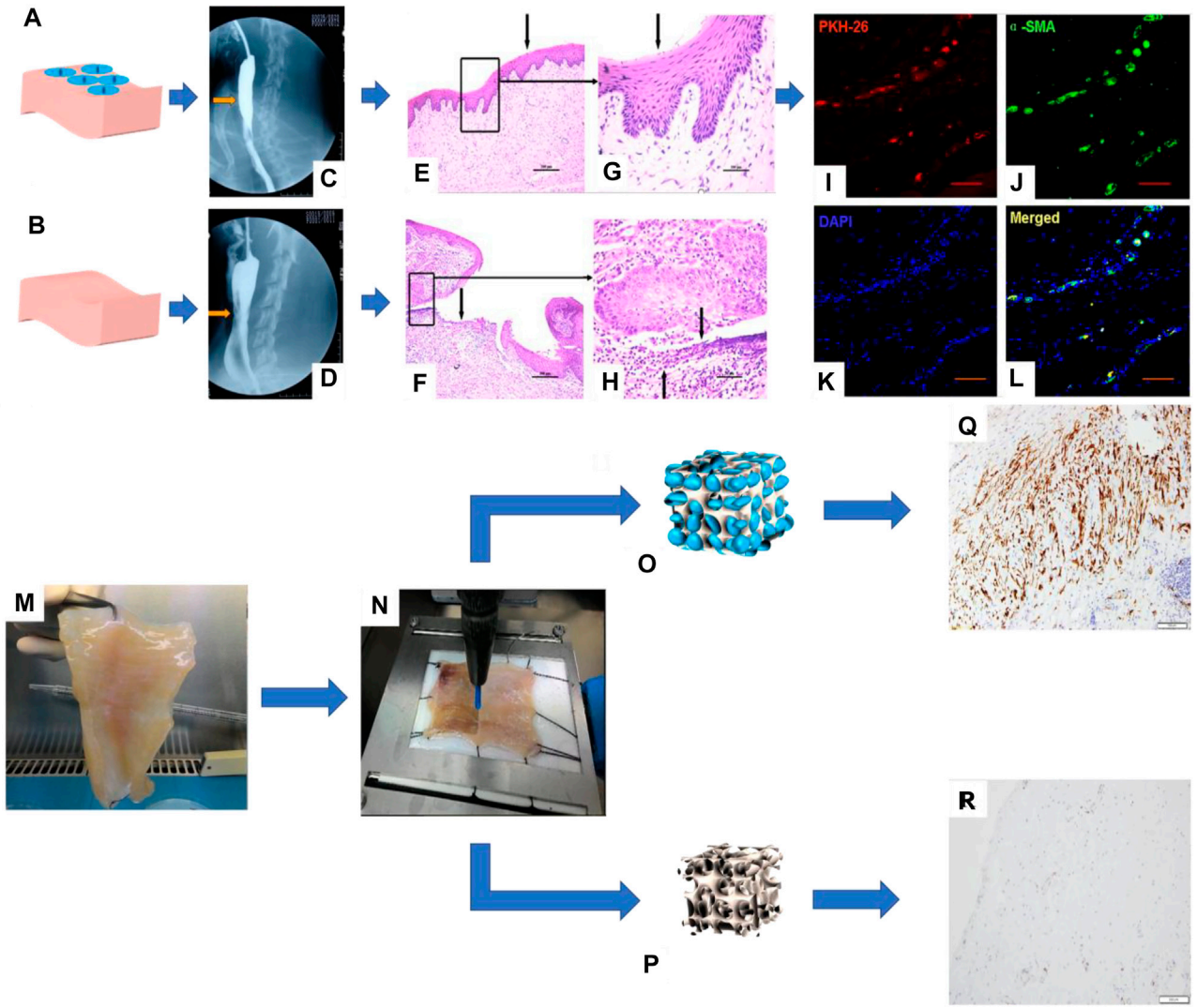


**FIGURE 2 |** I. Repair of a canine esophageal defect with SIS combined with MSCs. **(A)** SIS + MSCs. **(B)** Simple SIS. **(C, D)** Barium esophagus examination. **(E, F)** H&E staining of canine esophagus tissue and **(G, H)** its partial magnification. **(I–L)** Immunofluorescence staining to detect the expression of living cell marker proteins PKH-26 and $\alpha$-SMA in canine esophagus tissue (Tan et al., 2013). II. Esophageal muscular acellular matrix repairs porcine esophageal defects: **(K)** Porcine esophageal muscular acellular matrix. **(L)** Microscopic perforation treatment. **(M, N)** Schematic diagram of MSC growth in the acellular matrix scaffold. **(O, P)** Immunohistochemical staining to detect the expression of actin and desmin in porcine esophagus tissue (Marzaro et al., 2020).

esophageal muscle tissue to repair the esophagus *in situ* in pigs, which showed new muscle tissue compared with the decellularized esophageal muscle layer alone (Marzaro et al., 2020) (**Figure 2**). Aho et al. Using PU material, autologous adipose-derived mesenchymal stem cells were seeded to form a cell-span esophageal implant (CEI). After resection of the patient's esophageal cancer, *in situ* repair was performed using CEI and followed by esophagogastroduodenoscopy (EGD). After the patient's death, histological examination revealed esophageal luminal epithelialization and partial muscle regeneration 7.5 months after scaffold implantation (Aho et al., 2021) (**Figure 3**).

Therefore, single-layer bionic scaffold combined with stem cells to repair the mucosal layer or muscle layer is the current main research direction. On the basis of mucosal layer or muscle layer repair, higher clinical requirements for esophageal repair are proposed, such as full-thickness or circumferential defect, which requires simultaneous repair of the mucosal layer, submucosal layer, and muscle layer of the esophagus. Therefore, it is particularly important to design a multi-layer functional bionic scaffold.

## MULTI-LAYER ESOPHAGEAL SCAFFOLDS

### Construction Method of Scaffolds

Researchers have studied full-thickness or circumferential defects by designing lamellar or tubular bionic scaffolds. According to the

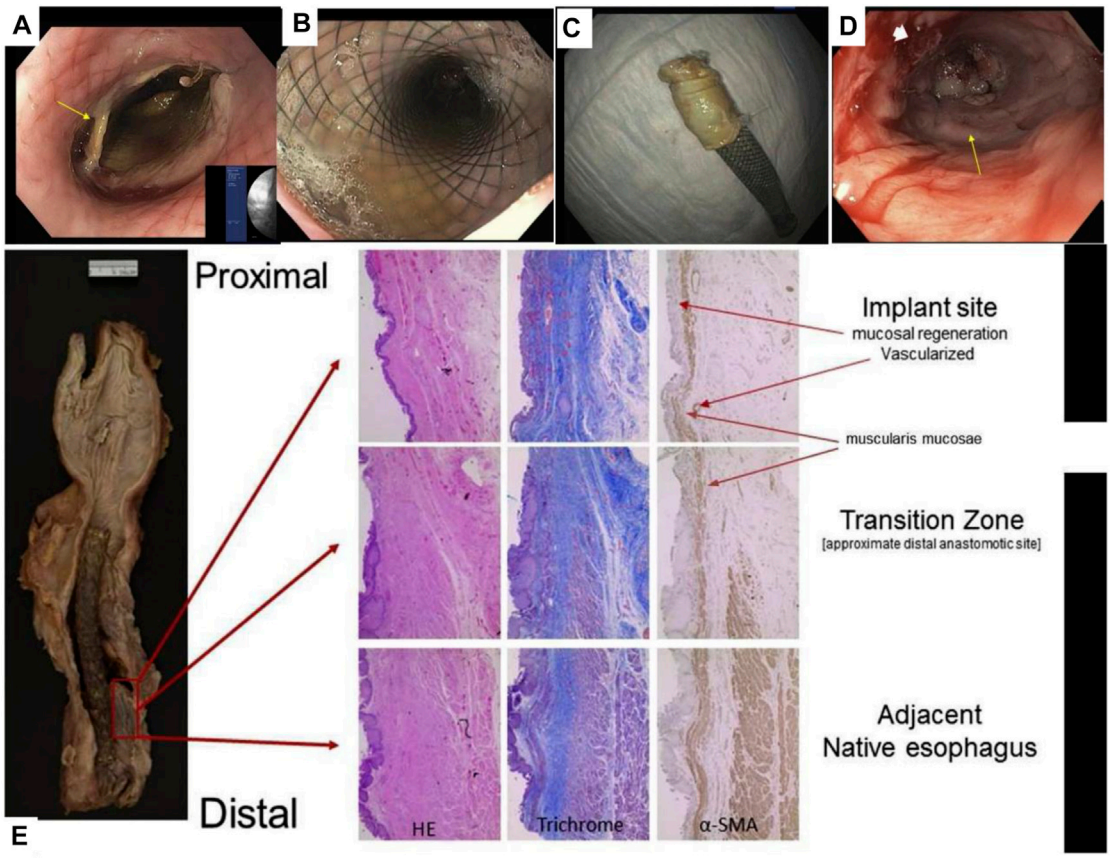


**FIGURE 3 |** PU combined with MSCs for reconstruction of the human esophagus. **(A)** EGD image of the esophagus after scaffold placement. **(B)** EGD image of the esophagus after scaffold deployment. **(C)** The removed CEI scaffold assembly is adhered to the scaffold. **(D)** EGD image of esophageal neoplastic tissue. **(E)** Histological examination of esophageal sections, including H&E staining, Masson staining, and immunohistochemical staining to detect the expression of α-SMA (Aho et al., 2021).

research methods, it is mainly divided into two categories: scaffolds and scaffolds/cells composite. The scaffolds were prepared by the one-step method or multi-step method. The one-step method is to mix the scaffold material into a whole through melting, electrostatic spinning, temperature-induced sedimentation, etc., and different components complement each other and work in synergy. For example, Tan et al. melted PCL/PLA and stretched it into a directional spinning tubular structure (Tan et al., 2016). The multi-step method is based on the perspective of esophageal structure bionics, combining different layers of scaffold materials through a certain link method. Joshua et al. prepared the silk fibroin double-layer scaffold by solution pouring (Gundogdu et al., 2021). Rossella et al. used electrospinning and temperature-induced sedimentation to construct two double-layer scaffolds (Pisani et al., 2020). Saverio et al. designed a PU electrospinning three-layer scaffold (inner and outer layer pore diameter>10 μm; middle layer <10 μm) (Soliman et al., 2019) (**Table 3**).

## Study on Scaffolds/Cells

Through the abovementioned research and analysis, it can be seen that the design of multi-layer scaffolds is the guiding ideology of bionics, but these scaffolds still cannot completely induce the structural growth of tissues. Therefore, researchers have constructed scaffolds with cells to enhance the repair function of tissue. Natural materials such as esophageal acellular matrix, SIS, and collagen scaffold are compounded with cells.

Guillaume et al. designed the esophageal mucosal acellular matrix/omentum double-layer scaffold, in which MSCs were cultured on the acellular matrix, and the omentum re-matured in pigs. As a result, it was found that 3 months after the esophageal replacement surgery, a new epithelium and muscle regeneration were visible (Levenson et al., 2021) (**Figure 4**). Paola et al. used the method of organoid culture to construct a multi-layer esophageal scaffold with cells *in vitro*. The researchers re-seeded ECs on the acellular matrix of the rat esophageal mucosa and allowed the cells to grow in the lumen of the acellular scaffold to construct the esophageal mucosal layer and co-cultured human or mouse fibroblasts and mouse neural crest cells *in vitro*. The muscle layer is constructed and then implanted into the rat omentum for *in vivo* culture to promote angiogenesis and build a multi-layer esophageal structure together with the mucosal layer. This kind of esophageal tissue composed of cells is more complete than the commonly used acellular matrix and other natural materials, but it needs to be verified

**TABLE 3 |** Classification according to the construction of bionic scaffolds.

| Author | References | Scaffolds | Formation method | Loading cell | Study | Biota | Outcomes |
|---|---|---|---|---|---|---|---|
| Joshua et al. | Gundogdu et al. (2021) | SF | Bilayer silk fibroin | — | Partial-thickness esophageal implantation | Pig | 0% mortality. Scaffold shifts, esophageal stenosis, and other complications were seen |
| Rossella et al. | Pisani et al. (2020) | PLA, PCL | Temperature-induced settlement double-layer scaffold, electrospinning double-layer scaffold | MSCs | *In vitro* | — | Scaffolds constructed in two ways are suitable for esophageal regeneration |
| Saverio et al. | Soliman et al. (2019) | PU | Three-layer bracket | MSCs, SMCs | *In vitro* | — | Cells can survive on three layers of scaffold and be separated by the middle layer |

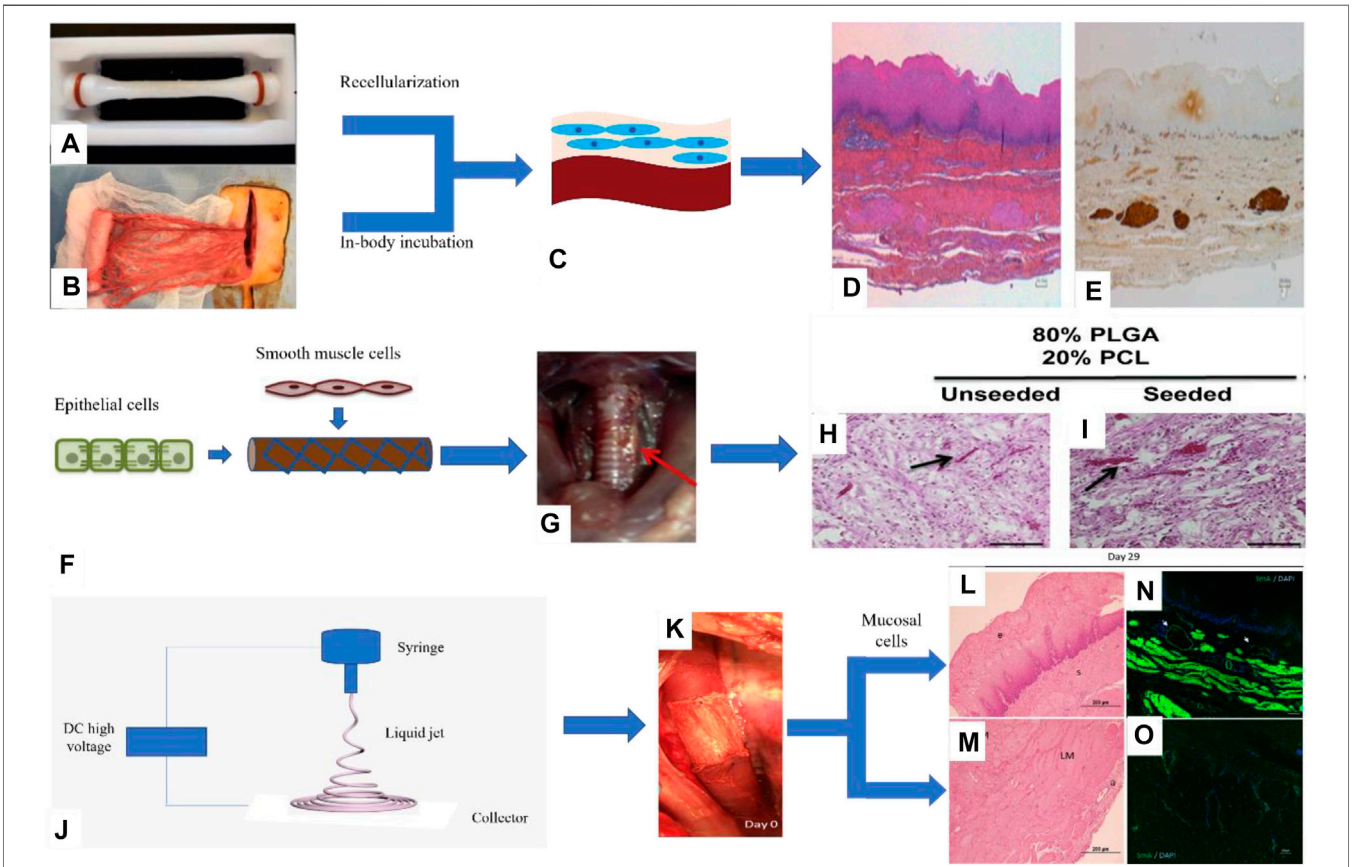


**FIGURE 4 |** Porcine esophageal acellular matrix and omentum construct a double-layer scaffold to repair esophageal defects. **(A)** Acellular matrix. **(B)** Decellularized matrix composite omentum. **(C)** Omentum maturation in pigs. **(D)** H&E staining of pig esophagus sections. **(E)** Immunohistochemical staining to detect the expression of desmin in porcine esophagus tissue (Levenson et al., 2021). II. The PLGA/PCL electrospinning scaffold was prepared by the one-step method combined with ECs and myocytes to repair esophageal defects: **(F)** Cells were cultured on the inner and outer surfaces of the scaffold. **(G)** The scaffold is a patch to repair esophageal injury in rats. **(H, I)** H&E staining of rat esophagus sections (Jensen et al., 2015). III. PU electrospun scaffolds combined with mucosal cells to construct composite scaffolds involved in porcine esophagus reconstruction: **(J)** Schematic diagram of electrospinning. **(K)** Composite scaffold for *in situ* replacement of the esophagus. **(L, M)** H&E staining of porcine esophagus sections. **(N, O)** Immunofluorescence staining was used to detect the expression of α-SMA in porcine esophagus tissue (Barron et al., 2018).

by animal experiments to prove its positive significance (Urbani et al., 2018) (**Figure 4**).

In addition to natural materials, synthetic polymer materials such as PLGA, PCL, and PU have also been studied in combination with cells. For example, Christine et al. prepared a PLGA/PCL electrospun tubular esophageal scaffold, the inner cavity of the scaffold was compounded with autologous ECs, and the outer side was compounded with autologous SMCs. The composite scaffolds containing cells were cultured in an *in vitro* bioreactor for a period of time and then implanted into the mouse

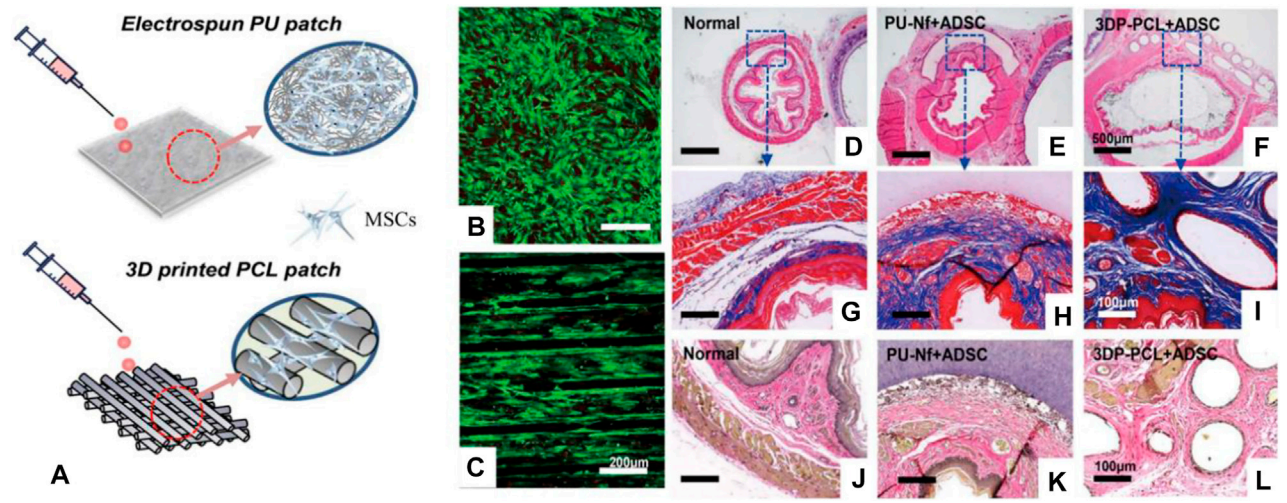


**FIGURE 5 |** 3D printed PCL scaffold and electrospun PU scaffold combined with MSCs to repair the esophageal defect. **(A)** Schematic diagram of the 3D printed PCL scaffold and electrospun PU scaffold. **(B,C)** The live/dead cell assay on the scaffold surface was studied. **(D–F)** H&E staining of rat esophagus sections. **(G–I)** Masson staining of rat esophagus sections. **(J–L)** Elastic fiber staining of rat esophagus sections (Park et al., 2021).

esophagus *in situ*, the esophagus is still viable after 2 weeks, and the cells maintain the phenotype (Jensen et al., 2015) (**Figure 4**). Dennis et al. combined porcine esophageal mucosal cells and electrospun PU scaffold into a tubular scaffold and implanted it into the whole-peripheral defect of the porcine esophagus, and the results showed that the mucosal layer, submucosa, and muscle layer of the esophagus regenerate simultaneously and have abundant blood vessels (Barron et al., 2018) (**Figure 4**).

Different from the traditional scaffolds, 3D printing scaffolds have many advantages, such as the flexibility of preparation methods, the customization of irregular tissue damage parts, and the ability to prepare scaffolds with very complex structures (Memic et al., 2017; Matai et al., 2020; Wan et al., 2020; Barros et al., 2021; Wu et al., 2021; Yang et al., 2021). The 3D printing scaffolds have been studied in esophageal repair. For example, Chung et al. used a 3D melt extrusion method to construct a polycaprolactone (PCL) 3D printing scaffold, seeded MSCs on the scaffold to participate in esophageal reconstruction, cells grew along the direction of the scaffold, and implanted it in the defect of the rat esophagus. The results show that the new tissue repaired by the 3D printing scaffold is similar to natural tissue and has obvious advantages compared with electrospun PU scaffolds (**Figure 5**) (Park et al., 2021). Although 3D printing scaffolds have many advantages, this method also has its own limitations, such as lack of diversity of bio-ink, harsh printing conditions (high temperature or UV curing), and expensive equipment for printing cells.

The mixed use of polymer synthetic materials and natural materials has gradually become the focus of research. For example, Jonathan et al. used electrospinning technology to make PLGA fiber layers on the SIS acellular matrix to form a double-layer esophageal scaffold, the results showed that human esophageal smooth muscle cell culture experiments and subcutaneous embedding presented good biocompatibility (Syed et al., 2019), but further research is needed for *in vivo* repair.

Our group's previous study used micro-pattern technology to construct a three-layer scaffold, which corresponds to the inner ring muscle (S1), outer longitudinal muscle (S2), and mucosal layer (S3) of the esophagus. After inoculating MSCs on the composite scaffold, it was implanted into the esophageal defect. The results showed that there was new esophageal tissue, including the muscle layer and mucosal layer. However, the PU material can still be found in the tissue 180 days after implantation, which may affect the speed of muscle regeneration (Wang X. et al., 2020) (**Figure 6**).

## PROBLEMS AND CHALLENGES

In conclusion, although studies on the repair of the full-thickness or circumferential defect of the esophagus have achieved many tentative results, the following key issues still need to be further developed and improved, in order to obtain a bionic scaffold that is closer to the natural esophageal structure and function, so as to be used in the clinical treatment of esophageal cancer patients as soon as possible and benefit mankind.

### Precision Bionics

At present, there are two main construction methods of esophageal scaffold, one-step construction and multi-step construction. The advantage of one-step construction is that it is relatively simple, only need one or more types of biomaterials are required, and generally, the binding force between the support layers is strong and stable. However, the disadvantage is that the material and function are relatively

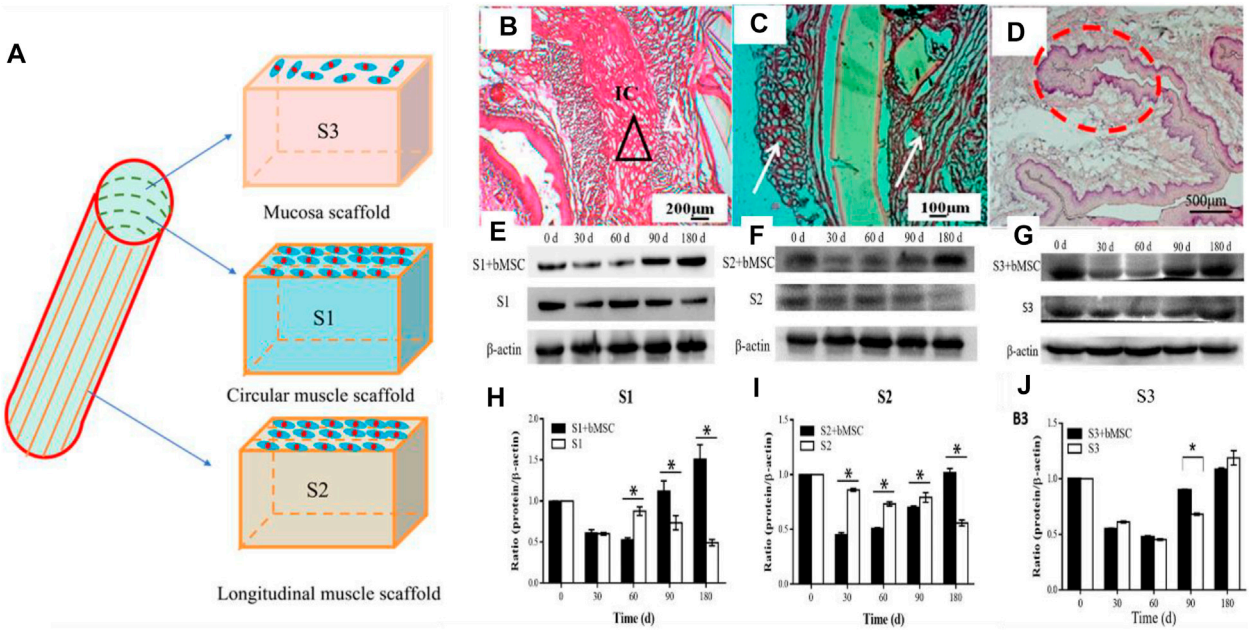


**FIGURE 6 |** Multi-layer esophageal scaffold combined with stem cells to repair esophageal defect in rabbits. **(A)** Schematic diagram of the three-layer scaffold; S1, S2, and S3, respectively, represent the inner ring muscle, outer longitudinal muscle, and mucosal layer of the esophagus. **(B–D)** H&E staining of rabbit esophagus sections at 180 days **(E–G)** Western blot evaluated the expression of α-SMA (S1, S2) and CK-14 (S3), respectively, in rabbit esophageal defect. **(H–J)** Quantitative calculation of (E–G) using ImageJ software ($n = 3$). *$p < 0.05$ (Wang X. et al., 2020).

single, so it is very difficult to accurately simulate the multi-layer structure of the esophagus and give specific functions to each layer of the scaffold. Since the multi-layer scaffold prepared by the multi-step construction method is flexible, it can provide different materials (natural materials, synthetic materials, or both) and cells (ECs, SMCs, or stem cells) for each layer of the scaffold, so as to more accurately mimic the structure and function of the esophagus. Therefore, it is the current development direction to prepare an accurate bionic multi-layer esophageal scaffold by multi-step construction.

## The Firmness Between Multi-Layer Esophageal Scaffolds

For multi-layer scaffolds prepared by multi-step construction, the firmness between the scaffolds is another key issue. If the adhesion between scaffolds is poor, the multi-layer scaffolds will fall off or shift, which will seriously affect the repair effect of the esophagus. The connection modes between the layers of multi-layer scaffolds include the solution casting method (Gundogdu et al., 2021), temperature-induced precipitation method (Dorati et al., 2017), solvent volatilization method of electrospinning (Chung et al., 2015), and glue bonding (Deng et al., 2019). The first three methods are not universally applicable because solutions or solvents may dissolve the active components such as protein, growth factor in the scaffold, and too high or low temperature is not conducive to the introduction of proteins and cells into the scaffold. Glue bonding does not affect the design of each layer of the scaffold, as long as the scaffold prepared separately is combined, which is a simple combination method with universal applicability. Generally, it is relatively easy for the glue to adhere to objects in a dry environment, but it remains a great challenge for repair in a wet environment (exudate or blood at the injury) or dynamic adhesion (human movement).

At present, the tissue glue used in the clinical treatment of esophageal anastomotic fistula is mainly cyanoacrylate (superglue, highly toxic, and rarely used) and fibrin glue (fibrin glue, frequently used, but with low adhesion ability) (Rao et al., 2018). The adhesion strength and adhesion energy of fibrin glue are about 10 kPa and 10 $Jm^{-2}$, respectively (Deng et al., 2019). As the esophagus is a soft tissue with peristalsis and swallowing functions, higher requirements are put forward for the glue used to bond the multi-layer esophageal scaffold (>>10 kPa and >>10 $Jm^{-2}$). New adhesives, such as nano-clay/multi-walled carbon nanotubes/isopropylacrylamide hydrogel (adhesive strength 7 kPa) (Deng et al., 2019), sodium p-styrene sulfonate/chloromethane quaternized dimethylaminoethyl acrylate hydrogel (adhesive strength 25 kPa, adhesive energy 50 $Jm^{-2}$) (Rao et al., 2018), chitosan/double-bonded phenylalanine hydrogel (adhesive strength 14 kPa) (Sharma et al., 2019), aldehyde functionalized hyaluronic acid/3,3′-dithiobis (propionyl hydrazide) hydrogel (adhesive strength 120 kPa) (Sigen et al., 2021), polyethylene glycol/lysozyme hydrogel (adhesive strength 32 kPa) (Tan et al., 2019), folic acid/polydimethyl diallyl ammonium chloride hydrogel (adhesive strength 150 kPa) (Gao et al., 2021), and hyaluronic acid/

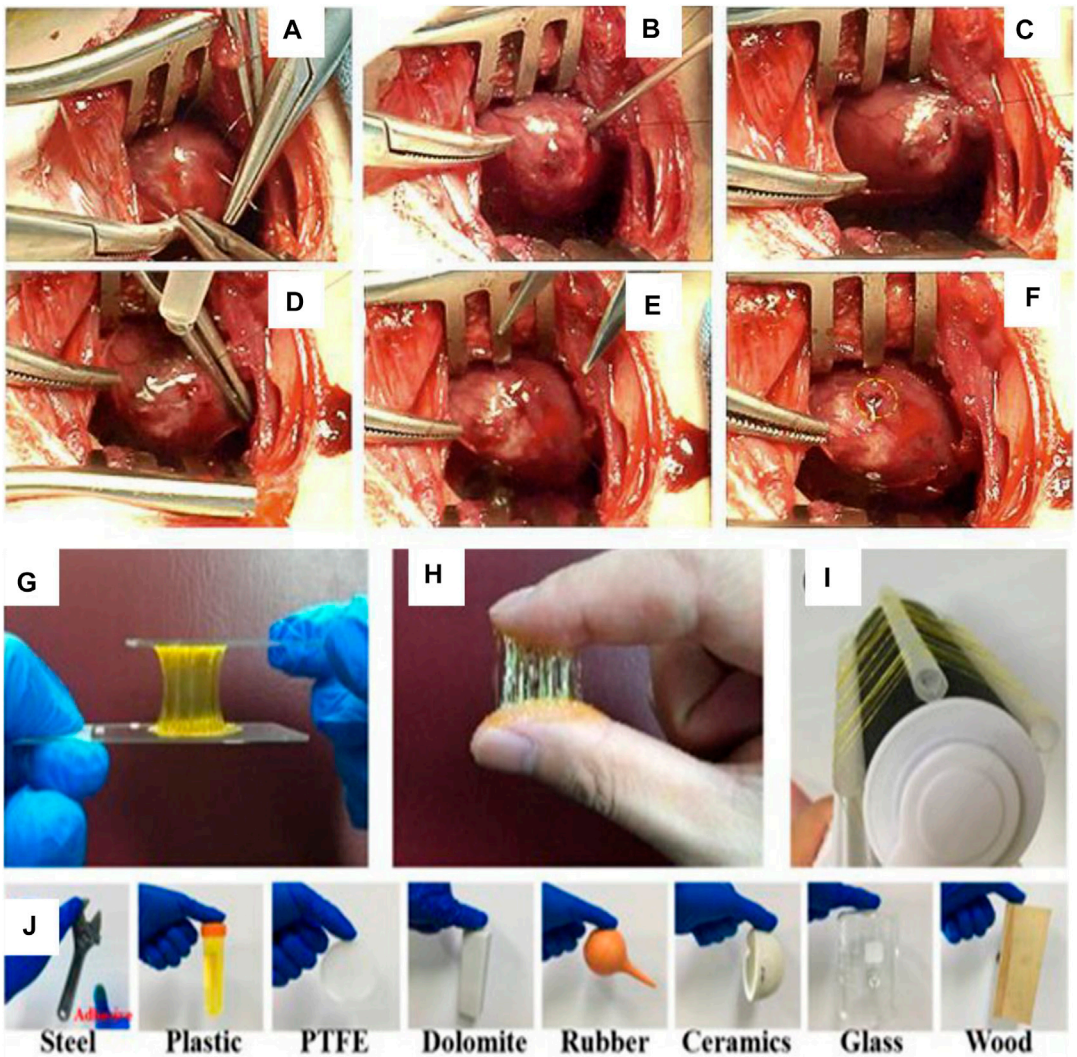


**FIGURE 7 |** Polyethylene glycol/lysozyme hydrogel adheres to the defect site of the left ventricular wall in rabbits. **(A–F)** Hydrogel participates in the process of sealing the left ventricular defect (Tan et al., 2019). II. Adhesion experiments of aldehyde-functionalized hyaluronic acid/3,3′-dithiobis (propionyl hydrazide) hydrogels. **(G,J)** Hydrogels adhered to various substrate surfaces (Sigen et al., 2021).

catechol/horseradish peroxidase hydrogels (17 kPa) (Wang D. et al., 2020) (**Figure 7**), are used. The hydrogels mentioned above can only meet one of the requirements of adhesion or cytocompatibility. Therefore, it is the research direction of adhesiveness of hydrogel to satisfy high adhesion and biocompatibility in a complex environment.

## CONCLUSION

Compared with traditional methods, esophageal tissue engineering technology has become a promising alternative method for the treatment of esophageal injury. The multi-layer complex structure of the esophagus should be considered in the repair of the full-thickness or circumferential defect of the esophagus, and how to obtain an ingenious design and retain the bionic structure and bionic function are the research direction. To solve these problems, the multi-step method is more favorable for the preparation of scaffolds; for example, glue bonding and 3D printing methods are two of the flexible styles to fabricate bionic scaffolds. It is believed that more and more perfect scaffolds will emerge in the near future and achieve more effective repair effects.

## AUTHOR CONTRIBUTIONS

RH conceived the initial idea and the conceptualization. RX drafted the manuscript. XF, SW, YW, YZ, LZ, LS, and QP participated in data collection. RH, JZ, XC, RZ, LY, and YZ revised the manuscript. All authors contributed to the article and approved the submitted version.

## FUNDING

This work was supported by the National Natural Science Foundation of China (No. 32000942), the Natural Science Foundation of Zhejiang (No. LY20C100001), the Natural Science Foundation of Ningbo (Nos. 2021J071 and 202003N4238), the Major Project of 2025 Sci and Tech Innovation of Ningbo (Nos. 2018B10052 and 2020Z096), the State Key Laboratory of Fluid Power and Mechatronic Systems (No. GZKF-202024), and the General scientific Research Project of Zhejiang Education Department (No. Y202044155).

## ACKNOWLEDGMENTS

The authors would like to thank the Core Facilities, Ningbo University School of Medicine, for the technical support.

## REFERENCES

A, S., Xu, Q., Johnson, M., Creagh-Flynn, J., Venet, M., Zhou, D., et al. (2021). An Injectable Multi-Responsive Hydrogel as Self-Healable and On-Demand Dissolution Tissue Adhesive. *Appl. Mater. Today* 22, 100967. doi:10.1016/j.apmt.2021.100967

Aho, J. M., La Francesca, S., Olson, S. D., Triolo, F., Bouchard, J., Mondano, L., et al. (2021). First-in-Human Segmental Esophageal Reconstruction Using a Bioengineered Mesenchymal Stromal Cell-Seeded Implant. *JTO Clin. Res. Rep.* 2 (9), 100216. doi:10.1016/j.jtocrr.2021.100216

Arakelian, L., Kanai, N., Dua, K., Durand, M., Cattan, P., and Ohki, T. (2018). Esophageal Tissue Engineering: from Bench to Bedside. *Ann. N.Y. Acad. Sci.* 1434 (1), 156–163. doi:10.1111/nyas.13951

Badylak, S., Meurling, S., Chen, M., Spievack, A., and Simmons-Byrd, A. (2000). Resorbable Bioscaffold for Esophageal Repair in a Dog Model. *J. Pediatr. Surg.* 35 (7), 1097–1103. doi:10.1053/jpsu.2000.7834

Barron, M. R., Blanco, E. W., Aho, J. M., Chakroff, J., Johnson, J., Cassivi, S. D., et al. (2018). Full-thickness Oesophageal Regeneration in Pig Using a Polyurethane Mucosal Cell Seeded Graft. *J. Tissue Eng. Regen. Med.* 12 (1), 175–185. doi:10.1002/term.2386

Barros, A. S., Costa, A., and Sarmento, B. (2021). Building Three-Dimensional Lung Models for Studying Pharmacokinetics of Inhaled Drugs. *Adv. Drug Deliv. Rev.* 170, 386–395. doi:10.1016/j.addr.2020.09.008

Blank, R. S., Collins, S. R., Huffmyer, J. L., and Jaeger, J. M. (2019). "Anesthesia for Esophageal Surgery," in *Principles and Practice of Anesthesia for Thoracic Surgery*. Editor P. Slinger (Cham: Springer International Publishing), 609–649. doi:10.1007/978-3-030-00859-8_38

Chaitin, H., Lu, M. L., Wallace, M. B., and Kang, Y. (2021). Development of a Decellularized Porcine Esophageal Matrix for Potential Applications in Cancer Modeling. *Cells* 10 (5), 1055. doi:10.3390/cells10051055

Chang, J., Tan, W., Ling, Z., Xi, R., Shao, M., Chen, M., et al. (2017). Genomic Analysis of Oesophageal Squamous-Cell Carcinoma Identifies Alcohol Drinking-Related Mutation Signature and Genomic Alterations. *Nat. Commun.* 8, 11. doi:10.1038/ncomms15290

Chen, W., Zheng, R., Baade, P. D., Zhang, S., Zeng, H., Bray, F., et al. (2016). Cancer Statistics in China, 2015. *CA: A Cancer J. Clinicians* 66 (2), 115–132. doi:10.3322/caac.21338

Chung, E.-J., Ju, H. W., Park, H. J., and Park, C. H. (2015). Three-layered Scaffolds for Artificial Esophagus Using Poly(ε-Caprolactone) Nanofibers and Silk Fibroin: An Experimental Study in a Rat Model. *J. Biomed. Mater. Res.* 103 (6), 2057–2065. doi:10.1002/jbm.a.35347

Deng, Z., Hu, T., Lei, Q., He, J., Ma, P. X., and Guo, B. (2019). Stimuli-Responsive Conductive Nanocomposite Hydrogels with High Stretchability, Self-Healing, Adhesiveness, and 3D Printability for Human Motion Sensing. *ACS Appl. Mater. Inter.* 11 (7), 6796–6808. doi:10.1021/acsami.8b20178

Dorati, R., De Trizio, A., Marconi, S., Ferrara, A., Auricchio, F., Genta, I., et al. (2017). Design of a Bioabsorbable Multilayered Patch for Esophagus Tissue Engineering. *Macromol. Biosci.* 17 (6), 1600426. doi:10.1002/mabi.201600426

Dua, K. S., Hogan, W. J., Aadam, A. A., and Gasparri, M. (2016). *In-vivo* Oesophageal Regeneration in a Human Being by Use of a Non-biological Scaffold and Extracellular Matrix. *The Lancet* 388 (10039), 55–61. doi:10.1016/s0140-6736(15)01036-3

Farhat, W., Chatelain, F., Marret, A., Faivre, L., Arakelian, L., Cattan, P., et al. (2021). Trends in 3D Bioprinting for Esophageal Tissue Repair and Reconstruction. *Biomaterials* 267, 120465. doi:10.1016/j.biomaterials.2020.120465

Gao, S., Wang, W., Wu, T., Jiang, S., Qi, J., Zhu, Z., et al. (2021). Folic Acid-Based Coacervate Leading to a Double-Sided Tape for Adhesion of Diverse Wet and Dry Substrates. *ACS Appl. Mater. Inter.* 13 (29), 34843–34850. doi:10.1021/acsami.1c06844

Gong, C., Hou, L., Zhu, Y., Lv, J., Liu, Y., and Luo, L. (2013). *In Vitro* Constitution of Esophageal Muscle Tissue with Endocyclic and Exolongitudinal Patterns. *ACS Appl. Mater. Inter.* 5 (14), 6549–6555. doi:10.1021/am401115z

Gundogdu, G., Morhardt, D., Cristofaro, V., Algarrahi, K., Yang, X., Costa, K., et al. (2021). Evaluation of Bilayer Silk Fibroin Grafts for Tubular Esophagoplasty in a Porcine Defect Model. *Tissue Eng. A* 27 (1-2), 103–116. doi:10.1089/ten.tea.2020.0061

Hou, L., Gong, C., and Zhu, Y. (2016). *In Vitro* construction and *In Vivo* Regeneration of Esophageal Bilamellar Muscle Tissue. *J. Biomater. Appl.* 30 (9), 1373–1384. doi:10.1177/0885328215627585

Hou, R., Wang, X., Wei, Q., Feng, P., Mou, X., Zhu, Y., et al. (2019). Biological Properties of a Bionic Scaffold for Esophageal Tissue Engineering Research. *Colloids Surf. B: Biointerfaces* 179, 208–217. doi:10.1016/j.colsurfb.2019.03.072

Huang, X., Zhou, X., Hu, Q., Sun, B., Deng, M., Qi, X., et al. (2018). Advances in Esophageal Cancer: A New Perspective on Pathogenesis Associated with Long Non-coding RNAs. *Cancer Lett.* 413, 94–101. doi:10.1016/j.canlet.2017.10.046

Jensen, T., Blanchette, A., Vadasz, S., Dave, A., Canfarotta, M., Sayej, W. N., et al. (2015). Biomimetic and Synthetic Esophageal Tissue Engineering. *Biomaterials* 57, 133–141. doi:10.1016/j.biomaterials.2015.04.004

Kuppan, P., Sethuraman, S., and Krishnan, U. M. (2016). Fabrication and Investigation of Nanofibrous Matrices as Esophageal Tissue Scaffolds Using Human Non-keratinized, Stratified, Squamous Epithelial Cells. *RSC Adv.* 6 (31), 26461–26473. doi:10.1039/c5ra24303c

Kuppan, P., Sethuraman, S., and Krishnan, U. M. (2017). *In Vitro* Co-culture of Epithelial Cells and Smooth Muscle Cells on Aligned Nanofibrous Scaffolds. *Mater. Sci. Eng. C* 81, 191–205. doi:10.1016/j.msec.2017.07.050

Levenson, G., Berger, A., Demma, J., Perrod, G., Domet, T., Arakelian, L., et al. (2022). Circumferential Esophageal Replacement by a Decellularized Esophageal Matrix in a Porcine Model. *Surgery* 171, 384–392. doi:10.1016/j.surg.2021.07.009

Luc, G., Charles, G., Gronnier, C., Cabau, M., Kalisky, C., Meulle, M., et al. (2018). Decellularized and Matured Esophageal Scaffold for Circumferential Esophagus Replacement: Proof of Concept in a Pig Model. *Biomaterials* 175, 1–18. doi:10.1016/j.biomaterials.2018.05.023

Lv, J., Chen, L., Zhu, Y., Hou, L., and Liu, Y. (2014). Promoting Epithelium Regeneration for Esophageal Tissue Engineering through Basement Membrane Reconstitution. *ACS Appl. Mater. Inter.* 6 (7), 4954–4964. doi:10.1021/am4059809

Marzaro, M., Algeri, M., Tomao, L., Tedesco, S., Caldaro, T., Balassone, V., et al. (2020). Successful Muscle Regeneration by a Homologous Microperforated Scaffold Seeded with Autologous Mesenchymal Stromal Cells in a Porcine Esophageal Substitution Model. *Therap Adv. Gastroenterol.* 13, 175628482092322. doi:10.1177/1756284820923220

Matai, I., Kaur, G., Seyedsalehi, A., McClinton, A., and Laurencin, C. T. (2020). Progress in 3D Bioprinting Technology for Tissue/organ Regenerative Engineering. *Biomaterials* 226, 119536. doi:10.1016/j.biomaterials.2019.119536

Memic, A., Navaei, A., Mirani, B., Cordova, J. A. V., Aldhahri, M., Dolatshahi-Pirouz, A., et al. (2017). Bioprinting Technologies for Disease Modeling. *Biotechnol. Lett.* 39 (9), 1279–1290. doi:10.1007/s10529-017-2360-z

Nieponice, A., Ciotola, F. F., Nachman, F., Jobe, B. A., Hoppo, T., Londono, R., et al. (2014). Patch Esophagoplasty: Esophageal Reconstruction Using Biologic Scaffolds. *Ann. Thorac. Surg.* 97 (1), 283–288. doi:10.1016/j.athoracsur.2013.08.011

Park, H., Kim, I. G., Wu, Y., Cho, H., Shin, J. W., Park, S. A., et al. (2021). Experimental Investigation of Esophageal Reconstruction with Electrospun Polyurethane Nanofiber and 3D Printing Polycaprolactone Scaffolds Using a Rat Model. *Head & Neck* 43 (3), 833–848. doi:10.1002/hed.26540

Peirlinck, M., Debusschere, N., Iannaccone, F., Siersema, P. D., Verhegghe, B., Segers, P., et al. (2018). An In Silico Biomechanical Analysis of the Stent-Esophagus Interaction. *Biomech. Model. Mechanobiol* 17 (1), 111–131. doi:10.1007/s10237-017-0948-9

Pennathur, A., Gibson, M. K., Jobe, B. A., and Luketich, J. D. (2013). Oesophageal Carcinoma. *The Lancet* 381 (9864), 400–412. doi:10.1016/s0140-6736(12)60643-6

Pisani, S., Croce, S., Chiesa, E., Dorati, R., Lenta, E., Genta, I., et al. (2020). Tissue Engineered Esophageal Patch by Mesenchymal Stromal Cells: Optimization of Electrospun Patch Engineering. *Ijms* 21 (5), 1764. doi:10.3390/ijms21051764

Rao, P., Sun, T. L., Chen, L., Takahashi, R., Shinohara, G., Guo, H., et al. (2018). Tough Hydrogels with Fast, Strong, and Reversible Underwater Adhesion Based on a Multiscale Design. *Adv. Mater.* 30 (32), 1801884. doi:10.1002/adma.201801884

Sharma, S., Kumar, R., Kumari, P., Kharwar, R. N., Yadav, A. K., and Saripella, S. (2019). Mechanically Magnified Chitosan-Based Hydrogel as Tissue Adhesive and Antimicrobial Candidate. *Int. J. Biol. Macromolecules* 125, 109–115. doi:10.1016/j.ijbiomac.2018.12.018

Soliman, S., Laurent, J., Kalenjian, L., Burnette, K., Hedberg, B., and La Francesca, S. (2019). A Multilayer Scaffold Design with Spatial Arrangement of Cells to Modulate Esophageal Tissue Growth. *J. Biomed. Mater. Res.* 107 (2), 324–331. doi:10.1002/jbm.b.34124

Syed, O., Kim, J.-H., Keskin-Erdogan, Z., Day, R. M., El-Fiqi, A., Kim, H.-W., et al. (2019). SIS/aligned Fibre Scaffold Designed to Meet Layered Oesophageal Tissue Complexity and Properties. *Acta Biomater.* 99, 181–195. doi:10.1016/j.actbio.2019.08.015

Tan, B., Wei, R.-Q., Tan, M.-Y., Luo, J.-C., Deng, L., Chen, X.-H., et al. (2013). Tissue Engineered Esophagus by Mesenchymal Stem Cell Seeding for Esophageal Repair in a Canine Model. *J. Surg. Res.* 182 (1), 40–48. doi:10.1016/j.jss.2012.07.054

Tan, H., Jin, D., Qu, X., Liu, H., Chen, X., Yin, M., et al. (2019). A PEG-Lysozyme Hydrogel Harvests Multiple Functions as a Fit-To-Shape Tissue Sealant for Internal-Use of Body. *Biomaterials* 192, 392–404. doi:10.1016/j.biomaterials.2018.10.047

Tan, Y. J., Yeong, W. Y., Tan, X., An, J., Chian, K. S., and Leong, K. F. (2016). Characterization, Mechanical Behavior and *In Vitro* Evaluation of a Melt-Drawn Scaffold for Esophageal Tissue Engineering. *J. Mech. Behav. Biomed. Mater.* 57, 246–259. doi:10.1016/j.jmbbm.2015.12.015

Uhlenhopp, D. J., Then, E. O., Sunkara, T., and Gaduputi, V. (2020). Epidemiology of Esophageal Cancer: Update in Global Trends, Etiology and Risk Factors. *Clin. J. Gastroenterol.* 13 (6), 1010–1021. doi:10.1007/s12328-020-01237-x

Urbani, L., Camilli, C., Phylactopoulos, D.-E., Crowley, C., Natarajan, D., Scottoni, F., et al. (2018). Multi-stage Bioengineering of a Layered Oesophagus with *In Vitro* Expanded Muscle and Epithelial Adult Progenitors. *Nat. Commun.* 9, 16. doi:10.1038/s41467-018-06385-w

Wan, Z., Zhang, P., Liu, Y., Lv, L., and Zhou, Y. (2020). Four-dimensional Bioprinting: Current Developments and Applications in Bone Tissue Engineering. *Acta Biomater.* 101, 26–42. doi:10.1016/j.actbio.2019.10.038

Wang, D., Xu, P., Wang, S., Li, W., and Liu, W. (2020a). Rapidly Curable Hyaluronic Acid-Catechol Hydrogels Inspired by Scallops as Tissue Adhesives for Hemostasis and Wound Healing. *Eur. Polym. J.* 134, 109763. doi:10.1016/j.eurpolymj.2020.109763

Wang, X., Jin, J., Hou, R., Zhou, M., Mou, X., Xu, K., et al. (2020b). Differentiation of bMSCs on Biocompatible, Biodegradable, and Biomimetic Scaffolds for Largely Defected Tissue Repair. *ACS Appl. Bio Mater.* 3 (1), 735–746. doi:10.1021/acsabm.9b01063

Wei, Q., Jin, J., Wang, X., Shen, Q., Zhou, M., Bu, S., et al. (2018). The Growth and Pluripotency of Mesenchymal Stem Cell on the Biodegradable Polyurethane Synthesized with Ferric Catalyst. *J. Biomater. Sci. Polym. Edition* 29 (10), 1095–1108. doi:10.1080/09205063.2018.1426424

Wu, Y., Kennedy, P., Bonazza, N., Yu, Y., Dhawan, A., and Ozbolat, I. (2021). Three-Dimensional Bioprinting of Articular Cartilage: A Systematic Review. *Cartilage* 12 (1), 76–92. doi:10.1177/1947603518809410

Yang, Y., Yang, G., Liu, X., Xu, Y., Zhao, S., Zhang, W., et al. (2021). Construction of Lung Tumor Model for Drug Screening Based on 3D Bio-Printing Technology. *J Biomater. Tissue Eng.* 11 (7), 1213–1226. doi:10.1166/jbt.2021.2706

Zhu, Y., Chan-Park, M. B., and Sin Chian, K. (2005). The Growth Improvement of Porcine Esophageal Smooth Muscle Cells on Collagen-Grafted Poly(DL-Lactide-Co-Glycolide) Membrane. *J. Biomed. Mater. Res.* 75B (1), 193–199. doi:10.1002/jbm.b.30305

Zhu, Y., Chian, K. S., Chan-Park, M. B., Mhaisalkar, P. S., and Ratner, B. D. (2006). Protein Bonding on Biodegradable Poly(L-Lactide-Co-Caprolactone) Membrane for Esophageal Tissue Engineering. *Biomaterials* 27 (1), 68–78. doi:10.1016/j.biomaterials.2005.05.069

Zhu, Y., Yang, K., Cheng, R., Xiang, Y., Yuan, T., Cheng, Y., et al. (2017). The Current Status of Biodegradable Stent to Treat Benign Luminal Disease. *Mater. Today* 20 (9), 516–529. doi:10.1016/j.mattod.2017.05.002

Zhuravleva, M., Gilazieva, Z., Grigoriev, T. E., Shepelev, A. D., Kh. Tenchurin, T., Kamyshinsky, R., et al. (2019). In Vitroassessment of Electrospun Polyamide-6 Scaffolds for Esophageal Tissue Engineering. *J. Biomed. Mater. Res.* 107 (2), 253–268. doi:10.1002/jbm.b.34116

**Conflict of Interest:** The authors declare that the research was conducted in the absence of any commercial or financial relationships that could be construed as a potential conflict of interest.

**Publisher's Note:** All claims expressed in this article are solely those of the authors and do not necessarily represent those of their affiliated organizations, or those of the publisher, the editors, and the reviewers. Any product that may be evaluated in this article, or claim that may be made by its manufacturer, is not guaranteed or endorsed by the publisher.

frontiers in Bioengineering and Biotechnology

ORIGINAL RESEARCH
published: 02 March 2022
doi: 10.3389/fbioe.2022.855022

# Multifunctional Baicalin-Modified Contact Lens for Preventing Infection, Regulating the Ocular Surface Microenvironment and Promoting Corneal Repair

*Yue Luo[1,2†], Luying Liu[3†], Yuzhen Liao[3], Ping Yang[3], Xiaoqi Liu[1], Lei Lu[4], Jiang Chen[5*] and Chao Qu[1,2*]*

[1]Sichuan Provincial Key Laboratory for Human Disease Gene Study, The Department of Medical Genetics, The Institute of Laboratory Medicine, Sichuan Academy of Medical Sciences and Sichuan Provincial People's Hospital, University of Electronic Science and Technology, Chengdu, China, [2]The Department of Ophthalmology, Sichuan Provincial People's Hospital, University of Electronic Science and Technology of China, Chengdu, China, [3]Institute of Biomaterials and Surface Engineering Key Lab. for Advanced Technologies of Materials, Ministry of Education, Southwest Jiaotong University, Chengdu, China, [4]School and Hospital of Stomatology, Wenzhou Medical University, Wenzhou, China, [5]The Department of Neurosurgery, Sichuan Academy of Medical Science and Sichuan Provincial People's Hospital, Chengdu, China

OPEN ACCESS

**Edited by:**
Guicai Li,
Nantong University, China

**Reviewed by:**
Tao Huang,
The University of Melbourne, Australia
Liu Hengquan,
Chengdu University of Technology, China

***Correspondence:**
Jiang Chen
283876533@qq.com
Chao Qu
lucyjeffersonqu@hotmail.com

[†]These authors have contributed equally to this work

**Specialty section:**
This article was submitted to Biomaterials, a section of the journal Frontiers in Bioengineering and Biotechnology

**Received:** 14 January 2022
**Accepted:** 26 January 2022
**Published:** 02 March 2022

**Citation:**
Luo Y, Liu L, Liao Y, Yang P, Liu X, Lu L, Chen J and Qu C (2022) Multifunctional Baicalin-Modified Contact Lens for Preventing Infection, Regulating the Ocular Surface Microenvironment and Promoting Corneal Repair. Front. Bioeng. Biotechnol. 10:855022. doi: 10.3389/fbioe.2022.855022

Corneal injury inevitably leads to disruption of the ocular surface microenvironment, which is closely associated with delayed epithelial cell repair and the development of infection. Recently, drug-loaded therapeutic contact lenses have emerged as a new approach to treating corneal injury due to their advantages of relieving pain, promoting corneal repair, and preventing infection. However, few therapeutic contact lenses could modulate the ocular surface's inflammation and oxidative stress microenvironment. To address this, in this study, we covalently immobilized multifunctional baicalin (BCL), a flavon molecular with anti-inflammatory, anti-oxidative stress, and antibacterial capabilities, onto the surface of the contact lens. The BCL-modified contact lens showed excellent optical properties, powerful antibacterial properties, and non-toxicity to endothelial cells. Furthermore, the BCL-modified contact lens could significantly modulate the ocular surface microenvironment, including inhibition of macrophage aggregation and resistance to epithelium damage caused by oxidative stress. In animal models, BCL-modified corneal contact lens effectively promoted corneal epithelial cells repair. These excellent properties suggested that multifunctional BCL molecules had great application potential in the surface engineering of ophthalmic medical materials.

**Keywords: baicalin, contact lens, surface modification, ocular surface microenvironment, repair injury**

## INTRODUCTION

Ocular surface diseases caused by corneal injury afflict more than 23 million people worldwide (Stern et al., 2018), and are among the most common eye diseases worldwide. Generally, corneal tissue can self-healing through epithelial cell migration and proliferation when the injury is not severe (Luo et al., 2021). However, when the ocular surface has intense inflammation or oxidative stress caused by extensive epithelial damage, dry eye disease, diabetic keratopathy, etc., the self-healing of the corneal

epithelial becomes difficult (Ziaei et al., 2018). This difficult-to-heal epithelial injury makes the cornea susceptible to microbial infection, which can lead to corneal ulceration, corneal perforation, and even corneal blindness (Ljubimov and Saghizadeh, 2015). Therefore, preventing microbial infection and improving the ocular surface inflammatory and oxidative stress microenvironment are critical in treating corneal injuries.

Therapeutic contact lenses have become popular in treating corneal injury in clinical practice (Zidan et al., 2018) for their functions of moisturizing, relieving pain, promoting corneal epithelial repair, and reducing corneal stroma exposure (Nosrati et al., 2020). The non-drug-loaded contact lenses, namely corneal bandage lenses, were mainly used in clinical practice to treat bullous keratitis, exposure keratitis, neurotrophic keratitis, dry eye disease with epithelial lesions, trichiasis, corneal refractive surgery, and other non-infectious corneal diseases (Zidan et al., 2018). The main disadvantage of the bandage lenses was susceptibility to infection. In recent years, a new generation of drug-loaded contact lenses with infection resistance had emerged (Huang et al., 2016; Wei et al., 2019; Liu et al., 2020; Yin et al., 2021). These contact lenses could sustainably release drugs on the ocular surface, which solves the shortcomings of low drug bioavailability and poor patient compliance in traditional eye drop treatments (Jumelle et al., 2020; Lim and Lim, 2020). However, contact lenses with a microenvironment regulating ocular surface inflammation and oxidative stress are still rarely reported.

Baicalin (BCL) is a natural extract of plant origin. Due to its unique flavonoid polyphenol structure, BCL has a variety of pharmacological activities such as antibacterial, anti-inflammatory, and antioxidant properties (Zhao et al., 2016). Therefore, BCL has been extensively studied in cardiovascular (Yu et al., 2019; Xu et al., 2020), neurology (Guo et al., 2019; Li et al., 2020), and orthopedic fields (Zhao et al., 2016; Pan et al., 2019). In ophthalmology, BCL had therapeutic effects on autoimmune uveitis (Zhu et al., 2018), age-related macular degeneration (Sun et al., 2020), diabetic retinopathy (Pan et al., 2021), etc. However, at present, there is almost a gap in the application of BCL in ophthalmic materials. Therefore, we envision that modification of BCL on the surface of contact lenses could promote corneal damage repair by preventing infection and regulating the ocular surface's inflammatory and oxidative stress microenvironment. In recent years, mussel-inspired polydopamine (PDA) coating has become a star coating for medical materials' surface engineering because they can easily cover almost any material. Moreover, PDA coating has good biosafety and provides many secondary reactive active sites. Recently, PDA coatings have been used to modify contact lenses and exhibited good ocular surface biocompatibility (Liu et al., 2018).

In this study, we first prepared an amino-rich polydopamine-hexane diamine (PDA-HD) coating on the surface of the contact lens. Then, BCL was covalently immobilized on the PDA-HD layer by the amidation reaction. Then, we systematically studied the BCL-modified contact lens's optical properties and surface chemistry. After that, we systematically evaluated the epithelial cell safety, anti-oxidative stress capacity, anti-inflammatory properties, and anti-microbial activity of the BCL-modified contact lens. Finally, the ability of this contact lens to promote corneal injury repair was evaluated using a rabbit animal model. Our results indicated that the BCL-modified contact lens had the potential to prevent infection, regulate the ocular surface microenvironment, and promote corneal injury repair.

# MATERIALS AND METHODS

## Materials

Neifilcon A contact lenses (Alcon®) were purchased from CIBA Vision Corporation (Georgia, United States). Baicalin (BCL) and Hexamethylene diamine (HD) were obtained from Shanghai Aladdin Co. Ltd. (Shanghai, China). Dopamine hydrochloride (DA) and Rhodamine B were bought from Sigma-Aldrich Co. Ltd., (Shanghai, China). Dimethylformamide (DMF) was purchased from Chengdu Kelong Chemical Co., Ltd. (Chengdu, China) N-Hydroxysuccinamide (NHS) was supplied by Rhawn Co. Ltd. (China). 1-(3-Dimethylaminopropyl)-3-ethylcarbodiimide hydrochloride (EDC) was obtained from TCI Shanghai Co. Ltd. (Shanghai, China). MicroBCA kit was purchased from Pierce Biotechnology Inc. (Rockford, United States). $H_2O_2$ was supplied by Nanjing KeyGEN BioTECH Co., Ltd. (Nanjing, China).

MH broth was bought from HopeBio Co. Ltd. (Qingdao, China). Blood agar plates and DensiCHEK Plus were obtained from bioMerieux Co. Ltd. (France). Paraformaldehyde was purchased from Wuhan Servicebio Co., Ltd. (Wuhan, China).

*Staphylococcus aureus (S. aureus)* and *Pseudomonas aeruginosa* (*P. aeruginosa*) were obtained from Sichuan Provincial People's Hospital (Chengdu, China). Human corneal epithelial cells (HCECs) were supplied by BNCC Co. Ltd. (China). Mice macrophages were obtained from Guge Co. Ltd. (Wuhan, China). Japanese white rabbits (3 kg) were sourced from Chengdu Dashuo Laboratory Animal Co., Ltd. (Chengdu, China).

## Preparation of the BCL-Modified Contact Lens

The preparation process of the contact lens is shown in **Figure 1A**. The PDA-HD coating was deposited by immersing the corneal contact lens in dopamine-hexanediamine solution (DA: 1 mg/ml, Tris buffer; HD: 2.5 mg/ml; pH = 8.0, 20°C) for 24 h. After sufficient washing using distilled water, the monolayer modified PDA-HD coating of the corneal contact lens was PDA-HD.

Meanwhile, distilled water was mixed with dimethylformamide in a 1:1 volume for preparing three concentrations of BCL solutions. The concentrations of BCL were 1, 2, and 3 mg/ml, respectively. A mixture of 15.52 mg/ml EDC and 5.14 mg/ml NHS was prepared, and the BCL solutions of each concentration were activated for 15 min in a ratio of 1:10. The prepared PDA-HD-coated corneal contact lenses were immersed in the BCL solution at 20°C for 24 h. After sufficient washing with distilled water, corneal contact

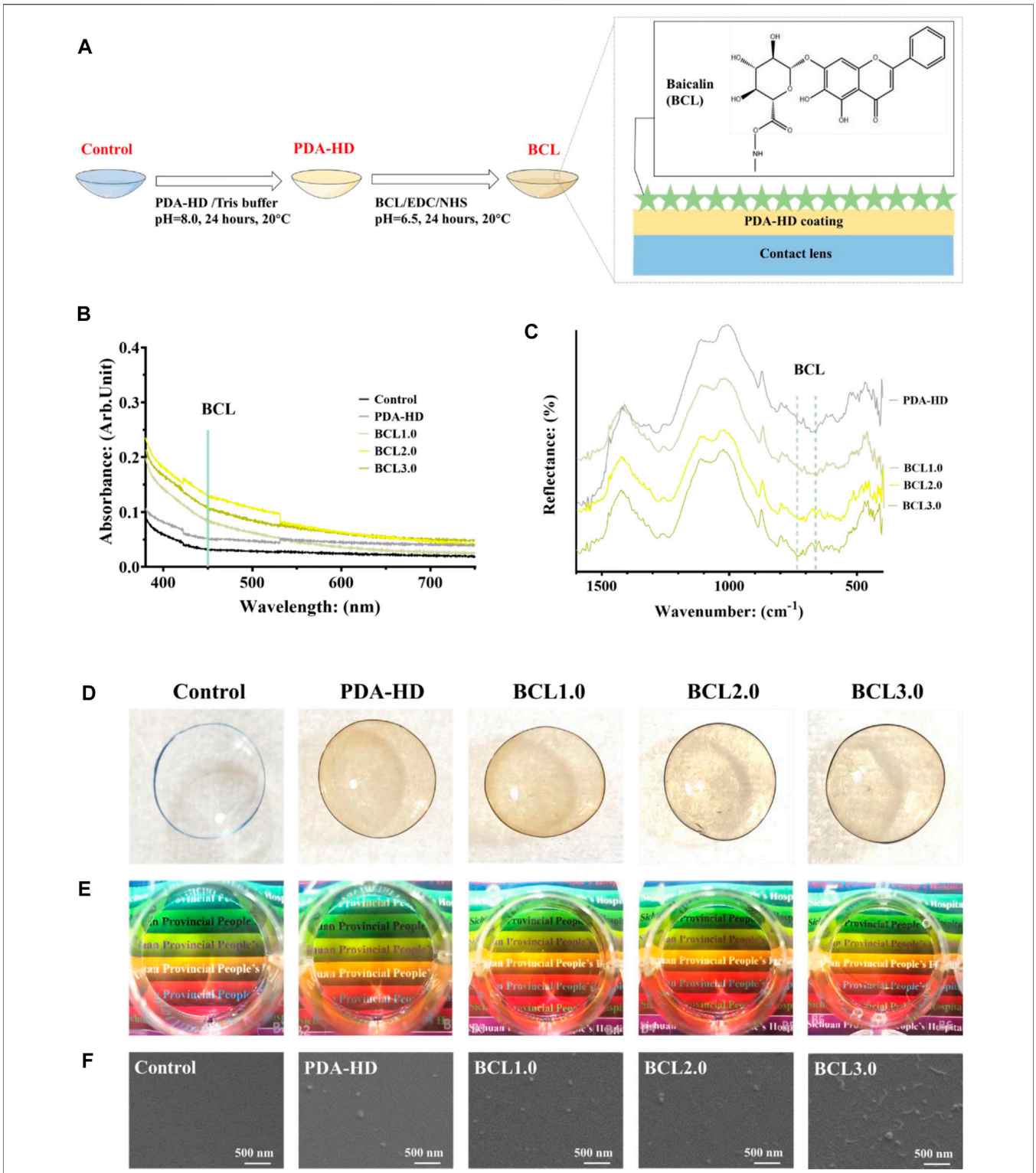


**FIGURE 1 | (A)** The preparation process of BCL-modified contact lens. **(B)** UV-vis measurements of contact lenses for Control, PDA-HD, BCL1.0, BCL2.0, and BCL3.0. **(C)** FTIR measurements of contact lenses. **(D,E)** Photographs of contact lenses. **(F)** SEM images of contact lens surfaces. The untreated contact lens was used as Control.

lenses modified with different concentrations of BCL were obtained as BCL1.0, BCL2.0, and BCL3.0, respectively.

## Characterization of the BCL-Modified Contact Lens

The surface morphology of the contact lens was characterized by scanning electron microscopy (SEM; Quanta 200, FEI, Netherlands). The optical properties of the contact lens were analyzed by a UV-visible spectrophotometer (UV-Vis; TU-1901, Persee, China). The surface structure of the contact lenses was analyzed by a Fourier transform infrared spectroscopy (NICOLET5700FT-IP, Thermoelectric co., ltd., United States). The contact lens's surface amino and phenolic hydroxyl contents were quantified by the acid orange method and MicroBCA kit, respectively. The hydrophilicity of the contact lens was detected by a drop shape analysis system (DSA 100, Krüss, Germany) in a static manner. X-ray photoelectron spectroscopy (XPS) was performed using the XSAM800 device (Kratos Ltd., United Kingdom) to detect the surface elements of the contact lens.

## Inflammatory Properties Test *in vitro*

Peritoneal macrophages from Sprague Dawley rats were cultured on samples at a cell concentration of $6 \times 10^4$/mL to test the inflammatory properties of contact lenses. After incubation at 37°C for 24 h, the culture medium was discarded, and the contact lenses were washed three times with saline and fixed for 24 h by adding 4% paraformaldehyde. Rhodamine stain was added to the surface of the contact lens, stained for 15 min for observation with an inverted fluorescence microscope, and cell adhesion density was calculated.

## Corneal Epithelial Cells Growth and $H_2O_2$ Damage

Human corneal epithelial cells (HCECs) were used for *in vitro* testing to verify their biocompatibility and resistance to oxidative stress.

The contact lenses without surface modification and the prepared contact lenses were cleaned and sterilized and then placed into a 24-well cell culture plate, cultured with HCECs for 12 h. After that, 100 μM $H_2O_2$ was added to each well for 12 h, and the medium was discarded. Then the contact lenses were thoroughly washed three times with physiological saline. The cells were stained with acridine orange/propidium iodide (AO-PI), incubated at 37°C for 3 min, and then observed with an inverted fluorescence microscope, and the cell survival rate was calculated.

## Evaluation of the Antibacterial Ability

*S. aureus* and *P. aeruginosa* were collected from the corneas of patients. Each species of bacteria was inoculated onto blood agar plates and incubated in a 37°C incubator. After the appearance of many colonies, they were eluted with saline and quantified with DensiCHEK Plus at $1 \times 10^8$ CFU/mL. And 10 μL of bacterial broth was added into 0.99 ml of MH broth to each well of a 24-well plate. The final concentration of *S. aureus* and *P. aeruginosa* in each well was $3 \times 10^6$ CFU/mL. The contact lenses were added to the above bacterial broth and incubated at 37°C for 24 h. Then the bacterial broth was discarded, and the contact lenses were washed three times with physiological saline and fixed with 4% paraformaldehyde for 24 h. A rhodamine stain was added to the contact lenses, stained for 15 min, and observed with an inverted fluorescence microscope. Bacterial adhesion on the surface of the corneal contact lens was observed by scanning electron microscopy (SEM) and fluorescence microscope. The ratio of bacterial adhesion area was calculated by ImageJ (National Institutes of Health, United States). The number of parallel samples tested was 3.

## *In vivo* Test of Wearing BCL-Modified Contact Lens

All animal experiments were approved by the Medical Ethics Committee of the Affiliated Hospital of University of Electronic Science and Technology & Sichuan Provincial People's Hospital. Japanese large-eared white rabbits (3 Kg) were obtained from Chengdu Dashuo Laboratory Animal Co. All animals were acclimated for 1 week. The rabbit corneal injury model was first established. Preoperatively, the whole layer of the epithelium was damaged with a cotton swab dipped in medical alcohol. After staying for a few seconds, the damaged corneal epithelium was scraped off with the back of a scraper blade, and the scraped epithelium continued to be cleaned with a moistened cotton swab. The selected BCL-modified (BCL2.0) contact lens was worn randomly to the left or right eye of the rabbit, and then the regular contact lens was worn on the opposite side as a control. Corneal epithelial healing was observed after 1 day of wearing the contact lens. After 1 day of wearing contact lenses, corneal samples were collected from rabbits for H&E staining and corneal morphology analysis.

## Data Statistics

All the above experiments were performed in triplicate ($n = 3$), and one-sided ANOVA was performed on all experimental results using GraphPad 8.0.2, with $p < 0.05$ being a statistically significant difference.

# RESULTS AND DISCUSSIONS

## Characterization of BCL-Modified Contact Lens

**Figure 1A** showed the preparation process of multifunctional BCL-modified contact lenses. As shown in **Figure 1B**, the UV-vis results showed a gentle shoulder peak at 450 nm for the BCL-modified samples emerged, implying the successful modification of BCL. In addition, the BCL-modified contact lens had a stronger absorption in the UV band than the Control, which implied that the BCL-modified contact lens had a stronger UV resistance, which had positive implications for the rehabilitation of eye diseases. **Figure 1C** showed FTIR measurements of contact lenses, and two BCL-specific absorption peaks could be observed around wavenumbers 660 and 740 $cm^{-1}$.

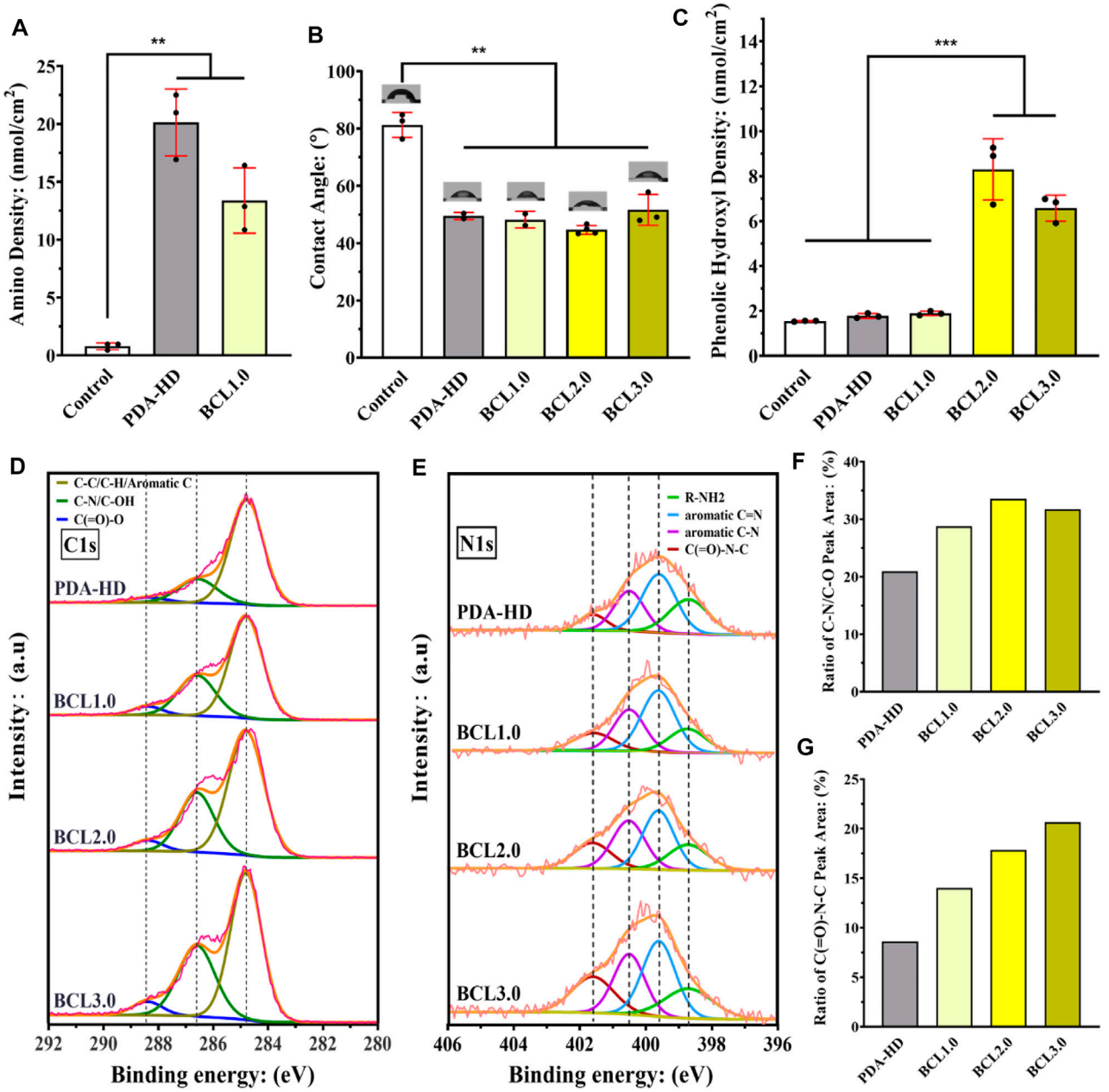


**FIGURE 2 | (A)** Amino density of contact lenses surface. **(B)** Water contact angle measurement on the contact lenses surface. **(C)** Phenolic hydroxyl density on the contact lenses surface. The close view of C1s peak **(D)** and N1s peak **(E)** on the surface of the contact lenses were detected using XPS, and the C-N/C-OH peak area in the C1s peak **(F)** and the C (=O)-N-C peak area in the N1s peak **(G)** were counted. The untreated contact lenses were used as Control. Data are presented as the mean ± SD of $n = 3$ and were analyzed using one–way ANOVA, $^{***}p < 0.001$.

As shown in **Figure 1D**, the colors of PDA-HD, BCL1.0, BCL2.0, and BCL3.0 turned slightly yellow compared to the Control. As shown in **Figure 1E**, when viewing the colored words through the contact lenses with surface deposited PDA-HD and different contents of BCL, on the one hand, the words were clear, which indicated good transparency of the contact lenses and could meet the daily visual needs. At the same time, the color of the colored backing of the words was easily distinguishable, which indicated that the wear of the contact lenses did not interfere with daily use, such as the discrimination of traffic lights. The above study illustrated that the multifunctional BCL-modified contact lens had an excellent optical performance.

**Figure 1F** showed SEM photos of several sets of contact lenses. The surfaces of PDA-HD, BCL1.0, and BCL2.0 were relatively smooth, and there were distributed nanoparticles, which might be the circular particles of PDA-HD formed during deposition (Lee et al., 2007). In the BCL3.0 sample, strip-shaped particles longer than 300 nm appeared on the surface, which might be caused by the high

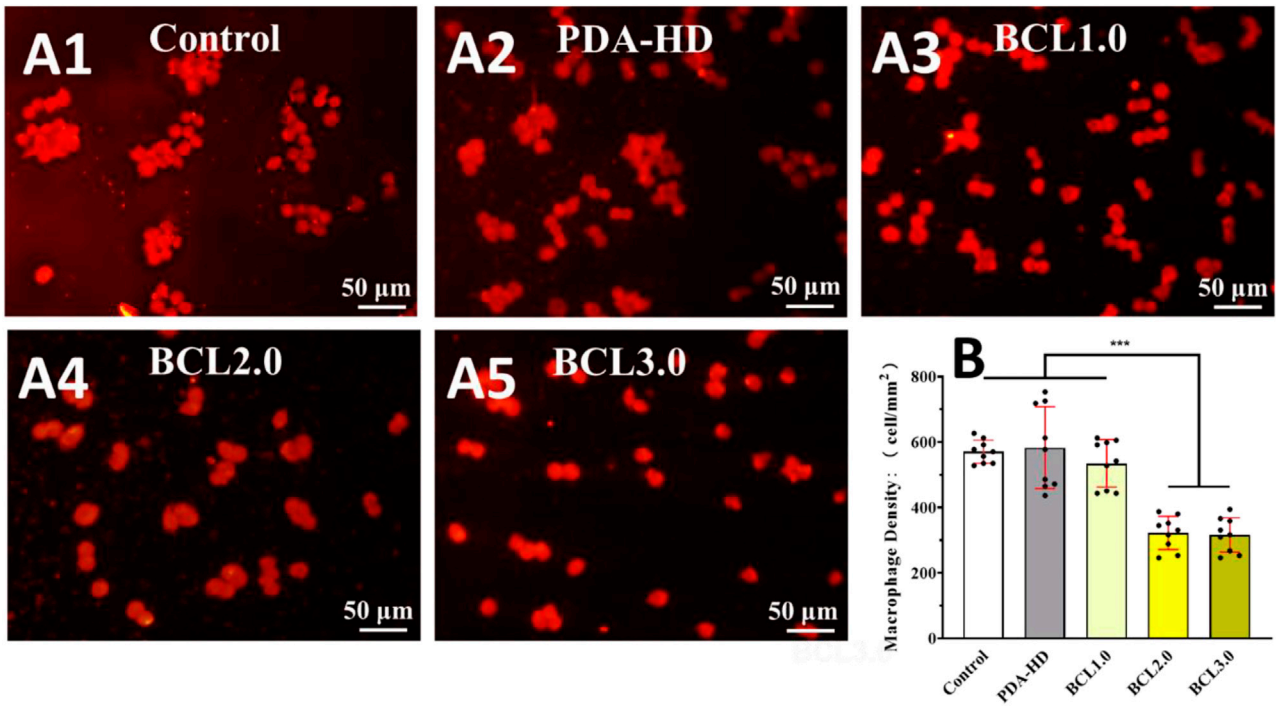


**FIGURE 3 |** Fluorescent staining of the contact lens surface for macrophage adhesion was photographed **(A1–A5)** and counted **(B)**. The untreated contact lenses were used as Control. Data are presented as the mean ± SD of $n = 3$ and were analyzed using one–way ANOVA, $^{***}p < 0.001$.

concentration of BCL solution during the sample preparation and the deposition of BCL agglomerates on the sample surface.

As shown in the results of the amino group quantification experiment in **Figure 2A**, there was almost no active amino group on the surface of the Control (the amino group density was about 0.79 nmol/cm$^2$). In contrast, after deposition of PDA-HD, the amino density on the sample surface increased to 20.13 nmol/cm$^2$, indicating a large number of amino groups on the contact lens surface after deposition of PDA-HD. Further, after grafting BCL on PDA-HD, the amino group on the BCL1.0 decreased to 13.38 nmol/cm$^2$, which implies that portion of the amino group of the PDA-HD coating was chemically bound to the carboxyl group of BCL, allowing covalently immobilized BCL. **Figure 2B** showed the results of the water contact angle measurements of contact lenses. The water contact angle of the Control was about 81.3°, which indicated that the silicone hydrogel corneal contact lens was hydrophobic and might have poor comfort during actual wear. However, in the PDA-HD, BCL1.0, BCL2.0, and BCL3.0, the water contact angle decreased to 49.5°, 48.3°, 44.7°, and 51.6°, respectively, indicating that the PDA-HD coating improved the hydrophilicity of the contact lens (Ho and Ding, 2014), which might be beneficial to the comfort of contact lens wear.

**Figure 2C** showed the results of phenolic hydroxyl quantification experiments. The phenolic hydroxyl density of the Control, PDA-HD, BCL1.0, BCL2.0, and BCL3.0 was 1.55, 1.78, 1.89, 8.3, and 5.03 nmol/cm$^2$, respectively. BCL2.0 had the most phenolic hydroxyl content among all BCL-modified samples, while the number of phenolic hydroxyl groups on BCL3.0 was rather inferior to that on BCL2.0. This might be due to the poor dissolution of the BCL solution used to prepare BCL3.0.

We analyzed the chemical state of the contact lenses surface using XPS. As shown in **Figure 2D**, the results of C1s peak detection showed that the peak at 285.6 eV (belonging to C-N or C-OH groups) increased when grafted with BCL, which implied an increase in hydroxyl content. **Figure 2F** showed that the area ratio of the peak of PDA-HD, BCL1.0, BCL2.0, and BCL3.0 at 285.6 eV was 20.95, 28.76, 33.59, and 31.73%, respectively. BCL2.0 had the highest elemental area ratio among all samples, which implied the most BCL molecules were modified on BCL2.0, which is consistent with the results of phenolic hydroxyl quantification experiments.

As shown in **Figure 2E**, the results of N1s high-resolution spectrum showed that the peak appearing at 401.5 eV represents C (=O)-N-C. The signal of this peak was significantly enhanced when the BCL was modified, suggesting the formation of the amide bond (Hao et al., 2019). **Figure 2G** showed the area ratio of the peak of PDA-HD, BCL1.0, BCL2.0, and BCL3.0 at 401.5 eV was 8.64, 14.02, 17.86, and 20.68%, respectively. The above results implied that BCL was covalently immobilized on the PDA-HD coating through the amide bond formation. Such covalently immobilized BCL molecules generally have excellent stability and are not easily shed by tear washout.

## The Ability of BCL-Modified Contact Lens to Modulate the Inflammatory Response

A series of immune responses often accompany corneal tissue injury or abrasion, including infiltration of inflammatory

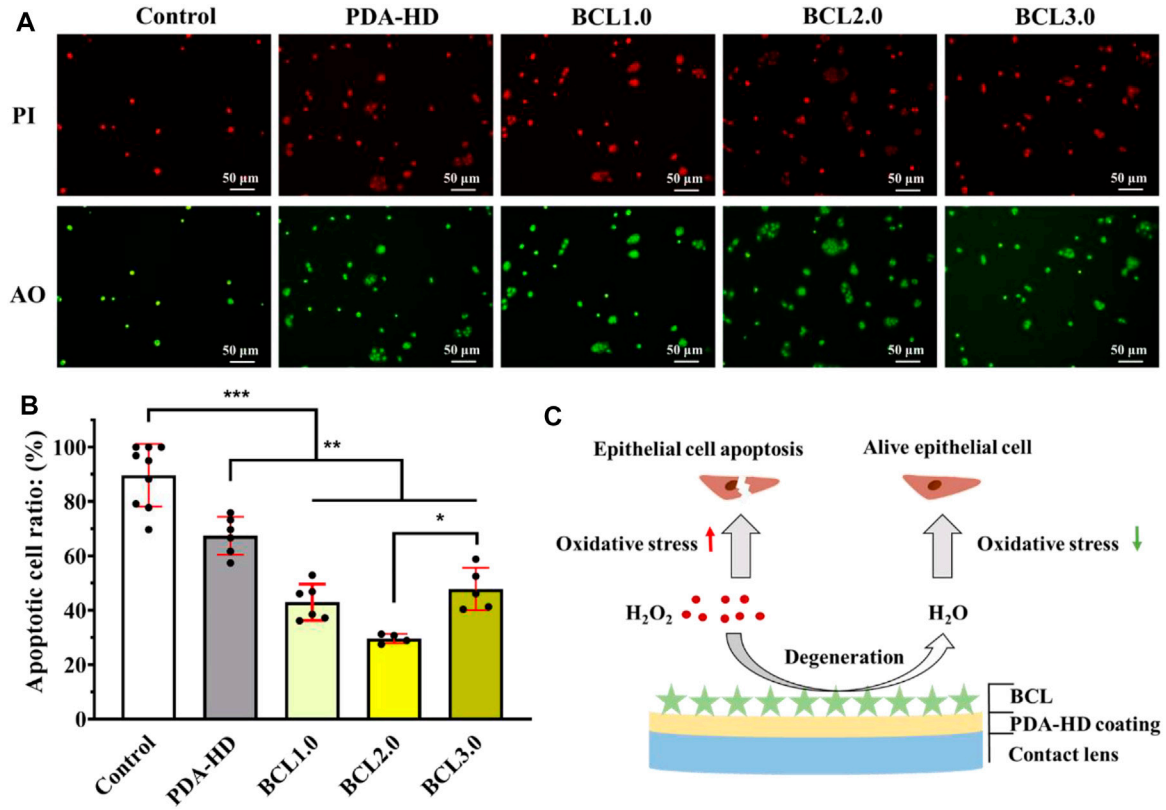


**FIGURE 4 | (A)** Fluorescence staining of HCECs growth and apoptosis on corneal contact lens after addition of hydrogen peroxide was photographed. **(B)** Survival statistics of HCECs on the contact lenses. **(C)** Schematic diagram of BCL-modified multifunctional corneal contact lens catabolizing hydrogen peroxide during cell culture. The untreated contact lenses were used as Control. Data are presented as the mean ± SD of $n = 3$ and were analyzed using one–way ANOVA, $^{*}p < 0.05$, $^{**}p < 0.01$, $^{***}p < 0.001$.

monocytes into the area of injury and differentiation into macrophage populations, which regulate tissue damage and repair, and release of pro-inflammatory cytokines and chemokines (Wynn and Vannella, 2016). The inflammatory response helps to destroy pathogens at the site of injury, but it also slows down the process of tissue repair. Therefore, controlling the unnecessary inflammatory response is beneficial to promote corneal repair. BCL had been reported to alter macrophage phenotype and attenuate the inflammatory response by inhibiting TLR4/NF-κB signaling pathway (Fu et al., 2021) and JAK/STAT pathway (Xu et al., 2020).

In this study, the modulatory effect of the BCL-modified contact lenses on the inflammatory response was assessed by macrophage culture. **Figures 3A1–A5** showed the growth of macrophages on the contact lenses after 24 h of culture in the high-sugar medium. **Figure 3B** showed the macrophage density on the contact lenses. As shown in **Figure 3**, the Control and PDA-HD groups had a large and aggregated number of macrophages adhering to the contact lenses. There was a slight decrease in the number of macrophages adhering to BCL1.0, but this decrease was not statistically significant. In contrast, there was a significant decrease in the number of adherent macrophages on BCL2.0 and BCL3.0. Such results suggested that the BCL modified on the contact lenses surface inhibited macrophage adhesion and exhibited anti-inflammatory properties. The above results implied that the multifunctional BCL-modified contact lenses could effectively regulate the ocular surface inflammatory microenvironment.

## The Ability of BCL-Modified Contact Lens to Modulate Oxidative Stress

Normal corneal epithelial tissue is rich in antioxidant enzymes to scavenge excess free radicals and reactive oxygen species (ROS). When the corneal epithelium is damaged, the oxidative stress response is triggered along with the activation of the inflammatory response, releasing large amounts of ROS, creating a vicious cycle of oxidative stress and inflammation (Kaluzhny et al., 2020). Therefore, there is a need to regulate the oxidative stress microenvironment of the ocular surface.

It has been reported that BCL had a powerful antioxidant capacity due to its special polyphenolic flavonoid structure, which significantly reduced mitochondrial and intracellular ROS levels, thus acting as a protective agent for cells (Song et al., 2020). As shown in **Figures 4A,B**, the cell growth and apoptosis of HCECs cultured on contact lenses and added with hydrogen peroxide were identified by acridine orange (green)/propidium iodide (red) (AO/PI) staining. The results showed that on Control

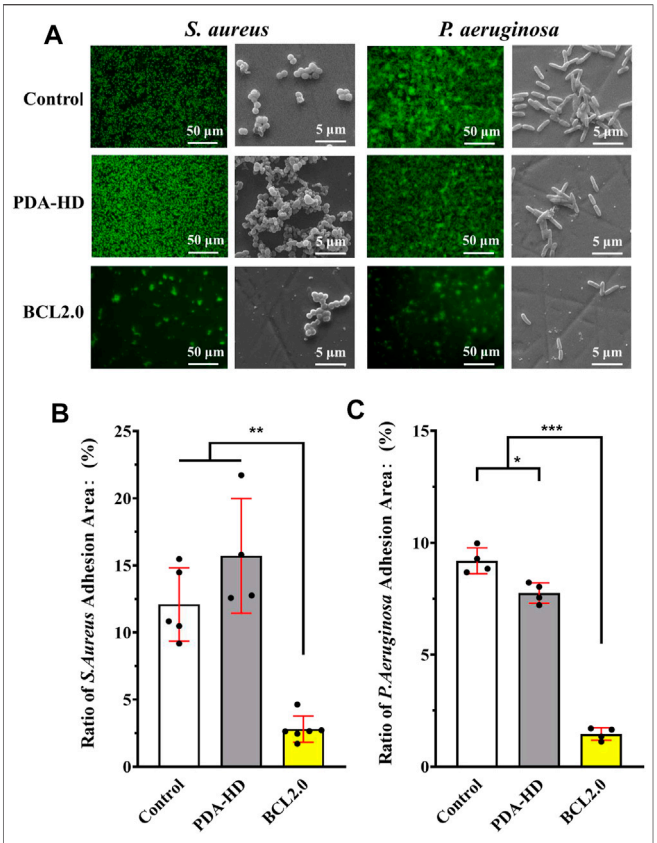


**FIGURE 5 | (A)** Fluorescence stained photographic and SEM scanned images of *S. aureus* and *P. aeruginosa* cultured on the contact lenses of Control, PDA-HD, and BCL2.0 for 24 h. **(B)** Statistics of the adherence area of *S. aureus* on the surface of the contact lenses. **(C)** Statistics of the adhesion area of *P. aeruginosa* on the surface of the contact lenses. The untreated contact lenses were used as Control. Data are presented as the mean ± SD of $n = 3$ and were analyzed using one–way ANOVA, $^{*}p < 0.05$, $^{**}p < 0.01$, $^{***}p < 0.001$.

samples with many PI-positive cells, the apoptosis rate was 88.97%, indicating a significant killing effect of $H_2O_2$ on HCECs. While on the surface of PDA-HD, BCL1.0, BCL2.0, and BCL3.0 samples, PI-positive cells were reduced with apoptosis rates of 67.42, 42.99, 29.63, and 47.84%, respectively. This trend of apoptosis rate was consistent with the trend of phenolic hydroxyl groups on the samples. (seen in **Figure 2C**). The above results indicated that the multifunctional BCL-modified contact lens could effectively inhibit the damage of HCECs by ROS.

Such results were also in line with our expectations. Firstly, the dopamine molecule, a constituent of the PDA-HD coating, has a catechol structure and has been shown to have free radical scavenging ability (Hu et al., 2020). Further, we modified the flavonoid polyphenol BCL on the surface of PDA-HD, thus enhancing the ability of the coating to regulate the oxidative stress microenvironment. A schematic diagram of the BCL-modified contact lens scavenging hydrogen peroxide during cell culture was shown in **Figure 4C**.

## *In vitro* Antimicrobial Properties of BCL-Modified Contact Lens

After a corneal injury, the barrier is disrupted, and ocular surface homeostasis is broken, at which time the normal flora or conditionally pathogenic bacteria in the conjunctival capsule can turn into pathogenic bacteria invasion, releasing various proteases and exotoxins to enhance the inflammatory response and oxidative stress response. If the infection is further aggravated, a biofilm can form and eventually lead to severe corneal disease (Zhang et al., 2020). Therefore, it is important to repair the damage while preventing microbial infections.

The results of antimicrobial experiments on contact lenses were shown in **Figure 5A**. After the Control, PDA-HD, and BCL2.0 contact lenses were incubated in *S. aureus* and *P. aeruginosa* bacterial solutions for 24 h, the adhesion of bacteria on the contact lenses were observed by fluorescence inverted microscopy and SEM, and the adhesion area was calculated (**Figures 5B,C**). The results showed that both *S. aureus* and *P. aeruginosa* adhered significantly less to the BCL2.0 surface compared to the Control. The adherence area ratios of *S. aureus* and *P. aeruginosa* were about 12.09 and 9.19% on Control samples, respectively, while they decreased to about 2.8 and 1.46% on BCL2.0, respectively., the above results indicated that the multifunctional BCL-modified contact lens had excellent antibacterial ability and was expected to prevent bacterial infections during wear.

## Effect of BCL-Modified Contact Lens on Corneal Injury Treatment

Corneal epithelial cell injury repair is a continuous and intersecting process involving epithelial cell proliferation, migration, and adhesion (Lu et al., 2001). In the early stages of trauma, necrotic shedding and progressive thinning of superficial epithelial cells around the corneal wound occurs, and flattened epithelial cells at the wound periphery extend pseudopods toward the wound surface. When the wound is close to the corneal rim, epithelial cells proliferate actively to fast repair the injury. When the wound is far from the corneal rim or located in the center of the pupil, the replenishment of epithelial cells at the wound moves centripetally from the normally proliferating epithelial cells at the corneal rim. The epithelial cells that add value and move to the wound then complete epithelial cell adhesion, i.e., tight epithelial cell-epithelial cell junctions and semi-bridging granule junctions between the epithelial cells and the basement membrane (Thill et al., 2007).

As shown in **Figure 6C**, we envisioned that the BCL-modified contact lens could promote corneal damage repair by preventing infection and regulating the ocular surface's inflammatory and oxidative stress microenvironment. We used animal experiments to verify this hypothesis.

The rabbit corneal epithelium was first disrupted and scraped in its entirety using 75% alcohol. Then the rabbit corneal morphology was observed by wearing the Control and BCL2.0 lenses for 24 h, respectively. As shown in **Figures 6A1,B1**, the Control lenses treated corneas were slightly cloudy, while the

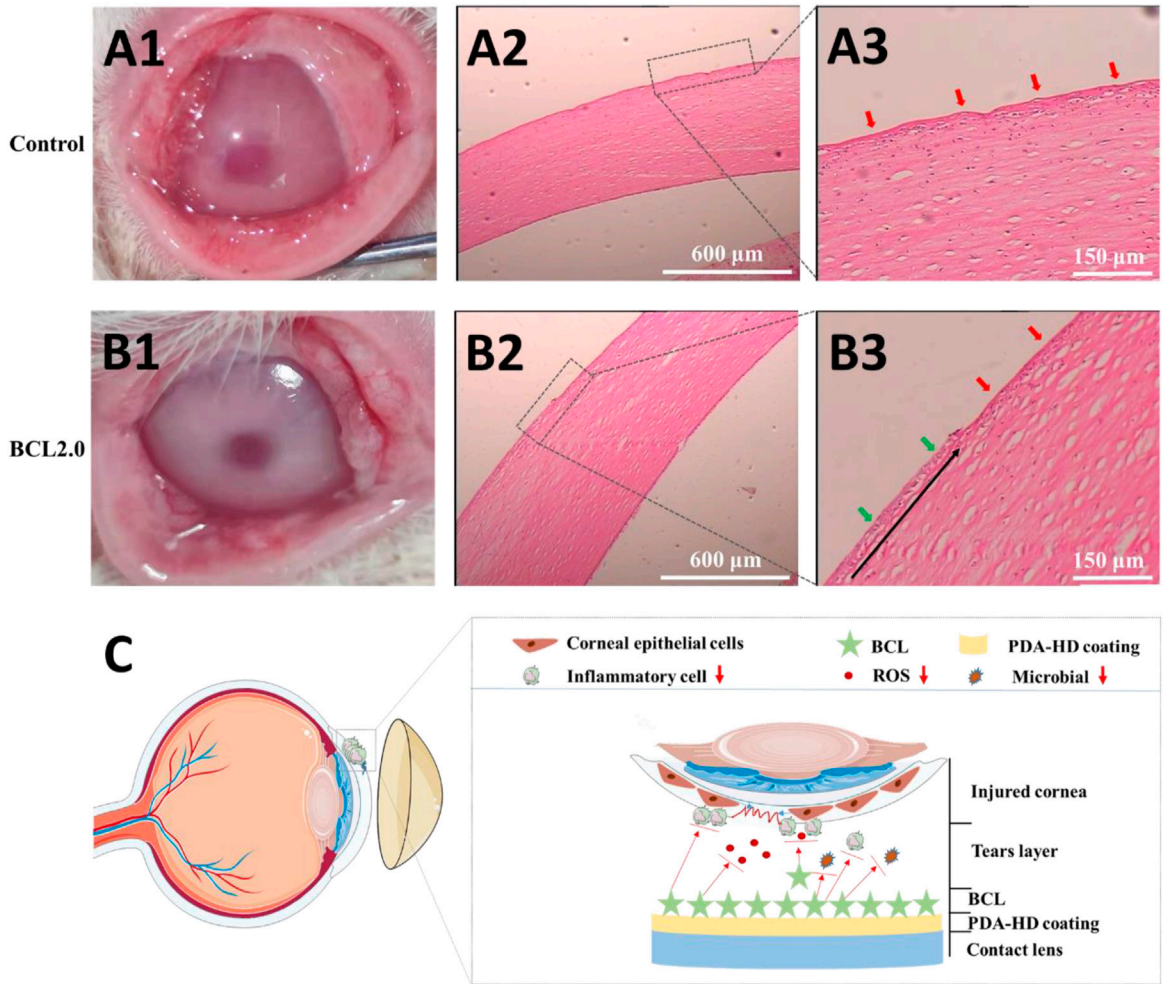


**FIGURE 6 |** The injured rabbits' cornea was treated by the Control or the BCL2.0 contact lenses for 24 h and observed by hematoxylin & eosin (H & E) staining. **(A1–A3)** Control group **(B1–B3)** BCL2.0 group. **(C)** Schematic diagram of the BCL-modified contact lens promoted corneal injury repair. The untreated contact lenses were used as Control.

BCL2.0 lenses treated corneas were clean. Furthermore, more lid conjunctiva and ocular secretions were observed in the Control group than in the BCL2.0 group. These results indicated that the BCL2.0 contact lens could more effectively relieve the inflammatory response and oxidative stress in the injury corneas than the Control contact lens.

As shown in **Figures 6A2,A3**, the entire cornea appeared uneven in the Control group (red arrows), with many immune cells collecting between the corneal stroma. The proliferating and migrating new corneal epithelium was not observed yet. As shown in **Figures 6B2,B3**, compared with the Control group, fewer immune cells accumulate between the corneal stroma in the BCL2.0 group. And new corneal epithelial cells (green arrows) that were proliferating and migrating from the corneal limbus to the pupil center could be observed (the black arrow in **Figure 6B3** shows the direction of corneal epithelial cell migration). The above results indicated that after a large area of corneal injury, wearing the multifunctional BCL-modified contact lenses could significantly boost the restoration of corneal injury at an early stage.

## CONCLUSION

In conclusion, we developed a simple and easy method to creatively covalently immobilize BCL onto a contact lens using dopamine-hexanediamine (PDA-HD) coating as a transition layer, thus endowing the contact lens with desirable multifunctions. The material science characterization showed that the BCL-modified contact lens had good optical properties and UV resistance. Besides, the BCL-modified contact lens also owned excellent hydrophilic and reductive properties. *In vitro* biological evaluation showed that the BCL-modified contact lens had epithelial cell safety and antibacterial activity. Moreover, the BCL-modified contact lens could regulate the inflammation and oxidative stress microenvironment, lacking in most current contact lenses. In the animal study, the multifunctional

BCL-modified contact lens was safe to wear and promoted injury repair of corneal epithelium. Thus, the BCL-modified contact lens has potential applications in preventing infection, regulating the ocular surface microenvironment, and promoting corneal injury repair. This study provides a new option for surface engineering of therapeutic contact lenses to treat ocular surface diseases.

## DATA AVAILABILITY STATEMENT

The original contributions presented in the study are included in the article/supplementary material, further inquiries can be directed to the corresponding authors.

## ETHICS STATEMENT

The animal study was reviewed and approved by the Medical Ethics Committee of the Affiliated Hospital of University of Electronic Science and Technology and Sichuan Provincial People's Hospital. Written informed consent was obtained from the owners for the participation of their animals in this study.

## AUTHOR CONTRIBUTIONS

YL and LYL: Experiment, Writing- Original draft preparation. YZL: Experiment, Data curation. PY and XL: Supervision and language polishment. LL: Writing- Reviewing. JC and CQ: Conceptualization and manuscript revision.

## FUNDING

This work was supported by the National Natural Science Foundation of China (82171026, 82070930, 81790643, 82121003, and 81970839), and the Sichuan Science and Technology Program (2020YFS0076, 2021YFS0369, 2021JDGD0036, 22ZDYF0869, and 2021YFS0033). And the CAMS Innovation Fund for Medical Sciences (2019-12M-5-032).

## REFERENCES

Fu, Y.-j., Xu, B., Huang, S.-w., Luo, X., Deng, X.-l., Luo, S., et al. (2021). Baicalin Prevents LPS-Induced Activation of TLR4/NF-Kb P65 Pathway and Inflammation in Mice via Inhibiting the Expression of CD14. *Acta Pharmacol. Sin* 42 (1), 88–96. doi:10.1038/s41401-020-0411-9

Guo, L.-T., Wang, S.-Q., Su, J., Xu, L.-X., Ji, Z.-Y., Zhang, R.-Y., et al. (2019). Baicalin Ameliorates Neuroinflammation-Induced Depressive-like Behavior through Inhibition of Toll-like Receptor 4 Expression via the PI3K/AKT/FoxO1 Pathway. *J. Neuroinflammation* 16 (1), 95. doi:10.1186/s12974-019-1474-8

Hao, X., Yeh, P., Qin, Y., Jiang, Y., Qiu, Z., Li, S., et al. (2019). Aptamer Surface Functionalization of Microfluidic Devices Using Dendrimers as Multi-Handled Templates and its Application in Sensitive Detections of Foodborne Pathogenic Bacteria. *Analytica Chim. Acta* 1056, 96–107. doi:10.1016/j.aca.2019.01.035

Ho, C.-C., and Ding, S.-J. (2014). Structure, Properties and Applications of Mussel-Inspired Polydopamine. *J. Biomed. Nanotechnol* 10 (10), 3063–3084. doi:10.1166/jbn.2014.1888

Hu, J., Yang, L., Yang, P., Jiang, S., Liu, X., and Li, Y. (2020). Polydopamine Free Radical Scavengers. *Biomater. Sci.* 8 (18), 4940–4950. doi:10.1039/d0bm01070g

Huang, J.-F., Zhong, J., Chen, G.-P., Lin, Z.-T., Deng, Y., Liu, Y.-L., et al. (2016). A Hydrogel-Based Hybrid Theranostic Contact Lens for Fungal Keratitis. *ACS Nano* 10 (7), 6464–6473. doi:10.1021/acsnano.6b00601

Jumelle, C., Gholizadeh, S., Annabi, N., and Dana, R. (2020). Advances and Limitations of Drug Delivery Systems Formulated as Eye Drops. *J. Controlled Release* 321, 1–22. doi:10.1016/j.jconrel.2020.01.057

Kaluzhny, Y., Kinuthia, M. W., Lapointe, A. M., Truong, T., Klausner, M., and Hayden, P. (2020). Oxidative Stress in Corneal Injuries of Different Origin: Utilization of 3D Human Corneal Epithelial Tissue Model. *Exp. Eye Res.* 190, 107867. doi:10.1016/j.exer.2019.107867

Lee, H., Dellatore, S. M., Miller, W. M., and Messersmith, P. B. (2007). Mussel-inspired Surface Chemistry for Multifunctional Coatings. *Science* 318 (5849), 426–430. doi:10.1126/science.1147241

Li, Y., Song, K., Zhang, H., Yuan, M., An, N., Wei, Y., et al. (2020). Anti-inflammatory and Immunomodulatory Effects of Baicalin in Cerebrovascular and Neurological Disorders. *Brain Res. Bull.* 164, 314–324. doi:10.1016/j.brainresbull.2020.08.016

Lim, L., and Lim, E. W. L. (2020). Therapeutic Contact Lenses in the Treatment of Corneal and Ocular Surface Diseases-A Review. *Asia Pac. J. Ophthalmol. (Phila)* 9 (6), 524–532. doi:10.1097/apo.0000000000000331

Liu, G., Li, K., Wang, H., Ma, L., Yu, L., and Nie, Y. (2020). Stable Fabrication of Zwitterionic Coating Based on Copper-Phenolic Networks on Contact Lens with Improved Surface Wettability and Broad-Spectrum Antimicrobial Activity. *ACS Appl. Mater. Inter.* 12 (14), 16125–16136. doi:10.1021/acsami.0c02143

Liu, X., Chen, J., Qu, C., Bo, G., Jiang, L., Zhao, H., et al. (2018). A Mussel-Inspired Facile Method to Prepare Multilayer-AgNP-Loaded Contact Lens for Early Treatment of Bacterial and Fungal Keratitis. *ACS Biomater. Sci. Eng.* 4 (5), 1568–1579. doi:10.1021/acsbiomaterials.7b00977

Ljubimov, A. V., and Saghizadeh, M. (2015). Progress in Corneal Wound Healing. *Prog. Retin. Eye Res.* 49, 17–45. doi:10.1016/j.preteyeres.2015.07.002

Lu, L., Reinach, P. S., and Kao, W. W.-Y. (2001). Corneal Epithelial Wound Healing. *Exp. Biol. Med. (Maywood)* 226 (7), 653–664. doi:10.1177/153537020222600711

Luo, Y., Kang, K. B., Sartaj, R., Sun, M. G., Zhou, Q., Guaiquil, V. H., et al. (2021). Silk Films with Nanotopography and Extracellular Proteins Enhance Corneal Epithelial Wound Healing. *Sci. Rep.* 11 (1), 8168. doi:10.1038/s41598-021-87658-1

Nosrati, H., Abpeikar, Z., Mahmoudian, Z. G., Zafari, M., Majidi, J., Alizadeh, A., et al. (2020). Corneal Epithelium Tissue Engineering: Recent Advances in Regeneration and Replacement of Corneal Surface. *Regenerative Med.* 15 (8), 2029–2044. doi:10.2217/rme-2019-0055

Pan, L., Cho, K.-S., Yi, I., To, C.-H., Chen, D. F., and Do, C.-W. (2021). Baicalein, Baicalin, and Wogonin: Protective Effects against Ischemia-Induced Neurodegeneration in the Brain and Retina. *Oxidative Med. Cell Longevity* 2021, 1–16. doi:10.1155/2021/8377362

Pan, Y., Song, D., Zhou, W., Lu, X., Wang, H., and Li, Z. (2019). Baicalin Inhibits C2C12 Myoblast Apoptosis and Prevents against Skeletal Muscle Injury. *Mol. Med. Rep.* 20 (1), 709–718. doi:10.3892/mmr.2019.10298

Song, X., Gong, Z., Liu, K., Kou, J., Liu, B., and Liu, K. (2020). Baicalin Combats Glutamate Excitotoxicity via Protecting Glutamine Synthetase from ROS-Induced 20S Proteasomal Degradation. *Redox Biol.* 34, 101559. doi:10.1016/j.redox.2020.101559

Stern, J. H., Tian, Y., Funderburgh, J., Pellegrini, G., Zhang, K., Goldberg, J. L., et al. (2018). Regenerating Eye Tissues to Preserve and Restore Vision. *Cell Stem Cell* 22 (6), 834–849. doi:10.1016/j.stem.2018.05.013

Sun, H.-J., Jin, X.-M., Xu, J., and Xiao, Q. (2020). Baicalin Alleviates Age-Related Macular Degeneration via miR-223/nlrp3-Regulated Pyroptosis. *Pharmacology* 105 (1-2), 28–38. doi:10.1159/000502614

Thill, M., Schlagner, K., Altenähr, S., Ergün, S., Faragher, R. G. A., Kilic, N., et al. (2007). A Novel Population of Repair Cells Identified in the Stroma of the Human Cornea. *Stem Cell Dev.* 16 (5), 733–746. doi:10.1089/scd.2006.0084

Wei, S., Yin, R., Tang, T., Wu, Y., Liu, Y., Wang, P., et al. (2019). Gas-Permeable, Irritation-free, Transparent Hydrogel Contact Lens Devices with Metal-Coated Nanofiber Mesh for Eye Interfacing. *ACS Nano* 13 (7), 7920–7929. doi:10.1021/acsnano.9b02305

Wynn, T. A., and Vannella, K. M. (2016). Macrophages in Tissue Repair, Regeneration, and Fibrosis. *Immunity* 44 (3), 450–462. doi:10.1016/j.immuni.2016.02.015

Xu, M., Li, X., and Song, L. (2020). Baicalin Regulates Macrophages Polarization and Alleviates Myocardial Ischaemia/reperfusion Injury via Inhibiting JAK/STAT Pathway. *Pharm. Biol.* 58 (1), 655–663. doi:10.1080/13880209.2020.1779318

Yin, C., Qi, X., Wu, J., Guo, C., and Wu, X. (2021). Therapeutic Contact Lenses Fabricated by Hyaluronic Acid and Silver Incorporated Bovine Serum Albumin Porous Films for the Treatment of Alkali-Burned Corneal Wound. *Int. J. Biol. Macromolecules* 184, 713–720. doi:10.1016/j.ijbiomac.2021.06.155

Yu, H., Chen, B., and Ren, Q. (2019). Baicalin Relieves Hypoxia-Aroused H9c2 Cell Apoptosis by Activating Nrf2/HO-1-Mediated HIF1α/BNIP3 Pathway. *Artif. Cell Nanomedicine, Biotechnol.* 47 (1), 3657–3663. doi:10.1080/21691401.2019.1657879

Zhang, S., Hu, B., Xu, J., Ren, Q., Wang, Z., Wang, S., et al. (2020). Baicalin Suppress Growth and Virulence-Related Factors of Methicillin-Resistant Staphylococcus aureus *In Vitro* and Vivo. *Microb. Pathogenesis* 139, 103899. doi:10.1016/j.micpath.2019.103899

Zhao, Q., Chen, X.-Y., and Martin, C. (2016). Scutellaria Baicalensis , the golden Herb from the Garden of Chinese Medicinal Plants. *Sci. Bull.* 61 (18), 1391–1398. doi:10.1007/s11434-016-1136-5

Zhu, W., Chen, X., Yu, J., Xiao, Y., Li, Y., Wan, S., et al. (2018). Baicalin Modulates the Treg/Teff Balance to Alleviate Uveitis by Activating the Aryl Hydrocarbon Receptor. *Biochem. Pharmacol.* 154, 18–27. doi:10.1016/j.bcp.2018.04.006

Ziaei, M., Greene, C., and Green, C. R. (2018). Wound Healing in the Eye: Therapeutic Prospects. *Adv. Drug Deliv. Rev.* 126, 162–176. doi:10.1016/j.addr.2018.01.006

Zidan, G., Rupenthal, I. D., Greene, C., and Seyfoddin, A. (2018). Medicated Ocular Bandages and Corneal Health: Potential Excipients and Active Pharmaceutical Ingredients. *Pharm. Dev. Tech.* 23 (3), 255–260. doi:10.1080/10837450.2017.1377232

**Conflict of Interest:** The authors declare that the research was conducted in the absence of any commercial or financial relationships that could be construed as a potential conflict of interest.

**Publisher's Note:** All claims expressed in this article are solely those of the authors and do not necessarily represent those of their affiliated organizations, or those of the publisher, the editors, and the reviewers. Any product that may be evaluated in this article, or claim that may be made by its manufacturer, is not guaranteed or endorsed by the publisher.

frontiers in Bioengineering and Biotechnology

ORIGINAL RESEARCH
published: 22 March 2022
doi: 10.3389/fbioe.2022.877738

# Ag-Incorporated Polydopamine/Tannic Acid Coating on Titanium With Enhanced Cytocompatible and Antibacterial Properties

*Hao Zhang[1], Xiaolong Shen[1], Zhikui Fei[1], Xingping Fan[1], Lan Ma[1]*, Haibo Wang[1], Congxue Tian[1], Bo Zhang[2], Rifang Luo[2], Yunbing Wang[2]* and Shengtian Huang[3]*

[1]School of Vanadium and Titanium, School of Biological and Chemical Engineering, Panzhihua University, Panzhihua, China, [2]National Engineering Research Center for Biomaterials, Sichuan University, Chengdu, China, [3]Material Corrosion and Protection Key Laboratory of Sichuan Province, Sichuan University of Science and Engineering, Zigong, China

OPEN ACCESS

**Edited by:**
Jingan Li,
Zhengzhou University, China

**Reviewed by:**
Yingqi Chen,
Peking University Shenzhen Hospital, China
Zhoujiang Chen,
Chengdu University, China
Peichuang Li,
Qilu University of Technology, China

***Correspondence:**
Lan Ma
hudie5656@163.com
Yunbing Wang
yunbing.wang@scu.edu.cn

**Specialty section:**
This article was submitted to Biomaterials, a section of the journal Frontiers in Bioengineering and Biotechnology

**Received:** 17 February 2022
**Accepted:** 28 February 2022
**Published:** 22 March 2022

**Citation:**
Zhang H, Shen X, Fei Z, Fan X, Ma L, Wang H, Tian C, Zhang B, Luo R, Wang Y and Huang S (2022) Ag-Incorporated Polydopamine/Tannic Acid Coating on Titanium With Enhanced Cytocompatible and Antibacterial Properties. Front. Bioeng. Biotechnol. 10:877738. doi: 10.3389/fbioe.2022.877738

Titanium (Ti) and its alloys are the most commonly used materials for bone implants. However, implant failure often happens due to bacterial infection. Developing antibacterial coatings on Ti implants is an effective strategy. Dopamine and tannic acid were cross-linked to form coating on Ti through Michael addition and Schiff base reaction. In addition, the Ag ions were grafted on the coating by the redox reaction of phenolic hydroxyl groups. Thus, an Ag-incorporated polydopamine/tannic acid coating was prepared on Ti substrate. SEM, EDS, water contact angle, FTIR, and XRD results demonstrated that the coating was formed on Ti successfully. The antibacterial activity of the coating against Gram-negative *E. coli* was examined, and the cytotoxicity of the coating was investigated by mouse fibroblast cells. The improvement of hydrophilicity, good cytocompatibility, and antibacterial effectiveness indicates that the coating has potential to surface modification of Ti implants.

**Keywords: titanium, antibacterial, silver, tannic acid, cytotoxicity**

## INTRODUCTION

Due to the favorable stability, mechanical properties, and biocompatibility, titanium and its alloys are the most commonly used materials for implants in dental and orthopedic (Elias et al., 2008; Suer et al., 2014; Scribante et al., 2018; Spriano et al., 2018). However, among titanium implant failures, bacterial infection and lack of osseointegration are the main causes (Jemat et al., 2015; Chouirfa et al., 2019). Titanium and its alloys have no antibacterial property and are sensitive to bacterial adhesion, which tends to bacterial infection (Spriano et al., 2018). Due to the presence of bacterial infection, a chronic inflammatory response may also develop at the infection site (Esposito and Leone, 2008; McConoughey et al., 2014; Høiby et al., 2015). In addition, titanium and its alloys are biologically inert, which made them that they can only be combined with the human body through physical chimerism. Such a combination lacks stability and may easily cause looseness and falloff in long-term use. Therefore, improving the antibacterial performance and osseointegration of Ti implants is necessary to improve the success rate of clinical implantation.

Surface modification is widely used to endow titanium and its alloys with osseointegration and antibacterial ability (Kulkarni et al., 2015; Ferraris and Spriano, 2016; Cheng et al., 2020; He et al., 2021). To achieve good osseointegration, the implants should trigger specific biological reactions at the interface to promote the combination between the tissue and the material (Hench et al., 1971). Ideal

antibacterial coatings should have proven antibacterial effects with no toxicity as well as easy to manufacture (Orapiriyakul et al., 2018). Surface modification of physical adsorption and chemical covalent conjugation with antibacterial entities [such as antibiotics (Cabal et al., 2012; Lee et al., 2013; Park et al., 2014), antibacterial metal elements (Mei et al., 2014; Janković et al., 2015; He et al., 2021), and antimicrobial peptides (Bronk et al., 2014; Chen et al., 2014)] has become a practical method to prepare antibacterial coatings on Ti implant. However, researchers still show continued interest in fabricating universal antibacterial coatings through simple and low-cost methods. Compared with most research studies, the preparation of Ag-incorporated polydopamine/tannic acid coating requires only simple soaking, which is easy to operate and low cost. Mussel-inspired coating has great potential for universal surface modification. Dopamine can form coatings on various substrates through self-polymerization by a simple dip process. Moreover, studies have shown that tea polyphenols extracted from plants have anti-inflammatory, antibacterial, and antioxidant properties and can improve the mineralization and differentiation of osteoblasts (Chen and Dou, 2008; Bancirova, 2010; Ferruzzi, 2010; Carloni et al., 2013; Srivastava et al., 2013; Vester et al., 2014). Tea polyphenols contain a large number of catechol groups, which can react with dopamine by Michael addition and Schiff base reaction (Xu et al., 2016). Using this reaction, tea polyphenols can be introduced into the dopamine coating. Studies have reported that green tea polyphenols have a stimulating effect on bone-forming cells. Surface treatment of titanium alloy (Ti6Al4V) by tea polyphenols can induce hydroxyapatite deposition in simulated body fluid, showing that polyphenols can improve cell differentiation and stimulate biomineralization (Bancirova, 2010). However, the antibacterial ability of a single polyphenol coating is insufficient, and it is usually necessary to combine it with antibacterial agents. Among them, Ag has attracted much attention due to its broad spectrum of antibacterial ability. Although Ag has cytotoxicity, the balance between effective antibacterial activity and cytotoxicity can be achieved by controlling its loading dose in the coating. Cheng et al. prepared $TiO_2$ nanotube (NT) by anodic oxidation on the Ti surface and then produced AgNT on the surface of NT through UV reduction of Ag ions. Ag-loaded $TiO_2$-NT showed strong antibacterial activity against *Staphylococcus aureus* (MRSA, AT43300) *in vitro* and maintained for at least 30 days (Cheng et al., 2014). Bai et al. prepared Ti–Ag coating with AgNPs on Ti by pulsed DC magnetron sputtering, which could kill *Staphylococcus aureus* and was valid for more than 75 days (Bai et al., 2015). Zhang et al. used 50 nm AgNP in the dopamine-modified alginate/chitosan (DAL/CHI) polyelectrolyte multilayer for surface modification of titanium alloys. The DAL/CHI layer can improve the wetting ability of titanium alloy and significantly promote the proliferation of fibroblasts. After incorporation of AgNP, although the L929 cell activity slightly decreased, the growth of *Escherichia coli* and *Staphylococcus aureus* was significantly inhibited (Zhang et al., 2013).

Most polyphenols can be complexed with metal ions and form stable complexes, such as Ag (I) and Cu (II) (Leopoldini et al., 2011; Rodríguez et al., 2016). Ag ions can be grafted onto the surface of medical titanium alloys by polyphenol coating due to their ability to complex metal ions. The electron-donating ortho-phenolic hydroxyls of polyphenol can serve as a reducing agent to reduce $Ag^+$ to $Ag^0$ (Huang et al., 2016). Tannic acid (TA) is a natural reducing agent, which is widely present in plants, has health benefits such as chemoprevention and antioxidant activity. The rich catechol groups of TA could reduce metal ions to metal nanoparticles in the solution (Sagbas et al., 2015; Luo et al., 2016). Furthermore, the catechol groups of TA could cross-link with amino groups of dopamine to form coatings on various substrates by Michael addition and Schiff base reaction (Luo et al., 2013; Zhang et al., 2018).

In this study, the Ag-incorporated polydopamine/tannic acid coating on the surface of Ti substrate was constructed to endow Ti implants with antibacterial properties. First, dopamine and tannic acid are co-deposited to construct a phenol–amine cross-linked coating on the titanium surface. During the co-deposition process, the phenolic hydroxyl groups of tannic acid were oxidized into quinones. The quinones can react with amine groups in dopamine via Michael addition and Schiff base reaction to construct covalent bonding of dopamine and tannic acid. Then, the Ag ions were grafted on the coating by the redox reaction of phenolic hydroxyl groups. The complexed Ag on the coating can effectively improve the antibacterial ability and avoid problems such as delayed inflammation. The surface morphology, hydrophilicity, surface chemical properties, antibacterial activity, and cytocompatibility of the coating were investigated.

# MATERIALS AND METHODS

## Preparation of Samples

Pure titanium plates (99.6 at%, Grade 2) were cut into rectangular samples with dimensions of 10 mm × 10 mm × 1 mm. The samples were polished to 2000 # grit level, ultrasonically cleaned with acetone, alcohol, and ultrapure water for 15 min each, and then dried at 40°C. To prepare polydopamine/tannic acid-decorated titanium (Ti-PT), 30 mg of tannic acid (Wuxi Taiyo Green Power Co., Ltd., Jiangsu, China) and 30 mg dopamine hydrochloride (Sigma-Aldrich Chemical Co.) were dissolved in 30 ml Tris–HCl solution (10 mM, pH = 8.5), and then the Ti substrates were immersed in the solution at 20°C for 24 h. Then, the samples were ultrasonically cleaned in ultrapure water and dried at 40°C. In order to further load Ag ions on the Ti-PT, the PT-coated samples were avoid-light placed in silver nitrate solution ($AgNO_3$, 0.1 mg/ml) at 20°C for 1 day. The obtained sample was denoted as Ti-PT-0.1Ag. Ag is a commonly used antibacterial metal, but high concentrations can cause cytotoxicity. In order to obtain the optimal process, three different $AgNO_3$ solution concentrations were set up to compare antibacterial activity and cytotoxicity. The Ti-PT samples were also immersed in 0.25 mg/ml and 0.5 mg/ml $AgNO_3$ solution, and the prepared samples were named Ti-PT-0.25Ag and Ti-PT-0.5Ag, respectively. The experimental procedure including the preparation of the polydopamine/tannic acid coating, complexation of $Ag^+$, and possible reaction mechanism are schematically illustrated in **Scheme 1**.

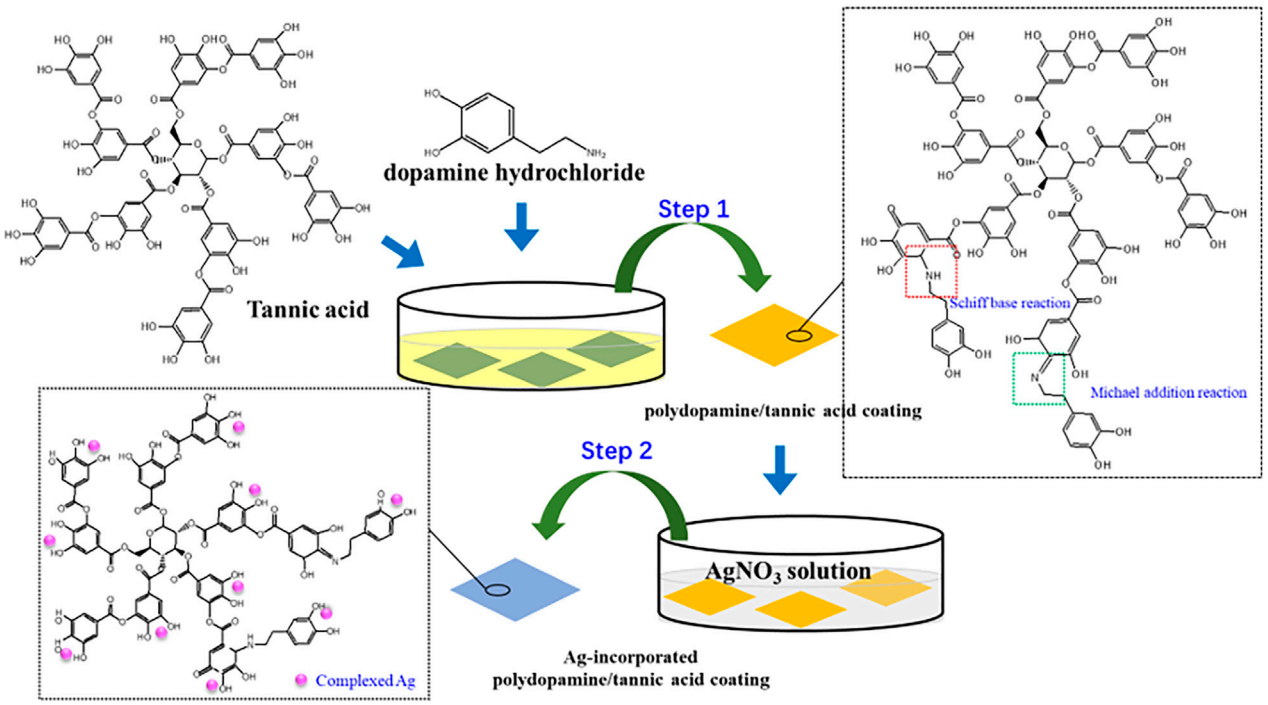


**SCHEME 1 |** Experimental procedure and possible reaction mechanism of Ag-incorporated polydopamine/tannic acid coating.

## Surface Characterization

FESEM (field emission scanning electron microscopy, JSM-7401F, JEOL, Japan) was used to observe the micromorphologies of samples. EDS (energy-dispersive X-ray spectrometry) was used to provide the element composition of the coatings. The optical contact angle system (Model SL200A/B/D) was employed to test the water contact angles of the samples by using a 2-μl deionized water droplet at room temperature. The attenuated total reflection FTIR infrared spectroscopy with a scan scope from 4,000 to 500 $cm^{-1}$ was employed for chemical characterization analysis of the coatings. The changes in the chemical states and the high resolution spectra of C 1s, O 1s, N 1s and Ag 3d were analyzed with an X-ray photoelectron spectroscopy system (XPS, XSAM800, Kratos Ltd., United Kingdom).

## Antibacterial Activity

The antibacterial capability of the samples was assessed by *Escherichia coli* (*E. coli*; ATCC 25922). The agar plating of colonies was carried out to investigate the bactericidal ability. Ti, Ti-PT, Ti-PT-0.1Ag, Ti-PT-0.25Ag, and Ti-PT-0.5Ag were sterilized by ultraviolet for 24 h. Each sample was incubated with 400 μl of solution containing *E. coli* suspension ($1 \times 10^6$ CFU $ml^{-1}$) at 37°C for 24 h. Then, the bacterial suspension was collected into the sterilized centrifugal tube with 4 ml physiological saline. The bacteria in the tube from different samples (Ti, Ti-PT, and Ti-PT-Ag) were dissociated using a vortex mixer. The dissociated bacteria solution was diluted with physiological saline and then added into the standard Luria–Bertani agars and incubated at 37°C for 24 h. The bacteria concentration of *E. coli* re-cultured on agars after dissociation from the samples was detected.

## Cytotoxicity Test

The mouse fibroblast cell line L929 was chosen for measuring the cytotoxicity of PT-Ag coating. Ti, Ti-PT, Ti-PT-0.1Ag, Ti-PT-0.25Ag, and Ti-PT-0.5Ag were sterilized by exposure to UV light overnight and then placed in 24-well plates. The fibroblast suspension (density $2 \times 10^4$ cells/$cm^2$) was seeded onto the samples and incubated for 1 day in 5% $CO_2$ at 37°C; the plates without samples were used as a blank control. CCK-8 assay was used to determine the cell viability. Subsequently, the samples were washed by phosphate buffer saline (PBS) three times and stained by rhodamine 123. The cells on the samples were visualized using an inverted fluorescence microscope (Leica, Germany).

# RESULTS AND DISCUSSION

## Surface Characterization

The optical images, SEM images, and the surface elemental composition of samples were studied and shown in **Figure 1**. As shown in **Figure 1A**, compared with bare Ti, the PDA/TA-coated surface (Ti-PT), especially the coatings grafted with $Ag^+$ (Ti-PT-0.1Ag) have obvious color change. The Ti-PT appears brown due to the presence of catechol and amine groups. It is speculated that after the phenol oxidized to quinone, the Michael

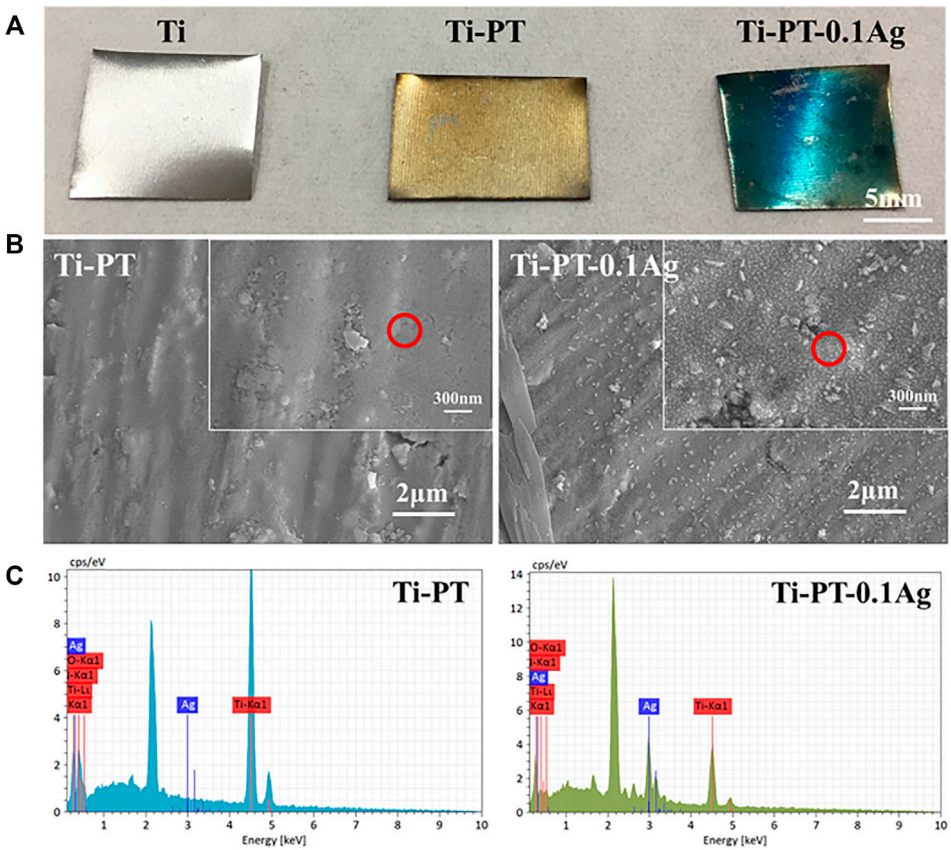


**FIGURE 1 | (A)** Digital pictures of Ti, Ti-PT, and Ti-PT-0.1Ag samples. **(B)** Surface morphology and microstructure of Ti-PT and Ti-PT-0.1Ag. **(C)** EDS spectra from the position marked by red circle.

addition reaction and Schiff base reaction occur with the amine donor, and the polymerization and cross-linking process is manifested by color. After immersing in silver nitrate solution, the surface of Ti-PT-0.1Ag turned blue due to the complexation of phenolic hydroxyl and silver ions. The color change of the sample surface preliminary indicates that the coating can be deposited on the Ti surface.

**Figure 1B** indicates SEM images of the Ti-PT and Ti-PT-0.1Ag. It can be clearly seen that the Ti-PT exhibited film-covered morphology. The addition of $Ag^+$ ion to the PT coating caused some particle depositions, and the size of the particles is about 30 nm. The catechol and hydroxyl groups on Ti-PT have the ability to complex and reduce $Ag^+$ ions to form metal silver. The elemental compositions of the surface were detected by EDS analysis (**Figure 1C**). The C, O, and Ti elements were detected on the Ti-PT and Ti-PT-0.1Ag, while the Ag element appeared on the surface of Ti-PT-0.1Ag. The EDS analysis confirmed the precipitated particles on Ti-PT-0.1Ag as silver. The presence of silver on Ti-PT-0.1Ag indicates the successful loading of silver on the coating.

The relatively hydrophilic surface has higher surface energy, which promotes the adhesion of cells, thus increasing the osteointegration ability between the implant and the host bone tissue. The hydrophilicity of the surface was characterized by the water contact angle, shown in **Figure 2**. The contact angle decreased from 80.13° ± 0.64° on the Ti surface to 72.50° ± 0.87° on the Ti-PT surface. The incorporated PDA/TA coating altered the contact angle on the Ti obviously, owing to the phenol and amino groups on the surface. After being grafted with $Ag^+$ ions, the contact angle of Ti-PT-0.1Ag further decreased to 50.14° ± 2.72°. These results indicate that the hydrophilicity is improved after surface modification.

In order to confirm the cross-linking of dopamine and tannic acid and identify the grafting principle of silver, FTIR infrared spectroscopy (**Figure 3**) and XPS (**Figure 4**) were used for further analysis. FTIR spectra exhibited the characteristic bands of Ti-PT and Ti-PT-0.1Ag, as shown in **Figure 3**. The basic feature peaks of dopamine and tannic acid were well preserved on both the surface of Ti-PT and Ti-PT-0.1Ag. The peaks around 3,500 $cm^{-1}$ are the phenolic hydroxyl groups. The peaks at 2,940 and 2,862 $cm^{-2}$ are C-H stretching vibration (Chen et al., 2015). The peak at 1,600 $cm^{-1}$ represents the aromatic nucleus, derived from the benzene ring structure of the dopamine and tannic acid. The formation of the vibration peak of aromatic O-H (1,265 $cm^{-1}$) and the stretching vibration peak of C-O (1,370 $cm^{-1}$) from the phenolic group could be observed. In addition, the stretching vibration peak of aliphatic primary amine C-N (1,080 $cm^{-1}$) and the N-H deformation vibration

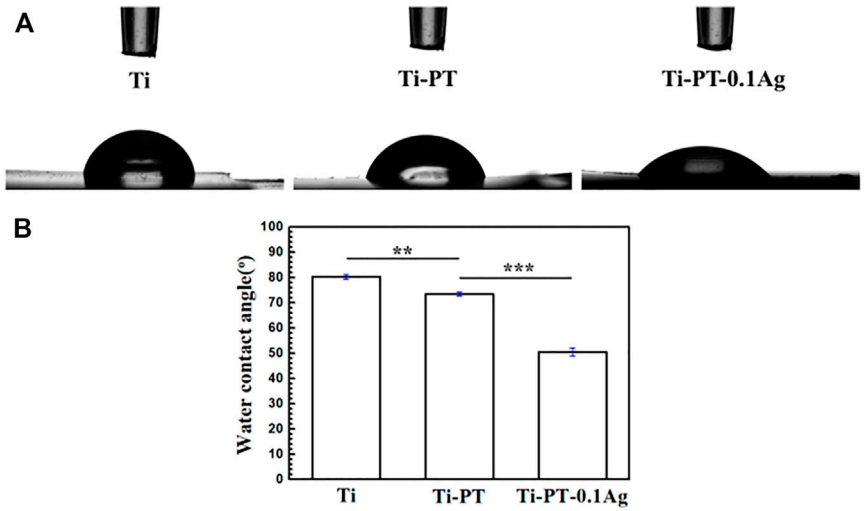


**FIGURE 2 | (A)** Shapes of water droplets on the Ti, Ti-PT, and Ti-PT-0.1Ag. **(B)** Static water contact angles of Ti, Ti-PT, and Ti-PT-0.1Ag. Data are presented as mean ± SD and analyzed by one-way ANOVA (**$p$ < 0.01, ***$p$ < 0.001).

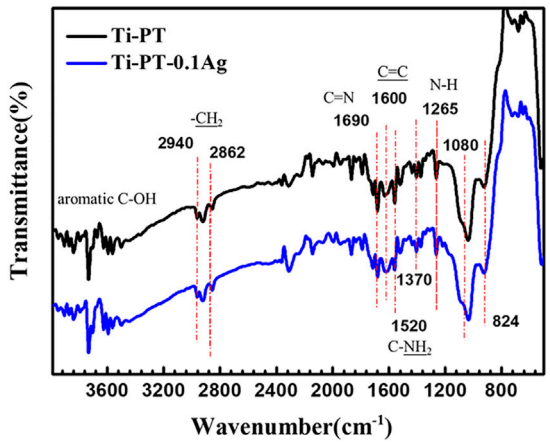


**FIGURE 3 |** FTIR spectra of Ti-PT and Ti-PT-0.1Ag.

peak of primary amine (827 $cm^{-1}$) from dopamine are shown (Zhang et al., 2019). It is noteworthy that the peaks at 1,690 $cm^{-1}$ and 1,520 $cm^{-1}$, which present C=N stretching vibration and N-H scissoring vibrations, respectively, confirmed the cross-link of dopamine and tannic acid. According to the analysis, although there is no significant difference in FTIR infrared spectroscopy between Ti-PT and Ti-PT-0.1Ag, detailed analysis is needed through XPS.

The XPS spectra survey of the surface was examined to further identify the presence of Ag ions and detect the chemical bonding states of the element on the surface. As shown in **Figure 4**, the Ti-PT and Ti-PT-0.1Ag showed the appearance of C 1s, O 1s, and N 1s. The signal peaks of ~600 and ~370 eV appeared on the Ti-PT-Ag, indicating successful grafting of $Ag^+$ ions on the surface. The atom content ratios of C, N, O, and Ag on the surface of Ti-PT and Ti-PT-0.1Ag are also listed in **Figure 4**. The high-resolution spectra and fitting results of C 1s, N 1s, O 1s, and Ag 3d on samples are shown in **Figure 5**. The grafted Ag has little effect on the chemical bonding states of C and N elements; therefore, only the high-resolution spectra of C1s and N1s of the Ti-PT are analyzed, as shown in **Figure 5A** and **Figure 5B**. The C 1s exhibited five bonding states: 1) 288.3 eV corresponding to the aromatic C=O; 2) 286.4 eV corresponding to the aromatic C-OH; 3) 285.6 eV corresponding to $C\text{-}NH_3^+$, aliphatic C-N, and aromatic C-N; 4) 284.9 eV corresponding to aliphatic C-C and C-H; and 5) 284.2 eV corresponding to aromatic C (Cheng et al., 2014). It should be noted that the fitting result of C 1s is not unique, and uncertainty cannot be completely avoided during the fitting process. However, if the fitting results of C 1s, N 1s, and O 1s show consistency, it can be mutually corroborated. **Figure 5B** shows the high-resolution fitting result of N 1s, which exhibit three bonding states: $C\text{-}NH_3^+$ at 401.4 eV, aromatic C-N at 400.5 eV, and aromatic C=N at 399.6 eV. The aromatic C-N obtained by the Michael addition reaction and the aromatic C=N obtained by the Schiff base reaction proved that the dopamine and tannic acid had cross-linked in the coating. The high-resolution spectra of O 1s on Ti-PT and Ti-PT-0.1Ag are compared in **Figure 5C**. The peak position of O 1s on Ti-PT-0.1Ag shifted to a higher binding energy than that on Ti-PT. This is caused by the complexation of the phenolic hydroxyl group or quinone group with the silver ion, which proves the occurrence of the complexation reaction. The binding energy of Ag at ~370 eV was amplified, and the peaks at 368.7 eV (3d 5/2) and 374.5 eV (3d 3/2) were found on Ti-PT-Ag, as shown in **Figure 5D**. The binding energy difference of nearly 6.0 eV between Ti-PT and Ti-PT-0.1Ag typically indicated the existence of Ag nanoparticles (Srivastava et al., 2013).

## Antibacterial Ability

The detached bacteria from the samples cultivated for 24 h were re-cultured on agar plates. The bacterial colony formation and the number of *E. coli* colonies with Ti, Ti-PT, Ti-PT-0.1Ag, Ti-PT-

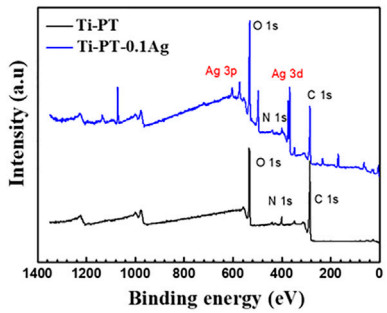


| Ti-PT | Ti-PT-0.1Ag |
|---|---|
| *Atom content (%)* | *Atom content (%)* |
| *C: 66.9* | *C: 49.61* |
| *N: 5.35* | *N: 7.25* |
| *O: 27.75* | *O: 38.84* |
| *Ag: 0* | *Ag: 3.48* |

**FIGURE 4 |** XPS spectra survey for Ti-PT and Ti-PT-0.1Ag surfaces with the surface elemental composition.

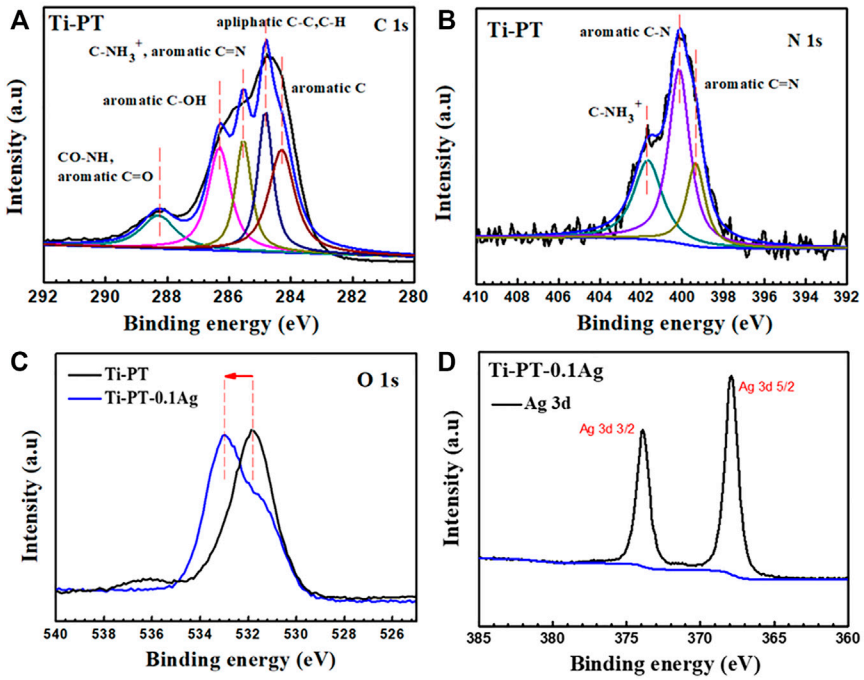


**FIGURE 5 |** High-resolution XPS spectra and fitting results of C 1s **(A)**, N 1s **(B)**, O 1s **(C)**, and Ag 3d **(D)** on Ti-PT and Ti-PT-0.1Ag.

0.25Ag, and Ti-PT-0.5Ag are shown in **Figure 6**. The agar plates of the bare Ti substrate displayed numerous bacterial colonies already after 24 h. Compared to those of Ti, significantly reduced bacteria were observed on those of the Ti-PT and Ti-PT-Ag groups. The tannic acid contained in the PT coating showed some antibacterial properties, especially the Ti-PT-Ag group, which showed 100% bacterial killing efficiency for *E. coli*. The silver normally exhibits antimicrobial properties, and the Ti-PT-Ag group showed antibacterial ability for *E. coli* within 12 h culture. The Ti-PT-0.1Ag group, with the lowest $AgNO_3$ concentration of 0.1 mg/ml, has shown the ability to inhibit *E. coli* colonies effectively.

## Cytotoxicity

The biocompatibility of the implant is crucial. Silver grafted onto the coating has antibacterial effect, but excessive concentration can lead to cytotoxicity. Therefore, the mouse fibroblast cell was used for cytotoxicity evaluation of the samples. The typical fluorescence images and CCK value of cells cultured on samples for 1 day are shown in **Figure 7**. After 24 h culture, the viability of cell growth on Ti, Ti-PT, and Ti-PT-0.1Ag showed no significant difference, which is similar to that of blank. There was a decrease in cell number observed when cultured on the 0.1 mM-$AgNO_3$-treated Ti metal surface. However, when fibroblast cells were cultured on the surface of Ti-PT-0.25Ag and Ti-PT-0.5Ag, the number and activity of cells were significantly reduced. The Ti-PT-0.1Ag did not cause significant cytotoxicity to fibroblast cells demonstrating its good biocompatibility. The results showed that the graft concentration of 0.1 mg/ml silver nitrate was safe, which

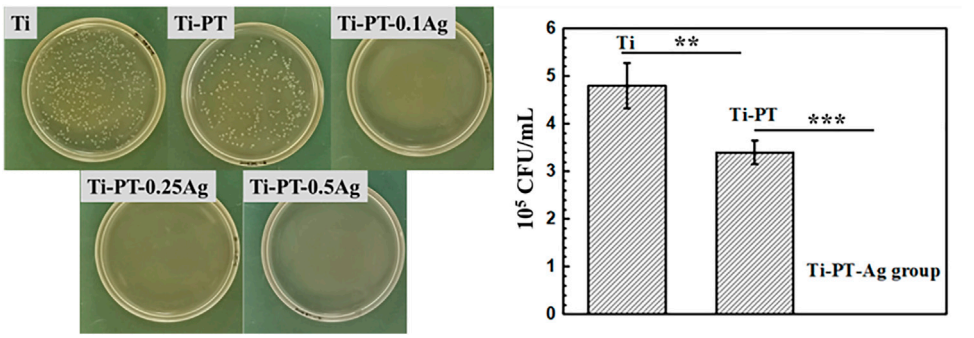


**FIGURE 6 |** Photographs (left) and the number (right) of *E. coli* colonies formation on Ti, Ti-PT, Ti-P-0.1Ag, Ti-PT-0.25Ag, and Ti-PT-0.5Ag. Data are presented as mean ± SD and analyzed by one-way ANOVA (**$p$ < 0.01, ***$p$ < 0.001).

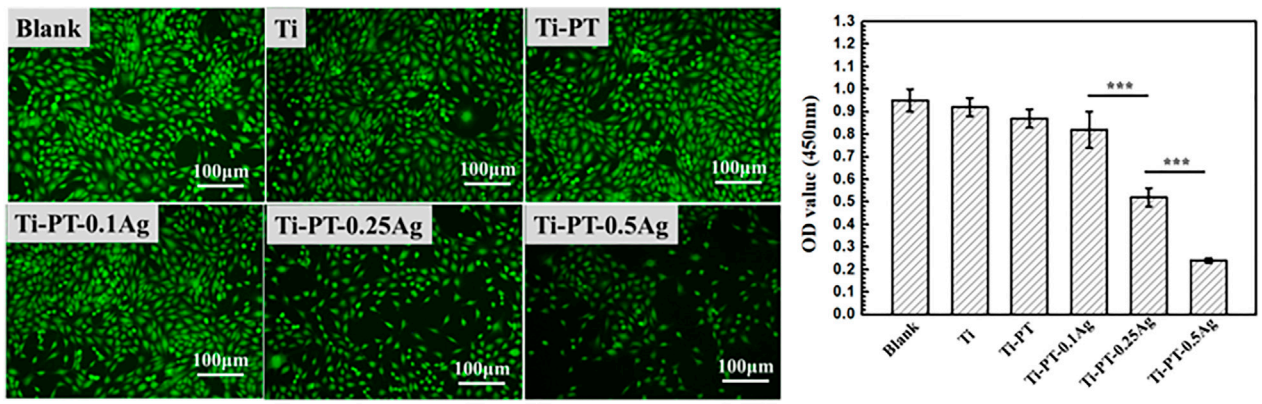


**FIGURE 7 |** Morphology of mouse fibroblast cells adhered on various samples and the viability of cells attached onto the samples after culture for 1 day (×100 magnification). Data are presented as mean ± SD and analyzed by one-way ANOVA (***$p$ < 0.001).

not only had no toxic effect on human cells but also had effective antibacterial activity.

## CONCLUSION

In this work, an Ag-incorporated polydopamine/tannic acid coating was prepared on pure titanium via the simple immersion method. Initially, dopamine and tannic acid formed a self-polymerizing coating on pure titanium via Michael-type addition and Schiff base reaction. Then, the phenolic hydroxyl functional groups on the coating were used to complex Ag ions. The results demonstrated that Ti-PT-Ag possesses antibacterial ability and cytocompatibility compared with bare Ti and Ti-PT. The Ti-PT-0.1Ag showed no significant cytotoxicity toward the mouse fibroblast cell and improved antibacterial properties toward *E. coli*. The result showed that the balance between effective antibacterial activity and cytotoxicity can be achieved by controlling the Ag-loading dose in the coating. The Ag-incorporated polydopamine/tannic acid coating might be used as an antibacterial and biocompatible platform for potential orthopedic implants.

## DATA AVAILABILITY STATEMENT

The original contributions presented in the study are included in the article/Supplementary Material, further inquiries can be directed to the corresponding authors.

## AUTHOR CONTRIBUTIONS

HZ, XS and ZF: work concept or design. HZ, XF, LM, BZ and RL: data collection. HZ, HW and CT: drafting the manuscript. YW, LM and SH: made important revisions to the manuscript. HZ, XS, ZF, XF, LM, HW, CT, BZ, RL, YW and SH: approval of the final version of the manuscript for publication.

## FUNDING

This work was supported by the National Natural Science Foundation of China (52101286), Opening Project of Sichuan University of Science and Engineering, Material Corrosion and

Protection Key Laboratory of Sichuan Province (2019CL18), Sichuan Province Science and Technology Support Program (2020YFG0215), Panzhihua Municipal Science and Technology Support Program (2019ZD-S-43), and Vanadium and Titanium Resource Comprehensive Utilization Key Laboratory of Sichuan Province (2018FTSZ29).

## REFERENCES

Bai, L., Hang, R., Gao, A., Zhang, X., Huang, X., Wang, Y., et al. (2015). Nanostructured Titanium-Silver Coatings with Good Antibacterial Activity and Cytocompatibility Fabricated by One-step Magnetron Sputtering. *Appl. Surf. Sci.* 355, 32–44. doi:10.1016/j.apsusc.2015.07.064

Bancirova, M. (2010). Comparison of the Antioxidant Capacity and the Antimicrobial Activity of Black and green tea. *Food Res. Int.* 43 (5), 1379–1382. doi:10.1016/j.foodres.2010.04.020

Bronk, J. K., Russell, B. H., Rivera, J. J., Pasqualini, R., Arap, W., Höök, M., et al. (2014). A Multifunctional Streptococcal Collagen-Mimetic Protein Coating Prevents Bacterial Adhesion and Promotes Osteoid Formation on Titanium. *Acta Biomater.* 10 (7), 3354–3362. doi:10.1016/j.actbio.2014.04.005

Cabal, B., Cafini, F., Esteban-Tejeda, L., Alou, L., Bartolomé, J. F., Sevillano, D., et al. (2012). Inhibitory Effect on *In Vitro* Streptococcus Oralis Biofilm of a Soda-Lime Glass Containing Silver Nanoparticles Coating on Titanium Alloy [J]. *PLoS One* 7 (8), e42393. doi:10.1371/journal.pone.0042393

Carloni, P., Tiano, L., Padella, L., Bacchetti, T., Customu, C., Kay, A., et al. (2013). Antioxidant Activity of white, green and Black tea Obtained from the Same tea Cultivar. *Food Res. Int.* 53 (2), 900–908. doi:10.1016/j.foodres.2012.07.057

Chen, D., and Dou, Q. (2008). Tea Polyphenols and Their Roles in Cancer Prevention and Chemotherapy. *Ijms* 9 (7), 1196–1206. doi:10.3390/ijms9071196

Chen, S., Zhang, J., Chen, Y., Zhao, S., Chen, M., Li, X., et al. (2015). Application of Phenol/Amine Copolymerized Film Modified Magnesium Alloys: Anticorrosion and Surface Biofunctionalization. *ACS Appl. Mater. Inter.* 7 (44), 24510–24522. doi:10.1021/acsami.5b05851

Chen, X., Hirt, H., Li, Y., Gorr, S.-U., and Aparicio, C. (2014). Antimicrobial GL13K Peptide Coatings Killed and Ruptured the Wall of Streptococcus Gordonii and Prevented Formation and Growth of Biofilms. *PLoS One* 9 (11), e111579. doi:10.1371/journal.pone.0111579

Cheng, H., Li, Y., Huo, K., Gao, B., and Xiong, W. (2014). Long-lastingin Vivoandin Vitroantibacterial Ability of Nanostructured Titania Coating Incorporated with Silver Nanoparticles. *J. Biomed. Mater. Res.* 102 (10), 3488–3499. doi:10.1002/jbm.a.35019

Cheng, Y. F., Pranantyo, D., Kasi, G., Lu, Z. S., Li, C. M., and Xu, L. Q. (2020). Amino-containing Tannic Acid Derivative-Mediated Universal Coatings for Multifunctional Surface Modification. *Biomater. Sci.* 8 (8), 2120–2128. doi:10.1039/d0bm00242a

Chouirfa, H., Bouloussa, H., Migonney, V., and Falentin-Daudré, C. (2019). Review of Titanium Surface Modification Techniques and Coatings for Antibacterial Applications. *Acta Biomater.* 83, 37–54. doi:10.1016/j.actbio.2018.10.036

Elias, C. N., Lima, J. H. C., Valiev, R., and Meyers, M. A. (2008). Biomedical Applications of Titanium and its Alloys. *Jom* 60 (3), 46–49. doi:10.1007/s11837-008-0031-1

Esposito, S., and Leone, S. (2008). Prosthetic Joint Infections: Microbiology, Diagnosis, Management and Prevention. *Int. J. Antimicrob. Agents* 32 (4), 287–293. doi:10.1016/j.ijantimicag.2008.03.010

Ferraris, S., and Spriano, S. (2016). Antibacterial Titanium Surfaces for Medical Implants. *Mater. Sci. Eng. C* 61, 965–978. doi:10.1016/j.msec.2015.12.062

Ferruzzi, M. G. (2010). The Influence of Beverage Composition on Delivery of Phenolic Compounds from Coffee and tea. *Physiol. Behav.* 100 (1), 33–41. doi:10.1016/j.physbeh.2010.01.035

He, X., Gopinath, K., Sathishkumar, G., Guo, L., Zhang, K., Lu, Z., et al. (2021). UV-assisted Deposition of Antibacterial Ag-Tannic Acid Nanocomposite Coating. *ACS Appl. Mater. Inter.* 13 (17), 20708–20717. doi:10.1021/acsami.1c03566

Hench, L. L., Splinter, R. J., Allen, W. C., and Greenlee, T. K. (1971). Bonding Mechanisms at the Interface of Ceramic Prosthetic Materials. *J. Biomed. Mater. Res.* 5 (6), 117–141. doi:10.1002/jbm.820050611

Høiby, N., Bjarnsholt, T., and Moser, C. (2015). ESCMID Guideline for the Diagnosis and Treatment of Biofilm Infections 2014. *Clin. Microbiol. Infec* 21, S1–S25.

Huang, S., Zhang, Y., Shi, J., and Huang, W. (2016). Superhydrophobic Particles Derived from Nature-Inspired Polyphenol Chemistry for Liquid marble Formation and Oil Spills Treatment. *ACS Sustain. Chem. Eng.* 4 (3), 676–681. doi:10.1021/acssuschemeng.6b00149

Janković, A., Eraković, S., Ristoscu, C., Mihailescu Serban, N., Duta, L., Visan, A., et al. (2015). Structural and Biological Evaluation of Lignin Addition to Simple and Silver-Doped Hydroxyapatite Thin Films Synthesized by Matrix-Assisted Pulsed Laser Evaporation. *J. Mater. Sci. Mater. Med.* 26 (1), 5333–5414. doi:10.1007/s10856-014-5333-y

Jemat, A., Ghazali, M. J., and Razali, M. (2015). Surface Modifications and Their Effects on Titanium Dental Implants. *Biomed. Res. Int.* 2015, 1–11. doi:10.1155/2015/791725

Kulkarni, M., Mazare, A., Gongadze, E., Perutkova, Š., Kralj-Iglič, V., Milošev, I., et al. (2015). Titanium Nanostructures for Biomedical Applications. *Nanotechnology* 26 (6), 062002. doi:10.1088/0957-4484/26/6/062002

Lee, J.-H., Moon, S.-K., Kim, K.-M., and Kim, K.-N. (2013). Modification of TiO2nanotube Surfaces by Electro-spray Deposition of Amoxicillin Combined with PLGA for Bactericidal Effects at Surgical Implantation Sites. *Acta Odontologica Scand.* 71 (1), 168–174. doi:10.3109/00016357.2011.654256

Leopoldini, M., Russo, N., and Toscano, M. (2011). The Molecular Basis of Working Mechanism of Natural Polyphenolic Antioxidants. *Food Chem.* 125 (2), 288–306. doi:10.1016/j.foodchem.2010.08.012

Luo, J., Lai, J., Zhang, N., Liu, Y., Liu, R., and Liu, X. (2016). Tannic Acid Induced Self-Assembly of Three-Dimensional Graphene with Good Adsorption and Antibacterial Properties. *ACS Sustain. Chem. Eng.* 4 (3), 1404–1413. doi:10.1021/acssuschemeng.5b01407

Luo, R., Tang, L., Wang, J., Zhao, Y., Tu, Q., Weng, Y., et al. (2013). Improved Immobilization of Biomolecules to Quinone-Rich Polydopamine for Efficient Surface Functionalization. *Colloids Surf. B: Biointerfaces* 106, 66–73. doi:10.1016/j.colsurfb.2013.01.033

McConoughey, S. J., Howlin, R., Granger, J. F., Manring, M. M., Calhoun, J. H., Shirtliff, M., et al. (2014). Biofilms in Periprosthetic Orthopedic Infections. *Future Microbiol.* 9 (8), 987–1007. doi:10.2217/fmb.14.64

Mei, S., Wang, H., Wang, W., Tong, L., Pan, H., Ruan, C., et al. (2014). Antibacterial Effects and Biocompatibility of Titanium Surfaces with Graded Silver Incorporation in Titania Nanotubes. *Biomaterials* 35 (14), 4255–4265. doi:10.1016/j.biomaterials.2014.02.005

Orapiriyakul, W., Young, P. S., Damiati, L., and Tsimbouri, P. M. (2018). Antibacterial Surface Modification of Titanium Implants in Orthopaedics. *J. Tissue Eng.* 9, 2041731418789838. doi:10.1177/2041731418789838

Park, S. W., Lee, D., Choi, Y. S., Jeon, H. B., Lee, C.-H., Moon, J.-H., et al. (2014). Mesoporous TiO2 Implants for Loading High Dosage of Antibacterial Agent. *Appl. Surf. Sci.* 303, 140–146. doi:10.1016/j.apsusc.2014.02.111

Rodríguez, A. R. C., Saiz-Poseu, J., and García-Pardo, J. (2016). Biocompatible Polydopamine-like Particles for the Removal of Heavy Metals at Extremely Low Concentrations. *RSC Adv.* 6 (46), 40058–40066.

Sagbas, S., Aktas, N., and Sahiner, N. (2015). Modified Biofunctional P(tannic Acid) Microgels and Their Antimicrobial Activity. *Appl. Surf. Sci.* 354, 306–313. doi:10.1016/j.apsusc.2015.06.163

Scribante, A., Montasser, M., Radwan, E., Bernardinelli, L., Alcozer, R., Gandini, P., et al. (2018). Reliability of Orthodontic Miniscrews: Bending and Maximum Load of Different Ti-6Al-4V Titanium and Stainless Steel Temporary Anchorage Devices (TADs). *Materials* 11 (7), 1138. doi:10.3390/ma11071138

Spriano, S., Yamaguchi, S., Baino, F., and Ferraris, S. (2018). A Critical Review of Multifunctional Titanium Surfaces: New Frontiers for Improving Osseointegration and Host Response, Avoiding Bacteria Contamination. *Acta Biomater.* 79, 1–22. doi:10.1016/j.actbio.2018.08.013

Srivastava, S., Bankar, R., and Roy, P. (2013). Assessment of the Role of Flavonoids for Inducing Osteoblast Differentiation in Isolated Mouse Bone Marrow Derived Mesenchymal Stem Cells. *Phytomedicine* 20 (8-9), 683–690. doi:10.1016/j.phymed.2013.03.001

Suer, B. T., Kocyigit, I. D., Kaman, S., Tuz, H. H., Tekin, U., and Atil, F. (2014). Biomechanical Evaluation of a New Design Titanium Miniplate for the

Treatment of Mandibular Angle Fractures. *Int. J. Oral Maxillofac. Surg.* 43 (7), 841–845. doi:10.1016/j.ijom.2014.01.011

Vester, H., Holzer, N., Neumaier, M., Lilianna, S., Nüssler, A. K., and Seeliger, C. (2014). Green Tea Extract (GTE) Improves Differentiation in Human Osteoblasts during Oxidative Stress. *J. Inflamm.* 11 (1), 15. doi:10.1186/1476-9255-11-15

Xu, Y. C., Wang, Z. X., Cheng, X. Q., Xiao, Y. C., and Shao, L. (2016). Positively Charged Nanofiltration Membranes via Economically Mussel-Substance -Simulated Co-deposition for Textile Wastewater Treatment. *Chem. Eng. J.* 303, 555–564. doi:10.1016/j.cej.2016.06.024

Zhang, H., Shen, X., Wang, J., Huang, N., Luo, R., Zhang, B., et al. (2019). Multistep Instead of One-step: A Versatile and Multifunctional Coating Platform for Biocompatible Corrosion Protection. *ACS Biomater. Sci. Eng.* 5 (12), 6541–6556. doi:10.1021/acsbiomaterials.9b01459

Zhang, H., Xie, L., Shen, X., Shang, T., Luo, R., Li, X., et al. (2018). Catechol/polyethyleneimine Conversion Coating with Enhanced Corrosion protection of Magnesium Alloys: Potential Applications for Vascular Implants. *J. Mater. Chem. B* 6 (43), 6936–6949. doi:10.1039/c8tb01574k

Zhang, X., Li, Z., Yuan, X., Cui, Z., Bao, H., Li, X., et al. (2013). Cytotoxicity and Antibacterial Property of Titanium alloy Coated with Silver Nanoparticle-Containing Polyelectrolyte Multilayer. *Mater. Sci. Eng. C* 33 (5), 2816–2820. doi:10.1016/j.msec.2013.03.010

**Conflict of Interest:** The authors declare that the research was conducted in the absence of any commercial or financial relationships that could be construed as a potential conflict of interest.

**Publisher's Note:** All claims expressed in this article are solely those of the authors and do not necessarily represent those of their affiliated organizations, or those of the publisher, the editors, and the reviewers. Any product that may be evaluated in this article, or claim that may be made by its manufacturer, is not guaranteed or endorsed by the publisher.

frontiers | Frontiers in Bioengineering and Biotechnology

ORIGINAL RESEARCH
published: 14 April 2022
doi: 10.3389/fbioe.2022.855013

# A Hydrogen Bonds-Crosslinked Hydrogels With Self-Healing and Adhesive Properties for Hemostatic

*Han Yu[1,2,3*†], Qiaohong Xiao[2†], Guilin Qi[2], Feixiang Chen[4], Biyue Tu[5], Suo Zhang[5], Yinping Li[3], Yun Chen[4], Hui Yu[2*] and Peng Duan[2*]*

[1]Department of Pathology, Xiangyang No.1 People's Hospital, Hubei University of Medicine, Xiangyang, China, [2]Key Laboratory of Zebrafish Modeling and Drug Screening for Human Diseases of Xiangyang City, Department of Obstetrics and Gynaecology, Xiangyang No.1 People's Hospital, Hubei University of Medicine, Xiangyang, China, [3]Department of Pathophysiology and Hubei Province Key Laboratory of Allergy and Immunology, School of Basic Medical Sciences, Wuhan University, Wuhan, China, [4]Department of Biomedical Engineering and Hubei Province Key Laboratory of Allergy and Immunology, School of Basic Medical Sciences, Wuhan University, Wuhan, China, [5]Fourth Clinical College, Hubei University of Medicine, Shiyan, China

OPEN ACCESS

**Edited by:**
Guicai Li,
Nantong University, China

**Reviewed by:**
Lidong Zhang,
East China Normal University, China
Hsiu-Wen Chien,
National Kaohsiung University of Science and Technology, Taiwan

***Correspondence:**
Han Yu
yuhanqh@163.com
Hui Yu
yuhui06127@163.com
Peng Duan
meduanpeng@163.com

[†]These authors have contributed equally to this work and share first authorship

**Specialty section:**
This article was submitted to Biomaterials, a section of the journal Frontiers in Bioengineering and Biotechnology

**Received:** 14 January 2022
**Accepted:** 21 March 2022
**Published:** 14 April 2022

**Citation:**
Yu H, Xiao Q, Qi G, Chen F, Tu B, Zhang S, Li Y, Chen Y, Yu H and Duan P (2022) A Hydrogen Bonds-Crosslinked Hydrogels With Self-Healing and Adhesive Properties for Hemostatic. Front. Bioeng. Biotechnol. 10:855013. doi: 10.3389/fbioe.2022.855013

Hydrogels with adhesive properties have the potential for rapid haemostasis and wound healing in uncontrolled non-pressurized surface bleeding. Herein, a typical hydrogen bond-crosslinked hydrogel with the above functions was constructed by directly mixing solutions of humic acid (HA) and polyvinylpyrrolidone (PVP), in which the HA worked as a crosslinking agent to form hydrogen bonds with the PVP. By altering the concentration of HA, a cluster of stable and uniform hydrogels were prepared within 10 s. The dynamic and reversible nature of the hydrogen bonds gave the HA/PVP complex (HPC) hydrogels injectability and good flexibility, as well as a self-healing ability. Moreover, the numerous functional groups in the hydrogels enhanced the cohesion strength and interaction on the interface between the hydrogel and the substrate, endowing them with good adhesion properties. The unique chemical composition and cross-linking mechanism gave the HPC hydrogel good biocompatibility. Taking advantage of all these features, the HPC hydrogels obtained in this work were broadly applied as haemostatic agents and showed a good therapeutic effect. This work might lead to an improvement in the development of multifunctional non-covalent hydrogels for application to biomaterials.

**Keywords: hydrogel, hydrogen bond, adhesive, self-healing, hemostatic**

## INTRODUCTION

Hydrogels, which are generated by exploiting covalent and/or noncovalent interactions between polymeric components, have been extensively studied due to their unique "human tissue-like" properties, such as their toughness, permeability, biocompatibility, self-healing ability and wettability (Li D. et al., 2020; Poupart et al., 2020; Chen et al., 2021; Kim et al., 2021). In particular, hydrogels with self-healing ability can spontaneously repair the cracked network when deformation occurs, without external stimuli, and maintain their efficacy and integrity in complex physiological environments; consequently, they have attracted great attention in recent years. Self-healing hydrogels have demonstrated tremendous superiority in a range of fields, including drug delivery, tissue engineering and cell therapy. Many strategies have been explored to develop self-healing hydrogels (Liu and Hsu 2018; Lin et al., 2021; Kim et al., 2022). The introduction of dynamic

and reversible noncovalent interactions, including coordination bonds, ionic bonds, host-guest interaction and hydrogen bonds, could endow a hydrogel with a self-healing ability, as well as stimuli-responsive and adaptive properties (Cao et al., 2018; Huang et al., 2018; Yan et al., 2020). Among the wide ranges of noncovalent bonds, hydrogen bonds are commonly found in natural systems, due to their bonding strength and low toxicity, and have been widely used to design functional hydrogels (Chen et al., 2016; Zhang et al., 2022). Moreover, the hydrogen bonds in a hydrogel serve as sacrificial bonds and show an excellent toughening effect, by effectively dissipating external energy (Zhang et al., 2018). Hydrogen bond-crosslinked hydrogels have attracted particular interest for polymeric biomaterials.

However, hydrogen bonds existing in a hydrogel might easily be disturbed by water molecules, which may severely reduce their stability and crosslinking effect in an aqueous environment (Long et al., 2018). Thus, the preparation of functional hydrogels based on hydrogen bonds is still challenging. Various strategies have been explored to develop hydrogen bond crosslinking systems that have high efficiency. In recent years, researchers have found that the introduction of hydrophobic domains can effectively improve the stability of the hydrogen bond (Zhang X. et al., 2019; Dompe et al., 2019; Wang et al., 2019; Criado-Gonzalez et al., 2020) For instance, Wu and co-workers have developed hydrogels with robust hydrogen bond networks using methacrylamide (MAAm) and methacrylic acid (MAAc) as raw monomers. The carboxyl and amide groups in the hydrogel formed stable hydrogen bond interactions that were effectively promoted by the hydrophobic methyl groups. The obtained hydrogels possessed excellent mechanical properties (elastic modulus: 2.3–217.3 MPa; fracture strength: 1.2–8.3 MPa; fracture strain: 200–620%), good shape memory performance, and cycling stability (Wang et al., 2019). According to this principle, molecules with both hydrophobic groups and active functional groups, including tannic acids (TA), lignin, and silicotungstic acid, were widely adopted as cross-linking agents to prepare hydrogen bond-crosslinked hydrogels (Zhang X. et al., 2019; Zhang Z.-X. et al., 2019; Peng et al., 2020). Humic acid (HA) is a degradation product of animals and plants, and contains almost 50% of the natural organic carbon source on earth (Ratie et al., 2021; Venezia et al., 2021). It is a versatile material in agricultural, environmental and healthcare applications due to its rich reserves, low cost and degradable features (Hou et al., 2018). In addition, the coexistence of hydrophobic groups and active functional groups make HA a potential candidate as a hydrogen bond crosslinking agent.

Hydrogels with a high adhesion strength to various substrates have also aroused growing interest in many practical applications, such as wound dressing, haemostatic agents and soft electronic devices (He et al., 2018; Wei et al., 2019; Zhang et al., 2020). Previous works have reported diverse strategies for the preparation of multifunction adhesive hydrogels, including chemical anchorage, physical adhesion, mechanical interlocking and bio-inspired means (Karami et al., 2018; Yang et al., 2018). Physical adhesion interactions, like hydrogen bonds, electrostatic and hydrophobic interactions, at the interface between the hydrogel and substrate were studied due to their multipurpose and reusable abilities (Xing et al., 2021; Li et al., 2022). For example, Guo developed adhesive hydrogels based on derivatives of hyaluronic acid, poly (ethylene glycol)-*co*-poly (glycerol sebacate) and cuttlefish melanin nanoparticles. The amino and catechol groups formed multiple interactions with tissue, which enabled the attachment to the skin surface to be maintained (Li et al., 2022).

Considering the requirements of hydrogel-based biomaterials, a novel HA/polyvinylpyrrolidone (PVP) complex (HPC) hydrogel with self-healing and adhesion properties has been developed in this work. The gelation process is forthright and rapid, using one-step mixing of aqueous solutions of HA and PVP. The construction of the HPC hydrogel is driven by the hydrogen bonds between HA and PVP, which are readily formed and adjusted. The dynamic and reversible hydrogen bond distributed in the hydrogel promotes the formation of a dynamic crosslinking network and endows the HPC hydrogel with good mechanical properties, injectability, self-healing properties and high adaptation to irregular substrates. In addition, the HPC hydrogels demonstrate good adhesion strength to multiple materials, which originates from the hydrogen bond between the HPC hydrogel and the surface of the substrates. The biologically compatible composition and gelation mechanism endows the HPC hydrogels with good biocompatibility, and they show good efficacy when serving as haemostatic agents in the bleeding model. The results suggest that this kind of self-healing, adhesive, injectable and haemostatic hydrogel exhibits great potential for application to biomedical materials.

## MATERIALS AND METHODS

### Materials

PVPs with Mw 8,000, 24,000, and 1,300,000 Da were bought from Aladdin (Shanghai, China). HA, NaOH, HCl, urea and dimethyl sulfoxide (DMSO) were bought from Sinopharm (Shanghai, China) and were used without any purification. Porcine skin was provided by the supermarket and was cleaned before use.

### Preparation of HA/PVP complex Hydrogel

HA and PVP were separately dissolved in water. The two solutions were then uniformly mixed and vigorously shaken. The pH value was adjusted to 7 using 0.1 M HCl aqueous solution. The solutions tended to gelation, and the HPC hydrogel was finally formed. The concentration of PVP was 15 wt%.

### Characterizations

All tensile tests of the HPC hydrogel were performed on a universal tensile tester (Instron machine 3343) at room temperature. The samples were stretched at a deformation rate of 100 mm/min. The toughness of the HPC was calculated by integrating the area under the stress-strain curve. The elastic modulus was determined by the slope of the initial stress-strain curves.

**TABLE 1 |** Composition and mechanical parameters of the prepared HPC hydrogels.

| Samples | $c_{HA}$ (wt%) | $c_{PVP}$ (wt%) | Fracture Stress (KPa) | Fracture Strain (%) |
|---|---|---|---|---|
| HPC-1 | 6 | 15 | 11.8 | 776 |
| HPC-2 | 8 | 15 | 18.9 | 643 |
| HPC-3 | 10 | 15 | 17.0 | 403 |
| HPC-4 | 4 | 15 | -[c] | -[c] |
| HPC-5 | 6 | 12 | -[c] | -[c] |

$C_{HA}$: *Concentration of HA.*
$C_{PVP}$: *Concentration of PVP.*
*c: Too weak to be meaningful.*

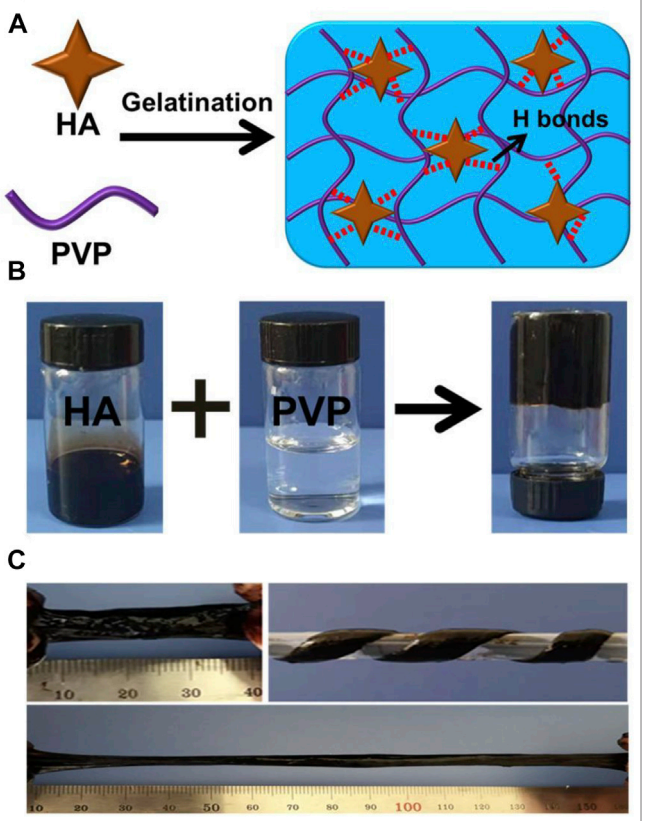


**FIGURE 1 | (A)** Schematic illustration of HPC hydrogels crosslinked by HA in an ultrafast process. **(B)** Images showing the preparation process of the HPC hydrogels. **(C)** Photographs of the HPC hydrogel. The obtained HPC-2 hydrogel was uniform and could be easily stretched and twisted.

## Dynamic Rheological Measurements of HA/PVP Complex Hydrogels

Dynamic rheological measurements were taken on the ARES RFSIII rheometer (TA Instruments, United States) using flat plates (40 mm). The gap spacing was set to 2 mm. Oscillatory frequency sweep measurements were carried out to determine the storage modulus (G′) and loss modulus (G″) of the hydrogels at 25°C. The strain was set to 10%, with the shear frequency ($\omega$) ranging from 0.1 to 100 rad/s. The temperature sweep test was conducted under the fixed frequency and strain of 10 rad/s and 10%, respectively.

## Adhesion Properties of HA/PVP Complex Hydrogels

Adhesion properties were measured using the lap-shear tension loading test. The HPC hydrogels were sandwiched between the overlap areas of two pieces of the substrate (for example, porcine skin with a regular rectangular shape), and the contact areas were measured and calculated. The samples to be tested were placed at room temperature for 15 min prior to the tensile test, which was carried out using a stretching rate of 20 mm/min. The adhesion strength of the samples to other materials was tested in the same way.

## Cytotoxicity of HA/PVP Complex Hydrogels

The biocompatibility of the HPC hydrogels was tested with the Calcein-AM/PI double staining method. The HPC hydrogels were freeze-dried and sterilized before testing. The HPC hydrogels were seeded with L929 cells with a density of $4 \times 10^4$ cells per sample, incubated for 24 h, and the cells then stained with calcein-AM and PI, respectively. The phalloidin staining evaluation was also performed according to the kit manufacturer's protocols. The cell morphology was observed by a laser confocal microscope (FV3000, Olympus).

## Haemolysis Evaluation of HA/PVP Complex Hydrogels

The haemolysis evaluation was conducted to assess the blood biocompatibility of the HPC hydrogel. In brief, rabbit blood was collected and diluted with PBS solution (2.5 ml). The series of HPC hydrogels were incubated in PBS solution (8 ml) in a water bath (37°C) for 1 h. Then, 0.2 ml diluted fresh blood was slowly added into the mixed solutions. The obtained mixture was incubated for 60 min, transferred into a centrifuge tube and centrifuged at 5,000 rpm for 8 min. Optical photos of the haemolysis results were taken. At the same time, the absorbance of the supernatant was measured at 540 nm using a UV spectrometer (UV-9200/VIS-7220G, China). A natural polymer-based hydrogel were chosen to be the control group. The haemolysis ratio was calculated as follows:

$$\text{Haemolysis ratio } \% = [(A_S - A_N)/(A_P - A_N)] \times 100\%$$

where $A_S$, $A_P$, and $A_N$ are the optical density values from the hydrogel, PBS solution, and deionized water, respectively.

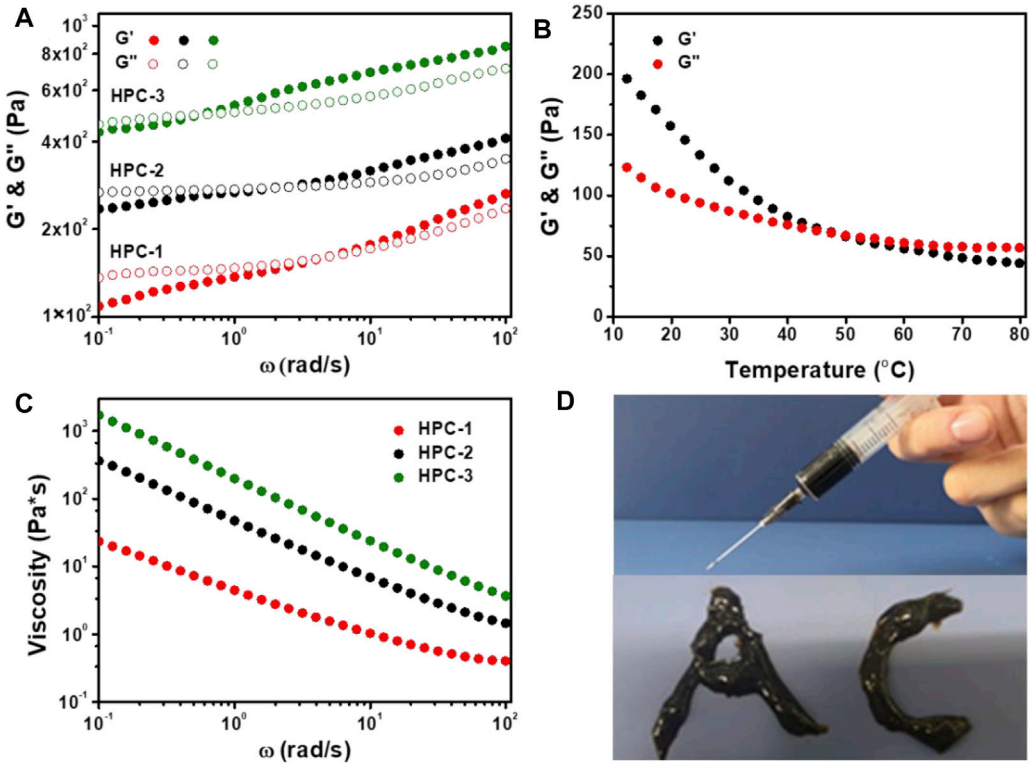


**FIGURE 2 | (A)** G′ and G″ as a function of $\omega$ for the HPC hydrogels. **(B)** Temperature dependence of G′ and G″ for the HPC-2 hydrogel **(C)** The shear viscosity of HPC hydrogels as a function of ω. **(D)** HPC-2 hydrogel used as ink to write words.

## Biohistocompatibility Evaluation of HA/PVP Complex Hydrogel

The HPC-2 hydrogel was transplanted into rats, and the heart, liver, spleen, lung and kidney tissues of the rats were harvested 14 days later. These tissue samples were observed in the HE staining.

## Haemostatic Performance and Wound Healing Behaviour of HA/PVP Complex Hydrogels

The liver bleeding model of the rat was selected to evaluate the *in vivo* haemostatic ability of HPC hydrogels. Before the animal experiments, male SD rats were subjected to abdominal anaesthesia. The anaesthetised rats were immobilized, and the abdomen of the rats was cut open with a scalpel to expose the liver. The liver of the rat was then cut open with a scalpel and a filter paper placed under the liver to collect the blood from the rat. HPC-2 hydrogel, with a weight of 2 g, was appended to the liver to treat the injury. No treatment was given in the control group.

The haemostatic index was tested through the whole blood coagulation experiment. Fresh samples of the rats' arterial blood were mixed evenly with gelatin sponge and freeze-dried hydrogel samples. $CaCl_2$ solution (20 μL, 0.2 mol/L) was then added and the mixture placed in a water bath (37°C). The light absorbance of the solutions at 540 nm was then measured, wherein deionized water was used as a control. The haemostatic index was calculated as follows:

$$\text{Haemostatic index}\,(\%) = A_h/A_c \times 100\%$$

where $A_h$ is the absorbency of HPC hydrogel group and $A_c$ represents the absorbency of the control group.

## Statistical Analysis

All statistical analyses were performed with SPSS software (SPSS software version 12.0, SPSS, Chicago, IL, United States). The data were expressed as the mean ± standard deviation (SD). All experiments were repeated at least three times. Statistical analysis across multiple groups was performed using one-way analysis of variance (ANOVA), followed by Fisher's LSD post-hoc test for homogeneity of variance. Two-sided $p$ values of <0.05, <0.01 and <0.001 were considered as statistically significant or highly significant, respectively. Line graphs and bar graphs were generated using GraphPad PRISM Version 8.0 (San Diego, CA, United States).

# RESULTS AND DISCUSSION

## Preparation of Various HA/PVP Complex Hydrogels

Various HPC hydrogels were successfully prepared by changing the HA content of the hydrogels. The specific parameters of the experiment are shown in **Table 1**.

We observed a rapid gelation phenomenon based on the crosslinking effect of the hydrogen bonds between HA and PVP.

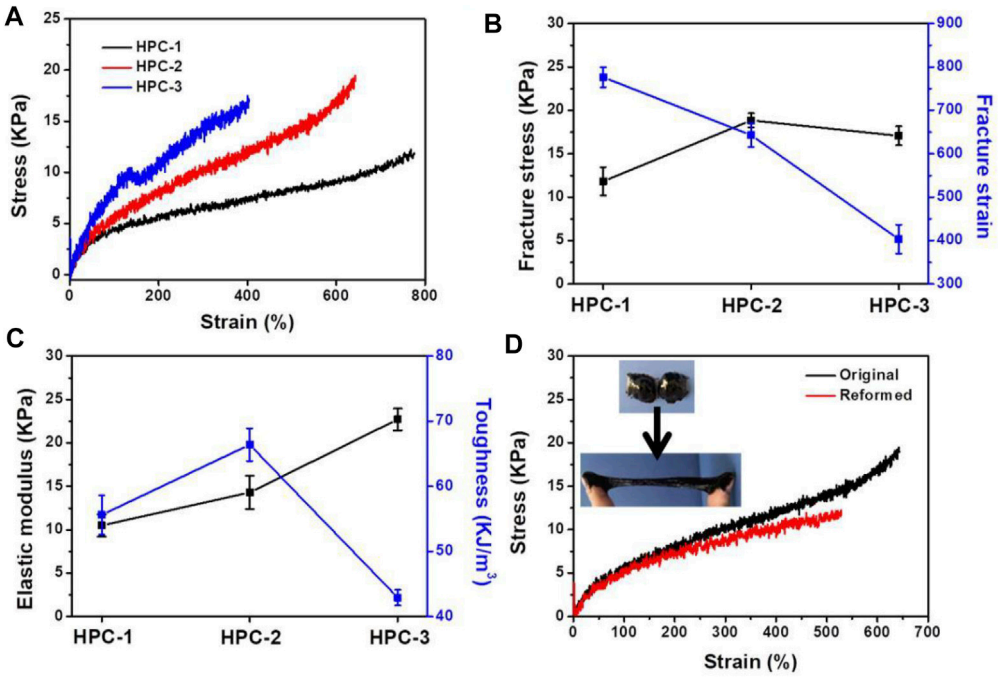


**FIGURE 3 | (A)** Tensile tests of the HPC hydrogels. **(B)** Fracture stress and strain. **(C)** Elastic modulus and toughness of the HPC hydrogels. **(D)** Tensile stress-strain curves of the integrated HPC-2 sample and the reformed one.

**Figures 1A,B** show the fast and convenient manufacturing procedure of the HPC hydrogels. Different concentrations of HA and PVP solutions were prepared in advance. It is noteworthy that HA was dissolved in a weakly alkaline aqueous solution (pH = 9) to convert the carboxyl groups to carboxylate and improve its solubility in water. By simply mixing the prepared HA and PVP solutions together and adjusting the pH value of the mixture to neutral, viscous and flexible hydrogels with a black homogeneous appearance were finally obtained within 10 seconds (**Figure 1C**). Thus, the Mw of PVP we used in this We then adjusted the ratio of HA to PVP, to prepare various HPC hydrogels with different characteristics. One of the most important factors that influenced the state of the hydrogel was the molecular weight of the polymer. The molecular weights (Mw) of PVP played an important role in the formation of the hydrogel. When the Mw of PVP was low, the hydrogel could not form and only solutions were obtained (**Supplementary Figure S1**). The Mw of PVP chosen to prepare the HPC hydrogel was 1,300,000 Da. It is worth noting that the concentration of PVP and HA could also affect the gelation process, as adequate polymer chains and crosslinking density were required to form the hydrogel (Dompé et al., 2019). Only when the concentration of both PVP and HA exceeded a certain value could HPC hydrogels with satisfactory performance be obtained. For example, when the concentration of PVP was lower than 15 wt% or the concentration of HA was 4 wt%, the obtained HPC samples were too weak to be tested. Based on this principle, the HPC-2 hydrogel was successfully prepared using 8 wt % HA and 15 wt% PVP, which has the highest fracture stress (18.9 kPa) and appropriate fracture strain (643%). Thus, HPC-2 was chosen as the model material to further explore the gelation mechanism of the hydrogel (**Table 1**). The FT-IR of PVP and HPC-2 samples was given in **Supplementary Figure S2**. The chemical shift of amide groups on PVP (1,662 $cm^{-1}$) decreased to 1,645 $cm^{-1}$, indicating the existence of hydrogen bonding interaction between HA and PVP in HPC-2. When temperature increased, part of hydrogen bonds broke and the signal at around 1,644 $cm^{-1}$ became weak. When the temperature returned, the signal recovered to original one, showing the "dynamics and reversibility" properties of hydrogen bonds. When DMSO, DMF, or urea was added, the hydrogen bonds broke and the HPC hydrogels changed to solutions. The HPC hydrogel also showed reversible responsivity to $H^+$ and $OH^-$, indicating the dynamic and reversible properties of the hydrogen bonds (**Supplementary Figure S3**). The swelling ratios of the HPC hydrogels were tested. The maximum swelling ratio gradually increased with the relative content of HA increased. Like other non-covalent supramolecular hydrogels, the HPC hydrogel would gradually disintegrate due to the hydration when immersed in water (**Supplementary Figure S4**).

## Rheological Properties of HA/PVP Complex Hydrogels

Firstly, the strength and structural stability of the HPC hydrogels were evaluated using dynamic frequency sweep tests. As shown in **Figure 2A**, the phase change could be obviously observed in all

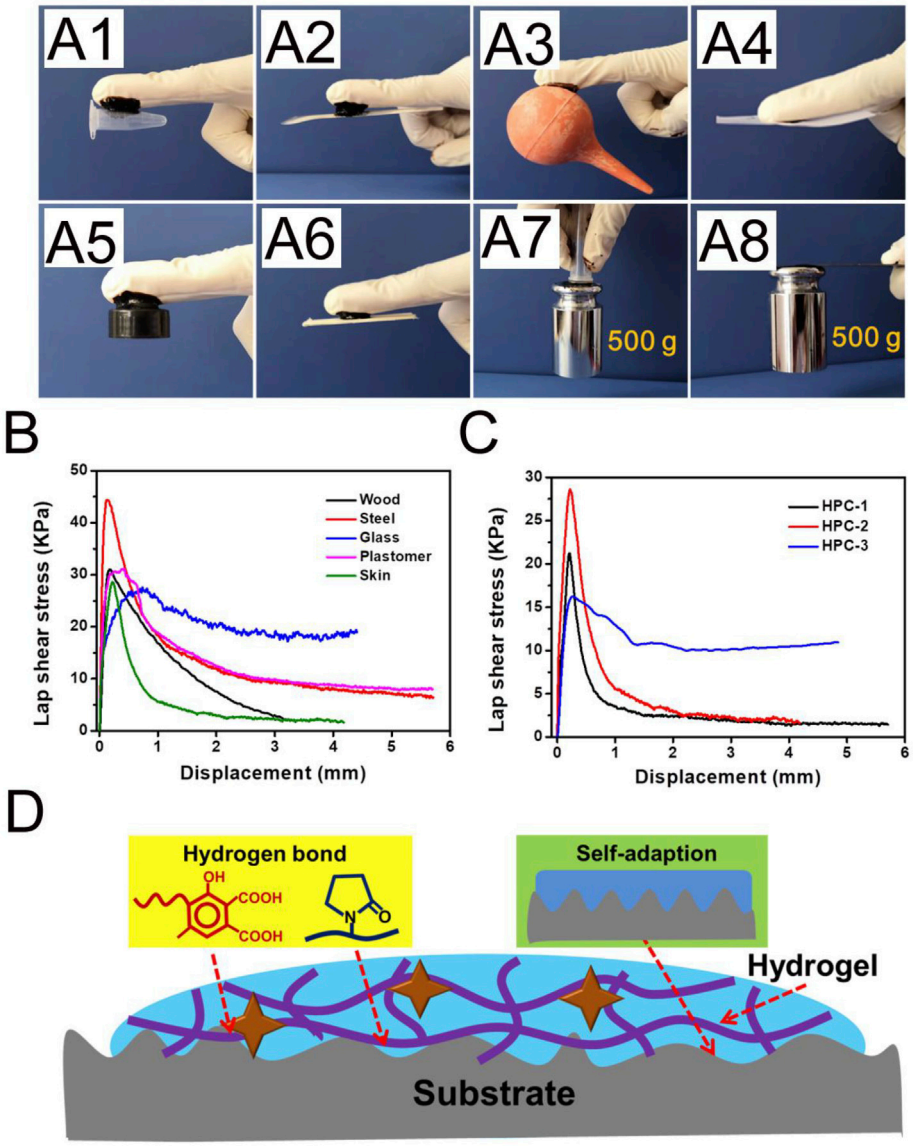


**FIGURE 4 | (A)** The HPC-2 hydrogel was used as glue to tightly adhere to plastomer, steel, rubber, paper and wood substrates, and put up the weight. **(B)** Adhesion mechanical curves of HPC-2 to various substrates. **(C)** Adhesion mechanical curves of HPC hydrogels to porcine skin. **(D)** The possible adhesion mechanism of the HPC hydrogels.

three samples, which showed similar characteristics to other noncovalent hydrogels. When the $\omega$ values were low, G′ was lower than G″, and the HPC samples behaved like viscous fluids, due to the stress dissipation (Grindy et al., 2015). As the strain frequency increased, G′ gradually exceed G″, and the HPC hydrogels exhibited obvious elastic behaviour (Chaudhuri et al., 2016). In addition, when the concentration of HA increased from 6 to 10 wt%, the crosslinking density increased and the critical frequencies (the intersection of G′ and G″) of the HPC hydrogels gradually reduced from 5.08 to 0.59 rad/s, which indicated that more compact and stable networks had finally formed.

We further employed rheological tests on the HPC-2 sample to measure its thermosensitivity. It was observed that G′ was higher than G″ at the initial temperature (**Figure 2B**). As the temperature increased, the hydrogen bonds in the HPC-2 hydrogel cracked, and G′ decreased obviously faster than G″, finally becoming lower than G″ when the temperature rose from 10°C to over 50°C. The inner hydrogen bond-crosslinked network disassembled, and the HPC-2 transformed to a liquid-like state. When the temperature decreased, the hydrogen bonds reformed and the HPC-2 returned to a solid-like gel state again. The reversible breakage and recombination of hydrogen bonds played an important role in this reversible thermosensitivity.

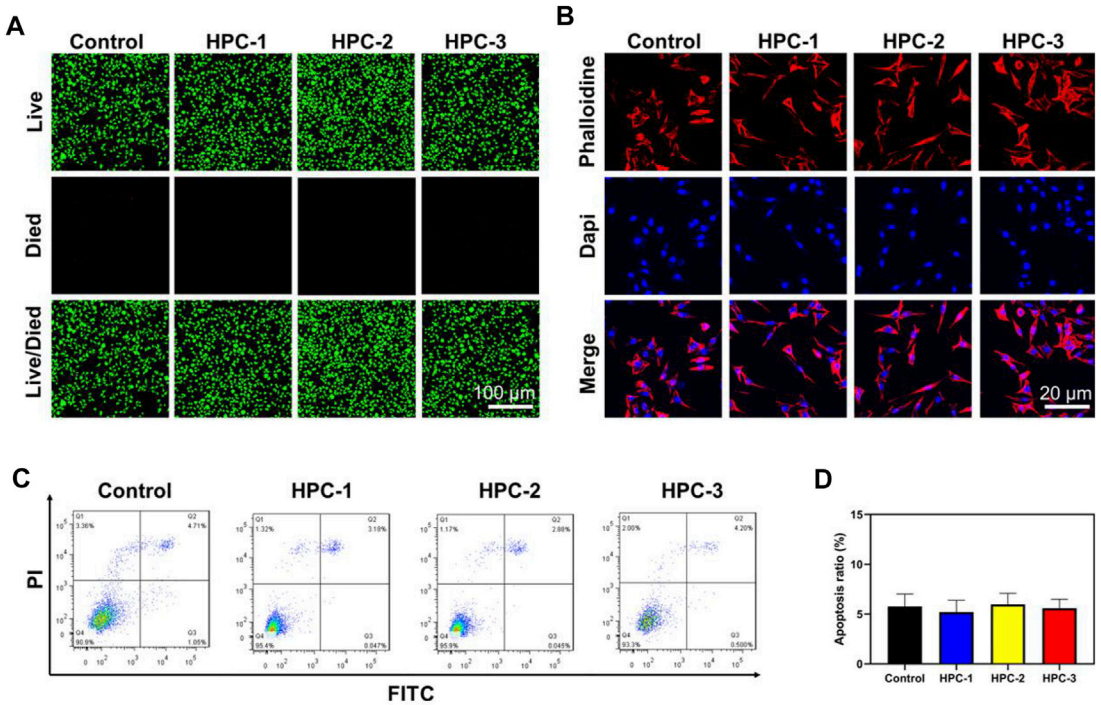


**FIGURE 5 |** The HPC hydrogels supported the adhesion of L929 cells. **(A)** Calcein-AM/PI double staining of L929 cells treated with HPC-1, -2 and -3 hydrogels. **(B)** IF images of F-actin. Blue signal: DAPI; red signal: F-actin. **(C)** Flow cytometry (FCM) analysis and **(D)** the corresponding apoptotic rate statistical result of the HPC hydrogels.

The HPC hydrogels also exhibited a typical shear-thinning behaviour. As shown in **Figure 2C**, when the shear rate increased, the viscosity of the HPC hydrogels obviously decreased, endowing them with good injectability. **Figure 2D** illustrates the letters "A" and "C" written with the HPC-2 hydrogel, further verifying its flexibility. The combination of thermosensitivity and injectability of the HPC hydrogels made it easy to add and extrude them from the syringe and then solidify them. The results suggest that HPC hydrogels have great potential in the field of biomaterials and 3D printing materials (Liu et al., 2020).

## Mechanical Properties of HA/PVP Complex Hydrogels

Typical stress-strain curves of the HPC hydrogels were used to measure their mechanical properties (**Figures 3A–C**). We fixed the concentration of PVP at 15 wt% to test the effect of crosslinking agents of HA on the mechanical properties of the obtained HPC hydrogels. The results showed that the mechanical performance of the HPC samples was highly dependent on the HA content in the hydrogel. When the concentration of HA was 6 wt%, the fracture stress and strain of HPC-1 were 11.8 KPa and 776%, respectively (**Figures 3A,B**). An increased content of HA could effectively improve the crosslinking density of the hydrogel: as the concentration of HA increased to 8 wt%, the fracture stress of HPC-2 increased to 18.9 KPa, while the fracture strain decreased to 643%. In addition, the toughness of the hydrogel increased from 55.6 to 66.4 kJ/m$^3$ (**Figure 3C**). As the concentration of HA further increased to 10 wt%, both the strength and flexibility of the HPC-3 hydrogel showed an apparent decrement, due to excessive crosslinking. The fracture stress of HPC-3 was 17.0 KPa, while the fracture strain and toughness of HPC-3 decreased to 403% and 42.9 kJ/m$^3$, respectively. The elastic modulus of the HPC hydrogels increased from 10.5 to 20.7 KPa when the concentration of HA increased from 6 to 10 wt%. This might mainly be due to the over-high crosslinking density causing the mobility of the polymer chains to decrease, leading to a more rigid polymeric network and heterogeneous structure, which finally reduced the toughness (Cao et al., 2020). In general, the HPC hydrogels showed good tensile properties.

Hydrogels possessing a self-healing ability can maintain their performance and play a unique role when there is external damage, and these hydrogels are in high demand in various areas, including tissue engineering and flexible electronics (Tian et al., 2020). The dynamic and reversible crosslinking of the hydrogen bonds between HA and PVP endowed the HPC hydrogel with self-healing properties. As shown in **Figure 3D**, the tensile tests were applied to the original and reformed HPC-2 hydrogels to quantitatively explore the healing effect. The cracked HPC-2 hydrogel was placed at 20°C for 10 min, and the fracture stress was tested to be 11.7 KPa, which was equal to 62% of its original value. The fracture strain and toughness of the reformed HPC-2 hydrogel recovered around 80% to its original level, and

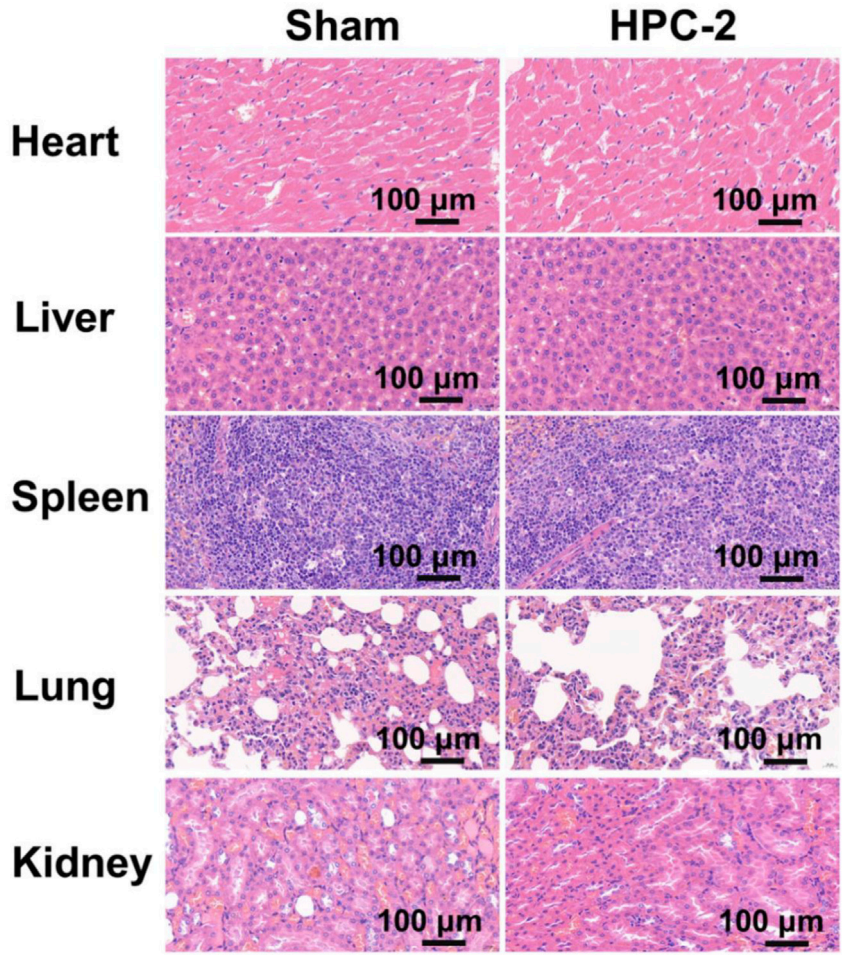


**FIGURE 6 |** Images of haematoxylin-eosin staining of the important organs of rats treated with HPC-2 hydrogel for 14 days.

the flexibility of the hydrogel was also well recovered. The insets in **Figure 3D** vividly show the self-healing performance of the HPC hydrogel. The two separated pieces of HPC-2 hydrogel could gradually rebuild to a single united piece within 10 min at room temperature, and the reformed HPC-2 hydrogel was easily stretched to a very large strain. The results indicate that the HPC hydrogel showed a good self-healing ability. The self-healing ability of HPC-2 hydrogel was further evaluated by alternate strains sweep of rheometer (**Supplementary Figure S5**). When a large strain (300%) was applied to HPC-2, the G' dramatically decreased and was less than G". When the strain recovered to 10%, the HPC-2 hydrogel showed rapid recovery with little hysteresis and the self-healing behavior was repeatable during the cyclic test.

## Adhesion Property of HA/PVP Complex Hydrogels

Adhesion is essential for the clinical-grade employment of hydrogels. As an example, hydrogels with adhesive ability could tightly adhere to organs and tissues, which has obvious advantages in biomedical materials. As shown in **Figure 4A**, the HPC-2 hydrogel could act as a binder, bonding different materials, including plastomers, steel, rubber, paper and wood. PE and stainless steel sheets bonded with HPC-2 hydrogel could withstand a large load of 500 g (**Figure 4A**). The lap shear strengths to several typical substrates were tested in order to quantitatively evaluate the adhesion property of the HPC-2 hydrogels. Typical force-extension curves are shown in **Figure 4B** and indicate that the adhesion strength rapidly reaches a peak and then gradually declines in the subsequent tensile process. The adhesion strength of the HPC hydrogels to wood, steel, glass, plastomer and porcine skin varied from 27.3 to 44.3 KPa, with the best adhesion strength being to steel. The adhesive strengths of different HPC hydrogels to porcine skin were further tested to investigate how the crosslinking agents affected the adhesion property of the hydrogels (**Figure 4C**). When the concentration of HA increased from 6 to 8 wt%, there was an increase of adhesion strength of around 30%, from 21.4 to 28.3 KPa. As the HA content further increased, the adhesion strength of HPC-3 decreased to 16.3 KPa, indicating that the excess amount of HA hinders the adhesion properties

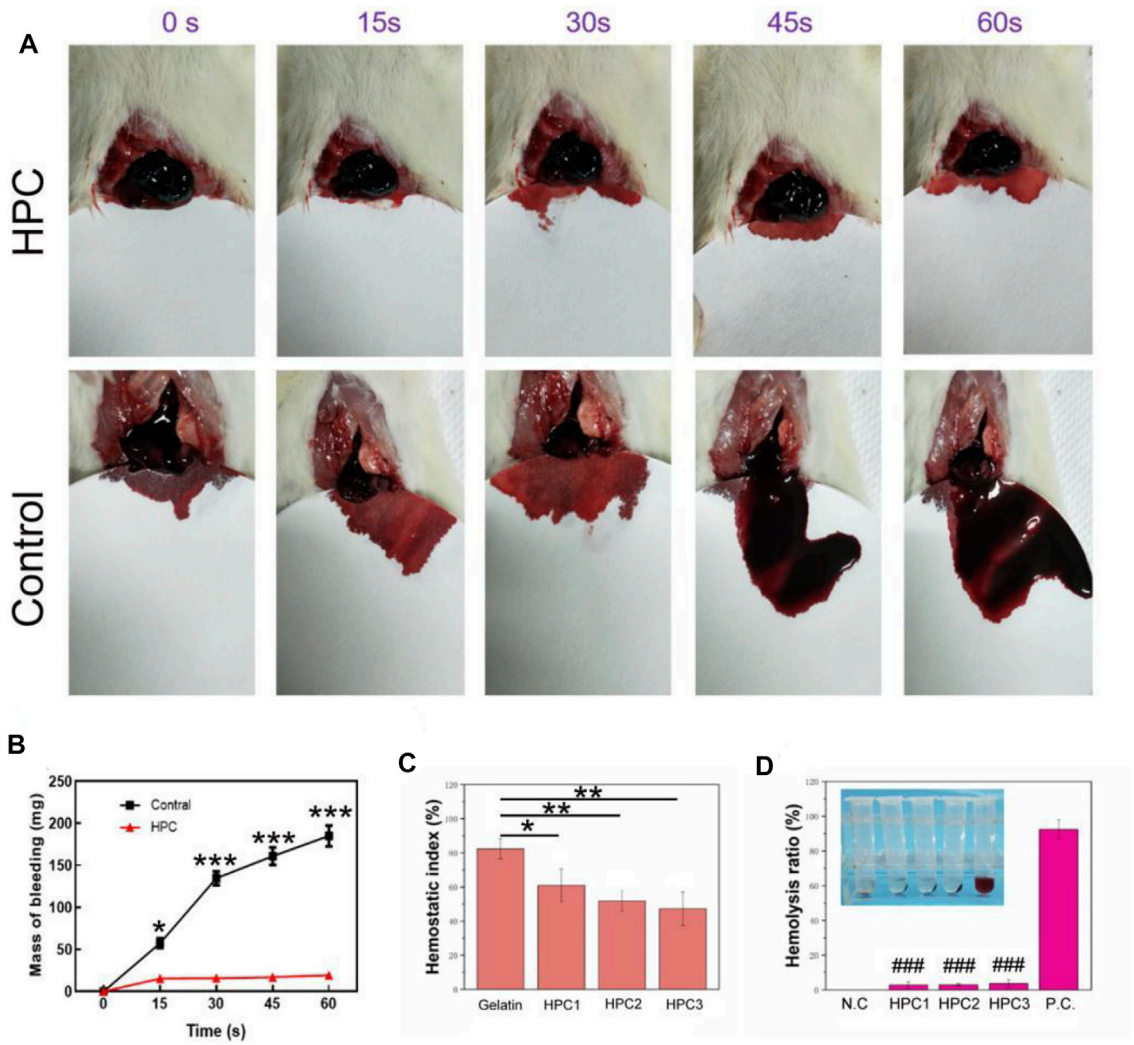


**FIGURE 7 |** Haemostatic performance of HPC hydrogels. **(A)** Haemostatic capability of the HPC-2 hydrogel. **(B)** Mass of bleeding with or without the treatment of HPC-2 hydrogel. **(C)** Haemostatic index of control and HPC samples. **(D)** Haemolysis ratio of HPC samples (**$p < 0.05$, **$p < 0.01$, ***$p < 0.001$ ; $^{\#\#\#}p < 0.001$vs P.C. group).

of the hydrogel. Thus, HPC-2 was chosen for subsequent experiments. The good skin adhesion property make the HPC hydrogels suitable for use as tissue engineering materials.

According to the above experimental results, the possible adhesion mechanism of the HPC hydrogels is shown in **Figure 4D**. Firstly, the components in the HPC hydrogels contain a variety of functional groups, such as carboxyl, hydroxyl and amide groups. The good adhesion property of the HPC hydrogels is derived from the hydrogen bond between the functional groups, which are the source of cohesion and interfacial interaction. The hydrogen bonds existing in the HPC hydrogels work as crosslinking domains to improve the cohesion strength, while the functional groups on the interface between the hydrogel and the substrate could form hydrogen bonds and increase the interfacial interaction (Feng et al., 2021). Secondly, the soft nature endows the HPC hydrogels with good adaption ability, making it easy to fill the irregular gaps on the surface, thus increasing the contact area and the binding capacity of the hydrogel to the substrate (Yang and Yuan 2019). However, an over-high crosslinking density might cause a reduction of both cohesion strength and adaption ability, which explains why the adhesion strength of HPC-3 decreased.

## Biocompatibility Evaluation

Biocompatibility is highly valued when hydrogels are used in biomedical areas. **Figure 5A** shows the Live/Died staining results, in which the green spots represent healthy cells, while the red spots represent apoptotic cells. In the images, a great number of green nuclei could be observed, while red nuclei were rarely observed, indicating that the HPC hydrogels showed very low cytotoxicity. To investigate the effect of HPC hydrogels on the attachment of cells, L929 cells were observed on HPC hydrogels using a confocal microscope. As

shown in **Figure 5B**, L929 cells attached on the HPC hydrogel well, indicating that the HPC hydrogels had good cytocompatibility. We then characterized the cytocompatibility of the HPC hydrogels through flow cytometry (FCM) tests. **Figures 5C,D** show the results of the cells in the control groups (PBS solutions) and those cultured with HPC hydrogels, respectively. The apoptosis rates of the hydrogel-treated group were fair to the negative control, indicating that there were no additional side effects when the hydrogel samples were introduced. We further explored the biocompatibility of the hydrogels by implanting the HPC-2 hydrogel into rats and observed the HE staining results of heart, liver, spleen, lung and kidney tissues of the rats (**Figure 6**). Apoptosis and necrosis were barely observed in the images, and the HPC hydrogel showed good biocompatibility (Wang et al., 2022).

The outstanding adhesive performance and good biocompatibility of the HPC hydrogels make them a promising candidate as haemostatic materials. The rat liver bleeding model was chosen as the *in vivo* animal model to investigate the haemostatic ability of the HPC hydrogels (**Figure 7A**). When the rat liver blood, the HPC hydrogels interacted with the damaged liver tissues, allowing the hydrogels to adhere to the haemorrhaging sites of the liver. The hydrogel could also work as a protective layer to stop the bleeding. The liver bleeding mass of the control group was 57.3, 134.7, 161 and 185 mg at 15, 30, 45 and 60 s, while the average bleeding mass with the HPC hydrogel treatment was 15.3, 15.7, 17 and 19.3 mg at 15, 30, 45 and 60 s (**Figure 7B**), indicating that the bleeding mass of the hydrogel-treated group decreased significantly. No excess bleeding was found at the site of injury after 1 minute of hydrogel treatment. The HPC hydrogel showed better haemostatic efficacy compared with the polyethylene glycol (PEG)-based hydrogel (control). The good haemostatic ability might be attributed to the high conglutination effect between the HPC hydrogel and the liver tissue. The haemostatic ability of the HPC hydrogel could also be monitored using the haemostatic index; a lower haemostatic index normally means a higher haemostatic ability (**Figure 7C**). The three HPC samples illustrated better haemostatic ability than gelatin. All in all, comparing our results to previous work, the HPC hydrogel also possessed an excellent haemostatic index as a local haemostatic agent (Li S. et al., 2020; Beaman et al., 2021).

**Figure 7D** shows the results of the haemolysis ratio test, which is significant for biomaterials to be applied in haemostatic areas. A haemolysis rate <5% is generally deemed to be appropriate for application in clinical haemostatic material, while a higher haemolysis ratio (>5%) suggests that the biomaterial could lead to the fracture of red blood cells. The haemolysis ratio of HPC-1, -2 and -3 were 2.8, 3 and 3.7%, respectively, demonstrating that the HPC hydrogels are nonhaemolytic materials and suitable for *in vivo* use.

## CONCLUSION

In this work, a typical hydrogel with injectability, good flexibility, self-healing ability, adhesion property and biocompatibility was prepared. The HA molecules worked as a crosslinking agent to form hydrogen bonds with PVP and induced the solution to gelation. The whole synthetic process was direct and lasted less than 10 s. The mechanical properties of the HPC samples were regulated by changing the HA content. With a gradual increase in HA content, the HPC hydrogels showed improved mechanical properties at the beginning, and the maximum value of the fracture stress reached 18.9 KPa. Excess HA led to a brittle network and a decreased fracture stress due to the over-high crosslinking density. The dynamic and reversible crosslinking of the hydrogen bonds between HA and PVP also endowed the hydrogel with a self-healing ability and injectability. When encountering large deformation, the internal structure of the hydrogel was damaged and could rapidly recover to its original state. The HPC hydrogels also showed good adhesion, which was attributed to the abundant hydrogen bonding and adaptation to the interfaces, and good biocompatibility. Taking advantage of all the above characteristics, the HPC hydrogels were used as haemostatic agents to treat damaged tissue, where the quantity of bleeding obviously decreased, from 185 to 19.3 mg, when injured liver was treated with HPC-2 hydrogel, showing an efficient haemostatic effect. Overall, the HPC hydrogel would be a good alternative to the current haemostatic dressings and could be widely applied in the biomaterials field.

## DATA AVAILABILITY STATEMENT

The original contributions presented in the study are included in the article/**Supplementary Material**, further inquiries can be directed to the corresponding authors.

## ETHICS STATEMENT

The animal study was reviewed and approved by Ethics Committee of Xiangyang No. 1 People's Hospital affiliated to Hubei University of Medicine; Xiangyang No. 1 People's Hospital affiliated to Hubei University of Medicine.

## AUTHOR CONTRIBUTIONS

HY, QX, and PD designed the study. HY, GQ, and FC performed the experiments. HY, QX, HY, and PD drafted the manuscript and interpreted the data. BT, SZ, YL, and YC revised the manuscript. All authors contributed to the article and approved the submitted version.

## FUNDING

This work was supported by research grants from the National Natural Science Foundation of China (81901567); the Natural Science Foundation of Hubei Province (2021CFB126); the Natural Science Foundation of Hubei Provincial Department of Education (B2016135, Q20202,105, JYT2021006); the Scientific and Technological Project of Xiangyang City of Hubei Province

(2021YL29, 2021ZD12, 2021YL22); the Innovative Research Program of Xiangyang No.1 People's Hospital (XYY2021M02, XYY2021Q04, XYY2021Q05); the Faculty Development Grants of Xiangyang No.1 People's Hospital Affiliated to Hubei University of Medicine (XYY2021D02, XYY2021D04).

## SUPPLEMENTARY MATERIAL

The Supplementary Material for this article can be found online at: https://www.frontiersin.org/articles/10.3389/fbioe.2022.855013/full#supplementary-material

## REFERENCES

Beaman, H. T., Shepherd, E., Satalin, J., Blair, S., Ramcharran, H., Serinelli, S., et al. (2022). Hemostatic Shape Memory Polymer Foams with Improved Survival in a Lethal Traumatic Hemorrhage Model. *Acta Biomater.* 137, 112–123. doi:10.1016/j.actbio.2021.10.005

Cao, J., Li, J., Chen, Y., Zhang, L., and Zhou, J. (2018). Dual Physical Crosslinking Strategy to Construct Moldable Hydrogels with Ultrahigh Strength and Toughness. *Adv. Funct. Mater.* 28 (23), 1800739. doi:10.1002/adfm.201800739

Cao, J., Zhao, X., and Ye, L. (2020). Facile Method to Fabricate Superstrong and Tough Poly(vinyl Alcohol) Hydrogels with High Energy Dissipation. *Ind. Eng. Chem. Res.* 59 (22), 10705–10715. doi:10.1021/acs.iecr.0c01083

Chaudhuri, O., Gu, L., Klumpers, D., Darnell, M., Bencherif, S. A., Weaver, J. C., et al. (2016). Hydrogels with Tunable Stress Relaxation Regulate Stem Cell Fate and Activity. *Nat. Mater.* 15 (3), 326–334. doi:10.1038/nmat4489

Chen, L., Hu, W., Du, M., Song, Y., Wu, Z., and Zheng, Q. (2021). Bioinspired, Recyclable, Stretchable Hydrogel with Boundary Ultralubrication. *ACS Appl. Mater. Inter.* 13 (35), 42240–42249. doi:10.1021/acsami.1c12631

Chen, Y.-N., Peng, L., Liu, T., Wang, Y., Shi, S., and Wang, H. (2016). Poly(vinyl Alcohol)-Tannic Acid Hydrogels with Excellent Mechanical Properties and Shape Memory Behaviors. *ACS Appl. Mater. Inter.* 8 (40), 27199–27206. doi:10.1021/acsami.6b08374

Criado-Gonzalez, M., Iqbal, M. H., Carvalho, A., Schmutz, M., Jierry, L., Schaaf, P., et al. (2020). Surface Triggered Self-Assembly of Fmoc-Tripeptide as an Antibacterial Coating. *Front. Bioeng. Biotechnol.* 8, 938. doi:10.3389/fbioe.2020.00938

Dompé, M., Cedano-Serrano, F. J., Heckert, O., van den Heuvel, N., van der Gucht, J., Tran, Y., et al. (2019). Thermoresponsive Complex Coacervate-Based Underwater Adhesive. *Adv. Mater.* 31 (21), 1808179. doi:10.1002/adma.201808179

Dompé, M., Cedano-Serrano, F. J., Vahdati, M., Westerveld, L., Hourdet, D., Creton, C., et al. (2019). Underwater Adhesion of Multiresponsive Complex Coacervates. *Adv. Mater. Inter.* 7 (4), 1901785. doi:10.1002/admi.201901785

Feng, H., Zhang, J., Yang, W., Ma, Y., Wang, R., Ma, S., et al. (2021). Transparent Janus Hydrogel Wet Adhesive for Underwater Self-Cleaning. *ACS Appl. Mater. Inter.* 13 (42), 50505–50515. doi:10.1021/acsami.1c12696

Grindy, S. C., Learsch, R., Mozhdehi, D., Cheng, J., Barrett, D. G., Guan, Z., et al. (2015). Control of Hierarchical Polymer Mechanics with Bioinspired Metal-Coordination Dynamics. *Nat. Mater* 14 (12), 1210–1216. doi:10.1038/nmat4401

He, X., Liu, L., Han, H., Shi, W., Yang, W., and Lu, X. (2018). Bioinspired and Microgel-Tackified Adhesive Hydrogel with Rapid Self-Healing and High Stretchability. *Macromolecules* 52 (1), 72–80. doi:10.1021/acs.macromol.8b01678

Hou, M., Yang, R., Zhang, L., Zhang, L., Liu, G., Xu, Z., et al. (2018). Injectable and Natural Humic Acid/Agarose Hybrid Hydrogel for Localized Light-Driven Photothermal Ablation and Chemotherapy of Cancer. *ACS Biomater. Sci. Eng.* 4 (12), 4266–4277. doi:10.1021/acsbiomaterials.8b01147

Huang, W., Wang, Y., Huang, Z., Wang, X., Chen, L., Zhang, Y., et al. (2018). On-Demand Dissolvable Self-Healing Hydrogel Based on Carboxymethyl Chitosan and Cellulose Nanocrystal for Deep Partial Thickness Burn Wound Healing. *ACS Appl. Mater. Inter.* 10 (48), 41076–41088. doi:10.1021/acsami.8b14526

Karami, P., Wyss, C. S., Khoushabi, A., Schmocker, A., Broome, M., Moser, C., et al. (2018). Composite Double-Network Hydrogels to Improve Adhesion on Biological Surfaces. *ACS Appl. Mater. Inter.* 10 (45), 38692–38699. doi:10.1021/acsami.8b10735

Kim, J.-N., Lee, J., Lee, H., and Oh, I.-K. (2021). Stretchable and Self-Healable Catechol-Chitosan-Diatom Hydrogel for Triboelectric Generator and Self-Powered Tremor Sensor Targeting at Parkinson Disease. *Nano Energy* 82, 105705–112855. doi:10.1016/j.nanoen.2020.105705

Kim, J. W., Kim, S., Jeong, Y. R., Kim, J., Kim, D. S., Keum, K., et al. (2022). Self-Healing Strain-Responsive Electrochromic Display Based on a Multiple Crosslinked Network Hydrogel. *Chem. Eng. J.* 430, 132685–138947. doi:10.1016/j.cej.2021.132685

Li, D., Chen, J., Wang, X., Zhang, M., Li, C., and Zhou, J. (2020a). Recent Advances on Synthetic and Polysaccharide Adhesives for Biological Hemostatic Applications. *Front. Bioeng. Biotechnol.* 8, 926. doi:10.3389/fbioe.2020.00926

Li, M., Liang, Y., Liang, Y., Pan, G., and Guo, B. (2022). Injectable Stretchable Self-Healing Dual Dynamic Network Hydrogel as Adhesive Anti-Oxidant Wound Dressing for Photothermal Clearance of Bacteria and Promoting Wound Healing of MRSA Infected Motion Wounds. *Chem. Eng. J.* 427, 132039. doi:10.1016/j.cej.2021.132039

Li, S., Wang, L., Zheng, W., Yang, G., and Jiang, X. (2020b). Rapid Fabrication of Self-Healing, Conductive, and Injectable Gel as Dressings for Healing Wounds in Stretchable Parts of the Body. *Adv. Funct. Mater.* 30 (31), 2002370. doi:10.1002/adfm.202002370

Lin, S.-H., Papadakis, C. M., Kang, J.-J., Lin, J.-M., and Hsu, S.-h. (2021). Injectable Phenolic-Chitosan Self-Healing Hydrogel with Hierarchical Micelle Architectures and Fast Adhesiveness. *Chem. Mater.* 33 (11), 3945–3958. doi:10.1021/acs.chemmater.1c00028

Liu, W., Erol, O., and Gracias, D. H. (2020). 3D Printing of an *In Situ* Grown MOF Hydrogel with Tunable Mechanical Properties. *ACS Appl. Mater. Inter.* 12 (29), 33267–33275. doi:10.1021/acsami.0c08880

Liu, Y., and Hsu, S.-h. (2018). Synthesis and Biomedical Applications of Self-Healing Hydrogels. *Front. Chem.* 6, 449. doi:10.3389/fchem.2018.00449

Long, T., Li, Y., Fang, X., and Sun, J. (2018). Salt-Mediated Polyampholyte Hydrogels with High Mechanical Strength, Excellent Self-Healing Property, and Satisfactory Electrical Conductivity. *Adv. Funct. Mater.* 28 (44), 1804416. doi:10.1002/adfm.201804416

Peng, Q., Chen, J., Zeng, Z., Wang, T., Xiang, L., Peng, X., et al. (2020). Adhesive Coacervates Driven by Hydrogen-Bonding Interaction. *Small* 16 (43), 2004132. doi:10.1002/smll.202004132

Poupart, O., Conti, R., Schmocker, A., Pancaldi, L., Moser, C., Nuss, K. M., et al. (2020). Pulsatile Flow-Induced Fatigue-Resistant Photopolymerizable Hydrogels for the Treatment of Intracranial Aneurysms. *Front. Bioeng. Biotechnol.* 8, 619858. doi:10.3389/fbioe.2020.619858

Ratié, G., Chrastný, V., Guinoiseau, D., Marsac, R., Vaňková, Z., and Komárek, M. (2021). Cadmium Isotope Fractionation during Complexation with Humic Acid. *Environ. Sci. Technol.* 55 (11), 7430–7444. doi:10.1021/acs.est.1c00646

Tian, Y., Pang, L., Zhang, R., Xu, T., Wang, S., Yu, B., et al. (2020). Poly-tetrahydropyrimidine Antibacterial Hydrogel with Injectability and Self-Healing Ability for Curing the Purulent Subcutaneous Infection. *ACS Appl. Mater. Inter.* 12 (45), 50236–50247. doi:10.1021/acsami.0c13822

Venezia, V., Matta, S., Lehner, S., Vitiello, G., Costantini, A., Gaan, S., et al. (2021). Detailed Thermal, Fire, and Mechanical Study of Silicon-Modified Epoxy Resin Containing Humic Acid and Other Additives. *ACS Appl. Polym. Mater.* 3, 5969–5981. doi:10.1021/acsapm.1c01240

Wang, K., Dong, R., Tang, J., Li, H., Dang, J., Zhang, Z., et al. (2022). Exosomes Laden Self-Healing Injectable Hydrogel Enhances Diabetic Wound Healing via Regulating Macrophage Polarization to Accelerate Angiogenesis. *Chem. Eng. J.* 430, 132664. doi:10.1016/j.cej.2021.132664

Wang, Y. J., Zhang, X. N., Song, Y., Zhao, Y., Chen, L., Su, F., et al. (2019). Ultrastiff and Tough Supramolecular Hydrogels with a Dense and Robust Hydrogen Bond Network. *Chem. Mater.* 31 (4), 1430–1440. doi:10.1021/acs.chemmater.8b05262

Wei, C., Zhu, X., Peng, H., Chen, J., Zhang, F., and Zhao, Q. (2019). Facile Preparation of Lignin-Based Underwater Adhesives with Improved Performances. *ACS Sust. Chem. Eng.* 7 (4), 4508–4514. doi:10.1021/acssuschemeng.8b06731

Xing, Y., Qing, X., Xia, H., Hao, S., Zhu, H., He, Y., et al. (2021). Injectable Hydrogel Based on Modified Gelatin and Sodium Alginate for Soft-Tissue Adhesive. *Front. Chem.* 9, 744099. doi:10.3389/fchem.2021.744099

Yan, B., Ma, C., Gao, J., Yuan, Y., and Wang, N. (2020). An Ion-Crosslinked Supramolecular Hydrogel for Ultrahigh and Fast Uranium Recovery from Seawater. *Adv. Mater.* 32 (10), 1906615. doi:10.1002/adma.201906615

Yang, B., and Yuan, W. (2019). Highly Stretchable, Adhesive, and Mechanical Zwitterionic Nanocomposite Hydrogel Biomimetic Skin. *ACS Appl. Mater. Inter.* 11 (43), 40620–40628. doi:10.1021/acsami.9b14040

Yang, J., Bai, R., and Suo, Z. (2018). Topological Adhesion of Wet Materials. *Adv. Mater.* 30 (25), 1800671. doi:10.1002/adma.201800671

Zhang, H., Tang, N., Yu, X., Guo, Z., Liu, Z., Sun, X., et al. (2022). Natural Glycyrrhizic Acid-Tailored Hydrogel with *In-Situ* Gradient Reduction of AgNPs Layer as High-Performance, Multi-Functional, Sustainable Flexible Sensors. *Chem. Eng. J.* 430, 132779–138947. doi:10.1016/j.cej.2021.132779

Zhang, L., Liu, M., Zhang, Y., and Pei, R. (2020). Recent Progress of Highly Adhesive Hydrogels as Wound Dressings. *Biomacromolecules* 21 (10), 3966–3983. doi:10.1021/acs.biomac.0c01069

Zhang, X., Liu, W., Yang, D., and Qiu, X. (2019a). Biomimetic Supertough and Strong Biodegradable Polymeric Materials with Improved Thermal Properties and Excellent UV-Blocking Performance. *Adv. Funct. Mater.* 29 (4), 1806912. doi:10.1002/adfm.201806912

Zhang, Y., Gao, H., Wang, H., Xu, Z., Chen, X., Liu, B., et al. (2018). Radiopaque Highly Stiff and Tough Shape Memory Hydrogel Microcoils for Permanent Embolization of Arteries. *Adv. Funct. Mater.* 28 (9), 1705962. doi:10.1002/adfm.201705962

Zhang, Z.-X., Liow, S. S., Xue, K., Zhang, X., Li, Z., and Loh, X. J. (2019b). Autonomous Chitosan-Based Self-Healing Hydrogel Formed through Noncovalent Interactions. *ACS Appl. Polym. Mater.* 1 (7), 1769–1777. doi:10.1021/acsapm.9b00317

**Conflict of Interest:** The authors declare that the research was conducted in the absence of any commercial or financial relationships that could be construed as a potential conflict of interest.

**Publisher's Note:** All claims expressed in this article are solely those of the authors and do not necessarily represent those of their affiliated organizations, or those of the publisher, the editors, and the reviewers. Any product that may be evaluated in this article, or claim that may be made by its manufacturer, is not guaranteed or endorsed by the publisher.

# Advantages of publishing in Frontiers

**OPEN ACCESS**
Articles are free to read for greatest visibility and readership

**FAST PUBLICATION**
Around 90 days from submission to decision

**HIGH QUALITY PEER-REVIEW**
Rigorous, collaborative, and constructive peer-review

**TRANSPARENT PEER-REVIEW**
Editors and reviewers acknowledged by name on published articles

**Frontiers**
Avenue du Tribunal-Fédéral 34
1005 Lausanne | Switzerland

**Visit us:** www.frontiersin.org
**Contact us:** frontiersin.org/about/contact

**REPRODUCIBILITY OF RESEARCH**
Support open data and methods to enhance research reproducibility

**DIGITAL PUBLISHING**
Articles designed for optimal readership across devices

**FOLLOW US**
@frontiersin

**IMPACT METRICS**
Advanced article metrics track visibility across digital media

**EXTENSIVE PROMOTION**
Marketing and promotion of impactful research

**LOOP RESEARCH NETWORK**
Our network increases your article's readership